Physics of Atomic Nuclei, Vol. 66, No. 7, 2003, pp. 1211–1218. Translated from Yadernaya Fizika, Vol. 66, No. 7, 2003, pp. 1251–1258.

NUCLEI
Experiment

Independent Yields of Kr and Xe Isotopes in the Photofission of Heavy Nuclei

Yu. P. Gangrsky*, V. I. Zhemenik, N. Yu. Maslova, G. V. Mishinsky, Yu. E. Penionzhkevich, and O. Szöllös

Joint Institute for Nuclear Research, Dubna, Moscow oblast, 141980 Russia

Received July 15, 2002

Abstract—The yields of Kr ($A = 87$–93) and Xe ($A = 138$–143) primary fission fragments produced in ^{232}Th, ^{238}U, and ^{244}Pu photofission upon the scission of a target nucleus and neutron emission were measured in an experiment with bremsstrahlung from electrons accelerated to 25 MeV by a microtron, and the results of these measurements are presented. The experimental procedure used involved the transportation of fragments that escaped from the target by a gas flow through a capillary and the condensation of Kr and Xe inert gases in a cryostat at liquid-nitrogen temperature. The fragments of all other elements were retained with a filter at the capillary inlet. The isotopes of Kr and Xe were identified by the γ spectra of their daughter products. The mass-number distributions of the independent yields of Kr and Xe isotopes are obtained and compared with similar data on fission induced by thermal and fast neutrons; the shifts of the fragment charges with respect to the undistorted charge distribution are determined. Prospects for using photofission fragments in studying the structure of highly neutron-rich nuclei are discussed. © *2003 MAIK "Nauka/Interperiodica".*

INTRODUCTION

The distributions of product fragments with respect to their mass numbers A and charge numbers Z are among the main properties of the nuclear-fission process. The shape of these distributions is controlled by the dynamics of the fission process from the saddle to the scission point. This intricate process depends on a number of factors, including the relief of the energy surface, the configurations of nuclear shapes at the instant of scission, and the nuclear viscosity of collective motion. Therefore, measurements of the isotopic and isobaric distributions of fragments (that is, those in A at given Z and those in Z at given A, respectively) provide important data on the dynamics of the fission process. The distributions of fragments produced after fissile-nucleus scission and the emission of neutrons (primary fragments) are the most informative of them.

However, measurement of such distributions involves some difficulties. Each of the techniques used has its limitations and can be applied efficiently only to a certain range of fission fragments. Therefore, isotopic and isobaric distributions of primary fragments have received adequate study only for the fission of the Th, U, and Pu isotopes that is induced by low-energy neutrons and for the spontaneous fission of ^{252}Cf. Data on these distributions are compiled in [1, 2].

At the same time, a wider range of experimental data and new theoretical approaches to describing them are required for obtaining deeper insight into the dynamics of the fission process. Measurement of the isotopic and isobaric distributions of fragments originating from reactions induced by γ rays is one of the promising lines of investigation in this region of nuclear fission since such reactions possess some special features:

(1) The interaction of γ radiation with nuclei is purely electromagnetic, and its properties are well known; therefore, an adequate calculation of this interaction can be performed without resort to additional model concepts.

(2) In the energy range 10–16 MeV, the interaction of photons with nuclei is of resonance origin (this is the region of a giant dipole resonance); the energy of this resonance corresponds to the frequency of proton oscillations with respect to neutrons in a nucleus.

(3) The absence of the binding energy and of the Coulomb barrier allows one to obtain fissile nuclei of any (even extremely low) excitation energy immediately after photon absorption.

(4) Over a wide range of γ-ray energies, the angular-momentum transfer to the irradiated nucleus undergoes virtually no change—it is as low as $1\hbar$ in the dipole absorption of photons.

These features peculiar to reactions induced by γ rays allow one to obtain new information about the

*e-mail: gangr@cv.jinr.ru

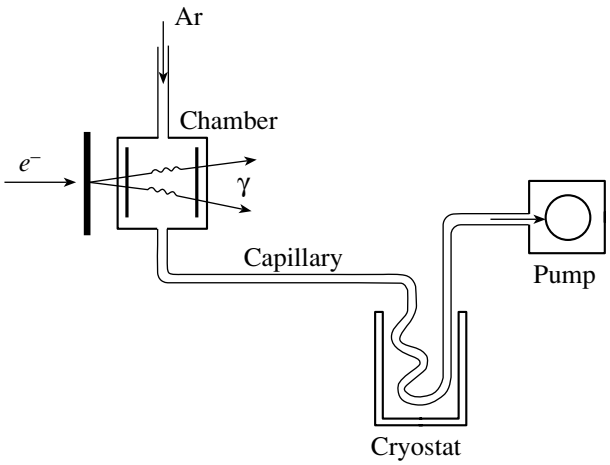

Fig. 1. Layout of the experimental setup.

nuclear-fission process. For example, experiments that studied the photofission of nuclei furnished a wide set of data on the structure of the fission barrier and the shape of the potential surface [3]. The above features of γ-ray interaction with nuclei are expected to manifest themselves in the process of fission-fragment formation as well. This can be illustrated by the results presented in [4], according to which the γ-ray-energy dependence of the yield of fragments (^{115}Cd, ^{117}Cd) from symmetric fission has a rather unusual character, with a maximum at 6 MeV and a kink at 5.3 MeV.

However, data on the isotopic and especially isobaric distributions of photofission fragments (first of all, on their independent yields) are considerably scarcer than data on reactions induced by neutrons and charged particles. We can mention only the results of the experiments performed in Ghent (Belgium) for a limited set of nuclei [5–8].

The objective of this study is to measure the independent yields of fragments (these are the isotopes of Kr and Xe inert gases) produced directly in ^{232}Th, ^{238}U, and ^{244}Pu fission induced by γ rays of energy corresponding to a giant dipole resonance and to compare these yields with similar data obtained in neutron-induced fission. The measurements of the cumulative yields of these isotopes in ^{238}U photofission are reported in [9]; preliminary results on the independent yields of Xe fragments in ^{232}Th and ^{238}U fission are given in [10].

Table 1. Properties of the targets used

Target	^{232}Th	^{238}U	^{244}Pu
Material	Metal	U_3O_8	PuO_2
Content (%)	100	99.85	96
Admixtures (%)	–	0.15 (^{235}U)	4 (^{240}Pu + ^{242}Pu)
Thickness (mg/cm^2)	25	3	0.3
Dimensions (mm)	∅15	∅20 and 30	10 × 10
Substrate	–	Al	Ti

EXPERIMENTAL PROCEDURE

The extraction of Kr and Xe isotopes from the bulk of photofission fragments is based on the use of their special chemical properties, which differ significantly from the properties of other elements and which reveal themselves in a number of phenomena, including the adsorption of their atoms on a filter and the walls of the capillary through which the fragments are transported from the irradiated target to radioactive-radiation detectors. The point is that Kr and Xe inert gases are efficiently adsorbed only at liquid-nitrogen temperature (−195.8°C), while all other fragments are adsorbed even at room temperature. It is precisely this property that is employed in our experimental setup, which comprises a reaction chamber, a cryostat, and Teflon capillaries for a gas flow. The layout of the setup is displayed in Fig. 1, and a more detailed description of it is given elsewhere [11].

The irradiated targets were placed in the reaction chamber, which had the shape of a cylinder 30 mm in height, its inner diameter being 40 mm. The cylinder walls had a thickness of 1.5 mm. The inlet and outlet holes for a buffer gas were located symmetrically opposite each other along a diameter of the reaction chamber. One or two targets placed at the end faces of the cylinder were used in the experiments. The properties of the targets are presented in Table 1 (these are the chemical composition, admixtures, dimensions, layer thickness, and the substrates).

An inert gas was supplied from a gas-container to the reaction chamber through a polyethylene capillary 4 mm in diameter. The gas pressure in the chamber was adjusted by a container valve and measured with a manometer at the chamber inlet. Chemically pure He, Ar, and N_2 at a pressure of 1 to 2 atm were used as buffer gases. The choice of inert gas and pressure in the chamber was determined by the conditions of the experiment (the efficiency of fragment collection, the rate of their transportation, the levels of the γ-radiation background caused by the activation of the inert gas owing to microtron bremsstrahlung).

The fission fragments were transported, together with the buffer gas, from the reaction chamber to the cryostat through a Teflon capillary of length 10 m and inner diameter 2 mm by means of evacuation with a pump. A fibrous filter placed at the capillary

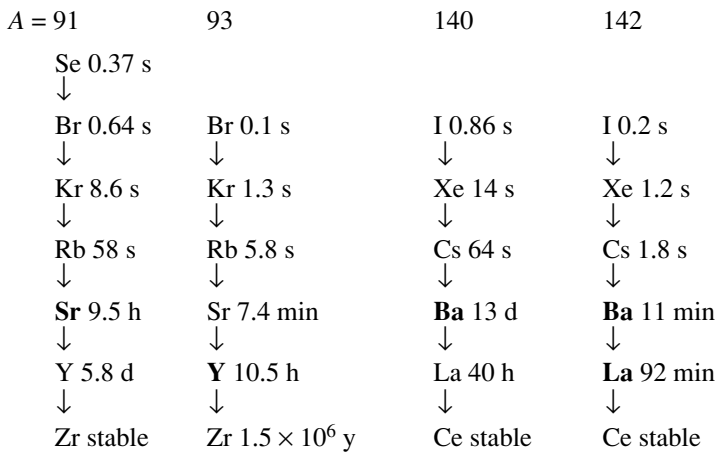

Fig. 2. Examples of the chains of β decays of the fission fragments that include Kr and Xe isotopes. The isotopes for which we measured γ spectra are given in boldface type.

inlet efficiently adsorbed all fission fragments, with the exception of Kr and Xe.

A spirally twisted copper tube placed in a Dewar vessel containing liquid nitrogen was used as a cryostat. The total length of the tube was 3 m, its inner diameter was 2 mm, and its walls had a thickness of 0.5 mm. This design of the cryostat enabled us to maintain the temperature at a level close to $-200°$C and, hence, to ensure the condensation of Kr and Xe (their temperatures of condensation are $-157°$C and $-112°$C, respectively). In this way, it was possible to separate Kr and Xe isotopes efficiently and quickly from the bulk of fission fragments, which remained on the filter and the capillary walls. A comparison of the spectra of γ radiation from fragments in the target, at the filter, and in the cryostat revealed that more than 90% of fragments not associated with the β decay chains involving Kr and Xe were retained by the filter and that more than 50% of Kr or Xe fragments were stopped in the cryostat.

The time it takes to transport Kr and Xe fragments from the reaction chamber to the cryostat was determined in dedicated tests that involved measuring the pressure drop in the chamber for the case where the valve was closed while the pump was operating. This time, which comprised the time of fragment diffusion to the outlet hole and the time of transportation through the capillary, ranged between 0.5 and 1.0 s, its specific value being dependent on the type of gas and its pressure [11]. It was the time period that determined the lower limit on the half-lives of the fragments under study (about 0.3 s). If the half-lives of the fragments that were the forerunners of Kr and Xe were greater than the time of their diffusion to the outlet chamber hole (0.1–0.2 s), they were also adsorbed on the filter, making no contribution to the yield of the Kr and Xe fragments transported to the cryostat. Therefore, only Kr and Xe fragments that were produced directly at the instant of the scission of a fissile nucleus reached the cryostat, and their yields can be considered to be independent. Fragments of other elements could appear in the cryostat only after the β decay of Kr and Xe isotopes, and their yields must also correspond to the independent yields of the inert gases. It was the yields of precisely these nuclides that were measured in the experiment, because they had longer half-lives and more easily observed γ lines. Short-lived fragments (forerunners of Kr and Xe) that decayed in the reaction chamber had low independent yields and did not distort the Kr and Xe yields. Figure 2 shows examples of β-decay chains involving the Kr and Xe isotopes; the nuclides that were used to determine the yields in question are given in boldface type. The properties of the radioactive decay of these nuclides (half-lives $T_{1/2}$, energies E_γ, intensities I_γ of measured γ lines) are listed in Table 2 [12]. The present approach to measuring independent yields enabled us to improve the accuracy of measurements and to observe fragments whose yields are as low as 10^{-3} of the number of fission events.

EXPERIMENTAL RESULTS

The experiments measuring the independent yields of Kr and Xe fragments were performed in a bremsstrahlung-photon beam from the MT-25 microtron of the Flerov Laboratory for Nuclear Reactions at the Joint Institute for Nuclear Research (JINR, Dubna). The description of this microtron and its basic properties were presented in [13]. The energy of accelerated electrons was 25 MeV (which determined the endpoint energy of the bremsstrahlung-photon spectrum); the beam current was 15 μA. A

Table 2. Properties of the radioactive decay of the nuclides explored in our experiments

Primary fragment	$T_{1/2}$	Daughter isotope	$T_{1/2}$	E_γ, keV	I_γ, %
^{89}Kr	3.2 min	^{89}Rb	15 min	1032	58
				1248	43
^{91}Kr	9 s	^{91}Sr	9.5 h	750	23.6
				1024	33.4
^{92}Kr	2 s	^{92}Sr	2.7 h	1384	90.1
		^{92}Y		934	13.9
^{93}Kr	1 s	^{93}Y	10.5 h	267	7.32
^{138}Xe	14 min	^{138}Cs	32 min	1436	76.3
				2218	15.2
^{139}Xe	40 s	^{139}Ba	83 min	166	23.6
^{140}Xe	14 s	^{140}Ba	12.8 d	537	24.4
		^{140}La	40 h	1596	95.4
^{141}Xe	1.8 s	^{141}Ba	18 min	190	46
		^{141}La	4 h	1355	1.64
^{142}Xe	1.2 s	^{142}La	93 min	641	47.4
				2398	13.3
^{143}Xe	0.8 s	^{143}Ce	33 h	293	42.8

water-cooled tungsten disk 4 mm thick was used as a converter. Behind the converter, there was a 20-mm-thick aluminum shield preventing electrons from entering the reaction chamber. The electron beam had the shape of an ellipse whose horizontal and vertical axes were 7 and 6 mm, respectively.

Typical periods of target irradiation were 30 min. After a time interval of 5 min, the copper spiral was removed from the Dewar vessel and brought to the γ-radiation spectrometer located in a room that was protected from microtron radiation; the β decay of Kr and Xe isotopes occurred within this period.

The areas of the γ lines associated with the nuclides of the daughter products of the β decay of the Kr and Xe isotopes were obtained from the γ-radiation spectra measured with this detector. These γ-line areas and the yields of the corresponding isotopes are related by the equation

$$Y(A) = \frac{S(1+\alpha)Nf(t)}{tI_\gamma \varepsilon_1 \varepsilon_2 \varepsilon_3 \eta}, \qquad (1)$$

where S is the γ-line area after background subtraction; t is the time of measurements; ε_1, ε_2, and ε_3 are the efficiencies of, respectively, the transportation of Kr and Xe fragments along the capillary, their adsorption in the cryostat, and the detection of their γ radiation; I_γ is the relative intensity of a γ line in the decay of the measured nuclide; α is the coefficient of the internal conversion of γ radiation; $f(t)$ is the time factor that takes into account the decay of Xe and Kr nuclei in the course of their transportation to the cryostat and the accumulation and decay of the measured nuclides; N is the number of decaying nuclei in the layer from which fission fragments escape; and η is the intensity of γ rays in the bremsstrahlung spectrum that induce the nuclear-fission process being considered. This method was used to measure, for the first time, the independent yields of four Kr isotopes ($A = 89$–93) and six Xe isotopes ($A = 138$–143) in ^{232}Th, ^{238}U, and ^{244}Pu photofission.

Since the Kr and Xe isotopes being studied were obtained within a single exposure and since the procedure of subsequent measurements was identical for all of them, the relative yields of these isotopes can be obtained from the measured γ-line areas by using the aforementioned parameters I_γ, α, ε_3, and $f(t)$ without recourse to the parameters ε_1 and ε_2, which are not known to a sufficient precision. The yields obtained by this method and normalized with respect to the ^{91}Kr and ^{139}Xe isotopes are given in Table 3.

Table 3. Independent yields of Kr and Xe fragments

Fragment	^{232}Th(γ, f)		^{238}U(γ, f)		^{244}Pu(γ, f)	
	Y_{rel}	Y_{fr}	Y_{rel}	Y_{fr}	Y_{rel}	Y_{fr}
^{89}Kr	0.15(2)	0.10(2)	0.29(1)	0.18(2)		
^{91}Kr	1.00	0.62(5)	1.00	0.60(5)		
^{92}Kr	0.95(1)	0.59(5)	0.80(2)	0.46(4)		
^{93}Kr	0.25(1)	0.15(2)	0.25(2)	0.15(2)		
^{137}Xe			0.27(3)	0.16(2)*		
^{138}Xe	0.85(1)	0.53(4)	0.65(3)	0.38(4)	0.84(4)	0.47(4)
^{139}Xe	1.00	0.63(5)	1.00	0.59(5)	1.00	0.56(5)
^{140}Xe	0.85(7)	0.53(5)	0.94(7)	0.56(5)	1.03(8)	0.57(5)
^{141}Xe	0.19(1)	0.12(1)	0.53(3)	0.31(3)	0.73(4)	0.41(4)
^{142}Xe	0.09(1)	0.06(1)	0.26(2)	0.16(2)	0.46(4)	0.26(3)
^{143}Xe			0.08(2)	0.05(1)	0.24(4)	0.14(2)

Note: The value labeled with an asterisk was borrowed from [6].

The absolute values of the independent yields of ^{91}Kr and ^{139}Xe isotopes can be deduced by employing the known data on their yields in the reactions induced by γ rays [6–8, 14] and by fission-spectrum and 14.7-MeV neutrons [2] (the isotopic distributions are similar for these reactions, and the yields are close in magnitude [15]). On the basis of an analysis of these data, the independent ^{91}Kr and ^{139}Xe yields divided by the sums of the yields of all $A = 91$ and 139 isobars (fractional yields), respectively, were assigned values that are given in Table 3, and these values were used to determine the fractional independent yields for the rest of the measured Kr and Xe isotopes with allowance for the variation in the total yields of fragments with a specific mass number and the emission of delayed neutrons from the fragments (these results are also presented in Table 3). The above yields divided by the total number of fission events are shown in Fig. 3 versus the mass number.

Owing to the fact that the bremsstrahlung spectrum is continuous, these yields are associated with a particular range of excitation energies. This range can be obtained from the experimentally measured excitation function for the reaction ^{238}U(γ, f) [16] (the excitation functions for the remaining fissile nuclei were assumed to be similar to that) and from the bremsstrahlung spectrum calculated for the specific conditions of the present experiment [17]. The mean excitation energy appears to be 12.5 MeV, and the half-width of the distribution is about 5 MeV.

DISCUSSION OF THE RESULTS

The curves in Fig. 3 have a typical shape characterized by a maximum at a specific value of A and a smooth decrease to the right and to the left of it. Such

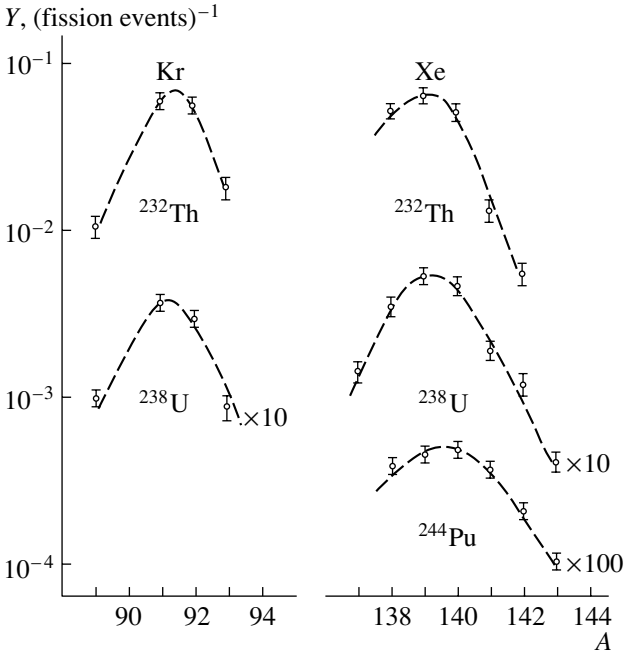

Fig. 3. Mass-number distributions of the independent yields of Kr and Xe isotopes in the photofission of ^{232}Th, ^{238}U, and ^{244}Pu nuclei. The circles represent experimental data, while the dashed curves correspond to their approximation by Gaussian curves.

Table 4. Parameters of the isotopic distribution of Kr and Xe fragments

Reaction	$\frac{N-Z}{N}$	Kr		Xe		References
		$\bar{A}$	σ	$\bar{A}$	σ	
^{232}Th(γ, f)	0.366	91.3(2)	1.1(1)	138.9(2)	1.2(1)	This study
^{238}U(γ, f)	0.370	91.1(2)	1.3(1)	139.4(2)	1.5(1)	This study
				138.9(3)		[5]
^{244}Pu(γ, f)	0.373			139.7(2)	1.8(2)	This study
^{235}U(γ, f)	0.357	89.4(3)	1.3(1)	137.4(4)	1.4(1)	[5]
^{233}U(n, f)	0.352	89.3(1)	1.5(1)	137.8(1)	1.5(1)	[1]
^{235}U(n, f)	0.364	90.1(1)	1.5(1)	138.4(1)	1.6(1)	[1]
^{238}U(n, f)	0.379	91.5(1)	1.6(1)	139.5(1)	1.8(2)	[1]

Table 5. Shifts of charges of Kr and Xe fragments with respect to the undistorted charge distribution

Reaction	Z_0/A_0	Z		$\bar{A}$		ν		ΔZ	
		Kr	Xe	Kr	Xe	Kr	Xe	Kr	Xe
^{232}Th(γ, f)	0.388	36	54	91.3(2)	138.9(2)	1.0	0.8	−0.19(8)	+0.20(8)
^{238}U(γ, f)	0.387	36	54	91.1(2)	139.4(2)	1.0	0.8	−0.36(9)	+0.25(8)
^{244}Pu(γ, f)	0.385		54		139.7(2)		0.8		+0.13(6)

curves can be described by a Gaussian distribution,

$$Y(A) = K \exp\left[-\frac{(A-\bar{A})^2}{2\sigma^2}\right], \qquad (2)$$

where K is the normalization factor, $\bar{A}$ is the mean mass number, and σ is the standard deviation.

The experimental values of the yields were approximated by such distributions, which are shown in Fig. 3, the fitted values of their parameters being given in Table 4 (the $\bar{A}$ value for ^{238}U is in agreement with that obtained in [7]). The corresponding parameters for ^{235}U and ^{233}U fission induced by thermal neutrons and for ^{238}U fission induced by 14.7-MeV neutrons [2] are also presented for the sake of comparison. A comparison of these parameters leads to the following conclusions:

(i) The mean mass number for Kr and Xe fragments exhibits a slow growth with increasing Z and A of the fissile nucleus and is close to the $\bar{A}$ value in ^{238}U fission induced by 14.7-MeV neutrons, but it is noticeably greater than that in ^{235}U and ^{233}U fission induced by thermal neutrons. This suggests the growth of $\bar{A}$ with increasing neutron excess in the fissile nucleus [this excess can be characterized by the ratio $(N-Z)/N$, whose values are quoted in Table 4].

(ii) The standard deviation of the distribution shows a sizable growth with increasing charge number of the fissile nucleus (by way of example, we indicate that, in going over from ^{232}Th to ^{244}Pu, it increases by a factor of 1.5). This implies a considerable distinction between the yields of the most neutron-rich fragments. For example, the yield of ^{143}Xe in ^{244}Pu photofission is an order of magnitude higher than that for ^{232}Th, and this difference grows fast with increasing number of neutrons in the fragment.

(iii) Deviation of the experimental values of the yields from the Gaussian distribution, as well as their odd–even differences, is small and does not go beyond the uncertainties of the measurement.

In ^{232}Th photofission, the Kr and Xe fragments are conjugate—that is, they are produced in a single fission event. In comparing the sum of their mean mass numbers [$\bar{A}$(Xe) = 138.9, $\bar{A}$(Kr) = 91.3] with the mass number of the fissile nucleus ($\bar{A} = 232$), one can assess the number of neutrons emitted from these fragments. It appears to be $\nu = 1.8(2)$. If it is considered that the fractional yields of ^{91}Kr and ^{139}Xe are, respectively, 0.62(5) and 0.63(5) (see Table 3), this value is in satisfactory agreement with the known values of the number of fission neutrons from the fragments with a specific mass number and their depen-

dence on the excitation energy [15, 18]. It follows from these data that the ratio of the numbers of neutrons from a light and the complementary heavy fragment is 1.3 in the fragment-mass-number range under study and that it varies only slightly in the excitation-energy range being considered. This corresponds to the value of $\nu = 1.0$ for Kr isotopes and to the value of $\nu = 0.8$ for Xe isotopes.

By using the above values of ν, we can assess the shift of the fragment charge with respect to the undistorted charge distribution, which corresponds to the ratio Z_0/A_0 of the charge number of the fissile nucleus to its mass number. The expression for the charge shift in the fragment of charge number Z has the form

$$\Delta Z = \frac{Z_0}{A_0}\left(\bar{A} + \nu\right) - Z. \qquad (3)$$

The ΔZ values obtained by this method for the mean mass numbers of Kr and Xe fragments in ^{232}Th, ^{238}U, and ^{244}Pu photofission are presented in Table 5. They appear to be close to the corresponding ΔZ values in the neutron-induced fission of heavy nuclei [1, 19].

A wide variety of models have been used to describe the isotopic and isobaric distributions of fission fragments. In recent years, the diffusion model [20, 21] has become widely accepted. Within this model, the breakup of a fissile nucleus is a quasiequilibrium process with respect to the charge mode, so that the statistical approach can be used to describe the charge distribution. In this case, the collective motion of nucleons, which manifests itself as dipole isovector vibrations, will be the main mechanism of formation of the isobaric charge distribution of fragments. However, the single-particle motion of nucleons can also make a nonvanishing contribution. The characteristic time of both kinds of motion (about 10^{-22} s) is much shorter than the time it takes for the nucleus to descend from the saddle to the scission point (about 3×10^{-20} s). The criterion of potential-energy minimum is used to determine the fragment charge. The deformation dependence of the potential energy was calculated on the basis of the liquid-drop model with allowance for shell corrections. For the fission of nuclei in the Th–Pu region, the calculations of the isobaric charge distributions within this model showed that the shift of the charge with respect to the undistorted charge distribution is 0.2–0.4 [22]. These values of ΔZ are consistent with the experimental data obtained in our study of photofission, as well as with those from other studies of the fission process induced by various particles.

The results of our experiments reveal that the isotopic distributions of fragments originating from the photofission of heavy nuclei are similar to the corresponding distributions obtained in neutron-induced fission. It is obvious that photon-absorption-induced dipole vibrations of the electric charge of nuclei are damped completely by the instant of fragment formation. Probably, some other of the aforementioned features of γ-radiation interaction with nuclei can affect fragment formation at lower excitation energies (in the vicinity of the fission barrier or below it).

The results of this study give sufficient grounds to conclude that photofission of nuclei is an efficient means for obtaining the most neutron-rich nuclides. A high yield of such nuclides is caused by a low excitation energy of nascent fission fragments (and, consequently, by a small number of neutrons emitted from them), by a high penetration capacity of bremsstrahlung radiation (this makes it possible to employ large amounts of fissile substance), and by a rather large standard deviation of the isotopic distribution of fission fragments. Therefore, photofission provides a promising method both for exploring the nuclear structure of fission fragments and for obtaining intense beams of accelerated neutron-rich radioactive nuclei by using these fragments. Investigation of reactions induced by such nuclei is of great interest since they permit obtaining radically new information about the properties of nuclei, which is inaccessible with other methods. A large number of projects devoted to the acceleration of fission fragments have been developed in recent years or are being executed at present. These include DRIBs project, which is being carried out at the Laboratory for Nuclear Reactions at JINR. In DRIBs, fission fragments are obtained by irradiating a thick uranium target with bremsstrahlung from the microtron and are accelerated at the 4-m isochronous cyclotron [23].

ACKNOWLEDGMENTS

We are grateful to Yu.Ts. Oganessian, M.G. Itkis, and S.N. Dmitriev for support of our studies; to Ya. Kliman and V.V. Pashkevich for stimulating discussions; and to A.G. Belov and G.V. Buklanov for assistance in performing the experiments.

This work was supported by the Russian Foundation for Basic Research (project nos. 01-02-97038, 01-02-16455) and INTAS (grant no. 2000-00463).

REFERENCES

1. A. C. Wahl, At. Data Nucl. Data Tables **39**, 1 (1988).
2. T. R. England and B. E. Rides, Preprint La-Ur-94-3106, LANL (Los Alamos, 1994).
3. Yu. M. Tsipenyuk, Yu. B. Ostapenko, G. N. Smirenkin, and A. S. Soldatov, Usp. Fiz. Nauk **144**, 3 (1984) [Sov. Phys. Usp. **27**, 649 (1984)].
4. B. V. Kurchatov, V. I. Novgorodotseva, V. A. Pchelin, *et al.*, Yad. Fiz. **7**, 521 (1968) [Sov. J. Nucl. Phys. **7**, 326 (1968)].

5. E. Jacobs, H. Thierens, D. De Frenne, *et al.*, Phys. Rev. C **19**, 422 (1979).
6. D. De Frenne, H. Thierens, B. Proot, *et al.*, Phys. Rev. C **26**, 1356 (1982).
7. D. De Frenne, H. Thierens, B. Proot, *et al.*, Phys. Rev. C **29**, 1908 (1984).
8. H. Thierens, A. De Clercq, E. Jacobs, *et al.*, Phys. Rev. C **29**, 498 (1984).
9. F. Ibrahim, J. Obert, O. Bajeat, *et al.*, Eur. Phys. J. A **15**, 357 (2002).
10. Yu. P. Gangrskiĭ, S. N. Dmitriev, V. I. Zhemenik, *et al.*, Fiz. Élem. Chastits At. Yadra **6**, 5 (2000).
11. Yu. P. Gangrskiĭ, V. P. Domanov, V. I. Zhemenik, *et al.*, Prib. Tekh. Éksp. **3**, 67 (2002).
12. E. Broune and R. B. Firestone, *Table of Radioactive Isotopes* (Wiley, New York, 1986).
13. A. G. Belov, Preprint No. D-15-93-80 (Joint Inst. for Nucl. Res., Dubna, 1993).
14. J. C. Hogan and A. E. Richardson, Phys. Rev. C **16**, 2296 (1977).
15. Yu. P. Gangrskiĭ, B. Dalkhsuren, and B. N. Markov, *Nuclear-Fission Fragments* (Énergoatomizdat, Moscow, 1986).
16. J. T. Cadwell, E. J. Dowly, B. L. Berman, *et al.*, Phys. Rev. C **21**, 1215 (1980).
17. Ph. Kondev, A. Tonchev, Kh. Khristov, and V. E. Zhuchko, Nucl. Instrum. Methods Phys. Res. B **71**, 126 (1992).
18. J. Terrell, Phys. Rev. **127**, 880 (1962).
19. A. C. Wahl, R. L. Fergusson, D. R. Nethaway, *et al.*, Phys. Rev. **126**, 1112 (1962).
20. G. D. Adeev, I. I. Gonchar, V. V. Pashkevich, *et al.*, Fiz. Élem. Chastits At. Yadra **19**, 1229 (1988) [Sov. J. Part. Nucl. **19**, 529 (1988)].
21. G. D. Adeev, Fiz. Élem. Chastits At. Yadra **23**, 1572 (1992) [Sov. J. Part. Nucl. **23**, 684 (1992)].
22. G. D. Adeev and T. Dossing, Phys. Lett. B **66B**, 11 (1977).
23. Yu. Oganessian, *Dubna Radioactive Ion Beams, Project,* Int. Report FLNR, Joint Inst. for Nucl. Res. (Dubna, 1998).

Translated by E. Kozlovskii

Physics of Atomic Nuclei, Vol. 66, No. 7, 2003, pp. 1219–1228. Translated from Yadernaya Fizika, Vol. 66, No. 7, 2003, pp. 1259–1268.

NUCLEI
Theory

Angular Distributions, Relative Orbital Angular Momenta, and Spins of Fragments Originating from the Binary Fission of Polarized Nuclei

S. G. Kadmensky and L. V. Rodionova

Voronezh State University, Universitetskaya pl. 1, Voronezh, 394693 Russia

Received June 17, 2002; in final form, November 5, 2002

Abstract—The angular distributions of fragments originating from the binary fission of odd and odd–odd nuclei capable of undergoing spontaneous fission that are polarized by a strong magnetic field at ultralow temperatures and from the low-energy photofission of even–even nuclei that is induced by dipole and quadrupole photons are investigated. It is shown that the deviations of these angular distributions from those that are obtained on the basis of the A. Bohr formula make it possible to estimate the maximum relative orbital angular momentum of fission fragments, this estimate providing important information about the relative orientation of the fragment spins. The angular distributions of fragments originating from subthreshold fission are analyzed for the case of the ^{238}U nucleus. A comparison of the resulting angular distributions with their experimental counterparts leads to the conclusion that the maximum relative orbital angular momentum of binary-fission fragments exceeds 20, the fragment spins having predominantly a parallel orientation. The possibility is considered for performing an experiment aimed at measuring the angular distributions of fragments of the spontaneous fission of polarized nuclei in order to determine both the spins of such nuclei and the maximum values of the relative orbital angular momenta of fission fragments. © *2003 MAIK "Nauka/Interperiodica"*.

1. INTRODUCTION

The problem of determining the relative orbital angular momenta l and spins J_i ($i = 1, 2$) of fission fragments is one of the key problems in the physics of binary nuclear fission. The conservation of the total angular momentum J of a fissile nucleus in the fission process leads to the vector relation

$$\mathbf{J} = \mathbf{l} + \mathbf{F}; \quad \mathbf{F} = \mathbf{J}_1 + \mathbf{J}_2. \tag{1}$$

It was shown in [1] that, because of the validity of the adiabatic approximation in the asymptotic region of a fissile system, where primary fission fragments are already formed, their deformation parameters having nonequilibrium values in this region, rotational bands characterized by rather wide sets of values of the fragment spins J_1 and J_2 are excited in these fragments. In the course of a further evolution, primary fission fragments go over to excited states that have equilibrium values of the deformation parameters, but which retain the initial values of the spins J_1 and J_2. At the next stage, these states of the fragments undergo transitions, via the emission of, first, prompt neutrons and, then, prompt photons, to predominantly the ground states of final fragments that are recorded in experiments. Upon the emission of prompt neutrons, the spins of fission fragments change values, from J_i to J_i^0, J_i^0 being the initial values of the fragment spins for the stage within which the fragments in question emit prompt photons. Upon photon emission, the fragment spins assume values of J_{if} that correspond to the states of final fragments. We denote by J_{in} and $J_{i\gamma}$ the total spins of, respectively, prompt neutrons and prompt photons emitted from the ith fragment. From the spin-conservation law, it then follows that $\mathbf{J}_i = \mathbf{J}_{in} + \mathbf{J}_{i\gamma} + \mathbf{J}_{if}$. Experiments devoted to measuring the multipole orders and multiplicities of prompt photons emitted by fission fragments revealed [2] that the mean values $\bar{J}_{i\gamma}$ of the total spins $J_{i\gamma}$ carried away by photons can be estimated (in $\hbar$ units) at $\bar{J}_{i\gamma} \approx 6$–$8$.

In the case of predominantly antiparallel orientation of fragment spins, which follows from the mechanism proposed by Mikhailov and Quentin [3], who considered the orientation pumping of fragment spins, the mean value of the total spin of primary fragments, $\bar{F}$, is close to zero. Therefore, the mean value of the relative orbital angular momentum of fragments is $\bar{l} \approx J$, so that the values of $\bar{l}$ are small for typical values of the spin J of fissile nuclei undergoing spontaneous or low-energy induced fission (these values do not exceed a few units, being much less than the mean spins $\bar{J}_1$ and $\bar{J}_2$).

This conclusion is at odds with another important result that was obtained, within the quantum-mechanical theory of binary nuclear fission [1], from an analysis of the angular distributions of fragments

1063-7788/03/6607-1219$24.00

originating from the fission of polarized nuclei. These distributions depend on the solid angle $\Omega = (\theta, \varphi)$ determining, in the laboratory frame, the direction of the radius vector $\mathbf{R}$ of the relative motion of fission fragments, $\mathbf{R} = \mathbf{R}_1 - \mathbf{R}_2$, where $\mathbf{R}_1$ and $\mathbf{R}_2$ are the coordinates of the centers of mass of, respectively, the first and the second fragment. The A. Bohr formula (see [4]) was successfully used in describing these angular distributions for the binary fission of polarized nuclei [4] and in describing the coefficient of P-even and P-odd asymmetry in the angular distributions of fission fragments [5–8]. It was shown in [1] that, for this formula to be approximately valid, it is necessary that fission fragments have coherently coupled relative orbital angular momenta l lying in a rather wide range $0 \le l \le l_m$; that is, the maximum possible value l_m of the relative orbital angular momentum must be quite large. Therefore, the mean value $\bar{l}$ is also large; if $\bar{l}$ is much greater than the spin J of a fissile nucleus, formula (1) then leads to the relation $\bar{l} \approx \bar{F} = \overline{|\mathbf{J}_1 + \mathbf{J}_2|} > \bar{J}_1, \bar{J}_2$, whence it follows that the spins $\bar{J}_1$ and $\bar{J}_2$ are predominantly parallel to each other, but this contradicts the results presented in [3].

The upper limit l_m^0 on l_m can be deduced from the law of conservation of the fissile-nucleus spin [see Eq. (1)]: $l_m^0 = J_{1m} + J_{2m} + J$. In order to assess the maximum values J_{im} of the fragment spins, we will make make use of the relation $J_{im} = (J_{in})_m + (J_{i\gamma})_m + (J_{if})_m$, which follows from the law of conservation of the fragment spin. If we assume that the values of the maximum possible spin carried away by photons $[(J_{i\gamma})_m]$ differ by a few units from the mean value $\bar{J}_{i\gamma}$ obtained in [2] for this spin, consider that the maximum value of the total spin carried away by neutrons $[(J_{in})_m]$ is about a few units, and use values of about a few units for the fissile-nucleus spin J and for the maximum spins $(J_{if})_m$ of final fission fragments, we can derive an estimate of the upper limit l_m^0 on l_m: $l_m^0 \approx 25$. It follows that the possible values of the relative orbital angular momenta l of fission fragments are constrained by the condition $l \le l_m < 25$.

With the aid of the methods proposed in [9, 10], a quantum-mechanical theory of the nuclear-fission process was developed in [1] by introducing the concepts of fission phases and the amplitudes of partial-wave fission widths and by relying on the adiabatic approximation in describing the asymptotic region of a fissile system, the idea of A. Bohr [4] that transition fission states formed at the saddle point of the deformation potential of a fissile nucleus play a crucial role in the fission process being taken into account in that theory. Concurrently, the concept of angular distributions of fission fragments in the internal coordinate frame of a fissile nucleus was also introduced in [1].

The objective of the present study is to analyze, within the approaches proposed in [1], the angular distributions of fragments originating from the low-energy photofission of even–even nuclei into two fragments that is induced by dipole and quadrupole photons (the angular distributions for this case have already been investigated experimentally) and the angular distributions for the as-yet-unexplored case of the binary fission of $J > 1/2$ odd and odd–odd nuclei capable of undergoing spontaneous fission that are polarized by a strong magnetic field at ultralow temperatures, these analyses being aimed at deducing information about the values of the relative orbital angular momenta and spins of fission fragments.

2. ANGULAR DISTRIBUTIONS OF FRAGMENTS ORIGINATING FROM THE BINARY FISSION OF POLARIZED NUCLEI

Since the nuclear-fission process induced by specific particle species $(n, \alpha, \gamma, ...)$ proceeds through the formation of a compound nucleus [4] having a spin J and a spin projection M onto the z axis in the laboratory frame (this axis is chosen to be aligned with the incident-beam axis), the differential cross section for the emission of fragments from the binary fission of nuclei can be represented in the form

$$\sigma_f(\theta) \equiv \frac{d\sigma_f(\Omega)}{d\Omega} = \sum_J \sum_{M=-J}^{J} \sigma(JM) \sum_{K=0}^{J} \frac{\Gamma_f(JK)}{\Gamma(J)} T_{MK}^J(\theta), \quad (2)$$

where $\sigma(JM)$ is the cross section for the formation of a compound nucleus, $\Gamma_f(JK)$ is the partial-wave decay width of this nucleus with respect to the channel characterized by a specific value of the projection K of the spin J of the axisymmetric compound nucleus onto the z' axis of the internal coordinate frame, and $\Gamma(J)$ is the total decay width of the compound nucleus.

In the K channel, the angular distribution $T_{MK}^J(\theta)$ of fission fragments that is normalized to unity is usually calculated on the basis of the A. Bohr formula [4]; that is,

$$T_{MK}^J(\theta) = \frac{2J+1}{8\pi} \times \left[\left| D_{MK}^J(\omega) \right|^2 + \left| D_{M,-K}^J(\omega) \right|^2 \right]_{\beta=\theta}, \quad (3)$$

where $D^J_{MK}(\omega)$ is a generalized spherical harmonic that depends on the Euler angles $\alpha, \beta, \gamma \equiv \omega$ characterizing the orientation of the axes of the internal coordinate frame with respect to the axes of the laboratory frame. In applying this formula, it is considered that $\left|D^J_{MK}(\omega)\right|^2$ is independent of the angles α and γ. Formula (3) is based on the qualitative physical assumption [4] according to which fission fragments are emitted only along or against the direction of the symmetry axis (z' axis) of the fissile nucleus being considered. This means that, in the internal coordinate frame, the angular distribution of fission fragments has a delta-function-like character of the form $\delta(\xi' \mp 1)$, where $\xi' = \cos\theta'$, θ' being the angle between the vector $\mathbf{R}$ and the symmetry axis (z' axis) of the fissile nucleus. Taking into account the azimuthal symmetry of the angular distribution of fission fragments, going over from the argument θ' to the argument ξ' in the spherical harmonic $Y_{l0}(\theta')$, redenoting the resulting function by the symbol $Y_{l0}(\xi')$ as before, and using the completeness of the set of functions $\sqrt{2\pi}Y_{l0}(\xi')$ in the space of ξ' ($-1 \le \xi' \le 1$), we can recast the aforementioned delta functions into the form

$$\delta(\xi' \mp 1) = \sum_{l=0}^{l_m} 2\pi Y_{l0}(\xi')Y_{l0}(\pm 1) \qquad (4)$$
$$= \sum_{l=0}^{l_m} \sqrt{(2l+1)}\pi Y_{l0}(\xi')P_l(\pm 1),$$

where $P_l(\xi')$ is a Legendre polynomial [$P_l(+1) = 1$, $P_l(-1) = (-1)^l$] and the quantity l_m is considered in the limit $l_m \to \infty$. Formula (4) reflects the quantum-mechanical uncertainty relation between the operator of the square of the orbital angular momentum of a particle, $\mathbf{l}^2$, and the square of the angle θ', which characterizes the direction of the radius vector $\mathbf{R}$ of this particle. From this relation, it follows that the angle θ' can be specified exactly only if the orbital angular momentum l of the particle is absolutely uncertain ($0 \le l \le \infty$).

Since only finite values of the spins J_1 and J_2 and of the relative orbital angular momentum l of fission fragments may appear in the nuclear-fission process, formula (3) is only approximate. At the same time, an analysis of the angular distributions of fragments originating from the fission of polarized nuclei [4] and an analysis of the coefficients of P-even and P-odd asymmetries in the angular distributions of fission fragments [5–8] on the basis of expression (3) reveal that this expression reflects actual properties of the nuclear-fission process. This means that angular distributions of fission fragments do not vanish only at values of the angle θ' that are close to 0 and π. Such a situation can be simulated mathematically [1] by describing the distribution of θ' by a formula of the type in (4) under the condition that the quantity l_m in it takes finite, albeit rather large, values. In that case, nonzero values of the angle θ' lie within cones whose axes correspond to the values of $\theta' = 0$ and $\theta' = \pi$ and whose opening angle at a cone apex is $\Delta\theta' \approx 1/l_m$.

The investigation performed in [1] by using the adiabatic approximation in the asymptotic region of a fissile system showed that the generalization of the A. Bohr formula (3) to this case can be represented as

$$\bar{T}^J_{MK}(\theta) = \frac{2J+1}{16\pi^2} \qquad (5)$$
$$\times \int d\omega \left[\left|D^J_{MK}(\omega)\right|^2 + \left|D^J_{M,-K}(\omega)\right|^2\right] F^2_{l_m}(\theta'),$$

where the function $F^2_{l_m}(\theta')$ is a smeared delta function of the form in (4) with an amplitude; that is,

$$F_{l_m}(\theta') \qquad (6)$$
$$= b(l_m)\left\{\sum_{l=0}^{l_m} Y_{l0}(\xi')Y_{l0}(1)\left[1 + \pi\pi_1\pi_2(-1)^l\right]\right\}.$$

In expression (6), the factor $[1 + \pi\pi_1\pi_2(-1)^l]$, where π, π_1, and π_2 are the parities of, respectively, the parent nucleus, the first fission fragment, and the second fission fragment, takes into account the parity-conservation law, while the quantity $b(l_m)$ is determined from the condition requiring that the angular distribution in (5) be normalized to unity. As a result, we obtain

$$b(l_m) = \left\{\sum_{l=0}^{l_m} \frac{(2l+1)}{4\pi}\left[1 + \pi\pi_1\pi_2(-1)^l\right]^2\right\}^{-1/2}. \qquad (7)$$

Formula (5) reduces to formula (3) for $l_m \to \infty$. But at finite and rather small values of l_m, the angular distribution of fission fragments in (5) differs significantly from the angular distribution of fission fragments in (3).

With an eye to applying the above formulas to a more general case, we will analyze the angular distributions of fission fragments in (3) and (5) at arbitrary values of J, M, and K. By employing the definition of a complex-conjugate generalized spherical harmonic [4],

$$D^{J*}_{MK}(\omega) = (-1)^{M-K} D^J_{-M,-K}(\omega), \qquad (8)$$

and the multiplication theorem for D functions,

$$D^{J_1}_{M_1K_1}(\omega) D^{J_2}_{M_2K_2}(\omega) \qquad (9)$$
$$= \sum_{J=|J_1-J_2|}^{J=J_1+J_2} C^{JM_1+M_2}_{J_1J_2M_1M_2} C^{JK_1+K_2}_{J_1J_2K_1K_2} D^J_{M_1+M_2,K_1+K_2}(\omega),$$

we can recast the A. Bohr formula (3) for the angular distribution of fission fragments into the form

$$T^J_{MK}(\theta) = \sum_L B^0_{JMKL} P_L(\xi), \qquad (10)$$

where

$$B^0_{JMKL} = \left(1 + (-1)^L\right) \qquad (11)$$
$$\times \frac{2J+1}{8\pi} C^{L0}_{JJM-M} C^{L0}_{JJK-K} (-1)^{M+K}$$

and L takes only even values in the range from 0 to $2J$. We note that, by virtue of the properties of Clebsch–Gordan coefficients, the quantity B^0_{JMKL} is equal to $1/4\pi$ at $L = 0$.

Let us now reduce the normalized (to unity) angular distribution of fission fragments in (5) to the form of an expansion in Legendre polynomials that is analogous to the expansion in (10). We introduce the notation

$$A^J_{M,\pm K}(\omega, \Omega') \equiv D^J_{M,\pm K}(\omega) F_{l_m}(\theta') \qquad (12)$$

and represent the angular distribution (5) as

$$\bar{T}^J_{MK}(\Omega) = \frac{2J+1}{16\pi^2} \qquad (13)$$
$$\times \int d\omega \left[\left|A^J_{M,K}(\omega, \Omega')\right|^2 + \left|A^J_{M,-K}(\omega, \Omega')\right|^2\right].$$

Making use of the Wigner transformation [4] for going over from the internal coordinate frame to the laboratory frame,

$$Y_{lk}(\Omega') = \sum_m D^{l*}_{mk}(\omega) Y_{lm}(\Omega), \qquad (14)$$

we can recast the function $F_{l_m}(\theta')$ (6) into the form

$$F_{l_m}(\theta') = b(l_m) \qquad (15)$$
$$\times \sum_{l=0}^{l_m} \sum_m D^{l*}_{m0}(\omega) Y_{lm}(\Omega) Y_{l0}(1) [1 + \pi\pi_1\pi_2(-1)^l].$$

Taking into account relation (15) and the representation of a complex-conjugate D function in the form (8), we can rewrite expression (12) as

$$A^J_{M,\pm K}(\omega, \Omega') = \tilde{A}^J_{M,\pm K}(\omega, \Omega) \qquad (16)$$
$$= b(l_m) \sum_{l=0}^{l_m} \sum_m \sum_{j=|J-l|}^{j=J+l} C^{jM-m}_{JlM-m} C^{j\pm K}_{Jl\pm K0}$$
$$\times D^j_{M-m,\pm K}(\omega) (-1)^m Y_{lm}(\Omega) Y_{l0}(1)$$
$$\times [1 + \pi\pi_1\pi_2(-1)^l].$$

Substituting expression (16) into (13) and performing integration with respect to the Euler angles with allowance for the orthogonality property of D functions [4], we obtain

$$\int d\omega |\tilde{A}^J_{M,\pm K}(\omega, \Omega)|^2 = |b(l_m)|^2 \qquad (17)$$
$$\times \sum_{l=0}^{l_m} \sum_{l'=0}^{l_m} \sum_{jm} C^{jM-m}_{Jl'M-m} C^{j\pm K}_{Jl'\pm K0} C^{jM-m}_{JlM-m}$$
$$\times C^{j\pm K}_{Jl\pm K0} \frac{8\pi^2}{2j+1} \sqrt{\frac{2l+1}{4\pi}} \sqrt{\frac{2l'+1}{4\pi}} Y^*_{l'm}(\Omega)$$
$$\times Y_{lm}(\Omega) [1 + \pi\pi_1\pi_2(-1)^l][1 + \pi\pi_1\pi_2(-1)^{l'}].$$

By using the multiplication theorem for spherical harmonics [4],

$$Y_{lm}(\Omega) Y^*_{l'm}(\Omega) = \frac{(-1)^m}{4\pi}$$
$$\times \sum_L \sqrt{(2l+1)(2l'+1)} C^{L0}_{ll'00} C^{L0}_{ll'm-m} P_L(\xi),$$

we can now recast expression (17) into the form

$$\int d\omega |\tilde{A}^J_{M,\pm K}(\omega, \Omega)|^2 = |b(l_m)|^2 \qquad (18)$$
$$\times \sum_{l=0}^{l_m} \sum_{l'=0}^{l_m} \sum_{jmL} C^{jM-m}_{Jl'M-m} C^{j\pm K}_{Jl'\pm K0} C^{jM-m}_{JlM-m} C^{j\pm K}_{Jl\pm K0}$$
$$\times C^{L0}_{ll'00} C^{L0}_{ll'm-m} P_L(\xi) \frac{(2l+1)(2l'+1)}{2(2j+1)}$$
$$\times [1 + \pi\pi_1\pi_2(-1)^l][1 + \pi\pi_1\pi_2(-1)^{l'}].$$

This formula can be significantly simplified by performing summation over the projection m of the relative orbital angular momentum l with the aid of the formula that makes it possible to evaluate sums of the products of Clebsch–Gordan coefficients [11],

$$\sum_{\alpha\beta\delta} C^{c\gamma}_{ab\alpha\beta} C^{e\varepsilon}_{db\delta\beta} C^{d\delta}_{af\alpha\varphi}$$
$$= (-1)^{b+c+d+f} \sqrt{(2c+1)(2d+1)}$$
$$\times C^{e\varepsilon}_{cf\gamma\varphi} \begin{Bmatrix} a & b & c \\ e & f & d \end{Bmatrix},$$

where $\begin{Bmatrix} a & b & c \\ e & f & d \end{Bmatrix}$ is a Wigner $6j$ coefficient, and the property of symmetry of Clebsch–Gordan coefficients under the permutation of angular momenta,

$$C^{JM}_{J_1J_2M_1M_2} = (-1)^{J_1-M_1} \sqrt{\frac{2J+1}{2J_2+1}} C^{J_2M_2}_{J_1JM_1-M}$$
$$= (-1)^{J_2+M_2} \sqrt{\frac{2J+1}{2J_1+1}} C^{J_1M_1}_{J_2J-M_2M}.$$

Table 1. Values of the coefficients α_{JK}, β_{JK}, and γ_{JK} for the A. Bohr angular distribution (10) and for the angular distribution (20) in the problem of the low-energy photofission of nuclei

l_m	α_{10}	α_{11}	α_{20}	α_{21}	α_{22}	β_{10}	β_{11}	β_{20}	β_{21}	β_{22}	γ_{20}	γ_{21}	γ_{22}
∞	0	0.75	0	1.25	0	0.75	−0.375	0	−0.625	0.625	0.9375	−0.625	0.15625
30	0.024	0.74	0.060	1.200	0.030	0.714	−0.357	−0.022	−0.580	0.592	0.854	−0.569	0.142
20	0.04	0.73	0.087	1.163	0.044	0.697	−0.349	−0.033	−0.560	0.576	0.815	−0.543	0.136
19	0.04	0.73	0.091	1.159	0.046	0.695	−0.348	−0.034	−0.557	0.574	0.809	−0.539	0.135
10	0.07	0.72	0.162	1.088	0.082	0.652	−0.326	−0.061	−0.503	0.533	0.709	−0.473	0.118
9	0.07	0.72	0.177	1.072	0.089	0.643	−0.322	−0.066	−0.492	0.525	0.688	−0.459	0.115
5	0.12	0.69	0.283	0.965	0.139	0.577	−0.289	−0.105	−0.411	0.463	0.538	−0.358	0.090
4	0.14	0.68	0.332	0.915	0.169	0.545	−0.272	−0.122	−0.372	0.434	0.468	−0.312	0.078

Expression (18) then assumes the form

$$\int d\omega |\tilde{A}^J_{M,\pm K}(\omega,\Omega)|^2 = |b(l_m)|^2 \qquad (19)$$
$$\times \sum_{l=0}^{l_m}\sum_{l'=0}^{l_m}\sum_{jL} C^{j\pm K}_{Jl'\pm K0} C^{j\pm K}_{Jl\pm K0} C^{L0}_{ll'00} C^{JM}_{JLM0}$$
$$\times \begin{Bmatrix} l & j & J \\ J & L & l' \end{Bmatrix} \frac{(2l+1)(2l'+1)}{2}$$
$$\times \sqrt{\frac{2L+1}{2J+1}}\,(-1)^{j+J+L} P_L(\xi)$$
$$\times [1+\pi\pi_1\pi_2(-1)^l][1+\pi\pi_1\pi_2(-1)^{l'}].$$

Since l and l' have the same parity, it follows from the properties of the Clebsch–Gordan coefficient $C^{L0}_{ll'00}$ that L can assume only the even values of $L = 0, 2, \ldots, 2J$. Upon the substitution of (19) into (13), the angular distribution $\bar{T}^J_{MK}(\Omega)$ of fission fragments, which is normalized to unity, can be reduced to a form that is analogous to (10). Specifically, we have

$$\bar{T}^J_{MK}(\theta) = \sum_L B_{JMKL} P_L(\xi), \qquad (20)$$

where

$$B_{JMKL} = \frac{2J+1}{16\pi^2}|b(l_m)|^2 \sum_{l=0}^{l_m}\sum_{l'=0}^{l_m}\sum_{jL} C^{jK}_{Jl'K0} \qquad (21)$$
$$\times C^{jK}_{JlK0} C^{L0}_{ll'00} C^{JM}_{JLM0} \begin{Bmatrix} l & j & J \\ J & L & l' \end{Bmatrix} (2l+1)$$
$$\times (2l'+1)\sqrt{\frac{2L+1}{2J+1}}\,(-1)^{j+J}$$
$$\times [1+\pi\pi_1\pi_2(-1)^l][1+\pi\pi_1\pi_2(-1)^{l'}].$$

At $L = 0$, the quantity B_{JMKL} is equal to $1/4\pi$.

3. ANGULAR DISTRIBUTIONS OF FRAGMENTS ORIGINATING FROM THE LOW-ENERGY PHOTOFISSION OF NUCLEI

Let us consider the case of the low-energy photofission of an even–even target nucleus in the ground state, its total angular momentum being $I = 0$. In order to describe the differential photofission cross section as a function of the angle θ between the directions of fission-fragment emission, which are defined with respect to the axis of the incident-photon beam, one can employ formula (2) at $M = \pm 1$, since the photon helicity is ± 1, and set the value of the compound-nucleus spin to $J = 1$ in the case of dipole photoabsorption and to $J = 2$ in the case of quadrupole photoabsorption.

Since the angular distribution of fission fragments that is specified by Eqs. (3) and (10) and the angular distribution that is specified by Eqs. (5) and (20) are invariant under the substitution of $-M$ for M, formula (2) can be represented in the form

$$\sigma_f(\theta) = a_0 + b_0 \sin^2\theta + c_0 \sin^2(2\theta), \qquad (22)$$

where the coefficients a_0, b_0, and c_0 are defined as

$$a_0 = \sum_{JK} \alpha_{JK} P(JK); \quad b_0 = \sum_{JK} \beta_{JK} P(JK); \qquad (23)$$

Table 2. Values of the coefficients G_{20}, a, and b for the A. Bohr angular distribution (10) and the angular distribution (20) in the problem of the low-energy fission of nuclei at $G_{22} = 0$ and $G_{22} = 1$

l_m	$G_{22} = 0$		$G_{22} = 1$	
	a	G_{20}	a	G_{20}
∞	0	0.73 ± 0.04	0	1.17 ± 0.07
30	0.096 ± 0.002	0.82 ± 0.04	0.098 ± 0.003	1.35 ± 0.08
20	0.15 ± 0.006	0.87 ± 0.05	0.15 ± 0.005	1.43 ± 0.08
10	0.29 ± 0.013	1.06 ± 0.06	0.29 ± 0.014	1.79 ± 0.11
Experiment [14]	0.09 ± 0.024		0.09 ± 0.024	

$$c_0 = \sum_{JK} \gamma_{JK} P(JK),$$

with

$$P(JK) = \frac{\Gamma_f(JK)}{\Gamma(J)} \sum_{M=-1}^{+1} \sigma(JM), \qquad (24)$$

while the coefficients α_{JK}, β_{JK}, and γ_{JK} are superpositions of the coefficients B_{J1KL} for $L = 0, 1, 2$.

It can be seen from Table 1 that, in the case of rather small values of l_m, the coefficients α_{JK}, β_{JK}, and γ_{JK} change significantly upon going over from the A. Bohr formula (10) to formula (20).

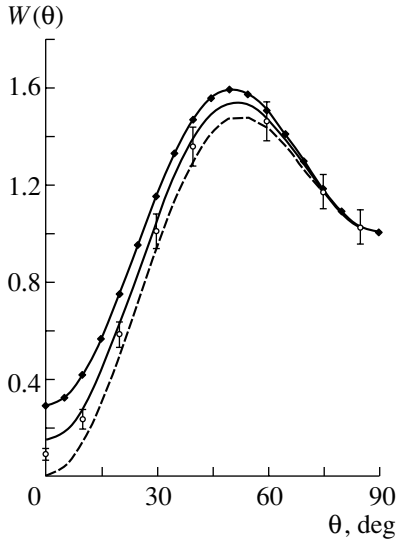

Fig. 1. Asymmetry $W(\theta)$ in the angular distribution of fragments originating from ^{238}U photofission induced by bremsstrahlung photons whose endpoint energy is 5.2 MeV, this asymmetry being defined with respect to the photon-beam axis. The curves depict theoretical results for various values of the maximum relative orbital angular momentum of fission fragments: (solid curve) $l_m = \infty$ (A. Bohr formula), (dashed curve) $l_m = 20$, and (solid curve labeled with a diamond) $l_m = 10$. Open circles represent experimental data reported in [14].

Our further analysis of low-energy photofission will be performed for the fission of ^{238}U nuclei that is induced by bremsstrahlung from 5.2-MeV electrons immediately below the fission threshold. We will investigate the quantity

$$W(\theta) = \frac{\sigma_f(\theta)}{\sigma_f(90^\circ)}, \qquad (25)$$

which characterizes the asymmetry in the angular distribution of fission fragments with respect to the photon-beam axis. From Eqs. (25) and (22), it follows that the asymmetry $W(\theta)$ is given by expression (22), where the coefficients a_0, b_0, and c_0 must be replaced by the coefficients $a = \dfrac{a_0}{a_0 + b_0}$, $b = \dfrac{b_0}{a_0 + b_0}$, and $c = \dfrac{c_0}{a_0 + b_0}$, which satisfy the relation $a + b = 1$.

The experimental values of the coefficients a and c are $a^{\text{expt}} = 0.04 \pm 0.04$ and $c^{\text{expt}} = 1.02 \pm 0.07$ [12], $a^{\text{expt}} = 0.10 \pm 0.035$ and $c^{\text{expt}} = 0.91 \pm 0.08$ [13], $a^{\text{expt}} = 0.09 \pm 0.024$ and $c^{\text{expt}} = 0.907 \pm 0.045$ [14], and $a^{\text{expt}} = 0.08^{+0.06}_{-0.03}$ and $c^{\text{expt}} = 0.97 \pm 0.10$ [15], whence we can see that the values c^{expt} change only slightly from measurements of one experimental group to measurements of another group, but that the values a^{expt} change more sharply, remaining, however, much smaller than b^{expt} and c^{expt}. As can be seen from Table 1, the coefficients α_{JK} are positive for all positive values of l_m; therefore, the smallness of the coefficient a may only be due to the smallness of the quantities $P(11)$ and $P(21)$ appearing as factors in front of the coefficients α_{11} and α_{21}, which are large in magnitude. Retaining, in (23), only the $K = 0$ and

$K = 2$ channels, we can then find for the coefficients a, b, and c that

$$a = \frac{\alpha_{10} + \alpha_{20}G_{20} + \alpha_{22}G_{22}}{d}; \quad (26)$$
$$b = \frac{\beta_{10} + \beta_{20}G_{20} + \beta_{22}G_{22}}{d};$$
$$c = \frac{\gamma_{20}G_{20} + \gamma_{22}G_{22}}{d};$$
$$d = (\alpha_{10} + \beta_{10}) + (\alpha_{20} + \beta_{20})\,G_{20} + (\alpha_{22} + \beta_{22})\,G_{22},$$

where $G_{JK} = P(JK)/P(10)$.

Let us first consider the situation where, in accordance with the concepts of low-energy photofission that were developed in [4], only the $K\pi = 0^+$ and $K\pi = 0^-$ transition fission states play an important role in subthreshold photofission. In this case, one can eliminate the $K = 2$ channels in formulas (26) by employing the value of $G_{22} = 0$ for the coefficient G_{22}, whereupon the coefficients a, b, and c in (26) appear to be dependent on only one unknown parameter, G_{20}. By using the experimental values of the coefficient c, c^{expt}, we can determine the coefficient G_{20} for various values of l_m. With the aid of these values of G_{20}, we can calculate the coefficients a and b by formulas (26). As can be seen from Table 2, where we present the results obtained by processing data from [14] and where the accuracy in determining the coefficient a^{expt} was the highest, the values found for the coefficients G_{20} grow with decreasing l_m, from 0.73 ± 0.04 at $l_m = \infty$ to 1.06 ± 0.06 at $l_m = 10$. Concurrently, the coefficient a increases (the coefficient b decreases) from $a = 0$ ($b = 1$) at $l_m = \infty$ to $a = 0.29$ ($b = 0.71$) at $l_m = 10$. A comparison of the values obtained for the coefficient a with its experimental counterpart, $a^{\text{expt}} = 0.09 \pm 0.024$, makes it possible to draw the conclusion that an l_m value that is consistent with the experimental angular distribution of photofission fragments at a level of two standard deviations must lie in the range $20 < l_m < 40$. We note that the inclusion of the $K = 2$ channel does not change the above conclusions. Indeed, it can be seen from Table 2 that, upon going over (for the coefficient G_{22}) from the value of $G_{22} = 0$ to the value of $G_{22} = 1$, the coefficients G_{20} change sizably, but the coefficients a and b remain virtually unchanged for all values of l_m.

As can be seen from Fig. 1, where the values calculated at $l_m = 10, 20, \infty$ for the asymmetry $W(\theta)$ (25) in the angular distribution of fragments originating from ^{238}U photofission induced by bremsstrahlung photons whose spectrum has an endpoint energy of 5.2 MeV, this asymmetry being defined with respect to the photon-beam axis, are displayed along with the analogous asymmetry obtained experimentally in [14], the A. Bohr formula (10) corresponding to $l_m = \infty$ is unable to reproduce the experimental asymmetry in the vicinity of the angle $\theta = 0$.

If we compare the interval $20 < l_m < 40$, which was obtained for l_m values, with the estimate $l_m^0 \approx 25$, which was derived above for the upper limit on l_m values, we can arrive at the conclusion that the interval of the possible values of l_m can be significantly constrained: $20 < l_m < 25$. Since the values obtained for l_m are much greater than the maximum values of the fragment spins, $(\mathbf{J}_1)_m$ and $(\mathbf{J}_2)_m$, it follows from relation (1) that the fragment spins $\mathbf{J}_1$ and $\mathbf{J}_2$ are predominantly parallel to each other and are antiparallel to the relative orbital angular momentum $\mathbf{l}$ of the fragments. Since the relative orbital angular momentum $\mathbf{l}$ is orthogonal to the direction of fragment emission and since, at high values of l_m, the emission of fragments occurs in the direction approximately parallel or antiparallel to the symmetry axis of the nucleus undergoing fission, the fission-fragment spins $\mathbf{J}_1$ and $\mathbf{J}_2$ are also orthogonal, to a high degree of precision, to the symmetry axis of this nucleus. This conclusion is confirmed by experimental results reported in [2].

4. ANGULAR DISTRIBUTIONS OF FRAGMENTS ORIGINATING FROM THE SPONTANEOUS FISSION OF POLARIZED NUCLEI

Let us consider the binary fission of spontaneously fissile odd or odd–odd nuclei whose total angular momentum J is greater than $1/2$. By applying a strong magnetic field at ultralow temperatures ($T \approx 1$ mK), the spin of the nucleus undergoing fission, $\mathbf{J}$, can be fully oriented along or against the direction of the magnetic-induction vector $\mathbf{B}$ (which provides a natural choice for the z axis in the laboratory frame), depending on the sign of the gyromagnetic ratio for this nucleus. In order to describe the angular distributions of fission fragments for such nuclei, we can use formula (3) or (5) at $M = K = J$, since, in the ground state of a deformed axisymmetric nucleus, the projection K of the spin J of this nucleus onto its symmetry axis coincides with the spin itself: $K = J$.

We can now estimate the degree to which the angular distributions $\bar{T}^J_{JJ}(\theta)$ (20) of fission fragments originating from the spontaneous binary fission of the ground states of polarized odd and odd–odd nuclei whose spin takes values in the region $J > 1/2$ and whose spin projections are $M = K = J$ deviate from the analogous angular distributions given by the A. Bohr formula (10) at the same values of K and M.

As can be seen from Figs. 2 and 3, the angular distribution $\bar{T}^J_{JJ}(\theta)$ (20) and the angular distribution

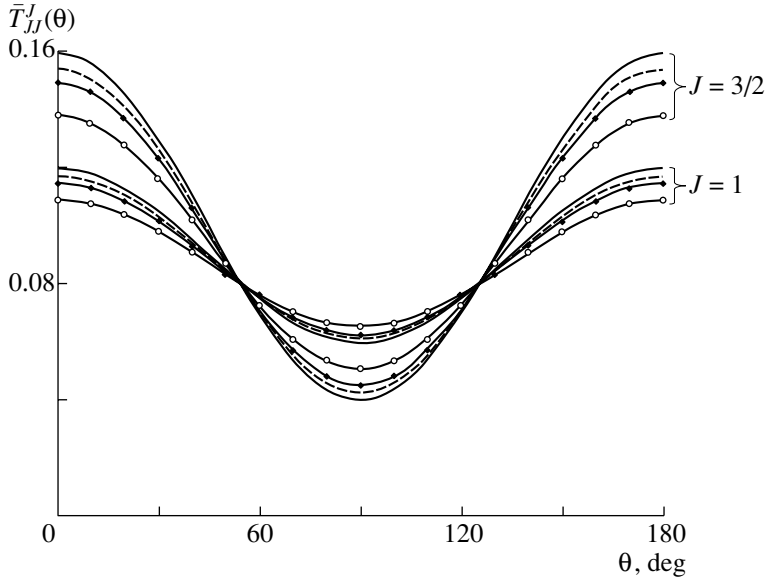

Fig. 2. Angular distributions $\bar{T}^J_{JJ}(\theta)$ ($J = 3/2, 1$) of fragments originating from the fission of polarized nuclei for various values of the maximum relative orbital angular momentum of fission fragments: (solid curve) $l_m = \infty$ (A. Bohr formula), (dashed curve) $l_m = 20$, (solid curve labeled with a diamond) $l_m = 10$, and (solid curve labeled with a circle) $l_m = 5$.

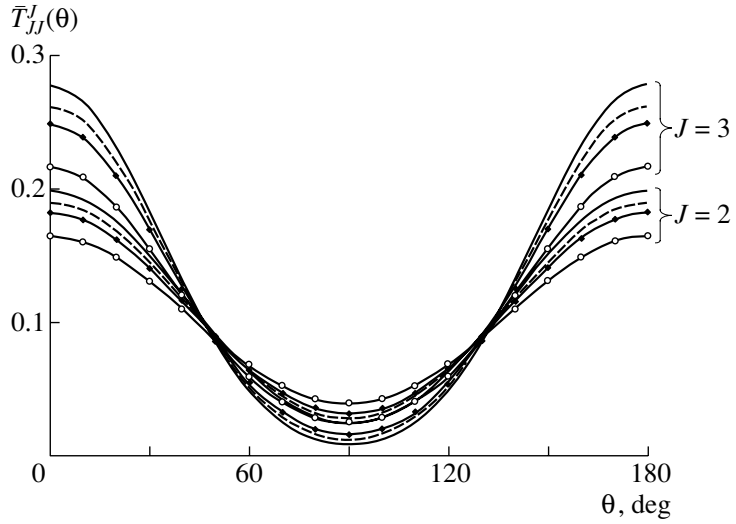

Fig. 3. Angular distributions $\bar{T}^J_{JJ}(\theta)$ of fragments originating from the fission of polarized nuclei for various values of the maximum relative orbital angular momentum of fission fragments: (solid curve) $l_m = \infty$ (A. Bohr formula), (dashed curve) $l_m = 20$, (solid curve labeled with a diamond) $l_m = 10$, and (solid curve labeled with a circle) $l_m = 5$.

$T^J_{JJ}(\theta)$ (10) are both symmetric with respect to an angle of $\theta = 90°$ and take maximum values at $\theta = 0°$ ($180°$). With increasing spin J of the parent nucleus, the ratios $T^J_{JJ}(0°)/T^J_{JJ}(90°)$ and $\bar{T}^J_{JJ}(0°)/\bar{T}^J_{JJ}(90°)$ grow rather fast, which makes it possible to use the angular distributions in (10) and (20) to determine the value of the spin J. We note that the angular distributions in (20) and (10) for polarized nuclei are qualitatively different from the angular distributions of protons emitted by polarized odd–odd nuclei capable of undergoing protonic decay [9], the latter having maxima at an angle of $\theta = 90°$. The deviations of the distributions in (20) from the A. Bohr distributions in (10) are the most pronounced at angles of $\theta = 0°(180°)$ and $90°$, growing in magnitude with increasing spin J of the parent nucleus and with decreasing maximum value l_m of the relative orbital angular momentum of fission fragments. At rather high values of l_m, the angular distributions $\bar{T}^J_{JJ}(\theta)$ of fission fragments in (20) change only slightly upon

Table 3. Deviation from the A. Bohr angular distribution in the problem of the spontaneous fission of polarized nuclei

l_m	$\frac{\bar{T}(0°)-T(0°)}{T(0°)}$, %				$\frac{\bar{T}(90°)-T(90°)}{T(90°)}$, %				$\frac{T(90°)}{T(0°)}$, %			
	$J=1$	$J=3/2$	$J=2$	$J=3$	$J=1$	$J=3/2$	$J=2$	$J=3$	$J=1$	$J=3/2$	$J=2$	$J=3$
20	−2.33	−3.49	−4.36	−5.72	2.34	6.96	14.83	48.62	0.5	0.25	0.125	0.03
19	−2.45	−3.66	−4.57	−6.00	2.45	7.31	15.56	51.00	0.5	0.25	0.125	0.03
10	−4.35	−6.52	−8.15	−10.69	4.32	13.04	27.70	90.92	0.5	0.25	0.125	0.03
9	−4.77	−7.14	−8.90	−11.70	4.78	14.27	30.36	99.70	0.5	0.25	0.125	0.03
5	−7.70	−11.54	−14.41	−18.85	7.69	23.07	49.10	161	0.5	0.25	0.125	0.03
4	−9.10	−13.63	−17.02	−22.24	9.10	27.27	58.02	191	0.5	0.25	0.125	0.03

going over from even values of l to their odd neighbors (that is, those that differ from their even counterparts by unity), as is illustrated in Table 3 at angles of 0° and 90°. Therefore, the angular distributions in (20), as well as the A. Bohr angular distributions in (10), are virtually independent of the parities of the parent nucleus and fission fragments. It can be seen from Table 3 that the relative deviations of the angular distributions in (20) from those in (10) at $\theta = 0°$ (180°) and 90° grow with decreasing l_m, reaching 20% for $\theta = 0°(180°)$ and 191% for $\theta = 90°$ at $l_m = 4$ and $J = 3$. The emergence of such large deviations of the angular distributions in (20) from the angular distributions in (10) at low values of l_m indicates that experiments aimed at studying the angular distributions of fragments originating from the spontaneous fission of polarized nuclei would make it possible to determine the lower limit on l_m.

5. CONCLUSION

From the analysis of angular distributions of fission fragments that was performed here for the case where parent nuclei are polarized, it was deduced that the maximum relative orbital angular momentum of fission fragments produced under such conditions is rather high, $l_m > 20$. It follows that the deviations of the angular distributions of fission fragments from that predicted by the A. Bohr formula (3) must be quite modest, so that this formula appears to be applicable in many cases.

At the same time, the fact that values obtained for the maximum relative orbital angular momentum l_m of fission fragments exceed 20 indicates that it is necessary to consider a specific physical mechanism that, at the stage of the scission of a fissile nucleus into fission fragments and the stage of their subsequent interaction via strongly nonspherical Coulomb and nuclear potentials, ensures the emergence of such high values of l_m and, hence, of the total fission-fragment spin F.

It would be of great interest to perform experiments devoted to studying angular distributions of fission fragments originating from the fission of odd nuclei capable of undergoing spontaneous fission that are polarized in a strong magnetic field at ultralow temperatures. We note that similar experiments that studied the angular distributions of alpha particles emitted by nuclei undergoing alpha decay that were polarized in strong magnetic fields at ultralow temperatures were successfully performed in [16, 17]. Because of small branching fractions of the fission process with respect to alpha decay or ε capture for known odd and odd–odd spontaneously fissile nuclei, it is necessary to overcome serious difficulties in order to record angular distributions for such nuclei with a high statistical accuracy. Nonetheless, such experiments are quite promising from the point of view of their theoretical treatment, since, in contrast to what occurs in the case of induced fission, one transition fission state characterized by only one value of K manifests itself in such experiments.

It also seems important to continue investigating the angular distributions of photofission fragments for various nuclei and various endpoint energies of incident photons.

In addition, it would be of interest to obtain an experimental corroboration of the conclusion drawn here that the spins of fragments originating from the binary fission of nuclei are predominantly parallel.

ACKNOWLEDGMENTS

We are grateful to V.E. Bunakov, W.I. Furman, and A.A. Barabanov for stimulating discussions.

This work was supported by INTAS (grant no. 99-00229) and by the foundation Universities of Russia (project UR-01.01.011).

REFERENCES

1. S. G. Kadmensky, Yad. Fiz. **65**, 1424 (2002) [Phys. At. Nucl. **65**, 1390 (2002)].
2. Yu. N. Kopach *et al.*, Phys. Rev. Lett. **82**, 303 (1999).
3. I. N. Mikhailov and P. Quentin, Phys. Lett. B **462**, 7 (1999).
4. A. Bohr and B. Mottelson, *Nuclear Structure* (Benjamin, New York; Amsterdam, 1969, 1975; Mir, Moscow, 1971, 1977), Vols. 1, 2.
5. A. K. Petukhov, G. V. Petrov, *et al.*, Pis'ma Zh. Éksp. Teor. Fiz. **30**, 324 (1979) [JETP Lett. **30**, 439 (1979)].
6. O. P. Sushkov and V. V. Flambaum, Usp. Fiz. Nauk **136**, 3 (1982) [Sov. Phys. Usp. **25**, 1 (1982)].
7. V. E. Bunakov and L. B. Pikel'ner, Fiz. Élem. Chastits At. Yadra **29**, 337 (1997).
8. A. Barabanov and W. Furman, Z. Phys. A **357**, 441 (1997).
9. S. G. Kadmensky and A. A. Sanzogni, Phys. Rev. C **62**, 054601 (2000).
10. S. G. Kadmensky, in *Proceedings of the IX International Seminar on Interaction of Neutrons with Nuclei, Dubna, 2001*, p. 128.
11. D. A. Varshalovich, A. N. Moskalev, and V. K. Khersonskiĭ, *Quantum Theory of Angular Momentum* (Nauka, Leningrad, 1975).
12. A. S. Soldatov, G. N. Smirenkin, *et al.*, Phys. Lett. **14**, 217 (1965).
13. N. S. Rabotnov, G. N. Smirenkin, *et al.*, Yad. Fiz. **11**, 508 (1970) [Sov. J. Nucl. Phys. **11**, 285 (1970)].
14. A. V. Ignatyuk, N. S. Rabotnov, *et al.*, Zh. Éksp. Teor. Fiz. **61**, 1284 (1971) [Sov. Phys. JETP **61**, 684 (1971)].
15. L. J. Lindgren, A. Alm, and A. Sandell, Nucl. Phys. A **298**, 43 (1978).
16. J. Wouters *et al.*, Phys. Rev. Lett. **56**, 1901 (1986).
17. P. Schuurmans *et al.*, Phys. Rev. Lett. **77**, 4420 (1995).

Translated by A. Isaakyan

Physics of Atomic Nuclei, Vol. 66, No. 7, 2003, pp. 1229–1238. Translated from Yadernaya Fizika, Vol. 66, No. 7, 2003, pp. 1269–1278.

NUCLEI
Theory

Semimicroscopic Description of the Gross Structure of a Giant Dipole Resonance in Light Nonmagic Nuclei

B. S. Ishkhanov and V. N. Orlin

Institute of Nuclear Physics,
Moscow State University, Vorob'evy gory, Moscow, 119899 Russia

Received April 15, 2002; in final form, August 12, 2002

Abstract—A simple model is formulated that makes it possible to describe the configuration and deformation splittings of a giant dipole resonance in light nonmagic nuclei. The gross structure of the cross sections for photoabsorption on ^{12}C, ^{24}Mg, and ^{28}Si nuclei is described on the basis of this model. © *2003 MAIK "Nauka/Interperiodica".*

1. INTRODUCTION

A giant dipole resonance in light nonmagic nuclei has a number of special features: (i) a very large width (up to 15 MeV in ^{23}Na [1]), (ii) a manifest intermediate structure that varies from one nucleus to another strongly, and (iii) a rather complicated gross structure. In order to explain these features, it is sufficient to recall that, in contrast to what we have in heavy nuclei, shell effects in light nuclei are much stronger than collective effects; as a result, the oscillator strengths of single-particle dipole transitions are not concentrated predominantly in one or two (if the nucleus being considered is deformed) collective states.

In the present study, we consider a number of problems connected with describing the gross structure of a giant dipole resonance in light nonmagic nuclei. This structure is formed, first, by the deformation splitting of a giant dipole resonance; second, by its configuration splitting, which is due to the fact that, in light nuclei, the energies of single-particle $E1$ transitions between principal (oscillator) shells (from a filled inner shell to the valence shell and from the valence shell to an unfilled outer shell) strongly differ from one another; and, finally, by the isospin splitting of a giant dipole resonance.

Each of the above types of giant-resonance splitting has received quite an adequate study in the literature. For example, a theoretical analysis of the spectrum of various isospin $E1$ modes was performed as far back as 1965–1968 in [2–5], where simple theoretical estimates were obtained for the isospin splitting of a giant dipole resonance. Ten years earlier, Danos [6] and Okamoto [7] successfully explained the deformation splitting of a giant dipole resonance within a hydrodynamic model. The configuration splitting of a giant resonance in light nonmagic nuclei was first considered in 1964 by Neudatchin and Shevchenko [8] and was then investigated in detail by the authors of [9–11]. Nonetheless, the problem of theoretically describing the gross structure of a giant resonance in light nonmagic nuclei has yet to be solved conclusively.

In the present study, we make an attempt at describing the gross structure of a giant dipole resonance within the semimicroscopic model of vibrations that was proposed in [12]. For the sake of simplicity, we take into account only the deformation and the configuration splitting of a giant dipole resonance, which are closely interrelated in light nonmagic nuclei (see, for example, [13]). For $N \neq Z$ nuclei, the isospin splitting of a giant dipole resonance can additionally be taken into account by using recipes proposed in [2–5].

2. CONFIGURATION SPLITTING OF SINGLE-PARTICLE $E1$ TRANSITIONS IN LIGHT NUCLEI

As was indicated above, principal (oscillator) shells in light nuclei are separated by unequal energy gaps. This is illustrated in Fig. 1, which displays data on the energies of the knockout of s-, p- and d-wave protons from the first three oscillator shells corresponding to the excitation of $\mathcal{N} = 0$, 1, and 2 oscillator quanta [9].

There is a wide scatter of the experimental values of the energies $E_{\mathcal{N}l}$ in the figure. This is due not only to errors in the relevant measurements but also to the effect of spin–orbit splitting of single-particle levels (for $l \neq 0$) and (in unfilled shells) the effect of nucleon–nucleon correlations on these levels. It can be seen from the figure that, for nuclei heavier than oxygen, the spacing between the "0s"

1063-7788/03/6607-1229$24.00

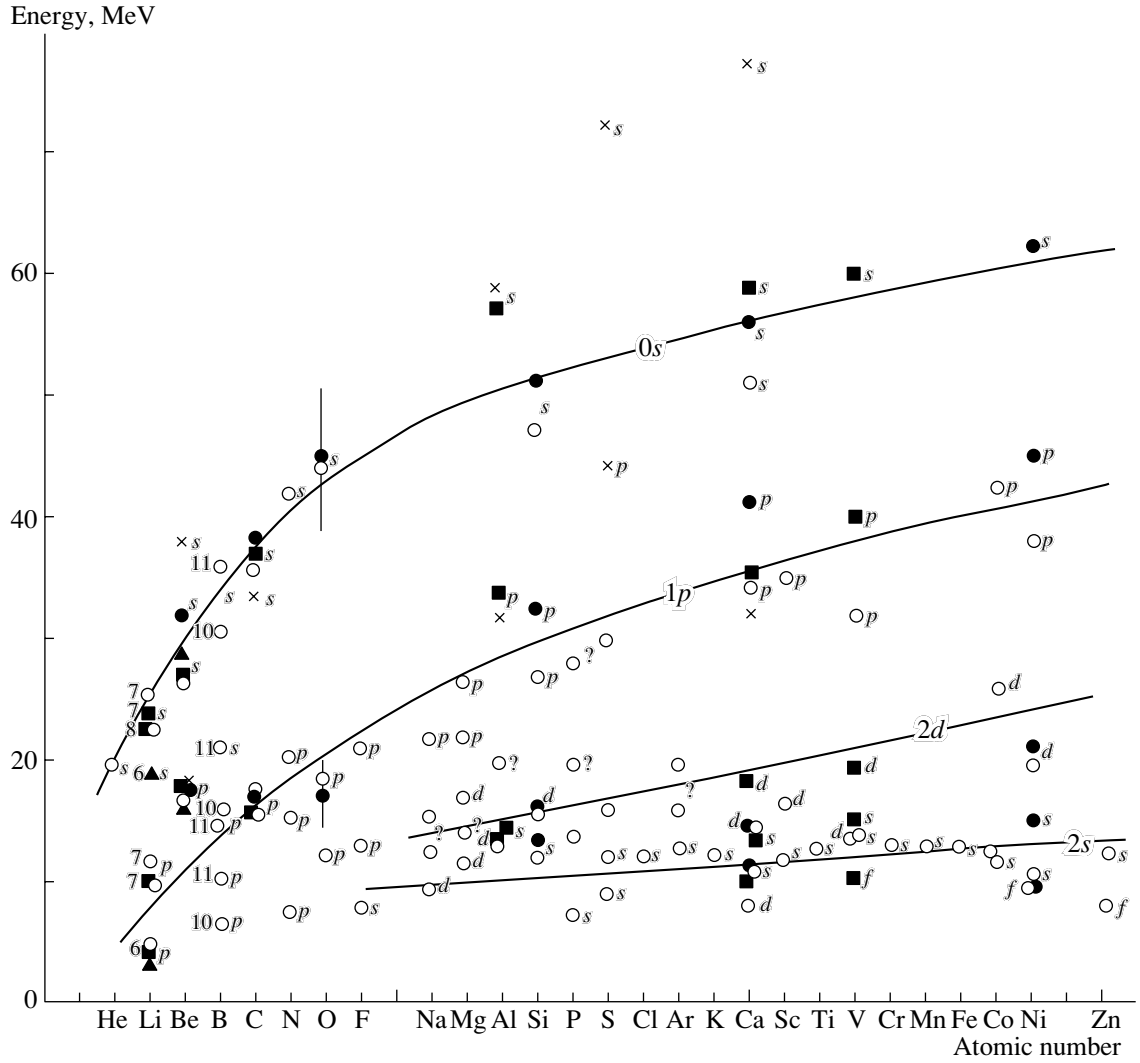

Fig. 1. Energies of the knockout of s-, p-, and d-wave protons from the first three oscillator shells [9].

and "$1p$" curves remains virtually unchanged as the charge number Z is increased. For nuclei lighter than oxygen—that is, in the region where the $1p$ shell is not closed—these curves somewhat approach each other, which may be attributed to the effect of residual forces (for example, pairing), which shift the energy E_{1p} upward. We are interested here in the mean spacing between the $0s$ and $1p$ single-particle oscillator shells. This quantity is not expected to depend on proton pairing. In estimating the difference $E_{0s} - E_{1p}$ over the $^4\mathrm{He} \rightarrow {}^{16}\mathrm{O}$ segment, where the filling of the $1p$ shell occurs, it is therefore necessary to take into account only data on odd-Z nuclei (see Fig. 1). After this correction, the quantity $E_{0s} - E_{1p}$ appears to be approximately constant for any values of Z greater than that for helium. This means that, for a first approximation, the mean energy of single-particle transitions from the filled $0s$ shell to the $1p$ shell is independent of the number of nucleons occurring in this shell and in higher lying shells.

Analyzing experimental data on the energies E_{1p}, E_{2d}, and E_{2s} and considering that the $2s$-wave protons shift the centroid of the $2d2s$ shell only slightly, we can arrive at the conclusion, in a similar way, that the mean energy of single-particle transitions from the filled $1p$ shell to the $2d2s$ shell is also independent of the number of protons occurring in states that lie higher than the $1p$ shell.

In all probability, this property is common to all closed shells. It implies a significant spatial separation of nucleons occurring in different principal shells of a nucleus. Indeed, it is clear that, if nucleons belonging to outer shells are situated by and large farther from the center of the nucleus being considered than nucleons belonging to inner shells, then the energy of a nucleon transition from a filled inner shell to the next higher lying shell will be determined

predominantly by the mean field generated by "internal" (core) nucleons. A spatial separation of shells is directly corroborated by fluctuations of the radial dependence of the nuclear density $\rho(r)$ (see, for example, [14]).

Let us now estimate the mean spacings between the $0s$, $1p$, and $2d2s$ shells. This can be done by two methods: either with the aid of experimental data presented in Fig. 1 or with the aid of the formula [15]

$$\hbar\omega_{\text{core}}^{(0)} \approx 41A_{\text{core}}^{-1/3}\ \text{MeV}, \quad (1)$$

where $\omega_{\text{core}}^{(0)}$ is the frequency parameter of the oscillator potential simulating the mean field that is generated by A_{core} core nucleons ($A_{\text{core}} = 4$ for the $0s \to 1p$ single-particle transition, and $A_{\text{core}} = 16$ for the $1p \to 2d2s$ transition).

Using the approximating curves in Fig. 1, we find, in the first case, that the $1p$ shell is separated by approximately 22.5 MeV from the $0s$ shell and by approximately 18.5 MeV from the $2d2s$ shell. In the second case, we instead obtain 25.8 and 16.3 MeV, respectively. It can easily be seen that the discrepancy between the two types of estimates does not exceed the uncertainty in the approximating curves "$0s$" and "$1p$." Indeed, perfect agreement between the estimates can be attained if we draw the first curve somewhat higher and the second curve somewhat lower (there are sufficient grounds for doing this).

We now have all the required data at our disposal for estimating the configuration splitting of single-particle dipole transitions. In a nonmagic nucleus, two types of single-particle $E1$ transitions are possible: type-1 transitions proceed from the valence shell of the nucleus to an empty outer shell, while type-2 transitions proceed from the last filled inner shell to the valence shell. The nuclear mean field in which valence nucleons move can be approximately described in terms of the oscillator potential corresponding to the oscillator-quantum energy of $\hbar\omega^{(0)} \approx 41A^{-1/3}$ MeV, where A is the mass number of the nucleus. Therefore, the mean energy of type-1 transitions is $\hbar\omega_1^{(0)} \approx \hbar\omega^{(0)}$. On the other hand, the mean energy of type-2 transitions can be calculated by formula (1), which yields $\hbar\omega_2^{(0)} \approx \hbar\omega_{\text{core}}^{(0)} \approx 41A_{\text{core}}^{-1/3}$ MeV.

Thus, the ratio of the mean energies for two types of single-particle $E1$ transitions in nonmagic nuclei can be approximated by the expression

$$\frac{\hbar\omega_2^{(0)}}{\hbar\omega_1^{(0)}} \approx \left(\frac{A}{A_{\text{core}}}\right)^{1/3}. \quad (2)$$

From this formula, it can be seen that the greater the contribution of valence nucleons to the total mass of the nucleus, the greater the configuration splitting. In light nonmagic nuclei, there can occur a situation where a major part of nucleons reside in the valence shell, while, in heavy nuclei, the greater part of the nuclear mass is always concentrated in filled inner shells. It therefore comes as no surprise that the configuration splitting of a giant dipole resonance manifests itself primarily in light nonmagic nuclei. (This statement can be illustrated by considering the example of the ^{12}C and ^{159}Tb nuclei, for which the above ratio of the mean transition energies, $\hbar\omega_2^{(0)}/\hbar\omega_1^{(0)}$, takes values of about 1.44 and 1.06, respectively.)

3. DESCRIPTION OF THE MODEL USED

In this section, we will first present fundamentals of the semimicroscopic model of dipole vibrations that was proposed in [12] and then show how it can be generalized to take into account the configuration and the deformation splitting of a giant dipole resonance.

3.1. Semimicroscopic Model of Dipole Vibrations

Basic properties of a nuclear dipole resonance can be explained in terms of the interplay of single-particle nucleon excitations and the isovector dipole field that is generated by these excitations and which, for vibrations along the x axis, is given by

$$F = \sum_{i=1}^{A}(2t_z x)_i = \sum_{\alpha>\beta}\langle\alpha|2t_z x|\beta\rangle a_\alpha^+ a_\beta + \text{h.c.}, \quad (3)$$

where a_λ^+ and a_λ are the operators of, respectively, creation and absorption of a nucleon in a single-particle state $|\lambda\rangle$ and $t_z = \pm 1/2$ is the isospin variable for a nucleon.

The application of the dipole operator F to the shell ground state of a nucleus (physical vacuum $|0\rangle$) generates a superposition of particle–hole ($1p1h$) states; that is,

$$F|0\rangle = \sum_{\alpha>\beta}\langle\alpha|2t_z x|\beta\rangle a_\alpha^+ a_\beta|0\rangle. \quad (4)$$

In the case of heavy and medium-mass spherical nuclei, the state $F|0\rangle$ is approximately an eigenstate of the single-particle Hamiltonian H_0, the corresponding excitation energy being

$$\hbar\omega^{(0)} \approx 41A^{-1/3}\ \text{MeV}, \quad (5)$$

since the energy scatter of single-particle $E1$ transitions is much less than $\hbar\omega^{(0)}$. The excitation $F|0\rangle$ is formed by a great number of single-particle excitations. In view of this, the operator F can be represented in the form

$$F = f^{(0)}c^{(0)+} + f^{(0)*}c^{(0)}, \quad (6)$$

where $c^{(0)+}$ and $c^{(0)}$ are the operators of creation and annihilation of a vibrational quantum of energy $\hbar\omega^{(0)}$, these operators approximately satisfying commutation rules for bosons, and $f^{(0)}$ is the probability amplitude for the production of such a quantum by the dipole field F.

The amplitude $f^{(0)}$ can be estimated with the aid of the classical sum rule

$$\hbar\omega^{(0)}|f^{(0)}|^2 = \frac{\hbar^2}{2M}A, \quad (7)$$

or it can be calculated directly by using the relation

$$|f^{(0)}|^2 = \langle 0|F^+F|0\rangle = \sum_{\alpha\beta}|\langle\alpha|2t_z x|\beta\rangle|^2, \quad (8)$$

where M is the nucleon mass and where summation is performed over filled (β) and free (α) single-particle levels.

Single-particle dipole vibrations cannot be considered as normal vibrations (eigenstates) of a nucleon system about the equilibrium position, since they effectively interact with one another via the excitation of the isovector single-particle potential. This circumstance can be taken into account by supplementing the single-particle Hamiltonian H_0 with that for dipole–dipole forces $\varkappa, F^2/2$, whereupon the vibrational Hamiltonian assumes the form

$$H = \hbar\omega^{(0)}c^{(0)+}c^{(0)} + \frac{1}{2}\varkappa F^2. \quad (9)$$

By using the semiempirical Weizsäcker mass formula, the coupling constant for dipole–dipole interaction can be expressed [12] in terms of the symmetry potential V as

$$\varkappa = \frac{V}{4A\langle x^2\rangle}, \quad (10)$$

where $\langle x^2\rangle \approx R^2/5 \approx (1.2A^{1/3})^2/5$ fm^2 is the mean-square value of the coordinate x of intranuclear nucleons.

With the aid of the linear canonical transformation

$$c^+ = Xc^{(0)+} - Yc^{(0)} \quad (X^2 - Y^2 = 1), \quad (11)$$

the Hamiltonian in (9) can be reduced to the diagonal form

$$H = \hbar\omega c^+c + \text{const}, \quad (12)$$

where

$$\hbar\omega = \sqrt{(\hbar\omega^{(0)})^2 + 2\varkappa\hbar\omega^{(0)}|f^{(0)}|^2} \quad (13)$$

is the energy of a normal mode of dipole vibrations.

From (5), (7), (10), and (13), we find at $V \approx 130$ MeV that

$$\hbar\omega \approx 80A^{-1/3}\ \text{MeV}. \quad (14)$$

This estimate of the energy of dipole vibrations is in good agreement with the experimental values of the giant-dipole-resonance energy for heavy nuclei.

In the representation of normal vibrations (eigenstates), the dipole-moment operator F has the form

$$F = fc^+ + f^*c, \quad (15)$$

where f is the probability amplitude for the excitation of normal vibrations. This amplitude is related to the amplitude $f^{(0)}$ by the equation

$$\hbar\omega|f|^2 = \hbar\omega^{(0)}|f^{(0)}|^2, \quad (16)$$

from which it follows that the canonical transformation (11) has no effect on the oscillator strength of dipole transitions.

3.2. Inclusion of the Configuration Splitting of a Giant Dipole Resonance

If there is a configuration splitting of $E1$ transitions, the dipole operator F must be broken down into two terms,

$$F = F_1 + F_2, \quad (17)$$

where the first term

$$F_1 = \sum_{\alpha<\beta}^{(1)}\langle\alpha|2t_z x|\beta\rangle a_\alpha^+ a_\beta + \text{h.c.} \quad (18)$$

exhausts single-particle transitions between the valence and outer shells, while the second term

$$F_2 = \sum_{\alpha<\beta}^{(2)}\langle\alpha|2t_z x|\beta\rangle a_\alpha^+ a_\beta + \text{h.c.} \quad (19)$$

takes into account transitions from a filled inner shell to the valence shell and the transitions inverse to these.

Following the same line of reasoning as in Subsection 3.1, we introduce the operators of creation ($c_1^{(0)+}$, $c_2^{(0)+}$) and annihilation ($c_1^{(0)}$, $c_2^{(0)}$) of single-particle quanta whose energies are (in MeV)

$$\hbar\omega_1^{(0)} \approx 41A^{-1/3} \text{ and } \hbar\omega_2^{(0)} \approx 41A_{\text{core}}^{-1/3} \quad (20)$$

(see Section 2); further, we employ the approximation

$$F_i = f_i^{(0)}c_i^{(0)+} + f_i^{(0)*}c_i^{(0)} \quad (i = 1, 2), \quad (21)$$

where the probability amplitudes for the excitation of single-particle vibrations are given by

$$|f_i^{(0)}|^2 = \sum_{\alpha<\beta}^{(i)}|\langle\alpha|2t_z x|\beta\rangle|^2 \quad (i = 1, 2). \quad (22)$$

The next step consists in representing the vibrational nuclear Hamiltonian in the form

$$H = H_1 + H_2 + H_{12}, \quad (23)$$

where

$$H_1 = \hbar\omega_1^{(0)} c_1^{(0)+} c_1^{(0)} + \frac{1}{2}\varkappa_1 F_1^2 \qquad (24)$$

is the Hamiltonian that describes normal vibrations for type-1 dipole transitions,

$$H_2 = \hbar\omega_2^{(0)} c_2^{(0)+} c_2^{(0)} + \frac{1}{2}\varkappa_2 F_2^2 \qquad (25)$$

is the analogous Hamiltonian for type-2 dipole transitions, and

$$H_{12} = \varkappa_{12} F_1 F_2 \qquad (26)$$

is the operator that takes into account the interaction of dipole transitions of the two types.

In order to take into account the possible distinctions for three types of $1p1h \rightleftarrows 1p1h$ interactions—$1 \rightleftarrows 1$, $2 \rightleftarrows 2$, and $1 \rightleftarrows 2$—we have introduced three different coupling constants for dipole–dipole forces ($\varkappa_1$, $\varkappa_2$, and $\varkappa_{12}$). This can be justified by the following considerations. According to the estimate in (10), the coupling constant for dipole–dipole forces is proportional to $A^{-5/3}$. This mass dependence is obviously appropriate for the constant $\varkappa_1$ and, to some extent, for the constant $\varkappa_{12}$, but the constant $\varkappa_2$ is most likely to be proportional to $A_{\text{core}}^{-5/3}$, since outer (valence) nucleons have but a slight effect on the oscillator excitations of nucleons belonging to a filled inner shell (see the analysis of data on quasielastic nucleon knockout in Section 2). Moreover, the interaction within the group of type-1 excitations is expected to be additionally suppressed in relation to the interaction within the group of type-2 excitations, since the former occurs at the nuclear periphery, where the mean density of nuclear matter is lower. Further, it can also be assumed that the intergroup interaction is weaker than the intragroup interaction because the overlap integral is small for type-1 and type-2 particle–hole states.

Taking the aforesaid into account, we represent the coupling constants for dipole–dipole interaction in the form

$$\varkappa_1 = \mathcal{K}_1 A^{-5/3}, \quad \varkappa_2 = \mathcal{K}_2 A_{\text{core}}^{-5/3}, \qquad (27)$$
$$\varkappa_{12} = \mathcal{K}_{12} A^{-5/3},$$

where the factors $\mathcal{K}_1$, $\mathcal{K}_2$, and $\mathcal{K}_{12}$ satisfy the relations

$$\mathcal{K}_{12} \lesssim \mathcal{K}_1 \lesssim \mathcal{K}_2 \approx 100 \text{ MeV}. \qquad (28)$$

We diagonalize the Hamiltonian in (23) in two steps: first, we find the eigenstates of the Hamiltonians H_1 and H_2, whereupon we take into account the interaction of these states. After the first step of the calculations, which reproduces the calculations described in Subsection 3.1, the Hamiltonian in Eq. (23) reduces to the form

$$H = \sum_{i=1}^{2} \hbar\omega_i c_i^+ c_i + \varkappa_{12} F_1 F_2 + \text{const}, \qquad (29)$$

where c_i^+ and c_i are the operators of, respectively, creation and annihilation of a quantum of eigenvibrations generated by the Hamiltonian H_i;

$$\hbar\omega_i = \sqrt{(\hbar\omega_i^{(0)})^2 + 2\varkappa_i \hbar\omega_i^{(0)} |f_i^{(0)}|^2} \qquad (30)$$

is the energy of such a quantum;

$$F_i = f_i c_i^+ + f_i^* c_i \qquad (31)$$

is operator F_i in the representation of the eigenstates of the Hamiltonian H_i; and f_i is the probability amplitude for the excitation of vibrations of the $c_i^+|0\rangle$ type, this amplitude being related to the amplitude $f_i^{(0)}$ by the equation

$$\hbar\omega_i |f_i|^2 = \hbar\omega_i^{(0)} |f_i^{(0)}|^2. \qquad (32)$$

Let us estimate the ratio of the energies $\hbar\omega_2$ and $\hbar\omega_1$. We assume that the fraction q of the valence shell is not occupied and that its fraction $(1-q)$ is accordingly filled. Using the dipole sum rule, we then obtain

$$\hbar\omega_2^{(0)} |f_2^{(0)}|^2 \approx \frac{\hbar^2}{2M} q A_{\text{core}}, \qquad (33)$$
$$\hbar\omega_1^{(0)} |f_1^{(0)}|^2 \approx \frac{\hbar^2}{2M} (A - q A_{\text{core}}).$$

By using these estimates and relations (20), (27), and (30), we obtain

$$\frac{\hbar\omega_2}{\hbar\omega_1} \approx \left(\frac{A}{A_{\text{core}}}\right)^{1/3} \sqrt{\frac{1 + 0.0247 q \mathcal{K}_2}{1 + 0.0247(1 - q A_{\text{core}}/A)\mathcal{K}_1}}. \qquad (34)$$

The configuration splitting of a giant dipole resonance does not play a significant role either in the case where the valence shell is nearly empty ($q \to 1$) or in the case where it is nearly filled ($q \to 0$). But in other cases, it can be seen from relations (28) that the second factor on the right-hand side of (34) is close to unity. Therefore, we assume that

$$\frac{\hbar\omega_2}{\hbar\omega_1} \approx \frac{\hbar\omega_2^{(0)}}{\hbar\omega_1^{(0)}} \approx \left(\frac{A}{A_{\text{core}}}\right)^{1/3}. \qquad (35)$$

In the representation specified by Eqs. (23)–(26), the coupling constants $\varkappa_1$, $\varkappa_2$, and $\varkappa_{12}$ play the role of free parameters of the model. Upon recasting the Hamiltonian H into the form (29), it becomes possible to choose parameters in an alternative way: $\hbar\omega_1$,

$\hbar\omega_2$, and $\mathcal{K}_{12} = \varkappa_{12}A^{5/3}$. This parametrization has a number of advantages: on one hand, the number of independent variable parameters decreases by virtue of the condition in (35); on the other hand, the region where phenomenological dipole–dipole forces are applied, which are only used to describe a relatively weak interaction of different configuration modes, shrinks.

The Hamiltonian in (29) can be diagonalized by means of the linear canonical transformation

$$\hat{c}_i^+ = \sum_{j=1}^{2}(X_{ij}c_j^+ - Y_{ij}c_j), \tag{36}$$

where the expansion coefficients X_{ij} and Y_{ij} satisfy the orthogonality conditions

$$\sum_{j=1}^{2}(X_{ij}X_{kj}^* - Y_{ij}Y_{kj}^*) = \delta_{ik}, \tag{37}$$

$$\sum_{j=1}^{2}(X_{ij}Y_{kj} - Y_{ij}X_{kj}) = 0.$$

The eigenenergies of the Hamiltonian H are given by

$$\hbar\hat{\omega}_i = \left(\frac{\hbar^2\omega_1^2 + \hbar^2\omega_2^2}{2} \mp \left(\frac{(\hbar^2\omega_1^2 - \hbar^2\omega_2^2)^2}{4}\right.\right. \tag{38}$$
$$\left.\left. + 4\varkappa_{12}^2\hbar\omega_1|f_1|^2\hbar\omega_2|f_2|^2\right)^{1/2}\right)^{1/2},$$

where $i = 1, 2$ and $\hbar\hat{\omega}_1 \leq \hbar\hat{\omega}_2$.

The dipole operator F reduces to the form

$$F = \sum_{i=1}^{2}(\hat{f}_i\hat{c}_i^+ + \hat{f}_i^*\hat{c}_i), \tag{39}$$

where $\hat{f}_i$ are the probability amplitudes for the excitation of the normal vibrations $\hat{c}_i^+|0\rangle$. These amplitudes can be found from the equation

$$\hbar\hat{\omega}_i|\hat{f}_i|^2 = [\hbar\omega_1|f_1|^2(\hbar^2\hat{\omega}_i^2 - \hbar^2\omega_2^2) \tag{40}$$
$$+ \hbar\omega_2|f_2|^2(\hbar^2\hat{\omega}_i^2 - \hbar^2\omega_1^2)$$
$$+ 4\varkappa\hbar\omega_1|f_1|^2\hbar\omega_2|f_2|^2]/(2\hbar^2\hat{\omega}_i^2 - \hbar^2\omega_1^2 - \hbar^2\omega_2^2)$$
$$(i = 1, 2).$$

Finally, the relations

$$|X_{i1}|^2 - |Y_{i1}|^2 = \frac{\hbar^2\hat{\omega}_i^2 - \hbar^2\omega_2^2}{2\hbar^2\hat{\omega}_i^2 - \hbar^2\omega_1^2 - \hbar^2\omega_2^2}, \tag{41}$$

$$|X_{i2}|^2 - |Y_{i2}|^2 = \frac{\hbar^2\hat{\omega}_i^2 - \hbar^2\omega_1^2}{2\hbar^2\hat{\omega}_i^2 - \hbar^2\omega_1^2 - \hbar^2\omega_2^2}$$

specify the contribution of type-1 and type-2 configurations to the dipole states $\hat{c}_i^+|0\rangle$ $(i = 1, 2)$.

3.3. Generalization to the Case of Deformed Nuclei

In a spherical nucleus, normal dipole vibrations in three mutually orthogonal directions are degenerate in energy. In view of this, we have only considered above vibrations along the x axis. In a deformed spheroidal nucleus, this degeneracy is partly removed. In that case, it is necessary to distinguish between vibrations along the symmetry axis of the nucleus (z axis) and vibrations along an orthogonal direction (say, along the x or the y axis). Each of these types of vibrations is described in precisely the same way as vibrations along the x axis of a spherical nucleus (see Subsection 3.2). It is only necessary to employ, in Eqs. (18), (19), and (22), the single-particle states $|\alpha\rangle$ and $|\beta\rangle$ of the deformed single-particle potential and to take into account the effect of deformation on the oscillator frequencies (20) of single-particle excitations—that is, to multiply the quantities $\hbar\omega_1^{(0)}$ and $\hbar\omega_2^{(0)}$ by the factor $\sqrt{1 - 4\delta'/3}$ (by δ', we mean here the deformation parameter that was introduced in [15]) for longitudinal vibrations (vibrations along the z axis) or by the factor $\sqrt{1 + 2\delta'/3}$ for transverse vibrations (vibrations along the x and y axes).

Relation (35) can now be recast into the form

$$\frac{\hbar\omega_2^{||}}{\hbar\omega_1^{||}} \approx \frac{\hbar\omega_2^{\perp}}{\hbar\omega_1^{\perp}} \approx \left(\frac{A}{A_{\text{core}}}\right)^{1/3}, \tag{42}$$

where $\hbar\omega_1^{||}$ and $\hbar\omega_2^{||}$ are the energies of, respectively, type-1 and type-2 intermediate normal vibrations for the longitudinal mode of a giant dipole resonance, while $\hbar\omega_1^{\perp}$ and $\hbar\omega_2^{\perp}$ are the analogous quantities for its transverse mode [compare with the energies $\hbar\omega_1$ and $\hbar\omega_2$ of the Hamiltonian in (29)].

The equalities in (42) make it possible to reduce the number of parameters varied in describing the structure of a giant resonance in deformed nuclei to three; for these, one can use, for example, the energies $\hbar\omega_1^{||}$ and $\hbar\omega_1^{\perp}$ and the constant $\mathcal{K}_{12}$.

4. APPLICATION TO LIGHT NONMAGIC NUCLEI

The model considered above was used to describe the gross structure of a giant dipole resonance in the ^{12}C, ^{24}Mg, and ^{28}Si nuclei. These are three self-conjugate nonmagic nuclei, for which the effects of both the configuration and the deformation splitting of a giant dipole resonance are of importance.

We employed the following computational scheme. First, the energies and oscillator strengths of normal excitations for longitudinal and transverse dipole vibrations were calculated on the basis of the formalism developed in Section 3. After that, the resulting dipole

resonances, whose number is equal to four with allowance for the degeneracy of vibrations along the x and y axes, were approximated by Lorentzian curves.

Below, we expound on the details of our computational procedure.

4.1. Choice of Single-Particle Potential

In order to calculate the single-particle states $|\alpha\rangle$, we employed the Nilsson spheroidal potential [16], setting its parameters to

$$\hbar\omega_z^{(0)} = 41A^{-1/3}\sqrt{1-\frac{4}{3}\delta'}, \tag{43}$$

$$\hbar\omega_x^{(0)} = \hbar\omega_y^{(0)} = 41A^{-1/3}\sqrt{1+\frac{2}{3}\delta'},$$

$$\delta' = \delta/(1+\frac{2}{3}\delta),$$

where δ is the parameter of the quadrupole deformation of a nucleus,

$$\delta = \frac{3}{4}\frac{Q_0}{Z\langle r^2\rangle}. \tag{44}$$

Here, Q_0 is the internal quadrupole moment and $\langle r^2\rangle$ is the mean-square radius of the nuclear-charge distribution.

For the nuclei considered here, the parameter δ was calculated theoretically by means of the procedure described in [17]. This procedure leads to overestimated values of the parameter δ for light nuclei, since it disregards the effect of nuclear-surface diffuseness on $\langle x^2\rangle$, $\langle y^2\rangle$, and $\langle z^2\rangle$. The value corrected with allowance for this effect can be obtained by the formula

$$\delta_{\rm corr} \approx \delta\frac{1+2\pi^2\eta^2+\frac{2}{15}\pi^4\eta^4}{1+\frac{10}{3}\pi^2\eta^2+\frac{7}{3}\pi^4\eta^4}, \tag{45}$$

where $\eta \equiv a/R_0$, with $a \approx 0.55$ fm and $R_0 \approx 1.07A^{1/3}$ fm being, respectively, the diffuseness parameter of the nuclear surface and the distance between the center of the nucleus and the point at which its density decreases by a factor of 2.

For the ^{12}C, ^{24}Mg, and ^{28}Si nuclei, the eventual values of the parameter δ' proved to be 0.13, 0.28, and 0.15, respectively.

4.2. Varying Model Parameters

We varied the following three parameters: $\hbar\omega_1^{||}$, $\hbar\omega_1^{\perp}$, and $\mathcal{K}_{12}$ (see Subsection 3.3). First, the value of the parameter $\mathcal{K}_{12}$ was fixed, whereupon the energies $\hbar\omega_1^{||}$ and $\hbar\omega_1^{\perp}$ were varied in such a way as to reproduce, in the calculations, the positions of the centroids $E_{\rm dip}^{||}$ and $E_{\rm dip}^{\perp}$ of dipole states for the longitudinal and transverse modes of vibrations. After that, a different value was chosen for the parameter $\mathcal{K}_{12}$, and the procedure was repeated.

The energies $E_{\rm dip}^{||}$ and $E_{\rm dip}^{\perp}$ were calculated with the aid of the relations

$$E_{\rm dip} = \frac{2E_{\rm dip}^{\perp}+E_{\rm dip}^{||}}{3}, \tag{46}$$

$$\frac{E_{\rm dip}^{\perp}}{E_{\rm dip}^{||}} = \sqrt{\frac{\langle z^2\rangle}{\langle x^2\rangle}} = \sqrt{\frac{1+2\delta'/3}{1-4\delta'/3}}.$$

The giant-resonance energy $E_{\rm dip}$, which appears in these relations, was estimated by the formula [18]

$$E_{\rm dip} \approx 86A^{-1/3}\sqrt{\frac{1+\pi^2\eta^2}{1+10\pi^2\eta^2/3+7\pi^4\eta^4/3}}\ \ [\text{MeV}], \tag{47}$$

where the quantity η was defined in (45).

The best agreement with experimental data for the nuclei considered here was obtained at $\mathcal{K}_{12} \approx 25$ MeV. As might have been expected, this value, which characterizes the strength of interaction of different dipole configurations, is rather small in relation to a value of about 100 MeV, which follows from the estimate in (10). In order to assess the sensitivity of calculations to the choice of value for the constant $\mathcal{K}_{12}$, we have performed calculations for the ^{28}Si nucleus, employing various values of this constant. The results are given in Fig. 2.

The intermediate energies $\hbar\omega_1^{||}$ and $\hbar\omega_1^{\perp}$ do not have an independent physical meaning. Nonetheless, it is interesting to note that, in varying the relevant model parameters, they are grouped around values that follow from formulas of the type in (30) if, in estimating the coupling constant for dipole–dipole forces [see Eq. (10)], use is made of a symmetry potential V that faithfully reproduces the position of the giant dipole resonance [compare the results in (14) and (47)]. The root-mean-square distinctions between the two types of estimates of the energies $\hbar\omega_1^{||}$ and $\hbar\omega_1^{\perp}$ are less than 1 MeV. This confirms that the approximations made in the model are physically justified.

4.3. Approximation of Resonance Widths

Our calculations revealed (see Figs. 3–5) that type-1 and type-2 dipole configurations are weakly mixed in light nonmagic nuclei. On the other hand, the damping of vibrations in light nuclei is governed

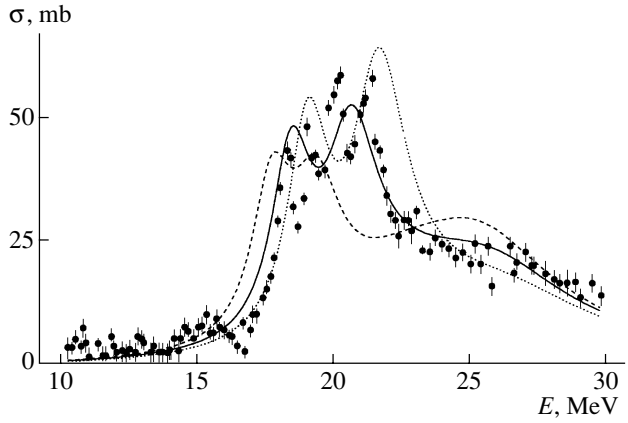

Fig. 2. Results of our calculations for the ^{28}Si nucleus at various values of the parameter $\mathcal{K}_{12}$. Points correspond to the experimental values of the photoabsorption cross section from [19], while the dashed, the solid, and the dotted curve represent the results of the calculations with $\mathcal{K}_{12} = 40$, 25, and 10 MeV, respectively.

by different mechanisms for vibrations of different types: these are predominantly the emission of an excited particle from a nucleus for type-1 vibrations and the spreading of a collective mode over a large number of noncollective nuclear states interacting with this mode for type-2 vibrations. It follows that, depending on the type of dominant configurations, the normal excitation $\hat{c}_i^+|0\rangle$ $(i = 1{-}4)$ of a light nucleus may be assigned either the emission width $\Gamma^{\uparrow}(\hbar\hat{\omega}_i)$ or the spreading width $\Gamma^{\downarrow}(\hbar\hat{\omega}_i)$.

For $16 \lesssim A \lesssim 240$ nuclei, the total width of a giant dipole resonance can be approximated by the formula [18]

$$\Gamma(E) \approx \frac{0.0293}{1+\pi^2\eta^2}\left[1 - 3\eta\frac{1+(\pi^2/3)\eta^2}{1+\pi^2\eta^2}\right]E^2, \quad (48)$$

where, by η, we imply the same quantity as in Eqs. (45) and (47).

As is well known, the approximate relation $\Gamma \approx \Gamma^{\uparrow} + \Gamma^{\downarrow}$ holds. We introduce the notation $\nu \equiv \Gamma^{\uparrow}/\Gamma$. We then find that $\Gamma^{\uparrow}(E) \approx \nu\Gamma(E)$ and $\Gamma^{\downarrow}(E) \approx (1-\nu)\Gamma(E)$, where $\Gamma(E)$ is given by expression (48).

In the present study, the dipole-resonance widths were estimated by using the values of $\nu = 0.6$, 0.4, and 0.3 for ^{12}C, ^{24}Mg, and ^{28}Si, respectively. In selecting these values, we have taken into account the experimental trend toward a decrease in the contribution to $\Gamma(E)$ from the emission width with increasing mass number A.

5. DISCUSSION OF THE RESULTS

The basic results of our calculations are given in Figs. 3–5.

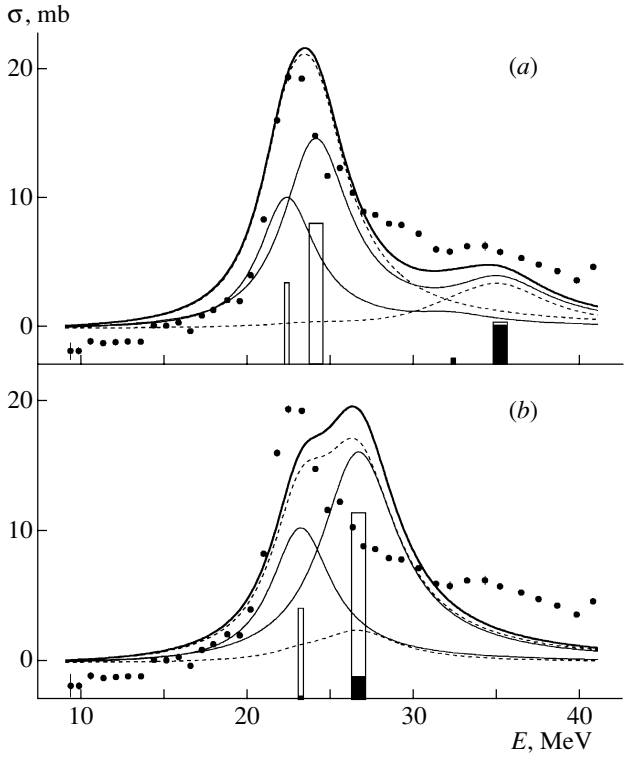

Fig. 3. Structure of the giant dipole resonance in the ^{12}C nucleus according to the calculations (*a*) with and (*b*) without allowance for the configuration splitting of the giant dipole resonance. Points represent the experimental values of the photoabsorption cross section from [20]. The description of the curves and histograms presented in this figure and in Figs. 4 and 5 below is given in the main body of the text.

Each of these figures consists of two panels (*a*, *b*). In the panels carrying the label *a*, the experimental values of the photoabsorption cross section (points) are contrasted against the results of the calculation based on the model described above (curves and histograms). The panels labeled with *b* display the results of the calculation that was performed under the assumption that a giant dipole resonance is split only into deformation modes whose energies are determined by relations (46) and (47). The thick solid curves represent the theoretical values of the photoabsorption cross section. In each case, two thin solid curves show the contributions to this cross section that come from, respectively, longitudinal and transverse dipole vibrations. Two dashed curves represent the configuration splitting of the giant dipole resonance. The histograms depict the distributions of the oscillator strengths of dipole states (in arbitrary units), the narrow and broad rectangles corresponding to, respectively, longitudinal and transverse dipole modes. The open (closed) part of a rectangle represents the contribution to a given state from type-1 (type-2) configurations.

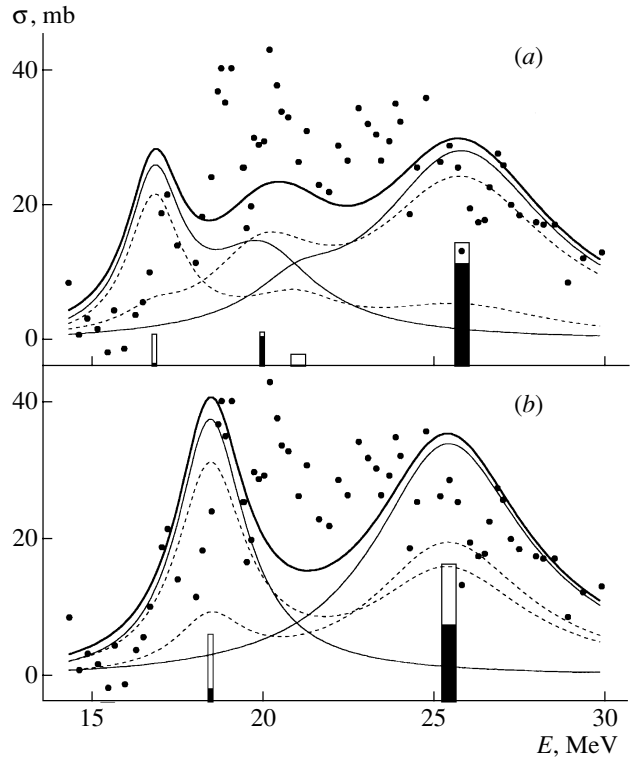

Fig. 4. Structure of the giant dipole resonance in the ^{24}Mg nucleus according to the calculations (*a*) with and (*b*) without allowance for the configuration splitting of the giant dipole resonance. Points represent the experimental values of the photoabsorption cross section from [21].

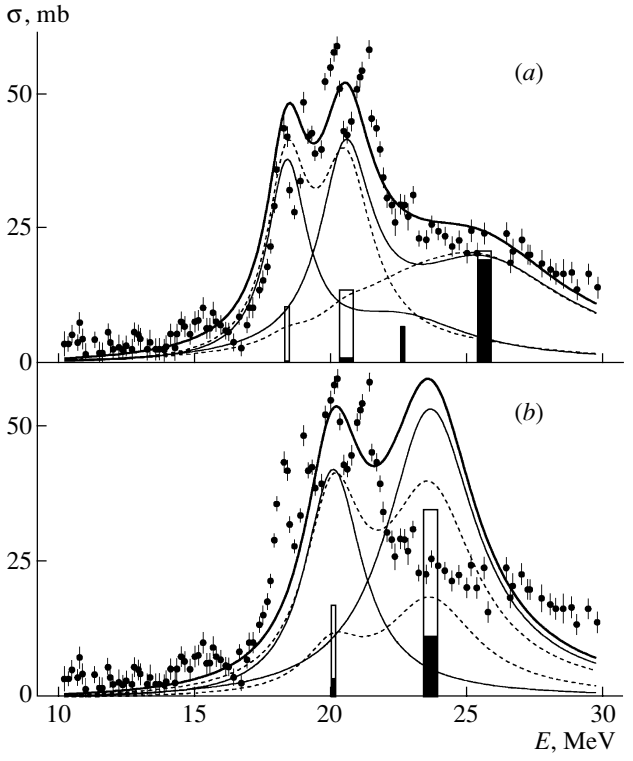

Fig. 5. Structure of the giant dipole resonance in the ^{28}Si nucleus according to the calculations (*a*) with and (*b*) without allowance for the configuration splitting of the giant dipole resonance. Points represent the experimental values of the photoabsorption cross section from [19].

Figures 3–5 clearly demonstrate that the configuration splitting of a giant dipole resonance plays a very important role in the formation of its gross structure in light nonmagic nuclei. Indeed, experimental data for any of the nuclei considered here cannot be adequately reproduced without taking this phenomenon into account (compare panels *a* and *b*). The effect of the configuration splitting of a giant dipole resonance is especially pronounced in nuclei characterized by a small deformation (^{12}C, ^{28}Si). However, it can easily be singled out in the structure of the cross section for photoabsorption on the strongly deformed nucleus of ^{24}Mg as well (see Fig. 4).

At the same time, the formation of the gross structure of a giant dipole resonance is also greatly affected by the deformation splitting of a giant dipole resonance (even in weakly deformed nuclei). This becomes obvious in comparing the rectangles of the histograms with the special features of the experimental photoabsorption cross sections.

In the literature, the high-energy tails of the cross sections for photoabsorption on nonmagic $1p$- and $2d2s$-shell nuclei (see the notation in Section 2) are usually associated with single-particle excitations from an inner filled shell [10]. The present calculation basically confirms this point of view, but with one important qualification: the main contribution to the high-energy region of a giant dipole resonance is formed by a collective mode that emerges from single-particle excitations under the effect of residual forces rather than by individual type-2 $1p1h$ configurations. Indeed, the residual interaction shifts this state (see extreme right rectangles in Figs. 3–5) by aproximately 8 MeV upward with respect to the energy position of type-2 single-particle transitions.

From the histograms presented in Figs. 3–5, it can be seen that type-1 and type-2 dipole configurations interact with each other rather weakly. This implies that normal vibrational modes are formed owing primarily to interactions of configurations belonging to the same type.

Finally, it should be noted that the main strength of dipole transitions from an inner shell to the valence shell (that is, of type-2 transitions) is associated with the transverse mode of dipole vibrations.

6. CONCLUSIONS

The model developed in the present study has been used to clarify the global features of the photoabsorp-

tion cross section in the mass range $10 < A < 40$, which is one of the most complicated for a theoretical description. The calculations performed on the basis of this model have enabled us to draw the following conclusions:

(i) In describing the gross structure of a giant dipole resonance in light nonmagic nuclei, it is necessary to take simultaneously into account the configuration and the deformation splitting of a giant resonance.

(ii) The configuration splitting of a giant dipole resonance arises because of a considerable difference of the mean energies of single-particle $E1$ transitions between a filled inner shell and the valence shell, on one hand, and the mean energies of such transitions between the valence shell and an empty outer shell, on the other hand. Nonetheless, the configuration maxima of a giant dipole resonance have a collective rather than a single-particle nature.

However, the proposed model is applicable not only to light nuclei. It can easily be understood that the representation of the vibrational Hamiltonian in the form (29) featuring the free parameters $\hbar\omega_1$, $\hbar\omega_2$, and $\mathcal{K}_{12} = \varkappa_{12}A^{5/3}$ is of a rather universal character and can be used in describing the gross structure of a giant dipole resonance both in light and in medium-mass and heavy nuclei. From Fig. 1, it can be seen that the curves representing the energies of nucleon knockout from different principal shells become parallel to one another as the mass number A grows. This suggests that, at large values of A, outer nucleons have but a slight effect on the energies of dipole transitions from inner shells. Therefore, relation (35) can also be extended to the region of medium-mass and heavy nuclei. In a forthcoming publication, we will present our theoretical results that will confirm the possibility of applying the model developed here to describing the gross structure of a giant dipole resonance over a very broad mass region—as a matter of fact, a region covering all cases where the concept of nucleon motion in a mean nuclear field is meaningful ($A \gtrsim 10$).

ACKNOWLEDGMENTS

We are grateful to V.V. Varlamov, M.E. Stepanov, V.V. Chesnokov, S.P. Likhachev, and E.N. Golovach (Institute of Nuclear Physics at Moscow State University) for stimulating discussions and assistance in this work.

REFERENCES

1. B. L. Berman, At. Data Nucl. Data Tables **15**, 319 (1975).
2. B. Goulard and S. Fallieros, Can. J. Phys. **45**, 3221 (1967).
3. V. M. Novikov and M. G. Urin, Yad. Fiz. **3**, 419 (1966) [Sov. J. Nucl. Phys. **3**, 302 (1966)].
4. D. F. Petersen and C. J. Veje, Phys. Lett. B **24B**, 449 (1967).
5. H. Ejiri and K. Ikeda, Phys. Rev. **176**, 1277 (1968).
6. M. Danos, Bull. Am. Phys. Soc. **1**, 135 (1956); Nucl. Phys. **5**, 23 (1958).
7. K. Okamoto, Prog. Theor. Phys. **15**, 75 (1956); Phys. Rev. **110**, 143 (1958).
8. V. G. Neudatchin and V. G. Shevchenko, Phys. Lett. **12**, 18 (1964).
9. R. A. Eramzhyan, B. S. Ishkhanov, I. M. Kapitonov, *et al.*, Phys. Rep. **136**, 230 (1986).
10. B. S. Ishkhanov, N. P. Yudin, and R. A. Éramzhyan, Fiz. Élem. Chastits At. Yadra **31**, 313 (2000) [Phys. Part. Nucl. **31**, 149 (2000)].
11. B. S. Ishkhanov, I. M. Kapitonov, V. G. Neudachin, *et al.*, Fiz. Élem. Chastits At. Yadra **31**, 1343 (2000).
12. A. Bohr and B. Mottelson, *Nuclear Structure*, Vol. 2: *Nuclear Deformations* (W. A. Benjamin, New York; Amsterdam, 1975; Mir, Moscow, 1977).
13. W. H. Bassichis and F. Scheck, Phys. Rev. **145**, 771 (1966).
14. V. M. Kolomiets *et al.*, Fiz. Élem. Chastits At. Yadra **3**, 392 (1972) [Sov. J. Part. Nucl. **3**, 204 (1972)].
15. S. G. Nilsson, K. Dan. Vidensk. Selsk. Mat.–Fys. Medd. **29**, No. 16 (1955).
16. C. Gustafson *et al.*, Ark. Fys. **36**, 613 (1967).
17. B. S. Ishkhanov and V. N. Orlin, Yad. Fiz. **65**, 1858 (2002) [Phys. At. Nucl. **65**, 1809 (2002)].
18. B. S. Ishkhanov and V. N. Orlin, Yad. Fiz. **66**, 688 (2003) [Phys. At. Nucl. **66**, 659 (2003)].
19. N. Bezic, D. Jamnik, G. Kernel, *et al.*, Nucl. Phys. A **117**, 124 (1968).
20. J. Ahrens *et al.*, Nucl. Phys. A **251**, 479 (1975).
21. B. S. Dolbilkin, V. I. Korin, L. E. Lazareva, *et al.*, Nucl. Phys. **72**, 137 (1965).

Translated by A. Isaakyan

Physics of Atomic Nuclei, Vol. 66, No. 7, 2003, pp. 1239–1241. Translated from Yadernaya Fizika, Vol. 66, No. 7, 2003, pp. 1279–1281.

NUCLEI
Theory

Charge-Exchange (p,n) Reaction on ^{48}Ca as a Means for Determining the Isospin Structure of the Mean Nuclear Spin–Orbit Field

V. I. Isakov*

Institute of Nuclear Physics, Russian Academy of Sciences, Gatchina, 188300 Russia

Received April 3, 2002

Abstract—The isotopic structure found previously in spin–orbit splitting by studying the spectra of heavy nuclei close to doubly magic ones is tested in polarization effects that arise in charge-exchange (p,n) reactions between the isobaric states of $A = 48$ nuclei. © *2003 MAIK "Nauka/Interperiodica".*

On the basis of an analysis of available experimental data for nuclei close to the doubly magic nuclides of ^{208}Pb and ^{132}Sn, it was shown in [1], by invoking various theoretical approaches, that neutron spin–orbit splitting in $N > Z$ nuclei is stronger, for identical orbitals, than the corresponding splitting for protons. It was found in [1], among other things, that various theoretical models lead to a stronger splitting for neutrons than for protons in the case of the $1d$ and $1p$ orbitals in ^{48}Ca, where experimental data on the energies of the corresponding single-particle levels are incomplete (in particular, because of their strong fragmentation). Also, it was revealed in [1] that, in terms of a phenomenological nuclear mean-field potential, the experimental values of "true" energies as determined for single-particle levels in nuclei with allowance for configuration mixing (averaged over the values of single-particle spectroscopic factors—see [2]), including spin–orbit splitting, can be well described by the potential

$$\hat{U}(r,\hat{\sigma},\tau_3) = V_0\left(1+\frac{1}{2}\beta\frac{N-Z}{A}\tau_3\right)f(r) \quad (1)$$
$$+ V_{ls}\left(1+\frac{1}{2}\beta_{ls}\frac{N-Z}{A}\tau_3\right)\frac{1}{r}\frac{df}{dr}\hat{\mathbf{l}}\cdot\hat{\mathbf{s}} + \frac{1+\tau_3}{2}U_{\rm Coul},$$
$$f(r) = \left[1+\exp\left(\frac{r-R}{a}\right)\right]^{-1}, \quad R = r_0A^{1/3},$$

where $V_0 = -51.5$ MeV; $r_0 = 1.27$ fm; $V_{ls} = 33.2$ MeV fm^2; $a \approx 0.6$ fm; $\beta = 1.39$; $\beta_{ls} \sim -0.6$; and $\tau_3 = -1$ for neutrons, and $\tau_3 = +1$ for protons.

Introducing the quantities $t_3 = -\tau_3/2$ and $T_3 = (N-Z)/2$ and making, as in [3], the substitution $T_3 \cdot t_3 \to \hat{\mathbf{T}}\cdot\hat{\mathbf{t}}$, where $\hat{\mathbf{T}}$ and $\hat{\mathbf{t}}$ are the isospin vector operators for the core and a nucleon, respectively, we obtain the nuclear component of the potential (1) in an isotopic-invariant form (Lane potential) that is appropriate for describing the processes that are both diagonal and nondiagonal in t_3 [single-particle spectra and elastic scattering in the first case and (p,n) reactions leading to the excitation of isoanalog states in the second case]:

$$\hat{U} = V_0\left(1-2\beta\frac{\hat{\mathbf{T}}\cdot\hat{\mathbf{t}}}{A}\right)f(r) \quad (2)$$
$$+ V_{ls}\left(1-2\beta_{ls}\frac{\hat{\mathbf{T}}\cdot\hat{\mathbf{t}}}{A}\right)\frac{1}{r}\frac{df}{dr}\hat{\mathbf{l}}\cdot\hat{\mathbf{s}}.$$

The spin–orbit term in the potential leads to polarization phenomena in scattering. From (2), it can be seen that, whereas polarization in elastic scattering is determined by a combination of parameters in the form

$$V_{ls}\left(1-\beta_{ls}\frac{N-Z}{A}t_3\right) \approx V_{ls},$$

similar effects in charge-exchange reactions involving the excitation of isoanalog states depend on $\beta_{ls}V_{ls}$ and are therefore controlled by the isovector parameter β_{ls} of the mean spin–orbit field, because the parameter V_{ls} is well known. Thus, all of the conclusions drawn in [1] on β_{ls} and based on the description of nuclear spectra can be verified by using the data on quasielastic (p,n) scattering. The corresponding information about polarization effects observed for nuclei in the vicinity of ^{48}Ca can be found in [4], where the reaction ^{48}Ca$(p,n)^{48}$Sc leading to the excitation of the 0^+ isoanalog state at 6.67 MeV was investigated with polarized protons, but the theoretical analysis was performed there in terms of a microscopic approach to describing the nuclear structure and in terms of nucleon–nucleon amplitudes for describing the scattering process (distorted-wave impulse approximation). Below, we perform our analysis within

*e-mail: visakov@thd.pnpi.spb.ru

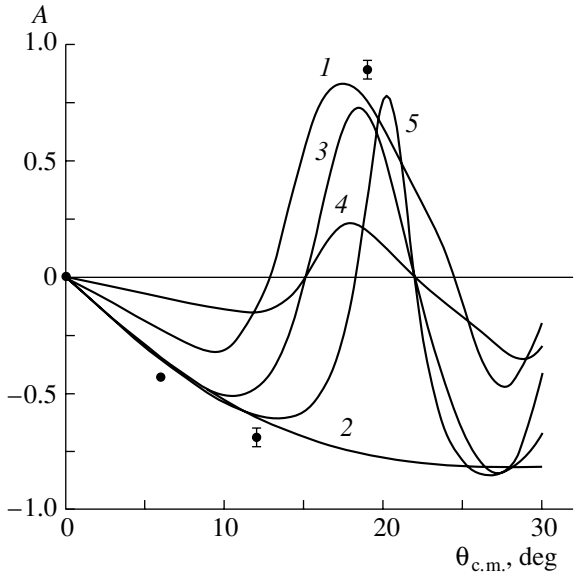

Fig. 1. Experimental data on the analyzing power from [4] (points) and results of various calculations (curves). Curve *1* corresponds to the microscopic calculation in the distorted-wave impulse approximation from [4]. Curves *2–5* were calculated in this study with (*2*) $\alpha = 1$ (volume absorption), $V_{ls} = 33.2$ MeV fm^2, and $\beta_{ls} = -0.6$; (*3*) $\alpha = 0$ (surface absorption), $V_{ls} = 33.2$ MeV fm^2, and $\beta_{ls} = -0.6$; (*4*) $\alpha = 0$, $\beta_{ls} = -0.6$, and an energy-dependent parameter V_{ls}; and (*5*) $\alpha = 0.5$, all other parameters being set to the same values as those for curves *2* and *3*.

the Lane model, relying on the mean-field parameters determined in [1]; in addition, we employ the Born approximation to describe the scattering process. In describing (p, n) reactions, Gosset *et al.* [5] also considered polarization effects in the Born approximation.

It is well known that, in the Born approximation, there are no polarization effects caused by a spin–orbit potential [6, 7] if use is made of a real-valued central potential. Therefore, an imaginary part (absorption) must be introduced in the optical potential in order to describe such effects. The energy dependence must also be taken into account in the real and imaginary parts of the potential, since the incident energy was quite high ($E = 134$ MeV) in [4]. In [8, 9], V_0 was parametrized as follows: $V_0 = V_0'(1 - 0.0058E)$, where $V_0' = -52$ MeV, which is very close to the value of -51.5 MeV obtained in [1]. In this case, the form proposed in [8] for the corresponding absorptive term in the optical potential is $iW_V f(r)$, where W_V (MeV) $= -3.3(1 + 0.03E)$. Surface absorption is usually taken into account via the term $iW_S(df/dr)$. For low momentum transfers (small angles), the two versions of absorption must provide an identical description of the scattering process. In the case of $a \ll R$, this leads to $W_S \approx -(R/3)W_V$. For the absorptive term, we therefore use the expression

$$iW_V\left[\alpha - (1-\alpha)\frac{R}{3}\frac{d}{dr}\right]f(r), \qquad (3)$$

where $0 \le \alpha \le 1$. This results in polarization effects that are independent of α for small scattering angles, but which are strongly dependent on α for high momentum transfers. Thus, the scattering process, along with polarization phenomena, is described here in terms of the optical potential in the form (2), where

$$V_0 \to -51.5(1 - 0.0058E) \qquad (4)$$
$$- i3.3 \cdot (1 + 0.03E)\left[\alpha - (1-\alpha)\frac{R}{3}\frac{d}{dr}\right],$$

identical energy dependences being assumed for the isoscalar and isovector components of the central nuclear potential.

The results of the present calculations for the analyzing power A in the (p, n) reaction occurring on ^{48}Ca and leading to the excitation of an isoanalog state,

$$A_{\text{theor}} = \frac{d\sigma_{\uparrow\uparrow}/d\omega - d\sigma_{\uparrow\downarrow}/d\omega}{d\sigma_{\uparrow\uparrow}/d\omega + d\sigma_{\uparrow\downarrow}/d\omega}, \quad |A| \le 1, \qquad (5)$$

are displayed in the figure, along with experimental data and the results of the microscopic calculations from [4]. The quantities $\sigma_{\uparrow\uparrow}$ and $\sigma_{\uparrow\downarrow}$ are the reaction cross sections for the cases where the proton polarization vector ε is, respectively, parallel and antiparallel to the vector $[\mathbf{k}_i \times \mathbf{k}_f]$. It can be seen that, in the case of surface absorption ($\alpha = 0$), our calculations in which we use the corresponding spin–orbit parameters from [1] agree well with experimental data up to large values of the scattering angle. At the same time, the description of the analyzing power becomes unsatisfactory upon introducing, in the spin–orbit parameter V_{ls}, an energy dependence similar to that for the central potential.

For the reaction ^{48}Ca(p, n) ^{48}Sc*(IAS) on unpolarized protons, where the abbreviation IAS stands for an isoanalog state, our calculations with $\alpha = 0$ yield a value of about 7.7 mb/sr for the differential cross section at zero angle, this cross section being a very slowly increasing function of the parameter α. The cross section decreases sharply with increasing scattering angle and exhibits some structure at $\Theta_{\text{c.m.}} \approx 20°$. The above value can be compared with the experimental result obtained in [10] for the differential cross section at zero angle (about 7 mb/sr) and with the theoretical result obtained in [10] on the basis of microscopic calculations (about 7.5 mb/sr).

The following conclusions can be drawn from the above results:

(i) Experimental data on the isotopic structure of spin–orbit splitting in nuclei are compatible with data on polarization effects in quasielastic (p, n) scattering. The mean-field parameters determined in [1], which made it possible to reproduce proton and neutron spin–orbit splitting in nuclei near ^{132}Sn and ^{208}Pb—in particular, the parameter β_{ls}—also faithfully reproduce experimental data for quasielastic (p, n) scattering on ^{48}Ca.

(ii) A good description of the analyzing power at high energies of incident protons with the values taken for spin–orbit parameters from low-energy spectroscopy is compatible with the assumption that these parameters of the optical model are weakly dependent on energy .

(iii) A satisfactory description of the cross section for the relevant (p, n) reaction involving the excitation of an isoanalog state indicates that the energy dependence of the isovector terms in the central nuclear potential was parametrized correctly.

(iv) The present results unambiguously corroborate the presence of a significant surface component $[(1 - \alpha) \gtrsim 0.5]$ in the imaginary part of the optical potential.

In conclusion, we note that, although spin–orbit interaction makes a relatively small contribution to the total mean-field potential for nuclear single-particle levels, it is of paramount importance for the formation of the nuclear shell structure. For example, the density of single-particle levels is high in superheavy nuclei; therefore, their small shifts due to refining the isospin dependence of the spin–orbit field can be decisive in determining shell corrections that control the stability of such nuclei. A correct inclusion of the isotopic dependence of spin–orbit splitting can also considerably affect the predictions for nucleon drip lines in nuclei characterized by an extremely high neutron excess or an extremely high neutron deficit.

ACKNOWLEDGMENTS

I am grateful to B. Fogelberg, H. Mach, V.E. Bunakov, and K.A. Mezilev for numerous stimulating discussions on the questions considered in this study—in particular, those concerning the problem of spin–orbit splitting in nuclei.

This work was supported by the Russian Foundation for Basic Research (project no. 00-15-96610).

REFERENCES

1. V. I. Isakov, K. I. Erokhina, H. Mach, *et al.*, Eur. Phys. J. A **14**, 29 (2002); nucl-th/0202044.
2. M. Baranger, Nucl. Phys. A **149**, 225 (1970).
3. A. M. Lane, Nucl. Phys. **35**, 676 (1962).
4. B. D. Anderson, T. Chittrakarn, A. R. Baldwin, *et al.*, Phys. Rev. C **34**, 422 (1986).
5. J. Gosset, B. Mayer, and J. L. Escudie, Phys. Rev. C **14**, 878 (1976).
6. L. D. Landau and E. M. Lifshitz, *Quantum Mechanics: Non-Relativistic Theory* (Nauka, Moscow, 1989, 4th ed.; Pergamon, Oxford, 1977, 3rd ed.).
7. A. S. Davydov, *Theory of the Nucleus* (Fizmatgiz, Moscow, 1958).
8. A. G. Sitenko, *Theory of Nuclear Reactions* (Énergoatomizdat, Moscow, 1983).
9. A. Bohr and B. Mottelson, *Nuclear Structure,* Vol. 1: *Single-Particle Motion* (Benjamin, New York, 1969; Mir, Moscow, 1971).
10. B. D. Anderson, T. Chittrakarn, A. R. Baldwin, *et al.*, Phys. Rev. C **31**, 1147 (1985).

Translated by V. Bukhanov

Physics of Atomic Nuclei, Vol. 66, No. 7, 2003, pp. 1242–1251. From Yadernaya Fizika, Vol. 66, No. 7, 2003, pp. 1282–1291.

NUCLEI
Theory

Thermal Multifragmentation of Hot Nuclei and Liquid–Fog Phase Transition*

V. A. Karnaukhov[1)], S. P. Avdeyev[1)], E. V. Duginova[1)], L. A. Petrov[†1)], V. K. Rodionov[1)], H. Oeschler[2)]***, A. Budzanowski[3)], W. Karcz[3)], M. Janicki[3)], O. V. Bochkarev[4)], E. A. Kuzmin[4)], L. V. Chulkov[4)], E. Norbeck[5)], and A. S. Botvina[6)]**

Received April 30, 2002; in final form, October 4, 2002

Abstract—Multiple emission of intermediate-mass fragments (IMF) in the collisions of protons (up to 8.1 GeV), ^{4}He (4 and 14.6 GeV), and ^{12}C (22.4 GeV) on Au has been studied with the 4π setup FASA. In all the cases, thermal multifragmentation of the hot and diluted target spectator takes place. The fragment multiplicity and charge distributions are well described by the combined model including the modified intranuclear cascade followed by the statistical multibody decay of the hot system. IMF–IMF-correlation study supports this picture, giving a very short time scale of the process ($\leq$70 fm/c). This decay process can be interpreted as the first-order nuclear "liquid–fog" phase transition inside the spinodal region. The evolution of the mechanism of thermal multifragmentation with increasing projectile mass was investigated. The onset of the radial collective flow was observed for heavier projectiles. The analysis reveals information on the fragment space distribution inside the breakup volume: heavier IMFs are formed predominantly in the interior of the fragmenting nucleus possibly due to the density gradient.

1. INTRODUCTION

Study of the decay properties of the hot nuclei is one of the most challenging topics of modern nuclear physics. The excitation energy of the hot nuclei (500–700 MeV) is comparable with the total binding energy. They disintegrate via a new multibody decay mode—thermal multifragmentation. This process is characterized by the copious emission of intermediate mass fragments that are heavier than alpha particles but lighter than fission fragments (IMF, $2 < Z \leq 20$). Such multibody disintegration is not exotic but the main decay channel of a very hot nuclear system.

The development of this field has been strongly stimulated by an idea that this process is related to the nuclear liquid–gas phase transition. One of the first nuclear models, suggested by N. Bohr, C. von Weizsäcker, and Ya.I. Frenkel 65 years ago, is the liquid-drop model, which has been successfully used up to now. The liquid–gas phase transition in nuclear matter was predicted much later [1–3] on the basis of the similarity between van der Waals and nucleon–nucleon interactions. In both cases, the attraction between particles is replaced by repulsion at a small interaction range. As a result, the equations of state are similar for such different systems. This is well seen in the phase diagram (Fig. 1) taken from [2]. The figure shows the isotherms for pressure as a function of volume calculated for the van der Waals system and the Fermi gas of nucleons interacting through Skyrme forces. The scales are the same for both cases due to the use of dimensionless variables: pressure, volume, and temperature are given as ratios to the critical values P_c, $V_c = 1/\rho_c$ (ρ_c is the critical density), and T_c. The very steep part of the isotherms (on the left) corresponds to the liquid phase. The gas phase is illustrated by the right parts of the isotherms, where pressure changes smoothly with increasing volume. A point of particular interest is the part of the diagram below the hatched line, where the isotherms correspond to negative compressibility. The density here is significantly reduced as compared to the liquid phase. This is a spinodal region characterized by the phase instability. One can imagine that a hot

*This article was submitted by the authors in English.
†Deceased.
1)Joint Institute for Nuclear Research, Dubna, Moscow oblast, 141980 Russia.
2)Institut für Kernphysik, Technische Universität Darmstadt, Germany.
3)Institute of Nuclear Physics, Cracow, Poland.
4)Russian Research Centre Kurchatov Institute, pl. Kurchatova 1, Moscow, 123182 Russia.
5)University of Iowa, Iowa City, IA, USA.
6)GSI, Darmstadt, Germany.
**e-mail: karna@nusun.jinr.ru
***e-mail: h.oeschler@gsi.de

nucleus expands due to thermal pressure and enters the metastable region. Due to density fluctuations, a homogeneous system converts into the mixed-phase state, consisting of droplets (IMFs) surrounded by nuclear gas (nucleons and light composite particles). In fact, the final state of this transition is a nuclear fog [3].

The neutrons fly away with energies corresponding to the system temperature (5–7 MeV), while the charged particles are additionally accelerated in the Coulomb field of the system. Disintegration time is determined by the time scale of the thermodynamic fluctuations and is expected to be very short. This is a scenario of nuclear multifragmentation as the spinodal decomposition, considered in a number of theoretical and experimental papers (see, for example, [4–10] and review papers [11, 12]). This picture was proved experimentally with a significant contribution from the FASA collaboration; a short review of the results obtained is presented below.

As for the critical temperature for the liquid–gas phase transition T_c (at which the surface tension vanishes), its value is not known definitely . There are many theoretical calculations of T_c for finite nuclei. In [1, 2], the calculation is done using a Skyrme effective interaction and thermal Hartree–Fock theory. The values of T_c were found to be 18.1 MeV [1] and in the range 8.1–20.5 MeV [2] depending on the chosen Skyrme interaction parameters. There are not yet reliable experimental data for T_c, despite the claims made in a number of papers. The latest of them is [13], where it is stated that $T_c = 6.7 \pm 0.2$ MeV. We return to the discussion of this point in Section 6.

2. HOW TO PRODUCE AND STUDY HOT NUCLEI

An effective way to produce hot nuclei is collisions of heavy ions with energies up to hundreds of MeV per nucleon. Around a dozen sophisticated experimental devices were created to study nuclear multifragmentation with heavy-ion beams. But in this case, heating of nuclei is accompanied by compression, strong rotation, and shape distortion, which may essentially influence the decay properties of hot nuclei.

Investigation of dynamic effects caused by excitation of collective (or "mechanical") degrees of freedom is interesting in itself, but there is a great problem of disentangling all these effects to get information on the thermodynamic properties of a hot nuclear system. One gains simplicity and the picture becomes clearer when light relativistic projectiles (first of all, protons, antiprotons, pions) are used. In contrast to heavy-ion collisions, fragments are emitted only by the source—the slowly moving target spectator. Its excitation energy is almost entirely thermal. Light relativistic projectiles therefore provide a unique possibility of investigating "thermal multifragmentation," which was realized in the FASA project.

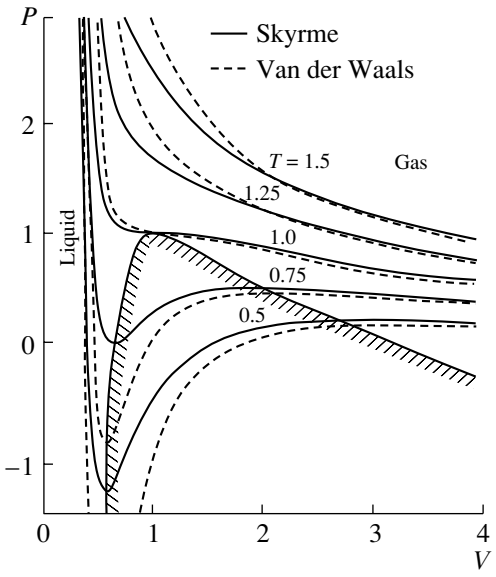

Fig. 1. Comparison of the equation of state for a van der Waals gas and for a nuclear system interacting through a Skyrme force (relative units are used).

To study multifragmentation with the beams of the Dubna synchrophasotron, a 4π setup FASA was created [14]. The device consists of two main parts:

(i) Five dE–E telescopes (at $\theta = 24°$, 68°, 87°, 112°, and 156° with the beam direction), which serve as triggers for the readout of the system allowing the measurement of the fragment charge and energy distributions. Ionization chambers and Si(Au) detectors are used as dE and E counters, respectively.

(ii) A fragment multiplicity detector (FMD) including 64 CsI(Tl) counters (with a scintillator thickness averaging 35 mg/cm^2), which cover 89% of 4π. The FMD gives the number of IMFs in the event and their angular distribution.

A self-supporting Au target 1.0 mg/cm^2 thick is located at the center of the FASA vacuum chamber ($\sim$1 m in diameter).

The following beams were used: protons at energies of 2.16, 3.6, and 8.1 GeV [15]; ^{4}He at 4 and 14.6 GeV; and ^{12}C at 22.4 GeV [16]. The mean beam intensity was around 7×10^8 p/spill for protons and helium and 1×10^8 p/spill for carbon projectiles (spill length 300 ms, spill period 10 s).

In recent years, FASA has been significantly upgraded, and a new counter array consisting of 25 dE–E telescopes was developed. At present, the total number of detectors in FASA is 129, supplied with 193 electronic channels.

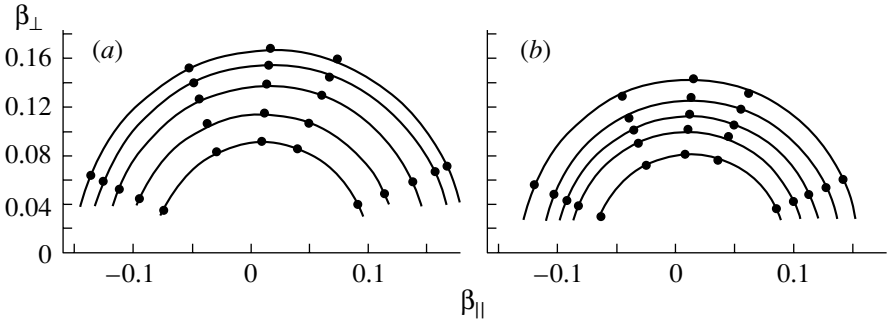

Fig. 2. Transverse vs. longitudinal velocity plot for carbon isotopes produced in ^{4}He (14.6 GeV) (*a*) and ^{12}C (22.4 GeV) (*b*) collisions with Au target. Circles are drawn through points of equal invariant cross section corresponding to isotropic emission in the moving source frame.

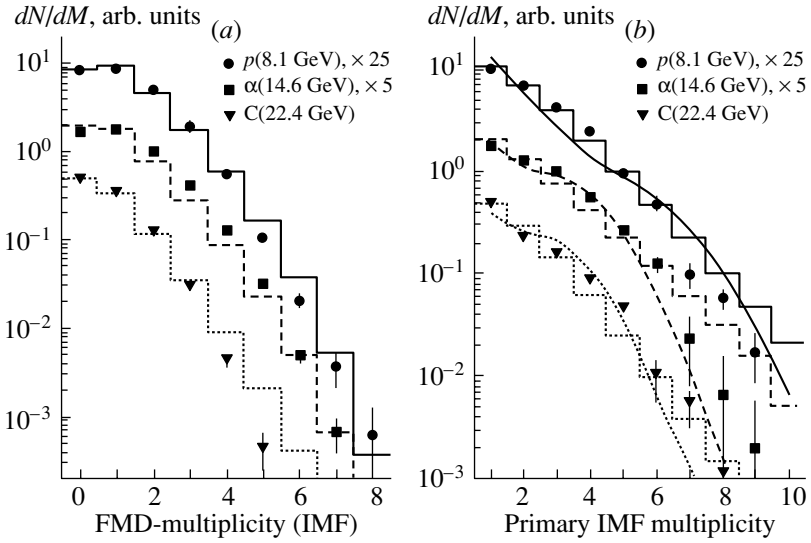

Fig. 3. (*a*) Associated IMF-multiplicity distributions and fits with Fermi functions (folded with the experimental filter) for p + Au collisions at 8.1 GeV, ^{4}He + Au at 14.6 GeV, and ^{12}C + Au at 22.4 GeV. (*b*) Symbols represent directly reconstructed primary IMF distributions; histograms are the Fermi distributions used to fit the data in the left part. The curves are calculated with the combined model INC + Expansion + SMM.

3. EVIDENCE FOR THERMALIZATION OF THE TARGET SPECTATOR AT BREAKUP

Let us consider a very important point of thermalization of the system at breakup. To check whether this state is close to thermal equilibrium, plots were composed for the fragment yields in terms of the longitudinal versus transverse velocity components. They look similar for all collisions investigated. Figure 2 shows such plots for ^{4}He + Au and ^{12}C + Au interactions [16]. The symbols correspond to the constant invariant cross sections taken for emitted carbon fragments. The lines connecting the experimental points form circles demonstrating isotropic emission in the frame of the moving source. This indicates that the fragment emission proceeds from a thermalized state. The center positions of circles determine the source velocities, which are found to be in the range of (0.01–0.02) c. The IMF angular distribution in the laboratory system exhibits a forward peak caused by the source motion.

Another finding in favor of the thermal equilibrium is that the fragment kinetic energy spectra look like Maxwellian ones with the maximum around the Coulomb barrier followed by an exponential tail. All these observations can be considered as good motivation for using statistical approaches to describe the data. It was done in our studies rather successfully. Some details of the model used are given in the next section, but here for illustration we present in Fig. 3 the fragment multiplicity distributions for different collisions in comparison with the model calculations.

4. DENSITY OF THE SYSTEM AT BREAKUP

What is the size of a fragmenting target spectator? Is it true that a very hot nucleus expands due to the thermal pressure to get into the phase instability (spinodal) region? To answer this question, we measured [17] the distribution of the relative velocities for coincident fragments at large correlation angles. The fragment kinetic energy is determined in the main by the acceleration in the Coulomb field of the fragmenting nucleus. Therefore, the fragment velocity is sensitive to the configuration of the system at the moment of breakup. In the upper part of Fig. 4, two variants of fragment emission are shown: evaporation from the surface of the nucleus with normal density (right) and the volume decay of the expanded system (left).

The measured distribution is shifted to lower velocities relative to the calculated one for the surface emission; this observation is in favor of the volume fragment emission. After quantitative analysis of the data by means of a combined model (see below), it was concluded that the fragment emission occurs from the expanded system with a mean density that is 3 to 4 times smaller than normal [18, 19]. The same conclusion is drawn from considerations of the fragment kinetic energy spectra [15]. Thus, one can say that thermal multifragmentation is indeed the spinodal decomposition process. This conclusion is supported by measuring the time scale of fragment emission, which is very fast (see the next section).

Now, let us consider the combined model. The reaction mechanism for light relativistic projectiles is usually divided into two steps. The first one is a fast energy deposition stage, during which energetic light particles are emitted and the nuclear remnant is excited. The fast stage is usually described by the intranuclear cascade model (INC). We use the version of the INC from [20] to get the distribution of the nuclear remnants in charge, mass, and excitation energy. The second stage is described by the statistical multifragmentation model (SMM) [21]. Within the SMM, the probability of different decay channels of the excited remnant is proportional to their statistical weight. The breakup volume determining the Coulomb energy of the system is taken to be $V_b = (1 + k)A/\rho_0$, where A is the mass number of the decaying nucleus, ρ_0 is the normal nuclear density, and k is the model parameter. Thus, thermal expansion before the breakup is assumed. The breakup density is $\rho_b = \rho_0/(1 + k)$. It is found that this traditional approach fails to describe the observed IMF multiplicities, whose mean values saturate at 2.2 ± 0.2. The expansion stage is inserted between the two parts of the calculation. In fact, the excitation energies and the residual masses are finely tuned to get agreement with the measured IMF multiplicities;

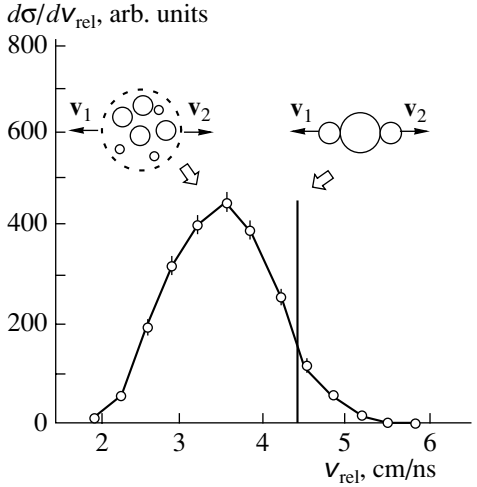

Fig. 4. Distribution of relative velocities for the coincident fragments from ^{4}He + Au collisions (at 14.6 GeV) measured at correlation angles of 150°–180°. The vertical line shows the expected maximum position for fragment evaporation from the nucleus surface. The data are shifted to lower velocities, corresponding to the volume disintegration of the expanded system (see text).

i.e., the values for the residual (after INC) masses and their excitation energies are scaled on an event-by-event basis (for details, see [15, 16]). The final stage of the combined model INC + Expansion + SMM is the multibody Coulomb trajectory calculations for all charged particles in the exit channel (again on an event-by-event basis). As a result, the fragment energies and momenta are obtained and can be compared with the experimental data.

5. THERMAL MULTIFRAGMENTATION—A NEW DECAY MODE OF HOT NUCLEI

The time scale of IMF emission is a crucial characteristic for understanding the mechanism of this decay process: whether it is a "slow" successive and independent evaporation of IMFs or a new (multibody) decay mode with "simultaneous" ejection of the fragments governed by the total accessible phase space. "Simultaneous" means that all the fragments are liberated during a time which is smaller than the characteristic Coulomb time $\tau_c \approx 10^{-21}$ s [22], which is the mean time of fragment acceleration in the Coulomb field of the system. In that case, emission of the fragments is not independent; they interact with each other via the Coulomb forces during the acceleration. Thus, measurement of the IMF emission time τ_{em} (the mean time separation between two consecutive fragment emissions) is a direct way to answer the question as to the nature of the multifragmentation phenomenon.

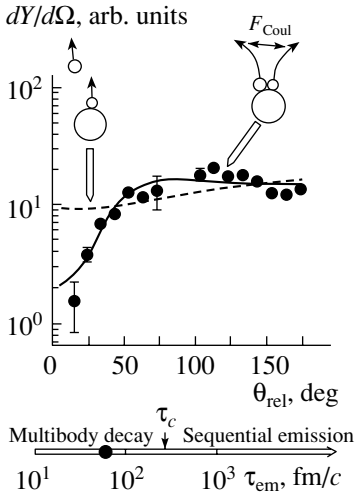

Fig. 5. Distribution of relative angles between coincident IMFs for ^{4}He (14.6 GeV) + Au collisions. The solid curve is calculated for the simultaneous emission of fragments; the dashed curve corresponds to the sequential, independent evaporation.

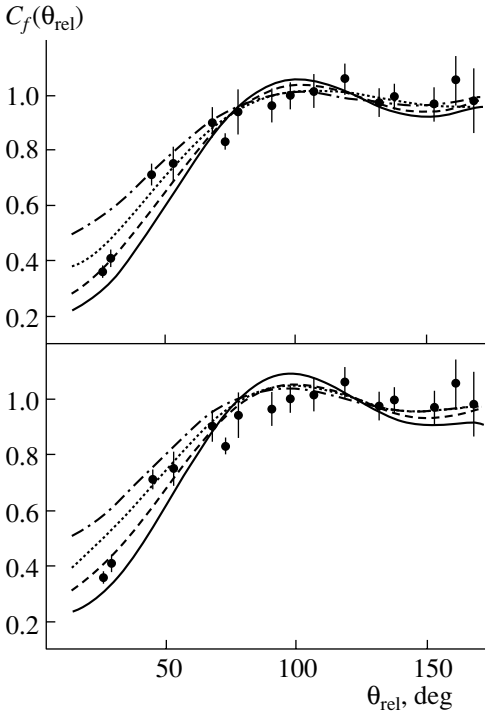

Fig. 6. Comparison of the measured correlation functions (for p + Au at 8.1 GeV) with the calculated ones for different mean decay times of the fragmenting system: solid, dashed, dotted, and dash-dotted curves for τ_{em} = 0, 50, 100, and 200 fm/c. Calculations are made with combined model INC + Expansion + SMM assuming two values of breakup volumes: $8V_0$ (upper panel) and $4V_0$ (lower panel).

There are two procedures to measure the emission time: analysis of the IMF–IMF correlation function with respect to the relative velocity and the relative angle. We used the second method. Figure 5 shows the IMF–IMF relative angle correlation for the fragmentation target spectator in ^{4}He (14.6 GeV) + Au collisions [18]. The correlation function exhibits a minimum at $\theta_{rel} = 0$ arising from the Coulomb repulsion between the coincident fragments. The magnitude of this effect drastically depends on the time scale of emission, since the longer the time distance between the fragments, the larger their space separation and the weaker the Coulomb repulsion. The multibody Coulomb trajectory calculations fit the data on the assumption that the mean emission time is $\tau_{em} \leq 70$ fm/c (2.3×10^{-22} s). This value is significantly smaller than the characteristic Coulomb time τ_c. The trivial mechanism of IMF emission (independent evaporation) is definitely excluded.

A similar result is obtained in our recent paper [23], devoted to the time scale measurement for multifragment emission in p + Au collisions at 8.1 GeV. The model dependence of the results was carefully investigated. Figure 6 shows the experimental correlation function and the calculated ones for two values of the breakup volumes: $V_b = 4V_0$ and $V_b = 8V_0$. The mean emission time is found to be $\tau_{em} = 50 \pm 10$ fm/c. One should notice that this value is in fact the mean time of fragment formation under breakup conditions. The total duration time of the reaction is larger. It includes the thermalization time (10–20 fm/c) and the mean expansion time before the disintegration of the hot nucleus, which is around 70 fm/c according to model estimation [15, 24].

6. EVOLUTION OF THE REACTION MECHANISM WITH INCREASING PROJECTILE MASS

It is shown in a number of papers that the multifragment emission in the central collisions of very heavy ions is not described by the statistical models. Initial compression of the system is tremendous and the collective part of the excitation energy is so large that the partition of the system into fragments is likely to be a very fast dynamic process [25]. In that case, the fragment kinetic energy is largely determined by the decompressional collective flow. It is interesting to follow the evolution of the multifragmentation mechanism (as the projectile mass increases) from pure thermal to that influenced by the dynamic effects.

6.1. Fragment Charge Distribution

We performed a comparative study of multifragmentation induced in a gold target by relativistic

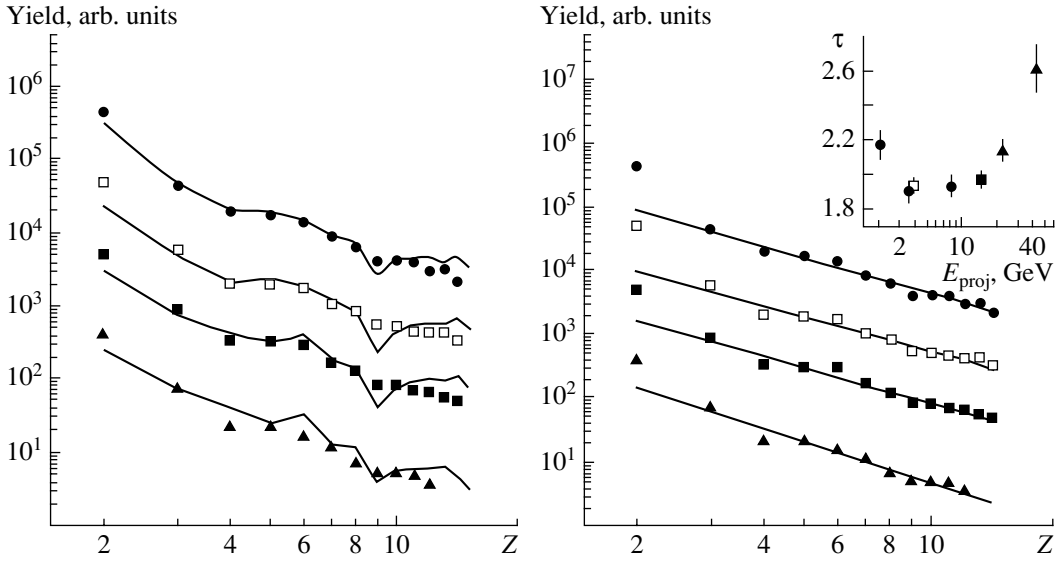

Fig. 7. Fragment charge distributions obtained at $\theta = 87°$ for p + Au at 8.1 GeV (●), ^{4}He + Au at 4 GeV (□), ^{4}He + Au at 14.6 GeV (■), and ^{12}C + Au at 22.4 GeV (▲). The lines (left side) are calculated by INC + Expansion + SMM (normalized at $Z = 3$). The power law fits are shown in the right panel with τ parameters given in the inset as a function of the beam energy. The last point in the inset is for ^{12}C + Au collisions at 44 GeV (from a preliminary experiment).

protons and helium and carbon ions [16, 26]. It was already demonstrated that, in all cases, one dealt with disintegration of a thermally equilibrated system (Fig. 2), and IMF multiplicity distributions were well reproduced by the statistical model (Fig. 3). It was also found that charge distributions of fragments were similar for all the collisions studied, and they are very well described by the combined model INC + Expansion + SMM (Fig. 7).

The general trend of the IMF charge distributions is also well reproduced by a power law $Y(Z) \sim Z^{-\tau}$. In earlier papers on multifragmentation [3, 27–29], such a power-law dependence for the fragment charge yield was interpreted as an indication of the proximity of the decaying state to the critical point for the liquid–gas phase transition in nuclear matter. This was stimulated by the application of the classical Fisher drop model [30], which predicted a pure power law droplet-size distribution with $\tau = 2$–3 at the critical point. According to this model, the τ parameter has a minimal value at the critical temperature. So, in the spirit of the Fisher model, the data in the inset of Fig. 7 should be considered as an indication of the "critical behavior" of the system at beam energies of 5–10 GeV. But this is not the case. The power law is well explained at temperatures far below the critical point. As is seen in Fig. 7, the pure thermodynamical SMM predicts that the IMF charge distribution is close to a power law at freeze-out temperatures of 5–6 MeV, while the critical temperature is assumed to be $T_c = 18$ MeV. The statistical model also predicts the parabolic dependence of the exponent τ on the excitation energy (E^*) with the minimal value around 2.0 at $E^*/A = 3$–5 MeV [31].

In [32], the value of the critical temperature is estimated from the data on the fission probabilities. In this paper, the temperature dependence of the liquid-drop fission barrier is calculated as in [1]. The critical temperature T_c (at which the surface tension vanishes) is taken as a parameter. It is found that the barrier height is very sensitive to the ratio T/T_c. Experimental data [33] and calculations are compared for highly excited ^{188}Os. It is concluded that T_c is definitely higher than 10 MeV. The results of recent paper [13] are in conflict with that conclusion. The fragment mass distributions obtained by the ISIS collaboration were analyzed in the framework of the Fisher model with the Coulomb energy taken into account. The extracted critical temperature $T_c = 6.7 \pm 0.2$ MeV. We believe that this result should be treated with caution, keeping in mind the shortcomings of the Fisher model in application to the hot nuclear system [34].[7)]

6.2. Fragment Kinetic Energy Spectra

The fragment kinetic energy spectra change with increasing projectile mass. The spectral shapes show an increase in the number of high-energy fragments

[7)] Note added in proof: In our recent article [Karnaukhov *et al.*, Phys. Rev. C **67**, 011601(R)(2003)], the critical temperature was found to be $T_c = 20 \pm 3$ MeV. This was done by analyzing the charge distribution of fragments within the statistical multifragmentation model.

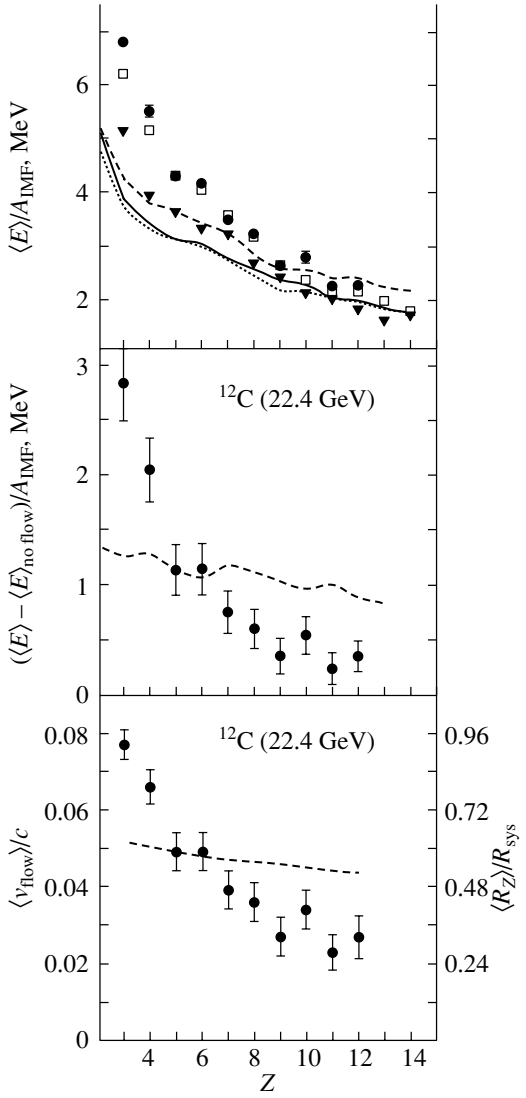

Fig. 8. Upper part: Mean kinetic energies of fragments per nucleon measured at $\theta = 87^\circ$ for p(8.1 GeV) (▼, dashed curve), ^{4}He(14.6 GeV) (□, dotted curve), and ^{12}C(22.4 GeV) (●, solid curve) collisions with Au. The curves are calculated within the INC + Expansion + SMM approach assuming no flow. Middle part: Flow energy per nucleon (dots) obtained as a difference of the measured fragment kinetic energies and the values calculated under the assumption of no flow in the system. The dashed curve represents a calculation assuming a linear radial profile for the expansion velocity with $v^0_{\rm flow} = 0.1c$. Lower part: Experimentally deduced mean flow velocities (dots) for ^{12}C + Au collisions as a function of the fragment charge (left scale) and the mean relative radial coordinates of fragments (right scale), obtained under the assumption of a linear radial profile for the expansion velocity. The dashed curve shows the mean radial coordinate according to SMM.

for heavier projectiles. This observation is summarized in Fig. 8 (upper panel), which shows the mean kinetic energies per nucleon as a function of the fragment charge. The figure reveals enhancement in the kinetic energies for the light fragments ($Z < 10$) emitted in ^{4}He(14.6 GeV) + Au and ^{12}C(22.4 GeV) + Au collisions as compared to the p(8.1 GeV) + Au case. The calculated values (curves) are obtained with the combined model INC + expansion + SMM. The measured energies are close to the calculated ones for p + Au collisions in the range of fragment charges between 4 and 9. However, the experimental values for heavier projectiles exceed the theoretical ones, which are similar for all three cases. What is the cause of that?

The kinetic energy of fragments is determined by four terms: thermal motion, Coulomb repulsion, rotation, and collective expansion energies, $E = E_{\rm th} + E_{\rm Coul} + E_{\rm rot} + E_{\rm flow}$. The Coulomb term is significantly larger than the thermal one, as was shown in [18, 23]. The contribution of the collective rotational energy is negligible even for C + Au collisions [16, 26]. We suggest that the observed energy enhancement is caused by the expansion flow in the system, which is assumed to be radial as the velocity plot (Fig. 2) does not show any significant deviation from circular symmetry. Note that the contribution of the collective flow for p(8.1 GeV) + Au collisions is inconspicuous. As was estimated in [15], the mean flow velocity for that case is less than $0.02c$. We believe that the observed flow for heavier projectiles is driven by the thermal pressure, which is expected to be larger than that for the proton beam.

An estimate of the fragment flow energies may be obtained as a difference between the measured IMF energies and those calculated without taking into account any flow in the system. This difference for ^{12}C + Au collisions is shown in Fig. 8 (middle panel).

In an attempt to describe the data, we modified the SMM code in the INC + Expansion + SMM concept by including a radial velocity boost for each particle at freeze-out. In other words, the radial expansion velocity was superimposed on the thermal motion in the calculation of the multibody Coulomb trajectories. Self-similar radial expansion is assumed when the local flow velocity is linearly dependent on the distance of the particle from the center of mass. The expansion velocity of particle Z located at radius $\mathbf{R}_Z$ is given by the following expression:

$$\mathbf{v}_{\rm flow}(Z) = v^0_{\rm flow}\mathbf{R}_Z/R_{\rm sys}, \qquad (1)$$

where $v^0_{\rm flow}$ is the radial velocity on the surface of the system. Note that, in this case, the density distribution changes in dynamic evolution in a self-similar way, being a function of the scaled radius $R_Z/R_{\rm sys}$.The use of the linear profile of the radial velocity is motivated by the hydrodynamic model calculations for an expanding hot nuclear system (see,

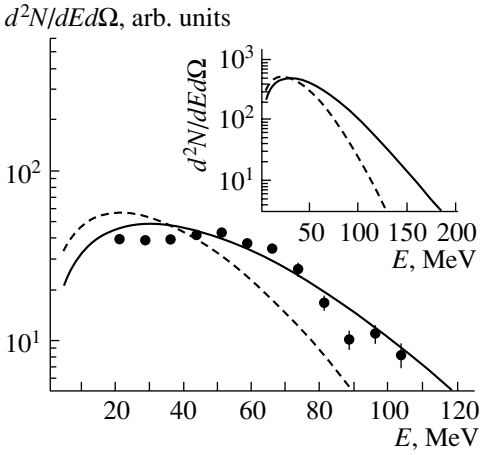

Fig. 9. Energy distribution of carbon fragments (at $\theta = 87°$) from $^{12}C + Au$ collisions. Solid curves are calculated assuming radial flow with the velocity on the surface equal to $0.1c$. Dashed curves are calculated assuming no flow.

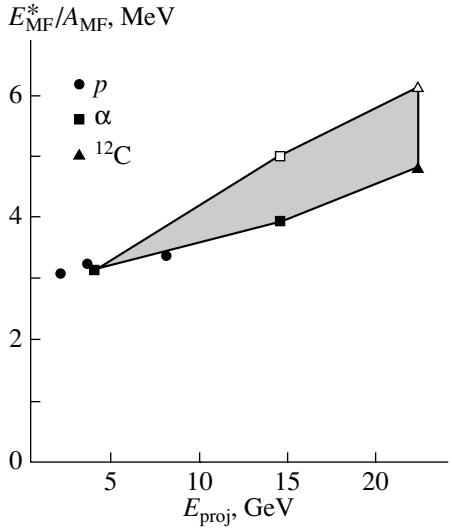

Fig. 10. Mean excitation energy of the fragmenting nucleus per nucleon E^*_{MF}/A_{MF} as a function of the beam energy: the closed points refer to the thermal part; the flow energy added is shown as open symbols and gray area.

for example, [35]). The value of v^0_{flow} was adjusted to describe the mean kinetic energy measured for the carbon fragment.

Figure 9 shows the comparison of the measured and calculated energy spectra (for $^{12}C + Au$ collisions) assuming $v^0_{flow} = 0.1c$. The agreement is good. The calculation without a flow deviates strongly. There is a longstanding problem of a qualitative difference between the chemical or thermal equilibrium temperature and the "kinetic" or so called "slope temperature." A recent discussion of that point can be found in [36]. The mean equilibrium temperature obtained in our calculations is 6.2 MeV. At the same time, the slope temperature found from the spectrum shape is $T_s = 14.5$ MeV for the "no-flow" case (see dashed curve in inset). This is the mutual result of the thermal motion, Coulomb repulsion during the volume disintegration, and the secondary decay of the excited fragments. Introducing a rather modest radial flow results in an increase in the slope temperature up to $T_s = 24$ MeV.

Let us return to Fig. 8 (middle). The model-calculated flow energy is given as the difference of the calculated fragment energies obtained for $v^0_{flow} = 0.1c$ and $v^0_{flow} = 0$. The data deviate significantly from the calculated values for Li and Be. This may be caused in part by the contribution of particle emission during the early stage of expansion from a hotter and denser system. This explanation is supported by the fact that the extra energy of Li fragments with respect to the calculated value is clearly seen in Fig. 8 (top) even for the proton-induced fragmentation, where no significant flow is expected.

As to fragments heavier than carbon, the calculated curve in Fig. 8 (middle) is above the data and only goes down slightly with increasing fragment charge. This trend of the calculations is to be expected. The mean fragment flow energy is proportional to $\langle R_Z^2 \rangle$. This value varies only slightly with the fragment charge in the SMM code due to the assumed equal probability for fragments of a given charge to be formed at any point of the available breakup volume. This assumption is a consequence of the model simplification that considers the system as a uniform one with $\rho(r) = \text{const}$ for $r \leq R_{sys}$. The data in Fig. 8 indicate that this is not the case. In fact, the dense interior of the expanded nucleus may favor the appearance of larger IMFs if fragments are formed via the density fluctuations. This observation is also in accordance with the analysis of the mean IMF energies performed in [15] for proton-induced fragmentation. It is also seen in Fig. 8 (top) that, for $p +$ Au collisions, the measured energies are below the theoretical curve for fragments heavier than Ne. This may be explained by the preferential location of the heavier fragments in the interior region of the freeze-out volume, where the Coulomb field is reduced.

The experimentally deduced mean flow velocities of IMFs for $^{12}C + Au$ collisions are presented in Fig. 8 (lower panel). The values for Li and Be are considered as upper limits because of the possible contribution of the preequilibrium emission. The corresponding values of $\langle R_Z/R_{sys} \rangle$, obtained under the assumption of the linear radial profile for the expansion velocity, can be read on the right-hand scale of the figure. The dashed curve shows the mean radial coordinates of the fragments according to the SMM code. The

calculated values of $\langle R_Z/R_{\rm sys}\rangle$ decrease only slightly with Z in contrast to the data.

The total expansion energy can be estimated by integrating the nucleon flow energy over the available volume at freeze-out. For a uniform system, one gets

$$E^{\rm tot}_{\rm flow} = (3/10)Am_N(v^0_{\rm flow})^2(1 - r_0/R_{\rm sys})^5, \quad (2)$$

where m_N and r_0 are the nucleon mass and radius. For ^{12}C + Au collisions, it gives $E^{\rm tot}_{\rm flow} \cong 115$ MeV, corresponding to the flow velocity on the surface equal to $0.1c$.

Similar results are obtained for ^{4}He(14.6 GeV) + Au collisions. The excitation energies of the fragmenting systems studied are largely thermal ones; therefore, we deal with thermal multifragmentation. It is reflected in Fig. 10, where the mean total excitation energy per nucleon $E^*_{\rm MF}/A_{\rm MF}$ is shown as a function of the incident energy. The closed symbols correspond to the thermal part of the excitation energy obtained via analysis of the data on fragment multiplicity and charge distributions with the combined model of the process. Open symbols include the flow energy. Thermal energies for these cases are 4 times larger than collective ones. The onset of the collective flow driven by the thermal pressure takes place at the excitation energy around 4 MeV/nucleon, which is in good agreement with the results of [37]. The mean fragmenting masses are equal to 158, 103, and 86 for proton (8.1 GeV), ^{4}He (14.6 GeV), and ^{12}C(22.4 GeV) collisions with Au, respectively. Note that selection of the events with the IMF multiplicity $M \geq 2$ (for the correlation measurements) results in an increase in the mean excitation energy by 0.5–0.7 MeV/nucleon [23].

7. CONCLUSION

In this work, we study the mechanism of multifragment emission in collisions of relativistic protons, ^{4}He, and ^{12}C with an Au target. The data obtained support the interpretation of this phenomenon as "thermal multifragmentation," which is a statistical breakup process of a diluted and hot system with the density 3–4 times smaller than the normal one. Thermal multifragmentation is a new multibody decay mode of an extremely excited nucleus with a very short lifetime. It was found via IMF–IMF relative angle correlations that the fragment mean emission time $\tau_{\rm em} \leq 70$ fm/c. This decay process can be interpreted as the first-order nuclear "liquid–fog" phase transition inside the spinodal region (spinodal decomposition).

The evolution of the thermal multifragmentation mechanism with increasing projectile mass was investigated. The onset of radial collective flow was observed for heavier projectiles. It is believed to be driven by the thermal pressure. The mean total flow energy at the moment of breakup is estimated to be around 115 MeV for both ^{4}He (14.6 GeV) and ^{12}C (22.4 GeV) beams, while the mean thermal excitation is around 400 MeV.

The flow energy of fragments decreases as their charge increases. The analysis of the data reveals interesting information on the fragment space distribution inside the breakup volume: heavier IMFs are formed predominantly in the interior of the fragmenting nucleus possibly due to the density gradient. This conclusion is in contrast to the predictions of the SMM.

This study of multifragmentation using a range of projectiles demonstrates a transition from pure "thermal decay" (for p + Au collisions) to disintegration "decorated" by the onset of a collective flow (for heavier projectiles). Nevertheless, the decay mechanism should be considered as thermal multifragmentation. The partition of the system is governed by the nuclear heating, and IMF charge distributions in all the cases considered are well described by the statistical model neglecting any flow.

ACKNOWLEDGMENTS

We are grateful to Profs. A. Hrynkiewicz, A.N. Sissakian, S.T. Belyaev, A.I. Malakhov, and N.A. Russakovich for support and to the staff of the JINR synchrophasotron for running the accelerator.

The research was supported in part by the Russian Foundation for Basic Research (project no. 03-02-17263), by a grant from the Polish Plenipotentiary in JINR, by grant NATO PST.CLG.976861, by grant no. 1P03 12615 from the Polish State Committee for Scientific Research, by contract no. 06DA453 with the Bundesministerium für Forschung und Technologie, and by the US National Science Foundation.

REFERENCES

1. G. Sauer, H. Chandra, and U. Mosel, Nucl. Phys. A **264**, 221 (1976).
2. H. Jaqaman, A. Z. Mekjian, and L. Zamick, Phys. Rev. C **27**, 2782 (1983).
3. P. J. Siemens, Nature **703**, 410 (1983); Nucl. Phys. A **428**, 189c (1984).
4. A. Guarnera, B. Jacquot, Ph. Chomaz, and M. Colonna, in *Proceedings of the XXXIII Winter Meeting on Nuclear Physics, Bormio, 1995*; Preprint GANIL P 95-05 (Caen, 1995).
5. S. J. Lee and A. Z. Mekjian, Phys. Rev. C **56**, 2621 (1997).
6. V. Baran, M. Colonna, M. Di Toro, and A. B. Larionov, Nucl. Phys. A **632**, 287 (1998).

7. M. D'Agostino *et al.*, Nucl. Phys. A **650**, 329 (1999); Phys. Lett. B **473**, 219 (2000).
8. L. Beaulieu *et al.*, Phys. Rev. Lett. **84**, 5971 (2000).
9. O. Lopez, Nucl. Phys. A **685**, 246c (2001).
10. B. Borderie *et al.*, Phys. Rev. Lett. **86**, 3252 (2001).
11. A. Bonasera, M. Bruno, C. O. Dorso, and P. F. Mastinu, Riv. Nuovo Cimento **23** (2), 1 (2000).
12. J. Richert and P. Wagner, Phys. Rep. **350**, 1 (2001).
13. J. B. Elliott, L. G. Moretto, L. Phair, *et al.*, Phys. Rev. Lett. **88**, 042701 (2002).
14. S. P. Avdeyev *et al.*, Nucl. Instrum. Methods Phys. Res. A **332**, 149 (1993); Prib. Tekh. Éksp., No. 2, 7 (1996).
15. S. P. Avdeyev *et al.*, Eur. Phys. J. A **3**, 75 (1998).
16. S. P. Avdeyev *et al.*, Yad. Fiz. **64**, 1628 (2001) [Phys. At. Nucl. **64**, 1549 (2001)].
17. V. Lips *et al.*, Phys. Rev. Lett. **72**, 1604 (1994).
18. V. Lips *et al.*, Phys. Lett. B **338**, 141 (1994); S. Y. Shmakov *et al.*, Yad. Fiz. **58**, 1735 (1995) [Phys. At. Nucl. **58**, 1635 (1995)].
19. Bao-An Li *et al.*, Phys. Lett. B **335**, 1 (1994).
20. V. D. Toneev *et al.*, Nucl. Phys. A **519**, 463c (1990); N. S. Amelin *et al.*, Yad. Fiz. **52**, 272 (1990) [Sov. J. Nucl. Phys. **52**, 172 (1990)].
21. J. Bondorf *et al.*, Phys. Rep. **257**, 133 (1995); Nucl. Phys. A **444**, 476 (1985).
22. O. Shapiro and D. H. E. Gross, Nucl. Phys. A **573**, 143 (1994).
23. V. K. Rodionov *et al.*, Nucl. Phys. A **700**, 457 (2002).
24. W. A. Friedman, Phys. Rev. C **42**, 667 (1990).
25. W. Reisdorf, Prog. Theor. Phys. Suppl., No. 140, 111 (2000).
26. S. P. Avdeyev *et al.*, Phys. Lett. B **503**, 256 (2001).
27. A. S. Hirsh *et al.*, Phys. Rev. C **29**, 508 (1984).
28. A. D. Panagiotou, M. W. Curtin, and D. K. Scott, Phys. Rev. C **31**, 55 (1985).
29. N. T. Porile *et al.*, Phys. Rev. C **39**, 1914 (1989).
30. M. E. Fisher, Physics (N.Y.) **3**, 255 (1967).
31. V. A. Karnaukhov *et al.*, Yad. Fiz. **62**, 272 (1999) [Phys. At. Nucl. **62**, 237 (1999)].
32. V. A. Karnaukhov, Yad. Fiz. **60**, 1780 (1997) [Phys. At. Nucl. **60**, 1625 (1997)].
33. L. G. Moretto *et al.*, Phys. Lett. B **38B**, 471 (1972).
34. J. Schmelzer, G. Roepke, and F.-P. Ludwig, Phys. Rev. C **55**, 1917 (1997).
35. J. P. Bondorf *et al.*, Nucl. Phys. A **296**, 320 (1978).
36. T. Odeh *et al.*, Phys. Rev. Lett. **84**, 4557 (2000).
37. T. Lefort *et al.*, Phys. Rev. C **62**, 031604 (2000).

Physics of Atomic Nuclei, Vol. 66, No. 7, 2003, pp. 1252–1259. Translated from Yadernaya Fizika, Vol. 66, No. 7, 2003, pp. 1292–1299.

ELEMENTARY PARTICLES AND FIELDS
Experiment

Small-Scale Anisotropy and Composition of $E_0 \approx 10^{17}$ eV Cosmic Rays According to Data from the Yakutsk Array for Studying Extensive Air Showers

A. V. Glushkov*

Institute for Cosmophysical Research and Aeronomy, Siberian Division, Russian Academy of Sciences, pr. Lenina 31, Yakutsk, 677891 Russia

Received May 13, 2002

Abstract—Results are presented that were obtained from an analysis of arrival directions for cosmic rays of energy in the range $E_0 \approx 10^{16.9-17.2}$ eV that were recorded by the Yakutsk array between 1974 and 2001 at zenith angles of $\theta \leq 45^\circ$. It is shown that a considerable part of them form clusters that have small-scale cellular structure. In all probability, these showers are generated by neutral particles of an extragalactic origin. © *2003 MAIK "Nauka/Interperiodica".*

1. INTRODUCTION

More than 40 years ago, a group from Moscow State University (MSU) discovered a knee in the spectra of the extensive air showers (EAS) at an energy of $E_0 \approx 3 \times 10^{15}$ eV [1]. Revealing its nature would greatly contribute to solving the problem of the origin of cosmic rays having extremely high energies, up to about 10^{20} eV. Many experiments have so far been performed to study this phenomenon, but there is still no an unambiguous understanding of it.

It is widely believed that, at energies in the range $3 \times 10^{15} < E_0 \leq 10^{17}$ eV, the composition of primary cosmic radiation (PCR) is noticeably enriched in heavy nuclei (see, for example, [2, 3]) and that, in the range $10^{17} < E_0 \leq 10^{18}$ eV, there is a fast increase in the fraction of protons [4]. The fraction of heavy nuclei is maximal at $E_0 \approx 10^{17}$ eV. These results are explained within the diffusion model [5], which also correctly predicts the shape of the PCR energy spectrum in the region of the aforementioned knee.

However, this explanation is questionable, because conclusions from EAS data are rather ambiguous and even inconsistent. Moreover, there are no direct measurements of the composition of extremely high-energy PCR. As was reported in [6–12], the arrival directions of $E_0 \geq 4 \times 10^{17}$ eV PCR exhibit numerous groups of showers in narrow solid angles. The distribution of these groups over the celestial sphere has a small-scale ordered structure that cannot be attributed to stochastic statistical processes. In my opinion, this structure can be associated with the distribution of extragalactic pointlike sources of PCR that generate neutral particles. Recently, this hypothesis was additionally confirmed in [13, 14] at energies of $E_0 \approx (1.3–4) \times 10^{17}$ eV. Several new experimental results supporting this opinion are given below.

2. FEATURES UNDER INVESTIGATION

In the present article, we consider showers of energy in the range $E_0 \approx (0.8–1.6) \times 10^{17}$ eV that were detected by the Yakutsk EAS array from 1974 to 2001 at zenith angles of $\theta \leq 45^\circ$. We select only those showers from the entire data sample whose arrival directions were found on the basis of data from four or more stations and whose axes traversed the central circle of the array with a radius not greater than 1000 m. These events give small errors in determining basic EAS parameters (direction and coordinates of the axis, E_0, etc.). The primary-particle energy E_0 was determined from the relations

$$E_0 = (4.8 \pm 1.6) \times 10^{17} (\rho_{s,600}(0^\circ))^{1.0 \pm 0.02} \text{ [eV]}, \quad (1)$$

$$\rho_{s,600}(0^\circ) = \rho_{s,600}(\theta) \times \exp((\sec\theta - 1) \times 1020/\lambda_\rho) \text{ [m}^{-2}\text{]}, \quad (2)$$

$$\lambda_\rho = (450 \pm 44) + (32 \pm 15) \log(\rho_{s,600}(0^\circ)) \text{ [g/cm}^2\text{]}, \quad (3)$$

where $\rho_{s,600}(\theta)$ is the charged-particle density measured by ground-based scintillation detectors at a distance of $R = 600$ m from the shower axis.

By using this method, we selected 14 318 showers. Figure 1 shows the chart of their arrival directions on the developed celestial sphere in galactic coordinates.

*e-mail: a.v.glushkov@ikfia.ysn.ru

1063-7788/03/6607-1252$24.00

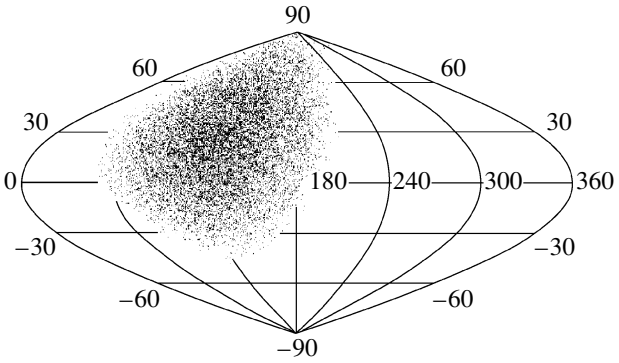

Fig. 1. Individual arrival directions of 14 318 showers with $E_0 \approx (0.8–1.6) \times 10^{17}$ eV and $\theta \leq 45°$ in galactic coordinates.

Equal areas in this chart correspond to sky regions of equal area. The coordinates of the North Pole of the Galaxy in right ascension are $\alpha_{1950} = 192.3°$ and $\delta_{1950} = 27.4°$.

In Fig. 1, one can see a small-scale anisotropy and numerous compact groups and chains. Let us consider some special features of these data. The distribution of showers presented in Fig. 1 with respect to arrival directions is displayed in Fig. 2 in terms of the galactic latitude of their arrival (with a step of $\Delta b_G = 1.5°$). Figure 2*a* shows the observed (N_{expt}) and expected (N_{ran}) distributions, while Fig. 2*b* presents the deviation of the number of observed events from the number of expected ones in units of the standard deviation $\sigma = \sqrt{N_{ran}}$; $n_\sigma = (N_{expt} - N_{ran})/\sigma$. The values N_{ran} were determined from a Monte Carlo simulation.

At first glance, the experimental data in Fig. 2 are quite consistent with an isotropic PCR flux. However, we would like to call the attention of the reader to the shaded area in the latitude range from 4.5° to 0°, where there is a pronounced dip of $|527 - 608|/\sqrt{608} \approx 3.3\sigma$. A similar dip, which is, however, more statistically significant ($\approx 9.2\sigma$), was obtained at energies of $E_0 \approx (1.3–4) \times 10^{17}$ eV in [13, 14]. In the present article, this dip is explained by the absorption of extragalactic PCR. This issue will be discussed in what follows.

In order to get a clearer idea of the structure of the data in Fig. 1, we broke down the whole sample of 14 318 showers into three energy ranges: $E_0 = 10^{16.9–17.0}$, $10^{17.0–17.1}$, and $10^{17.1–17.2}$ eV. In each of these, we took six independent samples that contained approximately 800 events each, but which differed from one another only in that their axes traversed different annular regions within the central circle of the array, all other conditions being the same. The presence of local shower groups over the celestial sphere was checked individually for each of the 18

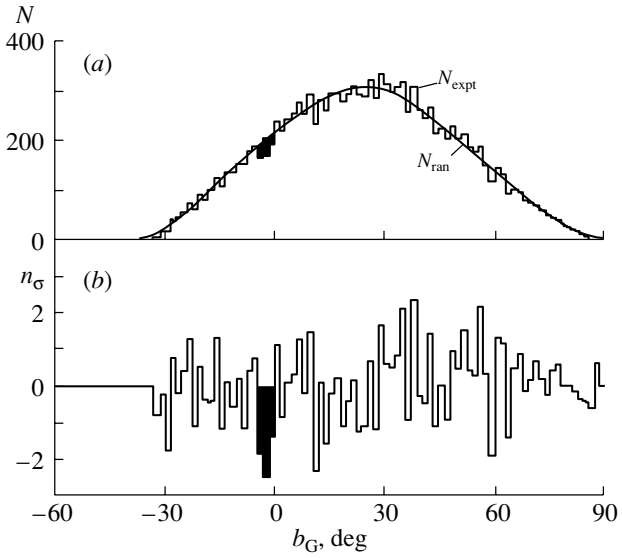

Fig. 2. The distribution of 14 318 showers with $E_0 \approx (0.8–1.6) \times 10^{17}$ eV and $\theta \leq 45°$ with respect to arrival directions in terms of the galactic latitude of their arrival: (*a*) observed (N_{expt}) and expected (N_{ran}) distributions for an isotropic flux and (*b*) deviation of the number of observed events from the number of expected ones, $n_\sigma = (N_{expt} - N_{ran})/\sqrt{N_{ran}}$. The shaded area corresponds to a 3.3σ dip.

($= 3 \times 6$) samples by using the same method as in [10–14]. For each shower, we determined all "neighbors" spaced in arrival direction by an angular distance of $d \leq 3°$. If a circle contained $n \geq 3$ showers, their coordinates were averaged and these averaged coordinates were used in the following as new points, referred to as nodes.

For each of the three energy ranges individually, we further analyzed nodes in any of the six samples for intersections of multiplicity not less than two (under the condition that their centers are within an angular distance of $d \leq 3°$). If such nodes were found, the arrival-direction coordinates of all showers belonging to them were averaged, and this new large node (referred to as a cluster) was used in the ensuing analysis.

3. SMALL-SCALE ANISOTROPY OF PCR

The superimposed chart of the positions of nodes for six samples of showers of energy in the range $E_0 = 10^{17.0–17.1}$ eV is shown in Fig. 3 in terms of supergalactic coordinates (the coordinates of the North Pole of the Supergalaxy are $\alpha = 286.2°$ and $\delta = 14.1°$). The longitude of the Supergalaxy was reckoned in the counterclockwise direction from the vector pointing to the anticenter. For the purpose of convenience, the equatorial coordinates are also shown in this chart.

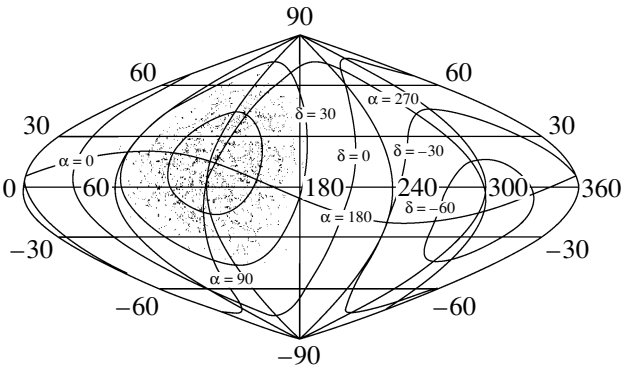

Fig. 3. Superimposed chart of the positions of nodes for six independent samples of 2439 showers with $E_0 = 10^{17.0-17.1}$ eV and $\theta \leq 45^\circ$ in supergalactic coordinates.

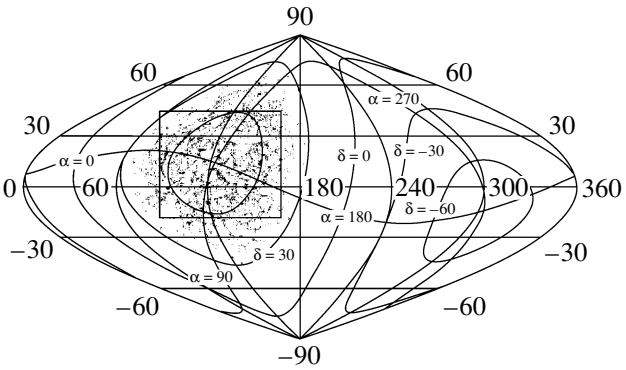

Fig. 4. Superimposed chart of the positions of clusters containing two or more nodes from three groups of showers with $E_0 = 10^{16.9-17.0}$, $10^{17.0-17.1}$, and $10^{17.1-17.2}$ eV in terms of the supergalactic coordinates. The rectangle singles out the fragment presented in Fig. 5.

One can see that this sample of 2439 showers (in all, there are 4861 showers in the $E_0 = 10^{17.0-17.1}$ eV group) forms chains, which in turn form a cellular structure. A similar pattern is observed at other values of the PCR energy. The positions of the clusters having different energies coincide in the majority of cases. This can be seen from Fig. 4, which displays the chart of clusters from three groups corresponding to $E_0 = 10^{16.9-17.0}$, $10^{17.0-17.1}$, and $10^{17.1-17.2}$ eV. This chart is a superposition of three original charts (one of these is shown in Fig. 3) obtained by the same methods. Here, the phenomenon in question becomes more pronounced, but the general structure of the distribution of clusters over the sky area under consideration remains unchanged.

A fragment of Fig. 4 is shown in Fig. 5. Points correspond to clusters where the number of showers, n, in one of these three groups in energy is not less than 10; crosses represent $n \geq 10$ clusters common to any two groups of these three; and closed circles correspond to $n \geq 10$ clusters common to all three groups in energy E_0. It can clearly be seen that the majority of clusters condense into chains separated by voids of characteristic angular dimension 5°–10°. According to a Monte Carlo simulation, the probability of such a result is less than 10^{-5}.

Observations reveal that the Universe contains large black holes of dimension 100–130 Mpc separated by relatively thin (20–30 Mpc) layers, and the theory confirms this. About 60 to 80% of galaxies are concentrated in these layers. These galaxies have a tendency to gather in extended and flattened superclusters. The Supergalaxy (of diameter 50 to 60 Mpc) considered here is one of such superclusters. In all probability, many of the superclusters are adjacent to one another, forming a unique cellular structure of the Universe [15–18]. There is the opinion that it may be a structure of the three-dimensional-chessboard type [19] or even something like a giant quasicrystal [20], with the bulk of matter being concentrated in its nodes.

One of the hypotheses concerning the formation of the cellular structure of the Universe was widely developed within the adiabatic theory of Zeldovich [21], where some stages of concentration of matter are represented in the evolution chain of the expanding Universe as bright surfaces–bright curves–bright drops sequence.

One cannot rule out the possibility that the nodes and clusters found above have some bearing on the cellular structure of the Universe. We will now estimate a typical size of the voids in Figs. 3–5; this is of interest since such voids may additionally characterize the small-scale anisotropy of ultrahigh-energy PCR. For this purpose, we analyze the distributions of angles between the nodes by using the $E_0 = 10^{17.0-17.1}$ eV data in Fig. 3 as an example. Let us consider any two (of six independent) samples containing equal numbers of events (370) and find the minimal angular distances $d_{\min}$ between the nodes from sample 1 with respect to the nodes from sample 2. To improve the statistical accuracy, we use all 15 pairs of such independent combinations. The eventual distribution (J_{expt}) is constructed as the sum of these distributions. In order to find the expected distribution for an isotropic flux (J_{ran}), we perform a such procedure once more (beginning from the selection of nodes), as was done in deriving the data presented in Fig. 3. The random directions are evaluated on the basis of real showers by replacing their measured right ascension by that determined from a Monte Carlo simulation in the angular range between 0° and 360°.

The angular correlation functions $k_\sigma = (J_{\text{expt}} - J_{\text{ran}})/\sigma(\sigma = \sqrt{J_{\text{ran}}})$ for $2220\,(= 370 \times 6)$ events con-

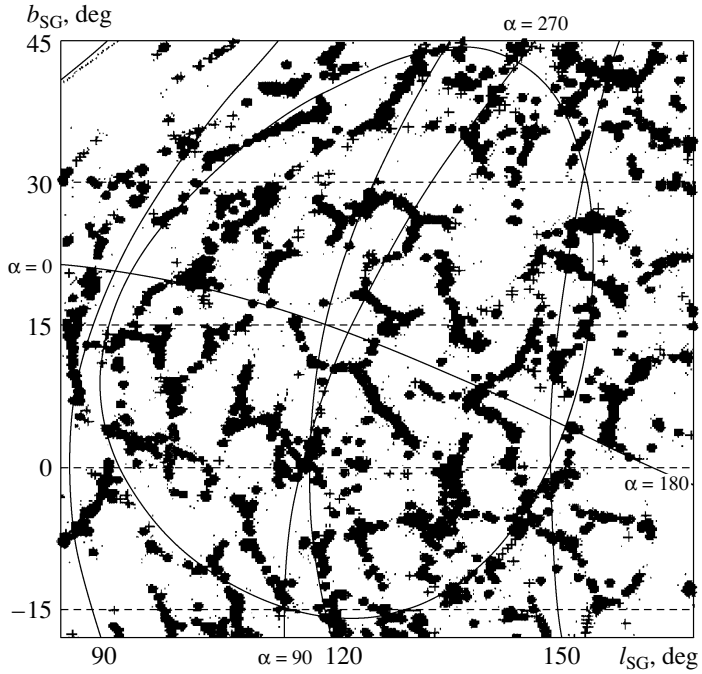

Fig. 5. Fragment singled out by the rectangle in Fig. 4 and (points) original data from Fig. 4 and (+ and •) clusters common to, respectively, any two and all three groups in energy (l_{SG} is the longitude of shower arrival from the Supergalactic disk).

sidered above are shown in Fig. 6. The closed circles in Fig. 6*a* correspond to showers from the nodes in Fig. 3, while those in Fig. 6*b* correspond to other showers not belonging to these nodes. It can be seen that, in Fig. 6*a*, there is a deficit of events (of about three standard deviations) for $d_{\min} \leq 2.5°$, but that, for $d_{\min} \approx 5°–10°$, there is a stable and statistically significant excess of events at a level of $(4–5.5)\sigma$. The correlation function k_σ in Fig. 6*b* exhibits an absolutely different behavior.

At first glance, this result is very strange. The presence of a dip in Fig. 6*a* instead of a peak at $d_{\min} \leq 2.5°$ is especially surprising. However, a further simulation revealed that such a pattern is quite possible if the data have a structure ordered in some specific way rather than a random one. For a rough model, we considered a rectangular network in equatorial coordinates that has a cell size of 5°. For the directions of initial events, we took the quantities obtained by smearing the celestial coordinates of the nodes of this network according to a normal law with a standard deviation of 2.5°. If we treat these simulated events [by using the same method as for the data in Figs. 3 and 6 (closed circles)], we arrive at the distribution represented by open circles in Fig. 6*a*.

One can see that this distribution is similar to the actual distribution even in many of its details. If we reduce the smearing of the network nodes to 0.5°–1°, then distinct peaks at angles of $d_{\min} \leq 2°$, 5°, and 10° will appear. Distributions similar to those presented in Fig. 6 are observed for other PCR energies considered in the present study.

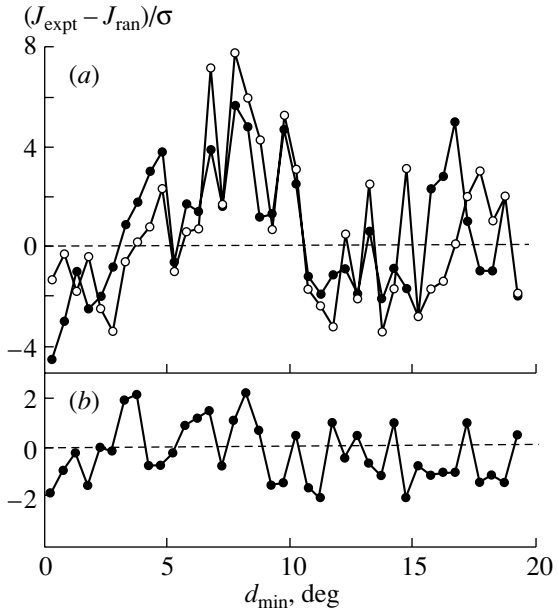

Fig. 6. Angular correlation functions for the $E_0 = 10^{17.0–17.1}$ eV sample. Closed circles represent (*a*) showers in nodes (see Fig. 3) and (*b*) showers outside these nodes, while open circles represent nodes from the rectangular network of size 5° in equatorial coordinates.

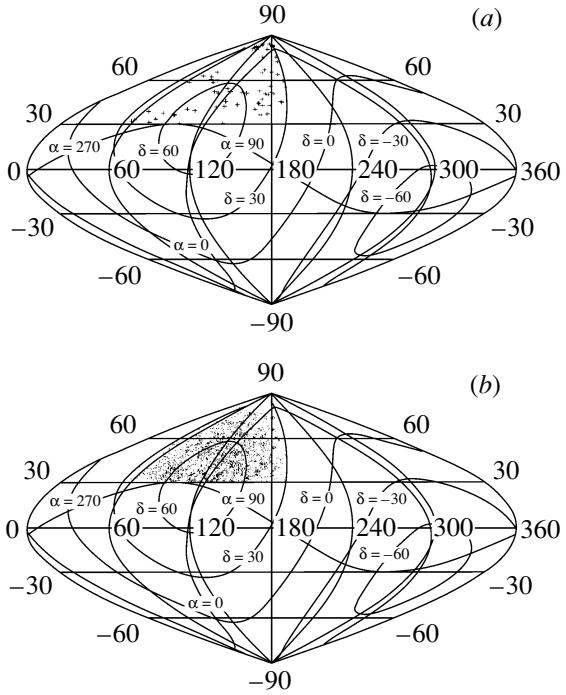

Fig. 7. Chart of the distributions in galactic coordinates: (*a*) 74 quasars with redshifts of $z \leq 0.3$ [22] and (*b*) nodes of PCR with $E_0 = 10^{16.9-17.2}$ eV and $\theta \leq 45^\circ$ from the data of Yakutsk EAS array.

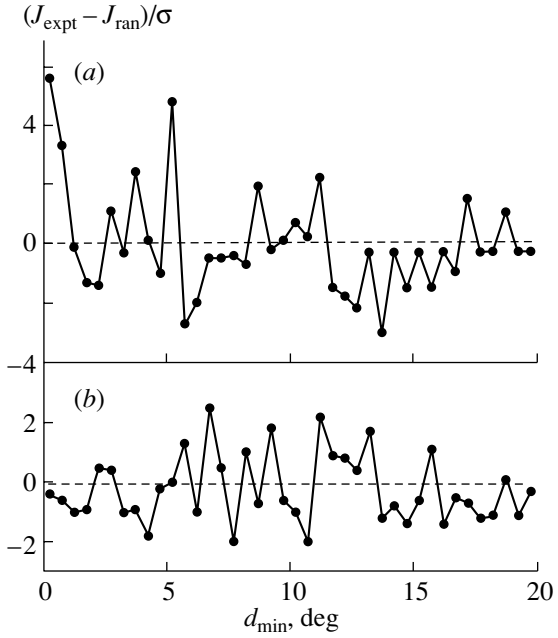

Fig. 8. Angular correlation between the nodes of $E_0 = 10^{16.9-17.2}$ eV PCR and quasars from the samples in Fig. 7: (*a*) showers in the nodes and (*b*) showers outside the nodes.

4. QUASARS AS A POSSIBLE SOURCES OF PCR

The above results give grounds to assume that the ultrahigh-energy cosmic rays forming nodes are in all probability of an extragalactic origin. It was shown in [8, 13, 14] that quasars might be one of their sources, since there is a similarity in the spatial distribution of PCR and quasars over the celestial sphere. We consider the correlation between them. In terms of the galactic coordinates, Fig. 7*a* shows the chart of 74 quasars with redshifts of $z \leq 0.3$ from the catalog [22] with declinations of $\delta \geq 30^\circ$. Since, in the catalog [22], there are virtually no data on the equatorial region of the Galaxy ($|b_G| \leq 30^\circ$) because of strong light absorption, all quasars and PCR nodes (Fig. 7*b*) from this area of the sky were eliminated from the ensuing analysis.

In Fig. 8, we present the angular correlation functions $k_\sigma = (J_{expt} - J_{ran})/\sigma$, which are similar to those in Fig. 6. The measured distributions (J_{expt}) and the distributions expected for random variables (J_{ran}) were evaluated as the sum of 18 ($= 3 \times 6$) original distributions of minimal angular distances d_{min} between the nodes (from 123 to 206) of the above groups of showers and 74 quasars. Figures 8*a* and 8*b* display the results for, respectively, showers from the nodes and showers not belonging to the nodes.

Figure 8*a* exhibits a statistically significant peak (5.5σ) at $d_{min} \leq 1^\circ$, but there is no peak in Fig. 8*b*. This suggests that primary particles forming nodes and clusters might have been generated by quasars. The peak in Fig. 8*a* at $d_{min} \approx 5^\circ$ can be related to the analogous peak in Fig. 6*b*; that is, it can be considered as an additional piece of evidence for the ordered character of the large-scale cellular structure of the Universe.

5. ESTIMATES OF THE PCR COMPOSITION

Most likely, primary particles entering into the clusters are neutral; otherwise, their motion in the galactic magnetic fields would destroy any correlation in direction with their production sources, and they could not reveal the structure that we see in Figs. 1 and 3–6.

Let us return once again to the distribution in Fig. 2. Figure 9 displays this distribution for 7104 showers entering into the clusters (Fig. 9*a*) and for the other 7214 showers, which do not belong to the clusters (Fig. 9*b*). There are substantial distinctions between these samples. First, the measured distribution (histogram) in Fig. 9*a* differs substantially, in terms of the χ^2 criterion, from that which is expected for random events (smooth curve). Indeed, one has $\chi^2 = 161$ for $k = 80$ degrees of freedom, which corresponds to a probability of $P < 10^{-5}$ for a random result. Second, there is a statistically significant

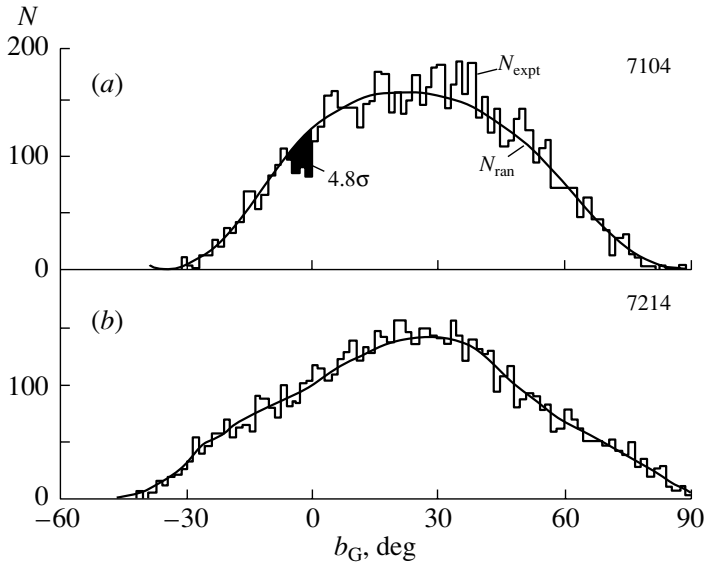

Fig. 9. Distributions similar to those in Fig. 2 for (a) showers in the clusters and (b) other showers not entering into the clusters. The numbers of showers are indicated in the corresponding panels.

deficit of events in the range from 4.5° to 0° (shaded area): $|259 - 350|/\sqrt{350} \approx 4.8\sigma$. On the other hand, the distribution in Fig. 9*b* has an absolutely different shape featuring no dip of the above type. It leads to the value of $\chi^2 = 93$ at $k = 90$ and suggests an isotropic flux of cosmic rays.

The result presented in Fig. 9 can be considered as a further piece of evidence that the PCR fraction inside the clusters is of an extragalactic origin. It seems that the Galaxy only absorbs this radiation, and it does this more strongly in the disk. The mean shift of the dip from the plane of the Galaxy is about −2.1°. In all probability, this shift is due to the fact that the Sun is not strictly situated in the symmetry plane of the disk, but it is slightly shifted to the Northern Hemisphere with respect to the plane of the Galaxy. If this is so, the PCR flux coming from southern latitudes at small angles with respect to disk must undergo much stronger absorption in relation to the analogous flux coming at the same angles from northern latitudes. This assumption is consistent with the distribution of neutral hydrogen in the disk of the Galaxy, where, according to data from [23], there is a −1.4° shift of the plane of the highest hydrogen concentration in relation to the commonly used position.

Let us assume that the dip in Fig. 9*a* is associated with a relatively stronger absorption of extragalactic PCR within the disk of the Galaxy in relation to that at higher latitudes. In this case, we can roughly estimate the absorption range of unknown extragalactic particles (for the sake of brevity, we refer to them as A particles) on the basis of the relation

$$N = N_0 \exp(-\langle l \rangle / \lambda_A), \qquad (4)$$

where $N_0 \approx 350$, $N \approx 259$ (see Fig. 9), and $\langle l \rangle$ is the average thickness (in g/cm^{-2}) of the disk of the Galaxy in our observation sector. From (4), we then obtain

$$\lambda_A \approx 3.3 \langle l \rangle.$$

In order to find the quantity $\langle l \rangle$, we assume that neutral hydrogen plays the most important role in the attenuation of PCR, because the dust contribution is very small (about 1%) [23]. It can be seen from Fig. 1 that, within the disk of the Galaxy, PCR arrives from the sector $\Delta l_G \approx 60°–180°$. Over this sector, the path r from an observer to the outer boundary of the Galaxy changes from about 10 to 5 kpc ($\langle r \rangle \approx$ 8 kpc). According to data from [23], the average hydrogen concentration in the latitude band $|b_G| \leq 10°$ decreases from $\rho \approx 0.5$ cm^{-3} (at the distance of $R =$ 10 kpc from the center of the Galaxy) to $\rho \approx 0.1$ cm^{-3} at $R = 15$ kpc ($\langle \rho \rangle \approx 0.25$ cm^{-3}). On this basis, we obtain

$$\langle l \rangle \approx \langle r \rangle \langle \rho \rangle m_p \approx 10^{-2} \text{ g cm}^{-2},$$

where $m_p = 1.67 \times 10^{-24}$ g is the proton mass. Finally, we arrive at

$$\lambda_A \approx 3.3 \times 10^{-2} \text{ g cm}^{-2}.$$

The value derived for the path of mysterious A particles appeared to be about 1000 times shorter than that for the nuclear interactions of $E_0 \sim 10^{17}$ eV protons. Nevertheless, these particles can arrive without losses almost from the horizon of the observed Universe. Considering that the age of the expanding

Universe is $t \approx 13 \times 10^9$ years and that the average matter density is $\rho_0 \approx 10^{-30}$ g cm^{-3}, we obtain

$$l_0 = \rho_0 ct \approx 1.23 \times 10^{-2} \text{ g cm}^{-2},$$

where c is the speed of light. Using Eq. (4), we find that the attenuation factor is $\exp(-\langle l_0 \rangle / \lambda_A) \approx 0.7$.

In the Earth's atmosphere, A particles begin to interact at an altitude h_A above sea level. This quantity can be found from the barometric equation

$$\lambda_A = p_0 \exp(-h_A/h_0), \quad (5)$$

where $p_0 = 1020$ g cm^{-2} is the air pressure at sea level and $h_0 = 6.85$ km. It follows that $h_A \approx 71$ km.

These particles initiate the development of EAS much earlier than particles belonging to the ordinary composition of cosmic rays. If we take, by way of example, protons of energy $E_0 \sim 10^{17}$ eV, their mean path in the Earth's atmosphere to the first event of nuclear interaction is about 50 g cm^{-2}. The analogous path of iron nuclei is shorter by a factor of about 2 to 3.

It is likely that, after the first interaction, these mysterious A particles disappear, giving way, in the development of EAS, to the ordinary cascade of secondary particles. Otherwise, showers initiated by these mysterious particles would be substantially different from ordinary ones and could easily be detected. Because of so short a range of A particles before the first nuclear interaction, showers initiated by them must lead to a very fast development of EAS, with a higher maximum of a cascade curve in relation to that for primary protons. In view of this, showers from A particles could be misidentified as showers from iron nuclei, especially as the majority of the methods for determining the composition of PCR are indirect: they are based on a comparison of the observed features of EAS with the results of calculations that rely on model assumptions concerning the development of EAS for one presumed composition of PCR or another. Therefore, one cannot rule out here the situation where the appearance of any new primary particles having a very short range is interpreted in terms of a noticeable increase in the fraction of heavy nuclei.

According to data from the Yakutsk EAS array [24], the global flux of PCR of energy $E_0 \approx 10^{17}$ eV does not exhibit any statistically significant anisotropy. From these data, it follows that the result obtained for the amplitude of the first harmonic in right ascension by the conventional method of harmonic analysis is $(0.45 \pm 0.55)\%$. However, special attention should be given to the phase of the first harmonic, $\varphi_1 = 192^\circ \pm 70^\circ$. Albeit involving a large uncertainty associated with the isotropy of PCR, it provides an indication of the center of the Supergalaxy.

The results presented in this article and in [24] could be explained if one assumes that PCR consists of two components. One is likely to contain charged particles, which are strongly mixed by the magnetic field of the Galaxy, while the other, which produces clusters, most probably features neutral particles of extragalactic origin.

6. CONCLUSION

The data presented above indicate that some fraction of cosmic rays of energy $E_0 \approx 10^{17}$ eV are grouped into numerous nodes and clusters within solid angles with $d \leq 3^\circ$. They form a cellular structure (see Fig. 3–5) having a characteristic angular scale of about 5°–10° (Fig. 6). This structure has a correlation with quasars characterized by a redshift of $z \leq 0.3$ (Fig. 8) and a negative correlation with the disk of the Galaxy (see Fig. 9). It can be conjectured that the nodes and clusters are an indication of some extragalactic pointlike sources of PCR and that these sources are associated with the large-scale structure of the Universe.

Primary particles forming the clusters are most likely neutral. Otherwise, they could not correlate in direction with their sources because of the motion in the magnetic fields of the Galaxy and exhibit the cellular structure of the matter distribution in the Universe.

In all probability, these particles have a very short range with respect to nuclear interaction ($\lambda_A \approx 3.3 \times 10^{-2}$ g cm^{-2}) and initiate an earlier development of EAS in relation to what occurs in the case of the usual composition of PCR. Their fraction in the whole flux of cosmic rays at $E_0 \approx 10^{17}$ eV is about $7104/14\,318 \approx 0.5$. This is severalfold greater than that in the adjacent energy range $E_0 = (1.3$–$4) \times 10^{17}$ eV [13, 14].

So fast an increase in the fraction of neutral particles at $E_0 \approx 10^{17}$ eV could be erroneously attributed to an increase in the content of heavy particles in PCR. We cannot rule out the possibility that such hypothetical unknown particles manifest themselves for $E_0 < 10^{17}$ eV as well. Further investigations are required for clarifying this point.

Showers that do not enter into the composition of the nodes and clusters are distributed almost isotropically over the celestial sphere. This PCR fraction is likely to consist of charged particles (protons and nuclei of various chemical elements) propagating through the Galaxy via diffusion. One of the intense sources occurs in the vicinity of the center of the Galaxy [25–27]. It is very difficult to observe other sources of charged particles at present, because their positions are strongly "smeared" by the magnetic field of the Galaxy.

ACKNOWLEDGMENTS

The financial support extended by the Ministry for Science of the Russian Federation to the Yakutsk multipurpose EAS array (grant no. 01-30) is gratefully acknowledged. This work was also supported by the Russian Foundation for Basic Research (project no. 00-15-96787).

REFERENCES

1. G. V. Kulikov and G. B. Khristiansen, Zh. Éksp. Teor. Fiz. **35**, 635 (1958) [Sov. Phys. JETP **8**, 441 (1958)].
2. V. I. Vishnevskaya, N. N. Kalmykov, G. V. Kulikov, *et al.*, Yad. Fiz. **62**, 300 (1999) [Phys. At. Nucl. **62**, 265 (1999)].
3. H. Ulrich, T. Antoni, W. D. Apel, *et al.*, in *Proceedings of the 27th ICRC, Hamburg, 2001,* p. 97.
4. T. Abu-Zayyad, K. Belov, D. J. Clay, *et al.*, astro-ph/0010652.
5. V. S. Ptuskin *et al.*, Astron. Astrophys. **268**, 726 (1993).
6. A. V. Glushkov, Pis'ma Zh. Éksp. Teor. Fiz. **48**, 513 (1988) [JETP Lett. **48**, 555 (1988)].
7. A. V. Glushkov, Priroda **5**, 111 (1989).
8. A. V. Glushkov, Pis'ma Zh. Éksp. Teor. Fiz. **73**, 355 (2001) [JETP Lett. **73**, 313 (2001)].
9. A. V. Glushkov and I. E. Sleptsov, Izv. Akad. Nauk, Ser. Fiz. **65**, 437 (2001).
10. A. V. Glushkov and M. I. Pravdin, Zh. Éksp. Teor. Fiz. **119**, 1029 (2001) [JETP **92**, 887 (2001)].
11. A. V. Glushkov and M. I. Pravdin, Pis'ma Astron. Zh. **27**, 577 (2001) [Astron. Lett. **27**, 493 (2001)].
12. A. V. Glushkov and M. I. Pravdin, Yad. Fiz. **66**, 886 (2003) [Phys. At. Nucl. **66**, 854 (2003)].
13. A. V. Glushkov, Pis'ma Zh. Éksp. Teor. Fiz. **75**, 3 (2002) [JETP Lett. **75**, 1 (2002)].
14. A. V. Glushkov and M. I. Pravdin, Pis'ma Astron. Zh. **28**, 341 (2002) [Astron. Lett. **28**, 296 (2002)].
15. B. A. Vorontsov-Vel'yaminov, I. D. Karachentsev, E. Turner, *et al.*, in *The Large-Scale Structure of the Universe*, Ed. by M. Longeir and J. Einasto (Reidel, Dordrecht, 1978; Mir, Moscow, 1981).
16. M. Seldner, B. Siebars, E. J. Groth, and P. J. E. Peebles, Astron. J. **82**, 249 (1977).
17. D. Layzer, *Constructing the Universe* (Sci. American, New York, 1984; Mir, Moscow, 1988).
18. A. V. Gurevich and K. P. Zybin, Usp. Fiz. Nauk **165**, 1 (1995) [Phys. Usp. **38**, 1 (1995)].
19. J. Einasto *et al.*, Nature **385**, 139 (1997).
20. S. G. Fedosin, *Physics and Philosophy of Similarity: from Preons to Metagalaxies* (Perm', 1999).
21. Ya. B. Zel'dovich, Pis'ma Astron. Zh. **8**, 195 (1982) [Sov. Astron. Lett. **8**, 102 (1982)].
22. A. Hewitt and G. Burbidge, Astrophys. J., Suppl. Ser. **63**, 1 (1987).
23. I. Oort, in *Handbuch der Physik. Bd. 53. Astrophysik IV: Sternesysteme* (West Berlin, 1959; Inostr. Lit., Moscow, 1962).
24. M. I. Pravdin, A. A. Ivanov, A. D. Krasil'nikov, *et al.*, Zh. Éksp. Teor. Fiz. **119**, 881 (2001) [JETP **92**, 766 (2001)].
25. N. Hayashida, M. Nagano, D. Nishikawa, *et al.*, Astropart. Phys. **10**, 303 (1999).
26. M. Teshima, M. Shikawa, M. Fukushima, *et al.*, in *Proceedings of the 27th ICRC, Hamburg, 2001,* p. 337.
27. J. A. Bellido, B. W. Clay, R. B. Dawson, and M. Johnston-Hollitt, astro-ph/0009039.

Translated by S. Slabospitsky

Physics of Atomic Nuclei, Vol. 66, No. 7, 2003, pp. 1260–1268. Translated from Yadernaya Fizika, Vol. 66, No. 7, 2003, pp. 1300–1308.

ELEMENTARY PARTICLES AND FIELDS
Theory

Contributions of Scalar Leptoquarks to the Cross Sections for the Production of Quark–Antiquark Pairs in Electron–Positron Annihilation

A. V. Povarov* and **A. D. Smirnov****

Yaroslavl State University, ul. Sovetskaya 14, Yaroslavl, 150000 Russia

Received May 13, 2002; in final form, November 5, 2002

Abstract—The contributions of scalar-leptoquark doublets to the cross sections $\sigma_{Q\tilde{Q}'}$ for the production of quark–antiquark pairs in electron–positron annihilation are calculated within the minimal model based on the four-color symmetry of quarks and leptons. These contributions are analyzed versus the scalar-leptoquark masses and the mixing parameters of the model at colliding-particle energies in the range 250–1000 GeV. It is shown that the contributions in question are of greatest importance for processes leading to t-quark production. In particular, it is found that, with allowance for the contribution of the scalar leptoquark of charge 5/3 and mass in the range 250–500 GeV, the cross section $\sigma_{t\tilde{t}}$ calculated at a mixing-parameter value of $k_t \sim 1$ may be severalfold larger than the corresponding cross section $\sigma_{t\tilde{t}}^{(\mathrm{SM})}$ within the Standard Model. The possibility of setting constraints on the scalar-leptoquark masses and on the mixing parameters by measuring such contributions at future electron–positron colliders is indicated.

1. INTRODUCTION

Searches for possible versions of new physics beyond the Standard Model form one of the lines of investigations into elementary-particle physics. Such versions include that which is based on a four-color symmetry of quarks and leptons [1] that belongs to the Pati–Salam type. This symmetry predicts vector leptoquarks of mass about the scale of breakdown of this symmetry; it also admits the existence of scalar leptoquarks [2–4] and of some other particles. If mass generation and the splitting of quark and lepton masses are due to the Higgs mechanism [5–7], the four-color symmetry of quarks and leptons predicts, in addition to vector leptoquarks, the existence of the doublets of scalar leptoquarks and the doublets of scalar gluons. In the approach being considered, these particles are responsible for the splitting of quark and lepton masses via the Higgs mechanism and appear to be some kind of partner of the standard Higgs doublet. Estimates of the masses of these particles—in particular, estimates obtained from the parameters S, T, and U of radiative corrections [8–10]—reveal that, in contrast to vector leptoquarks, these particles may be relatively light (of mass about 1 TeV or below) and, hence, lead to various manifestations of four-color symmetry at relatively low energies (about 1 TeV or below). We note that, because of their Higgs origin, the doublets of scalar leptoquarks and scalar gluons interact with fermions in a particular way: their fermionic coupling constants are proportional to the ratios of fermion masses to the Standard Model expectation value. It follows that, within the approach being considered, the characteristic values of these constants for specific processes are known (apart from mixing parameters), which makes it possible to obtain quantitative estimates for the contribution of these particles to processes involving quarks and leptons.

Within the minimal model involving the four-color symmetry of quarks and leptons [5–7], we calculate, in the present study, the contributions from the doublets of scalar leptoquarks to the production of quark–antiquark pairs in electron–positron annihilation, $e^+e^- \to Q_{ia}\tilde{Q}_{ja}$; also, we give a quantitative analysis of these contributions, contrasting them against the corresponding Standard Model cross sections at energies of about 1 TeV and below.

2. SCALAR-LEPTOQUARK INTERACTION WITH CHARGED LEPTONS IN THE MINIMAL MODEL INVOLVING QUARK–LEPTON SYMMETRY

We use here the minimal model involving quark–lepton symmetry [5, 6]. It is based on the $SU_V(4) \times$

*e-mail: povarov@univ.uniyar.ac.ru
**e-mail: asmirnov@univ.uniyar.ac.ru

1063-7788/03/6607-1260$24.00

$SU_L(2) \times U_R(1)$ group and is constructed by minimally extending the Standard Model in such a way as to include the four-color symmetry of quarks and leptons. In this model, the left-handed (L) and right-handed (R) quarks, $Q^{L,R}_{ia\alpha} = \psi^{L,R}_{ia\alpha}$, and leptons, $l^{L,R}_{ia} = \psi^{L,R}_{ia4}$—here, $a = 1, 2$ are the $SU_L(2)$ indices, while $\alpha = 1, 2, 3$ are the $SU_c(3)$ color indices—form the fundamental quartets $\psi^{L,R}_{iaA}$, $A = 1, 2, 3, 4$, of the $SU_V(4)$ group in each generation of number $i = 1, 2, 3\ldots$. With allowance for the possible mixing of fermions, the basis quark and lepton fields $Q'^{L,R}_{ia\alpha}$ and $l'^{L,R}_{ia}$, which form the basis quartets $\psi'^{L,R}_{iaA}$ of the $SU_V(4)$ group, can in general be represented as superpositions of the corresponding mass eigenstates $Q^{L,R}_{ia\alpha}$ and $l^{L,R}_{ia}$ of physical quarks and gluons; that is,

$$Q'^{L,R}_{ia\alpha} = \sum_j \left(A^{L,R}_{Q_a}\right)_{ij} Q^{L,R}_{ja\alpha}, \qquad (1)$$

$$l'^{L,R}_{ia} = \sum_j \left(A^{L,R}_{l_a}\right)_{ij} l^{L,R}_{ja},$$

where $A^{L,R}_{Q_a}$ and $A^{L,R}_{l_a}$ are unitary matrices that diagonalize the matrices of quarks and leptons, respectively.

Transformations of the basis fields in (1) under the $SU_V(4)$ group have a vectorial character; that is,

$$\psi'^{L,R}_{iaA} \to \psi''^{L,R}_{iaA} = \sum_B U_{AB} \psi'^{L,R}_{iaB},$$

where U is the 4×4 matrix of gauge $SU_V(4)$ transformations, which is common to the left- and right-handed fields. With respect to the $SU_L(2) \times U_R(1)$ group, left-handed fermions are doublets of zero hypercharge, while right-handed fermions are singlets of hypercharge $Y_R = \pm 1$ for up ($a = 1$) and down ($a = 2$) fermions, respectively.

In the gauge sector, this model predicts the existence of a charged color triplet of vector leptoquarks $V^{\pm}_{\alpha}$ and of an extra neutral Z' boson.

In general, the scalar sector of the model contains four multiplets $\Phi^{(1)}$, $\Phi^{(2)}$, $\Phi^{(3)}$, and $\Phi^{(4)}$ transforming according to the (4,1,1), (1,2,1), (15,2,1), and (15,1,0) representations of the $SU_V(4) \times SU_L(2) \times U_R(1)$ group and having vacuum expectation values η_1, η_2, η_3, and η_4, respectively. The multiplets $\Phi^{(1)}$ and $\Phi^{(4)}$ involve the scalar leptoquarks $S^{(1)}_{\alpha}$ and $S^{(4)}_{\alpha}$ of electric charge 2/3, which are singlets of the $SU_L(2)$ group, while the multiplet $\Phi^{(3)}$ contains two color $SU_L(2)$ doublets of scalar leptoquarks,

$$S^{(\pm)}_{a\alpha} = \begin{pmatrix} S^{(\pm)}_{1\alpha} \\ S^{(\pm)}_{2\alpha} \end{pmatrix}. \qquad (2)$$

The up components of these doublets, $S^{(\pm)}_{1\alpha}$, have electric charges of 5/3 and 1/3, while their down components $S^{(\pm)}_{2\alpha}$ have electric charges of $\pm 2/3$, respectively. From an analysis of the scalar sector of the model, it follows (see, for example, [9]) that, in general, the scalar leptoquarks $S^{(+)}_{2\alpha}, \overset{*}{S}{}^{(-)}_{2\alpha}$, $S^{(1)}_{\alpha}$, and $S^{(4)}_{\alpha}$ of electric charge 2/3 are superpositions of the Goldstone mode

$$S_0 = \left[-\frac{\eta_1}{2} S^{(1)} + \sqrt{\frac{2}{3}} \left(\eta_3 \frac{S^{(+)}_2 + \overset{*}{S}{}^{(-)}_2}{\sqrt{2}} + \eta_4 S^{(4)}\right)\right] \Bigg/ \sqrt{\frac{{\eta_1}^2}{4} + \frac{2}{3}({\eta_3}^2 + {\eta_4}^2)} \qquad (3)$$

and three physical scalar leptoquarks S_1, S_2, and S_3, which are orthogonal to it; that is,

$$S^{(+)}_2 = \sum_{k=0}^{3} C^{(+)}_k S_k, \quad \overset{*}{S}{}^{(-)}_2 = \sum_{k=0}^{3} C^{(-)}_k S_k, \qquad (4)$$

$$S^{(1)} = \sum_{k=0}^{3} C^{(1)}_k S_k, \quad S^{(4)} = \sum_{k=0}^{3} C^{(4)}_k S_k,$$

where $C^{(\pm)}_k$, $C^{(1)}_k$, and $C^{(4)}_k$ are complex numbers forming a 4×4 unitary matrix that describes the mixing of the scalar leptoquarks of electric charge 2/3. The elements $C^{(\pm)}_0$, $C^{(1)}_0$, and $C^{(4)}_0$ of this matrix, which correspond to the Goldstone mode, are equal to the coefficients of the fields $S^{(+)}_2, \overset{*}{S}{}^{(-)}_2$, $S^{(1)}$, and $S^{(4)}$ in Eq. (3), while its remaining elements must only satisfy constraints imposed by the unitarity of this matrix.

In the unitary gauge, two triplets of the up leptoquarks $S^{(+)}_{1\alpha}$ and $S^{(-)}_{1\alpha}$ of electric charge 5/3 and 1/3 and, in the general case of arbitrary mixing, three scalar leptoquarks $S_{k\alpha}$ ($k = 1, 2, 3$) of electric charge 2/3 appear as physical fields upon the elimination of Goldstone modes.

In a general form, the interactions of scalar doublets with fermions in the minimal model involving quark–lepton symmetry are presented in [7]. In order to perform calculations for processes like

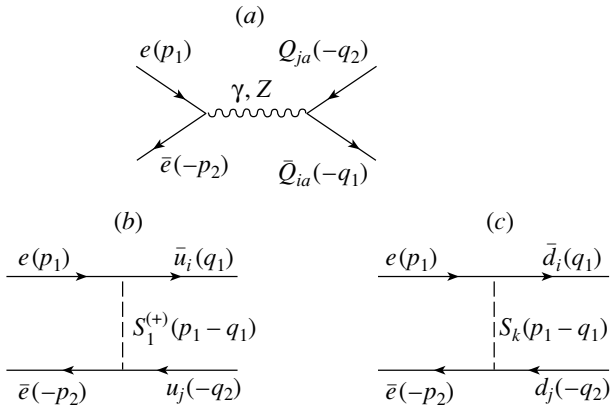

Fig. 1. Diagrams describing the production of quark–antiquark pairs in electron–positron annihilation with allowance for scalar leptoquarks, $e^+e^- \to Q_{ia}\tilde{Q}_{ja}$.

$e^+e^- \to Q_{ia}\tilde{Q}_{ja}$, we need the interactions of the scalar-leptoquark doublets (2) with charged leptons $l_{j2} = (e, \mu, \tau)$ and with up $[Q_{i1} \equiv u_i = (u, c, t)]$ and down $[Q_{i2} \equiv d_i = (d, s, b)]$ quarks ($i = 1, 2, 3$ are the indices of generations). These interactions can be represented as

$$L_{Q_1 l_2 S_1^{(+)}} = \bar{Q}_{i1\alpha}\Big[(g^S)_{ij} + (g^P)_{ij}\gamma_5\Big] l_{j2} S_{1\alpha}^{(+)} + \text{h.c.}, \tag{5}$$

$$L_{Q_2 l_2 S_k} = \bar{Q}_{i2\alpha}\Big[(g_k^S)_{ij} + (g_k^P)_{ij}\gamma_5\Big] l_{j2} S_{k\alpha} + \text{h.c.} \tag{6}$$

(hereafter, a tilde symbol above a fermion denotes its antiparticle, while an overbar denotes the Dirac conjugation of its wave function). In the minimal model featuring quark–lepton symmetry, the matrices that are formed by the scalar and pseudoscalar coupling constants and which are involved in Eqs. (5) and (6) are given by

$$(g^{S,P})_{ij} = \sqrt{3/2}\Big[\mp (C_Q M_2 K_2^R)_{ij} + (\overset{+}{M}_1 K_1^L C_l)_{ij}\Big]/(2\eta \sin\beta), \tag{7}$$

$$(g_k^{S,P})_{ij} = \sqrt{3/2}\Big[\mp (M_2 K_2^R)_{ij} C_k^{(+)} - (\overset{+}{M}_2 K_2^L)_{ij} C_k^{(-)}\Big]/(\sqrt{2}\eta \sin\beta), \tag{8}$$

where $M_a = M_{Q_a} - K_a^L M_{l_a} \overset{+}{K}_a^R$, with $(M_{Q_a})_{ij} = m_{Q_{ia}}\delta_{ij}$ and $(M_{l_a})_{ij} = m_{l_{ia}}\delta_{ij}$ being the diagonal mass matrices of the up ($a = 1$) and down ($a = 2$) quarks and leptons; $K_a^{L,R} = (A_{Q_a}^{L,R})^+ A_{l_a}^{L,R}$ are unitary mixing matrices that are due to the possible distinctions between the quarks and lepton mixing matrices $A_{Q_a}^{L,R}$ and $A_{l_a}^{L,R}$ in Eqs. (1); $C_Q = (A_{Q_1}^L)^+ A_{Q_2}^L$ is the Cabibbo–Kobayashi–Maskawa matrix, which is known to be due to the distinction between the mixing matrices $A_{Q_1}^L$ and $A_{Q_2}^L$ in (1) for up and down left-handed quarks; $C_l = (A_{l_1}^L)^+ A_{l_2}^L$ is the matrix that is analogous to the preceding one in the lepton sector and which is due to the possible distinction between the mixing matrices $A_{l_1}^L$ and $A_{l_2}^L$ in (1) for up and down left-handed leptons; β is the angle of mixing of two color-singlet scalar doublets available in the model, their expectation values being η_2 and η_3 ($\tan\beta = \eta_3/\eta_2$); and $\eta = \sqrt{\eta_2{}^2 + \eta_3{}^2} = (\sqrt{2}G_\text{F})^{-1/2} \approx 246$ GeV is the Standard Model expectation value. We note that, in general, there are five nonidentity matrices, $K_a^{L,R}$, $a = 1, 2$, and C_l, and this leads to [6] an additional mixing of quarks and leptons in their interaction with vector leptoquarks and to the additional mixing of leptons in their interaction with W bosons.

3. CROSS SECTIONS FOR THE PROCESS $e^+e^- \to Q_{ia}\tilde{Q}_{ja}$ OF THE PRODUCTION OF QUARK–ANTIQUARK PAIRS WITH ALLOWANCE FOR SCALAR LEPTOQUARKS

The production of a quark–antiquark pair in electron–positron annihilation with allowance for the scalar leptoquarks (2) and (4) is described by the diagrams in Fig. 1. The diagram in Fig. 1*a* corresponds to the contribution of a photon and a Z boson in the Standard Model to the process under consideration (the standard Higgs boson may also contribute within the Standard Model, but we disregard this contribution here since the constant of its coupling to the electron is small, $m_e/\eta \sim 10^{-6}$), while the diagrams in Figs. 1*b* and 1*c* describe the contributions to the production of up and down quarks from the scalar leptoquarks $S_1^{(+)}$ and S_k ($k = 1, 2, 3$), respectively.

3.1. Cross Section for the Process $e^+e^- \to u_i\tilde{u}_j$

The cross section for the process $e^+e^- \to u_i\tilde{u}_j$ of the production of up quarks is described by the sum of the diagrams in Fig. 1*a* and 1*b* and can be represented in the form

$$\sigma(e^+e^- \to u_i\tilde{u}_j) \equiv \sigma_{u_i\tilde{u}_j} = \delta_{ij}\left(\sigma_{u_i\tilde{u}_i}^{(\text{SM})} + \sum_{n=1,2}\sigma_{u_i\tilde{u}_i}^{X_n S_1^{(+)}}\right) + \sigma_{u_i\tilde{u}_j}^{S_1^{(+)}}, \tag{9}$$

where $\sigma^{(\mathrm{SM})}_{u_i\tilde{u}_i}$ is the cross section for this process in the Standard Model; $\sigma^{X_nS_1^{(+)}}_{u_i\tilde{u}_i}$ is the contribution that is due to the interference between the contributions of the X_n boson, $X_n = (\gamma, Z)$, $n = 1, 2$, and the scalar leptoquark $S_1^{(+)}$; and $\sigma^{S_1^{(+)}}_{u_i\tilde{u}_j}$ is the scalar-leptoquark ($S_1^{(+)}$) contribution associated with the diagram in Fig. 1*b*.

In the Standard Model, the cross section $\sigma^{(\mathrm{SM})}_{u_i\tilde{u}_i}$ has the form

$$\sigma^{(\mathrm{SM})}_{u_i\tilde{u}_i} = \frac{4\pi\alpha^2}{s} v(s, m_{u_i}, m_{\tilde{u}_i}) \Bigg\{ \left(1 + \frac{2m^2_{u_i}}{s}\right) \times \Bigg[Q^2_{u_i} + \frac{s^2}{(s - m_Z^2)^2} \left((v_e^Z)^2 + (a_e^Z)^2\right)(v_{u_i}^Z)^2 - \frac{2Q_{u_i}s}{s - m_Z^2} v_e^Z v_{u_i}^Z \Bigg] + v^2(s, m_{u_i}, m_{\tilde{u}_i}) \frac{s^2}{(s - m_Z^2)^2} \times \left((v_e^Z)^2 + (a_e^Z)^2\right)(a_{u_i}^Z)^2 \Bigg\}, \quad (10)$$

where

$$v(s, m_3, m_4) = \sqrt{1 - \frac{2(m_3^2 + m_4^2)}{s} + \frac{(m_3^2 - m_4^2)^2}{s^2}}; \quad (11)$$

$$v_{f_a}^Z = \frac{(\tau_3)_{aa} - 4Q_{f_a}s_{\mathrm{W}}^2}{4s_{\mathrm{W}}c_{\mathrm{W}}}, \quad a_{f_a}^Z = \frac{(\tau_3)_{aa}}{4s_{\mathrm{W}}c_{\mathrm{W}}}$$

are the vector and axial-vector fermionic coupling constants of the Z boson in the Standard Model; $s_{\mathrm{W}} = \sin\theta_{\mathrm{W}}$ and $c_{\mathrm{W}} = \cos\theta_{\mathrm{W}}$, θ_{W} being the Weinberg angle; τ_3 is the third Pauli matrix; and Q_{f_a} is the fermion electric charge expressed in units of the proton charge.

For the interference term $\sigma^{X_nS_1^{(+)}}_{u_i\tilde{u}_i}$, our calculations yield

$$\sigma^{X_nS_1^{(+)}}_{u_i\tilde{u}_i} = -\frac{N_c\alpha}{2(s - m^2_{X_n})} \sum_{\pm} \sum_{m=1,2} g_i^{(m)} \times V^{(m)X_n}_{u_i\pm} f_{\pm}(s, m_{S_1^{(+)}}, m_{u_i}), \quad (12)$$

where

$$g_i^{(1)} \equiv |(g^S)_{i1}|^2 + |(g^P)_{i1}|^2, \quad (13)$$
$$g_i^{(2)} \equiv (g^S)_{i1}(g^P)^*_{i1} + (g^P)_{i1}(g^S)^*_{i1},$$

$$V^{(1)X_n}_{Q_{ia}\pm} = v^{X_n}_{Q_{ia}} v_e^{X_n} \pm a^{X_n}_{Q_{ia}} a_e^{X_n}, \quad (14)$$
$$V^{(2)X_n}_{Q_{ia}\pm} = \pm a^{X_n}_{Q_{ia}} v_e^{X_n} + v^{X_n}_{Q_{ia}} a_e^{X_n},$$

$m_\gamma = 0$, $v^\gamma_{f_a} = Q_{f_a}$, and $a^\gamma_{f_a} = 0$. The functions $f_\pm(s, m, m_3)$ appearing in (12) are given by

$$f_+(s, m, m_3) = \frac{m_3^2}{s} \ln\left(\frac{w_+(s, m, m_3, m_3)}{w_-(s, m, m_3, m_3)}\right), \quad (15)$$

$$f_-(s, m, m_3) = \frac{2m^2 - 2m_3^2 - s}{s} \frac{v(s, m_3, m_3)}{2} + \frac{(m^2 - m_3^2)^2}{s^2} \ln\left(\frac{w_+(s, m, m_3, m_3)}{w_-(s, m, m_3, m_3)}\right), \quad (16)$$

where

$$w_\pm(s, m, m_3, m_4) = \pm sv(s, m_3, m_4) + m_3^2 + m_4^2 - s - 2m^2.$$

Similarly, the calculation of the contributions $\sigma^{S_1^{(+)}}_{u_i\tilde{u}_j}$ yields

$$\sigma^{S_1^{(+)}}_{u_i\tilde{u}_j} = \frac{N_c g_i^{(1)} (g_j^{(1)})^*}{16\pi s} f_{5/3}(s, m_{S_1^{(+)}}, m_{u_i}, m_{\tilde{u}_j}), \quad (17)$$

where

$$f_{5/3}(s, m, m_3, m_4) = \frac{2m^2 - m_3^2 - m_4^2}{s} \times \ln\left(\frac{w_+(s, m, m_3, m_4)}{w_-(s, m, m_3, m_4)}\right) + \frac{2m^4 + 2m_3^2m_4^2 - (2m_3^2 + 2m_4^2 - s)m^2}{m^4 + m_3^2m_4^2 - (m_3^2 + m_4^2 - s)m^2} \times v(s, m_3, m_4). \quad (18)$$

Formulas (9), (10), (12), and (17) determine the cross section for the process $e^+e^- \to u_i\tilde{u}_j$ of the production of up quarks in electron–positron annihilation with allowance for the contributions of the scalar leptoquark $S_1^{(+)}$. Upon taking into account Eq. (7), the constants that describe electron coupling to quarks of the ith generation and which appear in (13) take the form

$$(g^{S,P})_{i1} = \sqrt{3/2} \sum_{i'=1}^{3} \Bigg[\mp (C_Q)_{ii'} \times \left(m_{d_{i'}}(K_2^R)_{i'1} - (K_2^L)_{i'1}m_e\right) + \left(\pm (K_1^R)_{ii'}m_{\nu_{i'}} - m_{u_i}(K_1^L)_{ii'}\right)(C_l)_{i'1} \Bigg] / (2\eta \sin\beta), \quad (19)$$

where m_e is the electron mass, while m_{u_i}, m_{d_i}, and m_{ν_i} are the masses of, respectively, the up quark, the down quark, and the neutrino of the ith generation.

In the particular case where there is no additional mixing in the fermion sector—that is, $K^L = K^R =$

$C_l = I$—the coupling constants in (19) can be simplified to become

$$(g^{S,P})_{i1} = \sqrt{3/2}\,[\mp(C_Q)_{i1}(m_d - m_e) + \delta_{i1}(m_{\nu_e} - m_u)]\,/(2\eta\sin\beta). \quad (20)$$

It should be noted that, in the limit of massless quarks, the functions in (11) and (15) reduce to $v(s,0,0) = 1$ and $f_+(s,m,0) = 0$, respectively, while the functions in (16) and (18) take a much simpler form,

$$f_-(s,m,0) \equiv f_1(x) = x - 1/2 + x^2 \ln\frac{x}{1+x}, \quad (21)$$

$$f_{5/3}(s,m,0,0) \equiv f_2(x) = 2x\ln\frac{x}{1+x} + \frac{1+2x}{1+x}, \quad (22)$$

where $x = m^2/s$.

3.2. Cross Section for the Process $e^+e^- \to d_i\tilde{d}_j$

The process $e^+e^- \to d_i\tilde{d}_j$ of the production of down quarks with allowance for scalar leptoquarks is described by the sum of the diagrams in Figs. 1*a* and 1*c*. Similarly to (9), the cross section for this process can be represented in the form

$$\sigma(e^+e^- \to d_i\tilde{d}_j) \equiv \sigma_{d_i\tilde{d}_j} = \delta_{ij}\left(\sigma^{(\mathrm{SM})}_{d_i\tilde{d}_i} + \sum_{n=1,2}\sum_{k=1}^{3}\sigma^{X_nS_k}_{d_i\tilde{d}_i}\right) + \sigma^{S}_{d_i\tilde{d}_j}. \quad (23)$$

The Standard Model cross section $\sigma^{(\mathrm{SM})}_{d_i\tilde{d}_i}$ and the interference terms $\sigma^{X_nS_k}_{d_i\tilde{d}_i}$ appearing in (23) can be obtained from formulas (10) and (12) by means of the substitutions $u_i \to d_i$, $S_1^{(+)} \to S_k$, and $g_i^{(m)} \to (g_i^{(m)})_{kk}$. For the contribution $\sigma^{S}_{d_i\tilde{d}_j}$ from the diagram in Fig. 1*c*, the calculations yield

$$\sigma^{S}_{d_i\tilde{d}_j} = \frac{N_c}{16\pi s}\sum_{k,l=1}^{3}(g_i^{(1)})_{kl}(g_j^{(1)})^*_{kl} \times f_{2/3}(s, m_{S_k}, m_{S_l}; m_{d_i}, m_{\tilde{d}_j}), \quad (24)$$

where

$$(g_i^{(1)})_{kl} = (g_k^S)_{i1}(g_l^S)^*_{i1} + (g_k^P)_{i1}(g_l^P)^*_{i1}, \quad (25)$$
$$(g_i^{(2)})_{kl} = (g_k^S)_{i1}(g_l^P)^*_{i1} + (g_k^P)_{i1}(g_l^S)^*_{i1},$$

$$f_{2/3}(s,m_1,m_2;m_3,m_4) = \frac{m_1^4 + m_2^4 + 2m_3^2m_4^2 - 2(m_3^2+m_4^2)(m_1^2+m_2^2)}{2s(m_1^2-m_2^2)} \times \ln\left(\frac{w_+(s,m_1,m_3,m_4)w_-(s,m_2,m_3,m_4)}{w_-(s,m_1,m_3,m_4)w_+(s,m_2,m_3,m_4)}\right) + v(s,m_3,m_4) + \frac{m_1^2+m_2^2-m_3^2-m_4^2}{2s} \times \ln\left(\frac{(w_+(s,m_2,m_3,m_4) - m_1^2 + m_2^2)^2 - (m_1^2-m_2^2)^2}{(w_-(s,m_2,m_3,m_4) - m_1^2 + m_2^2)^2 - (m_1^2-m_2^2)^2}\right). \quad (26)$$

With allowance for formula (8), the constants describing scalar-leptoquark (S_k) coupling to the electron and the down quark and appearing in (25) assume the form

$$(g_k^{S,P})_{i1} = \sqrt{3/2} \times \left[\mp(m_{d_i}(K_2^R)_{i1} - m_e(K_2^L)_{i1})C_k^{(+)} - (m_{d_i}(K_2^L)_{i1} - m_e(K_2^R)_{i1})C_k^{(-)}\right]/(\sqrt{2}\eta\sin\beta). \quad (27)$$

In the particular case where there is no additional mixing in the fermion sector—that is, $K^L = K^R = I$—the nonvanishing (at $i = 1$) constant appearing in (27) has the form

$$(g_k^{S,P})_{11} = \sqrt{3/2}(m_d - m_e) \times \left[\mp C_k^{(+)} - C_k^{(-)}\right]/(\sqrt{2}\eta\sin\beta). \quad (28)$$

At equal masses of the scalar leptoquarks, the function in (26) coincides with that in (18), $f_{2/3}(s,m,m;m_3,m_4) = f_{5/3}(s,m,m_3,m_4)$, while, in the limit of massless quarks, it takes the form

$$f_{2/3}(s,m_{S_k},m_{S_l};0,0) \equiv f_3(x_k,x_l) = \frac{x_l}{x_l - x_k}\left(1 + x_l\ln\frac{x_l}{1+x_l}\right) - \frac{x_k}{x_l - x_k}\left(1 + x_k\ln\frac{x_k}{1+x_k}\right), \quad (29)$$

where $x_k = m^2_{S_k}/s$. At equal masses of the scalar

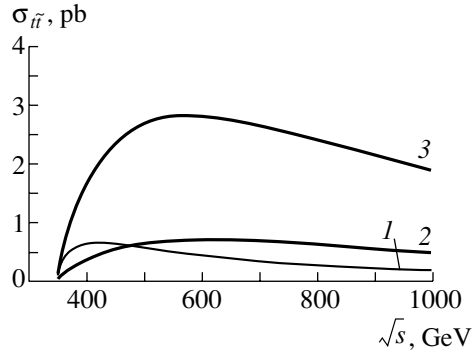

Fig. 2. Cross section for the process $e^+e^- \to t\tilde{t}$ as a function of the energy $\sqrt{s}$ at the scalar-leptoquark mass of $m_{S_1^{(+)}} = 300$ GeV for the mixing-parameter values of $k_t = (1)\,0$ (Standard Model), $(2)\,0.5$, and $(3)\,1.0$.

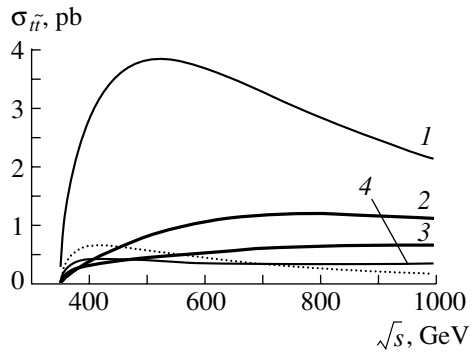

Fig. 3. Cross section for the process $e^+e^- \to t\tilde{t}$ as a function of the energy $\sqrt{s}$ at the mixing-parameter value of $k_t = 1$ for the scalar-leptoquark-mass values of $m_{S_1^{(+)}} = (1)\,250$, $(2)\,500$, $(3)\,700$, and $(4)\,1000$ GeV. The dotted curve represents the corresponding result in the Standard Model.

leptoquarks, the function in (29) coincides with the function $f_2(x_k)$ appearing in (22).

4. ANALYSIS OF THE SCALAR-LEPTOQUARK CONTRIBUTIONS TO THE CROSS SECTIONS FOR $e^+e^- \to Q_{ia}\tilde{Q}_{ja}$ PROCESSES

The constants in (19) and (27), which describe scalar-leptoquark coupling to the quarks and the electron and which lead to the processes being considered, are determined by the ratios of the quark, electron, and neutrino masses to the Standard Model vacuum expectation value; the Cabibbo–Kobayashi–Maskawa matrix C_Q; arbitrary unitary matrices K_a^L, K_a^R, and C_l describing additional fermion mixing; and the mixing angle β in the scalar sector. We note that, in the absence of additional fermion mixing [see formulas (20) and (28)], the above coupling constants prove to be on the order of the ratio of the masses of the first-generation quarks to the Standard Model vacuum expectation value—that is, on the order of $m_u/\eta \sim m_d/\eta \sim 10^{-5}$; in this case, the contributions of scalar leptoquarks to the process being studied are negligible. We note that the latest data on neutrino oscillations seem to suggest [11] that the lepton-mixing matrix C_l is nondiagonal—that is, an additional fermion mixing is possible, in particular, in the lepton sector. In the presence of an arbitrary fermion mixing, the coupling constants in (19) and (27) will be determined predominantly by the masses of the heavy t, c, and b quarks and by the mixing parameters.

4.1. Cross Sections for the Processes $e^+e^- \to t\tilde{t}, t\tilde{c}, c\tilde{c}$ of the Production of Heavy Up Quarks

Retaining, in (19), the contributions of the c and t quarks [the possible contribution of the b quark is suppressed by the additional element $(C_Q)_{i3}$ of the Cabibbo–Kobayashi–Maskawa matrix], we find that the coupling constants for processes involving c and t quarks have the form

$$(g^{S,P})_{i1} \approx -\frac{1}{2}\sqrt{\frac{3}{2}}\frac{m_{u_i}}{\eta}\sqrt{k_{u_i}}, \qquad (30)$$

where, by $k_{u_i}[i = 2, 3, u_i = (c, t)]$ we have denoted the effective mixing parameter for the c or the t quark,

$$k_{u_i} = \frac{|K_1^L C_l|^2_{i1}}{\sin^2\beta}. \qquad (31)$$

From (30), we obtain the coupling constants

$$(g^{S,P})_{21} \approx -0.3 \times 10^{-2}\sqrt{k_c}, \qquad (32)$$
$$(g^{S,P})_{31} \approx -0.43\sqrt{k_t}$$

for the c and the t quark, respectively. One can see that, in the case of identical assumptions on the mix-

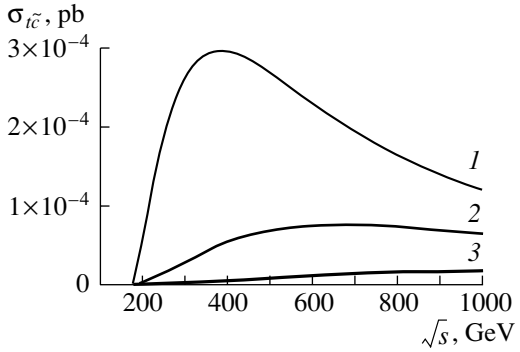

Fig. 4. Cross section for the process $e^+e^- \to t\tilde{c}$ as a function of the energy $\sqrt{s}$ at $k_c k_t = 1$ for the scalar-leptoquark-mass values of $m_{S_1^{(+)}} = (1)\,250, (2)\,500$, and $(3)\,1000$ GeV.

ing parameters, the coupling constants $(g^{(S,P)})_{31}$ for scalar-leptoquark interaction with the electron and the t quark appear to be dominant.

Taking into account expression (30) and using relations (9), (10), (12), and (17), we obtain the cross section for the production of a $t\tilde{t}$ pair in the form

$$\sigma_{t\tilde{t}} = \sigma_{t\tilde{t}}^{(\mathrm{SM})} + \sum_n \sigma_{t\tilde{t}}^{X_n S_1^{(+)}} + \sigma_{t\tilde{t}}^{S_1^{(+)}}, \qquad (33)$$

$$\sigma_{t\tilde{t}}^{X_n S_1^{(+)}} = \frac{-3N_c}{8}\left(\frac{m_t}{\eta}\right)^2 k_t \frac{\alpha}{(s-m_{X_n}^2)} \qquad (34)$$
$$\times \sum_{\pm}\sum_{m=1,2} V_{t\pm}^{(m)X_n} f_{\pm}(s, m_{S_1^{(+)}}, m_t),$$

$$\sigma_{t\tilde{t}}^{S_1^{(+)}} = \frac{9N_c}{256\pi}(\frac{m_t}{\eta})^4 k_t^2 \frac{1}{s} f_{5/3}(s, m_{S_1^{(+)}}, m_t, m_t), \qquad (35)$$

where the constants $V_{t\pm}^{(m)X_n}$ for the t quark are given by Eqs. (14), while the functions $f_{\pm}(s, m_{S_1^{(+)}}, m_t)$ and $f_{5/3}(s, m_{S_1^{(+)}}, m_t, m_t)$ are defined by Eqs. (15), (16), and (18).

The cross sections given by Eqs. (33)–(35) as a function of the energy $\sqrt{s}$ are determined by two parameters, the scalar-leptoquark mass $m_{S_1^{(+)}}$ and the mixing parameter k_t. According to the estimations of the scalar-leptoquark masses on the basis of currently available data on the parameters S, T, and U of radiative corrections [12], the scalar leptoquarks can be relatively light [10] (lighter than 1 TeV), a lower experimental limit on the mass of scalar leptoquarks from data on their direct production being about 250 GeV [12]. From Eqs. (31) and (32), it can be seen that, without disturbing the smallness of the perturbation-theory parameter $(g^{S,P})_{31}^2/4\pi$, the mixing parameter k_t can vary from zero to values of about unity or even somewhat greater. In the ensuing analysis, we restrict ourselves to values of the scalar-leptoquark masses in the range 250–1000 GeV and values of the mixing parameter k_t in the range 0.0–1.0.

Figure 2 shows the cross section $\sigma_{t\tilde{t}}$ as a function of the energy $\sqrt{s}$ at $m_{S_1^{(+)}} = 300$ GeV for $k_t =$ 0.0–1.0. For $k_t \leq 0.5$, the destructive-interference term is operative, which, in particular, leads, at energies of $\sqrt{s} \leq 500$ GeV, to a reduction of the cross section below that in the Standard Model, $\sigma_{t\tilde{t}}^{(\mathrm{SM})}$; at energies of $\sqrt{s} \geq 500$ GeV, however, the cross section $\sigma_{t\tilde{t}}$ already exceeds $\sigma_{t\tilde{t}}^{(\mathrm{SM})}$ considerably. At $k_t > 0.5$, the purely leptoquark contribution $\sigma_{t\tilde{t}}^{S}$ is dominant over the entire range of $\sqrt{s}$, and this leads to a significant excess of $\sigma_{t\tilde{t}}$ over $\sigma_{t\tilde{t}}^{(\mathrm{SM})}$ (by a factor greater than five at $k_t = 1.0$ and $\sqrt{s} \sim 600$ GeV).

In Fig. 3, the cross section $\sigma_{t\tilde{t}}$ as a function of the energy $\sqrt{s}$ is displayed at $k_t = 1$ for $m_{S_1^{(+)}} =$ 250–1000 GeV. From this figure, it can be seen that, if the scalar-leptoquark mass takes values in the range $m_{S_1^{(+)}} \sim 250$–500 GeV, the cross section $\sigma_{t\tilde{t}}$ (at $k_t = 1$) can be severalfold larger than the cross section $\sigma_{t\tilde{t}}^{(\mathrm{SM})}$, the characteristic value of the cross section $\sigma_{t\tilde{t}}$ being a few picobarns. We note that measurement of the cross section $\sigma_{t\tilde{t}}$ at electron–positron colliders of the TESLA type [13] could efficiently set constraints on the scalar-leptoquark mass and on the mixing parameter of the model.

Using Eqs. (9) and (17) and taking into account the coupling constants in (30), we can obtain the cross section for the process $e^+e^- \to t\tilde{c}$ in the form

$$\sigma(e^+e^- \to t\tilde{c}) \equiv \sigma_{t\tilde{c}} = \frac{9N_c}{256\pi}\left(\frac{m_c}{\eta}\right)^2$$
$$\times \left(\frac{m_t}{\eta}\right)^2 k_c k_t \frac{1}{s} f_{5/3}(s, m_{S_1^{(+)}}, m_t, m_c).$$

In Fig. 4, the cross section $\sigma_{t\tilde{c}}$ as a function of $\sqrt{s}$ is shown at $k_c k_t = 1$ for $m_{S_1^{(+)}} = 250$–1000 GeV. As can be seen from this figure, the cross section in question takes values of about 10^{-4} pb, which is much smaller, in particular, than the currently available upper limit from LEP II data [14]: $\sigma_{t\tilde{c}} < 0.55$ pb. We recall that this process cannot proceed in the Standard Model.

An analysis reveals that the cross section for the process $e^+e^- \to c\tilde{c}$ differs only slightly from the predictions of the Standard Model. By way of example, we indicate that, at $k_c \sim 1$ and $m_{S_1^{(+)}} = 250$ GeV, the scalar-leptoquark contribution is about 10^{-6} pb in the range $\sqrt{s} =$180–500 GeV. We also note that the scalar-leptoquark contribution to processes leading to the production of $t\tilde{u}$, $c\tilde{u}$, and $u\tilde{u}$ pairs involving a light u quark is negligible (10^{-8} pb) because of the smallness of the constants of scalar-leptoquark coupling to the electron and the u quark.

4.2. Cross Section for the Production of a $b\tilde{b}$ Pair in the Process $e^+e^- \to b\tilde{b}$

Disregarding the electron mass against the masses of down quarks and using Eq. (27), we approximately obtain

$$(g_k^{S,P})_{i1} \approx \sqrt{3/2} m_{d_i}$$

$$\times \left[\mp (K_2^R)_{i1} C_k^{(+)} - (K_2^L)_{i1} C_k^{(-)} \right] / (\sqrt{2}\eta \sin\beta).$$

The coupling constants in (25), which appear in the cross section for the production of down quarks, can be represented in the form

$$(g_i^{(m)})_{kl} \approx \frac{3}{2} \left(\frac{m_{d_i}}{\eta} \right)^2 (k_{d_i}^{(m)})_{kl},$$

where

$$(k_{d_i}^{(m)})_{kl} = \left(\delta_m |(K_2^R)_{i1}|^2 C_k^{(+)} \overset{*}{C}_l^{(+)} + |(K_2^L)_{i1}|^2 C_k^{(-)} \overset{*}{C}_l^{(-)} \right) / \sin^2\beta \quad (36)$$

is the effective mixing parameter for the production of down quarks d_i with $\delta_m = \pm 1$ at $m = 1, 2$.

Additionally disregarding the b-quark mass against $\sqrt{s}$ ($\sqrt{s} >> m_b$), we can represent the cross section (23) for the production of a $b\tilde{b}$ pair in the form

$$\sigma(e^+e^- \to b\tilde{b}) \equiv \sigma_{b\tilde{b}} = \sigma_{b\tilde{b}}^{(\mathrm{SM})} + \sigma_{b\tilde{b}}^{XS} + \sigma_{b\tilde{b}}^{S}, \quad (37)$$

where

$$\sigma_{b\tilde{b}}^{XS} = -\frac{3N_c\alpha}{4} \left(\frac{m_b}{\eta} \right)^2 \times \sum_{n=1,2} \sum_{m=1,2} \sum_{k=1}^{3} \frac{V_{b-}^{(m)X_n}}{(s - m_{X_n}^2)} (k_b^{(m)})_{kk} f_1(x_k), \quad (38)$$

$$\sigma_{b\tilde{b}}^{S} = \frac{9N_c}{64\pi} \left(\frac{m_b}{\eta} \right)^4 \frac{1}{s} \sum_{k,l=1}^{3} |(k_b^{(1)})_{kl}|^2 f_3(x_k, x_l). \quad (39)$$

Here, $V_{b-}^{(m)X_n}$ is given by (14); the functions $f_1(x_k)$ and $f_3(x_k, x_l)$ are specified by Eqs. (21) and (29), respectively; and $x_k = m_{S_k}^2/s$. A numerical analysis reveals that the contributions (38) and (39) of scalar leptoquarks to the cross section (37) are small. To illustrate this statement, we set $|(k_b^{(m)})_{kl}| \sim 1$ and $m_{S_k} \sim 500$ GeV by way of example and find from (37) that $\sigma_{b\tilde{b}} \sim 4$ pb at $\sqrt{s} = 180$ GeV in this case, the contribution of scalar leptoquarks, which is given by Eqs. (38) and (39), being about 10^{-5} pb. This is much smaller than known experimental errors, for example, in the experimental value of $\sigma_{b\tilde{b}} = 4.6 \pm 0.6 \pm 0.3$ pb, which was obtained by the OPAL Collaboration at $\sqrt{s} = 183$ GeV [15]. At $\sqrt{s} = 250$–1000 GeV, $|(k_b^{(m)})_{kl}| \sim 1$, and $m_{S_k} \sim 500$ GeV, the contribution of scalar leptoquarks, which is given Eqs. (38) and (39), remains small (about 10^{-5}–10^{-6} pb).

Thus, our analysis has revealed that the contribution of scalar leptoquarks to the cross sections for the processes considered here can be significant. In particular, this is so for the cross sections $\sigma_{t\tilde{t}}$ and $\sigma_{t\tilde{c}}$ for processes involving the production of a t quark—as can be seen from Figs. 2 and 3, the cross section $\sigma_{t\tilde{t}}$ for the production of a $t\tilde{t}$ pair due to the contribution of the scalar leptoquark $S_1^{(+)}$ can be severalfold as large as the corresponding cross section $\sigma_{t\tilde{t}}^{(\mathrm{SM})}$ in the Standard Model. Measurement of such cross sections will become possible at facilities of the TESLA type [13], and this would yield stringent constraints on the scalar-leptoquark masses and mixing parameters.

5. CONCLUSION

On the basis of the minimal model featuring the four-color symmetry of quarks and leptons, we have calculated the contribution of the scalar-leptoquark doublets to the cross section $\sigma_{Q_{ia}\tilde{Q}_{ja}}$ for processes of the $e^+e^- \to Q_{ia}\tilde{Q}_{ja}$ type. We have analyzed these cross sections versus the scalar-leptoquark masses and fermion-mixing parameters. This analysis has been performed for energies of a colliding electron–positron pair in the range $\sqrt{s} = 250$–1000 GeV.

It has been shown that, owing to special features of the interaction of the scalar-leptoquark doublets with fermions (because of the Higgs origin of these doublets, the respective coupling constants are proportional to the ratios of the fermion masses to the Standard Model expectation value), these contributions are the most significant for processes leading to the production of a heavy t quark. By way of example, we indicate that, at the scalar-leptoquark mass in the range $m_{S_1^{(+)}} \sim 250$–500 GeV and a mixing-parameter value of $k_t \sim 1.0$, the cross section $\sigma_{t\tilde{t}}$ for the production of a $t\tilde{t}$ pair in the energy range $\sqrt{s} = 400$–1000 GeV may be severalfold larger than the corresponding Standard Model cross section $\sigma_{t\tilde{t}}^{(\mathrm{SM})}$. Measurement of the cross section $\sigma_{t\tilde{t}}$ at electron–positron colliders of the TESLA type could set limits on the scalar-leptoquark mass and on the mixing parameter.

For the cross section $\sigma_{t\tilde{c}}$, which vanishes at the tree level in the Standard Model, we have obtained the estimate $\sigma_{t\tilde{c}} \sim 10^{-4}$ pb at $m_{S_1^{(+)}} \sim 250$–500 GeV and $k_c k_t \sim 1.0$.

It has been shown that the scalar-leptoquark contributions to the cross sections $\sigma_{c\tilde{c}}$ and $\sigma_{b\tilde{b}}$ are small—in the mass and mixing-parameter region considered here, they are below 10^{-5} pb.

Our results—in particular, estimates of the cross section $\sigma_{t\bar{t}}$—may be of interest for projects of the TESLA type that are being presently discussed in the literature.

ACKNOWLEDGMENTS

This work was supported in part by the program Universities of Russia—Basic Research (project no. 02.01.25) and by the Russian Foundation for Basic Research (project nos. 00-02-17883, 01-02-06221).

REFERENCES

1. J. C. Pati and A. Salam, Phys. Rev. D **10**, 275 (1974).
2. W. Buchmüller, R. Rückl, and D. Wyler, Phys. Lett. B **191**, 442 (1987).
3. J. L. Hewett and T. G. Rizzo, Phys. Rev. D **36**, 3367 (1987).
4. J. L. Hewett and T. G. Rizzo, Phys. Rev. D **56**, 5709 (1997).
5. A. D. Smirnov, Phys. Lett. B **346**, 297 (1995).
6. A. D. Smirnov, Yad. Fiz. **58**, 2252 (1995) [Phys. At. Nucl. **58**, 2137 (1995)].
7. A. V. Povarov and A. D. Smirnov, Yad. Fiz. **64**, 78 (2001) [Phys. At. Nucl. **64**, 74 (2001)].
8. A. D. Smirnov, Phys. Lett. B **431**, 119 (1998).
9. A. D. Smirnov, Yad. Fiz. **64**, 367 (2001) [Phys. At. Nucl. **64**, 318 (2001)].
10. A. D. Smirnov, Phys. Lett. B **531**, 237 (2002); hep-ph/0202229.
11. M. Fukugita and M. Tanimoto, Phys. Lett. B **515**, 30 (2001).
12. Particle Data Group (D. E. Groom *et al.*), Eur. Phys. J. C **15**, 1 (2000), and partial update for the edition of 2002 (http://pdg.lbl.gov).
13. R-D. Heuer *et al.*, DESY 2001-011; hep-ph/0106315.
14. DELPHI Collab., Phys. Lett. B **446**, 62 (1999).
15. OPAL Collab., Eur. Phys. J. C **6**, 1 (1999).

Translated by A. Isaakyan

Physics of Atomic Nuclei, Vol. 66, No. 7, 2003, pp. 1269–1281. From Yadernaya Fizika, Vol. 66, No. 7, 2003, pp. 1309–1321.

ELEMENTARY PARTICLES AND FIELDS
Theory

Wavelet Analysis of Data in Particle Physics: Vector Mesons in e^+e^- Annihilation*

T. S. Belozerova, P. G. Frick, and V. K. Henner**

Perm State University and Institute of Continuous Media Mechanics, Perm, Russia

Received February 28, 2002; in final form, November 26, 2002

Abstract—The advantages that wavelet analysis (WA) provides for resolving the structures in experimental data are demonstrated. Due to good scaling properties of the wavelets, one can consider data with various resolutions, which allows the resonances to be separated from the background and from each other. The WA is much less sensitive to noise than any other analysis and allows the role of statistical errors to be substantially reduced. The WA is applied to the e^+e^- annihilation into hadron states with quantum numbers of ρ and ω mesons, and to p-wave $\pi\pi$ scattering. Distinguishing the resonance structures from an experimental noise and the background allows us to make more reliable conclusions about the ρ' and ω' states. The WA yields a useful set of starting conditions for analysis of ω' states with the multiresonance Breit–Wigner method preserving unitarity in the case of overlapping resonances. We also apply the WA for the ratio $R_{e^+e^-}$. © *2003 MAIK "Nauka/Interperiodica"*.

1. INTRODUCTION

We consider the use of wavelet transforms to reduce the presence of statistical noise in experimental data and argue that the subsequent smoothed forms allow the extraction of physical parameters which would otherwise be obscured. The method is commonly used in image and signal processing and is potentially quite interesting in the context of experimental particle physics.

The data on e^+e^- annihilation in different hadron states in the energy range from ρ-meson mass to about 2 GeV indicate a behavior related to several resonances associated with states with quantum numbers of ρ and ω mesons. The properties of these states and even their number are not well defined. Major difficulties in understanding the situation with them are large statistical errors in the data and overlapping of these states decaying into several final channels. Correspondingly, the major goal of this paper is to resolve structures in the existing data relevant to this study and then to find parameters of the excitations related to these structures using an appropriate method. Such a method has to preserve unitarity even when the resonances r_i and r_j with the same quantum numbers overlap, i.e., $|E_{r_i} - E_{r_j}| \sim \Gamma_{r_i} + \Gamma_{r_j}$.

The experimental data on e^+e^- annihilation in $\pi\pi$, $\pi^+\pi^-\pi^+\pi^-$, $\pi^+\pi^-\pi^0\pi^0$, $\omega\pi^0$, $\eta\pi^+\pi^-$, $\pi^+\pi^-\pi^0$, and $\omega\pi\pi$ channels are described, as well as p-wave $\pi\pi$ scattering.

The two isovector $\rho'(1450)$ and $\rho'(1700)$ states were found many years ago. There are also some indications of the state with mass about 2.1–2.2 GeV. Another possible ρ' state has a mass in the range 1.1–1.3 GeV. The situation is probably similar to the isoscalar ω' states.

Parameters of all these resonances are not well established, which makes the nature of these states not clear. They are considered as two-quark states—radial and orbital excitations of the ρ and ω mesons—or as a mixture of two-quark, four quark, and hybrid states. The situation is really complicated and the poor accuracy of experimental data opens a possibility of drawing very different conclusions about these states. Therefore, an appropriate analysis of data, which allows one to extract all the important structures that can be of different scales, is useful before any model based on some physical assumptions is applied.

Section 2 features a brief discussion of the wavelets, their properties, and applicability to the purposes of resolving the resonance-like structures observed in high-energy and nuclear physics. In Section 3, the wavelet analysis (WA) of e^+e^- annihilation in different final hadron channels and of p-wave $\pi\pi$ scattering is presented. Then, in Section 4, these wavelet-analyzed data are used as an input to study ω' states with the Breit–Wigner method that preserves unitarity for overlapping multichannel resonances. The application of the WA to "smear" the ratio $R_{e^+e^-}$ is presented in the Conclusion.

*This article was submitted by the authors in English.

**e-mail: henner@psu.ru

1063-7788/03/6607-1269$24.00

2. WAVELETS AND STRUCTURE RECOGNITION

Our main goal is to detect essential structures in data sets in a wide range of scales using the most suitable tool for such purposes. A convenient method for such analysis is a wavelet transformation (WT), which is known to be an efficient multiscale technique (for example, see the books of Holschneider [1] or Torresani [2]). It is often said that the WA works like a "microscope" discriminating different scales—both the characteristic scales and the positions of any local structures are obtained independently of the general structure of the data.

Before giving a very brief introduction to wavelets, we would like to say that we are not the only ones performing a type of "optimization" of the data in elementary particle physics. Let us point out an analogy between this work and the works on optimization of the ratio $R_{e^+e^-}$ in QCD [3–5]. The data on $R_{e^+e^-}$ have a wide range of structures and large statistical errors, making a direct comparison with QCD impossible. However, a meaningful comparison can be done if some kind of smearing procedure is used. The smeared ratio

$$\bar{R}_{e^+e^-}(s,\Delta) = \frac{\Delta}{\pi}\int\limits_0^{s_{\max}} \frac{R_{e^+e^-}(s')}{(s'-s)^2+\Delta^2}ds' \quad (1)$$

was introduced [3] ($s = E^2$, and Δ is a smearing parameter) to even out any rapid variations in $R_{e^+e^-}$.

The difference between the described procedure and the analysis needed to obtain resonance parameters is that, contrary to the smearing, we need to resolve the structures and, what is most important, we want to detect structures corresponding to different scales (global and local). The WA seems to be a very good tool for that. We will return in the conclusion to the discussion of the ratio $R_{e^+e^-}$ to point out that the WA provides a very reasonable and simple way to smear this ratio.

Most of the applications of WA to physics are related to spectral analysis and turbulence, where scaling is its inherent feature. Over the past few years, WA has been getting more popular in different areas of physics and many applications have been described in reviews [6–8]. In high-energy nucleus–nucleus interactions, it was successfully applied for studying the angular distributions of secondary particles [9, 10]—more references related to the processes of multiple production can be found in [7, 8]. In particle physics, the WA was recently used for evaluations of a background in the $\pi^- p \to \eta\pi^0$ reaction [11].

The continuous WT of a function $f(t)$ representing the data is defined as

$$w(a,t) = C_\psi^{-1/2} a^{-1/2}\int\limits_{-\infty}^{+\infty}\psi^*\left(\frac{t'-t}{a}\right)f(t')dt', \quad (2)$$

where

$$C_\psi = \int\limits_{-\infty}^{+\infty}|\omega^{-1}||\hat{\psi}(\omega)|^2 d\omega \quad (3)$$

is a constant defined through the Fourier transformation of $\psi(t)$:

$$\hat{\psi}(\omega) = \int\limits_{-\infty}^{+\infty}\psi(t)e^{-i\omega t}dt. \quad (4)$$

Similar to most of the references, we call an argument t as "time," even though in our actual problem it is an energy variable. The decomposition (2) is performed by convolution of the function $f(t)$ with a biparametric family of self-similar functions generated by dilatation and translation of the analyzing function $\psi(t)$:

$$\psi_{a,b}(t) = \psi\left(\frac{t-b}{a}\right), \quad (5)$$

where a scale parameter a characterizes the dilatation and b characterizes the translation in time or space. Wavelet function $\psi(t)$ is a sort of "window function" with a nonconstant window width: high-frequency wavelets are narrow (due to the factor $1/a$), while low-frequency wavelets are much broader. Very important for WA is the choice of the proper analyzing wavelet, which depends on the goal of the study. The function $\psi(t)$ should be well localized in both time and Fourier spaces and must obey the admissibility condition, $\int_{-\infty}^{+\infty}\psi(t)dt = 0$. This condition implies that ψ is an oscillatory (but with limited support) function and, if the integrals (3) and (4) converge, provides the existence of the inverse transformation:

$$f(t) = C_\psi^{-1/2}\int\limits_{-\infty}^{+\infty}\int\limits_0^{+\infty}\psi\left(\frac{t-t'}{a}\right)w(a,t')\frac{dt'da}{a^{5/2}}. \quad (6)$$

The WT is usually used for two kinds of problems: time-frequency analysis and time-scale analysis. In the first case, one studies, for example, some quasi-periodic signals/data with time-dependent spectral properties. For these purposes, the wavelets with good spectral resolution (having enough oscillations) are required. The complex Morlet wavelet is commonly used for such purposes:

$$\psi(t) = e^{-t^2/2}e^{i\omega_0 t}, \quad (7)$$

where the proper frequency ω_0 defines its spectral resolution. The admissibility condition is satisfied exactly for the imaginary part of (7); for its real part, $\int_{-\infty}^{+\infty} e^{-t^2/2}\cos(\omega_0 t)dt = e^{-{\omega_0}^2/2}$ and, if we take ω_0 to be large enough, we can consider this average to be zero. A conventional choice is $\omega_0 = 2\pi$—in this case, a signal with the period T gives a stripe on a wavelet plane $w(a,t)$ just at the level $a = T^{-1}$.

For another kind of problem, the goal is to recognize the local features of data and to find the parameters of dominating structures (location and scale/width). For these purposes, wavelets with a good localization in physical space with a small number of oscillations are used. One of the most popular wavelets of this type is called "Mexican Hat" (MH),

$$\psi(t) = (1 - t^2)e^{-t^2/2}. \tag{8}$$

We end this short introduction to wavelets with two examples similar to real data in physics of resonances. They will give the reasons why the WA is so suitable for this situation and help to understand the figures that will be presented when we analyze real data.

The first example is the model signal composed of several Gaussians with different widths and intensities:

$$f(t) = e^{-5(t-1)^2} + 2e^{-(t-6)^2/20} + 3e^{-10(t-10)^2} + e^{-(t-14)^2/10} + e^{-(t-18)^2}. \tag{9}$$

Then it was discretized with a 0.1 step on the interval $0 < t < 20$ ($f(t) \approx 0$ outside this interval) and a random high-frequency noise was added at each point to make it similar to the real experimental data which will be analyzed in the next section. These simulated data are shown at the bottom of Fig. 1. In the left-hand part of this figure, above the simulated data, the Fourier reconstructions of the signal are given for different numbers of the Fourier harmonics. Keeping 20 harmonics is enough to localize all maxima except for the one at $t = 14$, which is not resolved due to the noise that still exists in a smoother form in the restored signal. Moreover, many false maxima appear for the reason that the nonperiodic signal is decomposed into a sum of periodic ones. When the number of harmonics is decreased, the restored signal becomes smoother, but the localization of maxima changes significantly. The widths and amplitudes of all maxima (which are crucial for finding the resonance parameters) have essentially changed. When the number of harmonics changes from $n = 100$ to $n = 5$, a high and narrow peak ($t = 10$) becomes two times lower and wider, and low and wide peaks ($t = 6$ and $t = 14$) become two times narrower and about 1.5 times higher. Thus, the Fourier reconstruction of nonperiodic noisy data is not suitable for our goals: when the number of harmonics is small enough to eliminate the noise, the restored signal does not reproduce many important features of the original data. It means that further theoretical analysis based on the Fourier-reconstructed data (for instance, to obtain the resonance masses and partial widths) would give wrong results, no matter what physical model is used for this analysis.

The situation is quite different when the WA is applied. A very helpful representation of the WT, which allows one to see the features of the signal, gives the "time–frequency" plane. This is a multiresolution spectrogram that shows the frequency (scale) contents of the signal as a function of time. Each pixel on the spectrogram represents $w(a,t)$ for a certain a (scale) and t (time). Figure 1 (top) shows the wavelet transformation $w(a,t)$ performed by the MH. The sequences of dark and light spots indicate variations at corresponding scales. The location of a spot on the vertical axis (scale axis, a) corresponds to the width of the extremum. The intensity of dark spots shows the amplitudes of maxima. The highest maximum at $t = 10$ corresponds to the darkest spot that is located at the smallest value of $a \approx 0.2$ corresponding to this narrowest maximum. The spot at $t \approx 1$ is located at larger $a \approx 0.35$ and is not so dark [lower and wider maximum in (9)]. The dark region at the top of the figure demonstrates that, in the large-scale region, the whole signal is nothing but a wide maximum. The reconstructed signal is stable under small perturbations, which enables one to distinguish between useful large-scale stains (low frequencies in Fourier space) and contributions of the small-scale features usually generated by noise. The noise is located at the bottom of the wavelet plane (small-scale regions, or high frequencies). In order to separate the signal from the background noise, the wavelet reconstruction is performed for scales (scale parameter values) greater than a certain scale a_{noise}, which we will call the boundary scale. Reconstructions for different boundary scales are shown in Fig. 1 (bottom, right-hand side). On the upper two graphs, the noise is practically damped, and even then the localization of all the maxima and their widths remains intact except for the width of the narrowest one at $t = 10$. The latter happens because the width of this peak is close to the width of noiselike fluctuations and this part of the signal is altered with noise filtering. The actual experimental data that we analyze below do not have very narrow peaks, and we included such a peak in the model signal (9) in order to be able to discuss more general cases. Thus, Fig. 1 illustrates that the WA is a substantially better description of the data at large enough values a than the Fourier description is

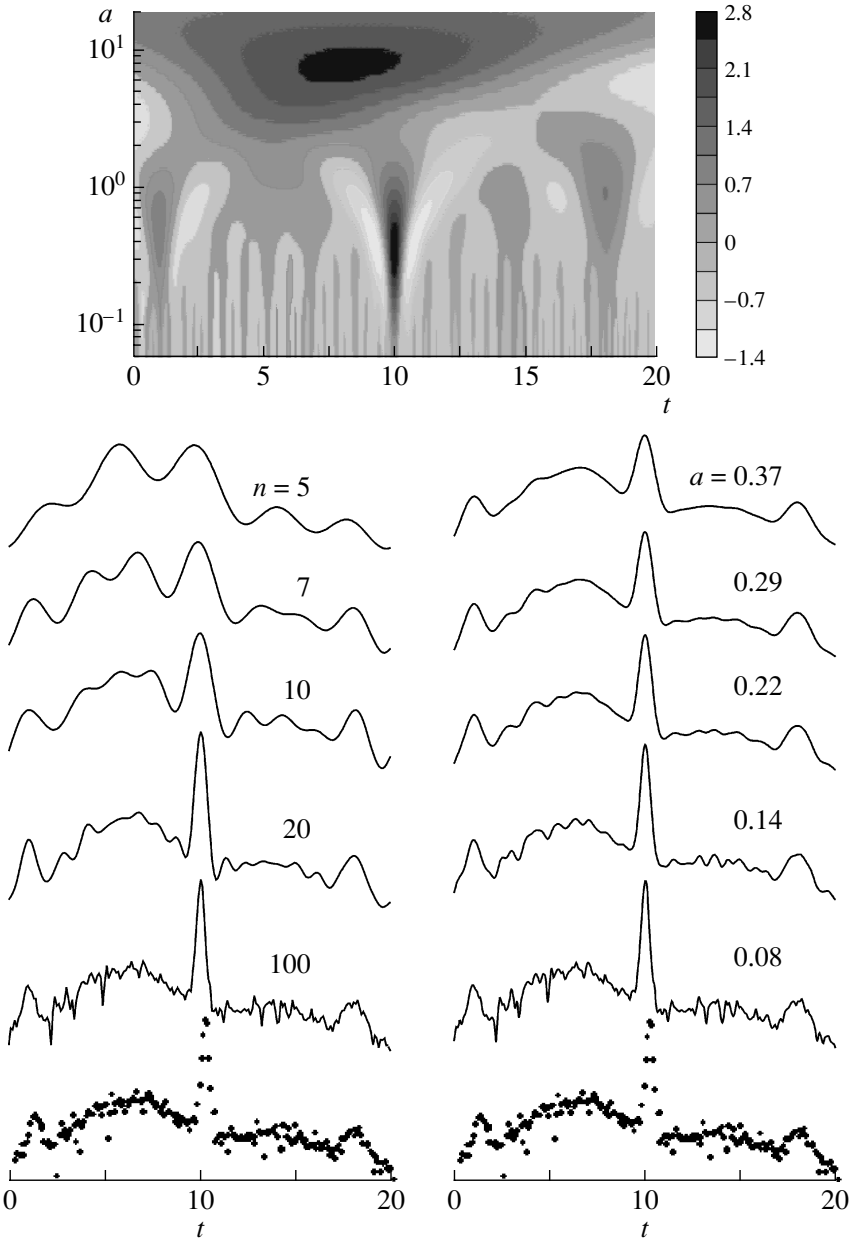

Fig. 1. (Top) Wavelet plane. (Bottom) Model signal based on Eq. (9) and its Fourier reconstruction for different n (n is the number of harmonics) (left side); wavelet reconstruction with MH wavelet for different values of the boundary scale (right side).

at small numbers n—both these cases correspond to damped noise.

Another signal, similar to physics-of-resonances data, is generated by discretizing a combination of several Lorentz-like peaks,

$$f(t) = \frac{8}{(t-2)^2+4} + \frac{1}{(t-5)^2+1} + \frac{48}{(t-10)^2+16} + \frac{1}{4(t-15)^2+1}. \quad (10)$$

The peaks have very different widths, and some of them substantially overlap. The signal was discretized with a step of 0.1 on the interval $0 < t < 20$ and a random high-frequency noise was added at each point (in the bottom of Fig. 2, we use a solid curve for the analyzed signal). Two different continuations for $f(t)$ below $t = 0$ were used to see the effect of the boundary conditions: $f(t) = 0$ and $f(t) = f(0)$. (Since $f(20) \approx 0$, a natural continuation above $t = 20$ is $f(t) = 0$.) Figure 2 gives the wavelet plane for the MH and the wavelet reconstruction of this signal. It is seen that the results of

the WA of the signal (10) + noise are similar to those obtained for the signal based on (9). Rigorously, the continuous Gaussian-shape MH wavelet may not be completely adequate for the problem of searching for Breit–Wigner resonances, but for practical purposes, as our examples demonstrate, it works well for both Gaussian- and Lorentz-like signals. It is important that the contributions of different bands to WT are reasonably separated along the vertical axis. That is why the reconstruction is stable under small variations of a_{noise}, which enables one to distinguish between the informative low-frequency bands and contributions of higher frequencies usually generated by noise.

Here, to choose a boundary scale, a_{noise}, that separates noiselike high-frequency components of data, we hold to a pragmatic line of reasoning: the best option of a_{noise} is the smallest one which will smooth out any rapid variations in data and enable us to reproduce stable results for low frequencies (resonances area). A similar pragmatic strategy was applied in [3, 4] to choose the parameter Δ that had to be large enough for a comparison of the smeared $\bar{R}_{e^+e^-}$ with QCD models, but not too large in order to keep some fine details of the data.

The reconstructed data are obtained using the inverse transformation (6)

$$f_r(t) = \langle f \rangle + C_\psi^{-1/2} \int_{a_{\text{noise}}}^{a_{\max}} \int_{t_{\min}}^{t_{\max}} \psi_{a,t}(t') w(a,t') \frac{dt'\,da}{a^{5/2}}. \tag{11}$$

The $\langle f \rangle$ must be added to the reconstructed signal to restore the mean value of the original signal (recall that the mean value of the WT is zero because an average value of any wavelet is zero). Formula (11) in the limit $a_{\text{noise}} \to 0$, $a_{\max} \to \infty$, $t_{\min} \to -\infty$, $t_{\max} \to +\infty$ is equivalent to the exact relation (6), but in practice a limited number of experimental points on the restricted energy interval leads to a limited domain in the integral (11). To fill in the gaps between experimental points, we use a linear interpolation. In practice, different interpolations lead to a small difference in the restored signal (which produces a very small difference on a lower part of the wavelet plane corresponding to noise). To show that, in the case of rather rare coverage on the energy scale in the data in Fig. 8 (below), we use two interpolations: linear and quadratic spline.

One of the big advantages of the WA is that the sensitivity of the restored signal to any physically reasonable continuation of the data outside the interval $(t_{\min}, t_{\max})$, where the data are known, is very low. Simply speaking, the Gaussian-like shape of wavelets makes the integration insensitive to any continuations outside of a few half-width intervals from the Gaussian center. We directly checked for several processes studied below that the WA procedure is very stable from this point of view—the WA is not sensitive to the behavior of the analyzed function beyond the region of reconstruction (region of the actual data).

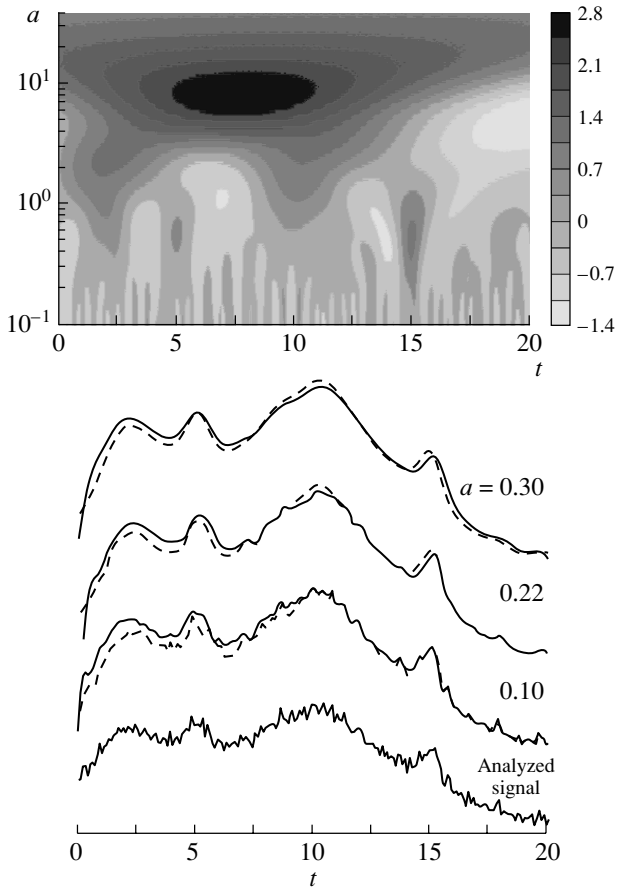

Fig. 2. (Top) Wavelet plane. (Bottom) Model signal based on Eq. (10) and its reconstructions for different boundary scale a and different continuations below $t_{\min}$: $f(t<0) = 0$ (solid curve); $f(t<0) = f(0)$ (dashed curve).

3. WAVELET ANALYSIS OF DATA

The experimental data relevant to ρ' and ω' states in e^+e^- annihilation and $\pi\pi$ scattering are available from a variety of sources and are shown in Figs. 3–10. The wavelet transformation images obtained with the MH wavelet are shown on the upper panels of Figs. 4–10. The WT localizes the structures in a fashion that allows us to estimate the masses of the resonances and their widths. Thus, the wavelet images themselves provide us with some useful information before the reconstruction of the data and their physical analysis is made. The straight horizontal lines correspond to the boundary scale a_{noise} which

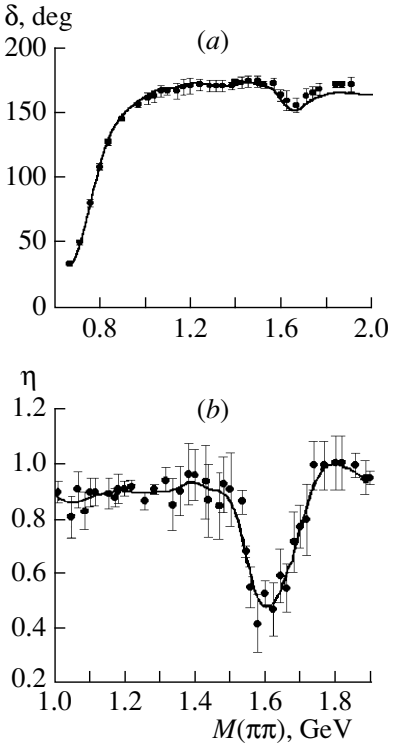

Fig. 3. Experimental data for the phase shift (a) and inelasticity (b) of the p-wave $\pi\pi$ scattering [12, 13] and their reconstruction.

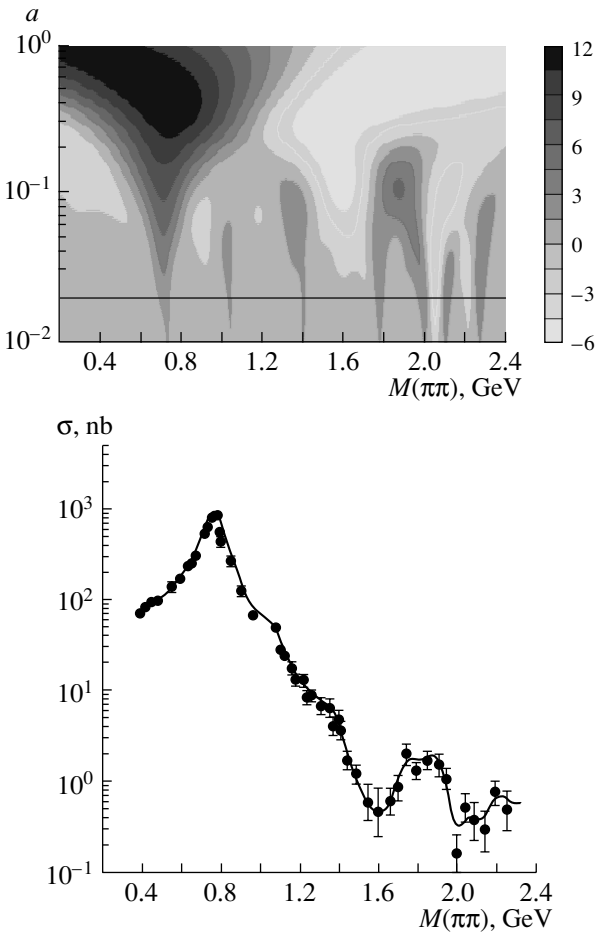

Fig. 4. Cross section of $e^+e^- \to \pi\pi$. (Top) Wavelet plane. (Bottom) Experimental data [14–16] and reconstruction.

cuts off the small scale structures. The curves in the figures are the reconstructed data obtained using the inverse transformation (11).

The cutoff value a_{noise} in the figures below corresponds to the smallest structure included in the reconstructed data. The width of such a structure can be estimated with the width of the MH wavelet at its half-height, $\Gamma \approx 1.5a$. It is reasonable to assume that a resonance structure to be reliably resolved should include at least three experimental points. In the data we analyze, the distance between the experimental points is 0.01 GeV or larger, and the smallest structures we are looking for have Γ_{min} not less than 0.03 GeV. This value 0.03 GeV corresponds to the value $a_{\text{noise}} = 0.02$ GeV, which we use in this section.

The data on $\pi\pi$ scattering do not contain much information about ρ' mesons. The dips at 1.6–1.7 GeV in Fig. 3 are clearly seen; that is why in order to save space we do not present the wavelet planes. The reconstruction of $\pi\pi$-scattering data is stable under variation of the boundary scale (the curves are plotted for $a_{\text{noise}} = 0.02$ GeV), which means that the experimental noise can be very reliably separated—here and elsewhere, this can be considered as one of the criteria of quality of the experiment.

Figure 4 shows that, on the wavelet plane of $e^+e^- \to \pi\pi$, along with the obvious ρ-meson contribution (large spot near 0.8 GeV), there are maxima around 1.03, 1.4, 1.65–1.85, and 2.2 GeV ($\ln\sigma$ was used for WA because of a logarithmic scale for σ in Fig. 4). The first one is the least stable to variation of value of a_{noise}.

For $e^+e^- \to \pi^+\pi^+\pi^-\pi^-$ (Fig. 5), the most obvious maxima are located at about 1.45 and 1.7 GeV with widths about 0.1 and 0.05 GeV, respectively. At greater values of a, these two maxima appear as one wide maximum around 1.55 GeV and width about 0.2 GeV. The situation we are describing recalls a former $\rho'(1600)$ that was later resolved into two states. For energy above the 1.7-GeV maximum, several small maxima unstable to a_{noise} variation are seen.

For $e^+e^- \to \pi^+\pi^-\pi^0\pi^0$ with subtracted contribution from $\omega\pi^0$ (Fig. 6), two obvious maxima are seen around 1.55 and 1.7 GeV with widths about 0.08 and 0.1 GeV. Two other maxima are seen to occur around 1.3 and 2.0 GeV. All these structures are stable for variation of the cutoff scale: a reduction

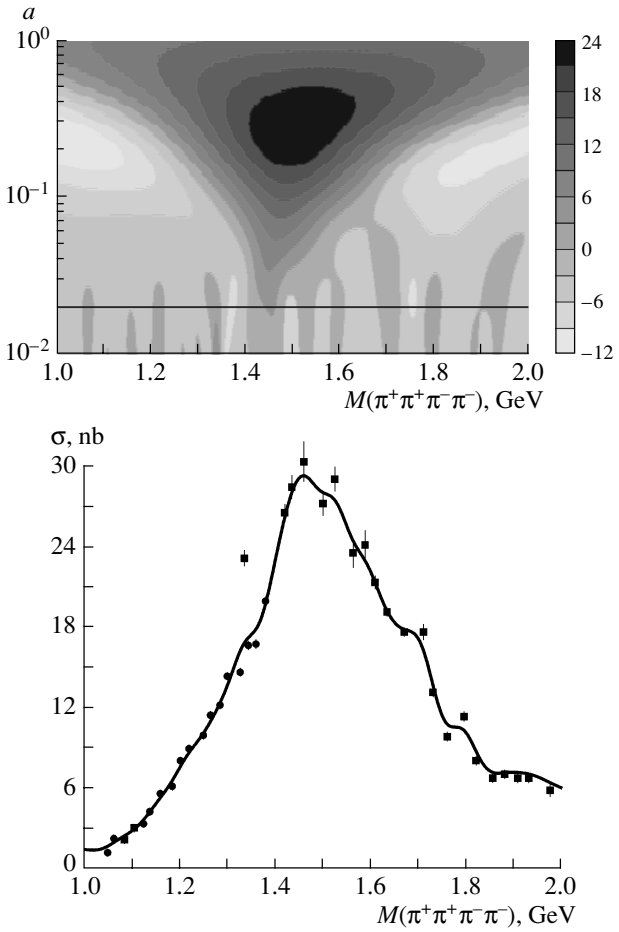

Fig. 5. Cross section of $e^+e^- \to 2\pi^+2\pi^-$. (Top) Wavelet plane. (Bottom) Experimental data [17, 18] and reconstruction.

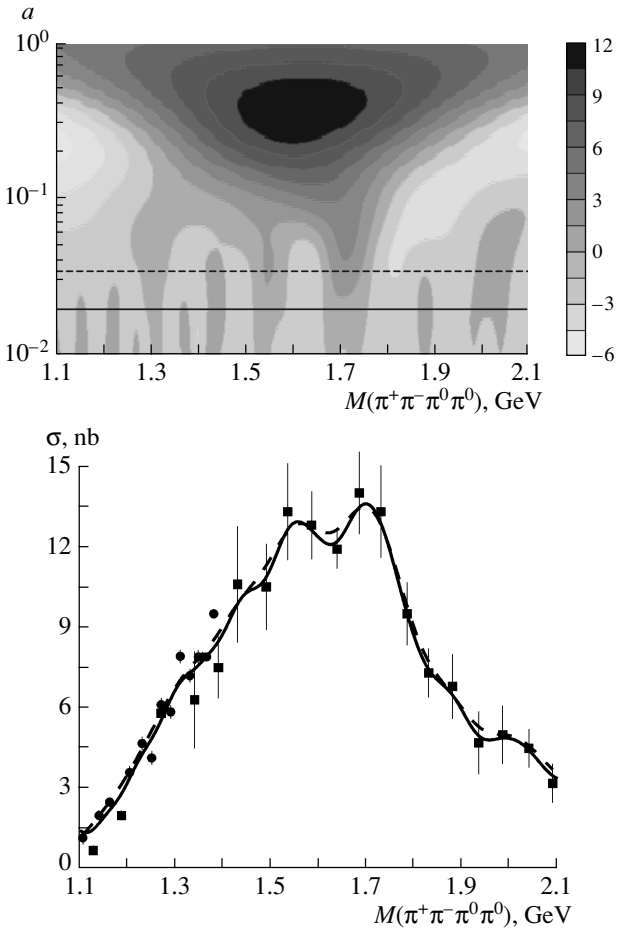

Fig. 6. Cross section of $e^+e^- \to \pi^+\pi^-2\pi^0$ with subtracted contribution from $\omega\pi^0$. (Top) Wavelet plane. (Bottom) Experimental data [17, 18] and two reconstructions for different cutoff values a_{noise}.

of a_{noise} by a factor of almost two does not change the locations of the peaks and their shapes.

For $e^+e^- \to \omega\pi^0$ (Fig. 7), a wide structure is located at about 1.25 GeV. A decrease in the cutoff scale causes splitting of that major maximum—two maxima occur at 1.05 and 1.45 GeV. Three more smaller structures can be recognized between these two. There are also two structures at about 1.85 and 2.0 GeV. The scale values corresponding to these structures are close to reliable values of a_{noise}. It can be observed that, except for the 1.25- and 1.45-GeV states, no dominating scales can be attributed to other states.

The $e^+e^- \to \eta\pi^+\pi^-$ data (Fig. 8) are rather poor and the only visible structure is a wide peak around 1.55 GeV. Here, to fill in rather big gaps between the experimental points, we use linear and quadratic spline interpolations. They lead to a small difference in the restored signal and to a tiny difference on a lower part of the wavelet plane corresponding to noise (on the wavelet plane, we present the plot corresponding to a linear interpolation).

Thus, the WA indicates the ρ' states with masses 1.05–1.25, 1.4, 1.6–1.85, and 2.0–2.2 GeV and widths of about 0.1 GeV, which makes sense to be included in further analysis that should be based on some physical models. The first and the last states are sensitive to high-frequency noise, which makes them questionable. A discussion above on the stability of those states under noise contribution can help evaluate the reliability of the results of further analyses. Note that the 1.01–1.25 GeV state has a long and complicated history; one of the last pieces of evidence was presented by the LASS group [25], but it still needs confirmation.[1)]

[1)]The likely existence of $\rho'(1200)$ with total width of about 0.2 GeV, the main decay mode into the $\omega\pi^0$ channel and smaller fractions into 2π and 4π states, was recently presented by Crystal Barrel [26].

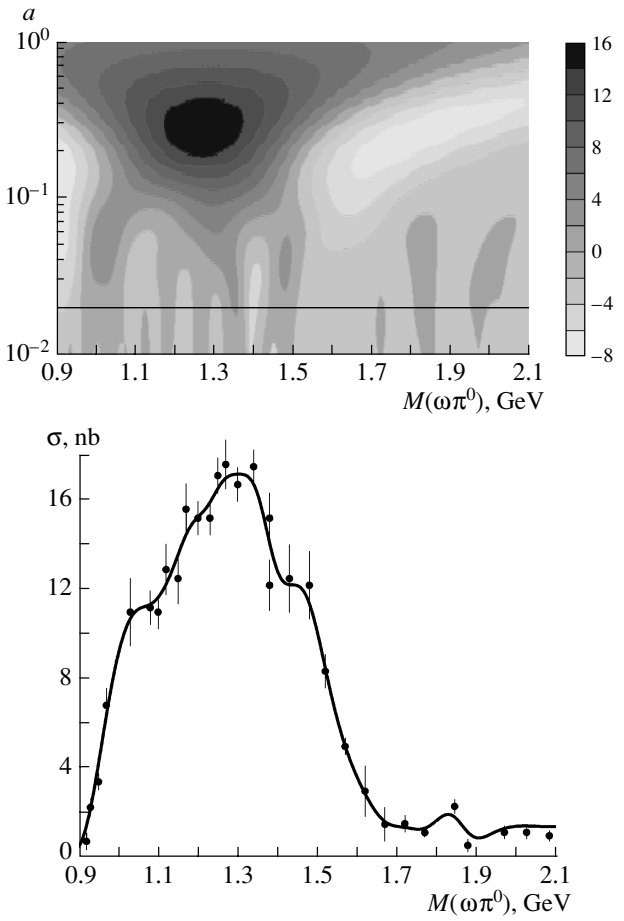

Fig. 7. Cross section of $e^+e^- \to \omega\pi^0$. (Top) Wavelet plane. (Bottom) Experimental data from [17, 19] and reconstruction.

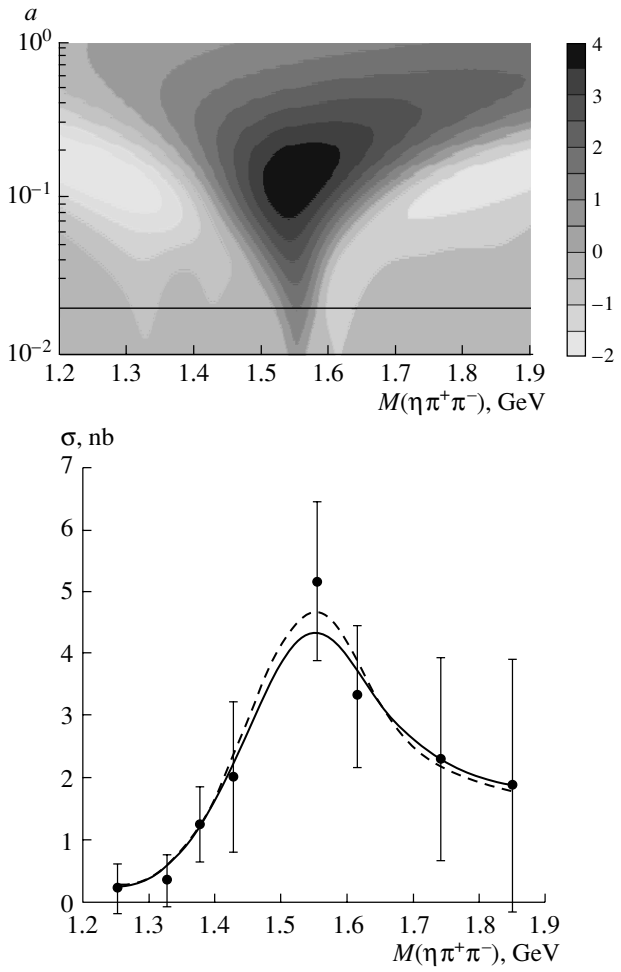

Fig. 8. Cross section of $e^+e^- \to \eta\pi^+\pi^-$. (Top) Wavelet plane. (Bottom) Experimental data [20, 21] and two reconstructions for different interpolations between experimental points: solid curve for linear interpolation and dashed curve for quadratic spline interpolation.

For the process $e^+e^- \to \pi^+\pi^-\pi^0$ (Fig. 9), a wide ω' structure dominates at about 1.25 GeV. It decays into three "horns" without characteristic scales as the cutoff scale decreases. There is also a relatively stable state at about 1.65 GeV with a rather well resolved characteristic scale position a.

The wavelet plane in Fig. 10 for $e^+e^- \to \omega\pi\pi$ indicates a wide ω' state at about 1.68 GeV and a weaker state at around 1.8 GeV—both of these are rather well resolved in a.

As we noted above, the argument in favor of developing a further more comprehensive analysis is the fact that even data with good statistics do not directly provide masses and widths of the resonances. Due to overlapping, the observed positions of maxima can differ substantially from the physical resonance masses, and partial and total widths can differ significantly from preliminary estimations. The WA in this case yields a useful set of starting conditions for a more accurate analysis. For the sake of clarity in the following section, and because the main goal of this paper is the WA, we do such an analysis for the ω' states only (it involves a smaller number of states and channels than those related to the ρ' states).

Table 1. Parameters of two ω' mesons (in GeV)

Meson	Mass	Width
ω'_1	1.15 ± 0.033	0.197 ± 0.051
ω'_2	1.69 ± 0.014	0.297 ± 0.028

4. BREIT–WIGNER ANALYSIS OF ω' STATES USING THE WAVELET-ANALYZED DATA

The interference of the resonances with the same decay channels is the key aspect of any analysis and

Table 2. Branching ratios of two ω' mesons (in %) and phases of ω'_2 (relative to ω'_1, in deg)

Channel	$B_{\omega'_1}$	$B_{\omega'_2}$	$\varphi_{\omega'_2}$
e^+e^-	$(1.7 \pm 0.4) \times 10^{-5}$	$(1.4 \pm 0.6) \times 10^{-4}$	0.16 ± 1.9
$\rho\pi$	86.2 ± 53.6	13.9 ± 11.1	0.07 ± 13.3
$\omega\pi\pi$	13.8 ± 53.6	86.1 ± 11.1	0.14 ± 2.1

interpretation. In the Breit–Wigner (BW) approach, this interference is often taken into account by relative phases in BW terms that are treated as free parameters, the most often just 0 or π. The results of analysis critically depend on the choice of the phase set. Whether or not these phases are included, such a sum of BW terms is depleted of unitarity, which is the basic point in the BW description.

There are several unitarity-preserving approaches, such as an often used K-matrix method. Contrary to

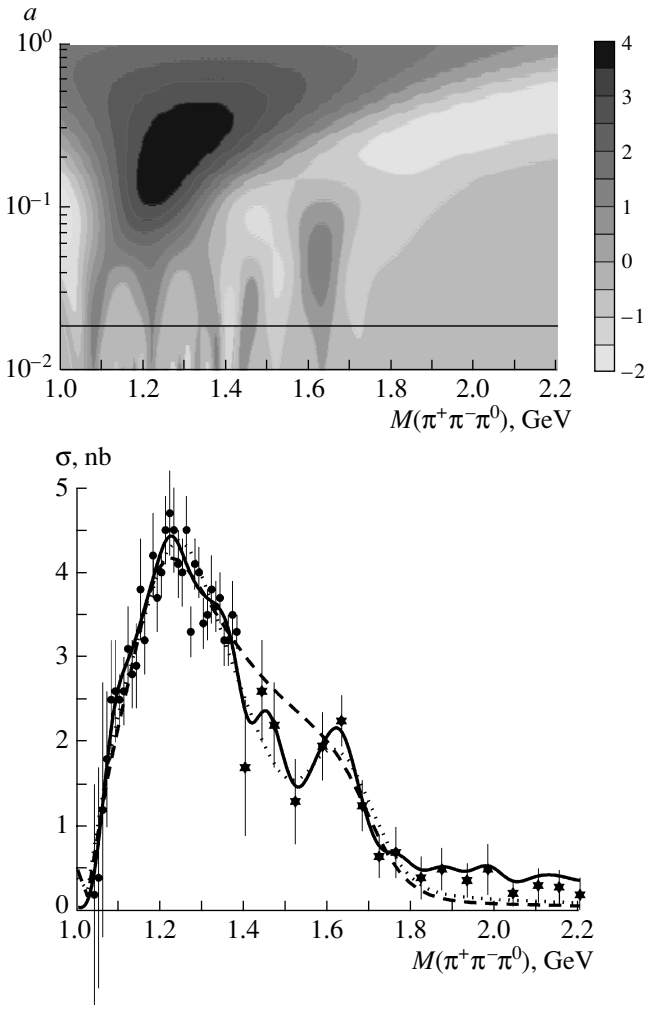

Fig. 9. Cross section of $e^+e^- \to \pi^+\pi^-\pi^0$. (Top) Wavelet plane. (Bottom) Experimental data [22, 23] and reconstruction (solid curve); fits with two ω' (dashed curve) and three ω' (dotted curve).

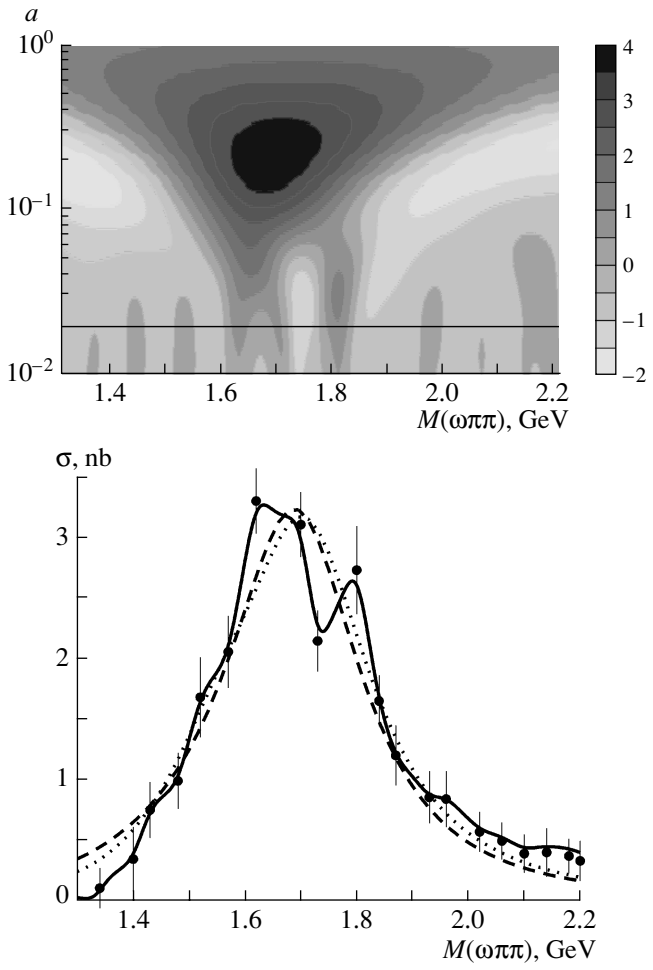

Fig. 10. Cross section of $e^+e^- \to \omega\pi\pi$. (Top) Wavelet plane. (Bottom) Experimental data [23, 24] (in the figure, the cross section from [23, 24] is multiplied by the factor 1.5 to include the nonobserved $\omega\pi^0\pi^0$ state) and reconstruction (solid curve); fits with two ω' (dashed curve) and three ω' (dotted curve).

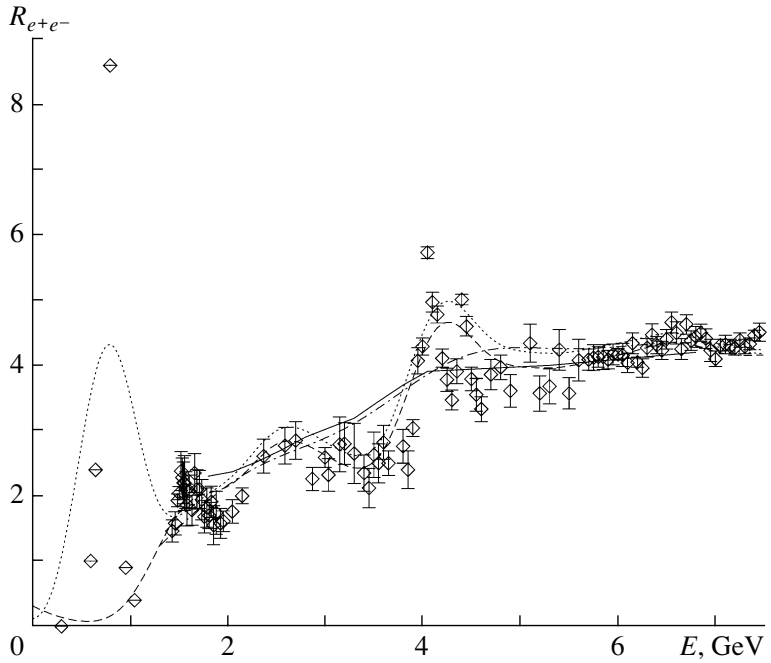

Fig. 11. Ratio $R_{e^+e^-}(E)$. Experimental points are from [29]. Dashed and dotted curves correspond to two different treatments of data reconstruction with $a_{\text{noise}} = 0.25$ GeV for energy below 1.5 GeV (see the text); solid curve represents the theoretical approach [5] Dash-dotted curve represents the result of wavelet reconstruction for $a_{\text{noise}} = 0.6$ GeV.

this approach, the BW method directly provides the physical parameters of the resonances, their masses, widths, and branching fractions.

Let us briefly formulate the unitarity-preserving BW method (details and connection to different methods are described in [27, 28]). Let the scattering amplitudes be written as

$$f_{ij}(s) = \sum_{r=1}^{N} \frac{m_r \Gamma_r g_{ri} g_{rj}}{s - m_r^2 + i m_r \Gamma_r} \qquad (12)$$

$$= \sum_{r=1}^{N} e^{i(\varphi_{ri}+\varphi_{rj})} \frac{m_r \Gamma_r |g_{ri}||g_{rj}|}{s - m_r^2 + i m_r \Gamma_r},$$

where the phases φ_{ri} are not free independent parameters and should be determined in such a way that preserves unitarity (note that the number of free parameters is smaller than or equal to that in a "naive" BW or K-matrix approach). As is often used for the vector states, here we use the approximation of energy-independent widths.

Index $i = 1$ corresponds to the initial state e^+e^- (or to the virtual photon), index $j = 2, 3$ corresponds to the final states $\pi^+\pi^-\pi^0$ and $\omega\pi\pi$ (which are the two main channels of the ω'-state decay [29]), and index r enumerates the ω' resonances. Here, we use data, some of which are rather recent [22–24], that lead to ω' states with masses rather different from those cited most often (at about 1.45 and 1.6 GeV) [29]. The ω' masses reported from the SND detector [24] are 1.25, 1.40, and 1.77 GeV. In the previous work of the same team [22], the PDG [29] resonance $\omega'(1420)$ was not observed and the $\omega'(1200)$ state was reported as a replacement for $\omega'(1420)$. Interestingly, the 1.2-GeV state is clearly observed on the wavelet plane in Fig. 9, and the important aspect is that $\omega'(1420)$ is rather sensitive to the a_{noise} value.

A comparison of the reconstructed data and expression (12) is seen in Figs. 9 and 10. For two ω', there are eight free parameters; for three ω', the number of free parameters is 12. The three-ω' fit better describes the region 1.4–1.5 GeV for the cross section of $e^+e^- \to \pi^+\pi^-\pi^0$, but the overall description for the two processes is about the same for both cases with $\chi^2/n_D \approx 1.3$. Starting from the

Table 3. Parameters of three ω' mesons (in GeV)

Meson	Mass	Width
ω'_1	1.204 ± 0.014	0.250 ± 0.048
ω'_2	1.550 ± 0.019	0.212 ± 0.077
ω'_3	1.700 ± 0.021	0.300 ± 0.039

Table 4. Branching ratios of three ω' mesons (in %) and phases of ω'_2 and ω'_3 (relative to ω'_1, in deg)

Channel	$B_{\omega'_1}$	$B_{\omega'_2}$	$\varphi_{\omega'_2}$	$B_{\omega'_3}$	$\varphi_{\omega'_3}$
e^+e^-	$(1.9 \pm 1) \times 10^{-5}$	$(1.1 \pm 0.5) \times 10^{-5}$	-24.4 ± 9.3	$(1.3 \pm 1) \times 10^{-4}$	-16.1 ± 2.5
$\rho\pi$	83.2 ± 35.1	81.6 ± 11.8	-34.5 ± 5.9	15.7 ± 10.5	-10.8 ± 6.4
$\omega\pi\pi$	16.8 ± 35.1	18.4 ± 11.8	-28.4 ± 10.9	84.3 ± 10.5	-21.5 ± 6.6

WA masses (and widths), we allow big deviations of about 150 MeV from these positions in either direction. The masses, widths, branching ratios, and relative phases of ω' states are presented in Tables 1–4.

5. CONCLUSION

Numerous applications of wavelets to data analysis in different fields of mathematics and physics have proved themselves to be a powerful tool for studying the fractal signals and data. This technique can be successfully applied to some problems of nuclear and high-energy physics where wavelet analysis will work as a tool for studying the energy scaling of the process.

When studying the data containing the information on ρ' and ω' states, we performed the WA of the data in order to single out their contribution. Due to good scaling properties of the wavelets, one can consider experimental data with various resolutions, which allows us to separate the resonances from noise and from each other. Such a local analysis (and the corresponding reconstruction) is very significant when it is necessary to distinguish between several resonances in experimental data with large errors, as in the case of ρ' and ω' mesons. The WA is much less sensitive to the noise than any other analysis and allows us to reduce the role of statistical errors substantially.

In the case of one isolated resonance (or several resonances that are very distant from each other), the wavelet image of data gives practically direct information about the mass and total width of each resonance. When resonances overlap, their physical parameters are found by applying the BW approach that preserves unitarity of the amplitudes for such cases. Fitting the data with suppressed noise gives more reliable results for resonance parameters. The WA of the data we use indicates the ρ' states with masses of 1.05–1.25, 1.4, 1.6–1.85, and 2.0–2.2 GeV and the ω' states at about 1.2, 1.6, and maybe at 1.4 and 1.8 GeV. The Review of Particle Physics [29] contains the references to the experimental and theoretical works related to the ρ' and ω' states with the masses close to all the ones listed above. The parameters of these states are known with a large uncertainty due to the poor accuracy, troubles in analyzing overlapping states, and conflicting experimental data. The e^+e^- annihilation into hadrons gives the most direct observation of the vector states. Other processes (such as τ decays) also give very important information, but with substantially greater uncertainty in the parameters of resonances.

The WA shows that some experimental data are statistically inadequate in the sense that they do not allow the noise contribution to be separated. The method gives the criteria for distinguishing between "stable" and "unstable" data—the latter do not reproduce the same essential structures when a contribution of the experimental noise changes slightly. Technically, it means that the structure (resonance) is questionable if it is sensitive to the noise-cutoff value. Interestingly, this criterion supports ρ' at about 1.45 and 1.65–1.70 GeV, in accord with the assessment in the current PDG [29] compilation. (We cannot directly compare the parameters of ω' states that we obtained with those in [29], because the data on ω' we analyze [22, 24] are not included in [29] review yet.) The only conclusion that we can draw with help of the WA about other states (like $\rho'(1200)$) is that their existence is consistent with the experimental data, but improvement of the cross-section measurement accuracy is needed.

Let us note one more thing related to fluctuations. While small-scale structures located at the bottom of wavelet plane correspond to experimental noise, the structures in the intermediate part of the wavelet plane can be of a different nature. Dark spots (related to the large amplitude of the wavelet coefficient $w(a, E)$), resolved in frequency, occur where the structure of the signal is similar to the wavelet shape and size at this location (a, E). Thus, such spots are most likely associated with resonances. There might also be dark "horns" (usually less intense than in the previous case) reaching high frequencies from the area of low or intermediate frequencies, and not having a relatively well resolved maximum intensity

(looking like a kneecap). Such horns should also be checked for association with resonances (using some physical models), but most likely they are related to noise fluctuations of large amplitude (when one or a few experimental points substantially jump up or down with respect to their neighbors).

To conclude this paper, let us return to the ratio $R_{e^+e^-}$ to demonstrate another application of the wavelet technique to high-energy physics. To even out any rapid variations in $R_{e^+e^-}$, we remove high-frequency noise with WT, which provides the smearing alternative to the procedure (1). The wavelet approach corresponds remarkably to this goal because of its multiscale nature.

The restored data in Fig. 11 keep all the main features of $R_{e^+e^-}$ with statistical errors and threshold singularities damped, which makes a direct comparison with the corresponding QCD-smeared quantity possible. The restored data are stable under rather large variations of the cutoff scale, which reflects the quality of the $R_{e^+e^-}$ data.

We restore the $R_{e^+e^-}$ on the same interval as in [3, 4], from about 1.4 to 7.5 GeV. It is interesting to compare how the resonances and $E < 1.4$ GeV and $E > 7.5$ GeV regions have been treated in [3, 4] and in our approach. Using the approach of [3], it was necessary to exclude the sharp resonances, ψ, ψ', etc., from the data to calculate the integral (1). Moreover, it was necessary to exclude a rather wide ρ peak that substantially contributes to (1). A term was then added to account for the contribution from $s_{\max}$ to ∞, assuming that $R_{e^+e^-}$ remains constant above $s_{\max} \approx 60\ \mathrm{GeV}^2$. The initial idea of smearing [3] supposes a global constant value of Δ in (1) (in [3], a value $\Delta = 3\ \mathrm{GeV}^2$ was used), but it turned out [4] that, for different energy regions, it would be better to use different Δ—in our context, we can note that use of an energy-dependent Δ in (1) in some sense reflects the necessity to use different scales. The WA allows us to not remove the resonances by hand—the sharp resonances get just a part of the high-frequency noise background and the ρ-meson contribution in the smeared $R_{e^+e^-}$ can be evaluated. Above 1.5 GeV, for a big cutoff value a_{noise}, it just gives some small vertical shift for the restored curve—the dotted curve on Fig. 11 is obtained by including all experimental points above the $2m_\pi$ threshold, and the dashed curve is obtained when the data from the threshold are continued to the first experimental point in the figure at about 1.4 GeV using a linear approximation (thus excluding the ρ peak). When the cutoff value increases, the difference between these two curves becomes very small—corresponding reconstructed data for the value $a_{\mathrm{noise}} = 0.6$ GeV are indicated by the dashed-dotted curve. The data from an energy interval well beyond 8 GeV (we use the data from [29] up to 60 GeV) contribute a negligible amount below 8 GeV in the restored data. As seen in Fig. 11, our WA-smeared ratio $R_{e^+e^-}$ corresponds very well to the theoretical prediction for the QCD-smeared ratio.

ACKNOWLEDGMENTS

We thank V.G. Solovyev for helping with the computing part of this study. We also thank M.N. Achasov for providing us with the recent e^+e^- data. One of the authors (V.H.) thanks D.V. Shirkov for attracting attention to the smearing of the ratio R, thus inspiring our application of the WA to that ratio, and S.B. Gerasimov for very useful discussions.

The research described in this publication was made possible in part by award no. PE-009-0 of the US Civilian Research and Development Foundation for the Independent States of the Former Soviet Union (CRDF).

REFERENCES

1. M. Holschneider, *Wavelets: An Analysis Tool* (Oxford Univ. Press, Oxford, 1995).
2. B. Torresani, *Analyse continue par ondelettes. Savoirs actuels* (Savoirs Actuals, Paris, 1995).
3. E. C. Poggio, H. R. Quinn, and S. Weinberg, Phys. Rev. D **13**, 1958 (1976).
4. A. C. Mattingly and P. M. Stevenson, Phys. Rev. D **49**, 437 (1994).
5. I. L. Solovtsov and D. V. Shirkov, Teor. Mat. Fiz. **120**, 1220 (1999).
6. N. M. Astafyeva, Usp. Fiz. Nauk **166**, 1145 (1996) [Phys. Usp. **39**, 1085 (1996)].
7. I. M. Dremin, Usp. Fiz. Nauk **170**, 1235 (2000) [Phys. Usp. **43**, 1137 (2000)].
8. I. M. Dremin, O. V. Ivanov, and V. A. Nechitailo, Usp. Fiz. Nauk **171**, 465 (2001) [Phys. Usp. **44**, 447 (2001)].
9. S. Afanasiev, M. Altaisky, and Yu. Zhestkov, Nuovo Cimento A **108**, 919 (1995).
10. V. V. Uzinski, G. A. Osokov, A. Polyanski, *et al.*, Preprint No. P1-2001-119 (Joint Inst. for Nucl. Res., Dubna, 2001) (and references therein).
11. V. L. Korotkikh and L. I. Sarycheva, in *Proceedings of the 9th International Conference on Hadron Spectroscopy, "Hadron 2001", Protvino, 2001*, p. 615.
12. B. Hyams *et al.*, Nucl. Phys. B **64**, 134 (1973).
13. S. D. Protopopescu *et al.*, Phys. Rev. D **7**, 1279 (1973).
14. A. Quenzer *et al.*, Phys. Lett. B **76B**, 512 (1978).
15. L. M. Barkov *et al.*, Nucl. Phys. B **256**, 365 (1985).
16. D. Bisello *et al.*, Preprint LAL 85-15 (Orsay, 1985).
17. L. Stanco, in *Proceedings of the International Conference on Hadron Spectroscopy, College Park, Maryland, 1991*, p. 84.

18. R. R. Akhmetshin *et al.*, Phys. Lett. B **446**, 392 (1999).
19. M. N. Achasov *et al.*, Phys. Lett. B **486**, 29 (2000).
20. V. P. Druzhin *et al.*, Phys. Lett. B **174**, 115 (1986).
21. B. Delcourt *et al.*, Phys. Lett. B **113B**, 93 (1982).
22. M. N. Achasov *et al.*, Phys. Lett. B **462**, 365 (1999).
23. A. Antonelly *et al.*, Z. Phys. C **56**, 15 (1992).
24. M. N. Achasov *et al.*, in *Proceedings of the 9th International Conference on Hadron Spectroscopy, "Hadron 2001", Protvino, 2001*, p. 30.
25. D. Aston *et al.*, Preprint SLAC-PUB 5657 (1991); Preprint SLAC-PUB 5606 (1994).
26. B. Pick, in *Proceedings of the 9th International Conference on Hadron Spectroscopy, "Hadron 2001", Protvino, 2001*, p. 683.
27. V. K. Henner and T. S. Belozerova, Fiz. Élem. Chastits At. Yadra **29**, 148 (1998) [Phys. Part. Nucl. **29**, 63 (1998)].
28. V. K. Henner and T. S. Belozerova, Yad. Fiz. **60**, 2180 (1997) [Phys. At. Nucl. **60**, 1998 (1997)].
29. D. E. Groom *et al.*, Eur. Phys. J. C **15**, 1 (2000).

Physics of Atomic Nuclei, Vol. 66, No. 7, 2003, pp. 1282–1288. Translated from Yadernaya Fizika, Vol. 66, No. 7, 2003, pp. 1322–1328.

ELEMENTARY PARTICLES AND FIELDS
Theory

Helicity Components of the Cross Section for Double Charged-Pion Production by Real Photons on Protons

V. I. Mokeev[1)], M. Ripani[2)], M. Anghinolfi[2)], M. Battaglieri[2)], R. De Vita[2)], E. N. Golovach[1)], B. S. Ishkhanov[1)], N. S. Markov[3)], M. V. Osipenko[1)], G. Ricco[2)], V. V. Sapunenko[2)], M. Taiuti[2)], and G. V. Fedotov[3)]

Institute of Nuclear Physics, Moscow State University, Vorob'evy gory, Moscow, 119899 Russia

Received October 9, 2002

Abstract—The helicity components $\sigma_{1/2}$ and $\sigma_{3/2}$ of the cross section for double charged-pion production by real photons on a nucleon are calculated within a phenomenological approach developed previously. A high sensitivity of the $\sigma_{1/2}-\sigma_{3/2}$ asymmetry to the contribution of nucleon resonances having strongly different electromagnetic helicity amplitudes $A_{1/2}$ and $A_{3/2}$ is demonstrated. This feature is of importance for seeking "missing" baryon states. © *2003 MAIK "Nauka/Interperiodica"*.

1. INTRODUCTION

Experiments with polarized electron (photon) beams and polarized proton targets made it possible to determine the cross sections $\sigma_{1/2}$ and $\sigma_{3/2}$ corresponding to the total proton and photon helicities of $1/2$ and $3/2$ in the initial states both for the inclusive channel and for various exclusive channels [1–6]. Interest in studying the helicity components $\sigma_{1/2}$ and $\sigma_{3/2}$ is motivated by the following factors.

On the basis of the most general theoretical principles, Gerasimov [7] and Drell and Hern [8] (GDH in the following) predicted the value of the integral

$$I_{\mathrm{GDH}} = \int (\sigma_{1/2} - \sigma_{3/2}) \frac{d\nu}{\nu}, \qquad (1)$$

where $\sigma_{1/2}$ and $\sigma_{3/2}$ are the total photoabsorption cross sections for the case in which the total photon–proton helicity is $1/2$ and $3/2$, respectively, while ν is the photon energy. It follows from [7, 8] that the GDH integral must take the value of -204 μb at the photon point. The experimental results reported in [1, 2] were compared with the predictions made in [7, 8]. The definition of I_{GDH} can be extended to the case of virtual-photon absorption, $I_{\mathrm{GDH}} = I_{\mathrm{GDH}}(Q^2)$, where Q^2 is the sign-reversed square of the virtual-photon 4-momentum. The investigation of the Q^2 dependence of I_{GDH} in [4] revealed that, for $Q^2 > 1.0$ GeV^2, its behavior obeys the $1/Q^2$ law. This behavior follows from the calculations within perturbative QCD in the region $Q^2 > 5$ GeV^2, but experimental data are in accord with the asymptotic behavior of photon–proton interaction at lower values of Q^2 down to 1 GeV^2.

The integral I_{GDH} grows fast from the photon point to $Q^2 \approx 1$–2 GeV^2, and its absolute value decreases approximately by an order of magnitude at $Q^2 = 1.0$ GeV^2. Under the assumption of photon interaction with proton partons, the difference $\sigma_{1/2} - \sigma_{3/2}$ is determined by the difference of the probabilities of finding a parton with spin orientation along and against the photon-spin direction. Thus, the integral I_{GDH} is related to the contribution of the parton spin to the total proton spin. According to the analyses performed in [9, 10], the contribution of the parton spin to the total nucleon spin in the asymptotic region ($Q^2 > 1.0$ GeV^2) does not exceed 30%; at the photon point ($Q^2 = 0$ GeV^2), the main contribution to the nucleon spin comes from constituent quarks.

Thus, the variation in the quantity Q^2 over the interval from 0 to 1.0 GeV^2 leads to a significant variation in the helicity amplitudes of photon–proton interaction and in the contribution of the quark spin to the total proton spin. In order to understand mechanisms behind such strong changes in the spin structure of the photon–proton interaction, it is necessary to analyze contributions of various exclusive channels to the cross-section difference $\sigma_{1/2} - \sigma_{3/2}$.

A detailed description of the Q^2 and W (W is the total energy in the c.m. frame) dependences of the cross sections $\sigma_{1/2}$ and $\sigma_{3/2}$ and of the GDH integral

[1)]Institute of Nuclear Physics, Moscow State University, Vorob'evy gory, Moscow, 119899 Russia.
[2)]Istituto Nazionale di Fisica Nucleare, Sezione di Genova, Genova, Italy.
[3)]Faculty of Physics, Moscow State University, Vorob'evy gory, Moscow, 119899 Russia.

in total-photoabsorption and single-pion-production reactions was given in [11]. At $W > 1.6$ GeV, double-pion-production reactions begin to contribute to the cross section for the total-photoabsorption reaction on a proton significantly; at $W > 1.9$ GeV, their contribution becomes dominant. Therefore, it is interesting to investigate the helicity components of the cross section for double pion production by photons on a proton. In [12–14], a model was developed for describing double pion production on a proton by virtual and real photons at $W < 4.0$ GeV and Q^2, $-t < 5.0$ GeV^2, where t is the square of the difference of the initial- and final-proton 4-momenta. In this kinematical region, the model proposed in [12–14] describes well the entire body of available data on the cross sections for double charged-pion production by real and virtual pions. This approach was used to analyze the first data of the CLAS Collaboration on the double production of charged pions by photons on a proton in the energy region corresponding to the excitation of nucleon resonances (E-93-006 experiment at JLAB; spokespersons V.D. Burkert and M. Ripani) [15, 16]. In the present study, we calculate the helicity components $\sigma_{1/2}$ and $\sigma_{3/2}$ of the cross section for double charged-pion production by real photons at $W < 2.0$ GeV, relying on the approach developed in [12–14]. We determine the model parameters from a fit to all available data on the cross sections for double charged-pion production by photons in the energy region of nucleon-resonance excitation.

2. DESCRIPTION OF THE CROSS SECTIONS FOR DOUBLE CHARGED-PION PRODUCTION ON PROTONS AND THEIR HELICITY COMPONENTS

Quasi-two-particle mechanisms involving the production and subsequent decay of Δ and ρ resonances in the intermediate state (see Fig. 1) are known to make the main contribution to the reaction of double charged-pion production on a proton target. The amplitude of each mechanism in Fig. 1 was calculated in the Breit–Wigner approximation as the product of the relevant two-particle amplitude, the amplitudes for the decay of unstable intermediate particles into stable final-state particles, and the corresponding Breit–Wigner propagators [13, 14]. We describe all other processes that contribute to the double-pion-production reaction in the phase-space approximation; that is, their total amplitude is approximated by a quantity $C(W, Q^2)$ that is independent of the final-state kinematical variables and which is a free model parameter to be determined from an analysis of experimental data. The amplitudes for the quasi-two-particle mechanisms in Fig. 2 are described by a superposition of the excitations of

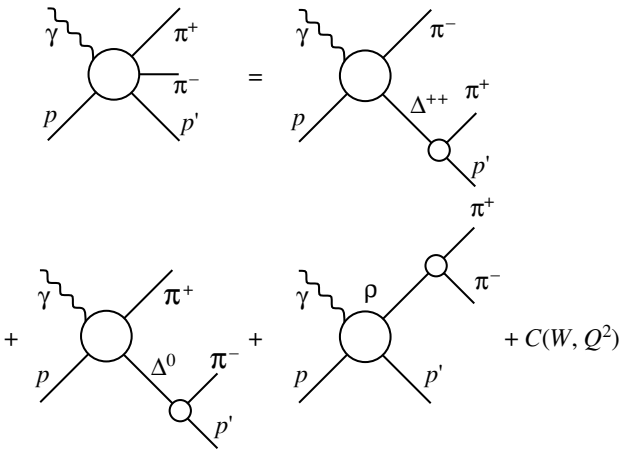

Fig. 1. Mechanisms of the production of $\pi^+\pi^-$ pairs by photons on a proton.

nucleon resonances in photon–proton interaction in the input channel (Figs. 2*a*, 2*f*) and nonresonance mechanisms (Figs. 2*b*–2*e* and 2*g*).

In calculating the resonance components in the amplitudes for the quasi-two-particle reactions (Fig. 2), we took into account all well-known nucleon resonances having masses below 2.0 GeV and significant widths with respect to decays through the $\pi\Delta$ and ρp channels [12, 13].

The resonance amplitudes were calculated in the Breit–Wigner approximation. The details of the calculations can be found in [12]. The electromagnetic amplitudes corresponding to the γpR vertex were calculated on the basis of data on the helicity amplitudes $A_{1/2}$ and $A_{3/2}$ from [17]. Here, a nucleon resonance is denoted by R. For these amplitudes, one can also use the results obtained within any quark model.

Having calculated the cross section for double charged-pion production within the model proposed in [12–14] with the model amplitudes $A_{1/2}$ and $A_{3/2}$ estimated on the basis of a quark model, we can compare the results with experimental data and, in this way, confirm that the model description of the electromagnetic form factors for nucleon resonances is adequate. On the other hand, we can treat the electromagnetic form factors as free parameters of the model and extract their values from a fit of the calculated cross sections to experimental data. We determined the amplitudes of the strong nucleon-resonance decays corresponding to the $Rp\rho$ ($R\pi\Delta$) vertex from the results obtained in [18] by analyzing the cross sections for $\pi N \to \pi\pi N$ reactions.

We described nonresonance processes in the quasi-two-particle reaction $\gamma p \to \rho p$ in the diffraction approximation [13, 14]. The common factor in the nonresonance amplitude is a free parameter that is

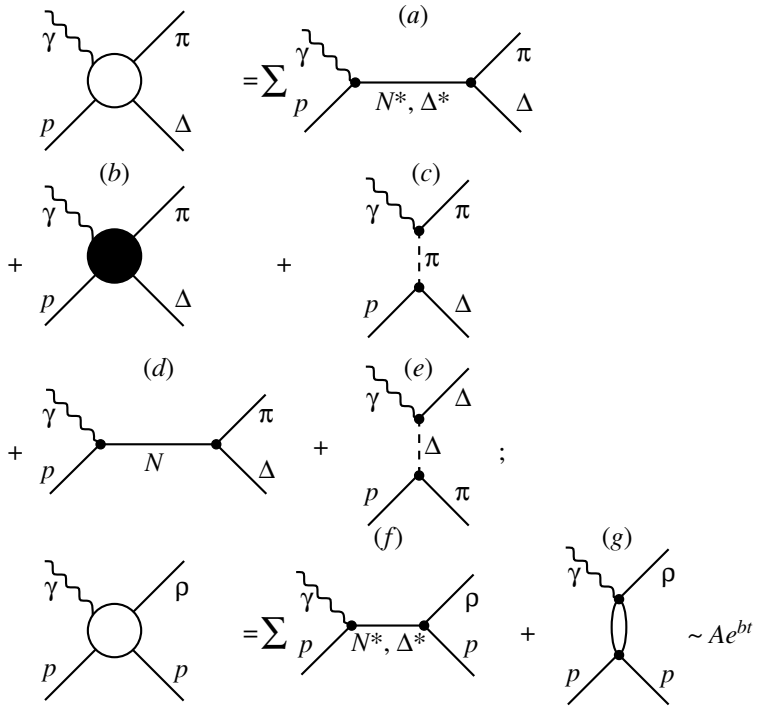

Fig. 2. Diagrams describing the quasi-two-particle reactions $\gamma p \to \pi\Delta$ [resonance mechanisms (a) and Born terms: (b) contact term, (c) on-flight pion, (d) nucleon term, and (e) on-flight delta] and $\gamma p \to \rho p$ [(f) resonance mechanisms and (g) diffractive production of a ρ meson].

independent of W and which must be determined from experimental data.

We described the nonresonance amplitude for the channel $\gamma p \to \pi\Delta$ by the set of gauge-invariant Born amplitudes corresponding to the diagrams in Figs. 2*b*–2*e*. Off-shell pion formation in the mechanism represented by the diagram in Fig. 2*c* was taken into account by introducing the $\pi N\Delta$ vertex function determined from data on NN scattering and the pion electromagnetic form factor [12]. The product of the strong and electromagnetic vertices for the diagram involving the exchange of a Δ isobar (Fig. 2*e*), as well as the t and Q^2 dependence of the contact term (Fig. 2*b*), was determined from the condition requiring that the sum of Born terms be gauge-invariant [12]. The possibility of the exchange of various mesons with pion quantum numbers via the mechanism in Fig. 2*c*—this possibility is of particular importance at $W > 1.7$ GeV—is effectively described by means of the substitution of the pion Regge trajectory for the one-pion propagator, as was proposed in [19]. To restore the gauge invariance of Born terms, we follow the procedure used in [19]. All Born amplitudes corresponding to one-pion exchange are multiplied by the common factor

$$\left(t - m_\pi^2\right) R_\pi(t), \qquad (2)$$

where $R_\pi(t)$ is the Regge propagator proposed in [19] for the pion trajectory, t is the Mandelstam variable corresponding to the amplitude in Fig. 2*c*, and m_π is the pion mass. The multiplication of the one-pion-exchange amplitude (Fig. 2*c*) by the factor in (2) corresponds to the substitution of the Reggeized propagator $R_\pi(t)$ for the one-pion propagator in this amplitude. Since the gauge-invariant sum of Born amplitudes involving one-pion exchange is multiplied by a common factor, the gauge invariance of the sum is preserved upon the substitution of the Reggeized propagator $R_\pi(t)$ for the one-pion-exchange propagator.

The use of the Reggeized gauge-invariant Born amplitudes made it possible to obtain a satisfactory description of experimental data from [20] on the angular distributions of π^- mesons in the quasi-two-particle channel $\gamma p \to \pi\Delta$ (see Fig. 3). Thereby, problems concerning the description of the π^--meson angular distribution in the reaction $\gamma p \to \pi\Delta$, which were discussed in [12], have been successfully solved; at the present stage, the Born terms in the channel $\gamma p \to \pi\Delta$ are gauge-invariant in our model.

Coupling to open inelastic channels in the initial and final states is of importance in describing the nonresonance Born amplitudes for the reaction $\gamma p \to \pi\Delta$. In [12], a dedicated approach was developed according to which this coupling is effectively taken into

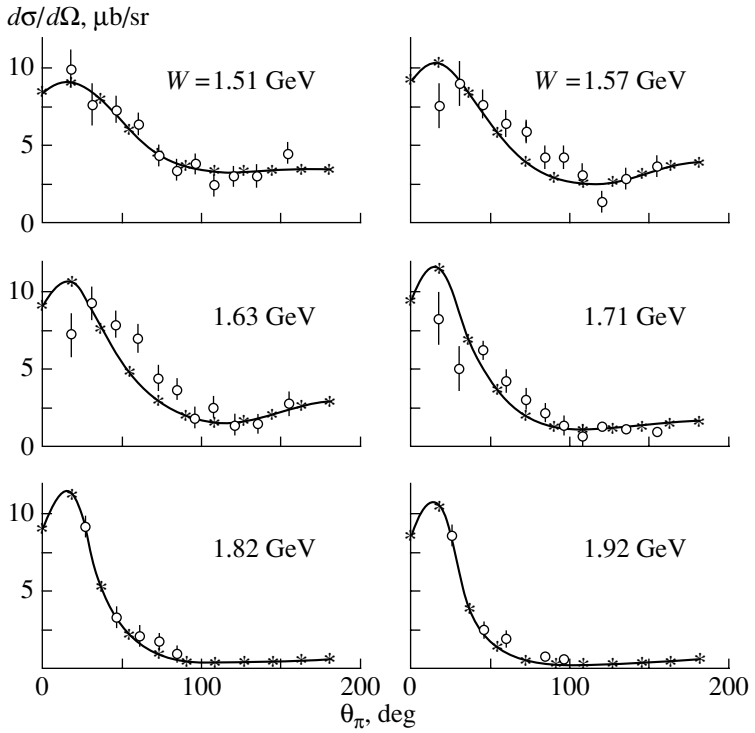

Fig. 3. Angular distribution of π^- mesons in the reaction $\gamma p \to \pi^- \Delta^{++}$ according to our calculations with Reggeized Born terms (see main body of the text), along with experimental data from [20]. The angle between the γ and π^- momenta in the c.m. frame is plotted along the abscissa.

account as the absorption of projectile particles in the initial state and the absorption of emitted particles in the final state. The absorption factors are determined from data on πN scattering.

The helicity differential-cross-section components $d\sigma_{1/2}$ and $d\sigma_{3/2}$ are defined as

$$d\sigma_{1/2(3/2)} = \frac{1}{2} 4\pi\alpha \frac{1}{4K_L M_N} \times \sum_{\lambda_\gamma \lambda_p \lambda_{p'}} \left| \langle \pi\pi\lambda_{p'} |T| \lambda_\gamma \lambda_p \rangle \right|^2 d\tau, \quad |\lambda_\gamma + \lambda_p| = 1/2(3/2), \tag{3}$$

where $\langle \pi\pi\lambda_{p'} |T| \lambda_\gamma \lambda_p \rangle$ are the helicity amplitudes for the reaction of double charged-pion production at the incident-photon helicity of λ_γ, the target-proton helicity of λ_p, and the final-state-proton helicity of $\lambda_{p'}$.

The quantity K_L is the equivalent-photon wave vector

$$K_L = \frac{W^2 - M_N^2}{2M_N}, \tag{4}$$

where M_N is the nucleon mass and $\alpha = 1/137$ is the fine-structure constant.

The element $d\tau$ of the final-state three-particle phase space is

$$d\tau = \frac{1}{32W^2} \frac{1}{(2\pi)^5} dS_{\pi^+ p} dS_{\pi^+\pi^-} d\Omega d\alpha, \tag{5}$$

where $S_{\pi^+ p}$ and $S_{\pi^+\pi^-}$ are the squares of the invariant masses of, respectively, the $\pi^+ p$ and the $\pi^+\pi^-$ system in the final state; Ω is the solid angle of proton (or π^--meson) emission; and α is the angle between the plane spanned by the photon and proton (or photon and π^--meson) 3-momenta and the plane spanned by the π^+- and π^--meson (or π^+-meson and proton) 3-momenta.

In calculating the helicity components $d\sigma_{1/2(3/2)}$, the terms characterized by the total helicities $\lambda_\gamma + \lambda_p$ are included in the sum in (3) according to the lower line in (3) and the conventions in [21]. The sum $d\sigma_{1/2} + d\sigma_{3/2}$ is related to the total unpolarized cross section as follows:

$$d\sigma_{1/2} + d\sigma_{3/2} = 2d\sigma. \tag{6}$$

The amplitudes parameterized in the phase-space approximation, $C(W, Q^2)$, are shared between the helicity components of $1/2$ and $3/2$ under the assumption of their equal contributions to all helicity states.

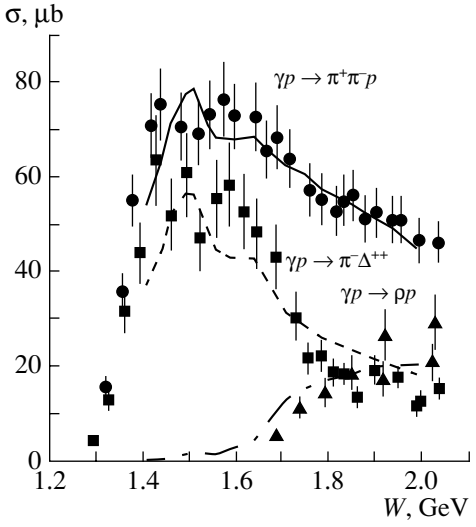

Fig. 4. Experimental data from [20] on the W dependence of the integrated cross sections for the reaction $\gamma p \to \pi^+\pi^- p$ (●) and contributions of the quasi-two-particle channels $\gamma p \to \pi^-\Delta^{++}$ (■) and $\gamma p \to \rho p$ (▲), along with the results of the calculations based on the model described in the main body of the text.

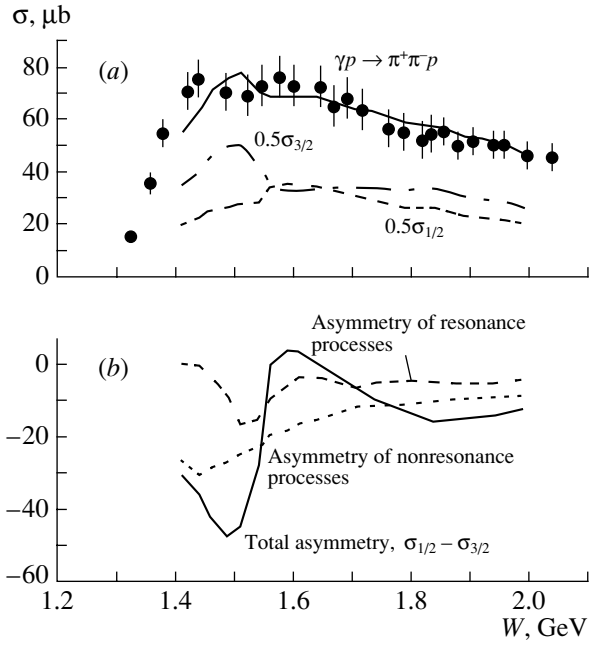

Fig. 5. (*a*) Total cross section (solid curve) and its helicity components for the reaction $\gamma p \to \pi^+\pi^- p$ along with experimental data from [20]; (*b*) $\sigma_{1/2}-\sigma_{3/2}$ asymmetry.

Upon including, in the model developed in [12–14], the calculations of the polarization components $d\sigma_{1/2(3/2)}$ of the cross sections, the values of the electromagnetic form factors for nucleon resonances can be extracted from a simultaneous fit to unpolarized differential cross sections $d\sigma$ and their helicity components $d\sigma_{1/2(3/2)}$. Such an extension of the range of fitted data may significantly improve the accuracy with which one extracts the electromagnetic form factors for nucleon resonances. In addition, a calculation of the helicity components $d\sigma_{1/2(3/2)}$ with the amplitudes $A_{1/2}$ and $A_{3/2}$ from various quark models and a comparison of the results obtained in this way with experimental data extend considerably the possibilities for validating the description of the structure of nucleon resonances as objects formed by interacting quarks and gluons.

The approach developed in the present study can also provide information about the contributions of resonance and nonresonance mechanisms and various two-quasi-particle channels to the cross-section components $d\sigma_{1/2(3/2)}$. This information is of great value for obtaining deeper insight into the spin structure of nucleons and into the dynamics of processes that are responsible for the evolution of the helicity structure of photon–proton interaction.

3. RESULTS OF THE CALCULATIONS FOR THE HELICITY COMPONENTS OF THE CROSS SECTIONS FOR DOUBLE CHARGED-PION PRODUCTION BY PHOTONS

Within the approach described above, we have calculated the W dependences of the helicity cross-section components $\sigma_{1/2}$ and $\sigma_{3/2}$ for the exclusive channel of double charged-pion production by photons. The electromagnetic form factors $A_{1/2}$ and $A_{3/2}$ for nucleon resonances were taken in accordance with data presented by the Particle Data Group [17]. The amplitudes of strong resonance decays were extracted from [18] by using the method described in [12]. The following parameters of the model were taken to be free: the amplitude of the three-particle phase space, $C(W, Q^2)$; the effective coupling constant for the π Regge trajectory; and the multiplicative factor of the diffractive nonresonance amplitude for ρ-meson production. The free parameters were determined from a fit to data of the ABBHM Collaboration [20] on the W dependences of the integrated cross sections for double charged-pion photoproduction.

The integrated cross sections that were calculated for double charged-pion photoproduction on the basis of our model with the parameter values corresponding to the best fit are displayed in Fig. 4 along with experimental data from [20]. The calculations are seen to reproduce these data well. In order to test our model, we

calculated the integrated cross sections for the quasi-two-particle reactions $\gamma p \to \pi^- \Delta^{++}$ and $\gamma p \to \rho p$, employing the parameters determined from a fit to the total cross section (solid curve in Fig. 4). The W dependences of the integrated cross sections for these reactions (dashed and dash-dotted curves in Fig. 4) are contrasted against experimental data from [20]. It can be seen that these theoretical results faithfully reproduce the data from [20] on the W dependences of the integrated cross sections for these quasi-two-particle channels.

The calculated helicity components $\sigma_{1/2}$ and $\sigma_{3/2}$ and their difference for the integrated cross sections are shown in Fig. 5 versus W. The lower panel in Fig. 5 displays the contributions of the resonance mechanisms (dashed curve) and nonresonance processes (dotted curve) to the difference $\sigma_{1/2} - \sigma_{3/2}$.

A feature peculiar to the difference $\sigma_{1/2} - \sigma_{3/2}$ is the formation of a dip at $W = 1.50$ GeV. Such a structure was observed in the MAMI experimental data [3] on the difference $\sigma_{1/2} - \sigma_{3/2}$ in double charged-pion production. The predicted structure is in qualitative agreement with the data from [3]. The W dependence for nonresonance processes is smooth, while the W dependence for the excitation of nucleon resonances features a structure at $W = 1.51$ GeV (Fig. 5*b*). The structure in the W dependence of the difference $\sigma_{1/2} - \sigma_{3/2}$ results from the contribution of the $D_{13}(1520)$ state, which is characterized by significantly different values of the electromagnetic helicity amplitudes $A_{1/2}$ and $A_{3/2}$ (-0.024 and 0.166 GeV$^{-1/2}$, respectively). So great a distinction between these helicity amplitudes leads to strongly different values of the helicity components of the resonance part of the cross section; this in turn leads to a dip in the W dependence of the difference of the helicity total-cross-section components $\sigma_{1/2}$ and $\sigma_{3/2}$ at a W value close to the mass of the $D_{13}(1520)$ resonance. Thus, measurement of the helicity components of the cross section for double pion photoproduction is sensitive to the existence of resonances characterized by significantly different values of the electromagnetic form factors $A_{1/2}$ and $A_{3/2}$ and can be used as an effective tool in searches for such states. In particular, measurements of the helicity components of the cross section will play an important role in seeking "missing" baryon states having significantly different electromagnetic form factors.

From the theoretical results presented in Fig. 5*b*, it follows that, in the energy region corresponding to the excitation of nucleon resonances, there is a strong interference between resonance and nonresonance amplitudes. Measurement of the helicity components of the cross section can aid in determining the relative phase of resonance and nonresonance amplitudes from experimental data, and this is of importance because it is difficult to do this theoretically.

4. CONCLUSION

On the basis of the model developed in [12–14] for describing double charged-pion photoproduction on a proton, we have predicted here the W dependence of the helicity cross-section components $\sigma_{1/2}$ and $\sigma_{3/2}$ and of their difference. The results exhibit a rather high sensitivity of the difference $\sigma_{1/2} - \sigma_{3/2}$ to the excitation of resonance states characterized by significantly different values of the electromagnetic form factors $A_{1/2}$ and $A_{3/2}$. The excitation of such resonances leads to the formation of resonance structures in the W dependence of the difference of the helicity cross-section components $\sigma_{1/2}$ and $\sigma_{3/2}$. Thus, measurement of the helicity components of the cross section for double charged-pion photoproduction will play an important role in the investigation of nucleon resonances having significantly different values of $A_{1/2}$ and $A_{3/2}$—in particular, in searches for "missing" baryon states that possess such properties.

Our approach makes it possible to extract the electromagnetic form factors for nucleon resonances from a global fit to data on the differential cross sections for double charged-pion photoproduction and their helicity components. The development of the model from [12–14] in the course of the present investigation, along with the extension of the range of data subjected to analysis, significantly enhances its potential for determining the electromagnetic form factors for nucleon resonances and improves the reliability of the results obtained in this way.

REFERENCES

1. J. Ahrens *et al.*, Phys. Rev. Lett. **84**, 5950 (2000).
2. P. Pedroni, in *Proceedings of the Symposium on the Gerasimov–Drell–Hern Sum Rule and the Nucleon Spin Structure in the Resonance Region, Germany, 2000*, Ed. by D. Drechsel and L. Tiator, p. 99.
3. M. Lang, in *Proceedings of the Symposium on the Gerasimov–Drell–Hern Sum Rule and the Nucleon Spin Structure in the Resonance Region, Germany, 2000*, Ed. by D. Drechsel and L. Tiator, p. 125.
4. K. Ackerstaff *et al.*, Phys. Lett. B **444**, 531 (1998).
5. R. C. Minechart, in *Proceedings of the NSTAR 2000 Conference, Newport News, USA, 2000*, Ed. by V. Burkert, L. Elouadrhiri, J. J. Kelly, and R. C. Minechart, p. 308.
6. R. De Vita, PhD Thesis (Universitá di Genova, 2000).

7. S. Gerasimov, Yad. Fiz. **2**, 598 (1965) [Sov. J. Nucl. Phys. **2**, 428 (1965)].
8. S. D. Drell and A. C. Hearn, Phys. Rev. Lett. **16**, 908 (1966).
9. V. D. Burkert, Preprint CEBAF PR-94-001.
10. V. D. Burkert and B. L. Ioffe, Preprint CEBAF PR-93-034.
11. D. Drechsel, O. Hanstein, S. S. Kamalov, and L. Tiator, Nucl. Phys. A **645**, 145 (1999).
12. M. Ripani, V. Mokeev, *et al.*, Nucl. Phys. A **672**, 220 (2000).
13. M. Ripani, V. I. Mokeev, M. Battaglieri, *et al.*, Yad. Fiz. **63**, 2036 (2000) [Phys. At. Nucl. **63**, 1943 (2000)].
14. M. Ripani, V. I. Mokeev, M. Anghinolfi, *et al.*, Yad. Fiz. **64**, 1368 (2001) [Phys. At. Nucl. **64**, 1292 (2001)].
15. M. Ripani, in *Proceedings of the NSTAR 2000 Conference, Newport News, USA, 2000*, Ed. by V. Burkert, L. Elouadrhiri, J. J. Kelly, and R. C. Minechart, p. 234.
16. V. Mokeev, M. Ripani, *et al.*, in *Proceedings of the NSTAR 2000 Conference, Newport News, USA, 2000*, Ed. by V. Burkert, L. Elouadrhiri, J. J. Kelly, and R. C. Minechart, p. 242.
17. Particle Data Group, Phys. Rev. D **54**, 1 (1996).
18. D. M. Manley and E. M. Salesky, Phys. Rev. D **45**, 4002 (1992).
19. M. Guidal, J.-M. Laget, and M. Vanderhaeghen, Phys. Lett. B **400**, 6 (1997).
20. ABBHM Collab., Phys. Rev. **175**, 1669 (1968).
21. L. Tiator, in *Proceedings of the Symposium on the Gerasimov–Drell–Hern Sum Rule and the Nucleon Spin Structure in the Resonance Region, Germany, 2000*, Ed. by D. Drechsel and L. Tiator, p. 97.

Translated by M. Kobrinsky

Physics of Atomic Nuclei, Vol. 66, No. 7, 2003, pp. 1289–1296. Translated from Yadernaya Fizika, Vol. 66, No. 7, 2003, pp. 1329–1336.

ELEMENTARY PARTICLES AND FIELDS
Theory

Transverse Polarization of the Lepton in the Decay Process $B \to Dl\nu_l$ due to Electromagnetic Final-State Interaction

V. V. Braguta, A. A. Likhoded, and A. E. Chalov

Institute for High Energy Physics, Protvino, Moscow oblast, 142281 Russia

Received May 31, 2002; in final form, October 18, 2002

Abstract—The emergence of transverse polarization of the lepton in the decay processes $B^0 \to D^- l^+ \nu_l$ and $B^+ \to \bar{D}^0 l^+ \nu_l$ for $l = \tau, \mu$ is studied on the basis of the Standard Model in the leading approximation of heavy-quark effective theory. It is shown that a nonzero transverse polarization appears owing to electromagnetic final-state interactions at the one-loop level. Diagrams involving D and D^* mesons in the intermediate state and making a nonzero contribution to the transverse polarization of the outgoing lepton are considered. If only these mesons are taken into account in evaluating the mean values of the τ-lepton polarization in the decays $B^0 \to D^- \tau^+ \nu_\tau$ and $B^+ \to \bar{D}^0 \tau^+ \nu_\tau$, the results are 2.60×10^{-3} and -1.59×10^{-3}, respectively. The corresponding values of the transverse muon polarization averaged over the Dalitz plot are 2.97×10^{-4} and -6.79×10^{-4}. © *2003 MAIK "Nauka/Interperiodica".*

1. INTRODUCTION

Although the Standard Model has correctly predicted the results of many experiments, the mechanism of CP violation has yet to be established conclusively. In the Standard Model, CP violation is due to the complex-valuedness of the Cabibbo–Kobayashi–Maskawa matrix; however, there are many models that offer different mechanisms of CP violation. The Weinberg model involving three doublets of Higgs bosons [1] provides an example of a model where CP violation occurs in the Higgs sector. Investigation of CP-odd phenomena may contribute to obtaining deeper insight into the mechanism of CP violation and, hence, to clarifying some basic questions of elementary-particle physics.

As an example of physical quantities sensitive to CP violation, we can consider the transverse polarization of leptons and T-odd correlations in weak decays. The transverse polarization of the muon in the decays $K^+ \to \mu^+ \nu \pi^0$ and $K^+ \to \mu^+ \nu \gamma$ has been the subject of many theoretical and experimental investigations. In some extensions of the Standard Model, it appears even at the tree level [2, 3]. In the Standard Model, the transverse polarization of an outgoing lepton is small because it vanishes in the tree approximation. A nonvanishing (CP-conserving) contribution to this quantity is due to final-state interaction. The transverse polarization of the muon in the decay $K^+ \to \mu^+ \nu \gamma$ arises at the one-loop level and varies in the range $(0.0–1.1) \times 10^{-3}$ over the Dalitz plot. Its average over the kinematical domain $E_\gamma \geq 20$ MeV amounts to 4.76×10^{-4} [2]. The transverse polarization of the muon in the decay $K^+ \to \mu^+ \nu \pi^0$ is as small as about 10^{-6} in the Standard Model [4, 5]; therefore, it is advisable to seek effects of new physics in this decay. The current experimental value obtained in the KEK-E246 experiment [6] for the transverse polarization of the muon in this process is

$$P_T = -0.0042 + 0.0049(\text{stat.}) + 0.0009(\text{syst.}). \quad (1)$$

This result does not give sufficient grounds to state that the transverse polarization of the muon in the process being discussed is due to new physics. However, the accuracy of the experiments will be improved in the near future, and this looks quite promising for studying CP violation.

The T-odd correlation in the decay $K^+ \to \pi^0 \mu^+ \nu \gamma$ (it is defined in terms of the distribution of the decay width with respect to the T-odd kinematical variable $\mathbf{p}_\pi \cdot [\mathbf{p}_\mu \times \mathbf{q}]$) is also small within the Standard Model [7]. The reason is identical to that in the case of the transverse polarization of the outgoing lepton in $K_{l2\gamma}$ decays. It is expected that this T-odd correlation will be measured in the OKA experiment [8] on the basis of some 7×10^5 events.

The transverse polarization of the outgoing lepton can be measured not only in the decays of K mesons, but also in the decays of B mesons. The latter decays are particularly sensitive to the CP-violating interactions of Higgs particles with fermions. Obviously, the transverse lepton polarization induced by the interactions of Higgs particles in the decay $K \to$

1063-7788/03/6607-1289$24.00

$\pi\mu\nu$ is $(m_b m_\tau)/(m_s m_\mu) \sim 800$ times less than the analogous polarization in the decay $B \to D(D^*)\tau\nu_\tau$.

In [9–11], effects associated with the emergence of a CP-violating component in the transverse polarization of the lepton in the decay $B \to D(D^*)l\nu$ were considered within various extensions of the Standard Model. If CP violation occurs in the Higgs sector, the transverse polarization of the τ lepton can take values in the region $P_T < 1$ [9, 10]; the corresponding constraint in the leptoquark model is $P_T < 0.26$ [11]. Thus, the magnitude of transverse polarization is expected to be quite large in some extensions of the Standard Model. In order to perform an exhaustive investigation of this issue, it is necessary, in our opinion, to begin by computing, within the Standard Model, the transverse polarization of outgoing leptons in the above decay processes. The present study is devoted to analyzing the CP-conserving component of the transverse polarization of the lepton in the decays $B^0 \to D^- l^+ \nu_l$ and $B^+ \to \bar{D}^0 l^+ \nu_l$, where $l = \tau, \mu$.

For the sake of simplicity, our calculations are performed on the basis of heavy-quark effective theory (HQET) in the leading order of the expansion in powers of $1/m_Q$. We show that the transverse polarization does not vanish only if the phases of the form factors that appear in the expression for the amplitude are different. It is electromagnetic final-state interaction that gives rise to a nonvanishing phase even in the one-loop approximation, and this in turn leads to a nonzero value of the transverse polarization. Also, we take into account the contribution of only the (D, D^*) doublet in our calculations.

The ensuing exposition is organized as follows. Expressions describing the form factors for the processes under study are given in Section 2. The procedure for computing the transverse polarization in question is outlined in Section 3. The results of numerical computations are presented and discussed in Section 4.

2. FORM FACTORS FOR THE PROCESS UNDER STUDY

In calculating the transverse polarization of the outgoing lepton (that is, the polarization component orthogonal to the decay plane), we will need some form factors; the most general expressions for them have the form

$$\langle D(k)|V^\mu|B(p)\rangle = f_+(p^\mu + k^\mu) + f_-(p^\mu - k^\mu), \quad (2)$$
$$\langle D(k)|A^\mu|B(p)\rangle = 0,$$
$$\langle D^*(k,\epsilon)|V^\mu|B(p)\rangle = -ive^{\mu\nu\alpha\beta}\epsilon^*_\nu k_\alpha p_\beta,$$
$$\langle D^*(k,\epsilon)|A^\mu|B(p)\rangle = a_1(\epsilon^*)^\mu + a_2(\epsilon^* p)p^\mu + a_3(\epsilon^* p)k^\mu,$$

where the quantities $V^\mu = \bar{b}\gamma^\mu c$ and $A^\mu = \bar{b}\gamma^\mu\gamma_5 c$ are associated with B-meson decays. The form factor $\langle D(k)|A^\mu|B(p)\rangle$ is equal to zero because an axial vector cannot be generated by the two momentum vectors that we have at our disposal. The definition of the Levi-Civita tensor appearing in the expression for the transition current $\langle D^*(k,\epsilon)|V^\mu|B(p)\rangle$ is such that $e^{0123} = 1$.

We calculate the transverse polarization in the leading order of HQET—that is, under the assumption that $m_b, m_c \to \infty$. In this approximation, all form factors can be expressed in terms of the Isgur–Wise function $\xi(\omega)$ [12, 13]; accordingly, expressions (2) can be recast into the form

$$\langle D(k)|V^\mu|B(p)\rangle = \frac{\xi(\omega)}{\sqrt{m_D m_B}}(m_D p^\mu + m_B k^\mu), \quad (3)$$
$$\langle D(k)|A^\mu|B(p)\rangle = 0,$$
$$\langle D^*(k,\epsilon)|V^\mu|B(p)\rangle = -i\frac{\xi(\omega)}{\sqrt{m_D m_B}}e^{\mu\nu\alpha\beta}\epsilon^*_\nu k_\alpha p_\beta,$$
$$\langle D^*(k,\epsilon)|A^\mu|B(p)\rangle = \frac{\xi(\omega)}{\sqrt{m_D m_B}} \times ((m_B m_D + pk)\epsilon^{*\mu} - (\epsilon^* p)k^\mu),$$

where $\omega = (pk)/(m_D m_B)$.

In addition to the matrix elements given above, we will need the matrix elements of the vector current describing the D–D and D^*–D transitions. Within HQET, the form factors that appear in the expressions for these matrix elements are expressed in terms of the Isgur–Wise function as

$$\langle D(p')|\bar{c}\gamma^\mu c|D(k)\rangle = \xi(\omega')(p'^\mu + k^\mu), \quad (4)$$
$$\langle D(p')|\bar{c}\gamma^\mu c|D^*(k,\epsilon)\rangle = -i\frac{\xi(\omega')}{m_D}e^{\mu\nu\alpha\beta}\epsilon_\nu p'_\alpha k_\beta,$$

where $\omega' = (kp')/(m_D m_B)$. In formulas (3) and (4), we disregard the difference of the D- and D^*-meson masses because, in the leading order of HQET, this difference does not contribute to the quantities in question.

For the function ξ, we use the standard parametrization

$$\xi(\omega) = 1 - \rho^2(\omega - 1). \quad (5)$$

In the numerical computations, we employ the value of $\rho^2 = 0.94$, which was obtained in [14] on the basis of the potential quark model and which is in agreement with experimental data from [13]. The ultimate result cannot change significantly upon replacing it by another value because the kinematical domain of the decay is rather narrow. The parameter ω for the decay $B \to D\tau\nu_\tau\omega$ varies from 1 to $(m_B^2 + m_D^2 - m_\tau^2)/(2m_B m_D) = 1.43$, whereas that for the decay $B \to D\mu\nu_\mu$ varies from 1 to 1.59.

In the calculations, we also use the matrix elements $\langle D|J^\mu_{\rm em}|D^*\rangle$ and $\langle D|J^\mu_{\rm em}|D\rangle$, where $J^\mu_{\rm em}$ is the electromagnetic current, which can be represented as the sum of the "heavy" and "light" components,

$$J^\mu_{\rm em} = J^\mu_h + J^\mu_l. \quad (6)$$

The matrix elements of the "heavy" component of the electromagnetic current can be expressed in terms of the transition amplitudes (4) as

$$\langle D(p')|J^\mu_h|D(k)\rangle = -q_c\xi(\omega')(p'^\mu + k^\mu), \quad (7)$$
$$\langle D(p')|J^\mu_h|D^*(k,\epsilon)\rangle = iq_c\frac{\xi(\omega')}{m_D}e^{\mu\nu\alpha\beta}\epsilon_\nu p'_\alpha k_\beta,$$

where q_c is the c-quark charge. The matrix elements of J^μ_l can be represented in the form

$$\langle D(p')|J^\mu_l|D(k)\rangle = q_l f^1_l(q^2)(p'^\mu + k^\mu), \quad (8)$$
$$\langle D(p')|J^\mu_l|D^*(k,\epsilon)\rangle = iq_l\beta f^2_l(q^2)e^{\mu\nu\alpha\beta}\epsilon_\nu p'_\alpha k_\beta,$$

where q_l is the charge of the light quark in the meson and $f^1_l(q^2)$ and $f^2_l(q^2)$ are the form factors describing the q^2 dependence of the matrix elements, these form factors being normalized in such a way that $f^{(1,2)}_l(0) = 1$. The constant β obtained in [15] is equal to 1.9 GeV^{-1}. The q^2 dependence of the form factors $f^i_l(q^2), i = 1, 2$, that is used in our computations was obtained under the assumption that the contribution of the ω and ρ resonances is dominant [16]. Disregarding the difference of the ω- and ρ-meson masses, we reduce the expressions for f^i_l to the form

$$f^i_l = f_l(q^2) = \frac{1}{1-\dfrac{q^2}{m^2_\rho}}, \quad i = 1, 2, \quad (9)$$

where m_ρ is the ρ-meson mass.

3. TRANSVERSE POLARIZATION OF THE LEPTON

The amplitude of the decays $B \to D(D^*)l^+\nu_l$ has the form

$$M = \frac{G_{\rm F}}{\sqrt{2}}V^*_{cb}\langle D|V^\mu - A^\mu|B\rangle\bar{u}(p_\nu)(1+\gamma_5)\gamma_\mu v(p_l), \quad (10)$$

where $G_{\rm F}$ is the Fermi constant and V^*_{cb} is the relevant element of the Cabibbo–Kobayashi–Maskawa matrix. The transition currents $\langle D|V^\mu - A^\mu|B\rangle$ are given in the preceding section. For the ensuing calculations, it is convenient to parametrize the amplitude for the process $B \to Dl^+\nu_l$ as follows:

$$M = \frac{G_{\rm F}}{\sqrt{2}}V^*_{cb}\bar{u}(p_\nu)(1+\gamma_5)(C_1\hat{p} + C_2)v(p_l). \quad (11)$$

It should be noted that expression (11) offers the most general form of the amplitude for the process under study for the case where only a left-handed neutrino is involved. Substituting the matrix elements (3) of the transition currents into (10), we obtain expressions for C_1 and C_2 in the leading order of HQET,

$$C_1 = \frac{\xi(\omega)}{\sqrt{m_B m_D}}(m_D + m_B), \quad (12)$$
$$C_2 = \frac{\xi(\omega)}{\sqrt{m_B m_D}}(m_B m_l).$$

In the B-meson rest frame, the partial width with respect to the decay $B \to Dl^+\nu_l$ has the form

$$d\Gamma = \frac{\sum|M|^2}{2m_B}(2\pi)^4\delta(p - p_D - p_l - p_{\nu_l}) \quad (13)$$
$$\times\frac{d^3p_D}{(2\pi)^3\cdot 2E_D}\frac{d^3p_l}{(2\pi)^3\cdot 2E_l}\frac{d^3p_{\nu_l}}{(2\pi)^3\cdot 2E_{\nu_l}},$$

where summation is performed over the spin states of the muon and photon involved.

We now introduce a unit vector directed along the spin of the lepton in its rest frame, $\mathbf{s}$, and unit vectors along the longitudinal, normal, and transverse polarizations of the lepton, $\mathbf{e}_i$ ($i = L, N, T$). In terms of these vectors, the expression for the square of the matrix element for a transition to a state characterized by a specific polarization of the lepton has the form

$$|M|^2 = \rho_0[1 + (P_L\mathbf{e}_L + P_N\mathbf{e}_N + P_T\mathbf{e}_T)\cdot\mathbf{s}], \quad (14)$$

where ρ_0 is the probability density averaged over spin states in the Dalitz plot. The unit vectors $\mathbf{e}_i$ are expressed in terms of the momenta of final particles as

$$\mathbf{e}_L = \frac{\mathbf{p}_l}{|\mathbf{p_l}|}, \quad \mathbf{e}_N = \frac{\mathbf{p}_l\times(\mathbf{p}_D\times\mathbf{p}_l)}{|\mathbf{p}_l\times(\mathbf{p}_D\times\mathbf{p}_l)|}, \quad (15)$$
$$\mathbf{e}_T = \frac{\mathbf{p}_D\times\mathbf{p}_l}{|\mathbf{p}_D\times\mathbf{p}_l|}.$$

For this definition of the vectors $\mathbf{e}_i$, P_T, P_L, and P_N stand for, respectively, the transverse, longitudinal, and normal components of the lepton polarization.

The probability density ρ_0 is given by

$$\rho_0 = G^2_{\rm F}|V_{cb}|^2(4|C_1|^2(pp_\nu)(pp_l) + 2|C_2|^2(p_\nu p_l) \quad (16)$$
$$- 2|C_1|^2(p_\nu p_l)m^2_B - 4m_l{\rm Re}(C_2C^*_1)(pp_\nu)).$$

The expression for the transverse polarization can then be represented in the form

$$P_T = \frac{\rho_T}{\rho_0}, \quad (17)$$

where ρ_T is given by

$$\rho_T = 4G^2_{\rm F}|V_{cb}|^2 m_B{\rm Im}(C_1C^*_2)|\mathbf{p}_D\times\mathbf{p}_l|. \quad (18)$$

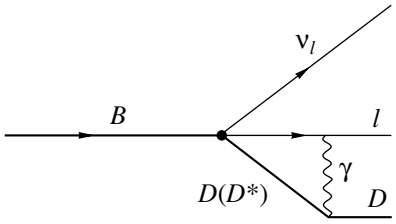

Fig. 1. Feynman diagrams describing the contribution to the transverse polarization of the muon in the decay $B^0 \to D^- l\nu_l$ in the one-loop approximation of the Standard Model.

From formula (18), it can be seen that the transverse polarization of the muon is nonzero only if the phases of the form factors C_1 and C_2 are different. In the tree approximation of the Standard Model, the transverse polarization of the muon vanishes because the above form factors are real-valued there. A nonvanishing transverse polarization results from final-state interaction. The relevant phase difference can be calculated on the basis of the unitarity condition, as was done in [17] for the decay $K^0 \to \pi\mu\nu$. The diagrams contributing to the transverse polarization of the muon are shown in Fig. 1. Here, we take into account the contribution to the transverse polarization of the muon only from D and D^* mesons. The contribution of the diagrams in Fig. 1 has the form

$$\mathrm{Im}M = \frac{G_\mathrm{F}}{\sqrt{2}} V_{cb}^* \frac{\alpha}{2\pi} \tag{19}$$
$$\times \int \frac{d\rho}{k_\gamma^2} \bar{u}(p_\nu)(1+\gamma_5)\gamma_\sigma(\hat{k}_l - m_l)\gamma_\lambda v(p_l)$$
$$\times \sum_{n=D,D^*} \langle D|J_\mathrm{em}^\lambda|n\rangle\langle n|V^\sigma - A^\sigma|B\rangle,$$

where k_l is the lepton momentum, k_D is the momentum of the D (or D^*) meson in the intermediate state, $k_\gamma^2 = (k_D - p_D)^2$ is the square of the momentum transfer, and $d\rho$ is an element of the two-body phase space. The expressions for the matrix elements of the transition currents $\langle D|J_\mathrm{em}^\lambda|n\rangle$ and $\langle n|V^\sigma - A^\sigma|B\rangle$ are given in Section 2.

It should be noted that the D-meson contribution in (19) involves an infrared divergence, but it does not contribute to the polarization. The soft-photon contribution factorizes completely; therefore, it does not give rise to a nonvanishing phase, which is necessary for the emergence of a nonzero transverse polarization. For this reason, we do not take the divergent terms into consideration [17]. The D^*-meson contribution in (19) does not involve an infrared divergence because, in this case, the lower bound on the momentum transfer is given by the expression

$$(-k_\gamma^2)_\mathrm{min} = (m_{D^*}^2 - m_D^2)\frac{m_l}{m_l + m_D}, \tag{20}$$

which is equal to 500 or 160 MeV for a τ lepton or a muon, respectively. These values indicate that the difference of the D- and D^*-meson masses must be taken into account in performing integration over the phase space.

It is obvious that the quantity under study receives contributions from the excited states of the D meson as well. We assume that such contributions have only a small effect on the results because the Isgur–Wise function describing a transition to an excited state of the D meson is smaller than the function defined in (5). For example, the Isgur–Wise function for the B-meson transition to the $(0^+, 1^+)$ doublet, $\tau_{1/2}(\omega)$, was evaluated in [18] by using QCD sum rules. The value of $\tau_{1/2}(1)$ obtained there is 0.24. It is obvious that the light-quark contribution is proportional to $\tau_{1/2}(1)$, whereas the heavy-quark contribution is proportional to the square of $\tau_{1/2}(1)$. Moreover, the diagrams involving a heavy D meson in the intermediate state make a nonvanishing contribution to the transverse polarization only in the domain bounded by the condition $(p_l + p_D)^2 \geq (m_D + m_l)^2$. For the D^* meson, this condition leads to only an insignificant decrease in the physical domain ($m_{D^*} - m_D \sim 0.15$ GeV), whereas, for the $(0^+, 1^+)$ doublet, it reduces the physical domain substantially, because the mass difference in this case ranges up to about 0.5 GeV. Therefore, the contribution to the average polarization in the latter case is considerably smaller than that in the former case.

The details of the procedure for computing the average polarization are presented in the Appendices. The integrals used in the computations by formula (19) are listed in Appendix 1, while the ultimate result is given in Appendix 2.

4. RESULTS AND DISCUSSION

Before proceeding to discuss the results, we introduce the notation

$$E_D = \frac{m_B}{2}x, \quad E_l = \frac{m_B}{2}y. \tag{21}$$

All the results will be formulated in terms of this notation.

Three-dimensional plots over the kinematical domain (x, y) for the transverse polarization of the lepton in the reactions $B^0 \to D^-\tau\nu_\tau, B^0 \to D^-\mu\nu_\mu$, $B^+ \to \bar{D}^0\tau\nu_\tau$, and $B^+ \to \bar{D}^0\mu\nu_\mu$ are given in Figs. 2, 3, 4, and 5, respectively. The corresponding isolines are depicted in Figs. 6–9. The average values of the transverse polarization are as follows:

$$P_T = 2.60 \times 10^{-3}, \quad B^0 \to D^-\tau\nu_\tau,$$
$$P_T = 2.97 \times 10^{-4}, \quad B^0 \to D^-\mu\nu_\mu,$$

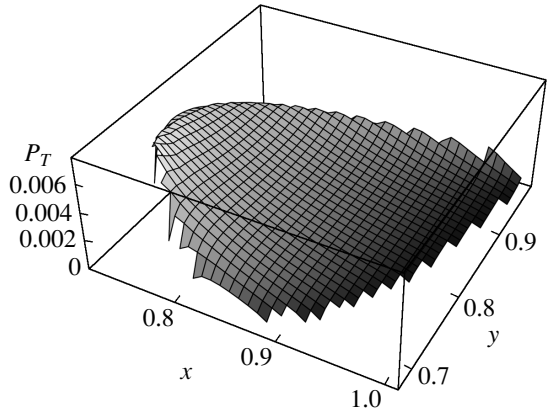

Fig. 2. Transverse polarization of the τ lepton in the decay $B^0 \to D^-\tau\nu_\tau$ on a three-dimensional plot.

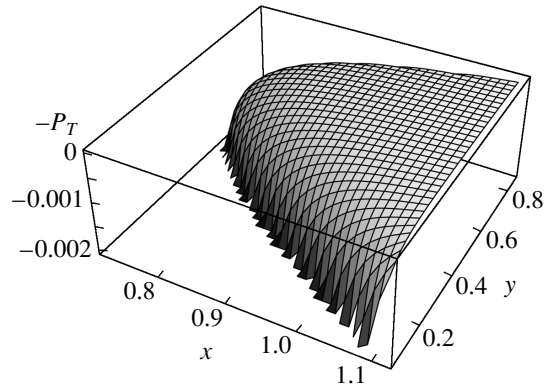

Fig. 3. Transverse polarization of the muon in the decay $B^0 \to D^-\mu\nu_\mu$ on a three-dimensional plot.

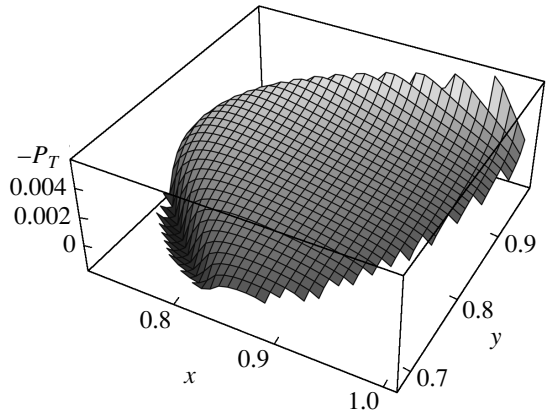

Fig. 4. Transverse polarization of the τ lepton in the decay $B^+ \to \bar{D}^0\tau\nu_\tau$ on a three-dimensional plot.

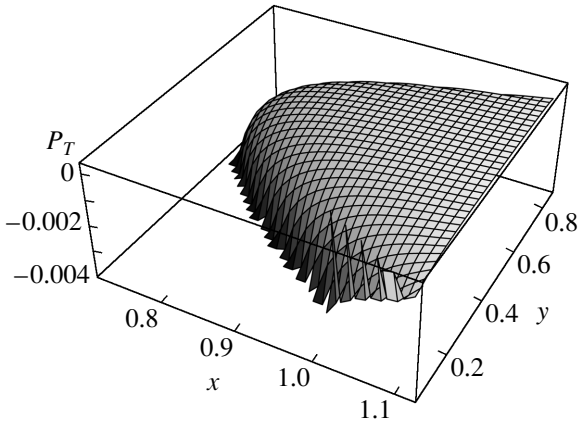

Fig. 5. Transverse polarization of the muon in the decay $B^+ \to \bar{D}^0\mu\nu_\mu$ on a three-dimensional plot.

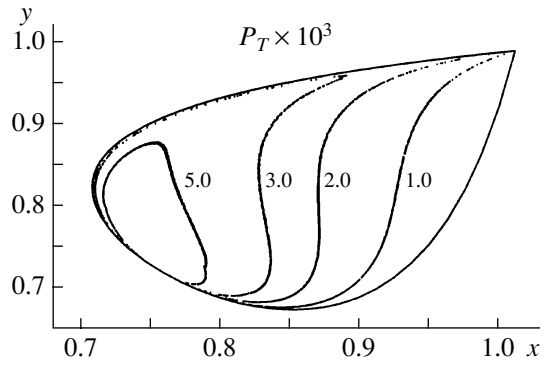

Fig. 6. Isolines for the transverse polarization of the τ lepton in the decay $B^0 \to D^-\tau\nu_\tau$.

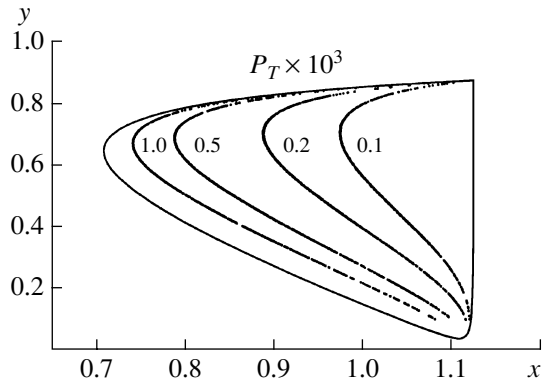

Fig. 7. Isolines for the transverse polarization of the muon in the decay $B^0 \to D^-\mu\nu_\mu$.

$$P_T = -1.59 \times 10^{-3}, \quad B^+ \to \bar{D}^0\tau\nu_\tau,$$
$$P_T = -6.79 \times 10^{-4}, \quad B^+ \to \bar{D}^0\mu\nu_\mu.$$

As was mentioned above, the transverse polarization of the lepton can be represented as the sum of the "heavy" and the "light" component. The form factors for photon–heavy-quark and photon–light-quark interactions depend on the scale parameter that varies from about m_ρ to about m_D over the range

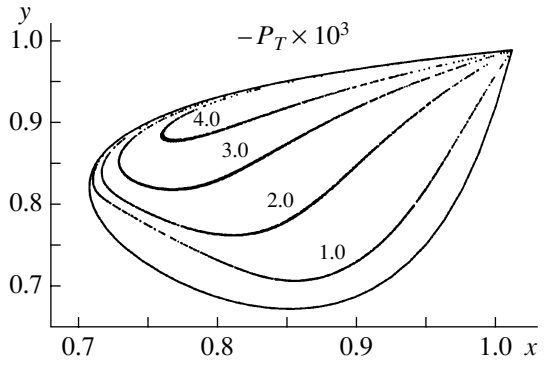

Fig. 8. Isolines for the transverse polarization of the τ lepton in the decay $B^+ \to \bar{D}^0 \tau \nu_\tau$.

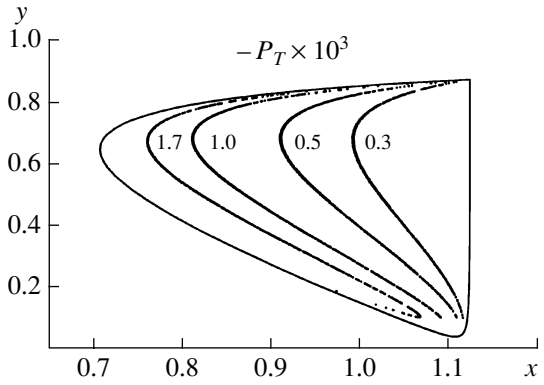

Fig. 9. Isolines for the transverse polarization of the muon in the decay $B^+ \to \bar{D}^0 \mu \nu_\mu$.

of variation of the momentum transfers k_γ. For this reason, the contribution of the diagrams involving a neutral $\bar{D}^0$ meson to the transverse polarization of the lepton in the decay $B^+ \to \bar{D}^0 l\nu$ is evanescently small at low momentum transfers ($k_\gamma^2 \ll m_\rho^2$) and is nonzero over the bulk of the kinematical domain, where $k_\gamma^2 \gg m_\rho^2$. However, the contributions of the light and heavy quarks partly cancel each other owing to the fact that the $\bar{D}^0$ meson is neutral. As a consequence, the contribution of the diagram involving a D^* meson in the intermediate state is greater than the analogous contribution involving a D meson. The distinction between these contributions accounts for the fact that the sign of the average polarization in the decay $B^+ \to \bar{D}^0 l\nu_l$ is opposite to that in the decay $B^0 \to D^- l\nu_l$.

In conclusion, we note that the average values of the transverse polarization in the Standard Model are considerably smaller than the corresponding average values in various extensions of this model [9–11]. The results obtained in [9–11] give sufficient grounds to conclude that B-meson decays may provide an efficient tool for seeking effects of new physics.

ACKNOWLEDGMENTS

We are grateful to V.V. Kiselev and A.K. Likhoded for stimulating discussions and enlightening comments.

This work was supported in part by the Russian Foundation for Basic Research (project nos. 99-02-16558, 00-15-96645), the Ministry of the Russian Federation for Higher Education (grant no. E00-3.3-62), and CRDF (grant no. MO-011-0).

APPENDIX 1

To perform integrations in formula (19), we use the following notation:

$$P^\mu = p_l^\mu + p_D^\mu,$$

$$l^\mu = p_D^\mu - \frac{(Pp_D)}{(P^2)} P^\mu,$$

$$Pk_D = \frac{1}{2}(P^2 + m_{D^*}^2 - m_l^2),$$

$$l^2 = m_D^2 - \frac{(Pp_D)^2}{P^2},$$

$$l_1^2 = m_{D^*}^2 - \frac{(Pk_D)^2}{P^2},$$

$$\eta^2 = m_D^2 + m_{D^*}^2 - 2\frac{(Pk_D)(Pp_D)}{P^2}.$$

In this notation, the integrals under consideration can be written as

$$J_1 = \int \frac{d\rho}{k_\gamma^2} f_l(k_\gamma^2)$$

$$= \frac{\pi}{4} \frac{1}{\sqrt{-l^2 P^2}} \left(\ln \left| \frac{-\eta^2 - 2\sqrt{l_1^2 l^2}}{-\eta^2 + 2\sqrt{l_1^2 l^2}} \right| - \ln \left| \frac{-\eta^2 - 2\sqrt{l_1^2 l^2} + m_\rho^2}{-\eta^2 + 2\sqrt{l_1^2 l^2} + m_\rho^2} \right| \right),$$

$$J_2 = \int d\rho f_l(k_\gamma^2) = -\frac{\pi}{4} \frac{m_\rho^2}{\sqrt{-l^2 P^2}} \times \left(\ln \left| \frac{-\eta^2 - 2\sqrt{l_1^2 l^2} + m_\rho^2}{-\eta^2 + 2\sqrt{l_1^2 l^2} + m_\rho^2} \right| \right),$$

$$J_3 = \int d\rho = \pi \frac{\sqrt{-l_1^2 P^2}}{P^2},$$

$$\int \frac{k_D^\alpha}{k_\gamma^2} f_l(k_\gamma^2) d\rho = a_1 P^\alpha + b_1 l^\alpha,$$

$$a_1 = \frac{Pk_D}{P^2} J_1,$$

$$b_1 = \frac{\eta^2}{2l^2}J_1 - \frac{1}{2l^2}J_2.$$

$$\int k_D^\alpha f_l(k_\gamma^2)d\rho = A_1 P^\alpha + B_1 l^\alpha,$$

$$A_1 = \frac{Pk_D}{P^2}J_2,$$

$$B_1 = \frac{\eta^2}{2l^2}J_2 - \frac{m_\rho^2}{2l^2}(J_2 - J_3).$$

$$\int \frac{k_D^\alpha k_D^\beta}{k_\gamma^2} f_l(k_\gamma^2)d\rho = a_2 g^{\alpha\beta} + b_2\frac{P^\alpha P^\beta}{P^2} + c_2(l^\alpha P^\beta + l^\beta P^\alpha) + d_2\frac{l^\alpha l^\beta}{l^2},$$

$$a_2 = \frac{l_1^2}{2}J_1 - \frac{\eta^2}{4}b_1 + \frac{B_1}{4},$$

$$b_2 = \frac{(Pk_D)^2}{P^2}J_1 - a_2,$$

$$c_2 = \frac{Pk_D}{P^2}b_1,$$

$$d_2 = \frac{\eta^2}{2}b_1 - \frac{B_1}{2} - a_2.$$

$$\int k_D^\alpha k_D^\beta f_l(k_\gamma^2)d\rho = A_2 g^{\alpha\beta} + B_2\frac{P^\alpha P^\beta}{P^2} + C_2(l^\alpha P^\beta + l^\beta P^\alpha) + D_2\frac{l^\alpha l^\beta}{l^2},$$

$$A_2 = \frac{l_1^2}{2}J_2 - \frac{\eta^2}{4}B_1 + \frac{m_\rho^2 B_1}{4},$$

$$B_2 = \frac{(Pk_D)^2}{P^2}J_2 - A_2,$$

$$C_2 = \frac{Pk_D}{P^2}B_1,$$

$$D_2 = \frac{\eta^2}{2}B_1 - \frac{m_\rho^2 B_1}{2} - A_2.$$

$$\int \frac{k_D^\alpha k_D^\beta k_D^\gamma}{k_\gamma^2}d\rho = a_3(g_{\alpha\beta}P^\gamma + g_{\alpha\gamma}P^\beta + g_{\beta\gamma}P^\alpha) + b_3(g_{\alpha\beta}l^\gamma + g_{\alpha\gamma}l^\beta + g_{\beta\gamma}l^\alpha) + c_3(l^\alpha P^\beta P^\gamma + l^\beta P^\alpha P^\gamma + l^\gamma P^\alpha P^\beta) + d_3(l^\alpha l^\beta P^\gamma + l^\beta l^\gamma P^\alpha + l^\gamma l^\alpha P^\beta) + e_3 l^\alpha l^\beta l^\gamma + f_3 P^\alpha P^\beta P^\gamma,$$

$$a_3 = \frac{Pk_D}{P^2}a_2,$$

$$b_3 = \frac{1}{2l^2}(\eta^2 a_2 - A_2),$$

$$c_3 = \frac{1}{2l^2P^2}(\eta^2 b_2 - B_2),$$

$$d_3 = \frac{Pk_D}{P^2l^2}d_2,$$

$$e_3 = \frac{1}{2(l^2)^2}(\eta^2 d_2 - D_2) - \frac{2}{l^2}b_3,$$

$$f_3 = \frac{Pk_D}{(P^2)^2}(b_2 - 2a_2).$$

$$\int k_D^\alpha k_D^\beta k_D^\gamma d\rho = A_3(g_{\alpha\beta}P^\gamma + g_{\alpha\gamma}P^\beta + g_{\beta\gamma}P^\alpha) + B_3(g_{\alpha\beta}l^\gamma + g_{\alpha\gamma}l^\beta + g_{\beta\gamma}l^\alpha) + C_3(l^\alpha P^\beta P^\gamma + l^\beta P^\alpha P^\gamma + l^\gamma P^\alpha P^\beta) + D_3(l^\alpha l^\beta P^\gamma + l^\beta l^\gamma P^\alpha + l^\gamma l^\alpha P^\beta) + E_3 l^\alpha l^\beta l^\gamma + F_3 P^\alpha P^\beta P^\gamma,$$

$$A_3 = \frac{Pk_D}{P^2}A_2,$$

$$B_3 = \frac{1}{2l^2}(\eta^2 A_2 - m_\rho^2 A_2 + \frac{1}{3}m_\rho^2 l_1^2 J_3),$$

$$C_3 = \frac{1}{2l^2P^2}\left(\eta^2 B_2 - m_\rho^2\left(B_2 - \frac{(Pk_D)^2}{P^2}J_3 + \frac{l_1^2}{3}J_3\right)\right),$$

$$D_3 = \frac{Pk_D}{P^2l^2}D_2,$$

$$E_3 = \frac{1}{2(l^2)^2}(\eta^2 D_2 - m_\rho^2 D_2) - \frac{2}{l^2}B_3,$$

$$F_3 = \frac{Pk_D}{(P^2)^2}(B_2 - 2A_2).$$

APPENDIX 2

Let us first consider the contribution of the D meson to the transverse polarization of the lepton. We represent the expression for the quantity $\mathrm{Im}(C_1C_2^*)$, which appears in formula (18), as the sum of the "heavy" and the "light" component,

$$\mathrm{Im}(C_1C_2^*) = \frac{\alpha}{2\pi}\xi(\omega)\frac{m_l}{m_B m_D} \times \left(q_l\left((1+\rho^2)C_l - \frac{\rho^2}{m_B m_D}C_l'\right) - q_c\left((1+\rho^2)C_h - \frac{\rho^2}{m_B m_D}C_h'\right)\right),$$

where $\xi(\omega)$ is the Isgur–Wise function; ρ^2 is the slope of this function; and q_l and q_c are the charges of the

light and the c quark, respectively. The coefficients C_l and C_l' appearing in the last formula are given by

$$C_l = 2b_1\frac{Pp_D}{P^2}(m_B^2 m_l^2 - M^2P^2),$$

$$\begin{aligned} C_l' = a_2(2P^2(m_B^2 - m_D^2) \\ + 4(Pp)Mm_D - 2m_B^2 m_l^2) \\ + 2b_2\frac{(Pp)}{P^2}(P^2M^2 - m_B^2 m_l^2)\frac{2}{P^2}c_2 \\ \times (m_B^2 m_l^2 - M^2P^2)(-(lp)P^2 + (Pp)(Pp_D)) \\ + \frac{2(Pp_D)(lp)}{P^2 l^2}d_2(m_B^2 m_l^2 - M^2P^2), \end{aligned}$$

where $M = m_B + m_D$. The expressions for the coefficients b_1, a_2, b_2, c_2, and d_2 for the D^* meson (provided that $m_{D^*} \neq m_D$) are given in Appendix 1. In order to derive these coefficients for the D meson, the D^*-meson mass must everywhere be replaced by the D-meson mass, whereupon the integral J_1 becomes divergent; however, this integral does not contribute to the transverse polarization because the transverse polarization does not involve divergences. For this reason, it can be safely set to zero in all formulas. In order to obtain the coefficients C_h and C_h', we must expand the coefficients C_l and C_l' in powers of $1/m_\rho^2$ up to linear terms and set $1/m_\rho^2$ to $\rho^2/(2m_D^2)$.

We do not present here the resulting formulas for the D^*-meson contribution to the transverse polarization since they are rather cumbersome.

REFERENCES

1. S. Weinberg, Phys. Rev. Lett. **37**, 657 (1976).
2. V. Braguta, A. Likhoded, and A. Chalov, hep-ph/0105111.
3. G. Belanger and C. Q. Geng, Phys. Rev. D **44**, 2789 (1991).
4. A. R. Zhitnitskiĭ, Yad. Fiz. **31**, 1024 (1980) [Sov. J. Nucl. Phys. **31**, 529 (1980)].
5. V. P. Efrosinin *et al.*, Phys. Lett. B **493**, 293 (2000).
6. M. Abe *et al.*, Phys. Rev. Lett. **83**, 4253 (1999).
7. V. Braguta, A. Likhoded, and A. Chalov, Phys. Rev. D **65**, 054038 (2002).
8. OKA Letter of Intent; V. F. Obraztsov, hep-ex/0011033.
9. R. Garisto, Phys. Rev. D **51**, 1107 (1995).
10. G. H. Wu, K. Kiers, and J. N. Ng, Phys. Rev. D **56**, 5413 (1997).
11. J. P. Lee, hep-ph/0111184.
12. N. Isgur and M. B. Wise, Phys. Lett. B **232**, 113 (1989); **237**, 527 (1990).
13. M. Neubert, Phys. Rep. **245**, 259 (1994).
14. V. V. Kiselev, Mod. Phys. Lett. **10**, 1049 (1995).
15. R. Casalbuoni *et al.*, hep-ph/9605342.
16. P. Colangelo *et al.*, Phys. Lett. B **316**, 555 (1993).
17. L. D. Okun' and I. B. Khriplovich, Yad. Fiz. **6**, 821 (1967) [Sov. J. Nucl. Phys. **6**, 598 (1967)].
18. P. Colangelo, G. Nardulli, and N. Paver, Phys. Lett. B **293**, 207 (1992).

Translated by R. Rogalyov

Physics of Atomic Nuclei, Vol. 66, No. 7, 2003, pp. 1297–1309. Translated from Yadernaya Fizika, Vol. 66, No. 7, 2003, pp. 1337–1349.

ELEMENTARY PARTICLES AND FIELDS
Theory

Energy and Momentum Losses of a Magnetized Plasma via Familon Emission

N. V. Mikheev* and **E. N. Narynskaya**

Yaroslavl State University, Sovetskaya ul. 14, Yaroslavl, 150000 Russia

Received February 19, 2002; in final form, December 5, 2002

Abstract—Familon emission from a dense magnetized plasma in the processes $e^- \to e^-\phi$ and $e^- \to \mu^-\phi$ is investigated. The contribution of these processes to the energy losses of a supernova remnant is calculated. It is shown that, at a late stage of the cooling of a supernova remnant, the energy loss of a plasma via familon emission may become commensurate with the loss via neutrino emission. It is found that, because of asymmetry of familon emission in the process $e^- \to \mu^-\phi$, there arises a force acting on the plasma. © *2003 MAIK "Nauka/Interperiodica".*

1. INTRODUCTION

In the past decades, there has been permanent interest in studying electroweak-interaction models that involve an extended Higgs sector. Special attention has been given to light and strictly massless particles playing the role of pseudo-Goldstone and Goldstone bosons, including axions, arions, familons, and Majorons [1]. The possible existence of such particles has many important implications both for the theoretical aspects of particle physics and for astrophysical applications.

At the present time, the Standard Model due to Weinberg, Salam, and Glashow is the most convenient theory that describes the physics of electroweak interactions. Despite its impressive successes in describing experimental data, some problems have remained, however, unsolved within this model. These include those concerning the existence of a few fermion generations and the mass difference between particles belonging different generations. These problems could possibly be solved by introducing an additional horizontal symmetry between fermion generations [2, 3]. A spontaneous breakdown of this symmetry may lead to the observed hierarchy in the fermion-mass spectrum, a Goldstone boson, referred to, in this case, as a familon, concurrently arising in the theory (see, for example, [4]).

In general, familon coupling to fermions is of a nondiagonal character and can be described in terms of the Lagrangian [5]

$$L = \frac{c_{ij}}{F}(\bar{\Psi}_i\gamma_\alpha(g_v + g_a\gamma_5)\Psi_j)\partial^\alpha\Phi + \text{h.c.}, \quad (1)$$

where c_{ij} is a model-dependent dimensionless factor on the order of unity; F is the scale of horizontal-symmetry breaking; Φ and Ψ_i are, respectively, the familon and the fermion wave function; the subscripts i and j indicate fermion flavors; and $g_a^2 + g_v^2 = 1$.

In the particular case of interaction diagonal in flavors ($i = j$), the conservation of the vector current makes it possible to recast the Lagrangian in (1) into the form

$$L = \frac{c_i}{F}(bar\Psi_i\gamma_\alpha\gamma_5\Psi_i)\partial^\alpha\Phi. \quad (2)$$

The existing astrophysical estimates are close to those that are based on laboratory experiments, both yielding $F > (1.1{-}3.1) \times 10^9$ GeV [6].

Since the familon is a particle whose interaction with matter is weak, it may penetrate deep into a substance, whence it follows that various processes involving its emission may provide an additional mechanism through which stars and other astrophysical objects lose energy. Moreover, the possible asymmetry of familon emission may generate a reactive force that in turn could clarify the problem of pulsar velocities.

In studying quantum processes under astrophysical conditions, it is necessary to take into account the effect of an active external medium, and not only may this be a plasma, but also a strong magnetic field is capable of playing such a role. By strong, one usually means a magnetic field whose strength considerably exceeds the critical value of $B_e = m_e^2/e = 4.41 \times 10^{13}$ G.[1)] According to the concepts adopted at present, fields of strength in

*e-mail: mikheev@uniyar.ac.ru

[1)]Here, use is made of a natural system of units where $c = \hbar = 1$, and $e > 0$ is an elementary charge.

1063-7788/03/6607-1297$24.00

the range $B \sim 10^{15}$–10^{17} G could be generated in astrophysical cataclysms, such a supernova explosion or the merger of neutron stars [7].

An external magnetic field playing, along with a plasma, the role of an active medium has a pronounced effect of the properties of particles and on their interactions. Owing to a change in the dispersion relation, channels forbidden in a vacuum may open in this case—for example, the splitting of a photon into two photons, $\gamma \to \gamma\gamma$ [8], and photon decay into an electron–positron pair, $\gamma \to e^-e^+$ [9], become possible. Further, we would like to emphasize that, in the presence of an external magnetic field, the interaction specified by Eq. (1) may lead to the synchrotron radiation of a familon, $e^- \to e^-\phi$, and the "decay" of an electron, $e^- \to \mu^-\phi$ [10].

It is important to note that an external magnetic field also induces a new effective familon–photon interaction of the form

$$L_{\phi\gamma} = g_{\phi\gamma}\tilde{F}^{\alpha\beta}(\partial_\beta A_\alpha)\Phi, \qquad (3)$$

where A_μ is the 4-potential of a quantized electromagnetic field, $F_{\alpha\beta}$ is the strength tensor of the external magnetic field, $\tilde{F}_{\alpha\beta} = (1/2)\varepsilon_{\alpha\beta\rho\sigma}F_{\rho\sigma}$ is its dual counterpart, and $g_{\phi\gamma}$ is the effective coupling constant for familon–photon interaction in the external magnetic field. Familon $\rightleftarrows$ photon transitions generate a new channel of synchrotron familon radiation from an electron through an intermediate plasmon, $e^- \stackrel{\gamma^*}{\to} e^-\phi$.

In the present study, we examine familon radiation from a dense magnetized plasma through the processes $e^- \to e^-\phi$ and $e^- \to \mu^-\phi$, which are forbidden in a vacuum by the law of energy–momentum conservation, but which become possible in an external magnetic field owing to a nontrivial particle kinematics.

We consider the physical situation in which the typical energy of plasma electrons is a dominant parameter of the problem; that is,

$$\mu^2, T^2 \gg eB \gg m_e^2. \qquad (4)$$

Such conditions could be realized, for example, in the core of a supernova, where, according to present-day concepts, the plasma chemical potential is $\mu \sim 500m_e$, while the plasma temperature is $T \sim 60\,m_e$ [1]. In this case, even very strong magnetic fields, those of strength $B \sim 10^{17}$ G, satisfy the condition in (4); therefore, they can be considered as relatively weak. In this case, plasma electrons occupy a large number of Landau levels. In order to demonstrate that this is indeed so, we will estimate the maximum number of populated Landau levels. Considering that the energy of an ultrarelativistic electron in a magnetic field in the Nth level is

$$E \simeq \sqrt{p_z^2 + 2eBN},$$

where p_z is the projection of the electron momentum onto the magnetic-field direction, we obtain

$$N_{\max} \simeq \frac{E^2}{2eB} \sim \frac{\mu^2}{2eB} \gg 1.$$

Under the physical conditions specified by (4), in which case a large number of Landau levels is excited, investigation of quantum processes effectively reduces to calculations in a constant crossed field ($\mathbf{B} \perp \mathbf{E}$, $|\mathbf{B}| = |\mathbf{E}|$), the technique of such calculations being well known [11, 12]. This is because an arbitrary relatively weak and slowly varying external electromagnetic field is close, in the rest frame of an ultarelativistic electron, to a crossed field. As a matter of fact, the result in the leading approximation then depends on only one dynamical invariant, $[e^2(pFFp)]^{1/2}$, where p_μ is the particle 4-momentum [here and below, it is assumed that the tensor indices of 4-vectors and tensors appearing within parentheses are consecutively contracted—for example: $(pFFp) = p_\alpha F_{\alpha\beta}F_{\beta\gamma}p_\gamma$]. We would like to note that calculations in a crossed field possess a high degree of generality and are of interest in and of themselves, since they appear to be a relativistic limit of the corresponding calculation in an arbitrary relatively weak electromagnetic field.

Under the conditions specified in (4), which are considered here, plasma electrons are ultrarelativistic particles. In the ensuing calculations, we will therefore disregard the electron mass in all cases where this does not lead to confusion.

For the processes being considered, the differential probability per unit time is given by

$$dW = \frac{|S|^2}{\mathcal{T}} dn_{f'}(1 - f'_{e^-})dn_\phi, \qquad (5)$$

where S is the S-matrix element for the relevant process; $\mathcal{T}$ is the total interaction time; and $dn_{f'}$ and dn_ϕ are, respectively, the number of states of a final fermion in a crossed field[2)] and the number of familon states,

$$dn_{f'} = \frac{2d^3p'}{(2\pi)^3}V, \quad dn_\phi = \frac{d^3k}{(2\pi)^3}V. \qquad (6)$$

Here, $V = L_xL_yL_z$ is a normalization volume; $\mathbf{k}$ is the familon-momentum vector; $\mathbf{p}'$ is the vector of the

[2)]It will be shown below that, in a relatively weak magnetic field, in which case electrons occupy a large number of Landau levels, the number of states is approximately described by the same formula.

momentum that fixes the state of the final fermion in a crossed field; and f'_{e^-} is the final-fermion distribution with allowance for the presence of a plasma, the invariant form of this distribution being

$$f'_{e^-} = \frac{1}{e^{((p'u)-\mu)/T}+1},$$

where u^α is the medium-velocity 4-vector, which, in the plasma rest frame has the form $u^\alpha = (1, \mathbf{0})$.

It is worthy of note that it is the mean energy and momentum losses of a magnetized plasma via familon emission rather than the probabilities of the processes that are of greatest practical interest for possible astrophysical applications. It is convenient to begin by calculating the mean energy and momentum losses of one plasma electron, which are determined by the 4-vector

$$Q^\mu = -E(\frac{dE}{dt}, \frac{d\mathbf{p}}{dt}), \tag{7}$$

where E and $\mathbf{p}$ are, respectively, the energy of this electron and its 3-momentum vector. The zeroth component Q^0 is associated with the mean energy lost by one plasma electron per unit time, while the spatial components $\mathbf{Q}$ are associated with the momentum loss of the electron per unit time. Therefore, the spatial components determine the force acting on the plasma electron from the emitted familon.

The components of 4-vector (7), which specifies the losses, can be calculated by the formula

$$Q^\mu = \int q^\mu E dW, \tag{8}$$

where $q^\mu = (\omega, \mathbf{k})$ is the familon 4-momentum.

In order to estimate the volume density of energy lost by a plasma per unit time via familon emission (familon luminosity), $\dot{\varepsilon}$, and the volume density of force acting on the plasma from the emitted familon, $\mathcal{F}$, it is necessary to sum the energy and momentum losses of one plasma electron over all states of primary electrons; that is,

$$(\dot{\varepsilon}, \mathcal{F}) = \sum_N \int dn_{e^-} f_{e^-} \frac{(Q^0, \mathbf{Q})}{VE}, \tag{9}$$

where f_{e^-} is the distribution of primary electrons.

In the plasma rest frame, where the electromagnetic field reduces to a purely magnetic field [$\mathbf{B} = (0, 0, B)$ in the gauge $A^\mu = (0, 0, Bx, 0)$], the number of electron states is

$$dn_{e^-} = \frac{dp_y dp_z}{(2\pi)^2} L_y L_z \tag{10}$$

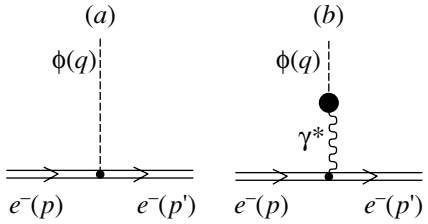

Fig. 1. Diagrams describing familon emission by an electron in a magnetized plasma.

Considering that integration with respect to p_y determines the degeneracy multiplicity s of an energy eigenstate according to the relation

$$s = 2\int \frac{L_y dp_y}{2\pi} = \frac{eBL_xL_y}{\pi}$$

and going over from summation over N to integration with respect to the transverse momentum $p_\perp$, we obtain the total number of primary-electron states in the form

$$\sum_N \int dn_{e^-} \simeq \int \frac{2d^3p}{(2\pi)^3} V. \tag{11}$$

Thus, we can see that, in a relatively weak field, the number of electron states is given by the same formula as in a crossed field [see (6)]. With allowance for Eq. (11), the definition in (9) can be recast into the form

$$(\dot{\varepsilon}, \mathcal{F}) = \int \frac{2d^3p}{(2\pi)^3} f_{e^-} \frac{(Q^0, \mathbf{Q})}{E}. \tag{12}$$

In the present study, we further calculate the energy and momentum losses of a magnetized plasma via familon emission. The ensuing exposition is organized as follows. In Section 2, we examine two channels of the synchrotron radiation of familons from electrons in a magnetized plasma. In Section 3, we consider the "decay" process $e^- \to \mu^- \phi$ for the case where both electrons and muons occupy a great number of Landau levels. In Section 4, we present numerical estimates of the results that we obtained. In particular, we estimate the contributions of the processes in question to the energy loss of the core of a supernova and the asymmetry of familon emission in the process $e^- \to \mu^- \phi$.

2. SYNCHROTRON RADIATION OF A FAMILON BY PLASMA ELECTRONS

2.1. Process $e^- \to e^- \phi$ in a Model Involving a Direct Familon–Fermion Coupling

In this section, we examine familon emission by plasma electrons due to a direct familon–fermion

coupling. This proceeds via the process $e^- \to e^-\phi$ (see Fig. 1*a*). The S-matrix element for this process can be obtained from the Lagrangian in (2) by directly substituting solutions to the Dirac equation into it; that is,

$$S_{(e^-\to e^-\phi)} = \frac{-c_e}{F\sqrt{2\omega V}} \times \int d^4x \bar{\psi}_e(p',x) q^\mu \gamma_\mu \gamma_5 \psi_e(p,x) e^{iqx}, \quad (13)$$

where ψ_e stands for solutions to the Dirac equation in a constant crossed field [12]; $q^\alpha = (\omega, \mathbf{k})$ is the familon 4-momentum; and $p^\alpha = (p_0, \mathbf{p})$ and $p'^\alpha = (p'_0, \mathbf{p}')$ are constant 4-vectors that characterize the states of, respectively, the primary and the final electron in a crossed field and which become coincident with the particle momentum upon switching the field.

By means of the procedure for performing calculations in a crossed field, the result for the probability (5) of the process $e^- \to e^-\phi$ can be expressed in terms of a single integral with respect to the dynamical parameter χ_q; that is,

$$W_{(e^-\to e^-\phi)} = \frac{c_e^2 m_e^4}{2\pi^2 F^2 p_0} \times \int_0^\chi \frac{d\chi_q}{(\chi-\chi_q)^{1/3}} \left(\frac{\chi_q}{\chi}\right)^{4/3} (-\Phi'(z))(1 - f'_{e^-}), \quad (14)$$

where f'_{e^-} is the distribution of the final electron and $\Phi(z)$ is the Airy function defined as

$$\Phi(z) = \int_0^\infty dx \cos\left(zx + \frac{x^3}{3}\right), \quad (15)$$

$$\Phi'(z) = \frac{d\Phi(z)}{dz}.$$

We have also used the following notation:

$$z = \left(\frac{\chi_q}{\chi(\chi-\chi_q)}\right)^{2/3}, \quad \chi_q^2 = \frac{e^2(qFFq)}{m_e^6}, \quad (16)$$

$$\chi^2 = \frac{e^2(pFFp)}{m_e^6}.$$

It should be noted that, apart from a change in the notation, expression (14) reproduces the result presented in Eq. (6) of [13] for the probability of the synchrotron radiation of axions in a weak magnetic field (that is, a field whose induction satisfies the condition $B \ll B_e$). In order to prove this statement, it is necessary to make the substitution $g_{ae} \to 2m_e c_e/F$ in Eq. (6) of [13]. In view of this, we immediately present the eventual expression for the familon luminosity due to the process $e^- \to e^-\phi$ induced by a direct familon–electron coupling. We have

$$\dot{\varepsilon}_{(e^-\to e^-\phi)} \simeq \frac{c_\phi c_e^2 m_e^2}{\pi^4 F^2} \left(\frac{eB}{\mu}\right)^{2/3} T^{13/3}, \quad (17)$$

where

$$c_\phi = \frac{14}{81}\left(\frac{3}{4}\right)^{1/6}\Gamma^3\left(\frac{1}{3}\right)\zeta\left(\frac{13}{3}\right) \simeq 3.38.$$

We note that our result in (17) is valid under the conditions in (4), which are more lenient than the condition $B \ll B_e$, which is necessary for the validity of the result in [13].

2.2. Process $e^- \to e^-\phi$ in a Model without Direct Familon–Fermion Coupling

In an external magnetic field, not only may a familon interact with an electron at the tree level, but it may also feature an induced interaction via an intermediate photon. As a result, the channel of familon emission from plasma electrons through a virtual plasmon as an intermediate state, $e^- \xrightarrow{\gamma^*} e^-\phi$ (see diagram in Fig. 1*b*), opens up in an active external medium (field + plasma).

The amplitude for this process can be obtained from the Lagrangian

$$L = g_{\phi\gamma}\tilde{F}^{\alpha\beta}(\partial_\beta A_\alpha)\Phi + e(\bar{\Psi}_e A^\mu \gamma_\mu \Psi_e), \quad (18)$$

where $g_{\phi\gamma}$ is the effective familon–photon coupling constant in a magnetized plasma. In general, this coupling involves a contribution induced by the external magnetic field and a contribution caused by the presence of an electron–positron plasma. Direct calculations (see Appendix) reveal that, under the physical conditions specified in (4), which correspond to the core of a supernova, the plasma contribution to $g_{\phi\gamma}$ is much smaller than the field contribution and can be discarded. In this case, the coupling constant $g_{\phi\gamma}$ proves to be independent of the familon (photon) momentum and has a simple form; that is,

$$g_{\phi\gamma} = \frac{2\alpha c_e}{\pi F}, \quad (19)$$

where $\alpha = e^2/4\pi$ is the fine-structure constant.

Although the process of familon emission through a virtual plasmon arises in a higher order of perturbation theory, its amplitude may appear to be on the same order of magnitude as the tree amplitude, especially in the case of a longitudinal plasmon. This is because the familon and longitudinal-plasmon dispersion curves intersect at some familon energy $\omega = \omega_0$ (see Fig. 2), with the result that the process of familon emission by plasma electrons has a resonance character. Concurrently, it turns out that, in the case

of ultrarelativistic plasma, the contribution from a transverse plasmon is negligible.

By using the Lagrangian in (18) and taking into account relation (19), we can represent the S-matrix element for the process under study in the form

$$S_{(e^-\xrightarrow{\gamma^*}e^-\phi)} = \frac{2\alpha e c_e}{\pi F\sqrt{2\omega V}}(q\tilde{F}G^L)^\mu J_\mu, \qquad (20)$$

where $J_\mu = \int d^4x\bar{\psi}_e(p',x)\gamma_\mu\psi_e(p,x)e^{iqx}$ and $G^L_{\alpha\beta}$ is the longitudinal-plasmon propagator, the rest of the notation being identical to that in Eq. (13). In a relatively weak external electromagnetic field, the longitudinal-plasmon propagator can be represented in the form

$$G^L_{\alpha\beta} \simeq \frac{l_\alpha l_\beta}{q^2-\Pi^L}, \qquad (21)$$

$$l_\alpha = \sqrt{\frac{q^2}{(uq)^2-q^2}}(u_\alpha - \frac{(uq)}{q^2}q_\alpha),$$

where q_μ is the virtual-plasmon 4-momentum, while l_α and Π^L are, respectively, the eigenvector and the eigenvalue of the polarization operator that correspond to the longitudinal plasmon.

The main contribution to the probability of the process $e^- \xrightarrow{\gamma^*} e^-\phi$ comes from the vicinity of the resonance, where $q^2 = 0$; throughout the ensuing calculations, we will therefore set $q^2 = 0$, unless this leads to confusion. Also, that part of l_α which is proportional to q_α does not contribute to the amplitude by virtue of gauge invariance and the asymmetry of the tensor $\tilde{F}_{\alpha\beta}$. Without loss of generality, the propagator in (21) can therefore be represented in the form

$$G^L_{\alpha\beta} \simeq \frac{u_\alpha u_\beta}{(uq)^2}\frac{q^2}{q^2-\Pi^L}. \qquad (22)$$

In general, Π^L is a complex-valued function,

$$\Pi^L = \mathrm{Re}\Pi^L + i\mathrm{Im}\Pi^L. \qquad (23)$$

In a weak field, the real part of Π^L is virtually coincident with its value in a nonmagnetized plasma and can be represented in the form [14]

$$\mathrm{Re}\Pi^L = q^2\frac{F(c)}{\mathbf{k}^2}, \quad c = \frac{|\mathbf{k}|}{\omega}, \qquad (24)$$

where

$$F(c) \simeq \frac{4\alpha}{\pi}\int\limits_0^\infty \frac{dpp}{E}\left(\frac{E}{c}\ln\left(\frac{E+pc}{E-pc}\right) - p - \frac{E^2p(1-c^2)}{E^2-c^2p^2}\right)(f_{e^-}+f_{e^+}).$$

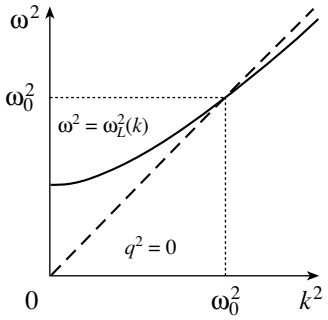

Fig. 2. Dispersion curves for (solid line) a longitudinal plasmon, $\omega^2 = \omega_L^2(k)$, and (dashed line) a familon, $\omega^2 = k^2$.

Here, E and p are, respectively, the energy and the momentum of plasma electrons (positrons) and f_{e^+} is the distribution of plasma positrons, which is obtained from the distribution f_{e^-} of electrons by means of the substitution $\mu \to -\mu$.

In order to find the resonance position, which is determined by the point of intersection of the longitudinal-plasmon and familon dispersion curves, $\omega \simeq \omega_0$, it is necessary to find a simultaneous solution to the dispersion equations for the longitudinal plasmon,

$$\mathbf{k}^2 = F(c), \qquad (25)$$

and the familon,

$$\mathbf{k}^2 = \omega^2. \qquad (26)$$

As a result, we obtain the familon energy at which the dispersion curves intersect:

$$\omega_0^2 = F(1). \qquad (27)$$

At the point $c = 1$, the function $F(c)$ can be reduced to the form

$$F(1) \simeq \frac{-2\alpha}{\pi} \qquad (28)$$

$$\times \int\limits_{m_e}^\infty dEE\left(E\ln\left(\frac{E+p}{E-p}\right) - 2p\right)\frac{d}{dE}(f_{e^-}+f_{e^+}).$$

It should be emphasized that formula (28) is universal—it is valid both for a cold ($\mu \gg T$) and for a hot ($\mu \ll T$) plasma. Upon the expansion of the function $F(c)/\mathbf{k}^2$ in a power series in the vicinity of the resonance, the expression for the real part of Π^L can be recast into the form

$$\mathrm{Re}\Pi^L \simeq q^2\frac{\omega^2}{\omega_0^2}. \qquad (29)$$

As to the imaginary part, it can undergo a significant change even under the effect of a relatively weak

field, since a magnetic field opens new channels of photon decay and new channels of photon absorption by plasma electrons and positrons, $\gamma \leftrightarrow e^-e^+$ and $e^\pm \leftrightarrow e^\pm\gamma$, these channels being forbidden in a nonmagnetized plasma. According to the unitarity condition, the imaginary part of Π^L and the total width with respect to longitudinal-plasmon "annihilation," $\Gamma^L(\omega)$, are related by the equation

$$Z^L \mathrm{Im}\Pi^L = -\omega\Gamma^L(\omega), \tag{30}$$

where Z^L is the renormalization factor for the plasmon wave function.

With allowance for relations (29) and (30), the longitudinal-plasmon propagator (22) in the vicinity of the resonance can be represented in the form

$$G^L_{\alpha\beta} \simeq \frac{u_\alpha u_\beta}{(\omega_0^2 - \omega^2 + i\gamma\omega_0^2)}, \tag{31}$$
$$\gamma = \frac{\omega_0\Gamma^L(\omega_0)}{q^2 Z^L}.$$

Substituting the explicit form (31) of the propagator into expression (20) for the relevant S-matrix element, we obtain

$$S_{(e^-\stackrel{\gamma^*}{\to}e^-\phi)} = \frac{2\alpha e c_e}{\pi F\sqrt{2\omega_0 V}}\frac{(q\tilde{F}u)(uJ)}{(\omega^2 - \omega_0^2 + i\gamma\omega_0^2)}. \tag{32}$$

From expression (32), it can clearly be seen that, at an emitted-famil on energy close to ω_0, the process of famil on emission by plasma electrons has a distinct resonance character.

The probability of the process $e^- \stackrel{\gamma^*}{\to} e^-\phi$ is calculated directly by formula (5) with the aid of expression (32) for the S-matrix element. After straightforward, albeit rather cumbersome, calculations, the result can be represented in the form

$$W_{(e^-\stackrel{\gamma^*}{\to}e^-\phi)} \simeq \frac{4c_e^2\alpha^3\omega_0^2}{\pi^3 F^2 p_0} \tag{33}$$
$$\times \int_0^\chi \frac{d\chi_q}{\chi_q^2}\frac{(\chi-\chi_q)(q\tilde{F}u)^2}{[(\omega^2-\omega_0^2)^2+\gamma^2\omega_0^4]}\Phi_1(z)(1-f'_{e^-}),$$

where

$$\Phi_1(z) = \int_z^\infty \Phi(x)dx,$$

with the argument z being given by (16). Under the conditions in (4), which are considered in the present study, the dynamical parameter χ for electrons is much greater than unity. The main contribution to the relevant integral with respect to the variable χ_q then comes from the region where $z \ll 1$. In this case, it is sufficient to know the value of the function $\Phi_1(z)$ at the origin.

It is convenient to perform a further integration in the rest frame of the plasma, where the electromagnetic field reduces to a purely magnetic one and where the dynamical parameters take the form

$$\chi = \frac{eBE}{m_e^3}\sin\theta, \quad \chi_q = \frac{eB\omega}{m_e^3}\sin\theta'. \tag{34}$$

Here, θ' is the angle between the famil on 3-momentum $\mathbf{k}$ and the magnetic-field direction and the effective angle θ is defined by the relation

$$\sin\theta = \frac{p_\perp}{\sqrt{p_\perp^2 + p_z^2}}. \tag{35}$$

An analysis reveals that, in a relatively weak magnetic field ($eB \ll \mu\omega$), we have

$$\sin\theta \simeq \sin\theta', \tag{36}$$

which means that, under the conditions being considered, the kinematics of the process $e^- \stackrel{\gamma^*}{\to} e^-\phi$ is collinear.

In expression (33), we further go over to the rest frame of the plasma with allowance for (34) and (36) and substitute the result into definition (8). In this way, we obtain, for the process $e^- \stackrel{\gamma^*}{\to} e^-\phi$, the zeroth component of the loss 4-vector in the form

$$Q^0_{(e^-\stackrel{\gamma^*}{\to}e^-\phi)} \simeq \frac{c_e^2\alpha^2\omega_0^3(eB)^2}{3\pi^3F^2}\cos^2\theta \tag{37}$$
$$\times \int_0^E \frac{(E-\omega)d\omega}{(\omega^2-\omega_0^2)^2+\gamma^2\omega_0^4}(1-f'_{e^-}),$$

where it has been considered that $\Phi_1(z) \simeq \Phi_1(0) = \pi/3$.

The resonance factor in expression (37) can be approximated by a delta function,

$$\frac{1}{(\omega^2-\omega_0^2)^2+\gamma^2\omega_0^4} \simeq \frac{\pi}{2\omega_0^3\gamma}\delta(\omega-\omega_0), \tag{38}$$

and this makes it possible to perform integration with respect to the famil on energy quite easily.

In order to calculate the dimensionless factor γ, it is necessary to know the total longitudinal-plasmon-annihilation width Γ^L, which is defined as the difference of the widths with respect to the absorption and the creation of a longitudinal plasmon in an electron–positron plasma and which can be represented in the form [15]

$$\Gamma^L = \Gamma^L_{\mathrm{abs}} - \Gamma^L_{\mathrm{cr}} = (1 - e^{-\omega/T})\Gamma^L_{\mathrm{abs}}. \tag{39}$$

An analysis reveals that the main contribution to $\Gamma^L_{\rm abs}$ comes from the process $e^-\gamma^L \to e^-$, where a longitudinal plasmon is absorbed by plasma electrons. The S-matrix element for this process can be obtained from the electromagnetic-interaction Lagrangian by directly substituting into it solutions to the Dirac equation in a crossed field. In the lowest order of perturbation theory, the result has the form

$$S = ie\int d^4x\bar{\psi}_e(p',x)A^\mu\gamma_\mu\psi_e(p,x). \qquad (40)$$

The plasmon-absorption width is determined in a standard way; that is,

$$\Gamma^L_{\rm abs} = \sum_{s,s'}\int\frac{|S|^2}{\mathcal{T}}\frac{d^3p}{(2\pi)^3}Vf_{e^-}\frac{d^3p'}{(2\pi)^3}V(1-f'_{e^-}). \qquad (41)$$

Omitting the details of integration over the phase spaces of the particles involved, we only present the result obtained by evaluating expression (41):

$$\Gamma^L_{\rm abs} \simeq \frac{2\alpha}{3}\frac{\mu^2}{\omega^3}\frac{q^2Z^L}{1-e^{-\omega/T}}. \qquad (42)$$

With allowance for (39) and (42), the dimensionless parameter γ reduces to the form

$$\gamma = \frac{2\alpha}{3}\frac{\mu^2}{\omega_0^2}. \qquad (43)$$

Substituting (37) into (12) and performing integration with respect to the primary-electron momentum and with respect to the familon energy with allowance for Eq. (38), we obtain the following expression for the familon luminosity due to the process $e^- \overset{\gamma^*}{\to} e^-\phi$:

$$\dot{\varepsilon}_{(e^-\overset{\gamma^*}{\to}e^-\phi)} \simeq \frac{\alpha c_e^2(eB)^2}{12\pi^4F^2}\frac{\omega_0^3}{(e^{\omega_0/T}-1)}. \qquad (44)$$

We note that the result in (44) is valid not only in a degenerate plasma but also in the general case. Only the energy ω_0 at which the familon and longitudinal-plasmon dispersion curves intersect depends on specific physical conditions. In the case of a degenerate ultrarelativistic plasma, we find from (27) with allowance for (28) that

$$\omega_0^2 \simeq \frac{4\alpha}{\pi}\mu^2(\ln\frac{2\mu}{m_e}-1).$$

In the case of a hot plasma, ω_0^2 is given by

$$\omega_0^2 \simeq \frac{4\pi\alpha}{3}T^2(\ln\frac{4T}{m_e}+\frac{1}{2}-\gamma_{\rm E}+\frac{\zeta'(2)}{\zeta(2)}),$$

where $\gamma_{\rm E}$ is the Euler constant ($\gamma_{\rm E}\simeq 0.577$) and $\zeta'(2)/\zeta(2)\simeq -0.570$.

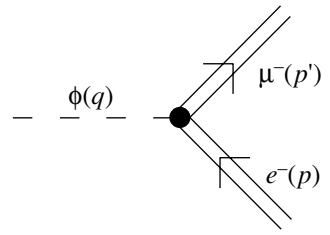

Fig. 3. Diagram describing familon emission in the process $e^- \to \mu^-\phi$ in an external field.

From the calculations, it follows that, under the conditions considered here, the effect of the interference between the contributions from the above two channels of the synchrotron radiation of familons is nonexistent.

3. TRANSITION $e^- \to \mu^-\phi$

In this section, we consider the electron-decay process $e^- \to \mu^-\phi$ as a possible additional source of the familon emissivity of a magnetized plasma (see Fig. 3). This process was previously studied by Averin *et al.* [10] in the limit of strong magnetic fields whose induction satisfies the condition $eB \gg \mu^2 - m_\mu^2$, in which case muons are produced only in the first Landau level. Among other things, those authors showed that, under the conditions that they considered, the familon emissivity is competitive with the neutrino emissivity caused by the magnetic bremsstahlung of neutrino pairs from electrons. It should be noted, however, that the magnetic bremsstrahlung of neutrinos does not saturate the actual emissivity of a supernova remnant or a nascent neutron star. As a matter of fact, the actual emissivity of these astrophysical objects is determined by modified URCA processes [16].

Here, we consider the limit of relatively weak magnetic fields, which corresponds to a situation that is inverse to that in [10] and which could occur, for example, in the core of a supernova, where $\mu^2 - m_\mu^2 \gg eB$ and where muons, as well as electrons, therefore populate a large number of Landau levels.

The general form of the S-matrix element for the process $e^- \to \mu^-\phi$ can be obtained from the Lagrangian in (1) by directly substituting into it solutions to the Dirac equation in a crossed field; that is,

$$S_{(e^-\to\mu^-\phi)} = \frac{-c_{\mu e}}{\sqrt{2\omega V F}}$$
$$\times\int d^4x\bar{\psi}_\mu(p',x)q^\mu\gamma_\mu(g_v+g_a\gamma_5)\psi_e(p,x)e^{iqx},$$

where $q^\alpha = (\omega,\mathbf{k})$ is the familon 4-momentum, while $p^\alpha = (p_0,\mathbf{p})$ and $p^{\alpha'} = (p'_0,\mathbf{p}')$ are constant vectors

that characterize the states of, respectively, the electron and the muon in a crossed field.

The probability of the process is determined according to Eq. (5), where a muon appears as the final fermion. In the relevant calculations, we will disregard the electron mass and the statistical factor of muons, assuming that the concentration of thermalized muons is low in the core of a supernova. The results of the calculations can be reduced to the form

$$W_{(e^-\to\mu^-\phi)} = \frac{c_{\mu e}^2 m_\mu^4}{8\pi^3 F^2 p_0} \tag{45}$$
$$\times \int_{-\infty}^{+\infty} d\tau \int_0^\chi \frac{\chi_q^2 d\chi_q}{r\chi^2(\chi-\chi_q)}[\Phi^2(y) r^2(\tau^2+\chi^2/\chi_q^2)$$
$$+ \Phi'^2(y) - 4g_a g_v \Phi(y)\Phi'(y) r\tau],$$

where the Airy function $\Phi(y)$ was defined in (15), its argument being

$$y = r^2\left(\tau^2 + \frac{\chi}{\chi_q}\right),$$

and where we have also introduced the following conventional notation [12]:

$$\tau = \frac{e(p\tilde{F}q)}{\chi_q m_\mu^4}, \quad r = \left(\frac{\chi_q}{2\chi(\chi-\chi_q)}\right)^{1/3}. \tag{46}$$

We recall that expression (45) was obtained in the ultrarelativistic limit, where the electron mass can be disregarded.

In contrast to what we had in (16), the dynamical parameters χ and χ_q are now naturally defined in terms of the muon mass; that is,

$$\chi_q^2 = \frac{e^2(qFFq)}{m_\mu^6}, \quad \chi^2 = \frac{e^2(pFFp)}{m_\mu^6}.$$

The last term in the bracketed expression on the right-hand side of (45) describes the interference between the vector and the axial-vector coupling constant entering into the Lagrangian in (1); although this term does not contribute to the total probability of the decay process in question, it leads to the asymmetry of familon emission in the process $e^- \to \mu^-\phi$.

Upon integration with respect to the variable τ, we obtain

$$W_{(e^-\to\mu^-\phi)} = \frac{c_{\mu e}^2 m_\mu^4}{16\pi^2 F^2 p_0}\int_0^\chi \frac{d\chi_q}{\chi} \tag{47}$$
$$\times\left(\Phi_1(z) - \frac{2\chi_q\Phi'(z)}{(\chi-\chi_q)z}\right),$$

$$z = \left(\frac{\chi}{\chi_q(\chi-\chi_q)^2}\right)^{1/3} > 0. \tag{48}$$

In a relatively weak external electromagnetic field, the dynamical parameter for electrons satisfies the condition $\chi \ll 1$, while, for the argument of the Airy function, we have $z \gg 1$. Performing integration with respect to the variable χ_q with allowance for the known asymptotic behavior of the functions $\Phi'(z)$ and $\Phi_1(z)$ at large values of the argument [12], we eventually obtain

$$W_{(e^-\to\mu^-\phi)} = \frac{c_{\mu e}^2 m_\mu^4 \chi}{36\sqrt{3}\pi F^2 p_0} e^{-\sqrt{3}/\chi}. \tag{49}$$

We would like to emphasize that the exponential smallness of the probability in (49) is characteristic of all processes that are forbidden in a vacuum, but which are allowed in a relatively weak field. However, the calculations reveal that, despite an exponential suppression, the decay probability $W_{(e^-\to\mu^-\phi)}$ proves to be on the same order of magnitude as the probabilities of the two channels of the synchrotron radiation of a familon from plasma electrons. This is because of the fact that, by virtue of (4), the last two probabilities also involve a small parameter that is associated either with the fine-structure constant α (33) or with the electron mass m_e (14) and which is the smallest parameter in the problem being considered.

According to our analysis, the main contribution to the integral with respect to the variable τ in expression (45) comes from the region around $\tau^2 \sim 1/r^3 \ll 1$; in the rest frame of the plasma and at relatively weak fields ($eB \ll \omega m_\mu$), this is equivalent to the collinearity condition. In order to make sure of this, it is sufficient to employ the explicit expressions for τ and r in the rest frame. We then have

$$\cos\theta - \cos\theta' \sim \left(\frac{eB}{\omega m_\mu}\right)^{1/2} \sin\theta(\sin\theta')^{1/2} \ll 1. \tag{50}$$

This makes it possible to go over, in expression (47), to the rest frame of the plasma prior to performing integration with respect to the variable χ_q and to recast this expression into the form

$$W_{(e^-\to\mu^-\phi)} = \frac{c_{\mu e}^2 m_\mu^4}{16\pi^2 F^2 E^2} \tag{51}$$
$$\times \int_0^E (\Phi_1(z) - \frac{2\omega\Phi'(z)}{(E-\omega)z})d\omega,$$

where the argument z of the Airy function becomes

$$z = \left(\frac{E}{\omega(E-\omega)^2}\frac{m_\mu^6}{(eB\sin\theta)^2}\right)^{1/3}.$$

Substituting expression (51) into the definition in (12) with allowance for (8) and performing integration

with respect to the familon energy and with respect to the primary-electron momenta, we obtain the familon luminosity due to the process $e^- \to \mu^- \phi$. The result of these calculations can be expressed in terms of a single integral as

$$\dot{\varepsilon}_{(e^- \to \mu^- \phi)} \simeq \frac{c_{\mu e}^2 \sqrt{2} m_\mu^4 \mu^3}{216 \pi^{5/2} F^2} \frac{I(y)}{y^{3/2}}, \qquad (52)$$

$$I(y) = \int_0^\infty x^{7/2} \frac{e^{-y/x} dx}{e^{\mu(x-1)/T} + 1}, \quad y = \sqrt{3} \frac{m_\mu^3}{eB\mu},$$

where the variable x is related to the primary-electron energy by the equation $x = E/\mu$.

The integral $I(y)$ in (52) can easily be calculated in two limiting cases.

First, there is the case of a cold plasma ($T \to 0$), where the distribution of primary electrons can be approximated by a Heaviside step function, $f \simeq \Theta(\mu - E)$. This leads to

$$\dot{\varepsilon}_{(e^- \to \mu^- \phi)} \simeq \frac{c_{\mu e}^2 \sqrt{2} m_\mu^4 \mu^3}{216 \pi^{5/2} F^2} \frac{e^{-y}}{y^{5/2}}, \qquad (53)$$

Second, there is the case of a relatively "warm" relativistic plasma: $T > \mu/y$, but $T \ll \mu$; in this case, where the main contribution comes from electrons of energy $E > \mu$, the result is

$$\dot{\varepsilon}_{(e^- \to \mu^- \phi)} \simeq \frac{c_{\mu e}^2 m_\mu^4 \mu^3}{216 \pi^2 F^2} \sqrt{2y} \left(\frac{T}{\mu}\right)^{5/2} e^{-y(2-1/t)/t}, \qquad (54)$$

$$t = \sqrt{\frac{yT}{\mu}}.$$

Since $t > 1$, the density of losses, $\dot{\varepsilon}$, increases significantly in this case.

4. ASTROPHYSICAL APPLICATIONS

In this section, we present quantitative estimates of our results, choosing, for a scale of horizontal-symmetry breaking, the upper bound on the relevant constraints, $F \simeq 3.1 \times 10^9$ GeV.

The volume density of the energy loss of the plasma by familon radiation can be represented as the sum of the contributions from two processes:

$$\dot{\varepsilon}_\phi = \dot{\varepsilon}_{(e^- \to e^- \phi)} + \dot{\varepsilon}_{(e^- \to \mu^- \phi)}.$$

We further estimate the energy loss per unit volume of the plasma by familon radiation under the conditions prevalent in the core of a supernova ($\mu = 250$ MeV, $T = 35$ MeV), setting the magnetic field to $B = 10^{17}$ G. The results of these numerical calculations are given in Fig. 4, which shows that, under such conditions, the contributions from the two processes in question are commensurate.

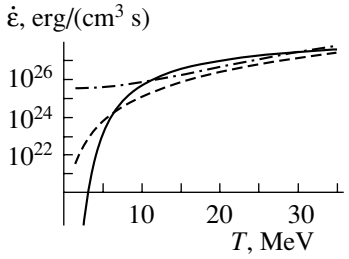

Fig. 4. Familon luminosity of a degenerate plasma ($\mu \gg T$) as a function of temperature: (solid curve) contribution of the synchrotron radiation of a familon through a virtual plasmon ($e^- \overset{\gamma^*}{\to} e^- \phi$), (dashed curve) contribution of the synchrotron radiation of a familon due to direct coupling ($e^- \to e^- \phi$), and (dash-dotted curve) contribution of the transition $e^- \to \mu^- \phi$.

A comparison of the familon luminosity with the known neutrino luminosity under the same conditions, $\dot{\varepsilon}_\nu \sim 10^{34}$ erg/(cm^3 s) [1], reveals that, at the initial stage of cooling, when the plasma temperature is $T \sim 35$ MeV, the processes being considered do not have a significant effect on the dynamics of cooling.

It is interesting to note, however, that, at a later stage of cooling, when the plasma temperature decreases to values of about a few MeV units, the contribution of the process $e^- \to \mu^- \phi$ with respect to the contribution of the synchrotron-radiation process $e^- \to e^- \phi$ becomes dominant. In this case, the energy loss of the plasma by familon radiation is given by

$$\dot{\varepsilon}_{(e^- \to \mu^- \phi)} \simeq 3.4 \times 10^{25} \frac{\text{erg}}{\text{cm}^3\ \text{s}}$$

and can be commensurate with the loss by neutrino radiation at the same stage, $\dot{\varepsilon}_\nu \sim 10^{26}$ erg/(cm^3 s)[1].

The asymmetry of familon emission is yet another interesting feature of radiation processes. This asymmetry can be defined as

$$\mathbf{A} = \left(0, 0, \frac{\mathcal{F}_3}{\dot{\varepsilon}}\right), \qquad (55)$$

where it is considered that the asymmetry does not vanish only in the magnetic-field direction (which is coincident with the direction of the z axis) and where $\mathcal{F}_3$ is the force acting on the plasma from the familon along the magnetic field. This force can be calculated by formula (12).

Direct calculations reveal that only the transition $e^- \to \mu^- \phi$ contributes to the asymmetry given by (55), which proved to be independent of either the

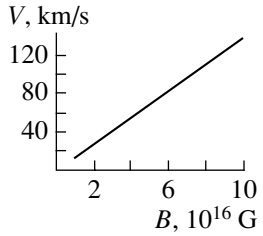

Fig. 5. Velocity of a supernova remnant with a mass on the order of the Sun's mass versus the magnetic-field induction.

chemical potential of the plasma or its temperature and which has the simple form

$$A \simeq \frac{g_a g_v}{3}\frac{eV}{m_\mu^2}. \qquad (56)$$

We note that the emergence of the asymmetry in (56) is due to the interference between the vector and the axial-vector coupling constant entering into the Lagrangian in (1).

Owing to this asymmetry, the total momentum carried away by a familon is nonzero, which in turn leads to a "push" velocity V of a supernova remnant. This velocity can be estimated as

$$V = \frac{\varepsilon A}{M}, \qquad (57)$$

where $\varepsilon = \int dt\dot{\varepsilon}$ is the total energy loss of the plasma by familon radiation in the process $e^- \to \mu^-\phi$ and M is the mass of the supernova remnant.

Figure 5 shows a numerical estimate of the velocity of a supernova remnant versus the magnetic-field induction. It can be seen that, even in strong magnetic fields ($B \sim 10^{17}$ G), the velocity of a supernova remnant with a mass on the order of the Sun's mass does not exceed 130 km/s. Thus, we conclude that, while being of interest in and of itself, the effect of the asymmetry of familon emission in the process $e^- \to \mu^-\phi$ unfortunately cannot clarify the problem of pulsar velocities.

5. CONCLUSION

We have considered familon emission from a magnetized plasma in the electron-"decay" process $e^- \to \mu^-\phi$ and in the process of synchrotron radiation of a familon by plasma electrons, $e^- \to e^-\phi$. New transitions of the familon $\rightleftarrows$ photon type, which generate an additional channel of the synchrotron radiation of a familon by an electron through a virtual plasmon as an intermediate state, $e^- \xrightarrow{\gamma^*} e^-\phi$, become possible in an external magnetic field. In the case where a virtual plasmon is longitudinal, the process $e^- \xrightarrow{\gamma^*} e^-\phi$ has been shown to be of a resonance character at a certain value of the emitted-familon energy.

As a possible astrophysical application, the volume density of the energy loss of a plasma by familon radiation has been calculated under the conditions of the core of a supernova. The estimates obtained in this way indicate that, under realistic conditions prevalent in the core of a supernova at the initial stage of cooling, the contributions to the energy loss of the plasma from the two processes being considered are on the same order of magnitude, but that they are insufficient for significantly affecting the dynamics of supernova cooling.

At the same time, the contribution to the energy loss from the transition $e^- \to \mu^-\phi$ at a later stage of cooling considerably exceeds the contribution from the synchrotron radiation of a familon and becomes commensurate with the energy loss by neutrino radiation under the same conditions. It follows that, at the stage of cooling, the role of processes involving familons may become significant against the background of neutrino processes when the plasma temperature decreases to a value of $T \sim 1$ MeV.

It has also been found that, in the case of familon emission by plasma electrons in the process $e^- \to \mu^-\phi$, there occurs an interesting interference effect that leads to the asymmetry of the familon momentum with respect to the direction of the magnetic field of a supernova remnant. In magnetic fields of induction $B \sim 10^{17}$ G, this generates a push velocity of the supernova remnant on the order of 100 km/s.

Our results may be of use in performing a detailed investigation into, for example, astrophysical phenomena that accompany the creation of a magnetized neutron star (pulsar) upon supernova explosion and in describing the dynamics of its cooling.

ACKNOWLEDGMENTS

This work was supported in part by the Ministry for Higher Education of the Russian Federation (project no. E02-11.0-48) and by the Russian Foundation for Basic Research (project nos. 01-02-17334, 03-02-06215).

APPENDIX

In general, the familon $\to$ photon conversion in a magnetized plasma is affected both by the magnetic field and by the plasma itself.

The one-loop external-field-induced contribution to the amplitude for the familon $\to$ photon transition, $M^{\text{field}}_{\phi\to\gamma}$, is described by the diagram in Fig. 6, where double lines denote that the effect of the external field

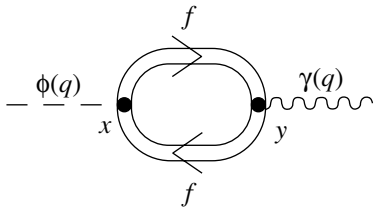

Fig. 6. Diagram describing the familon → photon transition in an external magnetic field through a fermionic loop.

has been taken into account in the propagators for virtual charged fermions f.

The plasma contribution $M^{\text{plasma}}_{\phi\to\gamma}$ comes from Compton-like processes of familon-to-photon transitions occurring on plasma electrons and positrons (see Fig. 7).

The expression for the amplitude $M^{\text{field}}_{\phi\to\gamma}$ can be derived, for example, from the results presented in [17], where the one-loop contributions to the generalized amplitude for the transition $j \to f\bar{f} \to j'$ in an external electromagnetic field were calculated for arbitrary combinations of the scalar, pseudoscalar, vector, and pseudovector coupling of the currents j and j' to fermions. Performing, in Eq. (3.9) of [17], the substitutions $j_{A\mu} \to (ic_f/F)q_\mu$ and $j_{V\mu} \to -e_f\varepsilon_\mu$ and setting $q^2 = 0$, one can obtain the transition amplitude in the form

$$M^{\text{field}}_{\phi\to\gamma} = \frac{i(q\tilde{F}\varepsilon^*)}{2\pi^2 F}\sum_f c_f e_f^2 J, \qquad \text{(A.1)}$$

where e_f is the charge of a virtual fermion in the loop; q_μ is the familon (photon) 4-momentum; ε_μ is the photon polarization 4-vector; $\tilde{F}_{\alpha\beta}$ is the dual counterpart of the strength tensor of the external electromagnetic field; and J is a field form factor that, in general, depends both on the field and on the 4-momentum q_μ.

Under physical conditions corresponding to a magnetized plasma in the core of a supernova ($B \ll 10^{18}$ G, $\mu \simeq 250$ MeV), the limit of a relatively weak external magnetic field is realized, in which case many Landau levels are excited [see (4)]. The form factor J then proves to be dependent only on the combination $(qFFq)$ and has the form

$$J(\chi_f) = \int_0^1 \eta f(\eta)dt, \qquad \text{(A.2)}$$

$$f(\eta) = i\int_0^\infty dz \exp\left[-i\left(\eta z + \frac{1}{3}z^3\right)\right],$$

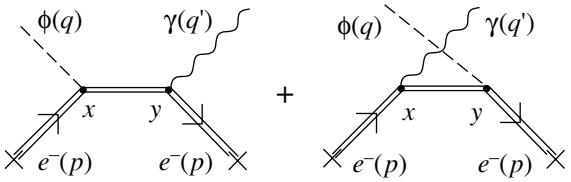

Fig. 7. Contribution of a magnetized plasma to the familon → photon transition.

$$\eta = \left[\frac{4}{\chi_f(1-t^2)}\right]^{2/3},$$

where $f(\eta)$ is the Hardy–Stokes function and $\chi_f^2 = e_f^2(qFFq)/m_f^6$ is the dynamical parameter of the relevant virtual fermion f.

The asymptotic behavior of the integral J in (A.2) at small and large values of the dynamical parameter χ_f is as follows:

$$J \simeq 1 + O(\chi_f^2), \qquad \chi_f \ll 1, \qquad \text{(A.3)}$$
$$J \simeq O(\chi_f^{-2/3}), \qquad \chi_f \gg 1.$$

Considering that the familon–photon interaction is free from the Adler anomaly, we can recast expression (A.1) into a form from which it is clearly seen that the amplitude for the familon → photon transition does not involve a term that is linear in the field; that is,

$$M^{\text{field}}_{\phi\to\gamma} = \frac{i(q\tilde{F}\varepsilon^*)}{2\pi^2 F}\sum_f c_f e_f^2[J-1]. \qquad \text{(A.4)}$$

By virtue of the asymptotic expressions in (A.3), only relatively light fermions, those for which $\chi_f \gg 1$, contribute to the transition amplitude (A.4). In view of the fermion-mass hierarchy, a virtual electron makes a dominant contribution under the conditions being considered:

$$M^{\text{field}}_{\phi\to\gamma} \simeq \frac{2i\alpha c_e}{\pi F}(\varepsilon^*\tilde{F}q). \qquad \text{(A.5)}$$

Comparing expression (A.5) with the Lagrangian in (3), we find that the external-electromagnetic-field-induced contribution to the effective familon–photon coupling constant $g_{\phi\gamma}$ can be represented in the form

$$g^{\text{field}}_{\phi\gamma} = \frac{2\alpha c_e}{\pi F}. \qquad \text{(A.6)}$$

We note that, in contrast to axion–photon interaction, the effective coupling $g^{\text{field}}_{\phi\gamma}$ features no vacuum term, because, as was indicated above, the familon does not involve the vacuum anomalies $\Phi(G\tilde{G})$ and $\Phi(F\tilde{F})$ (G and F are, respectively, the gluonic and

electromagnetic field tensors), so that its interaction with photons becomes possible only in an external electromagnetic field.

Let us now consider the plasma contribution to the amplitude for the familon → photon transition corresponding to the diagrams in Fig. 7.

The S-matrix element for the process $\phi \to \gamma$ occurring on plasma electrons can be obtained from the Lagrangian

$$\mathcal{L} = \frac{-2im_e c_e}{F}(\bar{\Psi}_e\gamma_5\Psi_e)\Phi + e(\bar{\Psi}_e\gamma_\alpha\Psi_e)A^\alpha \quad \text{(A.7)}$$

and, with allowance for coherent scattering on all plasma electrons, is given by

$$S^{(e^-)} = \frac{2iem_e c_e}{F}\int\int\int d^4x d^4y[\Phi(q,x)S(y,x)\gamma_5\psi_e(p,x)\bar{\psi}_e(p,y)\gamma_\alpha A^\alpha(q',y) \quad \text{(A.8)}$$
$$+ \Phi(q,y)\bar{\psi}_e(p,y)\gamma_5 S(y,x)\gamma_\beta A^\beta(q',x)\psi_e(p,x)]dn_{e^-}f_{e^-},$$

where A_μ is the 4-potential of a quantized electromagnetic field, Φ is the familon wave function, ψ_e stands for solutions to the Dirac equation, $S(y,x)$ is the electron propagator in an external magnetic field (see, for example, [18]), dn_{e^-} is an element of the phase space of a plasma electron, and f_{e^-} is its distribution. The S-matrix element for the familon → photon transition occurring on positrons, $S^{(e^+)}$, is obtained from expression (A.8) by means of the substitution $p \to -p$ in the solutions to the Dirac equation and the substitution $\mu \to -\mu$ in the distributions of the primary electron.

Upon integration with respect to the coordinates x and y and over the phase space of electrons and positrons, the four-dimensional delta function $\delta^4(q - q')$ can be singled out in the relevant S-matrix element. Owing to this, the standard invariant amplitude for the familon → photon transition in a relatively weak magnetic field can be written in the form

$$M^{\text{plasma}}_{\phi\to\gamma} = \frac{2i\alpha c_e}{\pi F}(\varepsilon^*\tilde{F}q) \quad \text{(A.9)}$$
$$\times\int_0^\infty dv(z_1 f(z_1) - z_2 f^*(z_2))(f_{e^-} + f_{e^+}),$$

where $f(z)$ is the Hardy–Stokes function, its argument being

$$z_{1,2} = (\chi_q v(1 \mp v))^{-2/3}.$$

The plasma contribution to the coupling constant $g_{\phi\gamma}$ from the amplitude in (A.9) has the form

$$g^{\text{plasma}}_{\phi\gamma} = \frac{2\alpha c_e}{\pi F} \quad \text{(A.10)}$$
$$\times\int_0^\infty dv(z_1 f(z_1) - z_2 f^*(z_2))(f_{e^-} + f_{e^+}).$$

Under the conditions of a degenerate ultrarelativistic plasma, the dynamical parameter χ_q is much greater than unity, in which case the integral with respect to the variable v can easily be calculated. As a result, the coupling constant can be represented in the form

$$g^{\text{plasma}}_{\phi\gamma} = \frac{\alpha c_e 3^{1/3}}{\pi^2 F}\Gamma\left(\frac{1}{3}\right)^4\frac{1}{\chi_q^{2/3}}. \quad \text{(A.11)}$$

Comparing expression (A.11) with the field contribution given by (A.6), one can see that, under the physical conditions being considered, the plasma contribution to the coupling constant $g_{\phi\gamma}$ is relatively small and can be discarded.

REFERENCES

1. G. G. Raffelt, *Stars as Laboratories for Fundamental Physics* (Univ. of Chicago Press, Chicago, 1996).
2. Dzh. L. Chkareuli, Pis'ma Zh. Éksp. Teor. Fiz. **32**, 684 (1980) [JETP Lett. **32**, 671 (1980)].
3. Z. G. Berezhiani and Dzh. L. Chkareuli, Pis'ma Zh. Éksp. Teor. Fiz. **35**, 494 (1982) [JETP Lett. **35**, 612 (1982)].
4. A. A. Ansel'm and N. G. Ural'tsev, Zh. Éksp. Teor. Fiz. **84**, 1961 (1983) [Sov. Phys. JETP **57**, 1142 (1983)].
5. J. L. Feng *et al.*, Phys. Rev. D **57**, 5875 (1998).
6. D. E. Groom *et al.* (Particle Data Group), Eur. Phys. J. C **15**, 1 (2000).
7. G. S. Bisnovatyi-Kogan, Astron. Astrophys. Trans. **3**, 287 (1993).
8. S. L. Adler, Ann. Phys. (N.Y.) **67**, 599 (1971).
9. N. P. Klepikov, Zh. Éksp. Teor. Fiz. **26**, 19 (1954).
10. A. V. Averin, A. V. Borisov, and A. I. Studenikin, Yad. Fiz. **50**, 1058 (1989) [Sov. J. Nucl. Phys. **50**, 660 (1989)].
11. A. I. Nikishov and V. I. Ritus, Zh. Éksp. Teor. Fiz. **46**, 776 (1964) [Sov. Phys. JETP **19**, 529 (1964)].

12. V. I. Ritus, *Quantum Electrodynamics of Intense Field Phenomena*, Tr. FIAN SSSR **111** (Nauka, Moscow, 1979).
13. A. V. Borisov and V. Yu. Grishina, Zh. Éksp. Teor. Fiz. **106**, 1553 (1994) [JETP **79**, 837 (1994)].
14. T. Altherr, Astropart. Phys. **1**, 289 (1993).
15. H. A. Weldon, Phys. Rev. D **28**, 2007 (1983).
16. M. Kachelriess, C. Wilke, and G. Wunner, Phys. Rev. D **56**, 1313 (1997).
17. M. Yu. Borovkov, A. V. Kuznetsov, and N. V. Mikheev, Yad. Fiz. **62**, 1714 (1999) [Phys. At. Nucl. **62**, 1601 (1999)].
18. C. Itzykson and J.-B. Zuber, *Quantum Field Theory* (McGraw-Hill, New York, 1980; Mir, Moscow, 1984), Vol. 1.

Translated by A. Isaakyan

Physics of Atomic Nuclei, Vol. 66, No. 7, 2003, pp. 1310–1318. Translated from Yadernaya Fizika, Vol. 66, No. 7, 2003, pp. 1350–1358.

ELEMENTARY PARTICLES AND FIELDS
Theory

Effect of Nuclear Matter on the Production of Hadrons in Deep-Inelastic Neutrino Scattering

N. M. Agababyan[1),2)], V. V. Ammosov, M. R. Atayan[2)], N. G. Grigoryan[2)], G. R. Gulkanyan[2)], A. A. Ivanilov[*], Zh. K. Karamyan[2)], and V. A. Korotkov

Institute for High-Energy Physics, Protvino, Moscow oblast, 142284 Russia

Received June 28, 2002; in final form, October 29, 2002

Abstract—The inclusive spectra of hadrons are measured with the aid of the SKAT propane–freon bubble chamber irradiated with a beam of 3- to 30-GeV neutrinos from the Serpukhov accelerator. The resulting data indicate that the intranuclear absorption of leading quark-fragmentation products is enhanced as the energy transfer to the quark involved decreases or as the quark-energy fraction z acquired by the product hadron increases. An analysis of the data on the basis of the color-string model reveals that the cross section for the intranuclear absorption of positively charged hadrons that are characterized by z values in the range between 0.7 and 0.9 is close to the inelastic cross section for pion–nucleon interaction.

INTRODUCTION

Deep-inelastic lepton–nucleon scattering is accompanied by the formation of a color string between the knock-on quark and the nucleon residue. In scattering on a peripheral intranuclear nucleon, the fragmentation of such a string is analogous to its fragmentation in the case of a hydrogen or a deuterium target. In the case of scattering on a nonperipheral nucleon, the fragmentation process is affected to some extent by a nuclear medium.

According to some theoretical predictions (see, for example, [1–5]), the mean spacetime gap l_h required for the formation of a hadron having a mass m_h and an energy E_h is determined by the Lorentz factor ($l_h \sim E_h/m_h$). In a number of other models, it is assumed that l_h is proportional to the Lorentz factor of the parent quark $l_h \sim \nu/m_q^*$, where ν is the energy transfer to the quark involved, the virtual-quark mass m_q^* being dependent on the momentum transfer squared Q^2 [6] or being determined by the kinematics of hadron "emission" from the quark [7].

From a more detailed treatment of the hadron-formation process on the basis of the Lund fragmentation model [8], as well as on the basis of models that take into account quark moderation either owing to the tension of a color string [9] or owing to gluon emission [10, 11], it follows that l_h depends on the quark-energy fraction transferred to the hadron, $z = E_h/\nu$, this dependence being such that, with decreasing z, the length of formation of the most energetic fragmentation products decreases, which entails an increase in the probability of their absorption in a nuclear medium.

A comparison of the inclusive spectra of hadrons that are produced on nuclei and the analogous spectra for the production process on a deuteron [12–16] corroborates the predicted weakening of nuclear-absorption effects with increasing ν and their enhancement for $z \to 1$. These data were obtained at comparatively high energies (up to 400 GeV); at the same time, data at intermediate energies ($\nu < 10$ GeV) are rather scanty. For the sake of completeness, it would be of interest to perform detailed investigations in this energy region as well, where the nuclear-medium effect on the fragmentation process is expected to be more pronounced.

Of special interest is a comparison of the spectra of hadrons from different samples of events of lepton scattering on the same nucleus—namely, samples that feature no explicit indication of secondary nuclear interactions and samples where there are such indications (in the following, samples of quasinucleonic and cascade events, respectively). In this comparison, manifestations of nuclear effects are expected to be more distinct in cascade events. Such a comparison was performed for νNe interactions at comparatively high values of the hadron-system energy W (up to about 25 GeV) [17].

[1)]Joint Institute for Nuclear Research, Dubna, Moscow oblast, 141980 Russia.
[2)]Yerevan Physics Institute, ul. Brat'ev Alikhanian 2, Yerevan, 375036 Armenia.
[*]e-mail: ivanilov@mx.ihep.su

The objective of the present study is to explore nuclear-absorption effects in neutron–nucleus interactions at intermediate energies, $\nu = 2$-15 GeV and $W = 2$–5 GeV. The ensuing exposition is organized as follows. The experimental procedure used is described in Section 1. An account of our methods for selecting interactions of the cascade and quasinucleonic types is given in Section 2. In Section 3, the spectra of hadrons from cascade events are compared with those for quasinucleonic events. A quantitative estimate of intranuclear-interaction effects is presented in Section 4. In Section 5, data obtained in our experiment are compared with the predictions of the color-string model. The basic results of this study and conclusions drawn from them are summarized in the Conclusion.

1. EXPERIMENTAL PROCEDURE

Our experiment employed the SKAT bubble chamber [18] irradiared with a wideband neutrino beam from the Serpukhov accelerator at a primary-proton energy of 70 GeV. The chamber was filled with a mixture containing 87% (in volume) propane (C_3H_8) and 13% freon (CF_3Br), the percentage of nuclei in this mixture being H : C : F : Br = 67.9 : 26.8 : 4.0 : 1.3. The density of admixtures was 0.55 g/cm^3; the radiation length was $X_0 = 50$ cm; and the nuclear-interaction range was 149 cm. The total volume of the chamber was 6.5 m^3, its effective volume used being 1.73 m^3. A uniform magnetic field of strength 20 kG was maintained in the chamber.

We selected charged-current-interaction events at negative-muon momenta satisfying the condition $p_\mu > 0.5$ GeV/c. A muon was identified as a negative particle that possessed the highest transverse momentum among particles that did not suffer a secondary interaction in the chamber. Other negative particles were assumed to be π^- mesons. Protons of momentum below 0.6 GeV/c and some protons of momentum in the range $0.6 < p < 0.85$ GeV/c were identified by ionization stopping in the chamber. In determining the energy transfer to the hadronic system, nonidentified positively charged particles of momentum satisfying the condition $p < 0.85$ GeV/c were assigned the proton or the pion mass in accordance with the preliminarily estimated branching fraction. All positively charged particles whose momenta took values in the region $p > 0.85$ GeV/c were assumed to be π^+ mesons. In order to improve the accuracy in reconstructing the energy transfer to the quark, ν, and the neutrino energy E_ν, we selected events in which errors in measuring the momenta of all charged secondaries and photons were less than 27% and 100%, respectively. Each selected event was assigned a weight that took into account losses of events. The mean weight of the sample used in the present study was 1.43.

For the quantity ν, the eventual value that takes into account undetected neutrons and photons was determined on the basis of the measured value of ν_{vis} by using the relation $\nu = a + b\nu_{\text{vis}}$, where the coefficients $a = 0.15 \pm 0.24$ GeV and $b = 1.07 \pm 0.05$ were found by means of the procedure applied in [19]. Close values of a and b were obtained from a Monte Carlo simulation of neutrino interactions in the chamber [20].

For a further analysis, we selected 2223 events where $3 < E_\nu < 30$ GeV, $W > 2$ GeV, the square of the momentum transfer lies in the region $Q^2 > 1\,(\text{GeV}/c)^2$, and $y = \nu/E_\nu < 0.95$.

2. SELECTION OF QUASINUCLEONIC, CASCADE, AND DEUTERON EVENTS

The selection of quasinucleonic and cascade events according to the procedure described in detail in [21] was performed by using a number of topological and kinematical criteria. The subsample B_N of quasinucleon interactions included events exhibiting no indication of a secondary interaction in the target nucleus: the total charge of secondary hadrons was required to be $q = +1$ (for the subsample B_n of interactions with a neutron) or $q = +2$ (for the subsample B_p of interactions with a proton), while the number of recorded baryons (these included identified protons and Λ hyperons, along with neutrons that suffered a secondary interaction in the chamber) was forbidden to exceed unity, baryons flying in the backward directions being required to be absent among them. Moreover, a constraint from above was imposed on the effective target mass M_t, $M_t < 1.2$ GeV/c^2, this mass being defined as $M_t = \sum(E_i - p^i_{||})$, where summation is performed over the energies E_i of secondary particles and over the longitudinal components $p^i_{||}$ of their momenta. Events that did not satisfy the above criteria were included in the subsample B_S of cascade events. As a result, the numbers of events in the subsamples B_p, B_n, and B_S proved to be 480, 555, and 1188, respectively, the numbers of the corresponding weighted events being 685, 751, and 1731.

With allowance for the content of protons and neutrons in the target nuclei, the ratio of the cross sections for νn and νp interactions that corresponds to the above relationships between the numbers of events is $r = \sigma(\nu n \to \mu^- X)/\sigma(\nu p \to \mu^- X) = 1.83 \pm 0.11$, which is close to the well-known value of $r \approx 2$ [22]. It was also verified [21] that the W dependences (in the range $2 \le W \le 5$ GeV) of

Mean features of deep-inelastic neutrino scattering for the total sample of events and for the subsamples B_p, B_n, and B_S

Sample	$\langle E_\nu \rangle$, GeV	$\langle \nu \rangle$, GeV	$\langle W^2 \rangle$, GeV^2	$\langle Q^2 \rangle$, GeV^2	$\langle x \rangle$
Total	10.8 ± 0.1	6.5 ± 0.1	9.5 ± 0.1	3.6 ± 0.1	0.30 ± 0.001
B_p	11.0 ± 0.3	6.6 ± 0.2	9.8 ± 0.3	3.5 ± 0.1	0.29 ± 0.001
B_n	10.9 ± 0.2	6.5 ± 0.2	9.3 ± 0.3	3.9 ± 0.1	0.33 ± 0.001
B_S	10.7 ± 0.2	6.5 ± 0.1	9.5 ± 0.2	3.5 ± 0.1	0.29 ± 0.001

the mean multiplicities of positively and negatively charged hadrons in the subsamples B_p and B_n are in satisfactory agreement with data from [23] on νp and νn interactions, this agreement being observed both at negative and at positive values of the Feynman variable. In addition, the inclusive spectra of hadrons were compared with available data for a hydrogen (deuterium) target in the region $2 \le W \le 5$ GeV. Here, we obtained satisfactory agreement between the inclusive spectra of π^- mesons in νp interactions [24] and those in the subsample B_p and between the inclusive spectra of hadrons in νD interactions [25] and those in the combined subsample B_{D} of quasideuteron events. The subsample of quasideuteron events contained the subsample B_n and 60% of the subsample B_p (this fraction effectively corresponds to νD interactions), the remaining 40% of the subsample B_p corresponding to interactions with hydrogen of the propane–freon mixture.

The satisfactory agreement of the above multiplicities and inclusive features of quasinucleonic subsamples with data for a proton (deuterium) target [22–25] gives sufficient grounds to conclude that the subsamples B_p and B_n may contain only an insignificant admixture of events where there occurred a secondary intranuclear interaction.

Some averaged kinematical features of the total sample and of the subsamples of events are listed in the table.

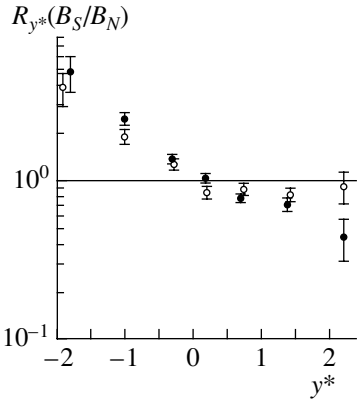

Fig. 1. Ratio of the pseudorapidity (y^*) distributions of charged hadrons in the subsamples B_S and B_N for two regions of the invariant energy W: (closed circles) $2 < W < 3$ GeV and (open circles) $3 < W < 5$ GeV.

3. COMPARISON OF THE INCLUSIVE SPECTRA OF HADRONS IN THE SUBSAMPLES OF CASCADE AND QUASINUCLEONIC EVENTS

The ratio $R_{y^*}(B_S/B_N)$ of the pseudorapidity (y^*) distributions of charged particles in the c.m. frame of the hadronic system in the subsamples B_S and B_N is shown in Fig. 1 for two intervals of the invariant energy, $2 < W < 3$ GeV and $3 < W < 5$ GeV. It can be seen that the spectrum of hadrons in the subsample B_S is shifted toward negative values of y^*, this being due to secondary intranuclear collisions and the hadron energy losses accompanying these collisions. In the target-fragmentation region ($y^* < -1$), the ratio $R_{y^*}(B_S/B_N)$ is about a few units. But in the region of quark fragmentation, the yield of hadrons is suppressed in the subsample B_S, this suppression being especially pronounced at low W—for the fastest particles ($y^* > 1.8$), we have $R_{y^*}(B_S/B_N) = 0.44 \pm 0.13$, which is compatible with the results presented in [17], where a value of 0.6 ± 0.1 at $W = 2$–7 GeV was obtained for the ratio of the yields of $y^* > 2$ charged hadrons in the cascade and quasinucleonic subsamples of νNe interactions. We also note that, with increasing W, effects associated with the absorption of fast quark-fragmentation products become weaker, disappearing almost completely, according to data from [17], in the region $W > 7$ GeV.

For the subsamples B_S and B_N, the distributions $\rho(z) = (1/N_{\mathrm{tot}})dN/dz$ with respect to the variable z are displayed in Fig. 2 separately for positively charged hadrons (identified protons are not included in these distributions) and for π^- mesons. It can be seen from this figure that, because of energy

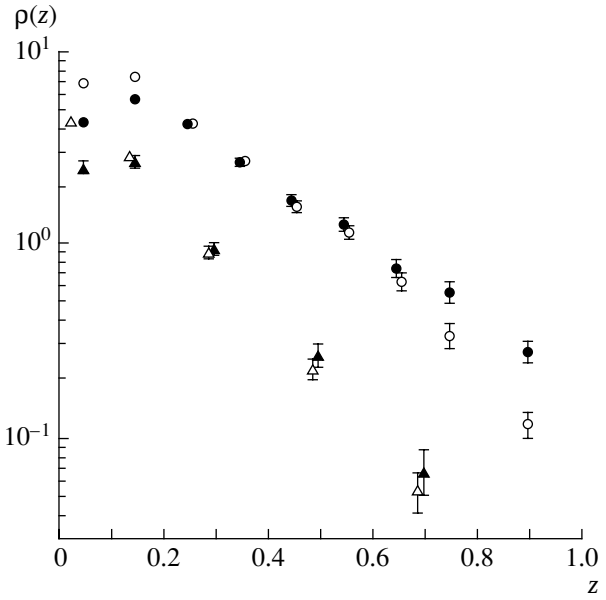

Fig. 2. Distributions of (circles) positively charged hadrons and (triangles) π^- mesons with respect to the variable z in the subsamples (open symbols) B_S and (closed symbols) B_N .

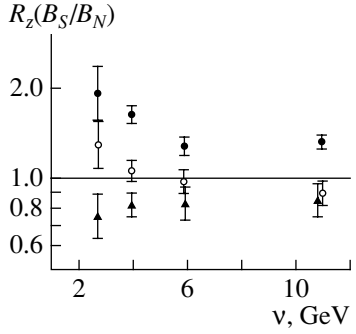

Fig. 3. Ratio of the yields of charged hadrons in the subsamples B_S and B_N as a function of ν for various regions of the variable z: (closed circles) $z < 0.2$, (open circles) $0.2 < z < 0.4$, and (closed triangles) $z > 0.4$.

losses in a nuclear medium, the spectra of hadrons in the subsample B_S are shifted toward small values of z. According to the data in Fig. 3, which illustrates the ν dependence of the ratio $R_z(B_S/B_N) = \rho^{\rm ch}_{B_S}(z)/\rho^{\rm ch}_{B_N}(z)$ of the analogous charged-hadron distributions integrated over three ranges of the variable z—$z < 0.2$, $0.2 < z < 0.4$, and $z > 0.4$—this shift, which manifests itself in the enhancement of the yield of hadrons characterized by low values of the variable z ($z < 0.2$) and in the suppression of the yield of hadrons at high values of this variable ($z > 0.4$), is especially pronounced at low values of the energy ν. From the results presented in Figs. 2 and 3, it follows that, in studying nuclear-absorption effects, one can hardly extract valuable information from data at $z < 0.4$, since these effects do not lead to the suppression of the yield of hadrons, at least in the region of comparatively low values of the energy ν, $\nu < 7$ GeV. Data for leading hadrons ($z > 0.4$) are more informative in this respect, because these data reveal that their yield is suppressed over the entire region of ν values being considered. These data also indicate that the suppression in question tends to become less pronounced with increasing ν.

Below, the nuclear-medium effect on the yield of leading hadrons, for which $z > 0.4$, will be considered versus kinematical variables (or their combinations) that presumably determine the hadron-formation length l_h. It is expected that the experimentally measured ratio $R_\eta(B_S/B_N)$ of the yields of hadrons will be a monotonically growing function of the kinematical variable $\eta \sim l_h$. Otherwise, the theoretical prediction that there is a linear relation between η and l_h would be at odds with experimental data on the leptonic production of hadrons. The data in Fig. 4 make it possible to test various theoretical predictions qualitatively.

From the data in Fig. 4*a*, it follows that, in contrast to the input assumption that the length l_h of formation of a leading hadron is linearly related to $E_{\rm ch}/m_\pi$, the degree of suppression of its yield and, hence, the path that it travels in a nuclear medium after formation undergo virtually no changes over a broad region of these variables. For the variable ν/m^*_q, which is the Lorentz factor of the quark whose effective mass is determined by the kinematics of the decay $u \to \pi^+ d$ or $\bar{d} \to \pi^+ \bar{u}$ of the knock-on virtual quark—$m^*_q = p^*_T\sqrt{z(1-z)}$, where p^*_T is the π^+-meson-momentum component orthogonal to the intermediate-boson momentum—a similar conclusion can be drawn from the data in Fig. 4*b*. Thus, our data on the neutrino-induced production of leading hadrons on nuclei do not support the conjecture that nuclear-absorption effects become weaker with increasing E_h or z.

A qualitatively different functional dependence of the length of leading-hadron formation on kinematical variables follows from models that consider the spacetime evolution of the color string that is formed between the knock-on quark and the nucleon residue [8–11]. As the string is stretched, the quark is moderated, its energy ν being expended into gluon emission; the production of quark–antiquark pairs; and, eventually, multiparticle hadron production. According to [9–11], the more extended the spacetime gap preceding the formation of a leading hadron, the smaller the fraction z of the energy ν that it can possess. At rather large z, this gap (or the hadron-formation length) is given by $l_h \sim \nu(1-z)$. For

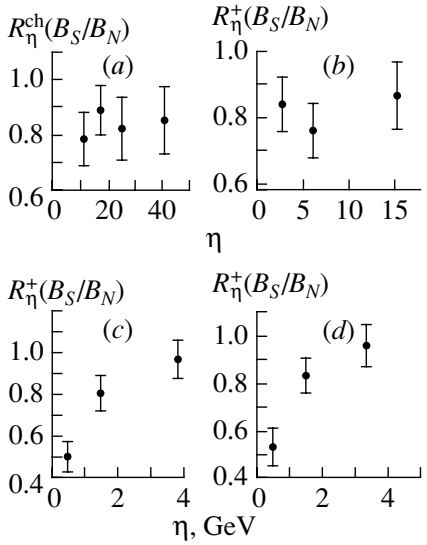

Fig. 4. Ratios of the yields of (a) charged hadrons and (b, c, d) positively charged hadrons in the subsamples B_S and B_N versus the kinematical variables defined in the main body of the text and denoted generically by η: (a) $\eta = E_{\rm ch}/m_\pi$, (b) $\eta = \nu[z(1-z)]^{-1/2}/p_T^*$, ($c$) $\eta = \nu(1-z)$, and (d) $\eta = \nu z[-1+\ln(z^{-2})/(1-z^2)]$.

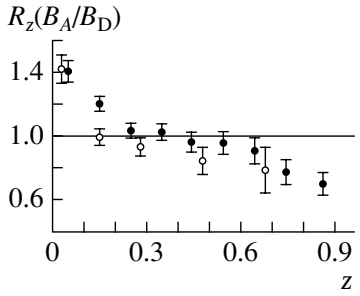

Fig. 5. Ratio of the yields of (closed circles) of positively charged hadrons and (open circles) π^- mesons in the subsamples B_A and $B_{\rm D}$ versus the variable z.

$z \to 1$, a similar dependence was obtained within the Lund string model [8]: $l_h \sim \nu z[-1+\ln(z^{-2})/(1-z^2)]$. In either case, l_h decreases monotonically with increasing z (over the region $z > 0.3$ in the second case); therefore, the suppression of the hadron yield becomes more pronounced.

The dependence of the ratio $R^+_\eta(B_S/B_N)$ on these variables in Figs. 4c and 4d is in qualitative agreement with this prediction. As was shown in [16], theoretical predictions based on the dependence $l_h \sim \nu(1-z)$ agree satisfactorily with data on the electroproduction of $z > 0.2$ hadrons on a nitrogen nucleus in the energy range $7 < \nu < 24$ GeV, which, on average, lies noticeably higher than the energy

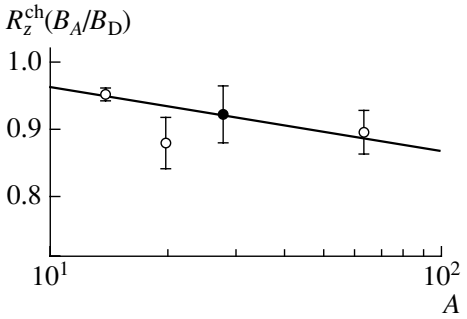

Fig. 6. Ratio $R^{\rm ch}_z(B_A/B_{\rm D})$ for $z > 0.2$ charged hadrons at the mean energy of $\langle\nu\rangle = 11.5$ GeV versus the mass number A of the target nucleus: (closed circles) data from our present study and (open circles) data from [13, 15, 16]. The description of the straight line is given in the main body of the text.

range $2 < \nu < 15$ GeV, which was studied in our experiment described here.

4. RATIO OF THE INCLUSIVE SPECTRA OF HADRONS IN THE SUBSAMPLES OF NUCLEAR AND QUASIDEUTERON EVENTS

In order to obtain quantitative estimates and to perform a comparison with the results of other experimental studies, it is necessary to represent data in the form of the ratio of the inclusive spectra in question for neutrino interactions with nuclei of the propane–freon mixture to those for neutrino interactions with deuterons. The subsample B_A of nuclear interactions can be obtained by eliminating the contribution that comes from events of interaction with hydrogen and which, in our experiment, is about 40% of the number of events in the subsample B_p. Thus, the subsample B_A can be symbolically represented as $B_A = B_S + B_n + 0.6B_p = B_S + B_{\rm D}$.

The ratio of the inclusive spectra in the subsamples B_A and $B_{\rm D}$, for example, with respect to the variable z is given by

$$R_z(B_A/B_{\rm D}) = \rho_A(z)/\rho_{\rm D}(z) = \frac{N_n^{\rm tot} + 0.6N_p^{\rm tot}}{N_S^{\rm tot} + N_n^{\rm tot} + 0.6N_p^{\rm tot}} \times \left[1 + \frac{\Delta N_S^h(z)}{\Delta N_n^h(z) + 0.6\Delta N_p^h(z)}\right],$$

where $N_S^{\rm tot}$, $N_n^{\rm tot}$, and $N_p^{\rm tot}$ are the total numbers of weighted events in the subsamples B_S, B_n, and B_p, respectively, while $\Delta N_S^h(z)$, $\Delta N_n^h(z)$, and $\Delta N_p^h(z)$ are the numbers of hadrons having a given value of z in the corresponding subsamples.

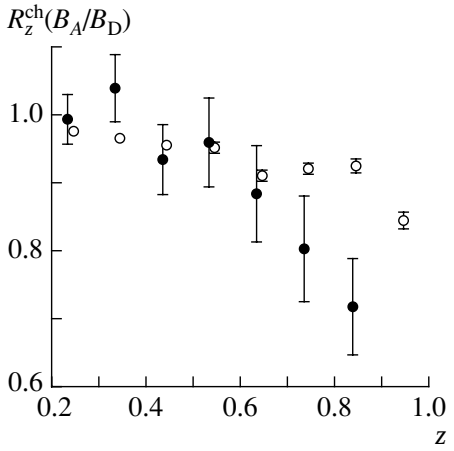

Fig. 7. Ratio of the yields of charged hadrons in the subsamples B_A and B_D (closed circles; $2 < \nu < 15$ GeV) and in the interactions of electrons with nitrogen nuclei and deuterons [16] (open circles; $7 < \nu < 24$ GeV) versus z.

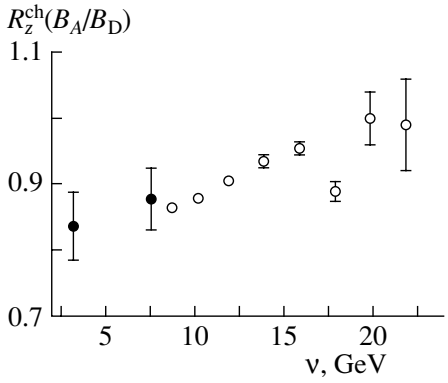

Fig. 8. Yields of $z > 0.5$ charged hadrons in the subsamples B_A and B_D (closed circles) and in the interactions of electrons with nitrogen nuclei and deuterons [16] (open circles) versus ν.

The ratio $R_z(B_A/B_D)$ as a function of z is shown in Fig. 5 individually for positive hadrons (in which case no account is taken of identified protons) and π^- mesons. From these data, it follows that the suppression of the yield of π^- mesons become significant for $z > 0.4$; for positive hadrons (primarily, π^+ mesons), this occurs for $z > 0.6$, the corresponding ratio becoming as low as $R_z(B_A/B_D) = 0.65 \pm 0.05$ for $z > 0.8$.

The yields of $z > 0.2$ charged hadrons from nuclear targets with respect to the corresponding yield from a deuterium target were measured in e^{64}Cu and e^{14}N interactions in [13, 16], as well as in $\nu(\bar{\nu})$Ne interactions in [15] at $\langle\nu\rangle \approx 11.5$ GeV, which, in our experiment, corresponds to the region $\nu > 7.5$ GeV.

The value of $R^{ch}_{z>0.2}(B_A/B_D) = 0.92 \pm 0.04$, which was obtained in the present study and which corresponds to the mean mass number $\bar{A} = 28$ of the target nucleus, is given in Fig. 6, along with data from [13, 15, 16]. Also presented in this figure is the result obtained by approximating the data in question by an exponential form (A^α), the fitted value of the exponent being $\alpha = -0.043 \pm 0.027$. So weak a dependence on A may be caused by a partial compensation of the possible suppression of the yield of $0.2 < z < 0.4$ hadrons because of the energy losses of hadrons initially possessing higher values of z. Owing to this, the integrated yield of hadrons that are characterized by values in the region $z > 0.2$ is suppressed only slightly (approximately by 10%) even for $A = 64$ nuclei.

A clear illustration of this effect is provided by Fig. 7, which displays our data ($\bar{A} = 28$) on the ratio $R_z^{ch}(B_A/B_D)$ at energies in the range $2 < \nu <$ 15 GeV, along with data obtained at higher energies of $7 < \nu < 24$ GeV for nitrogen nuclei ($A = 14$) [16]. Although stronger intranuclear-absorption effects are expected here, values that the ratio $R_z^{ch}(B_A/B_D)$ takes in the region $0.2 < z < 0.4$ are greater in the first than in the second case. The energy and the A dependence of the suppression of the hadron yield begin to manifest themselves in the region $z > 0.6$, becoming much more pronounced for the most energetic hadrons, which are characterized by values in the region $z > 0.8$.

The ν dependence of the ratio $R_z^{ch}(B_A/B_D)$ for leading charged hadrons with $z > 0.5$ is illustrated in Fig. 8, which shows our data for $2 < \nu < 4$ GeV ($\langle\nu\rangle = 3.3$ GeV) and $\nu > 4$ GeV ($\langle\nu\rangle = 7.7$ GeV), along with data on e^{14}N interactions in the region $\nu > 8$ GeV [16]. According to these data, the effect observed in [16] that the intranuclear absorption of leading hadrons becomes more pronounced with increasing ν tends to persist up to a value of $\nu \approx 3$ GeV, at which $R^{ch}_{z>0.5}(B_A/B_D)$ becomes as large as 0.84 ± 0.05.

5. COMPARISON OF EXPERIMENTAL DATA WITH PREDICTIONS OF THE COLOR-STRING MODEL

Below, we present the results obtained by comparing the ratio $R_z(B_A/B_D)$ measured for positively charged leading hadrons (which include, with a high probability, the quark knocked out by the incident lepton) with the predictions of the color-string model [9–11]. According to this model, the stretching of a color string between the nucleon residue and the knock-on quark leads to a linear decrease in the energy of this quark, ν_q, with increasing string length l: $\nu_q = \nu - \kappa l$, where the string-tension coefficient κ characterizes the quark energy

loss per unit length. In the approximation where the emission of gluons from the quark is disregarded, we have $\kappa \approx 1$ GeV/fm [26, 27], while, upon the inclusion of this emission, the effective value of κ is given by [10] $\kappa = 8\alpha_s(Q^2)Q^2/9\pi \approx 1.8$ GeV/fm at $\langle Q^2 \rangle = 3.6$ $(\mathrm{GeV}/c)^2$ and $\alpha_s = 0.35$ [28]. If the production of a leading $q\bar{q}$ pair (predominantly, a $u\bar{d}$ pair in the present case) proceeds through the rupture of the string at $l = l_h$, then its energy—that is, the energy of the leading final hadron (predominantly, a π^+ meson in our case)—is $E_h \approx \nu_q = \nu - \kappa l_h$, where $l_h = \nu(1-z)/\kappa$.

Immediately after the formation of a $q\bar{q}$ pair, its mean transverse dimension may be smaller than the pion radius, in which case the color quark charge is partly screened; as a result, the interaction of this $q\bar{q}$ pair in a nucleus is characterized by an effective cross section that is smaller than the cross section for inelastic pion–nucleon interaction, $\sigma_{\pi N}^{\mathrm{in}} \approx 20$ mb. From theoretical predictions obtained in [10, 11], it follows that, with increasing ν, the effective cross section σ_h averaged along the trajectory of the $q\bar{q}$ pair in a nucleus decreases, becoming much smaller than $\sigma_{\pi N}^{\mathrm{in}}$ for $\nu \gg 5$ GeV. But at energies in the region $\nu \leq 5$ GeV, the color-screening effect is expected to be insignificant. If the incident neutrino interacted with a nucleon whose transverse and longitudinal coordinates with respect to the center of the nucleus are $\mathbf{b}$ and ξ, respectively, and if the production of the leading $u\bar{d}$ pair occurred at the point $(\mathbf{b}, \xi + l_h)$, where $l_h = \nu(1-z)/\kappa$, then the suppression of the yield of a π^+ meson carrying the fraction z of the initial quark energy is given by

$$S_z^A(\mathbf{b}, \xi) = \exp\left(-\sigma_h \int\limits_{\xi + l_h}^{\infty} \rho_A(\mathbf{b}, \xi')\, d\xi'\right),$$

where $\rho_A(\mathbf{r})$ is the nuclear-matter density, for which, in the calculations, we used the Woods–Saxon parametrization

$$\rho_A(\mathbf{r}) = \frac{\rho_0}{1 + \exp\left(\dfrac{|\mathbf{r}| - r_A}{a}\right)}$$

with the parameter values extracted from data on eA scattering [29]: $r_A = 1.16A^{1/3} - 1.35A^{-1/3}$ (fm) and $a = 0.54$ fm. The parameter ρ_0 is determined from the normalization condition and is equal to 0.193, 0.186, and 0.163 fm^{-3} for the C, F, and Br nuclei, respectively.

For each nucleus of the propane–freon mixture and for each interval of the kinematical variable $z = E_h/\nu$, the expression for $S_z^A(\mathbf{b}, \xi)$ was averaged over the coordinates $(\mathbf{b}, \xi)$, as well as over the quantity $\nu(1-z)$, which is a combination of our kinematical variables; averaging over this quantity was performed by using its experimental distribution in the subsample B_{D}. The mean values $\langle R_z^A \rangle$ calculated in this way were averaged over target nuclei, and the resulting theoretical value $\langle R_z \rangle$ was compared with the experimentally measured ratio $R_z(B_A/B_{\mathrm{D}})$.

The calculations were performed at two values of the parameter κ, 1.0 and 1.8 GeV/fm. The parameter σ_h was fitted in such a way as to obtain the best description of data in the region of large z, $z = 0.7$–0.9. The region $z < 0.7$ was not included in the fitting procedure because a partial compensation of the suppression of the hadron yield due to the secondary interactions of more energetic particles was disregarded in the calculations.

Our fit resulted in the value of $\sigma_h = 19^{+6}_{-4.5}$ mb at $\kappa = 1$ GeV/fm and the value of $\sigma_h = 15.5^{+4.6}_{-3.8}$ mb at $\kappa = 1.8$ GeV/fm. In Fig. 9, the curves calculated at these parameter values are contrasted against experimental data. For $0.7 < z < 0.9$, good agreement is observed both for the entire energy range $\nu = 2$–15 GeV ($\langle \nu \rangle = 6.5$ GeV) and for the ranges of low and intermediate energies—that is, the range $\nu = 2$–5 GeV ($\langle \nu \rangle = 3.8$ GeV) and the range $\nu = 5$–15 GeV ($\langle \nu \rangle = 8.7$ GeV), respectively. It should be emphasized that a somewhat smaller suppression of the yield of the fastest hadrons for $\nu > 5$ GeV (Fig. 9*c*) in relation to the region $\nu < 5$ GeV (Fig. 9*b*) is explained by an increase in the mean formation length with increasing ν, $l_h \sim \nu(1-z)$, rather than by a decrease in the effective cross section σ_h. For the same reason, the interaction of the fastest hadrons in the nucleus for $\nu > 5$ GeV occurs with a lower probability, so that such hadrons make a relatively smaller contribution to the region $z < 0.7$. In all probability, this is the reason why the description of data in the region $0.4 < z < 0.7$ is satisfactory for $\nu > 5$ GeV and $\kappa = 1$ GeV/fm (Fig. 9*c*).

The description at $\kappa = 1.8$ GeV/fm is somewhat poorer, which may suggest that, in the region of intermediate energies, which are considered in the present study, the mechanism of gluon emission does not play a significant role in the leptonic production of quarks, so that the estimate obtained for the cross section σ_h at $\kappa = 1$ GeV/fm is preferable. Nonetheless, we have taken into account the possible uncertainty in the parameter κ, $\kappa = 1.4 \pm 0.4$ GeV/fm, and, as a consequence, in the cross section σ_h, $\sigma_h = 18.1 \pm 6.4$ mb, where the quoted errors include statistical uncertainties as well. Within the errors, σ_h does not differ from $\sigma_{\pi N}^{\mathrm{in}}$, whence we can conclude that the leading $q\bar{q}$ pair acquires the properties of the nascent hadron with a relatively short spacetime interval that

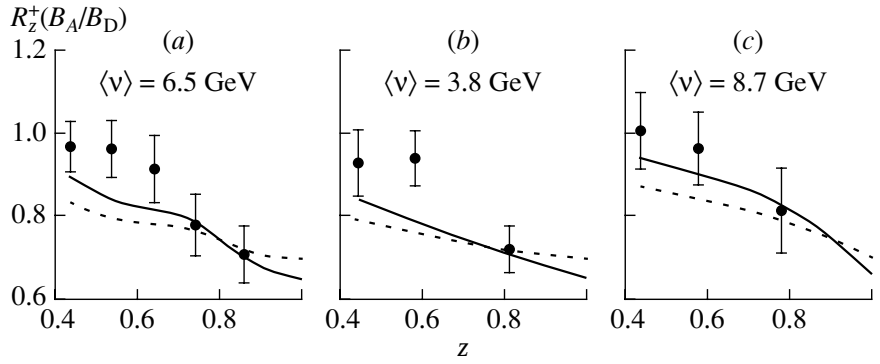

Fig. 9. Comparison of data on the ratio $R_z^+(B_A/B_D)$ for positively charged hadrons (points) along with the predictions of the color-string model (the solid and dashed curves calculated, respectively, at $\sigma_h = 19$ mb and $\kappa = 1$ GeV/fm and at $\sigma_h = 15.5$ mb and $\kappa = 1.8$ GeV/fm) for (*a*) $2 < \nu < 15$ GeV, (*b*) $2 < \nu < 5$ GeV, and (*c*) $5 < \nu < 15$ GeV.

is commensurate with internucleon distances in a nucleus.

CONCLUSION

New experimental data on the neutrino-induced production of hadrons on nuclei have been obtained in the intermediate-energy region specified by the inequalities $2 < W < 5$ GeV and $2 < \nu < 15$ GeV. The procedure applied in this study makes it possible to select the subsample of quasinucleonic (quasideuteron) events whose features are in accord with data obtained for a hydrogen (deuterium) target, as well as the subsample of cascade events exhibiting an indication of a secondary interaction in the target nucleus.

A comparison of the inclusive spectra of hadrons in these subsamples indicates that the yield of the fastest fragmentation products is suppressed, this suppression becoming more pronounced as W or ν decreases. It has been shown that the degree to which the yield of leading hadrons characterized by z values in the region $z > 0.4$ is suppressed (and, hence, their formation length) is not directly related to their energy, but it depends, in accordance with the predictions of the color-string model, on the quantity $\nu(1 - z)$, which is a combination of kinematical variables. With the aim of performing a comparison with the predictions of this model, as well as with other experimental data, the results of our measurements were represented in a form that is equivalent to the ratio $R_z(B_A/B_D)$ of inclusive spectra with respect to the variable z in νA and νD interactions. It has been shown that, for the fastest hadrons with $z = 0.7$–0.9, the effective cross section of $\sigma_h \approx 18 \pm 6$ mb for their absorption in a nuclear medium corresponds to the extracted value of $R_z(B_A/B_D)$, this value of the effective cross section being close to the known cross section for inelastic pion–nucleon interaction. This result suggests that the prehadronic $q\bar{q}$ state acquires the properties of the nascent pion within a spacetime interval that is commensurate with internucleonic distances in a nucleus. We have also obtained a piece of evidence in favor of the statement that gluon emission from a knock-on quark does not play a significant role in the evolution of the color string at moderately low values of $\langle Q^2 \rangle \approx 3.6$ (GeV/c)^2 and $\langle \nu \rangle \approx 6.5$ GeV, which were considered in the present study.

REFERENCES

1. L. Landau and I. Pomeranchuk, Dokl. Akad. Nauk SSSR **95**, 535 (1953).
2. V. N. Gribov, Yad. Fiz. **9**, 640 (1969) [Sov. J. Nucl. Phys. **9**, 369 (1969)].
3. K. Gottfried, Phys. Rev. Lett. **32**, 957 (1974).
4. F. E. Low and K. Gottfried, Phys. Rev. D **17**, 2487 (1978).
5. N. N. Nikolaev, Usp. Fiz. Nauk **134**, 369 (1981) [Sov. Phys. Usp. **24**, 531 (1981)].
6. A. Bialas and T. Chmaj, Phys. Lett. B **133B**, 24 (1983).
7. E. L. Berger, Z. Phys. C **4**, 289 (1980).
8. A. Bialas and M. Gyulassy, Nucl. Phys. B **291**, 793 (1987).
9. B. Z. Kopeliovich, Phys. Lett. B **243**, 141 (1990).
10. B. Z. Kopeliovich and J. Nemchic, Preprint No. E2-91-150 (Joint Inst. for Nucl. Res., Dubna, 1991).
11. B. Z. Kopeliovich, J. Nemchic, and E. Predazzi, in *Proceedings of the Workshop on Future Physics at HERA, DESY,* 1996; nucl-th/9607036.
12. L. S. Osborne *et al.*, Phys. Rev. Lett. **40**, 1624 (1978).
13. J. Ashman *et al.*, Z. Phys. C **52**, 1 (1991).
14. M. R. Adams *et al.*, Phys. Rev. D **50**, 1836 (1994).
15. W. Burkot *et al.*, Z. Phys. C **70**, 47 (1996).
16. A. Airapetian *et al.*, Eur. Phys. J. C **20**, 479 (2001).
17. E. S. Vataga, V. S. Murrin, M. Adernohz, *et al.*, Yad. Fiz. **63**, 1660 (2000) [Phys. At. Nucl. **63**, 1574 (2000)].

18. V. V. Ammosov *et al.*, Fiz. Élem. Chastits At. Yadra **23**, 648 (1992) [Sov. J. Part. Nucl. **23**, 283 (1992)].
19. A. É. Asratyan *et al.*, Yad. Fiz. **41**, 1193 (1985) [Sov. J. Nucl. Phys. **41**, 763 (1985)].
20. N. Agababyan *et al.*, Preprint No. 1539 (Yerevan. Phys. Inst., Yerevan, 1999).
21. N. Agababyan *et al.*, Preprint No. 1578 (Yerevan. Phys. Inst., Yerevan, 2002).
22. D. Zieminska *et al.*, Phys. Rev. D **27**, 47 (1983).
23. J. Brunner *et al.*, Z. Phys. C **45**, 361 (1989).
24. P. Allen *et al.*, Nucl. Phys. B **214**, 369 (1983).
25. D. Allasia *et al.*, Z. Phys. C **24**, 119 (1984).
26. A. Casher, H. Neuberger, and S. Nussinov, Phys. Rev. D **20**, 179 (1979).
27. E. G. Gurvich, Phys. Lett. B **87B**, 386 (1979).
28. *Review of Particle Physics,* Eur. Phys. J. C **3**, 87 (1998).
29. H. De Vries, C. W. De Jager, and C. De Vries, At. Data Nucl. Data Tables **36**, 495 (1987).

Translated by A. Isaakyan

Physics of Atomic Nuclei, Vol. 66, No. 7, 2003, pp. 1319–1327. Translated from Yadernaya Fizika, Vol. 66, No. 7, 2003, pp. 1359–1367.

ELEMENTARY PARTICLES AND FIELDS
Theory

Correlation between the Properties of the Deuteron and the Low-Energy Triplet Parameters of Neutron–Proton Scattering

V. A. Babenko and N. M. Petrov*

Bogolyubov Institute for Theoretical Physics, National Academy of Sciences of Ukraine, Metrologicheskaya ul. 14b, Kiev, 03143 Ukraine

Received June 4, 2002; in final form, October 9, 2002

Abstract—The correlation between the asymptotic normalization constant for the deuteron, A_S, and the neutron–proton scattering length for the triplet case, a_t, is investigated. It is found that 99.7% of the asymptotic constant A_S is determined by the scattering length a_t. It is shown that the linear correlation between the quantities A_S^{-2} and $1/a_t$ provides a good test of correctness of various models of nucleon–nucleon interaction. It is revealed that, for the normalization constant A_S and for the root-mean-square deuteron radius r_d, the results obtained with the experimental value recommended at present for the triplet scattering length a_t are exaggerated with respect to their experimental counterparts. By using the latest experimental data obtained for phase shifts by the group headed by Arndt, it proved to be possible to derive, for the low-energy parameters of scattering (a_t, r_t, P_t) and for the properties of the deuteron (A_S, r_d), results that comply well with experimental data. © *2003 MAIK "Nauka/Interperiodica".*

1. Basic features of the deuteron—such as the binding energy ε_d; the electric quadrupole moment Q; the root-mean-square radius r_d; the asymptotic normalization constants for the S and the D wave, A_S and A_D; and the corresponding mixing parameter $\eta = A_D/A_S$—play a significant role in constructing realistic models of nucleon–nucleon interaction and are important physical characteristics of nuclear forces. Of equally great importance are low-energy parameters of neutron–proton scattering in the triplet state. These include the scattering length a_t; the effective range r_t; and the shape parameters v_2, v_3, v_4, ... appearing in the effective-range expansion

$$k\cot\delta_t(k) = -\frac{1}{a_t} + \frac{1}{2}r_t k^2 + v_2 k^4 + v_3 k^6 + v_4 k^8 + \ldots, \quad (1)$$

where $\delta_t(k)$ is the triplet neutron–proton phase shift proper corresponding to the $^3S_1$ state. For this reason, much attention has been given to these quantities both in theoretical and in experimental studies [1–17]. At the present time, the experimental value of the deuteron binding energy ε_d is known to a high precision [9]:

$$\varepsilon_d = 2.22458900\ \text{MeV}. \quad (2)$$

The value of the asymptotic constant for S–D mixing, η, was also determined to a fairly high precision, both theoretically and experimentally (see [4, 7, 15–17]). The majority of the theoretical estimates of this quantity are in perfect agreement with its experimental value of $\eta = 0.0272$ [15]. At the same time, the values of some features of the deuteron, such as the asymptotic normalization constant A_S and the root-mean-square radius r_d, were the subject of controversy. For example, the value obtained for A_S directly from experimental data by analyzing elastic proton–deuteron scattering [18],

$$A_S = 0.8781\ \text{fm}^{-1/2}, \quad (3)$$

is at odds with the theoretical estimates derived for this quantity for many realistic potentials [19–26], as well as with those found from an analysis of phase shifts [17, 27] and on the basis of the effective-range expansion [4, 8]. Values of the asymptotic constant A_S that are discussed in the literature vary within a rather broad range—from 0.7592 to 0.9863 $\text{fm}^{-1/2}$ [28, 29].

In a number of studies, the result reported by Ericson in [5], $A_S = 0.8802\ \text{fm}^{-1/2}$, is used for an "experimental" value. It should be noted, however, that this value was obtained from an analysis of the linear relationship between the asymptotic constant A_S and the root-mean-square radius r_d rather than from experimental data directly. This linear correlation between A_S and r_d was established empirically for various models of nucleon–nucleon interaction [5, 30]. The procedure that Ericson used to obtain the above value of $A_S = 0.8802\ \text{fm}^{-1/2}$ on the basis of

*e-mail: pet@gluk.org

this relationship involved averaging the values of the root-mean-square radius r_d that were found experimentally in [10, 11]. In view of this, the use of Ericson's result for an experimental value is not quite correct. The value that is presented in (3) and which was derived in [18] on the basis of a direct method for determining this normalization constant from an analysis of data on elastic proton–deuteron scattering is more justified.

Other values sometimes used for the experimental asymptotic normalization constant include $A_S = 0.8846$, 0.8848, and 0.8883 fm$^{-1/2}$ (see [4], [30, 31], and [8], respectively). In just the same way as Ericson's result, they can hardly be treated, however, as correct experimental values, since they were found in the effective-range approximation with allowance for some corrections associated with the form of interaction; moreover, the low-energy triplet parameters of neutron–proton scattering that were employed in doing this were not determined from experimental data unambiguously. By way of example, we indicate that, in [1–3, 12–14, 32], values between 5.377 fm [1] and 5.424 fm [32] are given for experimental values of the triplet scattering length a_t, but the asymptotic normalization constant A_S greatly depends on a_t. As will be shown below, 99.7% of the normalization constant A_S is determined by the triplet scattering length a_t.

In the following, the value in (3) from [18] will be used for the experimental value of the normalization constant A_S. It is close to the value of $A_S = 0.8771$ fm$^{-1/2}$, which corresponds to the vertex-constant value of $G_d^2 = 0.427$ fm for the $d \to n + p$ vertex function and which was obtained earlier in [33]. As we have already indicated, the authors of [18, 33] employed a direct method for determining the constants A_S and G_d^2 that relies on extrapolating the experimental cross sections for elastic proton–deuteron scattering to the exchange-singularity point.

In just the same way as the constant A_S, the root-mean-square radius r_d of the deuteron is determined, to a great extent, by the triplet scattering length a_t. A linear correlation between the quantities r_d and a_t was established empirically in [6, 30]. To a high precision, this relationship can be approximated as follows:

$$r_d = 0.4a_t - 0.1985 \text{ (fm)}. \tag{4}$$

At present, the following experimental values are used in the literature for the root-mean-square radius of the deuteron:

$$r_d = 1.9635 \text{ fm [10] (B)}, \tag{5a}$$

$$r_d = 1.9560 \text{ fm [11] (S)}, \tag{5b}$$

$$r_d = 1.950 \text{ fm [30] (K)}. \tag{5c}$$

According to Eq. (4), the following values of the scattering length a_t correspond to the values of the radius r_d in (5):

$$a_t = 5.4050 \text{ fm (B)}, \tag{6a}$$

$$a_t = 5.3863 \text{ fm (S)}, \tag{6b}$$

$$a_t = 5.3713 \text{ fm (K)}. \tag{6c}$$

On the other hand, the values of the triplet scattering length that were calculated for many realistic nucleon–nucleon potentials [19–21, 24, 25] are close to the experimental value [32]

$$a_t = 5.424 \text{ fm}, \tag{7}$$

which is recommended at present, but which, in accordance with Eq. (4), leads to a root-mean-square radius exaggerated in relation to the experimental values in (5a)–(5c); that is,

$$r_d = 1.9711 \text{ fm}. \tag{8}$$

Thus, we can see that, frequently, values obtained and used in various studies for the features of the deuteron and for the triplet low-energy parameters of neutron–proton scattering are contradictory and deviate from experimental results.

2. In accordance with [8], the asymptotic normalization constant A_S for the deuteron can be represented in the form

$$A_S^2 = \frac{2\alpha}{1 - \alpha\rho_d}, \tag{9}$$

where α is the deuteron wave number defined by the relation $\varepsilon_d = \hbar^2\alpha^2/m_N$ and $\rho_d \equiv \rho(-\varepsilon_d, -\varepsilon_d)$ is the deuteron effective radius corresponding to S-wave interaction. The definition and properties of the radius ρ_d and of the function $\rho(E_1, E_2)$ are discussed in detail elsewhere [1]. The quantity ρ_d appears in the expansion of the function $k \cot \delta_t(k)$ at the point $k^2 = -\alpha^2$—that is, at the energy value equal to the deuteron binding energy. The expansion at the point $k^2 = -\alpha^2$ is similar to the expansion in (1), which is performed at the origin, involving the ordinary effective range $r_t \equiv \rho(0, 0)$ of scattering theory—that is, the effective range at zero energy. It can easily be found that the quantities ρ_d and r_t are expanded in powers of the parameter α^2 as

$$\rho_d = \rho_m - 2v_2\alpha^2 + 4v_3\alpha^4 - 6v_4\alpha^6 + \ldots, \tag{10}$$

$$r_t = \rho_m + 2v_2\alpha^2 - 2v_3\alpha^4 + 2v_4\alpha^6 - \ldots, \tag{11}$$

where $\rho_m \equiv \rho(0, -\varepsilon_d)$ is the so-called mixed effective range [1], for which the following relation holds:

$$\rho_m = \frac{2}{\alpha}\left(1 - \frac{1}{\alpha a_t}\right). \tag{12}$$

The shape parameters v_n in expansions (1), (10), and (11) are dimensional quantities. Instead of them, one

often introduces the dimensionless shape parameters P_t, Q_t, ... related to the parameters v_n by the equations

$$v_2 = -P_t r_t^3, \qquad v_3 = Q_t r_t^5, \ldots. \tag{13}$$

From the expansions in (10) and (11), it follows that the quantities r_t, ρ_d, and ρ_m are related as

$$\rho_d + r_t = 2\rho_m + 2v_3\alpha^4 - 4v_4\alpha^6 + \ldots, \tag{14}$$

$$\rho_d + 2r_t = 3\rho_m + 2v_2\alpha^2 - 2v_4\alpha^6 + \ldots. \tag{15}$$

The asymptotic normalization constant A_S for the deuteron is directly expressed in terms of the residue of the S matrix $S(k)$ at the pole $k = i\alpha$ corresponding to a bound state of the two-nucleon system; that is,

$$A_S^2 = i \operatorname*{Res}_{k=i\alpha} S(k). \tag{16}$$

Along with the constant A_S, other physical quantities, such as the nuclear vertex constant G_d and the dimensionless asymptotic normalization constant C_d, are frequently used in the literature [28, 29]. These two quantities are directly related to the constant A_S by the equations

$$G_d^2 = \pi\lambda\!\!\!^{-2} A_S^2, \tag{17}$$

$$C_d^2 = A_S^2/2\alpha, \tag{18}$$

where $\lambda\!\!\!^{-} = 2\lambda\!\!\!^{-}_N$, with $\lambda\!\!\!^{-}_N \equiv \hbar/m_N c$ being the Compton wavelength of the nucleon.

In the approximation where there is no dependence on the form of interaction ($v_2 = v_3 = \ldots = 0$),

$$k\cot\delta_t(k) = -\frac{1}{a_t} + \frac{1}{2}r_t k^2, \tag{19}$$

the quantities r_t, ρ_d, and ρ_m are equal to each other, as follows from Eqs. (10) and (11):

$$r_t = \rho_d = \rho_m. \tag{20}$$

In this approximation, the use of relations (12) and (20) makes it possible to recast Eq. (9) into the more convenient form

$$C_d^{-2} = -1 + 2\frac{R_d}{a_t}, \tag{21}$$

where the quantity

$$R_d \equiv 1/\alpha, \tag{22}$$

which characterizes the spatial dimensions of the deuteron, is referred to as the deuteron radius [2]. By using the value in (2) for the deuteron binding energy, one can easily obtain the following numerical value for the deuteron radius:

$$R_d = 4.317688 \text{ fm}. \tag{23}$$

In the approximation where there is no dependence on the form of interaction, the low-energy parameters of neutron–proton scattering—we mean here the scattering length a_t and the effective range r_t—are expressed in terms of bound-state parameters (deuteron radius R_d and dimensionless normalization constant C_d) as

$$a_t = \frac{2R_d}{1 + C_d^{-2}}, \tag{24}$$

$$r_t = R_d(1 - C_d^{-2}). \tag{25}$$

With the aid of parameters that characterize the bound state of the neutron–proton system (deuteron), the behavior of the phase shift at low energies can be predicted in the effective-range approximation (19) with allowance for expressions (24) and (25).

3. As was indicated above, a great number of studies have been devoted to exploring and calculating the asymptotic normalization constant A_S. The values of the constant A_S (and of the quantities ε_d and a_t) for some realistic potentials [19–25, 27, 34–36] are quoted in Table 1, along with the values of A_S that were found from the analysis of phase shifts in [17, 27] and on the basis of the effective-range expansion in [4, 8]. Also given in the same table are the values of the constant A_S that were calculated in the present study by formulas (18) and (21), which correspond to the approximation where there is no dependence on the form of interaction. In addition, Table 1 presents the absolute (Δ) and the relative (δ) error in the calculation of A_S in this approximation.

It can be seen from Table 1 that, for the majority of the models, the relative error in the A_S value calculated in the effective-range approximation does not exceed 0.3%, while the absolute error is not greater than 0.003 fm$^{-1/2}$, as a rule. This is not so only for some early models of the Bonn potential (lines 15–17 in Table 1), in which case the relative error in the approximate value of the constant A_S is 2 to 3%. For the same potentials, the relative error in the approximate values of the root-mean-square radius r_d of the deuteron that were obtained by formula (4) is also overly large. For example, the relative error in r_d is 2.52% for the HM-2 potential and 1.49% for the Bonn F potential. At the same time, this error is small for more correct models of the Bonn potential, Bonn R and Bonn Q (0.081 and 0.137%, respectively). For the Paris potential, the error in question is 0.035%.

Thus, we can see from Table 1 that the values of the normalization asymptotic constant A_S for realistic potentials are strongly correlated with the values of the triplet neutron–proton scattering length a_t. The same is also true for the values of A_S that were found from the analysis of phase shifts (lines 18, 19) and on the basis of the effective-range expansion in [4] (line 20). As to the value of $A_S = 0.8883$ fm$^{-1/2}$ (line 21), which was calculated in [8] on the basis of the effective-range expansion,

Table 1. Asymptotic normalization constant A_S for the deuteron within various models of nucleon–nucleon interaction

no.	References	ε_d, MeV	a_t, fm	A_S, fm$^{-1/2}$		Δ, fm$^{-1/2}$	δ, %
				precise value	effective-range approximation		
1	RHC [34]	2.22464	5.397	0.88034	0.87867	0.00167	0.216
2	RSC [34]	2.2246	5.390	0.87758	0.87711	0.00047	0.054
3	Paris [19]	2.2249	5.427	0.8869	0.88528	0.00162	0.183
4	Moscow [35]	2.2246	5.413	0.8814	0.88211	0.00071	0.080
5	Nijm I [21, 27]	2.224575	5.418	0.8841	0.88272	0.00138	0.156
6	Nijm II [21, 27]	2.224575	5.420	0.8845	0.88316	0.00134	0.152
7	Reid 93 [21, 27]	2.224575	5.422	0.8853	0.88360	0.00170	0.193
8	Argonne v_{18} [25]	2.224575	5.419	0.8850	0.88341	0.00159	0.180
9	GK-4 [36]	2.226	5.364	0.87462	0.87201	0.00261	0.299
10	GK-8 [36]	2.226	5.413	0.88434	0.88262	0.00172	0.194
11	GK-7 [36]	2.226	5.477	0.89776	0.89678	0.00098	0.109
12	HM-1 [22, 23]	2.224	5.50	0.901	0.90119	0.00019	0.021
13	Bonn R [20]	2.2246	5.423	0.8860	0.88430	0.00170	0.193
14	Bonn Q [20]	2.2246	5.424	0.8862	0.88452	0.00168	0.190
15	Bonn F [20]	2.2246	5.427	0.9046	0.88517	0.01942	2.195
16	HM-2 [22, 23]	2.2246	5.45	0.919	0.89024	0.02876	3.230
17	M [24]	2.22469	5.424	0.9043	0.8845	0.01975	2.233
18	SCSS [17]	2.224575	5.4193	0.8838	0.88300	0.00079	0.089
19	STS [27]	2.224575	5.4194	0.8845	0.88303	0.00147	0.166
20	ER-C [4]	2.224575	5.424	0.8846	0.88451	0.00009	0.011
21	KMMA [8]	2.224644	5.412	0.8883	0.88191	0.00639	0.725

it is strongly overestimated in relation to the value of $A_S = 0.88191$ fm$^{-1/2}$, which was found in the present study in the approximation where there is no dependence on the form of interaction. In that case, the relative error in the approximate value was 0.725%. An incorrect choice of the shape parameter P_t in [8] is the reason for this discrepancy—namely, the following data from [37] on the low-energy parameters of scattering were used in [8] to calculate the constant A_S: $a_t = 5.412$ fm and $r_t = 1.733$ fm; however, the value of $P_t = -0.0188$, chosen there for the shape parameter, corresponded to the Paris potential, for which the scattering length and the effective range take values ($a_t = 5.427$ fm, $r_t = 1.766$ fm) that considerably exceed those that were employed in [8].

Considering that the deuteron binding energy has been determined to a high degree of precision and is taken to have approximately the same value in all of the calculations, one can conclude on the basis of the results in Table 1 that 99.7% of the asymptotic normalization constant A_S is determined by the triplet scattering length a_t. The inverse also holds: knowing the values of the constant A_S, one can determine the triplet scattering length a_t to a high degree of precision.

Taking the aforesaid into consideration, we will investigate the asymptotic constant A_S as a function of the triplet scattering length a_t. It is convenient to perform this investigation for the dimensionless quantity C_d^{-2}, which, in the approximation where there is no dependence on the form of interaction, is a linear function of the quantity R_d/a_t [see Eq. (21)]. The R_d/a_t dependence of C_d^{-2} is shown in the figure. The straight line represents the results of the calculation based on the approximate formula (21),

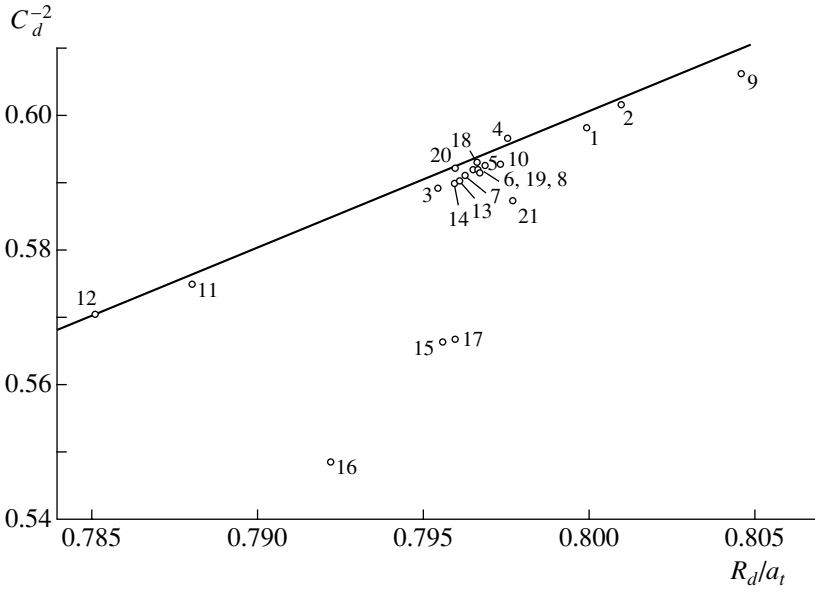

Correlation between the dimensionless asymptotic normalization constant for the deuteron, C_d, and the triplet scattering length a_t. Points represent values obtained within the various models of nucleon–nucleon interaction in Table 1 (the numerals in the figure correspond to the numbers of the lines in this table), while the straight line was calculated by the approximate formula (21).

while the points in the figure correspond to ε_d, a_t, and A_S values computed by various authors and quoted in Table 1. As can be seen from the figure, there is a linear relationship between the quantities C_d^{-2} and R_d/a_t. Points corresponding to their values lie in a close proximity of the straight line specified by Eq. (21). As was mentioned above, this is not so only for points corresponding to early models of the Bonn potential and the point corresponding to the values of the quantities in question from [8]. Points that represent values of C_d^{-2} and R_d/a_t for more correct versions of the Bonn potential model (Bonn R, Bonn Q) lie near the straight line specified by Eq. (21) (points 13, 14).

Thus, it follows from Table 1 and from the figure that the asymptotic normalization constant A_S and the triplet scattering length a_t are well correlated quantities, so that any of these can be determined to a high degree of precision if the other is known. For the experimental value presented in (3) for the constant A_S, the corresponding value of the scattering length a_t can easily be determined in the effective-range approximation by formulas (18) and (21). The result is

$$a_t = 5.395 \text{ fm}. \tag{26}$$

At the same time, the currently recommended experimental value of the triplet scattering length in (7) leads, in the effective-range approximation, to the asymptotic-normalization-constant value

$$A_S = 0.88451 \text{ fm}^{-1/2}, \tag{27}$$

which is well above the experimental value of this quantity in (3). As was indicated above, the experimental scattering-length value in (7) also leads to the exaggerated value in (8) for the root-mean-square radius r_d of the deuteron.

Thus, it can be concluded from the above analysis that the currently recommended experimental value of the triplet neutron–proton scattering length in (7) does not comply with the experimental values of the asymptotic normalization constant A_S for the deuteron and its root-mean-square radius r_d in (3) and (5a)–(5c), respectively. Therefore, it is of paramount importance to determine, for the features of the deuteron and for the parameters of low-energy neutron–proton scattering in the triplet case, such values that would be consistent with one another, on one hand, and which would be compatible with experimental data on the other hand.

4. Fixing the features ε_d, A_S, and r_d of the deuteron, we will study the behavior of the S-wave phase shift at low energies in the approximation that takes into account the shape parameter P_t in the effective-range expansion; that is,

$$k \cot \delta_t(k) = -\frac{1}{a_t} + \frac{1}{2} r_t k^2 - P_t r_t^3 k^4. \tag{28}$$

For the scattering length a_t, use is made here of the values in (6a)–(6c), which correspond to the values of the root-mean-square radius r_d of the deuteron in (5a)–(5c), while, in accordance with (10), (13),

Table 2. Parameters of effective-range theory that were calculated on the basis of the experimental values of ε_d, A_S, and r_d, as well as those found from the analysis of the experimental phase shifts for neutron–proton scattering

Version	a_t, fm	r_t, fm	P_t	ρ_m, fm	ρ_d, fm
B	5.4050	1.75047	−0.02312	1.73716	1.72385
S	5.3863	1.70257	0.02010	1.71321	1.72385
K	5.3713	1.66391	0.06064	1.69388	1.72385
ER	5.395	1.72385	0	1.72385	1.72385
PWA	5.4030	1.7495	−0.02592	1.73461	1.7197

Table 3. Triplet phase shift calculated for neutron–proton scattering in the shape-parameter approximation (28) with the parameter values from Table 2 as a function of the laboratory energy E_{lab}

E_{lab}, MeV	Phase shift δ_t, deg					
	experimental data [38]	PWA	B	S	K	ER
0.1	169.32	169.315	169.311	169.349	169.380	169.331
0.5	156.63	156.645	156.637	156.728	156.802	156.686
1.0	147.83	147.823	147.812	147.954	148.068	147.889
2.0	136.56	136.548	136.536	136.770	136.958	136.664
5.0	118.23	118.236	118.228	118.750	119.168	118.516
10.0	102.55	102.598	102.612	103.672	104.521	103.200
20.0	85.84	86.049	86.127	88.385	90.211	87.379
30.0	75.61	76.043	76.195	79.702	82.592	78.131
40.0	68.11	68.822	69.046	73.796	77.806	71.652
45.0	64.96	65.843	66.103	71.462	76.050	69.032
50.0	62.11	63.171	63.466	96.424	74.602	66.709
100.0	42.34	45.705	46.265	57.612	69.487	52.131

and (14), the effective range r_t and the shape parameter P_t are given by

$$r_t = 2\rho_m - \rho_d, \tag{29}$$

$$P_t = \frac{\rho_d - \rho_m}{2r_t^3\alpha^2}, \tag{30}$$

where the effective radius ρ_d of the deuteron and the mixed effective range ρ_m are determined from Eqs. (9) and (12), respectively. The parameters a_t, r_t, P_t, ρ_m, and ρ_d calculated in this approximation on the basis of the experimental values of the deuteron binding energy ε_d in (2), the asymptotic normalization constant A_S in (3), and the root-mean-square radius r_d of the deuteron in (5a)–(5c) are given in Table 2 (versions B, S, K), along with the values calculated for these parameters in the effective-range approximation (ER) on the basis of the experimental values of ε_d and A_S, as well as values found in the present study from the latest partial-wave analysis (PWA) reported by Arndt *et al.* [38] for the case of nucleon–nucleon scattering, which, as can be seen from this table, are in very good agreement with the corresponding values for version B, where the features of the deuteron were set to $\varepsilon_d = 2.22458900$ MeV [9], $A_S = 0.8781$ fm$^{-1/2}$ [18], and $r_d = 1.9635$ fm [10].

The quantity $\delta\rho$ defined as the difference of the effective radius ρ_d of the deuteron and the mixed effective range ρ_m,

$$\delta\rho = \rho_d - \rho_m, \tag{31}$$

is often discussed in the literature. According to the estimates obtained by Noyes in [3] on the basis of dispersion relations, this difference arises owing to one-pion exchange and is positive, its magnitude being 0.016 fm. For many potential models, the difference $\delta\rho$ is also positive; as was established in [5, 6, 31], it

Table 4. Difference Δ of the experimental value of the phase shift and its theoretical value calculated in the shape-parameter approximation (28) with the parameter values from Table 2

E_{lab}, MeV	Δ, deg				
	PWA	B	S	K	ER
0.1	0.005	0.009	−0.029	−0.060	−0.011
0.5	−0.015	−0.007	−0.098	−0.172	−0.056
1.0	0.007	0.018	−0.124	−0.238	−0.059
2.0	0.012	0.024	−0.210	−0.398	−0.104
5.0	−0.006	0.002	−0.520	−0.938	−0.286
10.0	−0.048	−0.062	−1.122	−1.971	−0.650
20.0	−0.209	−0.287	−2.545	−4.371	−1.539
30.0	−0.433	−0.585	−4.092	−6.982	−2.521
40.0	−0.712	−0.936	−5.686	−9.696	−3.542
45.0	−0.883	−1.143	−6.502	−11.090	−4.072
50.0	−1.061	−1.356	−7.314	−12.492	−4.599
100.0	−3.365	−3.925	−15.272	−27.147	−9.791

correlates well with the triplet scattering length a_t. In our case, this difference is given by

$$\delta\rho = 2P_t r_t^3 \alpha^2; \qquad (32)$$

for the parameter values used in the S and K versions from Table 2, it is positive, taking the values of 0.011 and 0.030 fm, respectively. For the cases of B and PWA in Table 2, the difference $\delta\rho$ is negative, its values being −0.013 and −0.015 fm. For this reason, the problem of the sign and magnitude of the difference of the effective radius ρ_d of the deuteron and the mixed effective range ρ_m calls for a further investigation.

For the low-energy parameters given in Table 2, we have calculated the triplet phase shift $\delta_t(k)$. The results are displayed in Table 3, along with the latest experimental data of Arndt *et al.* [38] on the triplet phase shift. Table 4 presents the energy dependence of the difference

$$\Delta = \delta_{expt} - \delta_{theor} \qquad (33)$$

of the experimental value of the phase shift and its theoretical counterparts calculated by formula (28) and quoted in Table 3. As can be seen from Tables 3 and 4, all sets of low-energy parameters a_t, r_t, and P_t from Table 2 describe well experimental data up to an energy value of 5 MeV (the absolute error being less than 1°). Nonetheless, the distinction between the sets of low-energy parameters in describing experimental data becomes noticeable at an energy as low as 1 MeV, and we can see that preference should be given to the parameter sets employed in the B and PWA versions. These sets provide a nearly precision description (with a relative error of about 0.005%) of experimental phase shifts up to an energy value of 5 MeV. Thus, the accuracy of existing experimental data that is available at present is quite sufficient for removing ambiguities that arise in determining the scattering length a_t and the effective range r_t [1] and which are associated with the form of the potential. In view of this, the problem of deducing the scattering length, the effective range, and parameters of higher order (shape parameters) in expansion (1) directly from experimental data is pressing. It should be noted that the B and PWA sets describe well, in contrast to other parameter sets, experimental phase shifts up to an energy value of 50 MeV. For the B and PWA sets, the absolute error is about 0.5° at $E_{lab} = 30$ MeV and about 1° at $E_{lab} = 50$ MeV. From Table 4, it can be seen that, for other parameter sets, the absolute error is much greater.

Thus, neutron–proton scattering in the triplet state can be described rather well within the B set up to an energy value of 50 MeV, the experimental values used in this description for the features of the deuteron being that in (2) for the binding energy, that in (3) for the asymptotic normalization constant, and that in (5a) for root-mean-square radius. On the other hand, parameters that characterize the neutron–proton bound state (deuteron) can be determined from experimental data on neutron–proton scattering. By using the values

$$a_t = 5.4030 \text{ fm}, \quad r_t = 1.7495 \text{ fm}, \qquad (34)$$

$$P_t = -0.0259,$$

which we found here for the low-energy parameters of scattering from an analysis of the latest data on phase shifts [38], we will now determine the asymptotic normalization constant A_S for the deuteron and its root-mean-square radius r_d. In accordance with Eqs. (4), (9), (10), (12), and (13), we obtain

$$A_S = 0.8774 \text{ fm}^{-1/2}, \quad (35)$$

$$r_d = 1.9627 \text{ fm}. \quad (36)$$

As might have been expected, these results are in very good agreement with the experimental values of $A_S = 0.8781$ fm$^{-1/2}$ [18] and $r_d = 1.9635$ fm [10].

5. To summarize, we will formulate our basic results and conclusions. We have investigated the correlation between the asymptotic normalization constant for the deuteron, A_S, and the triplet neutron–proton scattering length a_t. It has been established that 99.7% of the asymptotic constant A_S is determined by the triplet scattering length a_t. It has been shown that, in the effective-range approximation, the linear correlation between the quantities $2\alpha/A_S^2$ and R_d/a_t provides a good test of correctness of various potential models and methods that are used in studying nucleon–nucleon interaction.

It has been found that evaluating the asymptotic normalization constant for the deuteron and its root-mean-square radius with the currently recommended triplet-scattering-length value of $a_t = 5.424$ fm [32] leads to results, $A_S \simeq 0.8845$ fm$^{-1/2}$ and $r_d = 1.9711$ fm, that are exaggerated in relation to the corresponding experimental values in (3) and (5a)–(5c).

By using the experimental values of $\varepsilon_d = 2.22458900$ MeV [9], $A_S = 0.8781$ fm$^{-1/2}$ [18], and $r_d = 1.9635$ fm [10] for, respectively, the binding energy of the deuteron, its asymptotic normalization constant, and its root-mean-square radius, we have obtained the following results for the low-energy parameters of scattering: $a_t = 5.4050$ fm, $r_t = 1.7505$ fm, and $P_t = -0.0231$. It turned out that, with these parameter values, the respective experimental phase shift is faithfully reproduced up to an energy value of 50 MeV. The absolute error in the phase shift at this energy value is about 1°. As the energy decreases, the absolute error becomes smaller, taking the value of 0.06° at an energy of 10 MeV. If the root-mean-square radius of the deuteron is set to the experimental value of $r_d = 1.9560$ fm from [11] or the experimental value of $r_d = 1.950$ fm from [30], the corresponding low-energy parameters of scattering lead to a much poorer description of the experimental phase shift in the shape-parameter approximation. Even at an energy of 10 MeV, the absolute error exceeds 1° in this case.

The values found for the low-energy parameters of scattering with the aid of the latest experimental results reported by Arndt *et al.* [38] for the phase shifts are $a_t = 5.4030$ fm, $r_t = 1.7495$ fm, and $P_t = -0.0259$. They are in good agreement with the parameter values of $a_t = 5.4050$ fm, $r_t = 1.7505$ fm, and $P_t = -0.0231$, which were obtained on the basis of the experimental values of the features of the deuteron. Both sets of these parameters make it possible to describe well, in the shape-parameter approximation, the experimental phase shift up to an energy of 50 MeV, this indicating that the parameter Q_t and parameters of higher order in the effective-range expansion are small.

On the basis of the parameter values of $a_t = 5.4030$ fm, $r_t = 1.7495$ fm, and $P_t = -0.0259$, which correspond to the experimental phase shifts obtained by Arndt *et al.* [38], we have found the asymptotic normalization constant for the deuteron, $A_S = 0.8774$ fm$^{-1/2}$, and its root-mean-square radius, $r_d = 1.9627$ fm, these results being in excellent agreement with the experimental values of $A_S = 0.8781$ fm$^{-1/2}$ [18] and $r_d = 1.9635$ fm [10].

In summary, we arrive at the basic conclusion that the latest experimental results of Arndt *et al.* [38] for the phase shift comply very well with the experimental values of parameters that characterize the deuteron—specifically, with the binding energy in (2), the asymptotic normalization constant determined in [18] and given in (3), and the root-mean-square radius of the deuteron as obtained in [10] and presented in (5a).

REFERENCES

1. L. Hulthén and M. Sugawara, Handb. Phys. **39**, 1 (1957).
2. R. Wilson, *The Nucleon–Nucleon Interaction* (Interscience, New York, 1963).
3. H. P. Noyes, Annu. Rev. Nucl. Sci. **22**, 465 (1972).
4. T. E. O. Ericson and M. Rosa-Clot, Nucl. Phys. A **405**, 497 (1983).
5. T. E. O. Ericson, Nucl. Phys. A **416**, 281 (1984).
6. D. W. L. Sprung, in *Proceedings of the IX European Conference on Few-Body Problems in Physics, Tbilisi, Georgia, USSR, 1984* (World Sci., Singapore; Philadelphia, 1984), p. 234.
7. S. Klarsfeld, J. Martorell, and D. W. L. Sprung, Nucl. Phys. A **352**, 113 (1981).
8. M. W. Kermode, A. McKerrell, J. P. McTavish, and L. J. Allen, Z. Phys. A **303**, 167 (1981).
9. G. L. Greene, E. G. Kessler, Jr., R. D. Deslattes, and H. Boerner, Phys. Rev. Lett. **56**, 819 (1986).
10. R. W. Bérard, F. R. Buskirk, E. B. Dally, *et al.*, Phys. Lett. B **47B**, 355 (1973).
11. G. G. Simon, Ch. Schmitt, and V. H. Walther, Nucl. Phys. A **364**, 285 (1981).

12. T. L. Houk, Phys. Rev. C **3**, 1886 (1971).
13. W. Dilg, Phys. Rev. C **11**, 103 (1975).
14. T. L. Houk and R. Wilson, Rev. Mod. Phys. **39**, 546 (1967).
15. I. Borbély, W. Grüebler, V. König, *et al.*, Phys. Lett. B **109B**, 262 (1982).
16. J. Horáček, J. Bok, V. M. Krasnopolskij, and V. I. Kukulin, Phys. Lett. B **172**, 1 (1986).
17. V. G. J. Stoks, P. C. van Campen, W. Spit, and J. J. de Swart, Phys. Rev. Lett. **60**, 1932 (1988).
18. I. Borbély, W. Grüebler, V. König, *et al.*, Phys. Lett. B **160B**, 17 (1985).
19. M. Lacombe, B. Loiseau, J. M. Richard, *et al.*, Phys. Rev. C **21**, 861 (1980).
20. R. Machleidt, K. Holinde, and Ch. Elster, Phys. Rep. **149**, 1 (1987).
21. V. G. J. Stoks, R. A. M. Klomp, C. P. F. Terheggen, and J. J. de Swart, Phys. Rev. C **49**, 2950 (1994).
22. K. Holinde and R. Machleidt, Nucl. Phys. A **256**, 479 (1976).
23. N. J. McGurk, Phys. Rev. C **15**, 1924 (1977).
24. R. Machleidt, in *Proceedings of the IX European Conference on Few-Body Problems in Physics, Tbilisi, Georgia, USSR, 1984* (World Sci., Singapore; Philadelphia, 1984), p. 218.
25. R. B. Viringa, V. G. J. Stoks, and R. Schiavilla, Phys. Rev. C **51**, 38 (1995).
26. J. W. Humberstone and J. B. G. Wallace, Nucl. Phys. A **141**, 362 (1970).
27. J. J. de Swart, C. P. F. Terheggen, and V. G. J. Stoks, *3rd International Symposium "Dubna Deuteron 95", Dubna, Russia, 1995*, Invited Talk; nucl-th/9509032.
28. L. D. Blokhintsev, I. Borbely, and É. I. Dolinskiĭ, Fiz. Élem. Chastits At. Yadra **8**, 1189 (1977) [Sov. J. Part. Nucl. **8**, 485 (1977)].
29. M. P. Locher and T. Misutani, Phys. Rep. **46**, 43 (1978).
30. S. Klarsfeld, J. Martorell, J. A. Oteo, *et al.*, Nucl. Phys. A **456**, 373 (1986).
31. S. Klarsfeld, J. Martorell, and D. W. L. Sprung, J. Phys. G **10**, 165 (1984).
32. O. Dumbrajs, R. Koch, H. Pilkuhn, *et al.*, Nucl. Phys. B **216**, 277 (1983).
33. A. M. Mukhamedzhanov, I. Borbeĭ, V. Grubler, *et al.*, Izv. Akad. Nauk SSSR, Ser. Fiz. **48**, 350 (1984).
34. R. V. Reid, Jr., Ann. Phys. (N. Y.) **50**, 411 (1968).
35. V. I. Kukulin, V. M. Krasnopol'skiĭ, V. N. Pomerantsev, and P. B. Sazonov, Yad. Fiz. **43**, 559 (1986) [Sov. J. Nucl. Phys. **43**, 355 (1986)].
36. N. K. Glendenning and G. Kramer, Phys. Rev. **126**, 2159 (1962).
37. J. J. de Swart, in *Few-Body Problems in Nuclear and Particle Physics,* Ed. by J. R. Slobodrian *et al.* (Laval, Quebec, 1975), p. 235.
38. R. A. Arndt, W. J. Briscoe, R. L. Workman, and I. I. Strakovsky, Partial-Wave Analysis Facility SAID, URL http://gwdac.phys.gwu.edu.

Translated by A. Isaakyan

Physics of Atomic Nuclei, Vol. 66, No. 7, 2003, pp. 1328–1334. Translated from Yadernaya Fizika, Vol. 66, No. 7, 2003, pp. 1368–1374.

ELEMENTARY PARTICLES AND FIELDS
Theory

Nucleon Structure Functions, Resonance Form Factors, and Duality

V. V. Davidovsky and B. V. Struminsky[†1)]

Institute for Nuclear Research, National Academy of Sciences of Ukraine, pr. Nauki 47, Kiev, 03680 Ukraine

Received April 3, 2002

Abstract—The behavior of nucleon structure functions in the resonance region is explored. For form factors that describe resonance production, expressions are obtained that are dependent on the photon virtuality Q^2, which have a correct threshold behavior, and which take into account available experimental data on resonance decay. Resonance contributions to nucleon structure functions are calculated. The resulting expressions are used to investigate quark–hadron duality in electron–nucleon scattering by taking the example of the structure function F_2. © *2003 MAIK "Nauka/Interperiodica"*.

1. INTRODUCTION

To obtain deeper insights into the structure of hadrons and their interactions in terms of quark and gluon degrees of freedom is the most important theoretical problem in nuclear and elementary-particle physics.

Quark and gluon degrees of freedom provide a convenient basis for constructing QCD as a gauge-invariant theory of strong interaction. Hadronic degrees of freedom form a different basis. Since no physical observable can be dependent on the choice of basis, the description of processes in terms of quark–gluon degrees of freedom is expected to be equivalent to the corresponding description in terms of hadronic degrees of freedom.

The choice of degrees of freedom for describing hadronic processes depends on specific kinematical conditions. By way of example, we indicate that, in lepton–nucleon scattering, the resonance-production region is usually described in terms of hadronic degrees of freedom, while the region of deep-inelastic scattering is naturally described by using quark–gluon degrees of freedom. In the first region, a virtual photon that the lepton and the nucleon involved in lepton–nucleon scattering exchange interacts with the nucleon as a discrete unit, changing the orientation of the spins of relevant quarks and, hence, their angular momentum, whereby resonance production occurs. In the second region, a virtual photon undergoes scattering immediately on the quarks involved, causing the production of a large number of hadrons. Despite the distinction of mechanisms responsible for the interaction in the resonance and in the deep-inelastic region, it turns out that relevant amplitudes (or structure functions) behave similarly in these regions, and it is possible to describe them in terms of only quark or only hadronic degrees of freedom, irrespective of the kinematical region. The equivalence of quark and hadronic description is referred to as quark–hadron duality.

Formally, quark–hadron duality is exact; however, the fact that, in practice, we must truncate the expansion of any Fock state leads to different manifestations of this duality under different kinematical conditions and in different reactions.

We recall that the historically first concept of duality related resonances at low energies to Regge poles at high energies. Finite-energy sum rules that were independently introduced in [1–3] provided an exact mathematical formulation of the duality concept.

The Veneziano amplitude was the first example where hadron–Reggeon duality was fulfilled. A dual amplitude featuring Mandelstam analyticity [4, 5],

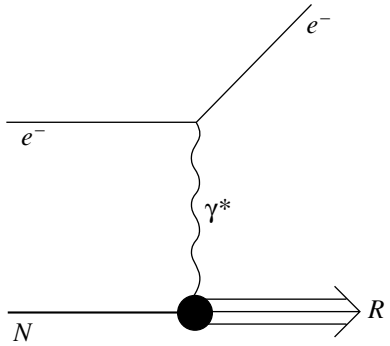

Fig. 1. Production of nucleon resonances in the lowest order in the electromagnetic-coupling constant.

[†] Deceased.

[1)] Bogolyubov Institute for Theoretical Physics, National Academy of Sciences of Ukraine, Metrologicheskaya ul. 14b, Kiev, 03143 Ukraine.

1063-7788/03/6607-1328$24.00

where one can introduce nonlinear complex Regge trajectories with correct thresholds, provides yet another example of this kind.

A manifestation of quark–hadron duality was first noticed by Bloom and Gilman [6] in analyzing data on nucleon structure functions in the region of nucleon-resonance excitation from experiments that studied electron–nucleon scattering. It turned out that, on average, the resonance curve for the structure function $F_2(x', Q^2)$ reproduces the scaling curve. In other words, the area under the resonance curve is equal to the area under the scaling curve. This is the so-called global duality. It was mentioned that, to some specific accuracy, a local duality holds. It means that all the aforesaid holds for averaging not only within the entire resonance region but also in the vicinity of an individual resonance.

The duality provided additional possibilities for studying the nucleon structure on the basis of data on the properties of nucleon resonances. For example, corrections to the scaling behavior of the structure function F_2—such corrections were calculated within QCD and have been measured over the past decade—can be extracted from resonance data [7].

Presently, it is of interest to describe duality theoretically—in particular, to construct nucleon structure functions in the resonance region (threshold energies and low values of the photon virtuality). For this, it is necessary to know the dependence of the form factors for resonance-production processes $\gamma^* N \to R$ on the photon virtuality Q^2.

Experimental data obtained recently in the Jefferson Laboratory [8, 9] provide a strong motivation for performing such investigations.

2. FORM FACTORS

In the lowest order in the electromagnetic coupling constant, the process of lepton–hadron scattering proceeds via the exchange of a virtual photon having a virtuality $Q^2 = -q^2$ (q is the photon 4-momentum) and an energy (in the nucleon rest frame) $\nu = (pq)/m$ (p is the nucleon 4-momentum, and m is the nucleon mass). In the case under consideration, Q^2 also plays the role of the square of the momentum transfer from the lepton to the nucleon involved.

The mechanism of virtual-photon interaction with a nucleon depends on the momentum transfer to the nucleon, Q^2, and on the photon energy. At high values of Q^2 and ν, there occur the noncoherent scattering of the virtual photon by the quarks of the nucleon and the production of a large number of hadrons. At $Q^2 \sim 1$ GeV^2 and moderate values of the energy ν, the excitation of internal spin states of the nucleon occurs, which leads to resonance production (see Fig. 1).

Let us introduce basic conventions and define the quantities that will be used below. We denote by p, q, and P, respectively, the nucleon, the photon, and the resonance 4-momenta. In the resonance rest frame, they are given by

$$p = \left(\frac{M^2 + m^2 + Q^2}{2M}, 0, 0, -\frac{\sqrt{(M^2 - m^2 - Q^2)^2 + 4M^2Q^2}}{2M}\right), \quad (1)$$

$$q = \left(\frac{M^2 - m^2 - Q^2}{2M}, 0, 0, \frac{\sqrt{(M^2 - m^2 - Q^2)^2 + 4M^2Q^2}}{2M}\right), \quad (2)$$

$$P = (M, 0, 0, 0), \quad (3)$$

where $p^2 = m^2$, $P^2 = M^2$, and M is the resonance mass.

The $\gamma^* N \to R$ vertex of virtual-photon absorption by a nucleon is described by three independent form factors $G_{\pm,0}(Q^2)$ (or by two form factors if the resonance is equal to 1/2, in which case $G_-(Q^2) \equiv 0$), which, apart from a factor, coincide (in the resonance rest frame) with the helicity amplitudes for the transition $\gamma^* N \to R$, these amplituces having the form

$$G_{\lambda_\gamma} = \frac{1}{2m}\langle R, \lambda_R = \lambda_N - \lambda_\gamma | J(0) | N, \lambda_N \rangle, \quad (4)$$

where λ_R, λ_N, and λ_γ are the helicities of the resonance, the nucleon, and the photon, respectively, λ_γ taking the values of $-1, 0, +1$, and $J(0)$ is the current operator.

The nucleon structure functions can be expressed in terms of form factors (4) [10] as

$$F_1(x, Q^2) = m^2 \delta(W^2 - M^2) \times \left[|G_+(Q^2)|^2 + |G_-(Q^2)|^2\right], \quad (5)$$

$$\left(1 + \frac{\nu^2}{Q^2}\right) F_2(x, Q^2) = m\nu\delta(W^2 - M^2) \times \left[|G_+(Q^2)|^2 + 2|G_0(Q^2)|^2 + |G_-(Q^2)|^2\right], \quad (6)$$

$$\left(1+\frac{Q^2}{\nu^2}\right)g_1(x,Q^2) = m^2\delta(W^2-M^2) \quad (7)$$
$$\times\left[|G_+(Q^2)|^2-|G_-(Q^2)|^2 + (-1)^{J-1/2}\eta\frac{Q\sqrt{2}}{\nu}G_0^*(Q^2)G_+(Q^2)\right],$$

$$\left(1+\frac{Q^2}{\nu^2}\right)g_2(x,Q^2) = -m^2\delta(W^2-M^2) \quad (8)$$
$$\times\left[|G_+(Q^2)|^2-|G_-(Q^2)|^2 - (-1)^{J-1/2}\eta\frac{\nu\sqrt{2}}{Q}G_0^*(Q^2)G_+(Q^2)\right],$$

where J and η are the resonance spin and the resonance parity, respectively; $W^2=(p+q)^2$ is the square of the total energy of the photon–nucleon system in the c.m. frame; and x is the Bjorken variable. We recall that the structure functions F_1 and F_2 are related to the quantities W_1 and W_2 by the equations $F_1(x,Q^2)=mW_1(\nu,Q^2)$ and $F_2(x,Q^2)=\nu W_2(\nu,Q^2)$.

Formulas (5)–(8) control the contribution of one infinitely narrow resonance to the nucleon structure functions. For a resonance of width Γ, it is necessary to replace, in these formulas, the delta function $\delta(W^2-M^2)$ by

$$\frac{1}{\pi}\frac{M\Gamma}{(W^2-M^2)^2+M^2\Gamma^2}. \quad (9)$$

In principle, this expression is not the only approximation of the resonance shape. However, a specific form of the resonance contribution is immaterial at this stage. It should be noted, however, that expression (9) originates from the resonance propagator.

The idea of the approach used in the present study is to take into account the contributions of all resonances for which there are data in the literature [11]. If we denote by $F_{1,2}^R$ and $g_{1,2}^R$, the contributions of the resonance R to, respectively, the spin-independent and the spin-dependent structure function, the resonance contributions to the structure functions can be represented as sums

$$F_{1,2}=\sum_R F_{1,2}^R; \quad g_{1,2}=\sum_R g_{1,2}^R. \quad (10)$$

In order to calculate the resonance contribution to the structure functions, it is necessary to construct the form factors for resonance production as functions of the photon virtuality Q^2. We note that the Q^2 dependence of the form factors of known resonances has not yet received adequate experimental study: the tables given in [11] only display their values at $Q^2=0$.

There are two types of $\gamma^*N\to R$ transitions in parity: normal transitions,

$$1/2^+\to 3/2^-, 5/2^+, 7/2^-, \ldots, \quad (11)$$

and anomalous transitions,

$$1/2^+\to 1/2^-, 3/2^+, 5/2^-, \ldots. \quad (12)$$

For the form factors $G_{\pm,0}(Q^2)$ corresponding to the above transitions, we know (i) their threshold behavior for $|\mathbf{q}|\to 0$ [12], (ii) their asymptotic behavior at high Q^2, and (iii) their values at $Q^2=0$ [11].

It was shown in [12] that, if a $\gamma^*N\to R$ transition is normal in parity [see (11)], the form factors for the production of a spin-J resonance have the following threshold behavior:

$$G_\pm(Q^2)\sim|\mathbf{q}|^{J-3/2}, \quad (13)$$

$$G_0(Q^2)\sim\frac{q_0}{|\mathbf{q}|}|\mathbf{q}|^{J-1/2}. \quad (14)$$

For transitions that are anomalous in parity [see (12)], we have

$$G_\pm(Q^2)\sim|\mathbf{q}|^{J-1/2}, \quad (15)$$

$$G_0(Q^2)\sim\frac{q_0}{|\mathbf{q}|}|\mathbf{q}|^{J+1/2}. \quad (16)$$

Transitions of the $1/2^+\to 1/2^+$ type stand out as a particular case. Specifically, they are controlled only by two form factors, G_+ and G_0—the form factor G_- corresponds to the helicity of a spin-3/2 resonance and, therefore, vanishes for a spin-1/2 resonance. For $1/2^+\to 1/2^+$, their threshold behavior is as follows:

$$G_+(Q^2)\sim|\mathbf{q}|, \quad (17)$$

$$G_0(Q^2)\sim\frac{q_0}{|\mathbf{q}|}|\mathbf{q}|^2. \quad (18)$$

The form factors for $1/2^+\to 1/2^-$ transitions are given by expressions (15) and (16) at $J=1/2$; that is,

$$G_+(Q^2)\sim\text{const}, \quad (19)$$

$$G_0(Q^2)\sim\frac{q_0}{|\mathbf{q}|}|\mathbf{q}|. \quad (20)$$

The high-Q^2 behavior of the form factors is determined by quark-counting rules [13, 14], according to which

$$G_+(Q^2)\sim Q^{-3}, \quad G_0(Q^2)\sim Q^{-4}, \quad (21)$$
$$G_-(Q^2)\sim Q^{-5}.$$

Thus, the expressions representing the form factors and possessing all of the aforementioned properties can be written as

$$|G_\pm(Q^2)|^2 = |G_\pm(0)|^2 \times \left(\frac{|\mathbf{q}|}{|\mathbf{q}|_{Q=0}}\frac{Q'^2_0}{Q^2+Q'^2_0}\right)^{2J-3}\left(\frac{Q^2_0}{Q^2+Q^2_0}\right)^{m_\pm}, \quad (22)$$

$$|G_0(Q^2)|^2 = C^2\left(\frac{Q^2}{Q^2+Q''^2_0}\right)^{2a}\frac{q_0^2}{|\mathbf{q}|^2} \times \left(\frac{|\mathbf{q}|}{|\mathbf{q}|_{Q=0}}\frac{Q'^2_0}{Q^2+Q'^2_0}\right)^{2J-1}\left(\frac{Q^2_0}{Q^2+Q^2_0}\right)^{m_0} \quad (23)$$

in the case of normal transitions and as

$$|G_\pm(Q^2)|^2 = |G_\pm(0)|^2 \times \left(\frac{|\mathbf{q}|}{|\mathbf{q}|_{Q=0}}\frac{Q'^2_0}{Q^2+Q'^2_0}\right)^{2J-1}\left(\frac{Q^2_0}{Q^2+Q^2_0}\right)^{m_\pm}, \quad (24)$$

$$|G_0(Q^2)|^2 = C^2\left(\frac{Q^2}{Q^2+Q''^2_0}\right)^{2a}\frac{q_0^2}{|\mathbf{q}|^2} \times \left(\frac{|\mathbf{q}|}{|\mathbf{q}|_{Q=0}}\frac{Q'^2_0}{Q^2+Q'^2_0}\right)^{2J+1}\left(\frac{Q^2_0}{Q^2+Q^2_0}\right)^{m_0} \quad (25)$$

in the case of anomalous transitions, where

$$|\mathbf{q}| = \frac{\sqrt{(M^2-m^2-Q^2)^2+4M^2Q^2}}{2M}, \quad (26)$$

$$|\mathbf{q}|_{Q=0} = \frac{M^2-m^2}{2M},$$

$m_+ = 3$, $m_- = 5$, and $m_0 = 4$.

The form factors for $1/2^+ \to 1/2^+$ transitions can be written in the form

$$|G_+(Q^2)|^2 = |G_+(0)|^2 \times \left(\frac{|\mathbf{q}|}{|\mathbf{q}|_{Q=0}}\frac{Q'^2_0}{Q^2+Q'^2_0}\right)^{2}\left(\frac{Q^2_0}{Q^2+Q^2_0}\right)^{m_+}, \quad (27)$$

$$|G_0(Q^2)|^2 = C^2\left(\frac{Q^2}{Q^2+Q''^2_0}\right)^{2a}\frac{q_0^2}{|\mathbf{q}|^2} \times \left(\frac{|\mathbf{q}|}{|\mathbf{q}|_{Q=0}}\frac{Q'^2_0}{Q^2+Q'^2_0}\right)^{4}\left(\frac{Q^2_0}{Q^2+Q^2_0}\right)^{m_0}. \quad (28)$$

In expressions (22)–(25), the quantities Q_0^2, Q'^2_0, Q''^2_0, and a are free parameters that can be determined from a fit to experimental data. The coefficient C can be found if there are experimental data on the ratio of the longitudinal and transverse cross sections for virtual-photon absorption, $R(Q^2) = \sigma_L(Q^2)/\sigma_T(Q^2)$, since the following relation holds:

$$R(Q^2) = \frac{2\sum\limits_R |G_0(Q^2)|^2}{\sum\limits_R (|G_+(Q^2)|^2 + |G_-(Q^2)|^2)}. \quad (29)$$

By the way, expression (29), together with expressions (22)–(25), makes it possible to determine the behavior of R, and this may be helpful in analyzing experimental data.

The values of the form factors at $Q^2 = 0$ and the helicity photoproduction amplitudes $A_{1/2}$ and $A_{3/2}$ presented in [11] are related by the equation [10]

$$|G_{+,-}(0)| = e^{-1}\sqrt{\frac{M^2-m^2}{m}}|A_{1/2,3/2}|, \quad (30)$$

where $e = \sqrt{4\pi/137}$ is the electron charge. We note that, at $Q^2 = 0$, the longitudinal form factor vanishes, $G_0(0) = 0$.

Substituting into (10) relations (5)–(8) written for each specific resonance, taking into account transition parities, and using the corresponding expressions for the form factors, we find that, in the resonance region, the structure functions have the form

$$F_1(x,Q^2) = \sum_R \frac{m^2}{\pi} \times \frac{M\Gamma}{(m^2+Q^2(1/x-1)-M^2)^2+M^2\Gamma^2} \times \left(\frac{|\mathbf{q}|}{|\mathbf{q}|_{Q=0}}\frac{Q'^2_0}{Q^2+Q'^2_0}\right)^{n_+}\left[|G_+(0)|^2 \times \left(\frac{Q^2_0}{Q^2+Q^2_0}\right)^{m_+} + |G_-(0)|^2\left(\frac{Q^2_0}{Q^2+Q^2_0}\right)^{m_-}\right], \quad (31)$$

$$F_2(x,Q^2) = \sum_R \frac{2m^2x}{1+4m^2x^2/Q^2}\frac{1}{\pi} \times \frac{M\Gamma}{(m^2+Q^2(1/x-1)-M^2)^2+M^2\Gamma^2} \times \left[\left(\frac{|\mathbf{q}|}{|\mathbf{q}|_{Q=0}}\frac{Q'^2_0}{Q^2+Q'^2_0}\right)^{n_+}\left(|G_+(0)|^2 \times \left(\frac{Q^2_0}{Q^2+Q^2_0}\right)^{m_+} + |G_-(0)|^2\left(\frac{Q^2_0}{Q^2+Q^2_0}\right)^{m_-}\right) + 2C^2\left(\frac{Q^2}{Q^2+Q''^2_0}\right)^{2a}\frac{q_0^2}{|\mathbf{q}|^2}\left(\frac{|\mathbf{q}|}{|\mathbf{q}|_{Q=0}}\frac{Q'^2_0}{Q^2+Q'^2_0}\right)^{n_0} \times \left(\frac{Q^2_0}{Q^2+Q^2_0}\right)^{m_0}\right], \quad (32)$$

$$g_1(x,Q^2)=\sum_R\frac{1}{1+4m^2x^2/Q^2}\frac{m^2}{\pi} \quad (33)$$
$$\times\frac{M\Gamma}{(m^2+Q^2(1/x-1)-M^2)^2+M^2\Gamma^2}$$
$$\times\left[\left(\frac{|\mathbf{q}|}{|\mathbf{q}|_{Q=0}}\frac{Q_0'^2}{Q^2+Q_0'^2}\right)^{n_+}\left(|G_+(0)|^2\right.\right.$$
$$\times\left(\frac{Q_0^2}{Q^2+Q_0^2}\right)^{m_+}-|G_-(0)|^2\left.\left(\frac{Q_0^2}{Q^2+Q_0^2}\right)^{m_-}\right)$$
$$+(-1)^{J-1/2}\eta\frac{2\sqrt{2}mx}{Q}C\left(\frac{Q^2}{Q^2+Q''^2_0}\right)^a|G_+(0)|$$
$$\times\frac{|q_0|}{|\mathbf{q}|}\left(\frac{|\mathbf{q}|}{|\mathbf{q}|_{Q=0}}\frac{Q_0'^2}{Q^2+Q_0'^2}\right)^{(n_0+n_+)/2}$$
$$\left.\times\left(\frac{Q_0^2}{Q^2+Q_0^2}\right)^{(m_0+m_+)/2}\right],$$

$$g_2(x,Q^2)=-\sum_R\frac{1}{1+4m^2x^2/Q^2}\frac{m^2}{\pi} \quad (34)$$
$$\times\frac{M\Gamma}{(m^2+Q^2(1/x-1)-M^2)^2+M^2\Gamma^2}$$
$$\times\left[\left(\frac{|\mathbf{q}|}{|\mathbf{q}|_{Q=0}}\frac{Q_0'^2}{Q^2+Q_0'^2}\right)^{n_+}\left(|G_+(0)|^2\right.\right.$$
$$\times\left(\frac{Q_0^2}{Q^2+Q_0^2}\right)^{m_+}-|G_-(0)|^2\left.\left(\frac{Q_0^2}{Q^2+Q_0^2}\right)^{m_-}\right)$$
$$-(-1)^{J-1/2}\eta\frac{Q}{\sqrt{2}mx}C\left(\frac{Q^2}{Q^2+Q''^2_0}\right)^a|G_+(0)|$$
$$\times\frac{|q_0|}{|\mathbf{q}|}\left(\frac{|\mathbf{q}|}{|\mathbf{q}|_{Q=0}}\frac{Q_0'^2}{Q^2+Q_0'^2}\right)^{(n_0+n_+)/2}$$
$$\left.\times\left(\frac{Q_0^2}{Q^2+Q_0^2}\right)^{(m_0+m_+)/2}\right],$$

where $n_+=2J-3$ and $n_0=2J-1$ for normal transitions, $n_+=2J-1$ and $n_0=2J+1$ for anomalous transitions, and summation is performed over resonances. We took into account the contributions of the following resonances: $N(1440)$, $N(1520)$, $N(1535)$, $N(1650)$, $N(1675)$, $N(1680)$, $N(1700)$, $N(1710)$, $N(1720)$, $N(1990)$, $\Delta(1232)$, $\Delta(1550)$, $\Delta(1600)$, $\Delta(1620)$, $\Delta(1700)$, $\Delta(1900)$, $\Delta(1905)$, $\Delta(1910)$, $\Delta(1920)$, $\Delta(1930)$, and $\Delta(1950)$.

The resulting formulas determine the resonance contribution to the nucleon structure functions. It is obvious that the production of resonances in electron–nucleon scattering is not the only process contributing to the structure functions. The production of mesons and other hadrons forms a nonresonance background, which must also be taken into account.

The contribution of the nonresonance background can be parametrized as [9]

$$F_2^{nr}(x,Q^2)=\frac{Q^2}{4\pi^2\alpha}\frac{1-x}{1+4m^2x^2/Q^2} \quad (35)$$
$$\times(1+R(x,Q^2))\sum_{n=1}^{N}C_n(Q^2)\,[W-W_{\rm th}]^{n-1/2},$$

where $N=3$, C_n are adjustable coefficients, and $W_{\rm thr}$ is the threshold energy.

3. DUALITY

Thus, we have obtained expressions that describe the nucleon structure functions in the resonance region and which depend on the Bjorken variable and the photon virtuality.

Following [6], we will consider how expressions (31)–(34) for the structure functions—these expressions involve resonance terms, which are strongly dependent on Q^2 owing to the form factors—reduce, in the high-Q^2 limit, to scaling expressions, which are weakly dependent on Q^2.

Let us go over to the variable $x'=Q^2/(Q^2+W^2)$, which is related to x by the equation

$$x'=\frac{xQ^2}{Q^2+xm^2}. \quad (36)$$

Let us consider the case of infinitely narrow resonances—that is, $\Gamma\to 0$. In this case, the structure function will be different from zero only for those values of x' at which $W^2=M^2$—that is, for $x'=Q^2/(M^2+Q^2)$. It can be seen that, with increasing Q^2, the resonance is shifted to a region around $x'\sim 1$. As is suggested by experimental data, the resonance then drifts along the scaling curve, whose form can be obtained from the expressions for the structure functions in the resonance region by means of the substitution $Q^2=M^2x'/(1-x')$.

In the case of finite-width resonances, the equality $W^2=M^2$ is approximate, which leads to corrections to the scaling behavior that are proportional to the ratio Γ/M.

In this study, we will consider only the structure function F_2. In what is concerned with the structure functions g_1, it should be noted that, in contrast to F_2, it is sensitive to the longitudinal form factor and to the relative values of G_+ and G_-—in (33), they appear in the form of the difference.

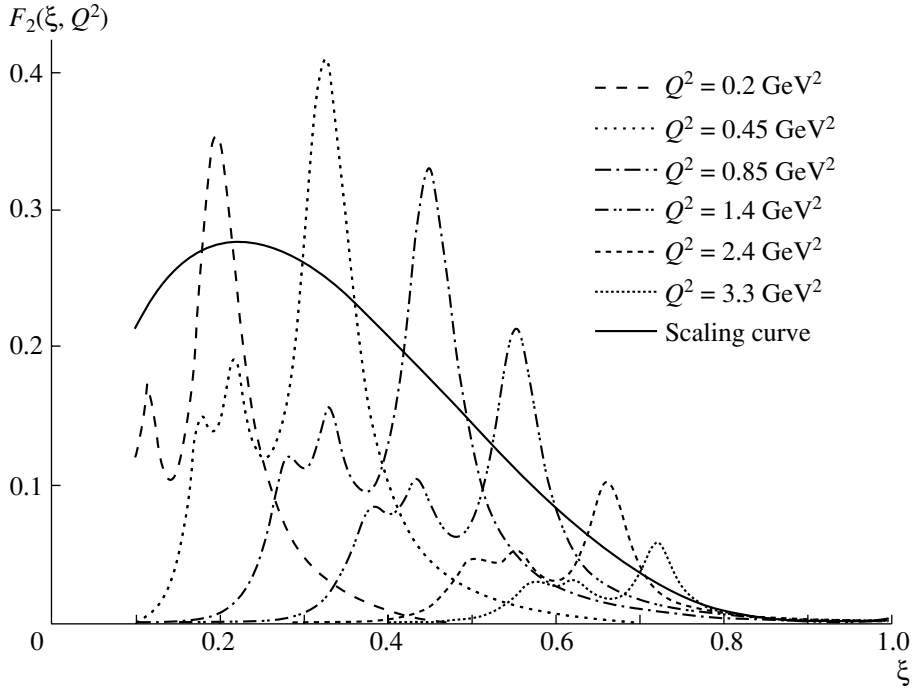

Fig. 2. Resonance contribution to the structure function $F_2(\xi, Q^2)$ in the resonance region.

Let us go over to the variable x' in (32). At high Q^2, we then obtain

$$F_2(x') = \sum_R \frac{2m^2x'}{\pi M\Gamma} \times \left[|G_+(0)|^2\left(\frac{Q_0^2}{M^2}\right)^{m_+}\left(\frac{1-x'}{x'}\right)^{m_+} + |G_-(0)|^2\left(\frac{Q_0^2}{M^2}\right)^{m_-}\left(\frac{1-x'}{x'}\right)^{m_-} + 2C^2\left(\frac{Q_0^2}{M^2}\right)^{m_0}\left(\frac{1-x'}{x'}\right)^{m_0}\right]. \quad (37)$$

From (37), it follows that, in the limit $x' \to 1$, the structure function under study behaves as $F_2(x') \sim (1-x')^{m_+}$.

In the resonance region, use is often made of the Nachtman variable $\xi = 2x/(1+\sqrt{1+4m^2x^2/Q^2})$ (the variable $x = Q^2/2m\nu$ is not convenient in analyzing structure functions in the resonance region, since all resonances are closely spaced in the region $x \sim 1$). Considering that $0 < x < 1$, one can find that $0 < \xi < (Q/m)(\sqrt{1+Q^2/4m^2} - Q/2m)$.

Figure 2 shows the resonance component of the structure function F_2 as a function of the Nachtman variable ξ at various values of Q^2. The solid curve corresponds to the function $F_2(\xi)$ that was presented in [8] and which was obtained from a fit to available data on deep-inelastic scattering.

It can be seen that a dominant contribution to the structure function comes from the $\Delta(1232)$ isobar. The resonance background is relatively small in this region, in contrast to what occurs in regions that correspond to more massive resonances. It can also be seen that, in response to variations in Q^2, the $\Delta(1232)$ peak exactly follows the scaling curve, in accord with the duality concept.

In order to perform a comparison with experimental data, it is necessary to parametrize the contribution of the nonresonance background. At this stage, however, this problem does not have an unambiguous solution.

The inclusion of the nonresonance background must lead to the growth of the structure function in the region of higher lying resonances to such an extent that it would follow the scaling curve (as Q^2 is varied) over a wide region of ξ.

4. CONCLUSION

The finding of Bloom and Gilman that the nucleon structure function F_2 averaged over a rather wide range of the scaling variable takes identical values in the resonance region and in the region of deep-inelastic scattering confirmed the existence of quark–hadron duality—that is, the possibility of describing

processes in terms of only hadronic or only quark degrees of freedom.

In practice, this implies that investigation of nucleon resonances—for example, in terms of form factors—would provide additional information about the properties of nucleons in the deep-inelastic region.

Expressions that were obtained in the present study for the form factors describing the production of nucleon resonances and which take into account a correct threshold behavior and experimental data on resonance decays can form a basis for studying the properties of nucleons in terms of hadronic degrees of freedom.

Expressions obtained here for the structure functions make it possible to demonstrate qualitatively the manifestation of duality by using the structure function F_2 as an example.

In the future, we plan to study the structure function g_1, which receives a significant contribution from the longitudinal form factor. A numerical test of the model upon the appearance of new experimental data would also be of interest.

ACKNOWLEDGMENTS

We are grateful to L.L. Jenkovszky for discussions.

REFERENCES

1. K. Igi and S. Matsuda, Phys. Rev. Lett. **18**, 625 (1967).
2. A. Logunov, L. Soloviev, and A. Tavkhelidze, Phys. Lett. B **24B**, 181 (1967).
3. R. Dolen, D. Horn, and C. Schmid, Phys. Rev. **166**, 1768 (1968).
4. A. I. Bugrij, L. L. Jenkovszky, and N. A. Kobylinsky, Nucl. Phys. B **35**, 120 (1971).
5. L. L. Jenkovszky, V. K. Magas, and E. Predazzi, Eur. Phys. J. A **12**, 361 (2001).
6. E. D. Bloom and F. J. Gilman, Phys. Rev. D **4**, 2901 (1971).
7. C. E. Carlson and N. C. Mukhopadhyay, Phys. Rev. Lett. **74**, 1288 (1995).
8. I. Niculescu, C. S. Armstrong, J. Arrington, *et al.*, Phys. Rev. Lett. **85**, 1186 (2000).
9. I. Niculescu, PhD Thesis (Hampton Univ., 1999).
10. C. E. Carlson and N. C. Mukhopadhyay, Phys. Rev. D **58**, 094029 (1998).
11. Particle Data Group, Phys. Lett. B **204**, 379 (1988).
12. J. D. Bjorken and J. D. Walecka, Ann. Phys. (N.Y.) **38**, 35 (1966).
13. S. J. Brodsky and G. Farrar, Phys. Rev. Lett. **31**, 1153 (1973).
14. V. A. Matveev, R. M. Muradian, and A. N. Tavkhelidze, Lett. Nuovo Cimento **7**, 719 (1973).

Translated by A. Isaakyan

Physics of Atomic Nuclei, Vol. 66, No. 7, 2003, pp. 1335–1341. From Yadernaya Fizika, Vol. 66, No. 7, 2003, pp. 1375–1381.

ELEMENTARY PARTICLES AND FIELDS
Theory

Fermion Production and Correlations due to Time Variation of Effective Mass*

I. V. Andreev**

Lebedev Institute of Physics, Russian Academy of Sciences, Leninskiĭ pr. 53, Moscow, 117924 Russia

Received May 22, 2002; in final form, August 20, 2002

Abstract—The fermion production arising due to time variation of effective mass has been considered. The diagonal polarization states have been found to be the definite helicity states. The strength of the production process and specific fermion–antifermion correlations have been calculated. The production of the fermion–antifermion pairs and the relative two-particle correlations appeared to be large for a sharp and significant change in the mass depending also on fermion occupancy in the initial state. © *2003 MAIK "Nauka/Interperiodica".*

1. INTRODUCTION

It is well known that, in quantum chromodynamics, the chiral invariance is spontaneously broken at low energies and the fermion masses (say, nucleon or constituent quark mass) arise essentially due to chiral-symmetry breaking. In the course of phase transition at high fermion density or at high temperature, the approximate chiral invariance is restored and the light (u, d, s) quark masses become small (ensuring small explicit violation of the symmetry). In practice, the change in the fermion masses is treated (semi)classically (for example, see [1]). However, it appears that, if the change in the mass is fast enough, then the quantum fermion field changes in a specific way producing correlated fermion–antifermion pairs.

Similar effects were considered earlier for bosons (mesons [2–5] and photons [6]) with application to heavy-ion collisions [6, 7]. Below, we consider the fermions in a spatially homogeneous large volume. Application of this effect to heavy-ion collisions will be given elsewhere.

Decomposition of the free fermion field is taken in the form

$$\psi(x) = \int \frac{d^3k}{(2\pi)^{3/2}} e^{i\mathbf{k}\cdot\mathbf{x}} \times \sum_{\nu=1}^{2} \left[u_\nu(\mathbf{k}) b_\nu(\mathbf{k}) e^{-iEt} + v_\nu(-\mathbf{k}) d_\nu^\dagger(-\mathbf{k}) e^{iEt} \right], \quad (1)$$

where $E = (\mathbf{k}^2 + m^2)^{1/2}$; m is the fermion mass; and b_ν, $b_\nu^\dagger$ and d_ν, $d_\nu^\dagger$ are annihilation and creation operators of particles and antiparticles, obeying standard anticommutation relations

$$[b_\nu(\mathbf{k}_1), b_\mu^\dagger(\mathbf{k}_2)]_+ = \delta_{\mu\nu}\delta(\mathbf{k}_1 - \mathbf{k}_2), \quad (2)$$
$$[d_\nu(\mathbf{k}_1), d_\mu^\dagger(\mathbf{k}_2)]_+ = \delta_{\mu\nu}\delta(\mathbf{k}_1 - \mathbf{k}_2).$$

Bispinors $u_\nu(\mathbf{k})$ and $v_\mu(\mathbf{k})$ are orthonormal,

$$u_\nu^\dagger(\mathbf{k}) u_\mu(\mathbf{k}) = v_\nu^\dagger(\mathbf{k}) v_\mu(\mathbf{k}) = \delta_{\mu\nu}, \quad (3)$$

and bispinors $u_\nu(\mathbf{k})$ and $v_\mu(-\mathbf{k})$ having opposite momenta are orthogonal,

$$u_\nu^\dagger(\mathbf{k}) v_\mu(-\mathbf{k}) = v_\nu^\dagger(\mathbf{k}) u_\mu(-\mathbf{k}) = 0. \quad (4)$$

For bispinors $u_\nu(\mathbf{k})$ and $v_\mu(\mathbf{k})$ related to the Dirac equation

$$\left(i\gamma^0 \frac{\partial}{\partial t} - \gamma^n k^n - m \right) \psi(\mathbf{k}, t) = 0, \quad n = 1, 2, 3, \quad (5)$$

we take the standard representation

$$u_\nu(\mathbf{k}) = \frac{1}{N} U_\nu(\mathbf{k}) = \frac{1}{N}(m + \gamma k) \begin{pmatrix} s_\nu \\ 0 \end{pmatrix}, \quad (6)$$
$$v_\nu(\mathbf{k}) = \frac{1}{N} V_\nu(\mathbf{k}) = \frac{1}{N}(m - \gamma k) \begin{pmatrix} 0 \\ s_\nu \end{pmatrix}$$

with two-component unit spinors $(s_1)_\rho = \delta_{1\rho}$, $(s_2)_\rho = \delta_{2\rho}$ and normalization factor

$$N \equiv N(E, m) = (2E(E + m))^{1/2}. \quad (7)$$

2. STEPWISE VARIATION OF THE FERMION MASS

Let the mass m in (5) depend on time, $m = m(t)$. We consider in this section the stepwise variation of the mass. This simple case reveals the main features

*This article was submitted by the author in English.

** e-mail: andreev@lpi.ac.ru

of the phenomenon. We suggest that at time $t = 0$ the mass changes instantly from m_i to m_f. According to Dirac Eq. (5), the time derivative of the field ψ has a jump discontinuity at $t = 0$. Therefore, the field $\psi(\mathbf{k}, t)$ is continuous at the point $t = 0$,

$$\psi_i(\mathbf{k}, -\delta t) = \psi_f(\mathbf{k}, +\delta t), \quad \delta t \to 0. \tag{8}$$

In view of continuity of the field ψ, we have

$$u_{i,\nu}(\mathbf{k})b_{i,\nu}(\mathbf{k}) + v_{i,\nu}(-\mathbf{k})d^\dagger_{i,\nu}(-\mathbf{k}) \tag{9}$$
$$= u_{f,\nu}(\mathbf{k})b_{f,\nu}(\mathbf{k}) + v_{f,\nu}(-\mathbf{k})d^\dagger_{f,\nu}(-\mathbf{k})$$

(sum over ν). Multiplying both sides of (9) by $u^\dagger_{f,\mu}(\mathbf{k})$ and then by $v^\dagger_{f,\mu}(-\mathbf{k})$ and using (3) and (4), we get the transformation of the annihilation and creation operators expressing final-state operators through initial-state operators:

$$b_{f,\nu}(\mathbf{k}) = \alpha_\nu(\mathbf{k})b_{i,\nu}(\mathbf{k}) + \beta_\nu(\mathbf{k})\tilde{d}^\dagger_{i,\nu}(-\mathbf{k}), \tag{10}$$
$$d^\dagger_{f,\nu}(-\mathbf{k}) = -\beta_\nu(\mathbf{k})\tilde{b}_{i,\nu}(\mathbf{k}) + \alpha_\nu(\mathbf{k})d_{i,\nu}(-\mathbf{k})$$

with coefficients

$$\alpha_\nu(\mathbf{k}) = \frac{(E_f + m_f)(E_i + m_i) + k^2}{N_i N_f}, \tag{11}$$
$$\beta_\nu(\mathbf{k}) = \mp\frac{k(E_f + m_f - E_i - m_i)}{N_i N_f}$$

for $\nu = 1, 2$, respectively, where N_i and N_f are normalization factors of the spinors u_ν, v_ν in the initial and final states given by (7). In (10), the combinations of the polarization states of b_1, b_2 operators arise:

$$\tilde{b}_1(\mathbf{k}) = n^3 b_1(\mathbf{k}) + (n^1 - in^2)b_2(\mathbf{k}), \tag{12}$$
$$\tilde{b}_2(\mathbf{k}) = -(n^1 + in^2)b_1(\mathbf{k}) + n^3 b_2(\mathbf{k})$$

(and also the same combinations $\tilde{d}^\dagger_\nu(-\mathbf{k})$ of the $d^\dagger_\nu(-\mathbf{k})$ operators), where $n^i = k^i/k$ are projections of the unit vector $\mathbf{n}$ directed along the momentum $\mathbf{k}$. The transformation (12) is the unitary $SU(2)$ transformation, and the operators $\tilde{b}_\nu(\mathbf{k}), \tilde{b}^\dagger_\nu(\mathbf{k})$ (as well as $\tilde{d}_\nu(\mathbf{k}), \tilde{d}^\dagger_\nu(\mathbf{k})$) satisfy canonical commutation relations. Their time evolution is given by (10) and it reads

$$\tilde{b}_{f,\nu}(\mathbf{k}) = \alpha_\nu(\mathbf{k})\tilde{b}_{i,\nu}(\mathbf{k}) + \beta_\nu(\mathbf{k})d^\dagger_{i,\nu}(-\mathbf{k}), \tag{13}$$
$$\tilde{d}^\dagger_{f,\nu}(-\mathbf{k}) = -\beta_\nu(\mathbf{k})b_{i,\nu}(\mathbf{k}) + \alpha_\nu(\mathbf{k})\tilde{d}^\dagger_{i,\nu}(-\mathbf{k}).$$

The closed transformations of the time evolution connect the pairs $b_\nu(\mathbf{k})$, $\tilde{d}^\dagger_\nu(-\mathbf{k})$ and $\tilde{b}_\nu(\mathbf{k})$, $d^\dagger_\nu(-\mathbf{k})$ for every ν, but they mix the initial polarizations, as follows from (10), (12), and (13).

It appears useful to introduce the normalized linear combinations of b_ν, $\tilde{b}_\nu$ and $d^\dagger_\nu$, $\tilde{d}^\dagger_\nu$ operators as follows:

$$\acute{b}_\nu(\mathbf{k}) = \frac{1}{\sqrt{2(1+n^3)}}(b_\nu(\mathbf{k}) + \tilde{b}_\nu(\mathbf{k})), \tag{14}$$
$$\acute{d}^\dagger_\nu(-\mathbf{k}) = \frac{1}{\sqrt{2(1+n^3)}}(d^\dagger_\nu(-\mathbf{k}) + \tilde{d}^\dagger_\nu(-\mathbf{k})),$$

so that, in accordance with (12) and (14),

$$\acute{b}_\mu(\mathbf{k}) = w_{\mu\nu}(\mathbf{n})b_\nu(\mathbf{k}), \tag{15}$$
$$\acute{d}^\dagger_\mu(-\mathbf{k}) = w_{\mu\nu}(\mathbf{n})d^\dagger_\nu(-\mathbf{k})$$

with

$$w = \frac{1}{\sqrt{2(1+n^3)}}\begin{pmatrix} 1+n^3 & n^1 - in^2 \\ -n^1 - in^2 & 1+n^3 \end{pmatrix} \tag{16}$$
$$= \begin{pmatrix} \cos(\theta/2) & \sin(\theta/2)e^{-i\phi} \\ -\sin(\theta/2)e^{i\phi} & \cos(\theta/2) \end{pmatrix},$$

where θ and ϕ are spherical angles of the momentum $\mathbf{k}$. The rotation matrix w is the $SU(2)$ matrix, and the operators $\acute{b}_\nu(\mathbf{k})$, $\acute{d}_\nu(\mathbf{k})$ obey correct commutation relations; satisfy the orthogonality conditions (3) and (4); and (contrary to input operators $b_\nu(\mathbf{k})$, $d_\nu(\mathbf{k})$) undergo a simple evolution transformation, which does not mix polarizations of the new operators $\acute{b}_\nu$, $\acute{d}_\nu$,

$$\acute{b}_{f,\nu}(\mathbf{k}) = \alpha_\nu(\mathbf{k})\acute{b}_{i,\nu}(\mathbf{k}) + \beta_\nu(\mathbf{k})\acute{d}^\dagger_{i,\nu}(-\mathbf{k}), \tag{17}$$
$$\acute{d}^\dagger_{f,\nu}(-\mathbf{k}) = -\beta_\nu(\mathbf{k})\acute{b}_{i,\nu}(\mathbf{k}) + \alpha_\nu(\mathbf{k})\acute{d}^\dagger_{i,\nu}(-\mathbf{k}),$$

for every ν. As can be seen from (11), the coefficients $\alpha_\nu(\mathbf{k})$ and $\beta_\nu(\mathbf{k})$ in (17) satisfy the condition

$$|\alpha_\nu(\mathbf{k})|^2 + |\beta_\nu(\mathbf{k})|^2 = 1, \tag{18}$$

so that the time evolution is described by the unitary Bogolyubov transformation [8] as it must be to preserve the anticommutation relations of the creation and annihilation operators in the course of the time evolution.

Therefore, it is useful to rewrite the fermion field decomposition (1) in terms of the new operators $\acute{b}_\nu(\mathbf{k})$, $\acute{d}^\dagger_\nu(-\mathbf{k})$ and corresponding bispinors $\acute{u}_\nu(\mathbf{k})$, $\acute{v}_\nu(-\mathbf{k})$ so that

$$u_\nu(\mathbf{k})b_\nu(\mathbf{k}) = \acute{u}_\nu(\mathbf{k})\acute{b}_\nu(\mathbf{k}), \tag{19}$$
$$v_\nu(-\mathbf{k})d^\dagger_\nu(-\mathbf{k}) = \acute{v}_\nu(-\mathbf{k})\acute{d}^\dagger_\nu(-\mathbf{k})$$

(sums over ν) with new bispinors

$$\acute{u}_\mu(\mathbf{k}) = w^{-1}_{\nu\mu}u_\nu(\mathbf{k}) = w^*_{\mu\nu}u_\nu(\mathbf{k}), \tag{20}$$
$$\acute{v}_\mu(-\mathbf{k}) = w^{-1}_{\nu\mu}v_\nu(-\mathbf{k}) = w^*_{\mu\nu}v_\nu(-\mathbf{k}),$$

where w^* is the matrix with complex-conjugated elements [that is, it differs from (16) by the sign of the azimuthal angle ϕ in (16)]. In explicit form,

$$\acute{u}_\nu(\mathbf{k}) = \frac{1}{\sqrt{N}} \begin{pmatrix} (E+m)\xi_\nu \\ \pm k\xi_\nu \end{pmatrix}, \qquad (21)$$

$$\acute{v}_\nu(-\mathbf{k}) = \frac{1}{\sqrt{N}} \begin{pmatrix} \mp k\xi_\nu \\ (E+m)\xi_\nu \end{pmatrix}, \quad \nu = 1,2,$$

with spinors

$$\xi_1 = \begin{pmatrix} \cos(\theta/2) \\ \sin(\theta/2)e^{i\phi} \end{pmatrix}, \quad \xi_2 = \begin{pmatrix} -\sin(\theta/2)e^{-i\phi} \\ \cos(\theta/2) \end{pmatrix} \qquad (22)$$

dependent on direction of the momentum $\mathbf{k}$. It can be seen that the spinors ξ_ν (and thus the bispinors $\acute{u}_\nu(\mathbf{k})$, $\acute{v}_\nu(-\mathbf{k})$) have definite helicities,

$$\frac{1}{2}\sigma^i n^i \xi_\nu = \pm\frac{1}{2}\xi_\nu, \quad \nu = 1,2 \qquad (23)$$

(σ^i are the Pauli matrices), which are conserved in the course of time evolution in view of (17).

Therefore, the Bogolyubov transformation (17) connects creation and annihilation operators that have opposite directions of momentum $\mathbf{k}$ and equal helicities (opposite spin projections). Let us note that, for a stepwise transition, the Bogolyubov coefficients (11) are real-valued. The coefficient $\beta_\nu(\mathbf{k})$ changes its sign if we change the sign of the momentum ($\mathbf{k} \to -\mathbf{k}$), or change $\nu(1 \leftrightarrow 2)$, or interchange the initial and final states ($f \leftrightarrow i$).

In general, the coefficients $\alpha_\nu(\mathbf{k})$ and $\beta_\nu(\mathbf{k})$ of the $SU(2)$ transformation (17) can be represented in the form

$$\alpha(\mathbf{k}) = \cos r(\mathbf{k}) e^{i\varphi_\alpha}, \quad \beta(\mathbf{k}) = \sin r(\mathbf{k}) e^{i\varphi_\beta}, \quad (24)$$

where

$$r(\mathbf{k}) = \tan^{-1}|\beta/\alpha| \qquad (25)$$

is the main evolution parameter and the phases φ_α and φ_β do not play an important role and will not be considered here. For a stepwise transition, the phases are absent.

Using (11), we get

$$\alpha^2(\mathbf{k}) = \frac{1}{2} + \frac{k^2 + m_i m_f}{2E_i E_f}, \qquad (26)$$

$$\beta^2(\mathbf{k}) = \frac{1}{2} - \frac{k^2 + m_i m_f}{2E_i E_f}.$$

As one can see from (26), the evolution parameter $r(\mathbf{k})$ is equal to zero at $\mathbf{k} = 0$; it is maximal at

$$k^2 = k_m^2 = m_i m_f + \frac{m_i^2 m_f^2}{(m_i - m_f)^2}; \qquad (27)$$

and it falls slowly at large k,

$$r(\mathbf{k}) \approx \frac{|m_i - m_f|}{2k}. \qquad (28)$$

At the point of the maximum, the parameter r depends only on the ratio m_f/m_i and it is not small if the mass ratio is small (or large), say, $m_i \gg m_f$. In this case,

$$\tan r_{\max} = |\beta/\alpha|_{\max} \approx 1 - 2\sqrt{m_f/m_i} \qquad (29)$$
$$\text{for} \quad k^2 \approx m_i m_f.$$

If one takes the fermion masses m_i and m_f to be the constituent quark mass ($\sim$350 MeV) and the current quark mass ($\sim$5 MeV), then $\tan r_{\max} \approx 0.76$ at $k \approx 42$ MeV.

In reality, the change in the fermion mass has finite time duration τ and the stepwise approximation is valid only if the momentum is much less than the inverse time duration, $k\tau \ll 1$. The effect of finite time duration will be discussed in the next section.

3. SMOOTH TRANSITION

Let us consider the smooth variation of the fermion mass $m(t)$. In this case, the coefficients $\alpha(\mathbf{k})$ and $\beta(\mathbf{k})$ of the Bogolyubov transformation can be expressed through solutions of Dirac Eq. (5) [9]. To solve this equation, it is helpful to use its squared form, representing the Dirac ψ function in (5) in the form

$$\psi(\mathbf{k},t) = \left(i\gamma^0 \frac{d}{dt} - \gamma^n k^n + m(t)\right)\chi(\mathbf{k},t). \quad (30)$$

Then Eq. (5) takes the form

$$\left(\frac{d^2}{dt^2} - i\gamma^0 \frac{dm}{dt} + k^2 + m^2(t)\right)\chi(\mathbf{k},t) = 0, \quad (31)$$

which splits into two complex-conjugated equations for two upper and two lower components of χ. The bispinor χ can be written in the form

$$\chi_\nu(\mathbf{k},t) = \begin{pmatrix} s_\nu \\ 0 \end{pmatrix}\varphi(\mathbf{k},t) + \begin{pmatrix} 0 \\ s_\nu \end{pmatrix}\varphi(\mathbf{k},t), \qquad (32)$$
$$\nu = 1,2,$$

where s_ν are unit two-component spinors [see (6)]. As a result, we have the second-order equation for scalar function $\varphi(\mathbf{k},t)$,

$$\left(\frac{d^2}{dt^2} - i\frac{dm}{dt} + k^2 + m^2(t)\right)\varphi(\mathbf{k},t) = 0, \qquad (33)$$

which is nothing but an oscillator equation with complex-valued variable frequency (energy).

Let us first consider the stepwise variation of the mass to establish the correspondence of the above approach with results of Section 2. In the region of constant mass, Eq. (33) is satisfied by arbitrary superposition of exponential functions $\exp(\pm iEt)$. Let us have in the initial state the function $\varphi(\mathbf{k},t)$ in the form of a single wave:

$$\varphi(t) = e^{-iE_i t}, \quad t < 0. \tag{34}$$

For $t > 0$, the general solution of (33) has the form

$$\varphi(t) = c^+ e^{-iE_f t} + c^- e^{iE_f t}, \quad t > 0. \tag{35}$$

Choosing one of the upper spinors s_ν (say, s_1) in (32) and substituting (32), (34), and (35) into (31), we get the corresponding (not normalized) expressions for the Dirac field $\psi(\mathbf{k},t)$ at $t < 0$ and at $t > 0$. Then the continuity condition (8) reads

$$U_1(\mathbf{k},m_i,E_i) = c_1^+ U_1(\mathbf{k},m_f,E_f) + c_1^- U_1(\mathbf{k},m_f,-E_f), \tag{36}$$

where bispinors U_1 are not normalized [see (6)], and we find the coefficients c_1^+ and c_1^-:

$$c_1^+ = \frac{E_f + E_i - m_f + m_i}{2E_f}, \qquad c_1^- = \frac{E_f - E_i + m_f - m_i}{2E_f}. \tag{37}$$

Note that bispinors on the right hand side of (36) are orthogonal. Using normalized bispinors u_ν instead of those in (36), we get

$$u_1(\mathbf{k},m_i,E_i) = \alpha_1(\mathbf{k})u_1(\mathbf{k},m_f,E_f) + \beta_1(\mathbf{k})u_1(\mathbf{k},m_f,-E_f) \tag{38}$$

with

$$\alpha_1(\mathbf{k}) = \frac{N(E_f,m_f)}{N(E_i,m_i)}c_1^+, \qquad \beta_1(\mathbf{k}) = \frac{N(-E_f,m_f)}{N(E_i,m_i)}c_1^-, \tag{39}$$

where $N(E,m)$ is given by (7). The coefficients $\alpha_1(\mathbf{k})$ and $\beta_1(\mathbf{k})$ coincide with Bogolyubov coefficients (11). Therefore, the solution of the classical Dirac equation can describe the evolution of the normalized fermion field [9],

$$\psi(\mathbf{k},t) = u_1(\mathbf{k},m_i,E_i)e^{-iE_i t}, \quad t < 0, \qquad \psi(\mathbf{k},t) = \alpha_1(\mathbf{k})u_1(\mathbf{k},m_f,E_f)e^{-iE_f t} + \beta_1(\mathbf{k})u_1(\mathbf{k},m_f,-E_f)e^{iE_f t}, \quad t > 0, \tag{40}$$

showing the appearance of the negative-energy wave (creation of antiparticles) with the correct Bogolyubov coefficient. The choice of another unit spinor in (40) gives a similar result. The momentum $\mathbf{k}$ in (40) may have arbitrary direction. If we take the $\mathbf{k}$ direction along the third (spin-quantization) axis, then bispinors u_1 in (40) have definite helicity $h = 1/2$ that is conserved in the course of transition. Note that the sign of the coefficient β_ν is not determined by the above procedure because the momentum k in $\beta_\nu(\mathbf{k})$ [see (11)] appears as the square root of $E_f^2 - m_f^2$ in (39). Considering below the smooth variation of the mass, we will use the squared Dirac equation to get the explicit expressions for Bogolyubov coefficients α_ν and β_ν. So we will keep in mind the sign assignment arising in (11) for stepwise transition.

Considering the smooth variation of the mass $m(t)$, we use the reference model with

$$m(t) = \frac{m_f + m_i}{2} + \left(\frac{m_f - m_i}{2}\right)\tanh(2t/\tau), \tag{41}$$

which has an exact solution and contains the important parameter τ giving the characteristic time of the mass variation.

Substituting (41) into (33), we get the equation

$$\left(\frac{d^2}{dt^2} + k^2 + e + f\tanh(2t/\tau) + g\tanh^2(2t/\tau)\right)\varphi(t) = 0 \tag{42}$$

with

$$e = \frac{(m_f + m_i)^2}{4} - \frac{i(m_f - m_i)}{\tau}, \qquad f = \frac{m_f^2 - m_i^2}{2}, \qquad g = \frac{(m_f - m_i)^2}{4} + \frac{i(m_f - m_i)}{\tau}. \tag{43}$$

Up to numerical coefficients e, f, and g, (42) coincides with the equation for charged particles in the electric field $E_{\rm el} = 1/\cosh^2(2t/\tau)$. The solution of (42) can be expressed through hypergeometric function F (see [9]):

$$\varphi(z) = (-z)^{-i\mu}(1-z)^{i\lambda}F(\alpha,\beta,\gamma|z), \qquad z = -e^{4t/\tau}, \tag{44}$$

with parameters of the hypergeometric function given by

$$\alpha = -i\mu + i\nu + i\lambda, \qquad \beta = -i\mu - i\nu + i\lambda, \quad \gamma = 1 - 2i\mu. \tag{45}$$

The parameters μ, ν, and λ are expressed through initial parameters of the problem as follows:

$$\mu = \pm E_i\tau/4, \quad \nu = \pm E_f\tau/4, \tag{46}$$

$$\lambda = (m_f - m_i)/4.$$

We choose the upper signs of μ and ν in (46). Then, in the initial state ($t \to -\infty$, $z \to 0$), we get from (44) the incoming wave of the form (34):

$$\varphi(t) = e^{-iE_i t}, \quad t \to -\infty. \tag{47}$$

To find the asymptotic behavior of $\varphi(t)$ at $t \to \infty$, one can use the relation [10]

$$F(\alpha, \beta, \gamma|z) \tag{48}$$
$$= \frac{\Gamma(\gamma)\Gamma(\beta-\alpha)}{\Gamma(\beta)\Gamma(\gamma-\alpha)} F(\alpha, \alpha+1-\gamma, \alpha+1-\beta|z^{-1}) + \{\alpha \leftrightarrow \beta\}.$$

Then, one gets the final state ($t \to \infty$, $z^{-1} \to 0$) of the form (35):

$$\varphi(t) = c^+(\tau)e^{-iE_f t} + c^-(\tau)e^{iE_f t}, \quad t \to \infty, \tag{49}$$

with

$$c^{\pm}(\tau) = \frac{\Gamma(\mp iE_f\tau/2)\Gamma(1-iE_i\tau/2)}{\Gamma\left(i\tau(-E_i \mp E_f + m_f - m_i)/4\right)\Gamma\left(1 + i\tau(-E_i \mp E_f - m_f + m_i)/4\right)}. \tag{50}$$

The coefficients α and β of the Bogolyubov transformation (17) are given by (39), where we can use the normalization factors (7) because these factors are related to asymptotic states and so they do not depend on the sharpness of the transition. Using Γ-function properties

$$\Gamma(z)\Gamma(1-z) = \frac{\pi}{\sin(\pi z)}, \quad |\Gamma(ix)|^2 = \frac{\pi}{\sinh(\pi x)}, \tag{51}$$

we get from (39) and (50) after some transformations

$$\left\{ \begin{matrix} |\alpha(\mathbf{k},\tau)|^2 \\ |\beta(\mathbf{k},\tau)|^2 \end{matrix} \right\} = \frac{\sinh\left(\pi\tau(\pm E_f + E_i - m_f + m_i)/4\right)\sinh\left(\pi\tau(E_f \pm E_i \pm m_f \mp m_i)/4\right)}{\sinh\left(\pi\tau E_f/2\right)\sinh\left(\pi\tau E_i/2\right)}, \tag{52}$$

where upper signs correspond to α and lower signs correspond to β. The Bogolyubov coefficients in (52) satisfy the crucial unitarity condition (18). In the limit of stepwise transition, they correspond to (11), as one can check by straightforward calculation.

As can be seen from (52), the coefficient $\beta(\mathbf{k},\tau) \to 0$ at $\mathbf{k} \to 0$ and it falls for large $\mathbf{k}$:

$$|\beta(\mathbf{k},\tau)| \approx r(\mathbf{k},\tau) \approx \frac{\sinh\left(\pi\tau|m_i - m_f|/4\right)}{\sinh\left(\pi\tau k/2\right)}, \quad k \gg m_i, m_f. \tag{53}$$

In the region $m_f \ll k \ll m_i$, where the coefficient $\beta(\mathbf{k})$ and the evolution parameter $r(\mathbf{k})$ are maximal for stepwise transition, we get

$$|\beta(\mathbf{k},\tau)|^2 \approx \frac{1}{2} - \frac{1}{2}\left(\frac{m_f}{k} + \frac{k}{m_i}h(\pi m_i\tau/2)\right) \tag{54}$$

with

$$h(x) = \frac{1}{2}(1 + x\coth x), \quad h(x) \geq 1, \tag{55}$$

where $m_i \gg m_f$ and $k\tau \ll 1$ were taken in accordance with typical parameters: $m_i \sim 350$ MeV, $m_f \sim 5$ MeV, and $k \sim 40$ MeV in Section 2 and with typical time duration $\tau \sim 1$ fm. As a result, the maximum of $\beta(\mathbf{k},\tau)$ and $r(\mathbf{k},\tau)$ is reduced for finite τ,

$$|\beta_{\max}(\mathbf{k},\tau)|^2 \approx \frac{1}{2} - \sqrt{h(\pi m_i\tau/2)m_f/m_i}, \tag{56}$$

and shifted to smaller momentum,

$$k_m \approx \sqrt{m_i m_f/h(\pi m_i\tau/2)}, \tag{57}$$

due to the h factor. At large $k \gg \tau^{-1}$, the evolution effect is exponentially small, $|\beta| \sim \exp(-\pi k\tau/2)$ for smooth transition.

4. CREATION OF FERMIONS AND THEIR CORRELATIONS

Using Bogolyubov transformation (17), one can find the final-state fermion momentum distributions and the final-state fermion correlations. We confine ourselves to the symmetric case where the fermions with opposite momenta are produced in an equivalent way (say, central collisions of identical nuclei). For simplicity, the Bogolyubov coefficients will be taken to be real-valued and $k = |\mathbf{k}|$ dependent. We also consider the simple model—fast simultaneous transition of a large homogeneous system at rest. The movement of the system can be taken into account by shifting each moving element to its rest frame and integrating over proper times and spacetime rapidities

of the elements of the system as was done for photon production [6] in heavy-ion collisions.

The final-state momentum distribution of the fermions (single-particle inclusive cross sections) is given by (below, we use notation b_ν, d_ν for operators having definite helicity $\nu = \pm 1/2$)

$$N_{f,\nu}(\mathbf{k}) = \frac{1}{\sigma}\frac{d\sigma_\nu}{d^3k} = \langle b^\dagger_{f,\nu}(\mathbf{k}) b_{f,\nu}(\mathbf{k})\rangle, \qquad (58)$$

where brackets mean averaging over initial state. Using (17), we get

$$N_{f,\nu}(\mathbf{k}) = |\alpha(\mathbf{k})|^2 \langle b^\dagger_{i,\nu}(\mathbf{k}) b_{i,\nu}(\mathbf{k})\rangle \qquad (59)$$
$$- |\beta(\mathbf{k})|^2 \langle d^\dagger_{i,\nu}(-\mathbf{k}) d_{i,\nu}(-\mathbf{k})\rangle + |\beta(\mathbf{k})|^2 \frac{V}{(2\pi)^3}$$

and a similar expression for antifermions (with interchange $b \leftrightarrow d$). The last term on the right-hand side of (59) reflects the result of the vacuum rearrangement (the initial vacuum of fermions having mass m_i is not the ground state of b_f, d_f operators). The factor $V/(2\pi)^3$ replaces $\delta^3(0)$ in the real case of large but finite volume V (see [2]).

It is convenient to introduce the level population function $n_\nu(\mathbf{k})$:

$$N_\nu(\mathbf{k}) = \frac{V}{(2\pi)^3} n_\nu(\mathbf{k}). \qquad (60)$$

Then, (59) and the corresponding equation for antiparticles take the simple form (independently for every helicity)

$$n_{f,\nu}(\mathbf{k}) = |\alpha(\mathbf{k})|^2 n_{i,\nu}(\mathbf{k}) + |\beta(\mathbf{k})|^2 \left(1 - \bar{n}_{i,\nu}(-\mathbf{k})\right), \qquad (61)$$

$$\bar{n}_{f,\nu}(\mathbf{k}) = |\alpha(\mathbf{k})|^2 \bar{n}_{i,\nu}(\mathbf{k}) + |\beta(\mathbf{k})|^2 \left(1 - n_{i,\nu}(-\mathbf{k})\right), \qquad (62)$$

where the notation $\bar{n}$ is used for antifermions. In general, one has to consider simultaneously the fermions and antifermions with momenta $\pm\mathbf{k}$ to get the full picture of the particle creation. For example, if there are no particles in the initial state, then we have $|\beta(\mathbf{k})|^2$ particles of each kind in the final state. If there is one particle having momentum $\mathbf{k}$ and helicity ν in the initial state, then we have

$$n_{f,\nu}(\mathbf{k}) = 1, \qquad \bar{n}_{f,\nu}(-\mathbf{k}) = 0, \qquad (63)$$

and $|\beta|^2$ particles in the rest of the states. If there is a fermion–antifermion (singlet) pair having zero momentum in the initial state, that is, $n_{i,\nu}(\mathbf{k}) = 1$, $\bar{n}_{i,\nu}(-\mathbf{k}) = 1$, then we get

$$n_{f,\nu}(\mathbf{k}) = \bar{n}_{f,\nu}(-\mathbf{k}) = |\alpha(\mathbf{k})|^2, \qquad (64)$$
$$n_{f,\nu}(-\mathbf{k}) = \bar{n}_{f,\nu}(\mathbf{k}) = |\beta(\mathbf{k})|^2$$

for the final state. Therefore, in zero-momentum states that are initially completely occupied (both with fermions and antifermions), the occupation number decreases, contrary to initially empty states, where the occupation number increases. For thermal equilibrium, $n(\mathbf{k})$ is the Fermi distribution, depending on temperature and chemical potential, and both effects are present.

The transition effect is better seen in two-particle correlations. Two-particle inclusive cross sections are given by

$$\frac{1}{\sigma}\frac{d^2\sigma^{++}_{\mu\nu}}{d^3k_1 d^3k_2} \qquad (65)$$
$$= \langle b^\dagger_{f,\nu}(\mathbf{k}_2) b^\dagger_{f,\mu}(\mathbf{k}_1) b_{f,\mu}(\mathbf{k}_1) b_{f,\nu}(\mathbf{k}_2)\rangle$$
$$= \langle b^\dagger_{f,\nu}(\mathbf{k}_2) b_{f,\nu}(\mathbf{k}_2)\rangle \langle b^\dagger_{f,\mu}(\mathbf{k}_1) b_{f,\mu}(\mathbf{k}_1)\rangle$$
$$- \delta_{\mu\nu} \langle b^\dagger_{f,\nu}(\mathbf{k}_2) b_{f,\mu}(\mathbf{k}_1)\rangle \langle b^\dagger_{f,\mu}(\mathbf{k}_1) b_{f,\nu}(\mathbf{k}_2)\rangle$$

for two fermions with helicities μ, ν (correlation of identical fermions) and

$$\frac{1}{\sigma}\frac{d^2\sigma^{+-}_{\mu\nu}}{d^3k_1 d^3k_2} \qquad (66)$$
$$= \langle b^\dagger_{f,\nu}(\mathbf{k}_2) d^\dagger_{f,\mu}(\mathbf{k}_1) d_{f,\mu}(\mathbf{k}_1) b_{f,\nu}(\mathbf{k}_2)\rangle$$
$$= \langle b^\dagger_{f,\nu}(\mathbf{k}_2) b_{f,\nu}(\mathbf{k}_2)\rangle \langle d^\dagger_{f,\mu}(\mathbf{k}_1) d_{f,\mu}(\mathbf{k}_1)\rangle$$
$$+ \delta_{\mu\nu} \langle b^\dagger_{f,\nu}(\mathbf{k}_2) d^\dagger_{f,\mu}(\mathbf{k}_1)\rangle \langle d_{f,\mu}(\mathbf{k}_1) b_{f,\nu}(\mathbf{k}_2)\rangle$$

for an fermion–antifermion pair. The last term on the right-hand side of (66) is essential only in the presence of the time evolution of the fermion field. Here, for simplicity, we do not take into account the dynamical correlations arising due to Coulomb and strong interactions of the fermions.

Considering correlations in finite volume V, we can use the modified creation and annihilation operators [2, 7] that are nonzero only in the volume V and satisfy modified anticommutation relations of the form

$$\left[b_\mu(\mathbf{k}_1), b^\dagger_\nu(\mathbf{k}_2)\right]_+ = \delta_{\mu\nu}\frac{V}{(2\pi)^3} G(\mathbf{k}_1 - \mathbf{k}_2), \qquad (67)$$
$$G(0) = 1,$$

where $G(\mathbf{k})$ is the normalized form factor of the fermion source (normalized Fourier transform of the source density). The corresponding correlator of the modified creation and annihilation operators has the form

$$\langle b^\dagger_\mu(\mathbf{k}_1), b_\nu(\mathbf{k}_2)\rangle \qquad (68)$$
$$\approx \delta_{\mu\nu}\frac{V}{(2\pi)^3} n((\mathbf{k}_1 + \mathbf{k}_2)/2) G(\mathbf{k}_1 - \mathbf{k}_2).$$

The right-hand side of (67) and (68) represents the smeared δ function having a width of the order of the

inverse size of the source, which is much less than the width of the momentum distribution $n(\mathbf{k})$.

Using Bogolyubov transformation (17), substituting (68) for arising fermion correlators of initial-state operators, and taking into account the small width of the form factor $G(\mathbf{k})$, one can express the final-state correlators through Bogolyubov coefficients α, β and the form factor G:

$$\langle b^\dagger_{f,\nu}(\mathbf{k}_2) b_{f,\nu}(\mathbf{k}_1)\rangle \langle b^\dagger_{f,\nu}(\mathbf{k}_1) b_{f,\nu}(\mathbf{k}_2)\rangle \quad (69)$$
$$= \frac{V^2}{(2\pi)^6}\left(|\alpha(\mathbf{k})|^2 n_{i,\nu}(\mathbf{k}) + |\beta(\mathbf{k})|^2(1-\bar{n}_{i,\nu}(\mathbf{k}))\right)^2 \times |G(\mathbf{k}_1-\mathbf{k}_2)|^2,$$

$$\langle b^\dagger_{f,\nu}(\mathbf{k}_2) d^\dagger_{f,\nu}(\mathbf{k}_1)\rangle \langle d_{f,\nu}(\mathbf{k}_1) b_{f,\nu}(\mathbf{k}_2)\rangle = \frac{V^2}{(2\pi)^6} \quad (70)$$
$$\times |\alpha(\mathbf{k})\beta(\mathbf{k})(1-n_{i,\nu}(\mathbf{k})-\bar{n}_{i,\nu}(\mathbf{k}))G(\mathbf{k}_1+\mathbf{k}_2)|^2,$$

where smooth functions $\alpha(\mathbf{k})$ and $\beta(\mathbf{k})$ can be evaluated at any of momenta $\mathbf{k}_1, \mathbf{k}_2 \approx \pm\mathbf{k}$ and we suggest that the process is $\mathbf{k} \leftrightarrow -\mathbf{k}$ symmetric. Taking the sum over helicities ν, we finally obtain the relative (divided by the product of single-particle distributions) correlation functions that are measured in experiment:

$$C^{++}(\mathbf{k}_1,\mathbf{k}_2) = 1 - \frac{1}{2}|G(\mathbf{k}_1-\mathbf{k}_2)|^2, \quad (71)$$

$$C^{+-}(\mathbf{k}_1,\mathbf{k}_2) = 1 + \frac{1}{2}R^2(\mathbf{k})|G(\mathbf{k}_1+\mathbf{k}_2)|^2, \quad (72)$$

with

$$R^2(\mathbf{k}) = \frac{|\alpha(\mathbf{k})\beta(\mathbf{k})(1-n_i(\mathbf{k})-\bar{n}_i(\mathbf{k}))|^2}{[|\alpha(\mathbf{k})|^2 n_i(\mathbf{k}) + |\beta(\mathbf{k})|^2(1-\bar{n}_i(\mathbf{k}))]\,[|\alpha(\mathbf{k})|^2\bar{n}_i(\mathbf{k}) + |\beta(\mathbf{k})|^2(1-n_i(\mathbf{k}))]}, \quad (73)$$

where we suggest that the helicities $\pm 1/2$ are equally represented in the initial state.

Equation (71) represents the identical-particle correlation in its simplest (no-interaction) form. The minus sign is a distinctive feature of the fermions and the factor $1/2$ arises due to the sum over polarizations (only two of four final polarization states contain identical particles).

Equation (72) describes the time evolution effect that depends on evolution parameter r (or β, α). For the vacuum initial state, the relative correlation function is big, being equal to $\alpha^2/2\beta^2 > 1/2$. It is especially big for small β, but in this case the pair production itself is weak [see (61), (62)]. In the case of cold dense matter, the correlation function is big for empty (high-momentum) initial states. In the case of hot quark–gluon plasma in the initial state, one has to take into account the presence of an effective thermal quark mass that is much bigger than the original quark mass ($m_i \sim gT$ for light quarks, where g is the QCD coupling constant and T is the temperature).

5. CONCLUSION

Calculation of the evolution effect for fermions shows that opposite-side fermion–antifermion correlations can be large. They can serve as a sign of chiral phase transition in quantum chromodynamics.

ACKNOWLEDGMENTS

The work was supported by the Russian Foundation for Basic Research (project no. 00-02-16101).

REFERENCES

1. L. P. Csernai, I. N. Mishustin, and A. Mocsy, in *Proceedings of the 4th Rio de Janeiro International Workshop on Relativistic Aspects of Nuclear Physics* (World Sci., Singapore, 1995), p. 137.
2. I. V. Andreev and R. M. Weiner, Phys. Lett. B **373**, 159 (1996).
3. M. Asakawa and T. Csorgo, Heavy Ion Phys. **4**, 233 (1996).
4. I. V. Andreev, Mod. Phys. Lett. A **14**, 459 (1999).
5. M. Asakawa, T. Csorgo, and M. Gyulassy, Phys. Rev. Lett. **83**, 4013 (1999).
6. I. V. Andreev, hep-ph/0105208; Yad. Fiz. **65**, 1961 (2002) [Phys. At. Nucl. **65**, 1908 (2002)].
7. I. V. Andreev, Yad. Fiz. **65**, 2088 (2002) [Phys. At. Nucl. **63**, 1988 (2000)].
8. N. N. Bogoliubov, Izv. Akad. Nauk SSSR, Ser. Fiz. **11**, 77 (1947).
9. A. I. Nikishov, Tr. Fiz. Inst. Akad. Nauk SSSR **111**, 152 (1979).
10. L. D. Landau and E. M. Lifshits, *Quantum Mechanics* (Nauka, Moscow, 1974), p. 746.

Physics of Atomic Nuclei, Vol. 66, No. 7, 2003, pp. 1342–1348. From Yadernaya Fizika, Vol. 66, No. 7, 2003, pp. 1382–1388.

ELEMENTARY PARTICLES AND FIELDS
Theory

Is the $a_0(1450)$ a Candidate for the Lowest $q\overline{q}\ ^3P_0$ State?*

A. M. Badalian

Institute of Theoretical and Experimental Physics,
Bol'shaya Cheremushkinskaya ul. 25, Moscow, 117259 Russia

Received December 23, 2002

Abstract—For $a_0(1450)$, considered as the $q\overline{q}\ 1^3P_0$ state, "experimental" tensor splitting, $c_{\rm exp} = -150 \pm 40$ MeV, appears to be in contradiction with the conventional theory of fine structure. There is no such discrepancy if $a_0(980)$ belongs to the $q\overline{q}\ 1^3P_J$ multiplet. The hadronic shift of $a_0(980)$ is shown to be greatly dependent on the value of strong coupling in spin-dependent interaction. © *2003 MAIK "Nauka/Interperiodica".*

1. TWO POSSIBLE CANDIDATES FOR THE GROUND $^3P_0$ STATE

At present, a few low-lying P-wave light mesons, in both isovector and isoscalar channels, were experimentally observed [1, 2]. However, theoretical identification of these states faces serious difficulties, first of all, because the $^3P_0$ member of the lowest ^3P_J multiplet has still not been identified in an unambiguous way. Here, we shall discuss only a simpler isovector multiplet, where mixing with other channels can be neglected.

As is well known, $a_0(980)$ couples strongly to $\eta\pi$ and $K\overline{K}$ channel, and therefore this state was suggested to be interpreted as a multiquark meson [3] or $K\overline{K}$ molecule [4]. Then, under such assumptions, the $q\overline{q}\ 1^3P_0$ state is to be identified with the $a_0(1450)$ meson [5]. There also exist many arguments in favor of considering the $a_0(980)$ as the ground $q\overline{q}\ ^3P_0$ state, which, however, has a large $K\overline{K}$ component in its wave function [6].

We shall discuss here both possibilities, performing a fine structure (FS) analysis of the lowest $q\overline{q}\ ^3P_J$ multiplet. It is evident that an identification of the members of this multiplet should be in accord with values and sign of FS parameters. We shall show here that, in two cases depending on whether $a_0(980)$ or $a_0(1450)$ is the $q\overline{q}\ 1^3P_0$ state, a drastic difference in value and even sign of tensor splitting takes place. In particular, if $a_0(1450)$ is identified as the $q\overline{q}\ 1^3P_0$ state, then the large magnitude and negative sign of tensor splitting appears to be in contradiction with conventional QCD theory of the FS. Also, in this case, the center of gravity of the 1^3P_J multiplet $M_{\rm cog}$ has a large value and large shift with respect to the mass of the $b_1(1235)$ meson (see the discussion in [7]). In the other case, if $a_0(980)$ is the 1^3P_0 state, FS splittings and $M_{\rm cog}$ appear to be in agreement with the theoretical picture, and the value of the hadronic shift is strongly correlated with the strong coupling in spin-dependent interaction. For large α_s(one-loop) $= 0.53$, the hadronic shift appears to be equal to zero and the masses of the a_0, a_1, a_2 mesons just coincide with their experimental values. For α_s(two-loop) $= 0.43$, the hadronic shift about 100 MeV is obtained.

2. FINE-STRUCTURE SPLITTINGS

For any n^3P_J multiplet, the FS parameters—spin–orbit (SO) splitting $a(nP)$ and tensor splitting $c(nP)$—can be expressed through the masses M_J $(J = 0, 1, 2)$ of the members of the multiplet in the standard way [8]:

$$a = \frac{5}{12}M_2 - \frac{1}{4}M_1 - \frac{1}{6}M_0, \qquad (1)$$

$$c = \frac{5}{6}M_1 - \frac{5}{18}M_2 - \frac{5}{9}M_0, \qquad (2)$$

where the experimental values of M_1 and M_2 for the a_1 and a_2 mesons are well known [1],

$$M_1 = 1230 \pm 40\ \text{MeV}, \qquad (3)$$
$$M_2 = 1318 \pm 0.6\ \text{MeV},$$

while the 1^3P_0 state will be identified either with $a_0(1450)$ with the mass $M_{0\rm A}$ [1],

$$\text{case A:}\quad M_{0\rm A} = 1452 \pm 8\ \text{MeV}, \qquad (4)$$

or with $a_0(980)$ having the mass $M_{0\rm B}$ [1],

$$\text{case B:}\quad M_{0\rm B} = 984.8 \pm 1.4\ \text{MeV}. \qquad (5)$$

*This article was submitted by the author in English.

1063-7788/03/6607-1342$24.00

Then, from Eqs. (1)–(4) in case A, the following "experimental" values of SO and tensor splittings can be extracted:

$$a_{\rm A}(\text{exp.}) = -0.3 \pm 11.6\ \text{MeV}, \tag{6}$$

$$c_{\rm A}(\text{exp.}) = -148 \pm 38\ \text{MeV}; \tag{7}$$

i.e, SO splitting is compatible with zero or even a small negative value, while tensor splitting (7) is always negative and has large magnitude:

$$-186 \le c_{\rm A}(\text{exp.}) \le -110\ \text{MeV}. \tag{8}$$

Note that large experimental error in $c_{\rm A}(\text{exp.})$ (7) comes from the error in the $a_1(1260)$ mass (3).

In case B, if $a_0(980)$ is the ground $q\overline{q}\ ^3P_0$ state, the situation is complicated by strong coupling of the $q\overline{q}$ channel with other hadronic channels, $\eta\pi$ and $K\overline{K}$, and for our analysis it is convenient to introduce the mass $\tilde{M}_0$ of the 1^3P_0 state in the one-channel approximation. Then,

$$M_{0\rm B}(\text{exp.}) = 985\ \text{MeV} = \tilde{M}_0 - \Delta_{\rm had}, \tag{9}$$

where the hadronic shift $\Delta_{\rm had}$ is an unknown value, while the mass $\tilde{M}_0$ can be calculated in different theoretical approaches, e.g., in the paper [9] of Godfrey and Isgur, $\tilde{M}_0(\text{GI}) = 1090$ MeV, which corresponds to $\Delta_{\rm had}(\text{GI}) = 105$ MeV. In the QCD string approach, our calculations give close number for the choice of $\alpha_s(\text{FS}) = 0.42$.

It is of interest to note that, if $a_0(980)$ is the $q\overline{q}\,1^3P_0$ state, then both SO and tensor splittings are positive and the situation looks like that in charmonium. For the $\chi_c(1P)$ mesons $a_{\rm exp}(c\overline{c})$ and $c_{\rm exp}(c\overline{c})$ are both positive with tensor splitting being 13% larger than the SO one [10]:

$$a_{\rm exp}(c\overline{c}) = 34.6 \pm 0.2\ \text{MeV}, \tag{10}$$
$$c_{\rm exp}(c\overline{c}) = 39.1 \pm 0.6\ \text{MeV}.$$

3. THEORY OF THE P-WAVE FINE STRUCTURE

Spin-dependent interaction in light $n\overline{n}$ mesons for the L-wave multiplets with $L \neq 0$ can be considered as a perturbation since FS splittings are experimentally small in relation to the meson masses. It is also assumed that the short-range one-gluon exchange (OGE) gives the dominant contribution to perturbative potentials, in particular, to SO potential $V^P_{\rm SO}(r)$ and tensor potential $V^P_T(r)$ [11]. As a result, the matrix elements (m.e.) $a_P = \langle V^P_{\rm SO}\rangle$ and $c_P = \langle V^P_T\rangle$ in light mesons are defined as the first-order terms in α_s. Note that the wave function for a given state of a light meson is calculated here by using the spinless Salpeter equation,

$$a_P(nP) = a^{(1)}_P = \frac{2\bar{\alpha}_s}{m_n^2}\langle r^{-3}\rangle_{nP}, \tag{11}$$
$$c_P(nP) = c^{(1)}_P = \frac{2}{3}a^{(1)}_P = \frac{4}{3}\frac{\bar{\alpha}_s}{m_n^2}\langle r^{-3}\rangle_{nP}.$$

These expressions contain the constituent mass m_n of a light quark, which was supposed to be fixed and just the same for all states with different quantum numbers nL; $m_n \cong 300$–350 MeV is usually taken [11]; the strong coupling α_s is denoted as $\bar{\alpha}_s$ since the renormalization scale in α_s is still not defined and also to distinguish between $\alpha_{\rm st}$ in the static potential and α_s in spin-dependent interaction. Here, $\langle\dots\rangle_{nP}$ denotes the m.e. over the wave function of the nP state.

More detailed analysis of spin-dependent potentials for light mesons, both perturbative and nonperturbative (NP), was done in [12], where the Feynman–Schwinger–Fock (FSF) representation of the light-meson Green's function was used. Keeping only bilocal correlators of the fields, the spin-dependent potentials were expressed through these correlators (see Appendix) which define perturbative SO and tensor splittings

$$a^{(1)}_P(nL) = \frac{2\bar{\alpha}_s}{\mu^2(nL)}\langle r^{-3}\rangle_{nL}, \tag{12}$$
$$c^{(1)}_P(nL) = \frac{2}{3}a^{(1)}_P(nL),$$

and NP contributions are

$$a_{\rm NP}(nL) = -\frac{\sigma}{2\mu^2(nL)}\,\langle r^{-1}\rangle_{nL}, \tag{13}$$
$$c_{\rm NP}(nL)\ \text{ is compatible with zero.}$$

It is important to stress that, in the FSF representation, the expansion in inverse quark masses as in heavy quarkonia is not used, and the constituent mass $\mu(nL)$ in Eqs. (12), (13) is defined by the average over the kinetic energy term of the string Hamiltonian [13, 14]. This "constituent," or dynamical, mass $\mu(nL)$ for a light quark with current mass $m = 0$ appears to be

$$\mu(nL) = \langle\sqrt{p^2}\rangle_{nL} = \frac{1}{2}\sigma\langle r\rangle_{nL} \tag{14}$$

for linear potential and can be expressed only through string tension σ and the universal number.

In contrast to the constant mass m_n in Eqs. (11), the mass $\mu(nL)$ depends on the quantum numbers n and L of a given state and increases with growing n and L.

In light mesons, which have large radii linear static potential σr dominates for all states with the exception of the $1S$ and $1P$ states, where the Coulomb term turns out to be important [14].

The choice of the string tension σ and coupling $\alpha_{\rm st}$ in the static potential can be fixed from the slope and the intercept of leading Regge L trajectory which is defined for spin-averaged masses $M_{\rm cog}(L)$ for the multiplets $1L$. As shown in [14], the experimental values of $M_{\rm cog}(L)$ put strong restrictions on σ and also on strong coupling $\alpha_{\rm st}$: $\sigma = 0.185 \pm 0.005$ GeV^2, $\alpha_{\rm st} \lesssim 0.40$. Here, we present our calculations for the linear σr potential with $\sigma = 0.18$ GeV^2 and also for the linear plus Coulomb potential with

$$\alpha_{\rm st} = 0.42, \quad \sigma = 0.18 \text{ GeV}^2, \tag{15}$$

and take into account that the experimental Regge L trajectory [14] gives

$$M_{\rm cog}(1P) = 1260 \pm 10 \text{ MeV}. \tag{16}$$

The linear potential with $\sigma = 0.18$ GeV^2 fits very well all orbital excitations with $L \geq 2$, and for this potential, the m.e. can be taken from [14],

$$\mu_0(1P) = 448 \text{ MeV}, \quad \langle r^{-1}\rangle_{1P} = 0.236 \text{ GeV}, \tag{17}$$
$$\langle r^{-3}\rangle_{1P} = 0.0264 \text{ GeV}^3,$$

and the calculated constituent mass for the $1S$ state,

$$\mu(1S) = 335 \text{ MeV}, \tag{18}$$

coincides with the conventional value $m_n \approx$ 300–350 MeV, usually used in potential models. For the $1P$ state, the calculated m.e. for the Cornell potential are

$$\mu(1P) = 486 \text{ MeV}, \quad \langle r^{-1}\rangle_{1P} = 0.260 \text{ MeV}, \tag{19}$$
$$\langle r^{3}\rangle_{1P} = 0.0394 \text{ GeV}^3;$$

i.e., in this case, $\langle r^{-3}\rangle_{1P}$ turns out to be 50% larger than for the linear potential.

Nonperturbative contributions to SO and tensor potentials can be correctly defined in a bilocal approximation (see Appendix) when the Thomas term dominates in NP SO splitting,

$$a_{\rm NP}(nP) = -\frac{\sigma}{2\mu^2(nP)}\langle r^{-1}\rangle_{nP}, \tag{20}$$

while NP tensor splitting $c_{\rm NP}(1P)$ for light mesons (as well as for heavy mesons) is compatible with zero,

$$0 \leq c_{\rm NP}(1P) < 5 \text{ MeV}, \tag{21}$$

and therefore can be neglected in our later analysis. This result follows from the fact, established in lattice QCD, that vacuum correlator D_1, which defines $c_{\rm NP}$, is small [15, 16].

Thus, the NP contribution is present only in SO splitting, so that total SO splitting is

$$a = a_P + a_{\rm NP} = \frac{2\bar{\alpha}_s}{\mu^2(1P)}\langle r^{-3}\rangle_{1P} \tag{22}$$
$$- \frac{\sigma}{2\mu^2(1P)}\langle r^{-1}\rangle_{1P}.$$

Due to the negative Thomas precession term, a cancellation of perturbative and NP terms in a(total) takes place and, in principle, a(total) could be small or a negative number.

In contrast to that, NP tensor splitting is small and positive, so that total tensor splitting appears to be always positive,

$$c = c_P = \frac{4\,\bar{\alpha}_s}{3\mu^2(1P)}\langle r^{-3}\rangle_{1P}. \tag{23}$$

Note that, in the χ_c mesons, the correction of order $\bar{\alpha}_s^2$ to c_P was found to be also positive and small [10].

4. REMARKS ABOUT STRONG COUPLING α_s

In heavy quarkonia, strong coupling $\alpha_s(\mu_{\rm ren})$ at the renormalization scale $\mu_{\rm ren}$ can explicitly be extracted from experimental values of FS splittings due to a rather simple, renorm-invariant relation between $\alpha_s(\mu_{\rm ren})$ and the combination $\eta = (3/2)c - a$ [10, 15]. In light mesons, one-loop perturbative corrections (α_s^2 order) are yet to be calculated and OGE contributions (12) with a fitting $\bar{\alpha}_s$ are assumed to be dominant.

However, at present, we know some useful features of α_s:

(i) The strong coupling freezes at large distances, and therefore $\bar{\alpha}_s$ in OGE terms have to be less than, or equal to, the critical value $\alpha_{\rm cr}$ [17, 9].

(ii) The critical value $\alpha_{\rm cr}$ was calculated in background field theory [17], and the value obtained for $\alpha_{\rm cr}(r)$ appears to be in good agreement with lattice measurement of the static potential in the quenched approximation [18]. For QCD constant $\Lambda^{(0)}_{\rm QCD} = 385 \pm 30$ MeV, defined in lattice calculations [19], the calculated $\alpha_{\rm cr}$ [17] is

$$\alpha_{\rm cr}(\text{one-loop}) = 0.59; \tag{24}$$
$$\alpha_{\rm cr}(\text{two-loop}) = 0.43^{+0.05}_{-0.04} \quad (n_f = 0),$$

where in the quenched approximation the number of flavors $n_f = 0$.

(iii) The characteristic size of FS interaction in the P waves, $R_{\rm FS}$, can be defined as

$$R_{\rm FS} = [\langle r^{-3}\rangle_{1P}]^{-1/3} \cong 0.60 \text{ fm}. \tag{25}$$

From the study of $\alpha_s(r)$ in coordinate space [17], it was observed that, at distances $r \sim 0.6$ fm, strong coupling $\alpha_s(r)$ is already close to the critical value (24), being only about 10% less. Therefore, one can expect that $\bar{\alpha}_s$ in OGE splittings (22), (23) has to be equal to

$$\bar{\alpha}_s(R_{\rm FS}) = 0.41 \pm 0.02. \quad (26)$$

(iv) The size $R_{\rm FS}$ (25) coincides remarkably with the radius of the $1P$ $c\bar{c}$ and also of the $2P$ $b\bar{b}$ state, which both are about 0.60 fm. For them, the strong coupling extracted from experiment is

$$\alpha_{\rm exp}(c\bar{c}, 1P) = 0.38 \pm 0.03(\text{exp.}); \quad (27)$$

i.e., this number is very close to that in Eq. (26). To check the sensitivity of FS splitting to the choice of $\bar{\alpha}_s$, here in our calculations we shall take

$$\bar{\alpha}_s(\text{two-loop}) = 0.43, \quad (28)$$
$$\bar{\alpha}_s(\text{one-loop}) = 0.53 \cong 0.9\alpha_{\rm cr}.$$

5. $a_0(1450)$ IS THE $q\bar{q}$ 1^3P_0 STATE

We start with the NP contribution to SO splitting $a_{\rm NP}$, and for $\sigma = 0.18$ GeV^2 ($\mu(1P) = 448$ MeV),

$$a_{\rm NP} = -106 \text{ MeV}. \quad (29)$$

It can be shown that $a_{\rm NP}$ is weakly dependent on the choice of parameters of static interaction varying in the range 99–106 MeV.

From Eq. (6), $a_{\rm A}(\text{exp.})$ is compatible with zero, and from Eq. (22), this condition can be reached only if $a_P = |a_{\rm NP}|$. Therefore, we have

$$a_P = 106 \text{ MeV} \quad \text{and} \quad \bar{\alpha}_s(\text{fit}) = 0.40. \quad (30)$$

Note that this $\bar{\alpha}_s$ is in agreement with expected value (26). Correspondingly, from (23) in theory tensor splitting $c_P = (2/3)a_P$ is positive,

$$c_P = c = 71 \text{ MeV}. \quad (31)$$

This positive sign of $c(1P)$ obtained within a conventional theoretical approach appears to be in contradiction with the "experimental" number (7): $c_{\rm A}(\text{exp.}) = -148 \pm 38$ MeV.

The second discrepancy is that spin-averaged mass considered in case A,

$$M_{\rm cog} = 1303 \text{ MeV}, \quad (32)$$

is larger than the experimental value (16) following from the linear Regge L trajectory for spin-averaged masses [14].

6. $a_0(980)$ IS THE $q\bar{q}$ 1^3P_0 STATE

Here, the mass $\tilde{M}_0(^3P_0)$ will be calculated in the one-channel approximation,

$$\tilde{M}_0 = M_{\rm cog}(1^3P_J) - 2a - c, \quad (33)$$

with $M_{\rm cog}(1^3P_J) = 1260 \pm 10$ MeV from the experimental Regge trajectory. We give below FS splittings $a(1P)$ and $c(1P)$ for two values of strong coupling (24).

For $\alpha_s = 0.43$, when radiative corrections of order α_s^2 were supposed to be small, $\langle r^{-3}\rangle_{1P} = 0.0394$ GeV^3, one obtains ($a_P = 143$ MeV, $a_{\rm NP} = -99$ MeV)

$$a = 44 \text{ MeV}, \quad c = 96 \text{ MeV} \quad (34)$$

and, from the definition (33),

$$\tilde{M}_0(\alpha_s = 0.43) = 1076 \pm 10 \text{ MeV}, \quad (35)$$

and the corresponding hadronic shift of the a_0 meson, according to the definition (9), is

$$\Delta_{\rm had}(\alpha_s = 0.43) = 91 \pm 10 \text{ MeV}. \quad (36)$$

If radiative corrections are not suppressed, then it would be more consistent to take in OGE terms the strong coupling in the one-loop approximation [17],

$$\bar{\alpha}_s(\text{one-loop}) \cong 0.9\alpha_{\rm cr}(\text{one-loop}) = 0.53. \quad (37)$$

Then, FS splittings appear to be in good agreement with the experimental numbers,

$$a(\text{theory}) = 78 \text{ MeV}, \quad c(\text{theory}) = 118 \text{ MeV}, \quad (38)$$
$$a_{\rm exp}(\Delta_{\rm had} = 0) = 77.5 \pm 10 \text{ MeV},$$
$$c_{\rm exp}(\Delta_{\rm had} = 0) = 112 \pm 34 \text{ MeV},$$

which correspond to the hadronic shift equal to zero, and

$$\tilde{M}_0 = 986 \pm 10 \text{ MeV} \quad (39)$$

coincides with the mass of $a_0(985)$. Thus, the hadronic shift turns out to be very sensitive to the choice of strong coupling and, for $\alpha_s = 0.53$, is compatible with zero,

$$\Delta_{\rm had}(\bar{\alpha}_s = 0.53) \cong 3 \pm 10 \text{ MeV}. \quad (40)$$

It is essential that, in [9], as well as in Eq. (37), a relatively large value of one-loop coupling was used. It assumes that α_s^2 corrections to FS splitting are not small, being about 20–30%. To understand which choice of $\bar{\alpha}_s$ is preferable, one needs to study many other P-wave multiplets. In any case, one can conclude that the predicted value of the hadronic shift is correlated with the choice of strong coupling in SO and tensor potentials.

For FS splittings (38), the masses of the a_1 and a_2 mesons are equal to 1242 and 1325 MeV, i.e., very close to their experimental values.

7. HYPERFINE SHIFT AS A TOOL TO IDENTIFY THE MEMBERS OF THE ^3P_J MULTIPLET

Hyperfine (HF) splitting of the P-wave multiplet which comes from spin–spin interaction, $\Delta_{\rm HF}(1P)$, is defined as

$$\Delta_{\rm HF}(1P) = M_{\rm cog}(1P_J) - M(1P_1), \qquad (41)$$

where $M_{\rm cog}$ is not sensitive to the taken value of $\tilde{M}_0$ since it enters $M_{\rm cog}$ with small weight equal to 1/9. In (41), $M(1P_1)$ is the mass of $b_1(1235)$.

Then, if the $a_0(1450)$ belongs to the lowest $q\overline{q}\,^3P_J$ multiplet, $M_{\rm cog} = 1303$ MeV and

$$\Delta_{\rm HF(1P)} = 73 \pm 3(\text{exp.})\ \text{MeV}, \ \text{ case A.} \qquad (42)$$

Identifying $a_0(980)$ as the $q\overline{q}$ ground $^3P_0$ state, one obtains $M_{\rm cog} = 1252$ MeV and

$$\Delta_{\rm HF(1P)} = 28 \pm 6(\text{theory}) \pm 3(\text{exp.})\ \text{MeV}, \ \text{ case B,} \qquad (43)$$

i.e. substantially smaller. One can compare these numbers with theoretical predictions from [7], where the perturbative contribution to the HF shift was shown to be small and negative, while the NP term is positive and not small,

$$\Delta_{\rm HF}(\text{theory}) = 30 \pm 10\ \text{MeV}. \qquad (44)$$

In $\Delta_{\rm HF}$(theory) (44), the theoretical error comes from uncertainty in our knowledge of gluonic correlation length T_g in lattice calculations: $T_g = 0.2$ fm in quenched QCD and $T_g = 0.3$ fm in full QCD [16]. From comparison of (44) and (43), one can see that theoretical number (44) appears to be in good agreement with experimental number (43) if $a_0(980)$ is the $q\overline{q}\,1^3P_0$ and this statement does not depend on a value of hadronic shift $\Delta_{\rm had}$.

On the contrary, if $a_0(1450)$ is considered to be the $q\overline{q}\,1^3P_0$ state, then "experimental" value (42) is two times larger than $\Delta_{\rm HF}$(theory).

8. CONCLUSIONS

Experimental data on FS splittings in light mesons appear to be a useful tool to identify the members of the ^3P_J multiplet. Our study of the FS has shown that $a_0(1450)$ cannot be a candidate for the ground $^3P_0$ state for several reasons:

(i) The "experimental" value of tensor splitting turns out to be negative (with large magnitude), $c_{(\text{exp.})} = -148 \pm 38$) MeV, in contradiction with the conventional theory.

(ii) Also for such interpretation, spin-averaged mass $M_{\rm cog} = 1303$ MeV would be too large and would lie above the linear Regge trajectory for spin-averaged masses.

(iii) The hyperfine shift of $b_1(1235)$ with respect to $M_{\rm cog}$ would be two times larger than the predicted number in [7].

There are no such discrepancies if $a_0(980)$ is the $q\overline{q}\ 1^3P_0$ state. In this case, the mass $\tilde{M}_0(^3P_0)$ can be calculated in the one-channel approximation, and from the difference $\tilde{M}_0(^3P_0) - M_0(a_0(980)) = \Delta_{\rm had}$, the hadronic shift is found to be very sensitive to the chosen value of strong coupling $\bar{\alpha}_s$.

If radiative corrections of order α_s^2 are small, as in charmonium, and $\bar{\alpha}_s \cong 0.40$ is used, then $\Delta_{\rm had}$ is large, $\Delta_{\rm had} = 100 \pm 10$ MeV. If for $\bar{\alpha}_s$ the value $\bar{\alpha}_s(\text{one-loop}) = 0.53$ is taken, the hadronic shift appears to be equal to zero.

ACKNOWLEDGMENTS

I am grateful to Yu.A. Simonov for fruitful discussions. This work has been supported by the Russian Foundation for Basic Research, project no. 00-02-17836, and INTAS, grant no. 00-00110.

APPENDIX

Spin-Dependent Potentials in Light Mesons

In [12, 20, 21], all NP spin-dependent potentials in light mesons, $\hat{V}_{LS} = \mathbf{L}\cdot\mathbf{S}V_{LS}$, tensor potential $\hat{V}_T = \hat{S}_{12}\,V_T$, and HF potential $\hat{V}_{\rm HF} = \mathbf{S}_1\cdot\mathbf{S}_2 V_{\rm HF}$, were obtained being expressed through bilocal vacuum correlation functions (v.c.f.) $D(x)$ and $D_1(x)$:

$$V_{LS}^{\rm NP}(r) = -\frac{1}{\mu_0^2 r}\int\limits_0^\infty d\nu \int\limits_0^r d\lambda\left(1 - \frac{4\lambda}{r}\right) \qquad (A.1)$$

$$\times\, D(\sqrt{\lambda^2+\nu^2}) + \frac{3}{2\mu_0^2}\int\limits_0^\infty d\nu D_1^{\rm NP}(\sqrt{r^2+\nu^2}),$$

$$V_T^{\rm NP}(r) = -\frac{2r^2}{3\mu_0^2}\int\limits_0^\infty d\nu \frac{\partial}{\partial r^2} D_1^{\rm NP}(\sqrt{r^2+\nu^2}), \quad (A.2)$$

$$V_{\rm HF}^{\rm NP}(r) = \frac{2}{\mu_0^2}\int\limits_0^\infty d\nu \Bigg[D(\sqrt{r^2+\nu^2}) \qquad (A.3)$$

$$+ D_1^{\rm NP}(\sqrt{r^2+\nu^2}) + \frac{2r^2}{3}\frac{D_1^{\rm NP}(\sqrt{r^2+\nu^2})}{\partial r^2}\Bigg]$$

(μ_0 is the average kinetic energy for a given state). Here, v.c.f. D and D_1 are defined through the gauge-invariant bilocal vacuum correlators over fields strengths $F_{\mu\nu}$:

$$\frac{g^2}{N_c}\langle F_{\mu\nu}(x)\phi(x,y)F_{\lambda\sigma}(y)\phi(y,x)\rangle \tag{A.4}$$
$$= (\delta_{\mu\lambda}\delta_{\nu\sigma} - \delta_{\mu\sigma}\delta_{\nu\lambda})D(x-y) + \frac{1}{2}$$
$$\times \partial_\mu\big\{[(h_\lambda\delta_{\nu\sigma} - h_\sigma\delta_{\nu\lambda}) + \text{permutation}]D_1(x-y)\big\},$$

where $h_\mu = x_\mu - y_\mu$ and the standard factor

$$\phi(x,y) = P\exp\int\limits_y^x A_\mu(z)dz_\mu \tag{A.5}$$

provides the gauge invariance of the correlators (A.4). It was shown in [22] that, in the bilocal approximation, there is no perturbative contribution to v.c.f. $D(x)$, while the correlator D_1 contains both perturbative and NP contributions:

$$D_1 = D_1^{\rm P} + D_1^{\rm NP} \tag{A.6}$$

with

$$D_1^{\rm P}(x) = \frac{16}{3\pi}\frac{\alpha_s}{x^4}. \tag{A.7}$$

We give some comments on how the average energy, or the constituent mass, μ_0^2, appears in the denominators in Eqs. (A.1)–(A.3). To derive the expressions (A.1)–(A.3), the meson Green's function $G_M(x,y)$ is studied in the FSF representation (which is gauge-invariant), where spin terms enter $G_M(x,y)$ through the exponential factors

$$\exp\left(g\int\limits_0^s d\tau\sigma_{\mu\nu}^{(1)}F_{\mu\nu}\right)\exp\left(-g\int\limits_0^{\bar s} d\bar\tau\sigma_{\mu\nu}^{(2)}F_{\mu\nu}\right). \tag{A.8}$$

Here, $\sigma_{\mu\nu}^{(i)} = (\gamma_\mu\gamma_\nu - \gamma_\nu\gamma_\mu)/4$, $i = 1, 2$ refer to the quarks (antiquarks), $F_{\mu\nu}$ is the field strength, and s ($\bar s$) is the proper time of the quark (antiquark). The proper time τ ($\bar\tau$) plays the role of ordering parameter along the quark (antiquark) trajectory $z(\tau)$ ($\bar z_\mu(\tau)$).

To obtain the Hamiltonian and potentials from the meson Green's function, it is necessary to go over from the proper time to the actual time t of the quark, thus defining the new quanity $\mu(t)$:

$$2\mu(t) = \frac{dt}{d\tau}, \quad 2\bar\mu(\bar t) = \frac{dt}{d\bar\tau}. \tag{A.9}$$

Then, in (A.8), the integrals can be rewritten as

$$J_q = \int\limits_0^s d\tau\sigma_{\mu\nu}^{(i)}F_{\mu\nu} = \int\limits_0^T \frac{dt}{2\mu(t)}\sigma_{\mu\nu}^{(1)}F_{\mu\nu}(z(t)), \tag{A.10}$$

and correspondingly the integral

$$\bar J_q = \int\limits_0^T \frac{dt}{2\bar\mu(t)}\sigma_{\mu\nu}^{(2)}F_{\mu\nu} \tag{A.11}$$

is defined for the antiquark. In the bilocal approximation after averaging, the exponents (A.8) will contain the bilocal correlators, or the cumulants. To obtain spin-dependent potentials, the important approximation is that the spin factors (A.8) are considered as a perturbation and therefore $\mu(t)$ and $\bar\mu(t)$ in (A.10), (A.11) can be changed by corresponding values μ_0 and $\bar\mu_0$ ($\mu_0 = \bar\mu_0$) calculated for the unperturbed Hamiltonian H_R which is defined for a meson with a spinless quark and antiquark. It is inportant that, to derive spin-dependent potentials in light mesons in the FSF representation, the expansion in inverse powers of the quark mass was not used.

The derivation of the meson relativistic Hamiltonian H_R and the definition of the constituent mass

$$\mu_0 = \langle\sqrt{p^2+m^2}\rangle_{nL}, \tag{A.12}$$

are discussed in detail in [12–13].

The v.c.f. D and D_1 were calculated in lattice QCD [16], where it was shown that $D_1^{\rm NP}$ is small when compared to $D(x)$ and even compatible with zero in full QCD. Therefore, in the potentials (A.1)–(A.3), the terms containing $D_1^{\rm NP}$ can be omitted, in particular, the NP contribution to tensor splitting,

$$c_{\rm NP} = \langle V_T\rangle \text{ is compatible with zero.} \tag{A.13}$$

The perturbative contribution to SO and tensor potentials that are defined by v.c.f. (A.7) just corresponds to OGE terms (12) in Section 3.

Lattice measurements have also shown that v.c.f. D can be parametrized with good accuracy as an exponential at distances $x \gtrsim 0.2$ fm, i.e.,

$$D(x) = d\exp\left(-\frac{x}{T_g}\right). \tag{A.14}$$

Then, from (A.1) and (A.9),

$$V_{LS}^{\rm NP}(r) = -\frac{\sigma}{\mu_0^2 r\pi}\int\limits_0^{r/T_g} dttK_1(t) \tag{A.15}$$
$$+\frac{4\sigma}{\pi\mu_0^2}\left[\frac{2T_g}{r^2} - \frac{1}{T_g}K_2\left(\frac{r}{T_g}\right)\right],$$

where the string tension,

$$\sigma = 2\int\limits_0^\infty d\nu\int\limits_0^\infty d\lambda\, D(\sqrt{\lambda^2+\nu^2}), \tag{A.16}$$

for the exponential form of $D(x)$ is

$$\sigma = \pi d T_g^2. \qquad \text{(A.17)}$$

From expression (A.15), it can easily be shown that the nonperturbative potential

$$V_{LS}^{\rm NP}(r \gg T_g) \to -\frac{\sigma}{2\mu^2 r}, \qquad \text{(A.18)}$$

i.e., it coincides with the Thomas precession term if T_g is supposed to be small. We shall not take into account here the positive correction to the Thomas potential coming from second term in (A.15) since there exist two other contributions: from the interference of perturbative and NP terms [23] and from the Coulomb term with correct strong coupling in background fields $\alpha_B(r)$, which imitates the linear $\sigma^* r$ potential at $r \lesssim 0.3$ fm [17, 18].

REFERENCES

1. Particle Data Group, Eur. Phys. J. C **15**, 1, 437 (2000).
2. T. Barnes, in *Proceedings of the Physics and Detectors for DAFNE, Frascati, 1999,* p. 16; hep-ph/0001326.
3. R. L. Jaffe, Phys. Rev. D **15**, 281 (1977); R. L. Jaffe and F. E. Low, Phys. Rev. D **19**, 2105 (1979); A. Alford and R. L. Jaffe, Nucl. Phys. B **578**, 367 (2000); hep-lat/0001023.
4. J. Weinstein and N. Isgur, Phys. Rev. Lett. **48**, 659 (1982); Phys. Rev. D **27**, 588 (1983); F. E. Close, N. Isgur, and S. Kumano, Nucl. Phys. B **389**, 513 (1993).
5. P. Geiger and N. Isgur, Phys. Rev. Lett. **67**, 1066 (1991); Phys. Rev. D **44**, 799 (1991); F. E. Close and N. A. Törnqvist, hep-ph/0204205 (and references therein).
6. K. Maltman, Nucl. Phys. A **680**, 171 (2000); N. A. Törnqvist and M. Ross, Phys. Rev. Lett. **76**, 1575 (1996); S. Narison, Nucl. Phys. B (Proc. Suppl.) **96**, 244 (2001).
7. A. M. Badalian and B. L. G. Bakker, Phys. Rev. D **64**, 114010 (2001); hep-ph/0105156.
8. J. Pantaleone, S.-H. H. Tye, and Y. J. Ng, Phys. Rev. D **33**, 777 (1986).
9. S. Godfrey and N. Isgur, Phys. Rev. D **32**, 189 (1985).
10. A. M. Badalian and V. L. Morgunov, Phys. Rev. D **60**, 116008 (1999).
11. A. De Rujula, H. Georgi, and S. L. Glashow, Phys. Rev. D **12**, 147 (1975).
12. Yu. A. Simonov, in *Proceedings of the XVII International School of Physics, Lisbon, 1999* (World Sci., Singapore, 2000), p. 60; hep-ph/9911237.
13. A. V. Dubin, A. B. Kaidalov, and Yu. A. Simonov, Phys. Lett. B **323**, 41 (1994); Yad. Fiz. **56**, 213 (1993) [Phys. At. Nucl. **56**, 1745 (1993)]; hep-ph/9311344.
14. A. M. Badalian and B. L. G. Bakker, Phys. Rev. D **66**, 034025 (2002); hep-ph/0202246.
15. A. M. Badalian and B. L. G. Bakker, Phys. Rev. D **62**, 094031 (2000); hep-ph/0004021.
16. A. DiGiacomo and H. Panagopoulos, Phys. Lett. B **285**, 133 (1992); M. D'Elia, A. DiGiacomo, and E. Maggiolaro, Phys. Lett. B **408**, 315 (1997).
17. A. M. Badalian, Yad. Fiz. **63**, 2269 (2000) [Phys. At. Nucl. **63**, 2173 (2000)]; A. M. Badalian and D. S. Kuzmenko, Phys. Rev. D **65**, 016004 (2002); hep-ph/0104097.
18. G. S. Bali, Phys. Lett. B **460**, 170 (1999).
19. S. Capitani, M. Lüsher, R. Sommer, and H. Witting, Nucl. Phys. B **501**, 471 (1997).
20. Yu. A. Simonov, Pis'ma Zh. Éksp. Teor. Fiz. **71** (4), 9 (2000) [JETP Lett. **71**, 127 (2000)]; V. I. Shevchenko and Yu. A. Simonov, Phys. Rev. Lett. **85**, 1811 (2000).
21. Yu. A. Simonov, Nucl. Phys. B **324**, 67 (1989); Preprint No. 97-89 (Inst. Theor. and Exp. Phys., Moscow, 1989).
22. Yu. A. Simonov, Usp. Fiz. Nauk **166**, 337 (1996) [Phys. Usp. **39**, 313 (1996)].
23. Yu. A. Simonov, Phys. Rep. **320**, 265 (1999); Pis'ma Zh. Éksp. Teor. Fiz. **69**, 471 (1999) [JETP Lett. **69**, 505 (1999)]; hep-ph/9902233.

Physics of Atomic Nuclei, Vol. 66, No. 7, 2003, pp. 1349–1356. Translated from Yadernaya Fizika, Vol. 66, No. 7, 2003, pp. 1389–1397.

ELEMENTARY PARTICLES AND FIELDS
Theory

Diquark Condensate and Quark Interaction with an Instanton Liquid

G. M. Zinovjev[1)] and S. V. Molodtsov

Institute of Experimental and Theoretical Physics,
Bol'shaya Cheremushkinskaya ul. 25, Moscow, 117259 Russia

Received May 23, 2002

Abstract—The interaction of light quarks with an instanton liquid is considered at nonzero density of quark/baryon matter in a phase where the diquark condensate is nonzero. It is shown that the inclusion of the relevant perturbation of the instanton liquid leads to an increase in the quark chemical potential μ_c. This in turn induces a considerable growth of the threshold quark-matter density at which one expects the emergence of color superconductivity. © *2003 MAIK "Nauka/Interperiodica".*

The possible existence of strongly interacting matter in the phase of quark–gluon plasma has remained one of the most fundamental and intriguing predictions of QCD nearly since the time of its advent. At a phenomenological level, this phase is treated as a state where quarks and gluons at finite values of temperature (T) and (or) the quark/baryon chemical potential (μ) can propagate rather freely over significant (naturally, with respect to the hadron scale) distances. Even the simplest qualitative estimates of physical features of this phase appeared to be so plausible that this made it possible to begin experimental searches for quark–gluon plasma in collisions of relativistic heavy ions. Although the first investigations yielded, in a sense, quite promising results, a new generation of experiments is required for drawing compelling conclusions. This in turn urgently calls for a serious quantitative analysis of the QCD phase diagram.

It seems that lattice QCD would make it possible to solve this problem on the basis of the first principles of the theory; however, a solution within this framework has so far been obtained (at a level that is rather far from reliability) mainly in the vicinity of the temperature axis of the μT plane. Nevertheless, the lattice approximation revealed that, in all probability, the phase structure of QCD is quite rich [1]. In particular, we firmly know at present that, if the temperature falls below some critical value, the chiral symmetry of the original Lagrangian is broken, whereupon quarks are bound by confinement forces. Moreover, lattice calculations indicate that these phenomena occur as the result of the corresponding phase transitions whose critical temperatures are virtually coincident. This observation shows that, most likely, the two phenomena in question are closely related, which may heuristically play an important role in obtaining deeper insight into the confinement mechanism.

The behavior of strongly interacting matter at finite quark/baryon densities has received much less study. From the theoretical point of view, the reason for this is that QCD runs into known serious difficulties in introducing fermions in the lattice model and especially in performing a generalization to nonzero quark/baryon densities. As to a phenomenological aspect, available experimental data proved to be of a low information value for developing the theory along these lines. It is obvious that, both at present and in the future, an increase in the energy of colliding heavy ions would result in the production of strongly interacting matter that occurs ever closer to the temperature axis of the μT plane. In view of this circumstance, a phenomenological development of investigations along the μ axis would predominantly rely on astrophysical observations of compact stars. In recent years, it has been revealed that the effect of diquark pairing in the $\bar{3}$ color channel owing to instanton-induced interaction may prove to be significantly stronger than attraction that is induced by one-gluon exchange and which was considered previously and may lead, in particular, at high quark/baryon densities, to the phase of color superconductivity; in general, the pattern that arises in the μT plane upon taking this into account is by no means trivial [2].

The present article reports on a continuation of our previous study [3], where, on the basis of the method proposed in [4], we examined, in the phase of

[1)]Bogolyubov Institute for Theoretical Physics, National Academy of Sciences of Ukraine, Metrologicheskaya ul. 14b, 03143 Kiev, Ukraine.

broken chiral symmetry, the effect of quarks on the instanton liquid at nonzero chemical potentials. These effects are rather weak and can manifest themselves in the second order of the expansion in the effective coupling constant. Nevertheless, we found that, at a qualitative level, allowance for quark interaction with the instanton liquid can lead to an increase in the threshold quark-matter density at which one can expect the emergence of color superconductivity. It is well known that, if there is no perturbation of the instanton liquid, this density appears to be paradoxically low ($n_q \sim 0.062\ \text{fm}^{-3}$), so that the diquark phase should be formed even in ordinary nuclei ($n_{\text{nucl}} \simeq 0.45\ \text{fm}^{-3}$—the quark-matter density is taken to be three times greater than the nuclear-matter density) [5, 6]. In this study, we will obtain a quantitative estimate for the critical value of the quark/baryon chemical potential μ_c. For this purpose, we will analyze the corresponding set of Gor'kov equations for a color superconductor. In doing this, we rely on an "exact" Lagrangian for four-quark interaction generated by (anti)instantons without resorting to extensively used simplifications of the original Lagrangian that are associated with isolating the channel where attraction is the strongest. We believe that this is dictated by the very formulation of the problem, where the instanton-liquid-perturbation effects being discussed may prove to be of the same order of smallness as effects induced by terms that are usually omitted.

We recall that, in the instanton-liquid model [7], the generating functional $\mathcal{Z}$ is represented as the product of a gluon and a quark component; that is,

$$\mathcal{Z} = \mathcal{Z}_g \cdot \mathcal{Z}_\psi.$$

The first factor provides information about the gluon condensate, while the fermion factor $\mathcal{Z}_\psi$ serves for describing quarks in an instanton medium [5, 7]. Hereafter, we everywhere use the notation borrowed from [3], where we introduced dimensionless variables (dictated by the form of the interquark-interaction kernel)—for example, we make the substitutions $\mu \to \mu\bar{\rho}/2$ and $k_i\bar{\rho}/2 \to k_i$, $i = 1, \ldots, 4$, for the chemical potential and for the momenta, respectively, with $\bar{\rho}$ being the mean size of pseudoparticles. With the aid of an auxiliary integration with respect to the parameter λ, the quark determinant $\mathcal{Z}_\psi$ can be reduced to the form [here, we consider the $SU(3)$ group for quarks of two flavors, $N_f = 2$]

$$\mathcal{Z}_\psi \simeq \int d\lambda \int D\psi^\dagger D\psi \exp\left\{nV_4\left(\ln\frac{n\bar{\rho}^4}{\lambda N} - 1\right)\right\} \times \exp\left\{\int \frac{dk}{\pi^4}\sum_{f=1}^{2}\psi_f^\dagger(k)\cdot 2(-\hat{k} - i\hat{\mu})\psi_f(k) + V\right\}, \quad (1)$$

$$V = 2\lambda(\psi_1^{\dagger L}L_1\psi_1^L)(\psi_2^{\dagger L}L_2\psi_2^L) + 2\lambda(\psi_1^{\dagger R}R_1\psi_1^R)(\psi_2^{\dagger R}R_2\psi_2^R),$$

where $\psi_f^T = (\psi_f^R, \psi_f^L)$, $f = 1, 2$, are the quark fields composed from spinors of specific helicity, $\psi_f^{L,R} = P_\pm\psi_f$ with $P_\pm = \dfrac{1 \pm \gamma_5}{2}$; n is the instanton-liquid density; V_4 is the 4-volume of the system; $\mu_\nu = (\mathbf{0}, \mu)$; and N is a renormalization factor, which, for the sake of definiteness, we set here to unity, but which can in principle be considered as a free parameter of the model. For models where the packing-fraction parameter $n\bar{\rho}^4$ is fixed, this factor is immaterial, while, if this parameter is variable, there appears a weak logarithmic dependence on N. The factors of 2 in expression (1) appear upon going over to dimensionless variables. The term V representing the four-fermion quark interaction can be directly expressed in terms of the helicity components; for example, we have

$$(\psi_f^{\dagger L}L_f\psi_f^L) = \int \frac{dp_f dq_f}{\pi^8}\psi^{\dagger L}_{f\alpha_f i_f}(p_f) \times L^{\beta_f j_f}_{\alpha_f i_f}(p_f, q_f; \mu)\psi_f^{L\beta_f j_f}(q_f).$$

For the right-handed fields, it is necessary to make the substitution $L \to R$. The kernels $L^{\beta_f j_f}_{\alpha_f i_f}$ are defined in terms of zero modes (solutions to the Dirac equation with the chemical potential μ) by means of the functions h_i, $i = 1, \ldots, 4$, which are given by

$$h_4(k_4, k; \mu) = \frac{\pi}{4k}\{(k - \mu - ik_4)[(2k_4 + i\mu)f_1^- + i(k - \mu - ik_4)f_2^-] + (k + \mu + ik_4)[(2k_4 + i\mu)f_1^+ - i(k + \mu + ik_4)f_2^+]\},$$

$$h_i(k_4, k; \mu) = \frac{\pi k_i}{4k^2}\Bigg\{(2k - \mu)(k - \mu - ik_4)f_1^- + (2k + \mu)(k + \mu + ik_4)f_1^+ + \Bigg[2(k - \mu)(k - \mu - ik_4) - \frac{1}{k}(\mu + ik_4)[k_4^2 + (k - \mu)^2]\Bigg]f_2^- + \Bigg[2(k + \mu)(k + \mu + ik_4) + \frac{1}{k}(\mu + ik_4)[k_4^2 + (k + \mu)^2]\Bigg]f_2^+\Bigg\}, \quad i = 1, 2, 3.$$

Here, $k = |\mathbf{k}|$ if we consider the spatial components of the 4-vector k_ν and

$$f_1^\pm = \frac{I_1(z^\pm)K_0(z^\pm) - I_0(z^\pm)K_1(z^\pm)}{z^\pm},$$

$$f_2^{\pm} = \frac{I_1(z^{\pm})K_1(z^{\pm})}{z_{\pm}^2}, z^{\pm} = \frac{\bar{\rho}}{2}\sqrt{k_4^2 + (k \pm \mu)^2},$$

where I_i and $K_i (i = 0, 1)$ are modified Bessel functions. In passing, we introduce the scalar function $h(k_4, k; \mu)$ associated with the three-dimensional component: $h_i(k_4, k; \mu) = h(k_4, k; \mu)\frac{k_i}{k}$, $i = 1, 2, 3$ (we will not present the arguments of the functions h_i explicitly unless this leads to confusion). We then have

$$L_{\alpha i}^{\beta j}(p, q; \mu) = S^{ik}(p; \mu)\epsilon^{kl}U_l^{\alpha}U_{\beta}^{\dagger\sigma}\epsilon^{\sigma n}S_{nj}^{+}(q; -\mu).$$

Here, $S(p; \mu) = (p + i\mu)^{-}h^{+}(p; \mu)$ and $S^{+}(p; -\mu) = \overset{*}{h}{}^{-}(p; -\mu)(p + i\mu)^{+}$, with the conjugate function being given by $\overset{*}{h}{}_{\mu}(p; -\mu) = h_{\mu}(p; \mu)$, while ϵ is an antisymmetric matrix, $\epsilon_{12} = -\epsilon_{21} = 1$. In these formulas, $p^{\pm}$ and similar symbols are used for 4-vectors associated with the matrices $\sigma_{\nu}^{\pm}$, where $\sigma_{\nu}^{\pm} = (\pm i\boldsymbol{\sigma}, 1)$, $\boldsymbol{\sigma}$ being the 3-vector of the Pauli matrices, $p^{\pm} = p^{\nu}\sigma_{\nu}^{\pm}$, while U is the matrix of rotations in color space. For the right-handed components, we have the analogous relations

$$(\psi_f^{\dagger R}R_f\psi_f^R) = \int \frac{dp_f dq_f}{\pi^8}\psi_{f\alpha_f i_f}^{\dagger R}(p_f) \times R_{\alpha_f i_f}^{\beta_f j_f}(p_f, q_f; \mu)\psi_f^{R\beta_f j_f}(q_f)$$

with the kernel

$$R_{\alpha i}^{\beta j}(p, q; \mu) = T^{ik}(p; \mu)\epsilon^{kl}U_l^{\alpha}U_{\beta}^{\dagger\sigma}\epsilon^{\sigma n}T_{nj}^{+}(q; -\mu),$$

where $T(p; \mu) = (p + i\mu)^{+}h^{-}(p; \mu)$ and $T^{+}(p; -\mu) = \overset{*}{h}{}^{+}(p; -\mu)(p + i\mu)^{-}$. Since the vector function $\mathbf{h}(p)$ is associated only with the vector $\mathbf{p}$, the components of the matrices $(p + i\mu)^{\pm}$ and $h^{\mp}(p; \mu)$ can be interchanged. As a result, it can easily be shown that the following identities hold:

$$T(p; \mu) = S^{+}(p; -\mu), \quad T^{+}(p; -\mu) = S(p; \mu).$$

Further, we will omit the dependence of the matrices T and T^{+} on μ since the chemical potential appears in the matrix T only with a plus sign and in the matrix T^{+} only with a minus sign. In addition, we present two useful identities

$$\sigma_2 T^T(p)\sigma_2 = T^{+}(p), \quad \sigma_2 T^{+T}(p)\sigma_2 = T(p).$$

where T^T is the transposed matrix.

For the expectation values

$$\langle\psi_{1\alpha i}^{L,R}(p)\psi_{2\beta j}^{L,R}(q)\rangle = \epsilon_{12}\epsilon_{\alpha\beta}\pi^4\delta(p + q)F_{ij}^{L,R}(p),$$

$$\langle\psi_{f\alpha i}^{L}(p)\psi_{g\beta j}^{\dagger R}(q)\rangle = \delta_{fg}\delta_{\alpha\beta}\pi^4\delta(p - q)G_{ij}^{LR}(p),$$

which are of interest in the case of a diquark condensate, the use of the expression that follows from (1) for the effective action makes it possible to obtain a set of Gor'kov equations that is similar to the set of equations obtained in [6]. The result is

$$\begin{aligned}
\left[G_0^{+}(p)\right]^{-1}F^L(p) - \Sigma^R(p)G^{LRT}(-p) &= 0, \quad (2)\\
\left[G_0^{+}(p)\right]^{-1}G^{LR}(p) - \Sigma^R(p)F^{+RT}(p) &= 1,\\
\left[G_0^{-}(p)\right]^{-1}F^R(p) - \Sigma^L(p)G^{RLT}(-p) &= 0,\\
\left[G_0^{-}(p)\right]^{-1}G^{RL}(p) - \Sigma^L(p)F^{+LT}(p) &= 1,
\end{aligned}$$

where $\left[G_0^{\pm}(p)\right]^{-1} = -2(p + i\mu)^{\pm}$ refers to a free Green's function, $\Sigma^R(p) = \Delta^R T(p)\epsilon T^T(-p)$, $\Sigma^L(p) = \Delta^L T^{+}(p)\epsilon T^{+T}(-p)$, and $\Delta^{L,R}$ is a gap. The form of the Σ matrices is determined by the structure of the kernels of the equations that arise upon averaging over color orientations (it should be recalled that we consider an ensemble that is stochastic in color). The set of Eqs. (2) can be closed by supplementing it with the gap equation

$$\epsilon\Delta^R = \frac{2\lambda}{N_c(N_c - 1)}\int\frac{dq}{\pi^4}[T^{+}(q)F^R(q)T^{+T}(-q) - T^{+}(-q)F^{RT}(q)T^{+T}(q)],$$

$$\epsilon\Delta^L = \frac{2\lambda}{N_c(N_c - 1)}\int\frac{dq}{\pi^4}[T(q)F^L(q)T^T(-q) - T(-q)F^{LT}(q)T^T(q)].$$

It can easily be seen that the right-hand sides of these equations involve the difference of a matrix and its transposed counterpart; therefore, the right-hand sides are automatically proportional to ϵ.

A similar set of equations is valid for the conjugate matrices; that is,

$$\begin{aligned}
F^{+LT}(p)\left[G_0^{-}(p)\right]^{-1} - G^{RLT}(-p)\Sigma^{+R}(p) &= 0, \quad (3)\\
G^{RL}(p)\left[G_0^{-}(p)\right]^{-1} - F^R(p)\Sigma^{+R}(p) &= 1,\\
F^{+RT}(p)\left[G_0^{+}(p)\right]^{-1} - G^{LRT}(-p)\Sigma^{+L}(p) &= 0,\\
G^{LR}(p)\left[G_0^{+}(p)\right]^{-1} - F^L(p)\Sigma^{+L}(p) &= 1.
\end{aligned}$$

The relevant closing gap equation has the form

$$\epsilon\Delta^{+R} = \frac{2\lambda}{N_c(N_c - 1)}\int\frac{dq}{\pi^4}[T^T(-q)F^{+RT}(q)T(q) - T^T(q)F^{+R}(q)T(-q)],$$

$$\epsilon\Delta^{+L} = \frac{2\lambda}{N_c(N_c - 1)} \times \int\frac{dq}{\pi^4}[T^{+T}(-q)F^{+LT}(q)T^{+}(q) - T^{+T}(q)F^{+L}(q)T^{+}(-q)],$$

where $\Sigma^{+R}(p) = \Delta^{+R}T^{+T}(-p)\epsilon T^{+}(p)$, $\Sigma^{+L}(p) = \Delta^{+L}T^{T}(-p)\epsilon T(p)$, and $\Delta^{+L,+R}$ are the corresponding gaps. We note that, in this study, we will restrict ourselves to the case of a diquark condensate; however, it is well known that, in the vicinity of the phase transition at $\mu_c \sim 300$ MeV, there exists a small intermediate region where the mixed phase of nonvanishing chiral and diquark condensates occurs [6], realizing the regime of a transition to the state of color superconductivity. In order to describe this phase, we must extend the set of equations by supplementing it with the additional expectation values

$$\langle \psi^{L,R}_{f\alpha i}(p)\psi^{\dagger L,R}_{g\beta j}(q)\rangle = \delta_{fg}\delta_{\alpha\beta}\pi^4\delta(p-q)G^{LL,RR}_{ij}(p).$$

From the sets of Eqs. (2) and (3), we obtain

$$G^{LR}(p) = G_0^{+}(p) + G_0^{+}(p)\Sigma^{R}(p)F^{+RT}(p),$$
$$F^{+RT}(p) = G^{LRT}(-p)\Sigma^{+L}(p)G_0^{+}(p).$$

Let us introduce auxiliary matrices $C^{+L}(p) = \Delta^{+L}T^{+}(-p)T(p)$ and $C^{R}(p) = \Delta^{R}T(p)T^{+}(-p)$. With the aid of them, the Σ matrices can be recast into the form

$$\Sigma^{+L}(p) = \epsilon C^{+L}(p), \quad \Sigma^{R}(p) = C^{R}(p)\epsilon.$$

By using identities that relate the T matrices, we can show that the following equalities hold:

$$\epsilon C^{+LT}(-p)\epsilon^{T} = C^{+L}(p),$$

$$\epsilon C^{RT}(-p)\epsilon^{T} = C^{R}(p).$$

For the Green's function, we have

$$G^{LR}(p) = G_0^{+}(p) + G_0^{+}(p)C^{R}(p)\epsilon \times G^{LRT}(-p)\epsilon C^{+L}(p)G_0^{+}(p).$$

By using the properties of C matrices and considering that the free Green's functions satisfy the identities

$$\sigma_2 G_0^{\pm T}(p)\sigma_2 = G_0^{\mp}(p),$$

we obtain a closed equation for determining the function G^{LR}:

$$\epsilon G^{LR}(-p)\epsilon^{T} = G_0^{-}(-p) + G_0^{-}(-p) \times C^{+L}(p)G^{LR}(p)C^{R}(p)G_0^{-}(-p).$$

The fact that the vector function $\mathbf{h}(p)$ is associated with the vector $\mathbf{p}$ leads to a useful property—all of the matrices $G_0^{\pm}$, C^{+L}, and C^{R} commute with one another. Seeking a solution for the Green's function G^{LR} in the form of an iterative series, one can see that it also commutes with these matrices. We can now easily derive a final equation for the Green's function in the form

$$G^{LR}(p) = [1 + H(p)]G_0^{+}(p) + H^2(p)G^{LR}(p)$$

or

$$[1 - H(p)]G^{LR}(p) = G_0^{+}(p),$$

where $H(p) = G_0^{+}(p)C^{R}(p)G_0^{-}(-p)C^{+L}(p)$.

The form of the matrices $H(p)$ is such that the sum

$$H(p) + H(-p) = \alpha(p)$$

and product

$$H(p)H(-p) = \beta(p)$$

are proportional to identity matrices [by definition, we see that $\alpha(-p) = \alpha(p)$; similarly, the relation $\beta(-p) = \beta(p)$ also holds]. Denoting the functions $h_\nu(p)$ of sign-reversed argument by $g_\nu = h_\nu(-p)$, we can write the functions $\alpha(p)$ and $\beta(p)$ in the compact form

$$\alpha(p) = 4\Delta^{R}\Delta^{+L} \times [-4A(p)(hg) + 2(p^2+\mu^2)(h^2)(g^2)],$$

where

$$A(p) = (p^2+\mu^2)(hg) - 2i\mu p(g_4 h - h_4 g).$$

In these expressions, we have used a natural definition of the scalar product in the form $(hg) = \sum_{i=1}^{4} h_i g_i$ and similar definitions for the squares of these functions, (h^2) and (g^2). In the last term appearing in the expression for $A(p)$, we have employed the aforementioned notation for the scalar function associated with the three-dimensional component $\mathbf{h}$. For the function β, we can in turn obtain

$$\beta(p) = 16\left(\Delta^{R}\right)^2\left(\Delta^{+L}\right)^2\left(p^2+\mu^2\right)^2(h^2)^2(g^2)^2.$$

Since the functions α and β are associated with identity matrices, the solution for the Green's function can be represented in the form

$$G^{LR}(p) = \frac{G_0^{+}(p)[1 - H(-p)]}{1 - \alpha(p) + \beta(p)}.$$

In this case, the gap equation can be rewritten as

$$\Delta^{L} = \frac{2\lambda}{N_c(N_c-1)}\int \frac{dp}{\pi^4}\frac{\alpha(p) - 2\beta(p)}{\Delta^{+L}(1 - \alpha(p) + \beta(p))}. \quad (4)$$

We are interested in a solution of the form $\Delta^{R} = \Delta^{+L} = \Delta^{L} = \Delta^{+R} = \Delta$ for $\lambda < 0$. This solution is dictated by the symmetry properties of the kernel of the four-quark interaction. We recall that, in the kernel, the factor for each sort of quarks is traditionally written with the factor of i [7, 8]. This explains the choice of the sign of λ. It should be noted, however, that, in principle, there exists an alternative—$\Delta^{R} = \Delta^{+L} = -\Delta^{L} = -\Delta^{+R}$ for $\lambda > 0$—if we redefine the kernels. An analysis shows that the denominator on the right-hand side of Eq. (4) is always positive;

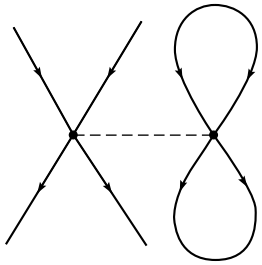

Fig. 1. Diagram of the tadpole approximation (see main body of the text): (solid lines) fermion fields and (dashed line) scalar field.

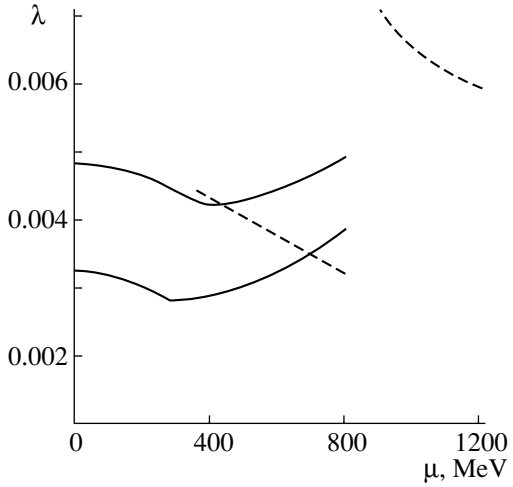

Fig. 2. Saddle-point value λ (to the one-loop approximation, it is proportional to the free energy of the system) as a function of the chemical potential μ at $N_c = 3$ and $N_f = 2$. The solid curves were obtained for the phase where chiral symmetry is broken (the lower curve was calculated with allowance for perturbations of the instanton liquid). The dashed curves correspond to the phase of color superconductivity (left curve) for the case where the tadpole contribution is disregarded and (right curve) for the case where the interaction of the instanton liquid is included.

hence, it is guaranteed that this equation has a solution at sufficiently large λ.

The state of quark matter at a specific value of the chemical potential is determined by the saddle point of the functional in (1). We consider this functional, retaining the first nonvanishing contribution and restricting ourselves to the right (figure-of-eight) diagram (see, for example, [5]), whose contribution I has the form

$$I = 2(N_c - 1)\int \frac{dp}{\pi^4}\frac{\alpha(p) - 2\beta(p)}{1 - \alpha(p) + \beta(p)}.$$

In our case, this contribution to the generating functional ($Z_\psi \sim e^W$) reduces to

$$W = -n\bar{\rho}^4 \ln\lambda + \lambda\langle Y\rangle, \langle Y\rangle \simeq I.$$

In the simplest case of a constant instanton-liquid density, the saddle-point equation can be written in the form

$$n\bar{\rho}^4 - \lambda\langle Y\rangle = 0.$$

Comparing this equation with the gap equation in (4), one can notice an interesting property: the saddle-point equation leads to the condition according to which the gap as a function of μ is constant. This property provides a useful test for numerical calculations.

It was shown in [4, 9] that the reaction of quarks to the instanton liquid can be described within perturbation theory in terms of small variations of the instanton-liquid parameters, δn and $\delta\rho$, in the vicinity of their equilibrium values n and $\bar{\rho}$. The variation of the parameters is included in the theory if use is made of deformable field configurations (crumpled instantons)—in our case, instantons of dimension ρ as a function of x and z: $\rho \to \rho(x, z)$—and if the variation of zero modes in the quark determinant is taken into account in the interaction vertices upon the substitution $\bar{\rho} \to \bar{\rho} + \delta\rho$. It appears that, for long-wave perturbations, such as π mesons, the deformation field describes scalar colorless excitations of the instanton liquid with mass gap M on the order of a few hundred MeV, $M^2 = \nu/\kappa$, where κ is the kinetic coefficient that is calculated within the semiclassical approach and $\nu = (b-4)/2$ with $b = (11N_c - 2N_f)/3$, N_c and N_f being the numbers of quark colors and flavors, respectively. For this kinetic coefficient, our estimations yield $\kappa \sim c\beta$ [9], where $\beta = 8\pi^2/g^2$ is the instanton action and $c \sim 1.5$–6, the specific value of the factor c being dependent on the ansatz adopted for the saturating configuration.

Eventually, we find that, in addition to the four-leg diagrams [see the term V in (1)], there appear diagrams featuring a scalar field connected through a vertex where differentiation with respect to ρ occurs and where it is necessary to take into account the variation of the functions describing zero modes,

$$h_i \to h_i + \frac{\partial h_i}{\partial\rho}\delta\rho, \quad i = 1, \ldots, 4. \qquad (5)$$

Owing to the presence of a condensate (in our case, this is a diquark condensate), we can significantly simplify the Lagrangian under consideration if we retain only the main contributions, which stem from the tadpole-type diagrams. The leading contribution actually comes from the term V and from the term associated with two four-leg diagrams connected by the scalar field whose propagator is $1/M^2$, one of these diagrams being closed into a figure-of-eight

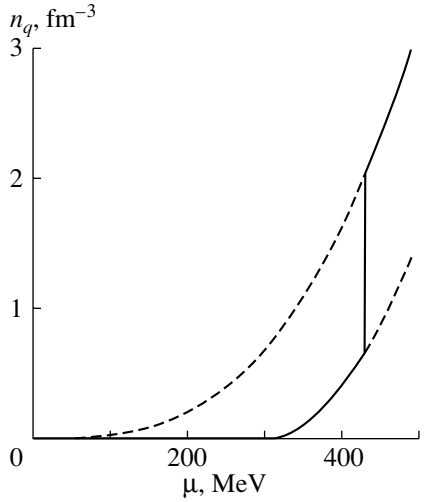

Fig. 3. Quark density determined from the intersection of the upper curve in Fig. 2 (for the chiral condensate) with the curve representing the diquark condensate (without including perturbations of the instanton liquid) in the same figure. The solid and the dashed curve show the result for the stable and metastable phases, respectively.

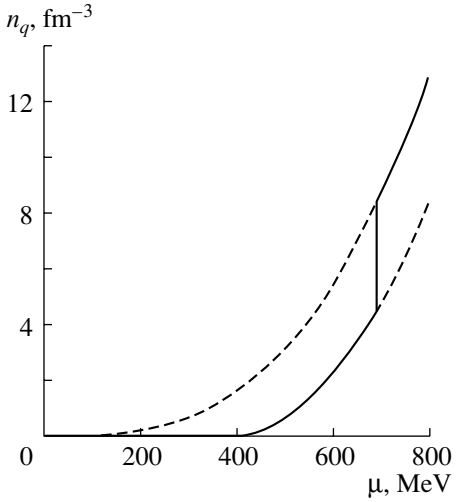

Fig. 4. Quark density determined from the intersection of the lower curve in Fig. 2 (for the chiral condensate, the diquark condensate being taken without allowing for the tadpole contribution) and the curve representing the diquark condensate (without allowing for the perturbations of the instanton liquid) in the same figure. The solid and the dashed curve depict the results for, respectively, the stable and the metastable phase.

(see Fig. 1); because of a condensate, it is considered with fully paired lines.

Analyzing the modified Lagrangian, we can easily see that the form of the set of Gor'kov equations remains unchanged except that, instead of Σ, we must everywhere use the corrected expression $\Sigma + \delta\Sigma$, where the correction $\delta\Sigma$ is constructed from the modified functions (5). Further, one can see that the result for the Green's function also remains unchanged. By Σ in final expressions, one should imply the corrected functions. In particular, the form of the gap equation does not change since, in the kernel, there arises once again the familiar combination of a matrix and its transposed counterpart, this combination being constructed from the matrix functions T and T^+ differentiated with respect to ρ (and considered, for example, in terms of finite differences) and being associated with an identity matrix. Finally, it turns out that, in the gap equation, we must make the substitutions

$$\alpha(p) \to \alpha(p) + \delta\alpha(p),$$

$$\beta(p) \to \beta(p) + \delta\beta(p),$$

where

$$\delta\alpha(p) = J\frac{\partial\alpha}{\partial\rho},$$

$$\delta\beta(p) = J\frac{\partial\beta}{\partial\rho},$$

with J describing the contribution of a diagram belonging to the figure-of-eight type and having, for the external line, the scalar-field propagator,

$$J = \frac{2\lambda}{N_c(N_c-1)}\frac{1}{n\bar\rho^4\kappa}\frac{1}{4M^2}I.$$

It should be emphasized that, with allowance for the explicit form of M, the dependence on the kinetic term κ is effectively canceled, so that its exact value is immaterial in the approximation being considered. By differentiating the figure-of-eight diagram, we obtain

$$\frac{\partial I}{\partial\rho} = 2(N_c-1)\int\frac{dp}{\pi^4}\left\{\frac{1-\beta(p)}{(1-\alpha(p)+\beta(p))^2}\delta\alpha(p) + \frac{\alpha(p)-2}{(1-\alpha(p)+\beta(p))^2}\delta\beta(p)\right\}.$$

We must also take into account the modification of the generating functional. It should be recalled that this functional is calculated to the first nonvanishing contribution,

$$W = -n\bar\rho^4\left(\ln\frac{n\bar\rho^4}{\lambda} - 1\right) + \lambda\langle Y\rangle.$$

With allowance for a variation of the instanton-liquid density, the saddle point is now determined from the equation

$$n\bar\rho^4 - \lambda(n\bar\rho^4)'\ln\frac{n\bar\rho^4}{|\lambda|} - \lambda\langle Y\rangle = 0.$$

As to the instanton-liquid density, it is given by [4]

$$n\bar\rho^4 = \frac{\nu}{2\beta\xi^2} \qquad (6)$$

$$+\left[\left(\frac{\nu}{2\beta\xi^2}\right)^2+\frac{\left(\frac{\delta I}{\delta\rho}\right)'}{\beta\xi^2}\frac{\Gamma(\nu+1/2)}{2\sqrt{\nu}\Gamma(\nu)}\right]^{1/2},$$

where the prime denotes differentiation with respect to λ, the constant $\xi^2=\frac{27}{4}\frac{N_c}{N_c^2-1}\pi^2$ characterizes interaction in the stochastic ensemble of pseudoparticles, and the mean size of pseudoparticles is defined as $\bar{\rho}\Lambda=\exp\left\{-\frac{2N_c}{2\nu-1}\right\}$.

The derivative of the figure-of-eight diagram with respect to λ is given by the expression

$$\left(\frac{\delta I}{\delta\rho}\right)'=4(N_c-1)\frac{\Delta'}{\Delta}\times\int\frac{dp}{\pi^4}\left\{\frac{1+\alpha-6\beta+\alpha\beta+\beta^2}{(1-\alpha+\beta)^3}\delta\alpha+\frac{-4+7\alpha+4\beta-\alpha\beta-\alpha^2}{(1-\alpha+\beta)^3}\delta\beta\right\}.$$

Finally, the derivative Δ' is determined from the relation

$$\frac{N_c(N_c-1)}{2\lambda^2}=\frac{2\Delta'}{\Delta^3}\int\frac{dp}{\pi^4}\frac{2\beta-2\beta^2+2\alpha\beta-\alpha^2}{(1-\alpha+\beta)^2}.$$

The calculations were performed to the one-loop approximation, where the saddle-point parameter λ is proportional to the free energy of the system. In Fig. 2, this parameter is represented by the dashed curves (the left curve was obtained without taking into account quark interaction with the instanton liquid). In the same figure, the solid curves represent similar results, but for the phase where chiral symmetry is broken (see [3]). It should be noted that the saddle-point parameter λ_1 from [3] and that which is used in the present study are related by the equation $\lambda_1^2=-\frac{\lambda n\bar{\rho}^4}{2(N_c-1)N_c}$. The intersection of the curves determines the point of the transition to the superconducting phase. It was mentioned above that, in fact, there exists a narrow intermediate zone of a mixed phase where a nonvanishing chiral and a nonvanishing diquark condensate coexist, so that the transition is not very sharp. But refinements following from this are not very important for our consideration. First of all, we note that the phase-transition point obtained without allowance for the tadpole contribution (the point at which the upper solid curve intersects the left-hand dashed curve) lies farther than the value of $\mu_c\simeq 300$ MeV, which was found previously in [5, 6]. However, the conclusion that the phase-transition is shifted toward greater values of μ owing to the use of the "exact" Lagrangian would be premature. We recall that the value of $\mu_c\simeq 300$ MeV is obtained if use is made of an approximate Lagrangian where the channel characterized by the strongest attraction is selected. The point is that the instanton-liquid parameters obtained within different approaches differ somewhat from one another, but optimal agreement with phenomenological results known from analyses of the QCD vacuum can be reached by adjusting the model parameters—for example, by changing the scale Λ. In this sense, the shift of the phase-transition point is probably within the accuracy that the instanton-liquid model can ensure.

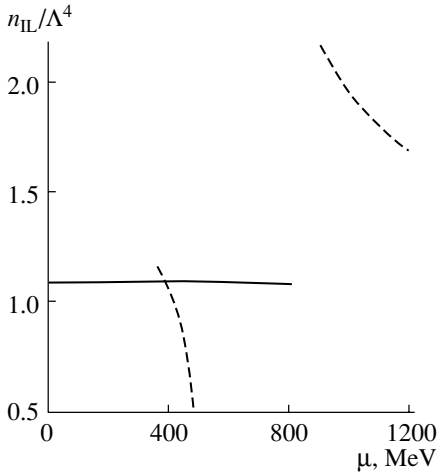

Fig. 5. Instanton-liquid density at $N_c=3$ and $N_f=2$ for two regimes. The solid curve and two dashed curves represent the results of the calculations with, respectively, the chiral and the diquark condensate. The lower dashed curve was obtained by estimating the instanton-liquid density without self-consistently taking into account quark interaction with the instanton liquid (one finds the diquark condensate and then determines the instanton-liquid density on the basis of it), while the upper curve is discussed in the main body of the text.

The situation becomes more certain if we take into account the disturbance of the instanton liquid by quarks. In this case, the phase-transition point is shifted noticeably toward greater values of μ_c (the point at which the lower solid curve intersects the left-hand dashed curve). The quark-matter density for the former version ("exact" Lagrangian) and for the version discussed immediately above versus the chemical potential is given in Figs. 3 and 4, whence it can be seen that the threshold densities at which the emergence of the phase involving color superconductivity is expected may significantly exceed the density of normal nuclear matter. In all probability, these results suggest that, in principle, additional weak (against the background of the instanton interaction) interactions of light quarks can significantly change

the estimate of the threshold nuclear-matter density at which diquark condensation occurs.

But if we also take into account the interaction of quarks in the phase involving a nonvanishing diquark condensate with the instanton liquid (right-hand dashed curve), the intersection point is shifted to unjustifiably large values of μ—that is, to the region where the simple instanton-liquid model can hardly be used to describe the QCD vacuum. The restriction from the side of large values of the chemical potential is due to the fact that, at some value of μ, interquark distances become so small that Coulomb (perturbative) fields become commensurate with instanton fields, with the result that a superposition of (anti)instantons ceases to be an appropriate configuration that saturates the relevant path integral. From our results, we can therefore draw only the conservative conclusion that the curves describing the chiral and diquark condensates move apart upon taking into account the perturbation of the instanton liquid by quarks. The chiral curve moves downward, while the diquark curve drifts toward larger values of μ, simultaneously displacing the phase-transition point. In order to obtain more accurate numerical data, it is necessary to improve the instanton-liquid model in such a way that the contribution of perturbative fields could be taken into account more reliably.

Figure 5 shows the instanton-liquid density as a function of μ with allowance for quark interaction with the instanton liquid in the phase where chiral symmetry is broken (solid curve) and in the phase of color superconductivity (dashed curves). The lower curve gives an estimate obtained for the instanton-liquid density without self-consistently taking into account quark interaction with the instanton liquid (one first finds the diquark condensate and then determines the instanton-liquid density on the basis of it). It is interesting to note that quarks may affect the instanton liquid differently. For quarks in the phase of broken chiral symmetry, the density remains virtually constant, while, for quarks in the phase of color superconductivity, the instanton-liquid density decreases sharply (a nonsmooth behavior of the curves is due here to the disregard of the mixed phase, which must describe a smooth transition to the aforementioned regimes, where only the quark or only the diquark condensate does not vanish). In the first case, the corresponding analog of the tadpole contribution $\delta I/(\delta\rho)'$ in (6) is strictly positive; therefore, the inclusion of instanton-liquid interaction with quarks in this phase may only lead to an increase in the instanton-liquid density (gluon condensate). However, this increase appears to be insignificant, merely reflecting the sensitivity of the model to variations in the dynamical quark mass [3]. In the phase of a nonvanishing diquark condensate, the tadpole contribution is alternating, which, as can be seen from Fig. 5, leads to a sharp change in the character of the chemical-potential dependence of the instanton-liquid density, causing a significant reduction of the gluon condensate. Yet, this effect was previously indicated in [10].

ACKNOWLEDGMENTS

This work was supported in part by CERN–INTAS (grant no. 2000-349) and NATO (grant no. 2000-PST.CLG 977482). We thank the Fabergé Foundation for providing excellent conditions for work. S.V. Molodtsov is grateful to Prof. M. Namiki and the HUUJUKAI Fund for financial support and to Prof. P. Giubellino for interesting discussions and support.

REFERENCES

1. F. Karsch, hep-ph/0103314.
2. K. Rajagopal, Nucl. Phys. A **651**, 150c (1999); M. Alford, hep-ph/0110150.
3. S. V. Molodtsov and G. M. Zinovjev, Nucl. Phys. B (Proc. Suppl.) **106**, 471 (2002).
4. G. M. Zinovjev, S. V. Molodtsov, and A. M. Snigirev, Yad. Fiz. **65**, 961 (2002) [Phys. At. Nucl. **65**, 929 (2002)]; hep-ph/0004212.
5. G. W. Carter and D. I. Diakonov, Phys. Rev. D **60**, 016004 (1999).
6. R. Rapp, T. Schäfer, E. V. Shuryak, and M. Velkovsky, Ann. Phys. (N.Y.) **280**, 35 (2000).
7. D. I. Diakonov and V. Yu. Petrov, Nucl. Phys. B **245**, 259 (1984); in *Hadronic Matter under Extreme Conditions*, Ed. by V. Shelest and G. Zinovjev (Nauk. Dumka, Kiev, 1986), p. 192; D. I. Diakonov, V. Yu. Petrov, and P. V. Pobylitsa, Phys. Lett. B **226**, 471 (1989); C. G. Callan, R. Dashen, and D. J. Gross, Phys. Rev. D **17**, 2717 (1978); E.-M. Ilgenfritz and M. Müller-Preussker, Nucl. Phys. B **184**, 443 (1981); T. Schäfer and E. V. Shuryak, Rev. Mod. Phys. **70**, 323 (1998).
8. D. I. Diakonov, M. V. Polyakov, and C. Weiss, Nucl. Phys. B **461**, 539 (1996); D. I. Diakonov, hep-ph/9802298.
9. S. V. Molodtsov, A. M. Snigirev, and G. M. Zinovjev, Phys. Rev. D **60**, 056006 (1999); in *Lattice Fermions and Structure of the Vacuum*, Ed. by V. Mitrjushkin and G. Schierholz (Kluwer Acad. Publ., Dordrecht, 2000), p. 307; G. M. Zinov'ev, S. V. Molodtsov, and A. M. Snigirev, Yad. Fiz. **63**, 975 (2000) [Phys. At. Nucl. **63**, 903 (2000)].
10. N. O. Agasyan, D. Ebert, and E.-M. Ilgenfritz, Nucl. Phys. A **637**, 135 (1998); N. O. Agasyan, B. O. Kerbikov, and V. I. Shevchenko, Phys. Rep. **320**, 131 (1999); D. Ebert, V. V. Khudyakov, K. G. Klimenko, and V. Ch. Zhukovsky, hep-ph/0106110; D. Ebert, V. V. Khudyakov, H. Toki, *et al.*, hep-ph/0108185.

Translated by A. Isaakyan

Physics of Atomic Nuclei, Vol. 66, No. 7, 2003, pp. 1357–1374. Translated from Yadernaya Fizika, Vol. 66, No. 7, 2003, pp. 1398–1415.

ELEMENTARY PARTICLES AND FIELDS
Theory

Application of the Unitarity Conditions to Calculating Interaction Amplitudes for Ramond States in Superstring Theory

G. S. Danilov

Petersburg Nuclear Physics Institute, Russian Academy of Sciences, Gatchina, 188350 Russia

Received July 9, 2002

Abstract—The unitarity conditions for superstring amplitudes of boson interaction are used to calculate the Green's function for Ramond states—that is, for 10-spinor states and Ramond bosons. It is shown that, from the unitarity conditions, it follows, among other things, that local quantities specifying the sought amplitudes satisfy some integral relations. The amplitude for the transition of two massless Neveu–Schwarz bosons into a system of two massless Ramond states is obtained in an arbitrary order in the number of loops. For this amplitude, the aforementioned integral relations are verified in the tree approximation. © *2003 MAIK "Nauka/Interperiodica".*

1. INTRODUCTION

Within Ramond–Neveu–Schwarz superstring theory [1], it is rather difficult to calculate the interaction amplitudes for Ramond states (ten-dimensional spinors and Ramond bosons) [1–3]. In order to calculate such amplitudes for an arbitrary number of loops, it is proposed in this study to use the unitarity conditions for the amplitudes of the interaction of Neveu–Schwarz boson states. These amplitudes were obtained in [4–6] for a closed oriented string to any order of the coupling constant. In this study, we derive the amplitude for the transition of two massless bosons from the gravitational multiplet to the system of two massless Ramond states. Here, local quantities that determine the amplitude in question for an arbitrary number of loops $(n-1)$ are expressed in terms of local quantities that determine the n-loop amplitude for the scattering of massless bosons in the region where one of the handles degenerates. In the future, we hope to generalize the proposed method for calculating more general amplitudes.

The problem of calculating multiloop superstring amplitudes was discussed by a number of authors [7–14]. In the scheme proposed in [10], supersymmetry is lost, since multiloop superstring amplitudes depend on the choice of basis for gravitino zero modes [11, 12]. Yet, Hoker and Phong [15] recently proposed a procedure for eliminating this dependence. Anyway, the approaches considered in [10, 13] require an intricate modular parametrization, and this complicates their application to specific calculations. There is no such drawback in the supercovariant calculation [4–9], which employs a parametrization in terms of supergroups that are superconformal extensions of the Schottky groups. Such a parametrization is especially convenient for investigating the unitarity conditions since it arises in a natural way in matching [8] tree amplitudes.

Although only the contributions from the Neveu–Schwarz sector were known explicitly within this supercovariant approach for a long time [7–9], all contributions to boson-emission amplitudes for an arbitrary number of loops, including the contribution from the Ramond sector, have been calculated by now [4–6]. The required amplitudes are given in the form of finite-dimensional integrals of explicit functions with respect to the parameters of the super Schottky groups [7, 8, 16, 17] and the coordinates of interaction vertices in the complex (1|1) supermanifold [18]. The relevant integrand is the sum over the superspin structures defined in terms of the super Schottky groups. For all spin structures, including the Ramond sector, the super Schottky groups were obtained in [4, 5, 17]. A supergroup transformation depends on three Riemann and two Grassmann (odd) complex-valued parameters [18, 19]. At nonzero odd parameters, this transformation mixes boson and fermions, whence it follows that a supermanifold of genus $n > 1$ is not split in accordance with [20]. Therefore, superspin structures differ from ordinary spin structures [21], where boson fields are single-valued on Riemann surfaces and where fermion fields can acquire, upon rounds about noncontractible cycles, only a sign factor. Functions that characterize a transition to the split description of supermanifolds are singular [22], and a superstring is not invariant under this transformation. It is for this reason that supersymmetry is lost in the approach [10] that implies the split description of supermanifolds. A more detailed comparison

1063-7788/03/6607-1357$24.00

of the supercovariant approach with the approaches proposed in [10, 15] is planned to be given in a forthcoming publication.

The contribution to the amplitude of each superspin structure is given by the product of an integration measure and the vacuum expectation value of the product of vertices. The integration measures for even superspin structures[1)] were calculated explicitly by solving equations that were obtained in [4] on the basis of the condition requiring that multiloop amplitudes not depend on the choice of gauge of the zweibein and gravitino fields. For odd superspin structures, the partition functions were calculated by factorizing appropriate even structures [6]. The vacuum expectation values of the product of vertices are expressed in terms of the vacuum correlation functions for matter superfields; in turn, these correlation functions are expressed in terms of holomorphic Green's functions and quantities related to them (period matrix and holomorphic superscalar functions having periods). For a handle of the Ramond type, a nonidentity transformation corresponds to a round about an A cycle. At nonzero Grassmann moduli, this transformation is not split, and neither is the transformation corresponding to a round about a B cycle. In this case, holomorphic Green's functions cannot be represented in the form of a series of the Poincaré type. A method for calculating such Green's functions and quantities related to them was proposed in [23, 24]. All of the functions being discussed, including those in the Ramond sector, were calculated in [4–6].

It will be shown in Section 4 below that boson amplitudes satisfy the unitarity conditions upon cutting boson loops. The unitarity condition upon cutting fermion loops can be used to calculate the interaction amplitudes for states of the Ramond type. For this purpose, the discontinuity in energy (more precisely, in the corresponding bilinear 10-invariant) in the Neveu–Schwarz boson-interaction amplitude must be represented in the form of a trace associated with a fermion loop. Since Ramond states are described by Majorana–Weyl spinors [1], there are in the interaction amplitudes for Ramond states, no 10-spinor structures featuring an even number of Dirac 10-matrices sandwiched between spinor states. Therefore, the number of 10-spinor structures that can be involved in the amplitude is in general less than the number of conditions that can be locally satisfied by representing the aforementioned discontinuity in the energy variable as the trace associated with a fermion loop. Thus, the unitarity conditions require fulfillment of specific integral relations for local quantities determining the amplitude in question. In this study, we obtain such relations for the aforementioned four-leg diagram, which involves two massless bosons and two massless Ramond particles. So far, we have verified these relations only for this four-leg diagram in the tree approximation. The relations that arise for loop amplitudes require a dedicated investigation. It should be noted that only some general properties of integration measures and of vacuum correlation functions upon the degeneration of handles are of importance in deriving the unitarity conditions for boson amplitudes—the details of the expressions obtained in [4–6] are immaterial.

This article is organized as follows. In Section 2, we present an original expression for the amplitudes describing boson emission and some formulas that will be used below. In Section 3, we derive the two-particle unitarity condition for the amplitude being considered. In Section 4, we discuss the unitarity condition for a boson loop. In Section 5, we discuss the amplitude describing the transition of two bosons to two Ramond particles in an arbitrary order in the coupling constant. In Appendix A, we present, for the sake of convenience, explicit expressions for integration measures and for vacuum correlation functions. Some details of the calculations are given in Appendix B.

2. EXPRESSIONS FOR AMPLITUDES

As was indicated in the Introduction, the superstring n-loop amplitude can be expressed in terms of an integral of the sum over superspin structures defined on a complex (1|1) supermanifold [18] in terms of super Schottky groups [4, 5, 17] of genus n. This supergroup is specified by the set of transformations $\Gamma_{a,s}(l_{1s})$ and $\Gamma_{b,s}(l_{2s})$ corresponding to rounds about A_s and B_s cycles on a Riemann surface of genus n, where $s = 1, 2, \ldots, n$. In general, each transformation depends on three even and two odd (Grassmann) parameters. Each pair including $\Gamma_{a,s}(l_{1s})$ and $\Gamma_{b,s}(l_{2s})$ is a superconformal extension of the Schottky transformations $\Gamma^{(0)}_{a,s}(l_{1s})$ and $\Gamma^{(0)}_{b,s}(l_{2s})$, which are given by (below, z is a local coordinate on the supermanifold and ϑ is its superpartner)

$$\Gamma^{(0)}_{b,s}(l_{2s}) = \left\{ z \to \frac{a_s z + b_s}{c_s z + d_s}, \quad \vartheta \to -\frac{(-1)^{2l_{2s}}\vartheta}{c_s z + d_s} \right\},$$
$$\Gamma^{(0)}_{a,s}(l_{1s}) = \{ z \to z, \quad \vartheta \to (-1)^{2l_{1s}}\vartheta \}, \tag{1}$$

where l_{1s} and l_{2s} are the characteristics of the theta function that are attributed to a particular handle s. They can only take values of 0 and 1/2—more specifically, $l_{1s} = 0$ for a boson loop and $l_{1s} = 1/2$ for a fermion loop. In the last case, $l_{2s} = 0$ and $l_{2s} = 1/2$

[1)] A superspin structure is even (odd) if the spin structure corresponding to it is even (odd).

define a loop of, respectively, even and odd spin structure. Further, we have $a_s d_s - b_s c_s = 1$ with

$$a_s = \frac{u_s - k_s v_s}{\sqrt{k_s}(u_s - v_s)}, \quad d_s = \frac{k_s u_s - v_s}{\sqrt{k_s}(u_s - v_s)}, \quad (2)$$
$$c_s = \frac{1 - k_s}{k_s(u_s - v_s)},$$

where k_s is the Schottky dilatation parameter and u_s and v_s are fixed points of the transformation. Without loss of generality, we can assume that $|k_s| < 1$ and $|\arg k_s| \le \pi$. Expressions (2) can be supersymmetrized in different ways, but in this case, the 1/2-form space will not in general have a basis [25]. There will then arise difficulties in constructing vacuum correlation functions for scalar superfields, with the result that such a supersymmetrization will be inappropriate for describing superstrings. In order to construct [4, 26] the required extension of formulas (1), it is necessary to consider that, at $n = 1$, superstring-interaction amplitudes are obtained by means of summation over ordinary spin structures. In calculating the pole contribution to the amplitude, in which case a given handle is separated from the others, the odd parameters of this handle therefore cease to be moduli. For each number s, all odd modular parameters in $\Gamma_{a,s}(l_{1s})$ and $\Gamma_{b,s}(l_{2s})$ must then reduce to zero by the same transformation $\tilde{\Gamma}_s$. Therefore, we have

$$\Gamma_{a,s}(l_{1s}) = \tilde{\Gamma}_s^{-1}\Gamma_{a,s}^{(0)}(l_{1s})\tilde{\Gamma}_s, \quad (3)$$
$$\Gamma_{b,s}(l_{2s}) = \tilde{\Gamma}_s^{-1}\Gamma_{b,s}^{(0)}(l_{2s})\tilde{\Gamma}_s,$$

where $\Gamma_{a,s}^{(0)}(l_{1s})$ and $\Gamma_{b,s}^{(0)}(l_{2s})$ are transformations of the type in (1), while $\tilde{\Gamma}_s$ is the $(z \to z_s, \vartheta \to \vartheta_s)$ transformation, which depends on the odd parameters μ_s and ν_s:

$$\tilde{\Gamma}_s = \{z = z_s + \vartheta_s \varepsilon_s(z_s), \quad (4)$$
$$\vartheta = \vartheta_s(1 + 1/2\varepsilon_s(z_s)\varepsilon_s'(z_s)) + \varepsilon_s(z_s)\},$$

where

$$\varepsilon_s' = \partial_z \varepsilon_s(z) \text{ and } \varepsilon_s(z) = \frac{\mu_s(z - v_s) - \nu_s(z - u_s)}{u_s - v_s}.$$

It follows from (1) and (4) that, under the transformations in (3), the points $(u_s|\mu_s)$ and $(v_s|\nu_s)$ on the complex (1|1) supermanifold remain unchanged. At $l_{1s} = 1/2$, the transformation $\Gamma_{a,s}(l_{1s} = 1/2)$ differs from the identity transformation, but $\Gamma_{a,s}^2 = 1$. This means that superfields develop a square-root cut on the complex plane of z. Each transformation in (3) converts the circle $C_s^{(+)}$ into the circle $C_s^{(-)}$, where

$$C_s^{(-)} = \{z : |c_s z_s + d_s| = 1\}, \quad (5)$$
$$C_s^{(+)} = \{z : |-c_s z_s + a_s| = 1\},$$

z_s being related to z by transformation (4). Under the transformations $\Gamma_{a,s} = \{t \to t_s^a\}$ and $\Gamma_{b,s} = \{t \to t_s^b\}$, the supersymmetric p tensors $\hat{F}_p(t)$ change as

$$\hat{F}_p(t_s^a) = \hat{F}_p^{(s)}(t)Q_{\Gamma_{a,s}}^p(t), \quad \hat{F}_p(t_s^b) = \hat{F}_p(t)Q_{\Gamma_{b,s}}^p(t), \quad (6)$$

where the function $\hat{F}_p^{(s)}(t)$ is obtained from $\hat{F}_p(t)$ by means of a round about the circle $C_s^{(-)}$ or $C_s^{(+)}$. By $Q_{\Gamma_{a,s}}(t)$ and $Q_{\Gamma_{b,s}}(t)$, we denote those factors that the spinorial derivative $D(t)$ acquires upon applying the transformations $\Gamma_{a,s}(l_{1s})$ and $\Gamma_{b,s}(l_{2s})$, respectively. For an arbitrary superconformal transformation $\Gamma = \{t \to t_\Gamma\}$, the factor $Q_\Gamma(t)$ is defined as follows:

$$D(t_\Gamma) = Q_\Gamma(t)D(t), \quad D(t) = \theta\partial_z + \partial_\theta. \quad (7)$$

Thus, (3|2) complex parameters (k_s, u_s, v_s) and (μ_s, ν_s) correspond to each handle. The n-loop superstring amplitude is given by an integral with respect to these parameters and their complex conjugate counterparts and with respect to the coordinates $t_j = (z_j|\vartheta_j)$ of interaction vertices on the relevant supermanifold. Any (3|2) complex variables $\{N_0\}$ are then fixed owing to $SL(2)$ symmetry, and this leads to emergence of an additional factor $|H(\{N_0\})|^2$ in the integrand. This factor was calculated in [4]. In the following, we fix two local variables u and v, together with their Grassmann partners, which are chosen to be zero, and the third local variable z_4. In this case, we have

$$|H(\{N_0\})|^2 = |(z_4 - u)(z_4 - v)|^2. \quad (8)$$

In the amplitude for the interaction of m bosons, each term of the sum over superspin structures is the product of the integration measure $Z_{L,L'}^{(n)}(\{q, \overline{q}\})$ and the vacuum expectation value $F_m^{(n)}(\{t_j, \overline{t}_j\}, \{p_j, \epsilon^{(j)}\}, \{q, \overline{q}\}; L, L')$ of the product of all interaction vertices (from $j = 1$ to $j = m$) with the coordinates $t_j = (z_j|\vartheta_j)$ on the supermanifold.[2)] We denote by $\{q\}$ the set of parameters of the super Schottky groups and by p_j and $\epsilon^{(j)}$ the momentum of the jth boson and its polarization tensor, respectively. By L and L', we denote the superspin structures of, respectively, holomorphic and antiholomorphic fields. According to (1) and (3), superspin structures are specified, in just the same way as ordinary spin structures [21], by the characteristics l_{1s} and l_{2s} of the theta function that are attributed to a given handle s. Thus, the n-loop amplitude $A_m^{(n)}(\{p_j, \epsilon^{(j)}\})$ for the interaction of m bosons has the form

$$A_m^{(n)}(\{p_j, \epsilon^{(j)}\}) = \frac{g^{2n+2}}{2^n n!} \quad (9)$$

[2)] Hereafter, an overbar denotes complex conjugation.

$$\times \int |H(\{N_0\})|^2 \sum_{L,L'} Z^{(n)}_{L,L'}(\{q,\bar{q}\})$$

$$\times F^{(n)}_m(\{t_j,\overline{t}_j\},\{p_j,\epsilon^{(j)}\},\{q,\bar{q}\};L,L')(dqd\bar{q}dtd\bar{t})',$$

where $(dqd\bar{q}dtd\bar{t})'$ stands for the product of the differentials of all coordinates of interaction vertices and modular parameters, with the exception of those $(3|2)$ that are fixed owing to $SL(2)$ symmetry. Further, g is the coupling constant and the rest of the notation was given above. Since we will discuss the four-leg diagram featuring massless bosons, only even superspin structures (including those that involve an even number of fermion loops of odd spin structures) are present in expression (9). The factor of $1/2^n$ takes into account symmetry under the permutation of the fixed points $U_s = (u_s|\mu_s)$ and $V_s = (v_s|\nu_s)$ for a given handle, while the factor of $1/n!$ reflects symmetry under the permutation of handles. For any boson variable x, we define $dxd\overline{x} = d(\mathrm{Re}x)d(\mathrm{Im}x)/(4\pi)$. For any Grassmann variable η, we define $\int d\eta\eta = 1$. The string tension will be taken to be $1/\pi$. Our normalization conditions correspond to the normalization conditions in [1]. The vertex describing the emission of a massless boson (in our normalization) characterized by a 10-momentum $p = \{p_M\}$ and polarization 10-vectors $\zeta = \{\zeta_M\}$ and $\zeta' = \{\zeta'_M\}$ for, respectively, left- and right-handed fields ($M = 0,\ldots,9$) has the form [2]

$$V(t,\overline{t};p;\zeta) \tag{10}$$

$$= 4[\zeta D(t)X(t,\overline{t})][\overline{\zeta' D(t)}X(t,\overline{t})]\exp[ipX(t,\overline{t})],$$

where, for the two 10-vectors a and b, the quantity $ab = a_M b^M$ denotes their scalar product, the mostly plus metric being predominantly used here. By $X^N(t,\overline{t})$, we imply the scalar superfield of a string. Further, $p\zeta = p\zeta' = 0$ and $p^2 = 0$; the spinorial derivative $D(t)$ was defined in (7). In this case, the quantity $F^{(n)}_m(\{t_j,\overline{t}_j\},\{p_j,\epsilon^{(j)}\},\{q,\bar{q}\};L,L') \equiv F^{(n)}_m(\{t_j,\overline{t}_j\},\{p_j,\epsilon^{(j)}\})$ appearing in (9) is expressed [1] in terms of the vacuum correlation function $\hat{X}_{L,L'}(t_j,\overline{t}_j;t_l,\overline{t}_l;\{q\}) \equiv \hat{X}(j,l)$ for scalar superfields in the form of an integral with respect to auxiliary Grassmann parameters $\{\eta_j,\overline{\eta}_j\}$ associated with each boson; that is,

$$F^{(n)}_m(\{t_j,\overline{t}_j\},\{p_j,\epsilon^{(j)}\}) = \int (d\eta d\bar{\eta}) \tag{11}$$

$$\times \exp\left[-\frac{1}{2}\sum_{j,l}(\hat{\kappa}_j + ip_j)(\hat{\kappa}_l + ip_l)\hat{X}(j,l)\right],$$

where the operator $\hat{\kappa}_j$ is defined as the sum $\hat{\kappa}_j = \kappa_j + \overline{\kappa'_j}$ of the two operators; here, $\kappa_j = 2\eta_j\zeta_{(j)}D(t_j)$ and, accordingly, $\kappa'_j = 2\eta_j\zeta'_{(j)}D(t_j)$. In these formulas, $\zeta_{(j)}$ and $\overline{\zeta'_{(j)}}$ describe the polarization of the jth boson, so that $\zeta_{(j)M}\overline{\zeta'_{(j)N}} = \epsilon^{(j)}_{MN}$. All of the momenta are considered to be entering the diagram.

A vacuum correlation function is expressed in terms of the holomorphic Green's function $R^{(n)}_L(t,t';\{q\})$ and the superscalar functions $J^{(n)}_s(t;\{q\};L)$, where $s = 1,\ldots,n$; that is,

$$4\hat{X}_{L,L'}(t,\overline{t};t',\overline{t}';\{q,\bar{q}\}) = R^{(n)}_L(t,t';\{q\}) \tag{12}$$

$$+ \overline{R^{(n)}_{L'}(t,t';\{q\})} + I^{(n)}_{LL'}(t,\overline{t};t',\overline{t}';\{q,\bar{q}\}),$$

$$I^{(n)}_{LL'}(t,\overline{t};t',\overline{t}';\{q,\bar{q}\}) = [J^{(n)}_s(t;\{q\};L) \tag{13}$$

$$+ \overline{J^{(n)}_s(t;\{q\};L')}][\Omega^{(n)}_{L,L'}(\{q,\overline{q}\})]^{-1}_{sr}$$

$$\times [J^{(n)}_r(t';\{q\};L) + \overline{J^{(n)}_r(t';\{q\};L')}],$$

where the matrix $\Omega^{(n)}_{L,L'}(\{q,\overline{q}\})$ is expressed in terms of the period matrix $\omega^{(n)}(\{q\},L)$ as

$$\Omega^{(n)}_{L,L'}(\{q,\overline{q}\}) = 2\pi i[\overline{\omega^{(n)}(\{q\},L')} - \omega^{(n)}(\{q\},L)]. \tag{14}$$

Because of boson–fermion mixing, the period matrix $\omega^{(n)}(\{q\},L)$ depends [4, 8] on the superspin structure L. The Green's function is normalized by the condition

$$R^{(n)}_L(t,t';\{q\}) = \ln(z - z' - \vartheta\vartheta') + \tilde{R}^{(n)}_L(t,t';\{q\}), \tag{15}$$

where $\tilde{R}^{(n)}_L(t,t';\{q\})$ is not singular at $z = z'$. As usual, the function $R^{(n)}_L(t,t';\{q\})$ at coinciding arguments $t = t'$ is taken to be $\tilde{R}^{(n)}_L(t,t;\{q\})$. The correlation function in (12) at coinciding arguments is calculated in the same way. When the coordinates change as $t \to t^b_s$ and $t \to t^a_s$ under the transformations of the super Schottky group that correspond to the rounds about, respectively, the B_s and the A_s cycle, the holomorphic Green's functions being discussed satisfy the relations

$$R^{(n)}_L(t^b_s,t';\{q\}) = R^{(n)}_L(t,t';\{q\}) + J^{(n)}_s(t';\{q\};L), \tag{16}$$

$$R^{(n)}_L(t^a_s,t';\{q\}) = R^{(n)(s)}_L(t,t';\{q\}),$$

where $R^{(n)(s)}_L(t,t';\{q\})$ is the function obtained from $R^{(n)}_L(t,t';\{q\})$ by means of a round about the Schottky circle (5) corresponding to the A_s cycle [it should be noted that, according to formulas (1) and (3), the

Green's function for a Ramond handle has a square-root branch point]. Further, we have

$$J_r^{(n)}(t_s^b;\{q\};L) = J_r^{(n)}(t;\{q\};L) + 2\pi i\omega_{sr}(\{q\},L), \quad (17)$$
$$J_r^{(n)}(t_s^a;\{q\};L) = J_r^{(n)(s)}(t;\{q\};L) + 2\pi i\delta_{rs},$$

where $J_r^{(n)(s)}$ is obtained by means of a round of $J_r^{(n)}$ about the A_s cycle [from (3), it follows that, because of boson–fermion mixing, $J_r^{(n)}$ at nonzero Grassmann moduli has a branch point associated with a round about the Schottky circle for a Ramond handle]. The problem of constructing the required functions will be solved if we construct functions that satisfy the conditions in (16) and (17). In the Neveu–Schwarz sector and for a bosonic string [7–9, 27, 28], these functions can be specified in the form of Poincaré-type series. In particular, the relevant expressions for a bosonic string are given in [4] (Appendix B). In the Neveu–Schwarz sector, the expressions for a superstring can be obtained from the expressions for a bosonic string by substituting the superinterval $\ell(t_1,t_2) = (z_1 - z_2 - \vartheta_1\vartheta_2)$ for the interval $(z_1 - z_2)$. In this case [$R_L^{(n)}(t,t') \equiv R_L^{(n)}(t,t';\{q\})$], we have

$$D(t')R_L^{(n)}(t,t') = \sum_\Gamma \frac{(\vartheta - \vartheta'_\Gamma)D(t')\vartheta'_\Gamma}{\ell(t,t'_\Gamma)}, \quad (18)$$
$$J_r^{(n)}(t;\{q\};L) = \sum_\Gamma{}' \ln\frac{\ell(t,U_\Gamma^{(r)})}{\ell(t,V_\Gamma^{(r)})},$$
$$2\pi i\omega_{sr}(\{q\},L) = \delta_{rs}\ln k_s + \sum_\Gamma{}'' \ln\frac{\ell(U^{(s)},U_\Gamma^{(r)})\ell(V^{(s)},V_\Gamma^{(r)})}{\ell(U^{(s)},V_\Gamma^{(r)})\ell(V^{(s)},U_\Gamma^{(r)})},$$

where, as before, $U^{(s)} = (u_s|\mu_s)$ and $V^{(s)} = (v_s|\nu_s)$ and $t_\Gamma = (z_\Gamma,\vartheta_\Gamma)$ is the result of applying the transformation Γ to $t = (z|\vartheta)$. In the first formula in (18), summation is performed over all group products Γ of the transformations $\Gamma_{b,s}(l_{2s})$ of the super Schottky group [see (3)]. In the second formula, the sum does not include those Γ that contain powers of the transformation $\Gamma_{b,r}(l_{2r})$ on the right. In the third formula, those Γ that involve powers of the transformation $\Gamma_{b,s}(l_{2s})$ on the left are additionally excluded from the sum. At $s = r$, the sum does not involve the term corresponding to the identity transformation either. In the Ramond sector, the Green's functions cannot be written in the form of Poincaré-type series at nonzero Grassmann moduli, since, according to (3), the transformation corresponding to a round about the circles in (5) is not split in this case. In any case, they can nevertheless be specified in the form of series where each term of the series can be represented in the form of an integral where known functions of genus 1 appear as integrands (Appendix A).

The integration measures in (9) are calculated from the equations derived in [4, 9] from the requirement that the relevant amplitude be independent of the choice of the zweibein and the field of the two-dimensional gravitino. Owing to the separation of holomorphic and antiholomorphic fields [29], the integration measure in (9) has the form [4]

$$Z_{L,L'}^{(n)}(\{q,\overline{q}\}) = (8\pi)^{5n}[\det\Omega_{L,L'}^{(n)}(\{q,\overline{q}\})]^{-5} \times Z_L^{(n)}(\{q\})\overline{Z_{L'}^{(n)}(\{q\})}, \quad (19)$$

where the matrix $\Omega_{L,L'}^{(n)}(\{q,\overline{q}\})$ is given by (14) and $Z_L^{(n)}(\{q\})$ is a holomorphic function of the variables $\{q\}$ that can be written as

$$Z_L^{(n)}(\{q\}) = \tilde{Z}^{(n)}(\{q\},L) \times \prod_{s=1}^n \frac{Z^{(1)}(k_s;l_{1s},l_{2s})}{k_s^{(3-2l_{1s})/2}(u_s - v_s - \mu_s\nu_s)}. \quad (20)$$

Here, l_{1s}, l_{2s} takes the values of 0 or 1/2, as was indicated above; the function $\tilde{Z}^{(n)}(\{q\},L)$ is given in Appendix A; and, for $Z^{(1)}(k;l_1)$, we have

$$Z^{(1)}(k;l_1,l_2) = (-1)^{2l_1+2l_2}16^{2l_1} \times \prod_{p=1}^\infty \frac{[1+(-1)^{2l_2}k^pk^{(2l_1-1)/2}]^8}{[1-k^p]^8}. \quad (21)$$

The domain of integration in (9) will be discussed in a future publication. We only note now that the integral with respect to the vertex coordinates in (9) is calculated over the fundamental domain [4, 5] of the super Schottky group—for this domain, one can choose the domain that is external with respect to the circles specified in (5). The domain of integration with respect to the modular parameters is predominantly determined by modular symmetry. Here, the dilatation parameters $|k_j| \to 1$ can be eliminated from the region being considered. There then appear unitarity discontinuities of the amplitudes [1] if some or all dilatation parameters tend to zero, $k_j \to 0$.

3. TWO-PARTICLE UNITARITY CONDITION

Two-particle discontinuities arise upon integration over the region where the only one dilatation parameter tends to zero, $k \to 0$. In this case, it is convenient to fix in (9) a local coordinate of one of the interaction vertices—for example, z_4—and both limiting points $U = (u|\mu)$ and $V = (v|\nu)$ of that transformation in (3) for which $k \to 0$. We set $\mu = \nu = 0$. The factor $|H(\{N_0\})|^2$ in (9) is then given by (8).

For the sake of definiteness, we will calculate the discontinuities in the invariant quantity $s = -(p_1 + p_2)^2 = -(p_3 + p_4)^2$. They emerge upon integration over the region where z_1 and z_2 tend to u or to v, remaining beyond the Schottky circles. The region where z_2 tends to v makes the same contribution to the integral as the region where $z_2 \to u$. Therefore, we assume that $z_2 \to u$ and then double the result obtained in this way. In addition, we must multiply the result by n since each of the n handles can play the role of the degenerate handle being considered.

If $z_2 \to u$, then $z_1 \to u$ or $z_1 \to v$. The second case reduces to the first by the corresponding Schottky transformation of the coordinate z_1, whereupon z_1 appears to be within a circle containing the point u. Therefore, we assume that $z_1 \to u$ and $z_2 \to u$, but z_1 can be either beyond or within the Schottky circle, while z_2 lies beyond this Schottky circle. According to (2) and (5), we then have

$$|z_2 - u| \geq \sqrt{k}|u - v|. \tag{22}$$

For the sake of simplicity, we will calculate that part of the discontinuity which is given by the product of the tree and the $(n-1)$-loop amplitude. It is determined by a configuration where the limiting points of the remaining basis transformations of the Schottky group are not close to u. We discuss only massless states.

In the limit $k \to 0$, the singularity of the integration measures in (19) emerges owing to the factor $1/k^{(3-2l_1)/2}$ in (20). The leading singularity of the $1/k^{3/2}$ form for a handle of the Neveu–Schwarz type (in this case, $l_1 = 0$; see Section 2) cancels in the sum of two terms corresponding to $l_2 = 0$ and $l_2 = 1/2$. Indeed, expression (9) is an even function of $\sqrt{k}$. Therefore, the leading singularity appears to be of the $1/|k|^2$ type, the coefficient of $1/|k|^2$ being logarithmically dependent on $|k|$ through the period matrix (see Appendix A). Terms of higher order in powers of k do not contribute to the sought discontinuity, which is caused by massless particles. To the required accuracy, we represent the contribution W of the region under discussion to the integral in (9) as an integral of the sum of expressions factorized in the initial and final states with respect to the momentum $\tilde{p}_1$ flowing along the loop in question; that is,

$$W = \int \frac{2d^{10}\tilde{p}_1}{\tilde{p}_1^2\tilde{p}_2^2} \sum_{\lambda,\lambda'} \hat{A}_{(0)}(\{p,\epsilon\}_{(i)}, \tilde{p}_1; \lambda, \lambda') \hat{A}_{(n-1)}(\lambda, \lambda'; \tilde{p}_1, \{p,\epsilon\}_{(f)}), \tag{23}$$

where $\tilde{p}_1 + \tilde{p}_2 = P = p_1 + p_2 = -(p_3 + p_4)$ and the summation is taken over the polarizations λ, λ' of intermediate states of holomorphic (λ) and antiholomorphic (λ') fields. In each term, the first factor depends on the momenta and polarizations of particles in the initial $[\{p,\epsilon\}_{(i)} = (p_1, p_2, \epsilon^{(1)}, \epsilon^{(2)})]$ and the intermediate state, while the second factor depends on the parameters of the intermediate and final $[\{p,\epsilon\}_{(f)} = (p_3, p_4, \epsilon^{(3)}, \epsilon^{(4)})]$ states. These factors were calculated at $\tilde{p}_1^2 = \tilde{p}_2^2 = 0$. The sought unitary discontinuity, which emerges from the vanishing of the denominator $(\tilde{p}_1^2\tilde{p}_2^2)$ can easily be calculated. From a comparison with the unitarity condition, it follows that, under the normalization condition adopted in this study, $\hat{A}_{(0)}(\{p,\epsilon\}_{(i)}, \tilde{p}_1; \lambda, \lambda')$ and $\hat{A}_{(n-1)}(\lambda, \lambda'; \tilde{p}_1, \{p,\epsilon\}_{(f)})$ are, respectively, the tree and the $(n-1)$-loop amplitude. In this case, the corresponding unitarity condition is satisfied for a boson loop and the sought interaction amplitudes for Ramond states are calculated from the unitarity condition for a fermion loop. In order to derive formula (23) itself, the vacuum expectation value in (9) is represented in the form of the integral (11) with respect to $(d\eta d\bar{\eta})$, whereupon, in the limit $k \to 0$, each term $\hat{W}$ in the integrand in (9) is written to the required accuracy in the form of a Gaussian integral with respect to the momentum flowing in the loop:

$$\begin{aligned}\hat{W} = \int d^{10}\tilde{p}_1 \exp[\tilde{G}_0 + \tilde{G}_1\tilde{p}_1^2 + \tilde{B}_1\tilde{p}_1] \\ \times \exp[G_1\tilde{p}_1^2 + G_{12}\tilde{p}_1\tilde{p}_2 + G_2\tilde{p}_2^2 + B_1\tilde{p}_1 \\ + B_2\tilde{p}_2 + G_0] O_{\tilde{L}}(\{p\}, \{\zeta\}, \tilde{p}_1, \{t\}, \{q\}) \\ \times \overline{O_{\tilde{L}'}(\{p\}, \{\zeta'\}, \tilde{p}_1, \{t\}, \{q\})} \\ \times \hat{Z}^{(n-1)}_{\tilde{L},\tilde{L}'}(\{q, \bar{q}\})|(z_4 - u)(z_4 - v)|^2.\end{aligned} \tag{24}$$

Below we demonstrate that, upon performing the above integrations in (9), expression (24) reduces to the sought form (23). In (24), all 10-vectors are assumed to be Euclidean. The quantities in the integrand depend on the type of the degenerate loop being considered. The coefficients $\tilde{G}_0$, $\tilde{G}_1$, and $\tilde{B}_1$ depend on the initial state, as well as on $y = \ln|k|$ and on $(u, \bar{u})$. The coefficients in the exponent of the second exponential function depend on the final state and on modular parameters (with the exception of the dilatation parameters $k = 0$). They also depend on the spin structures $(\tilde{L}, \tilde{L}')$ formed by all handles, apart from the degenerate one. The

expression $|(z_4-u)(z_4-v)|^2$ in (24) is the factor $|H(\{N_0\})|^2$ in (9) as specified by formula (8). The sets of the momenta, polarizations, and coordinates of the vertices describing boson emission in the initial and final states are denoted by $\{p\}$, $\{\zeta\}$, $\{\zeta'\}$, and $\{t,\bar{t}\}$. The factors $O_{\tilde{L}}(\{p\},\{\zeta\},\tilde{p}_1,\{t\},\{q\})$ and $\overline{O_{\tilde{L}'}(\{p\},\{\zeta'\},\tilde{p}_1,\{t\},\{q\})}$ emerged from the expansion of holomorphic and antiholomorphic functions in (19) and (11) in the small parameters k, (z_1-u), and (z_2-u). Owing to the nonholomorphic factor in (19) and the last term in (12), the factor $O_{\tilde{L}}(\{p\},\{\zeta\},\tilde{p}_1,\{t\},\{q\})$ at $n>1$ depends on $\{\bar{t}\}$, $\{\bar{q}\}$, and L' as well, while the factor $\overline{O_{\tilde{L}'}(\{p\},\{\zeta'\},\tilde{p}_1,\{t\},\{q\})}$ depends on $\{t\}$, $\{\bar{q}\}$, and L. These factors can depend polynomially on $\tilde{p}_1$. Each of the factors is the sum of expressions that are factorized with respect to the initial and the final state. The factor $\hat{Z}^{(n-1)}_{\tilde{L},\tilde{L}'}(\{q,\bar{q}\})$ is caused by the partition function. The explicit form of all of the quantities being discussed will be obtained in the sections that follow. In deriving expression (24), we use the following formulas for the determinant of the n-dimensional matrix Ω and for the quadratic form $J\Omega^{-1}J$ of n quantities J_s (where $s=1,\ldots,n$):

$$J\Omega^{-1}J=[J_1(1-\Omega_{1j_1}\tilde{\Omega}^{-1}_{j_1l_1})J_{l_1}]^2 \times[\Omega_{11}-\Omega_{1j}\tilde{\Omega}^{-1}_{jl}\Omega_{l1}]^{-1}+J_j\tilde{\Omega}^{-1}_{jl}J_l, \tag{25}$$

$$\det\Omega=\det\{\Omega_{jl}\}[\Omega_{11}-\Omega_{1j_1}\tilde{\Omega}^{-1}_{j_1l_1}\Omega_{l_11}].$$

Here, we imply summation over dummy indices, these running through the values from 2 to n. In addition, we have used the notation $\tilde{\Omega}=\{\Omega_{jl}\}$. The coefficients of J_pJ_s (including $p,s=1$) in (25) are nothing but the corresponding elements Ω^{-1}_{ps} expressed in terms of the elements of the matrix Ω. The second formula in (25) follows from the equality $\ln\det\Omega=\mathrm{tr}\ln\Omega$ if we calculate $\mathrm{tr}\ln\Omega$ in terms of Ω_{11}, Ω_{1j_1}, $\tilde{\Omega}^{-1}_{j_1l_1}$, and Ω_{l_11}.

If, instead of z_1, we introduce the variable $z=(z_1-u)/(z_2-u)$, the entire dependence on z_2 and y in (24) is factored out in the form $|z_2-u|^{-2}\exp[x(\tilde{p}_2^2-\tilde{p}_1^2)/4+y\tilde{p}_1^2/4]$, where $x=\ln|z_2-u|$. Here, $-\infty<y<0$ and, according to (22), $y/2<x<0$. Hence, the integral of expression (24) with respect to z_2 and y is $4/[\tilde{p}_1^2(\tilde{p}_1^2+\tilde{p}_2^2)]$. Since the product $O_{\tilde{L}}(\{p\},\{\zeta\},\tilde{p}_1,\{t\},\{q\})\times\overline{O_{\tilde{L}'}(\{p\},\{\zeta'\},\tilde{p}_1,\{t\},\{q\})}$ in (24) is symmetric under the substitution $\tilde{p}_1\rightleftharpoons\tilde{p}_2$, the result can be replaced by $2(\tilde{p}_1^2\tilde{p}_2^2)^{-1}$. In the resulting integral, we can additionally shift the contour of integration in the tenth component of the vector $\tilde{p}_1$ to the imaginary axis. As a result, we arrive at the required formula (23). Concurrently, the tree amplitude arises in the form of an integral where the coordinates $(0|0)$ and $(\infty|0)$ of the particles in the intermediate state (with momenta $\tilde{p}_1$ and $\tilde{p}_2$, respectively) and the local coordinate z_2 are fixed. In the integral for the $(n-1)$-loop amplitude, the coordinates $(v|0)$ and $(u|0)$ of the particles having the momenta $\tilde{p}_1$ and $\tilde{p}_2$, respectively, and the local coordinate z_4 are fixed.

4. UNITARITY FOR A BOSON LOOP

First, we discuss the unitarity condition for a boson loop. In the case of $k\to0$, we then have $J_1^{(n)}(t;\{q\};L)\equiv J_1(t)$. In addition, the elements $\omega^{(n)}(\{q\},L)_{11}\equiv\omega_{11}$ and $\omega^{(n)}(\{q\},L)_{1l}\equiv\omega_{1l}$ of the period matrix can be expressed in terms of the holomorphic Green's function $R^{(n-1)}_{\tilde{L}}(t,t';\{q\})\equiv R(t,t')$ and the scalar functions $J_1^{(n-1)}(t;\{q\};\tilde{L})\equiv J_l(t)$ on the supermanifold of genus $(n-1)$ formed by the remaining handles as

$$2\pi i\omega_{11}=\ln k+R(U,U)+R(V,V)-R(U,V)-R(V,U), \tag{26}$$

$$2\pi i\omega_{1l}=J_l(U)-J_l(V),$$

$$J_1(t)=R(t,U)-R(t,V),$$

where $U=(u|0)$ and $V=(v|0)$. Formula (26) directly follows from (18) for $k\to0$. We examine a loop that is bosonic both for holomorphic and for antiholomorphic fields—that is, $l_1=l_1'=0$. By taking into account (26), we then find that the coefficients determining the exponential functions in (24) are

$$B_1=-i\sum_{j=3}^{4}(\hat{\kappa}_j+ip_j)\hat{X}(t_j,\bar{t}_j;V,\bar{V}), \tag{27}$$

$$B_2=-i\sum_{j=3}^{4}(\hat{\kappa}_j+ip_j)\hat{X}(t_j,\bar{t}_j;U,\bar{U}),$$

$$G_0=-\frac{1}{2}\sum_{j,l=3}^{4}(\hat{\kappa}_j+ip_j)(\hat{\kappa}_l+ip_l)\hat{X}(t_3,\bar{t}_3;t_4,\bar{t}_4),$$

$$G_{12}=\hat{X}(U,\bar{U};V,\bar{V}),$$

$$G_1=\hat{X}(V,\bar{V};V,\bar{V})+\ln|u-v|,$$

$$G_2=\hat{X}(U,\bar{U};U,\bar{U}),$$

$$\tilde{G}_0=-(\hat{\kappa}_1+ip_1)(\hat{\kappa}_2+ip_2)\frac{1}{2}\ln|z_1-z_2-\vartheta_1\vartheta_2|,$$

$$\tilde{G}_1=\frac{1}{4}\ln|k|,\quad \tilde{B}_1=i\sum_{j=1}^{2}(\hat{\kappa}_j+ip_j)\frac{1}{2}\ln|z_j-u|,$$

where $U=(u|0)$ and $V=(v|0)$; the operators $\hat{\kappa}_j$ have the same form as in (11); and $\hat{X}(t,\bar{t};t',\bar{t}')$ is

the correlation function (12) on the supermanifold of genus $(n-1)$ formed by all handles, with the exception of the degenerate handle being considered. The quantity $\tilde{G}_0$, as well as each term in the expression for $\tilde{B}_1$, is a correlation function defined on a surface of genus 0 and calculated for the corresponding points. The nonexponential factors in (24) are independent of $\tilde{p}_1$ and $\tilde{p}_2$. In calculating them in the expansion in k, one must retain, in view of the estimates $|z_1-u| \sim |z_2-u| \sim \sqrt{|k|}$ and $\vartheta_1 \sim \vartheta_2 \sim |k|^{1/4}$, terms that are not less than unity. In order to verify the validity of expressions (27), we must substitute them into (24) and calculate the resulting integral. In performing a comparison with the amplitude in (9), use is made of formulas (25), where the subscript "1" is associated with the degenerate handle.

By way of example, we will consider a one-loop amplitude ($n=1$). The vacuum correlation function $\hat{X}(t,\bar{t};t',\bar{t}')$ in (27) is then equal to $(\ln|z_1-z_2-\vartheta_1\vartheta_2|)/2$, while the factor $\hat{Z}^{(n-1)}_{\tilde{L},\tilde{L}'}(\{q,\bar{q}\})$ in (24) reduces to unity. We note in addition that the product $O_{\tilde{L}}(\{p\},\{\zeta\},\tilde{p}_1,\{t\},\{q\})\overline{O_{\tilde{L}'}(\{p\},\{\zeta'\},\tilde{p}_1,\{t\},\{q\})}$ is written in the form $O_{(b)}(\{\zeta\})\overline{O_{(b)}(\{\zeta'\})}$, the holomorphic function $O_{(b)}(\{\zeta\})$ here being the sum over the polarization 10-vectors $\tilde{\zeta}_1$ and $\tilde{\zeta}_2$ of bosons whose momenta are $\tilde{p}_1$ and $\tilde{p}_2$; that is,

$$O_{(b)} = \sum_{\tilde{\zeta}_1,\tilde{\zeta}_2}\left[-\tilde{\zeta}_1\tilde{\zeta}_2 + \sum_{j=1}^{2}\tilde{\zeta}_1\frac{(\kappa_j+ip_j)\vartheta_j}{2(z_j-u)} \times \sum_{l=1}^{2}\tilde{\zeta}_2\frac{1}{2}(\kappa_l+ip_l)\vartheta_l\right]\left[-\frac{\tilde{\zeta}_1\tilde{\zeta}_2}{u-v} + \sum_{r=3}^{4}\tilde{\zeta}_1\frac{(\kappa_r+ip_r)\vartheta_r}{2(z_r-v)}\sum_{s=3}^{4}\tilde{\zeta}_2\frac{(\kappa_s+ip_s)\vartheta_s}{2(z_s-u)}\right] - \frac{2}{u-v}, \quad (28)$$

where κ is the holomorphic part of the operator $\hat{\kappa}$ [see the comments immediately after formula (11)]. In formula (28), summation is performed over all ten independent polarizations of each boson. The term $-2/(u-v)$ emerged because of the appearance of $8/(u-v)$ instead of $10/(u-v)$ from the expansion of expression (21) in powers of k. This term is the contribution from the loop of Faddeev–Popov ghosts, and it cancels the contribution of unphysical polarizations upon integration with respect to t_1, t_2, and $t_3=t$ (the proof of this natural cancellation of unphysical polarizations will be given elsewhere). Upon integration with respect to y, there then arises expression (23), where summation is performed only over physical polarizations.

For n-loop amplitudes, the function $\hat{Z}^{(n-1)}_{\tilde{L},\tilde{L}'}(\{q,\bar{q}\})$ in (24) is equal to the partition function on the supermanifold of genus $(n-1)$ that is formed by all handles, with the exception of the degenerate being under considered. For an arbitrary n, the right-hand part of the integral in (24) can be written, in just the same way as for $n=1$, in the form of the sum over physical polarizations of bosons in the intermediate state; upon integration with respect to y, t_1, t_2, $t_3=t$, and ϑ_4, there then arises expression (23). By applying a similar method, we can perform a complete verification of the unitarity of boson loops, at least for massless states (such a verification will be given elsewhere).

5. RAMOND INTERMEDIATE STATES

Let us now consider the two-particle unitarity condition for a loop involving Ramond states in the holomorphic sector ($l_1=1/2$). For $k\to 0$, the holomorphic Green's function then remains singular at the points u and v. Thus, this function, along with the other quantities in (12), differs from the corresponding functions of genus $(n-1)$. For example, the holomorphic Green's function $R_{(0)}(t_1,t_2)$ on a sphere as obtained upon going over to the above limit in the corresponding function of genus 1 (both at $l_2=0$ and at $2l_2=1$) has the form

$$R_{(0)}(t,t') = \ln(z-z') - \frac{\vartheta\vartheta'}{2(z-z')} \times \left[\sqrt{\frac{(z-u)(z'-v)}{(z-v)(z'-u)}} + \sqrt{\frac{(z-v)(z'-u)}{(z-u)(z'-v)}}\right]. \quad (29)$$

Formula (29) immediately follows from expressions (A.2) and (A.7) for the Green's functions (see Appendix A). Green's functions of higher genus also have a singularity of this type, as follows from (A.2) for the case where all Grassmann moduli are equal to zero. Of course, this singularity occurs in the case of nonzero Grassmann moduli as well (see Appendix B). It follows that, if $z\to u$ and if z' lies at a finite distance from the point u, the Green's function $R^{(n)}_L(t,t';\{q\}) \equiv R(t,t')$ has the form

$$R(t,t') = R_{(0)}(t,t') + R_{(r)}(U,t') - \frac{\vartheta\hat{\phi}(t')}{2\sqrt{(z-u)}}, \quad (30)$$

where $R_{(0)}(t,t')$ is given by formula (29), the function $R_{(r)}(U,t')$ is regular for $z\to u$, and $\hat{\phi}(t')$ is a factor in the singular part. The function $\hat{\phi}(t')$ is not singular for $z'\to u$ since the Green's function is symmetric (apart from the emergence of the term $\pm\pi i$) under the permutation of arguments. We recall that $U=(u|0)$.

In the limit $z \to v$, the Green's function has a similar form. The singularities being discussed are associated with the fermion part of the Green's function, but, in the presence of Grassmann modular parameters corresponding to nondegenerate handles, they also arise in its bosonic part and, hence, in the scalar functions $J_s^{(n)}(t;\{q\};L)$. The explicit form of the functions $R_{(r)}(U,t')$ and $\hat{\phi}(t')$ in (30) can be obtained (see Appendix B) from formulas presented in Appendix A, but this is immaterial for the ensuing analysis. If $z, z' \to u$, then

$$R(t,t') = R_{(0)}(t,t') + R_{(rr)}(U,U) \qquad (31)$$
$$- \frac{\vartheta\hat{\phi}(U)}{2\sqrt{(z-u)}} - \frac{\vartheta'\hat{\phi}(U)}{2\sqrt{(z'-u)}},$$

where $R_{(rr)}(U,U)$ is that part of $R_{(r)}(U,t')$ which is regular for $z' \to u$. The quantity $\hat{\phi}(U)$ is proportional to the Grassmann modular parameters corresponding to nondegenerate handles. If one argument of the function $R(t,t')$ tends to $U = (u|\mu = 0)$ or to $V = (v|\nu = 0)$ (or both of its arguments tend to these quantities), the Green's function has no singularity of the above type since $\vartheta = 0$ in this case. Therefore, relations (26) are valid in the case of a fermion loop as well (see Appendix B). In accordance with formula (29) in the limit $z, z' \to u$ and formula (12), the quantity $\tilde{G}_0$ in (24) is given by

$$\tilde{G}_0 = -(\hat{\kappa}_1 + ip_1)(\hat{\kappa}_2 + ip_2)\left[\frac{1}{2}\ln|z_1 - z_2| \qquad (32)\right.$$
$$\left. - \frac{\vartheta_1\vartheta_2}{8(z_1-z_2)}\left(\sqrt{\frac{z_1-u}{z_2-u}} + \sqrt{\frac{z_2-u}{z_1-u}}\right)\right].$$

In the case of a fermion loop and antiholomorphic fields (that is, $l_1' = 1/2$), the bracketed expression in (32) also involves the term that is complex conjugate to the last term in this bracketed expression. The remaining coefficients in the exponents appearing in (24) are given by formulas (27), where the correlation function $\hat{X}(t,\bar{t};t',\bar{t}')$ is defined as the limit of the vacuum correlation function (12) for $k \to 0$. According to the formulas obtained for the Green's functions, we can write the correlation function $\hat{X}(t,\bar{t};t',\bar{t}')$ in (27) as

$$\hat{X}(t,\bar{t};t',\bar{t}') = \hat{X}_{(r)}(U,\bar{U};t',\bar{t}') - \frac{\vartheta\varphi(t')}{2\sqrt{(z-u)}} \qquad (33)$$

for $z \to u$ and as

$$\hat{X}(t,\bar{t};t',\bar{t}') = \hat{X}_{rr}(U,\bar{U};U,\bar{U}) \qquad (34)$$
$$- \frac{\vartheta\varphi(U)}{2\sqrt{(z-u)}} - \frac{\vartheta'\varphi(U)}{2\sqrt{(z'-u)}}$$

in the limit $z \to u$ and $z' \to u$. Here, the function $\varphi(t)$ is not singular at $z = u$. In addition, the quantity $\varphi(U)$ is proportional to the Grassmann modular parameters that correspond to nondegenerate handles. If $l_1' = 1/2$, the two terms in (34) that are singular in the limit $z \to u$ must be supplemented with the terms that are complex conjugate to them. We note that, because of the presence of the Grassmann parameters, the function $\varphi(t)$ depends not only on t but also on $\bar{t}$. In this case, the singularity being studied does indeed appear in scalar functions and, hence, in the last term on the right-hand side of (12). The validity of these expressions for the coefficients in (24) is verified by a direct calculation of the integral in (24) upon substituting in it expressions (27) and (32) and expressions that are given below for nonexponential factors.

In particular, the function $\hat{Z}^{(n-1)}_{\tilde{L},\tilde{L}'}(\{q,\bar{q}\})$ in (24) has the form (19) where $Z_L^{(n)}(\{q\})$ must be replaced by the expression $kZ_L^{(n)}(\{q\})/16$ at $k = 0$[3] and where the period matrix $\omega^{(n)}(\{q\},L)$ in formula (14) for $\Omega^{(n)}_{L,L'}(\{q,\overline{q}\})$ is replaced by the period matrix $\tilde{\omega}^{(n-1)}(\{q\},\tilde{L})$ whose elements are equal to the elements $[\omega^{(n)}(\{q\},L)]_{jl}$ at $j,l = 2,\ldots,n$ of the period matrix at $k = 0$. As in formula (25), the subscripts $j,l = 2,\ldots,n$ number nondegenerate handles. If, in addition, $l_1' = 1/2$, a similar replacement must be made for the quantities $Z_{L'}^{(n)}(\{q\})$ and $\omega^{(n)}(\{q\},L')$. If $l_1' = 0$, then the quantities $Z_{L'}^{(n)}(\{q\})$ and $\omega^{(n)}(\{q\},L')$ are replaced by the corresponding values calculated on the supermanifold of genus $(n-1)$ that is formed by all handles, with the exception of the degenerate handle being studied. We note that all of the functions being discussed can be explicitly obtained (see Appendix B) from formulas given in Appendix A. Finally, we note that, for the fermion loop under study, the factor $O_{\tilde{L}}(\{p\},\{\zeta\},\tilde{p}_1,\{t\},\{q\})$ in (24) has the form

$$O_{\tilde{L}}(\{p\},\{\zeta\},\tilde{p}_1,\{t\},\{q\}) \qquad (35)$$
$$= \exp\left[\sum_{j=1}^{2}\frac{2\eta_j\zeta_{(j)} + ip_j\vartheta_j}{8\sqrt{z_j-u}}\hat{\Psi}\right],$$

where the Grassmann quantities η_j are identical to those in (11) and the 10-vector $\hat{\Psi}$ depends on the

[3] In this expression, the factor of 1/16 is due to the fact that, at $2l_1 = 1$, the factor of 16 in (21) at $2l_1 = 1$ arises from the trace of the products of Dirac 10-matrices in the fermion loop [see the text after formula (38) below].

parameters of the final state and on $\tilde{p}_1$; that is,

$$\hat{\Psi} = \sum_{j=3}^{4}[2\eta_j\zeta_{(j)}D(t_j) + ip_j\vartheta_j]\varphi(t_j) \qquad (36)$$
$$+ i\tilde{p}_1\varphi(V) + i\tilde{p}_2\varphi(U).$$

Here, the spinorial derivative $D(t)$ and the function $\varphi(t)$ were defined in (7) and (33), respectively. In just the same way as $\varphi(U)$, the quantity $\varphi(V)$ is proportional to the Grassmann modular parameters corresponding to nondegenerate handles. At $l_1' = 1/2$, the expression for the factor $\overline{O_{\tilde{L}'}(\{p\},\{\zeta'\},\tilde{p}_1,\{t\},\{q\})}$ in (24) has a similar form. At $l_1' = 0$, this factor is calculated by a method similar to that used for a boson loop. As has already been indicated, the expressions obtained above are verified according to the scheme where their substitution into (24) is followed by a calculation of the emerging integral with respect to $\tilde{p}_1$ and a comparison of the result with expression (9). The sought n-loop amplitude $\tilde{A}^{(n)}$ for the transition to Ramond states has the form

$$\tilde{A}^{(n)} = \bar{\psi}(\tilde{p}_2)(\tilde{T}_3^{(n)} + \tilde{T}_1^{(n)})\psi(\tilde{p}_1), \qquad (37)$$

where $\psi(p)$ is a Majorana—Weyl 10-spinor satisfying the condition $\Gamma_{11}\psi(p) = \psi(p)$ and the Dirac equation $(\Gamma^M p_M)\psi(p) = 0$. Here, Γ^M is a Dirac matrix, and Γ_{11} is the product of all ten matrices. The quantity $\tilde{T}_1^{(n)}$ in (37) involves one Dirac matrix, while $\tilde{T}_3^{(n)}$ contains the antisymmetrized product of three matrices. Therefore, $O_{\tilde{L}}(\{p\},\{\zeta\},\tilde{p}_1,\{t\},\{q\})$ must have the form

$$O_{\tilde{L}}(\{p\},\{\zeta\},\tilde{p}_1,\{t\},\{q\}) \qquad (38)$$
$$= \mathrm{tr}[(T_3^{(0)} + T_1^{(0)})(\Gamma\tilde{p}_1)(T_3^{(n-1)} + T_1^{(n-1)})(\Gamma\tilde{p}_2)]$$
$$+ \ldots,$$

where the ellipsis stands for the contribution that vanishes in (9) upon taking the relevant integrals and performing summation over spin structures. In (38), $T_1^{(n)}$ involves one Dirac matrix, while $T_3^{(n)}$ contains the antisymmetrization product of three Dirac matrices. Since the 10-spinors in (37) obey the Weyl condition, the trace of the identity matrix is equal to 16 in (38).

The expression for $O_{\tilde{L}}(\{p\},\{\zeta\},\tilde{p}_1,\{t\},\{q\})$ in (35) is a fourth-order polynomial in the exponent, which is the sum of the products of Grassmann variables. Odd powers of this polynomial vanish upon integration with respect to Grassmann variables. Even powers must be represented in the form (38), whereby one defines the integrand in the expressions for the amplitudes $\tilde{A}^{(0)}$ and $\tilde{A}^{(n-1)}$. Concurrently, it is convenient to recast (36) into the form

$$\hat{\Psi} = \Psi - iP\Phi + i\tilde{p}[\varphi(V) - \varphi(U)], \qquad (39)$$

where $P = p_1 + p_2 = \tilde{p}_1 + \tilde{p}_2$, $\tilde{p} = \tilde{(}p_1 - \tilde{p}_2)/2$,

$$\Phi = \frac{1}{2}[\varphi(t_3) + \varphi(t_4) - \varphi(U) - \varphi(V)], \qquad (40)$$

$$\Psi = 2\eta_3\zeta_{(3)}D(t_3)\varphi(t_3) + 2\eta_4\zeta_{(4)}D(t_4)\varphi(t_4) \qquad (41)$$
$$+ i(p_3 - p_4)\frac{1}{2}[\varphi(t_3) - \varphi(t_4)].$$

The function $\varphi(t)$ was defined in (33). In this case, expression (35) takes the form

$$O_{\tilde{L}}(\{p\},\{\zeta\},\tilde{p}_1,\{t\},\{q\}) \qquad (42)$$
$$= \exp\left[\sum_{r=1}^{2}\frac{4\eta_r\zeta_{(r)} + i(p_1 - p_2)(\vartheta_1 - \vartheta_2)}{16\sqrt{z_r - u}}\Psi\right.$$
$$- \sum_{j=1}^{2}\frac{2i\eta_j(P\zeta_{(j)}) + (p_1p_2)(\vartheta_1 + \vartheta_2)}{8\sqrt{z_j - u}}\Phi$$
$$+ i\sum_{j=1}^{2}\frac{\vartheta_1 + \vartheta_2}{16\sqrt{z_j - u}}(P\Psi)$$
$$+ \sum_{s=1}^{2}\frac{4\eta_s(\zeta_{(s)}\tilde{p}) + i(p_1 - p_2)\tilde{p}(\vartheta_1 - \vartheta_2)}{16\sqrt{z_s - u}}$$
$$\left.\times\,[\varphi(V) - \varphi(U)]\right].$$

The tree amplitude can be calculated by considering the case of $n = 1$, where there are no Grassmann modular parameters. Representing, in this case, the factor $O_{\tilde{L}}(\{p\},\{\zeta\},\tilde{p}_1,\{t\},\{q\})$ appearing in (24) in the form (38), we arrive at

$$4\sqrt{2}T_1^{(0)} = -\left(\Gamma[(\zeta_3\zeta_4)\frac{1}{2}(p_3 - p_4) \qquad (43)\right.$$
$$\left.- (\zeta_4p_3)\zeta_3 + (\zeta_3p_4)\zeta_4]\right)\frac{\eta_3\vartheta_3\eta_4\vartheta_4}{2(z_3 - z_4)}$$
$$\times\left[\frac{v - u}{(z_3 - u)(z_4 - v)} + \frac{v - u}{(z_3 - v)(z_4 - u)}\right]$$
$$+\frac{[(\zeta_3(\tilde{p}_3 - \tilde{p}_4))\zeta_4 + (\zeta_4(\tilde{p}_3 - \tilde{p}_4))\zeta_3](v - u)^2}{4(z_3 - u)(z_3 - v)(z_4 - u)(z_4 - v)},$$
$$4\sqrt{2}T_3^{(0)}$$
$$= \frac{[(\Gamma\zeta_3)(\Gamma\zeta_4)(\Gamma(p_3 - p_4))]_a\eta_3\vartheta_3\eta_4\vartheta_4(v - u)^2}{4(z_3 - u)(z_3 - v)(z_4 - u)(z_4 - v)},$$

where $[\ldots]_a$ symbolizes an antisymmetrized (with a factor of $1/6$) expression. In (43), we have discarded terms that vanish upon integration with respect to Grassmann variables. We recall that v and u are the coordinates of vertices describing the emission of a fermion with a momentum $\tilde{p}_1$ and $\tilde{p}_2$, respectively. For the amplitude involving bosons whose momenta

are p_1 and p_2, the corresponding expressions arise as the limit $u \to \infty$ of formulas (43), whereupon one must make the change of variable $v \to u$ and the substitutions $3 \to 1$ and $4 \to 2$ for the indices. The successive substitutions of formula (43) into the expression on the right-hand side of (38) and of the resulting expression into (24) lead (apart from normalization) to the amplitude obtained in [2]. In deriving (43), we integrated by parts those terms in (24) that are proportional to $\eta_1\eta_2 p_1 p_2/[(z_1-u)(z_1-z_2)]$ and $\eta_1\eta_2 p_1 p_2/[(z_2-u)(z_1-z_2)]$. The first and the second term were integrated with respect to z_2 and z_1, respectively. By using expression (32) for $\tilde{G}_0$, we eventually find that the first and the second term reduce to $-\eta_1\eta_2 p_2\tilde{p}_1/[(z_1-u)(z_2-u)]$ and $\eta_1\eta_2 p_1\tilde{p}_1/[(z_1-u)(z_2-u)]$, respectively. In some cases, the product of the last factor in the first term on the right-hand side of the first equation in (43) and $1/(z_3-z_4)$ can be written as

$$\frac{2(v-u)}{(z_4-u)(z_4-v)(z_3-z_4)} - \frac{(v-u)}{(z_3-u)(z_4-u)(z_4-v)} - \frac{(v-u)}{(z_3-v)(z_4-v)(z_4-u)}, \tag{44}$$

or as the expression obtained from (44) by means of the substitutions $z_3 \rightleftharpoons z_4$ and $v \rightleftharpoons u$. When expression (44) was multiplied by $\eta_3\eta_4 p_3 p_4$, the first term in (44) was integrated by parts with respect to z_3. As a result, the contribution of this term proved to be proportional to the expression

$$-\frac{2\eta_3\eta_4(v-u)}{(z_4-u)(z_4-v)}\left[\frac{p_3\tilde{p}_1}{z_3-v}+\frac{p_3\tilde{p}_2}{z_3-u}\right]. \tag{45}$$

From (29), it follows that, in the case of $n=1$, which is being considered at present, the function $\varphi(t)$ in (42) has the form

$$\varphi(t) = -\vartheta\sqrt{\frac{u-v}{(z-u)(z-v)}}. \tag{46}$$

For an arbitrary n (including $n=0$), the structure $T_3^{(n-1)}$ in (38) is obtained owing to the terms that are proportional to $\sim\Psi_{M_1}\Psi_{M_2}\Psi_{M_3}\Phi$. These terms arise upon expanding the exponential function in (42) in a series as the result of the multiplication of the third power of the sum over r in (42) by the term proportional to Φ. Here, Ψ_M is the component of the 10-vector Ψ. These $\Phi\Psi_{M_1}\Psi_{M_2}\Psi_{M_3}$ terms are also proportional to $(\tilde{p}_1\tilde{p}_2)$. They correspond to the $(\tilde{p}_1\tilde{p}_2)$ terms in (38), which originate from $\mathrm{tr}[T_3^{(0)}(\Gamma\tilde{p}_1)T_3^{(n-1)}(\Gamma\tilde{p}_2)]$. Here, the quantity $T_3^{(n-1)}$ is calculated unambiguously and is given by

$$T_3^{(n-1)} = \frac{i}{48}(\Gamma\Psi)(\Gamma\Psi)(\Gamma\Psi)\Phi. \tag{47}$$

Since the products of the Dirac matrices are antisymmetrized in $T_3^{(n-1)}$ and $T_3^{(0)}$, there are no terms in $\mathrm{tr}[T_3^{(0)}(\Gamma\tilde{p}_1)T_3^{(n-1)}(\Gamma\tilde{p}_2)]$ that are proportional to the scalar products of those vectors that are both contained in $T_3^{(0)}$ or $T_3^{(n-1)}$. For the same reason, the trace being studied does not involve terms in which each of the vectors $\tilde{p}_1$ and $\tilde{p}_2$ in (38) is scalarly multiplied by the vectors that are both included either in $T_3^{(0)}$ or in $T_3^{(n-1)}$. Only those terms in the expansion of the exponential function in (42) that involve the square of the sum over r can generate nonzero terms in the trace being studied. If the quantity $T_3^{(n-1)}$ is given by (47), the part of the trace that is quadratic in the components of the 10-vector $(\tilde{p}_1+\tilde{p}_2)$ stems from the term where the square of the above sum over r is multiplied by the product of the sum proportional to $P\Psi$ and the sum proportional to Φ. The remaining terms of this trace are quadratic in the components of the 10-vector $(\tilde{p}_1-\tilde{p}_2)$. They cannot be obtained by expanding the exponential function in (42) since the remaining terms of this expansion do not involve the quantities proportional to $\Psi\Psi\Psi\Phi$. For the required contribution to the unitarity condition for the boson amplitude to arise in spite of this, it is necessary that

$$\left\langle \Psi_M\Psi_N\left[1-\frac{1}{16}[\varphi(V)-\varphi(U)]\Big(P^2\Phi+i(P\Psi)\Big)\right]-\frac{i}{4}\Psi_M\Psi_N(\Psi\tilde{p})\Phi\right\rangle = 0, \tag{48}$$

where $\langle\ldots\rangle$ denotes integration of the expression obtained by multiplying that in (48) [for details, see formula (50) above and the text after it] by the factors remaining in (24) [all of the quantities there are factors, with the exception of $O_{\tilde{L}}(\{p\},\{\zeta\},\tilde{p}_1,\{t\},\{q\})$] and by summing the result over the superspin structures $(\tilde{L},\tilde{L}')$. The integral is calculated with respect to variables that determine the amplitude $\tilde{A}^{(n-1)}$. Relation (48) follows from a comparison of the corresponding contributions in the expansion of the exponential function (42) with the quantity $\mathrm{tr}[T_3^{(0)}(\Gamma\tilde{p}_1)T_3^{(n-1)}(\Gamma\tilde{p}_2)]$, where, for $T_3^{(0)}$ and $T_3^{(n-1)}$, we use the expressions obtained above [see formulas (43) and (47)]. Three independent conditions for

the coefficients of $\zeta_{(3)M}\zeta_{(4)N}$, $\zeta_{(3)M}\tilde{p}_N(\zeta_{(4)}p_3)$, and $\zeta_{(4)M}\tilde{p}_N(\zeta_{(3)}p_4)$, where, as before, $\tilde{p}=(\tilde{p}_1-\tilde{p}_2)/2$, follow from formula (48) if we take into account the identity of bosons. In order to calculate $T_1^{(n-1)}$ in (38), we consider the term $\mathrm{tr}[T_3^{(0)}(\Gamma\tilde{p}_1)T_1^{(n-1)}(\Gamma\tilde{p}_2)]$. Isolating this term from the terms appearing in the expansion of the exponential function in (42), we obtain

$$T_1^{(n-1)}=-i(\Gamma\Psi)\Phi+\frac{i}{8}(\Gamma\Psi)(P\Psi)[\varphi(V)-\varphi(U)]\Phi, \tag{49}$$

where the notation is identical to that in (42). With allowance for (49) and (48), the remaining terms in the expansion of the exponential function in (42) that are linear in Ψ yield all the remaining terms in (38), with the exception of the term proportional to the product of $\mathrm{tr}[(\Gamma\tilde{p})T_1^{(0)}]$ and $\mathrm{tr}[(\Gamma\tilde{p})T_1^{(n-1)}]$, where $\tilde{p}=(\tilde{p}_1-\tilde{p}_2)/2$ as before. This term cannot be obtained from the unit term in the expansion of expression (35) because it does not involve Ψ. For the required contribution to the unitarity condition for the boson amplitude to arise in spite of this, it is necessary that

$$\left\langle 16+\mathrm{tr}\left[\frac{1}{2}(\Gamma T_1^{(n-1)})(\Gamma\tilde{p})\right]+\sqrt{2}[\varphi(V)-\varphi(U)][P^2\Phi+(\Psi P)]\right\rangle=0, \tag{50}$$

where, as in (48), $\langle\ldots\rangle$ denotes integration of the expression obtained by multiplying that in (48) by all factors following from (24) and summing the result over the superspin structures $(\tilde{L},\tilde{L}')$. The rest of the notation is identical to that in (42).

Thus, the $(n-1)$-loop amplitude $\tilde{A}^{(n-1)}$ describing the transition of two massless Ramond states having the momenta $\tilde{p}_1$ and $\tilde{p}_2$ to two massless bosons whose momenta and polarizations are $(p_3,\zeta_{(3)})$ and $(p_4,\zeta_{(4)})$ is given by

$$A^{(n-1)}=\frac{2g^{2n}}{2^n(n-1)!}\int|(z_4-u)(z_4-v)|^2\times\sum_{\tilde{L},\tilde{L}'}\hat{Z}^{(n-1)}_{\tilde{L},\tilde{L}'}(\{q,\bar{q}\})\tilde{F}^{(n-1)}_{\tilde{L},\tilde{L}'}\mathcal{O}_{\tilde{L}}\overline{\mathcal{O}_{\tilde{L}'}}(dqd\bar{q}dtd\bar{t})', \tag{51}$$

where g is the coupling constant, as in (9), and summation is performed over superspin structures on a supermanifold of genus $(n-1)$. We note that, in contrast to the boson amplitudes for massless-boson scattering, the sum in question involves the contribution of odd superspin structures that is induced by the contribution to the unitarity condition from the $l_2=1/2$ fermion loop. The quantities in (51) are expressed in terms of the corresponding quantities for the n-loop amplitude (9). In addition, $\hat{Z}^{(n-1)}_{\tilde{L},\tilde{L}'}(\{q,\bar{q}\})$ is calculated in terms of $Z^{(n)}_{L,L'}(\{q,\bar{q}\})$, as was explained after formula (34). It should be noted that $\hat{Z}^{(n-1)}_{\tilde{L},\tilde{L}'}(\{q,\bar{q}\})$ depends, in particular, on the coordinates v and u of the vertices describing the emission of Ramond states. Further, $\tilde{F}^{(n-1)}_{\tilde{L},\tilde{L}'}$ is calculated in terms of the function $\hat{F}^{(n-1)}_{\tilde{L},\tilde{L}'}(\eta_1,\eta_2,\bar{\eta}_1,\bar{\eta}_2)$, which is given by the expression obtained by integrating the integrand in formula (11) with respect to $(\eta_3,\bar{\eta}_3)$ and $(\eta_4,\bar{\eta}_4)$. In this expression, the vacuum correlation functions (12) on a supermanifold of genus n must be replaced by the functions $\hat{X}(t,\bar{t};t',\bar{t}')$, which are the corresponding vacuum correlation functions (12) of genus n that are calculated for $k\to 0$ [see the explanation in the text after formula (27); see also formula (33) and Appendix B]. In the resulting expression, we must additionally make the substitutions $(z_1|\vartheta_1)\to(v|0)$, $(z_2|\vartheta_2)\to(u|0)$, $p_1\to\tilde{p}_1$, and $p_2\to\tilde{p}_2$. If states characterized by the momenta $\tilde{p}_1$ and $\tilde{p}_2$ are Ramond bosons, then we have

$$\mathcal{O}_{\tilde{L}}=\bar{\psi}(\tilde{p}_2)(T_3^{(n-1)}+T_1^{(n-1)})\psi(\tilde{p}_1), \tag{52}$$

where $\psi(p)$ is a Majorana–Weyl 10-spinor and other quantities are given by formulas (47) and (49). The quantity $\overline{\mathcal{O}_{\tilde{L}'}}$ is calculated in a similar way. Here, the function $\tilde{F}^{(n-1)}_{\tilde{L},\tilde{L}'}$ in (51) is equal to $\hat{F}^{(n-1)}_{\tilde{L},\tilde{L}'}(\eta_1,\eta_2,\bar{\eta}_1,\bar{\eta}_2)$ at $\eta_1=\eta_2=0$ and $\bar{\eta}_1=\bar{\eta}_2=0$; that is,

$$\tilde{F}^{(n-1)}_{\tilde{L},\tilde{L}'}=\hat{F}^{(n-1)}_{\tilde{L},\tilde{L}'}(0,0,0,0). \tag{53}$$

We recall that the function $\hat{F}^{(n-1)}_{\tilde{L},\tilde{L}'}(\eta_1,\eta_2,\bar{\eta}_1,\bar{\eta}_2)$ is defined in the text given between formulas (51) and (52). If the particles that we consider and which have the momenta $\tilde{p}_1$ and $\tilde{p}_2$ are Ramond fermions, either the holomorphic or the antiholomorphic part of the above two-particle state is described by a bosonic wave function. If it is the holomorphic part of the wave function that corresponds to it, then $\mathcal{O}_{\tilde{L}}=1$ and

$$\tilde{F}^{(n-1)}_{\tilde{L},\tilde{L}'}=\int d\eta_1 d\eta_2\hat{F}^{(n-1)}_{\tilde{L},\tilde{L}'}(\eta_1,\eta_2,0,0). \tag{54}$$

In addition, the quantity $\overline{\mathcal{O}_{\tilde{L}'}}$ is calculated according to (52). If the antiholomorphic part of the Ramond state under discussion corresponds to bosons, the factors in question are calculated in a similar way. In (37), the coordinates of the interaction vertices corresponding to Ramond particles are fixed along with the local coordinate of the vertex describing the emission of one of the bosons. Here, the Grassmann

partners of the local coordinates of the vertices corresponding to the Ramond particles are set to zero. Since the integrand in (51) possesses $SL(2)$ symmetry, any (3|2) variables could be fixed in the integral in (51); however, we will not discuss this subject in the present article.

One can verify that, if the conditions in (48) and (50) are satisfied, the amplitude in (51) vanishes in the case of longitudinal-boson emission, as is prescribed by gauge invariance (we plan to discuss this issue in detail elsewhere). The aforementioned conditions (48) and (50) and the analogous conditions arising in the case of $l_1' = 1/2$ can be obtained by replacing, in (51), the factor $\mathcal{O}_{\tilde{L}}$ (or the factor $\overline{\mathcal{O}_{\tilde{L}'}}$ or both these factors if $l_1 = l_1' = 1/2$) by the expressions within the angular brackets $\langle \dots \rangle$ in (48) and (50) (or by their complex conjugate counterparts). At present, we have proven the validity of the relations being discussed only for the tree amplitudes in (51). In this case, the first factor under the sum sign in (51) is equal to unity; the remaining quantities are calculated in terms of correlation functions on a sphere and in terms of expressions (32) and (46). In doing this, it is convenient to consider the limit $u \to \infty$ or $v \to \infty$; this is sufficient since the expressions being discussed possess $L(2)$ symmetry. In this case (for $u \to \infty$), expressions that involve $\eta_3\eta_4 p_3 p_4/[(z_4 - v)(z_3 - z_4)]$ are integrated by parts in just the same way as was done for the expressions considered after formula (43). This verification can also be performed for arbitrary u and v. In this case, it is convenient to use formula (44) and integration by parts leading to (45). The problem of verifying the relations in question for loop amplitudes requires a further investigation.

ACKNOWLEDGMENTS

This work was supported by the US Civilian Research and Development Foundation (CRDF) for the Independent States of the Former Soviet Union (grant no. RP1-2108) and by the Russian Foundation for Basic Research (project nos. 00-02-16691, 00-15-96610).

APPENDIX A

Here, we present expressions for holomorphic Green's functions and quantities related to them (in particular for the Ramond sector), as well as for the holomorphic function $\tilde{Z}^{(n)}(\{q\}, L)$ in (20) [it determines the integration measure (19)]. At zero Grassmann parameters, the sought holomorphic Green's functions $R_{(0)}(t, t'; L)$ have the form

$$R_{(0)}(t, t'; L) = R_b(z, z') - \vartheta\vartheta' R_f(z, z'; L), \quad \text{(A.1)}$$

where $R_b(z, z')$ and $R_f(z, z'; L)$ are the Green's functions for boson and fermion fields, respectively. For even spin structures, the fermion Green's functions can be written, for example, as [4]

$$R_f(z, z'; L) = \exp\left\{\frac{1}{2}[R_b(z, z) + R_b(z', z')] - R_b(z, z')\right\}\frac{\Theta[l_1, l_2](J|\omega^{(0)})}{\Theta[l_1, l_2](0|\omega^{(0)})}, \quad \text{(A.2)}$$

where $R_b(z, z)$ for $z' = z$ is defined as the limit $R_b(z, z') - \ln(z - z')$ for $z \to z'$, Θ is a theta function, and J stands for the set of scalar functions $(J_s(z) - J_s(z'))/2\pi i$ that are its arguments. Here, the quantities $R_b(z, z)$, $J_s(z)$, and $\omega^{(0)}$ are given by formulas (18) at zero values of the parameters μ and ν. For a surface of arbitrary genus n, in particular, we have

$$\partial_{z'} R_b(z, z') = \sum_g [z - g(z')]^{-1}(cz' + d)^{-2}, \quad \text{(A.3)}$$

where summation is performed over all elements of the Schottky group. Formula (A.2) can also be recast into the form of Poincaré series, but we do not dwell on this point here. At nonzero Grassmann moduli, the Green's functions in the Ramond sector cannot be directly expressed in terms of theta functions or written in the form of Poincaré-type series (see Introduction and Section 2). In any case, they can nevertheless be specified in the form of series where each term of a series is represented as the integral of an expression constructed from functions of genus 1 that are associated with each of the handles. Each such function $R_s^{(1)}(t, t)$ was calculated for the parameters (k_s, u_s, v_s) and (μ_s, ν_s) of a given handle and its spin structure $l_s = (l_{1s}, l_{2s})$. By virtue of relations (3), this function has the form

$$\begin{aligned} R_s^{(1)}(t, t') &= R_{(b)s}^{(1)}(z_s, z_s') - \vartheta_s\vartheta_s' R_{(f)s}^{(1)}(z_s, z_s'; l_{1s}, l_{2s}) \\ &+ \varepsilon_s'\vartheta_s' \Upsilon_s(\infty, z_s') + \varepsilon_s'\vartheta_s \Upsilon_s(z_s, \infty), \\ \Upsilon_s(z, z') &= (z - z') R_f^{(1)}(z, z'; l_{1s}, l_{2s}), \end{aligned} \quad \text{(A.4)}$$

where z_s and ϑ_s are given by (4) and $R_{(b)s}^{(1)}(z, z')$ and $R_{(f)s}^{(1)}(z, z'; l_{1s}, l_{2s})$ are the relevant boson and fermion functions. The terms proportional to Υ_s were added in order to ensure a decrease in $K_s^{(1)}(t, t')$ for $z \to \infty$ or $z' \to \infty$. Here, the function $K_s^{(1)}(t, t')$ has the form

$$K_s^{(1)}(t, t') = D(t') R_s^{(1)}(t, t'). \quad \text{(A.5)}$$

For the case of $n = 1$, the boson function is given by formula (A.3). The scalar function $J_s^{(1)}(t)$ of genus 1

is given by

$$J_s^{(1)}(t) = \ln\frac{z_s - u_s}{z_s - v_s}, \tag{A.6}$$

where, for z_s, we employ expressions (4). For even spin structures, the fermion function $R^{(1)}_{(f)s}(z, z'; l_{1s}, l_{2s})$ has the form (A.2), where $L = (l_{1s}, l_{2s})$, while, for odd spin structures, we use the function

$$R^{(1)}_{(f)s}(z, z'; 1/2, 1/2) \tag{A.7}$$
$$= \frac{\partial_z\{\Theta[1/2,1/2](J^{(1)}_{(0)s}|\omega_s^{(1)})\}}{\Theta[1/2,1/2](J^{(1)}_{(0)s}|\omega_s^{(1)})}\sqrt{\frac{\partial_{z'}J^{(1)}_{(0)s}(z')}{\partial_z J^{(1)}_{(0)s}(z)}},$$

where $J^{(1)}_{(0)s}(z)$ is given by (A.6) at $z_s = z$. In this case, we have

$$R_s^{(1)}(t_b, t') = R_s^{(1)}(t, t') + J_s^{(1)}(t') - \varphi_s(t)\varphi_s(t'), \tag{A.8}$$

where t_b corresponds to a round about the B_s cycle; the scalar function $J_s^{(1)}(t')$ has the form (A.6); and the spinor zero mode $\varphi_s(t)$ is

$$\varphi_s(t) = \frac{\vartheta_s(u_s - v_s)^{1/2}}{[(z_s - u_s)(z_s - v_s)]^{1/2}} + \varepsilon_s'(u_s - v_s)^{1/2}; \tag{A.9}$$

and $(z_s|\vartheta_s)$ is defined according to (4). The last term in (A.9) ensures a decrease of $\varphi_s(t)$ in the limit $z \to \infty$.

In order to construct the required Green's function, we define (see [4]) the matrix operator $\hat{K}^{(1)} = \{\hat{K}_{sr}\}$, where $\hat{K}^{(1)}_{sr}$ is an integral operator equal to zero for $s = r$. For $s \neq r$, the kernel of the operator is $\tilde{K}^{(1)}_s(t, t')dt'$. Here, the function $\tilde{K}^{(1)}_s(t, t')$ is related to $\tilde{R}^{(1)}_s(t, t')$ via (A.5); that is,

$$K_s^{(1)}(t, t') = \frac{\vartheta - \vartheta'}{z - z'} + \tilde{K}_s^{(1)}(t, t'), \tag{A.10}$$
$$\tilde{K}_s^{(1)}(t, t') = D(t')\tilde{R}_s^{(1)}(t, t').$$

Following [4], we define the kernel along with the differential $dt' = dz'd\vartheta'/2\pi i$. The operator under discussion integrates the above function multiplied by $\tilde{K}^{(1)}_s(t, t')$ with respect to t' along the contour C_r, which circumvents the limiting points of the Schottky supertransformation associated with the rth handle. This contour also circumvents the cuts that are present for handles of the Ramond type. The required expression for the Green's function has the form

$$R_L^{(n)}(t, t'; \{q\}) = \ln(z - z' - \vartheta\vartheta') + \sum_s \tilde{R}_s^{(1)}(t, t') \tag{A.11}$$
$$+ \sum_{r,s}\int\limits_{C_s}[(1 - \hat{K}^{(1)})^{-1}\hat{K}^{(1)}]_{rs}(t, t_1)dt_1\tilde{R}_r^{(1)}(t_1, t')$$
$$- \frac{1}{2}\sum_{m,m'}\Phi_m(t; L; \{q\})\hat{V}^{-1}_{mm'}\Phi_{m'}(t'; L; \{q\}),$$

where $[(1 - \hat{K}^{(1)})^{-1}\hat{K}^{(1)}]_{rs}(t, t_1)dt_1$ is the kernel of the operator

$$(1 - \hat{K}^{(1)})^{-1}\hat{K}^{(1)} = \hat{K}^{(1)} + \hat{K}^{(1)}\hat{K}^{(1)} + \ldots, \tag{A.12}$$

and the sum over m, m' is taken only over odd spin structures of genus 1. Here, $\hat{V}_{mm'}$ are defined only for those m, m' that number these odd spin structures. In this case, we have

$$\Phi_m(t; L; \{q\}) = \varphi_m(t) \tag{A.13}$$
$$+ \sum_p\int\limits_{C_m}[(1 - \hat{K}^{(1)})^{-1}\hat{K}^{(1)}]_{pm}(t, t')dt'\varphi_m(t'),$$

where $\varphi_m(t)$ is given by (A.9) and[4)]

$$\hat{V}_{mm'} = -\frac{1}{2}\sum_{p\neq m}\int\limits_{C_p} D(t)\varphi_m(t)dt \tag{A.14}$$
$$\times\int\limits_{C_{m'}}[(1 - \hat{K}^{(1)})^{-1}\hat{K}^{(1)}]_{pm'}(t, t')dt'\varphi_{m'}(t')$$
$$- \frac{1}{2}(1 - \delta_{mm'})\int\limits_{C_{m'}} D(t)\varphi_m(t)dt\varphi_{m'}(t),$$

with $\delta_{mm'}$ being the Kronecker delta. In the Neveu–Schwarz sector, where the function defined in (A.5) has no cuts, the integrals in (A.11) can easily be calculated. In this case, we can obtain a series for $R_L^{(n)}(t, t'; \{q\})$ by using the Poincaré series (18) at $n = 1$ for the Green's functions. In general, the proof of (A.11) reduces to verifying that expression (A.11) satisfies the conditions in (16). In order to test relations (16) for the transformations associated with the rth handle, we rewrite (A.11) as

$$R_L^{(n)}(t, t'; \{q\}) = R_r^{(1)}(t, t') \tag{A.15}$$
$$+ \sum_{s\neq r}\int\limits_{C_s} K_r^{(1)}(t, t_1)dt_1\hat{R}(t_1, t'),$$

where $R_r^{(1)}(t, t')$ and $K_r^{(1)}(t, t_1)$ are the total Green's functions of genus 1 with allowance for the singular terms in (15) and (A.10). Calculating the contribution to (A.15) from the pole term in (A.10), we do indeed

[4)] The matrix $\hat{V}_{mm'}$ differs slightly from the corresponding matrix in [4].

arrive at (A.11). Simultaneously, we calculate the quantity $\hat{R}(t_1, t'; \{q\}; s)$. For a handle of an odd spin structure, we obtain [4]

$$\varphi_r(t') + \sum_{s\neq r} \int\limits_{C_s} \varphi_r(t_1) dt_1 \hat{R}(t_1, t'; \{q\}; s) = 0. \tag{A.16}$$

For expression (A.15), relations (16) for the transformations associated with the rth handle obviously hold [upon taking into account relations (A.7) and (A.16) for the handle of odd spin structure]. Simultaneously, the scalar function $J_r^{(n)}(t; \{q\}; L)$ corresponding to the rth handle is determined in the form

$$\begin{aligned} J_r^{(n)}(t; \{q\}; L) &= J_r^{(1)}(t) \\ &+ \sum_{s\neq r} \int\limits_{C_s} D(t_1) J_r^{(1)}(t_1) dt_1 \tilde{R}_s^{(1)}(t_1, t) \\ &+ \sum_{p\neq r} \sum_{s} \int\limits_{C_p} D(t_1) J_r^{(1)}(t_1) dt_1 \\ &\times \int\limits_{C_s} [(1 - \hat{K}^{(1)})^{-1} \hat{K}^{(1)}]_{ps}(t_1, t_2) dt_2 \tilde{R}_s^{(1)}(t_2, t) \\ &- \frac{1}{2} \sum_{m,m'} \Phi_m^{(r)}(L; \{q\}) \hat{V}^{-1}_{mm'} \Phi_{m'}(t; L; \{q\}), \end{aligned} \tag{A.17}$$

where $J_s^{(1)}(t)$ is given by (A.6) and

$$\begin{aligned} \Phi_m^{(r)}(L; \{q\}) &= (1 - \delta_{mr}) \\ &\times \int\limits_{C_m} D(t_1) J_r^{(1)}(t_1) dt_1 \varphi_m(t_1) \\ &+ \sum_{p\neq r} \int\limits_{C_p} D(t_1) J_r^{(1)}(t_1) dt_1 \\ &\times \int\limits_{C_m} [(1 - \hat{K}^{(1)})^{-1} \hat{K}^{(1)}]_{pm}(t_1, t_2) dt_2 \varphi_m(t_2). \end{aligned} \tag{A.18}$$

The period matrix is calculated [4] on the basis of equalities (17) for the functions in (A.17). The matrix element $\omega_{rs}^{(n)}(\{q\}; L)$ of the period matrix then assumes the form

$$\begin{aligned} 2\pi i \omega_{rs}^{(n)}(\{q\}; L) &= \delta_{rs} \ln k_r + (1 - \delta_{rs}) \\ &\times \int\limits_{C_s} D(t) J_r^{(1)}(t) dt J_s^{(1)}(t) \\ &+ \sum_{p} \int\limits_{C_p} D(t) J_r^{(1)}(t) dt \\ &\times \int\limits_{C_s} [(1 - \hat{K}^{(1)})^{-1} \hat{K}^{(1)}]_{pr}(t, t') dt' J_s^{(1)}(t') \\ &- \frac{1}{2} \sum_{m,m'} \Phi_m^{(r)}(L; \{q\}) \hat{V}^{-1}_{mm'} \Phi_{m'}^{(s)}(L; \{q\}), \end{aligned} \tag{A.19}$$

where the quantities appearing in this expression are given by (A.18) and (A.6).

As was indicated in Section 2, the integration measures in (9) are calculated on the basis of the equations derived in [4, 9] by requiring that the amplitude be independent of the choice of the zweibein and the field of the two-dimensional gravitino. For the integration measures in question, we thereby obtain formulas (19)–(21), where the function $\tilde{Z}^{(n)}(\{q\}, L)$ in (20) can be written in the form

$$\begin{aligned} \ln \tilde{Z}^{(n)}(\{q\}, L) &= -5 \mathrm{tr} \ln(I - \hat{K}^{(1)}) \\ &+ 5 \ln \det \hat{V} + \mathrm{tr} \ln(I - \hat{G}^{(1)}) - \ln \det \hat{U}, \end{aligned} \tag{A.20}$$

where I is the identity operator and $\hat{K}^{(1)}$ is the same operator as in (A.11). The matrix $\hat{V}$ is defined in (A.14). The matrix operator $\hat{G}^{(1)}$ is calculated in terms of the Green's function $G_s^{(1)}(t, t')$ of genus 1 for ghosts (see below) in just the same way as the quantity $\hat{K}^{(1)}$ is calculated in terms of $K_s^{(1)}(t, t')$. Thus, we obtain $\hat{G}^{(1)} = \{\hat{G}_{sr}^{(1)}\}$, where the integral operator $\hat{G}_{sr}^{(1)}$ vanishes at $s = r$. For $s \neq r$, its kernel $\hat{G}_{sr}^{(1)}$ is equal to the regular part $\tilde{G}_{l_s}^{(1)}(t, t'; s) dt'$ of the ghost correlation function $G_s^{(1)}(t, t')$; that is,

$$G_s^{(1)}(t, t') = \frac{\vartheta - \vartheta'}{z - z'} - \tilde{G}_{l_s}^{(1)}(t, t'; s). \tag{A.21}$$

As in the case of the matrix in (A.14), the matrix elements $\hat{U}_{mn}$ are defined only for those m, m' that number odd spin structures of genus 1. They are calculated in terms of the (3/2) zero modes $\chi_m^{(1)}(t)$ and the $(-1/2)$ zero modes $\phi_m^{(1)}(t)$ of genus 1. As a result, we obtain

$$\begin{aligned} \hat{U}_{mm'} &= -\frac{1}{2} \sum_{p\neq m} \int\limits_{C_p} \chi_m^{(1)}(t) dt \\ &\times \int\limits_{C_{m'}} [(1 - \hat{G})^{-1} \hat{G}]_{pm'}(t, t') dt' \phi_{m'}^{(1)}(t') \\ &- \frac{1}{2}(1 - \delta_{mm'}) \int\limits_{C_{m'}} \chi_m^{(1)}(t) dt \phi_{m'}^{(1)}(t). \end{aligned} \tag{A.22}$$

Here, the zero modes are given by

$$\chi_m^{(1)}(t) = -\frac{(u_m - v_m)^2}{[(z_m - u_m)(z_m - v_m)Q_m^2(t)]^{3/2}}, \quad (A.23)$$

$$\phi_m^{(1)}(t) = \frac{\vartheta_m Q_m^2(t)\sqrt{(z_m - u_m)(z_m - v_m)}}{(u_m - v_m)},$$

where variables $(z_m|\vartheta_m)$ are defined in (4) at $s = m$, while the quantity Q_m defined in (7) corresponds to the aforementioned transformation (4) at $s = m$. As for scalar fields, the function $G_s^{(1)}(t,t)$ is expressed in terms of the boson function $G_{(b)s}^{(1)}(z,z')$ and the fermion function $G_{(f)s}^{(1)}(z,z';l_{1s},l_{2s})$ as [4]

$$G_s^{(1)}(t,t') = Q_s^2(t)[G_{(b)s}^{(1)}(z_s,z_s')\vartheta_s' \quad (A.24)$$
$$+ \vartheta_s G_{(f)s}^{(1)}(z_s,z_s';l_{1s},l_{2s}) - \varepsilon_s'\tilde{\Upsilon}_s(\infty,z_s')]Q_s^{-3}(t'),$$
$$\tilde{\Upsilon}_s(z,z') = (z-z')G_{(f)s}^{(1)}(z,z';l_{1s},l_{2s}),$$

where z_s and ϑ_s are defined in (4) and the terms proportional to $\tilde{\Upsilon}_s$ ensure a decrease in $G_{l_s}^{(1)}(t,t')$ for $z \to \infty$ or $z' \to \infty$. The boson part of the Green's functions in (A.24) has the form [4]

$$G_{(b)}^{(1)}(z,z') = -\sum_n \frac{1}{(z - g^n(z'))(c_n z' + d_n)^4}, \quad (A.25)$$

where we omit the subscript s for the sake of brevity. Summation is performed here over the group products of the corresponding Schottky transformation $g(z)$. The fermion Green's function $G_f^{(1)}(z,z';l_1,l_2)$ for even spin structures (we again omit the subscript s for the sake of brevity) has the form

$$G_f^{(1)}(z,z';l_1,l_2) \quad (A.26)$$
$$= \frac{(z-u)(z-v)}{(z'-u)(z'-v)}R_f^{(1)}(z,z';l_1,l_2)$$
$$- \frac{(z-v)W_1(z';l_1,l_2) + W_2(z';l_1,l_2)}{(z'-u)(z'-v)},$$

where the last term is calculated in terms of the asymptotic expression for $R_f^{(1)}(z,z';l_1,l_2)$ in the limit $z \to \infty$:

$$R_f^{(1)}(z,z';l_1,l_2) \to \frac{W_1(z;l_1,l_2)}{z-u} + \frac{W_2(z;l_1,l_2)}{(z-u)^2}. \quad (A.27)$$

It can easily be verified that $G_f^{(1)}(z,z';l_1,l_2)$ decreases for $z \to \infty$ for $z' \to \infty$. In addition, we have

$$(cz+d)G_f^{(1)}(g(z),z';l_1,l_2) \quad (A.28)$$
$$= G_f^{(1)}(z,z';l_1,l_2) + \frac{1-\sqrt{k}}{\sqrt{k}}p_\mu(z)\chi_\mu(z';l_1,l_2)$$
$$- (1-\sqrt{k})p_\nu(z)\chi_\nu(z';l_1,l_2),$$

where $(cz+d)$ corresponds to the transformation $g(z)$ being considered; $p_\mu(z)$ and $p_\nu(z)$ have the form

$$p_\mu(z) = \frac{2(z-v)}{u-v}, \quad p_\nu(z) = -\frac{2(z-u)}{u-v}; \quad (A.29)$$

and z'-dependent functions are

$$\chi_\mu(z;l_1,l_2) = -\frac{(u-v)W_1(z;l_1,l_2) + W_2(z;l_1,l_2)}{2(z-u)(z-v)}, \quad (A.30)$$

$$\chi_\nu(z;l_1,l_2) = -\frac{W_2(z;l_1,l_2)}{2(z-u)(z-v)}.$$

For an odd spin structure, where there are no Green's functions possessing the property specified by Eq. (A.28) because of the $(-1/2)$ zero mode, we define the Green's function by the formula

$$G_f^{(1)}(z,z';1/2,1/2) = G_{(\sigma=1)}^{(1)}(z,z') \quad (A.31)$$
$$- 2\left(\sqrt{\frac{z-u}{z-v}} - 1\right)\chi_\nu(z';1/2,1/2),$$
$$\chi_\nu(z;1/2,1/2) = -\frac{1}{2\sqrt{(z-u)(z-v)}}$$
$$\times \sum_n \frac{1}{(c_n z' + d_n)^2},$$

where $G_{(\sigma)}^{(1)}(z,z')$ has the form

$$G_{(\sigma)}^{(1)}(z,z') = \left[\frac{(z-u)(z'-v)}{(z-v)(z'-u)}\right]^{l_1\sigma} \quad (A.32)$$
$$\times \sum_n \frac{k^{-l_1\sigma n}(-1)^{(2l_2-1)n}}{(z - g^n(z'))(c_n z + d_n)^3}.$$

Here, summation is performed over all powers of the transformation $g(z)$. We also note that, for even spin structures, we have

$$G_f^{(1)}(z,z';l_1,l_2) = G_{(\sigma=1)}^{(1)}(z,z') \quad (A.33)$$
$$+ [p_\mu(z)\chi_\mu(z';l_1,l_2) - p_\nu(z)\chi_\nu(z';l_1,l_2)]$$
$$- \frac{1}{2}\sqrt{\frac{z-u}{z-v}}[p_\mu(z)(3\chi_\mu(z';l_1,l_2) + \chi_\nu(z';l_1,l_2))$$
$$- p_\nu(z)(\chi_\mu(z';l_1,l_2) - \chi_\nu(z';l_1,l_2))],$$

where the notation is specified by formulas (A.29) and (A.30). The distinction between formula (A.20) and the corresponding expression in [4] is due to the fact that, in [4], the function $G_{(\sigma=1)}^{(1)}(z,z')$ is used instead of $G_f^{(1)}(z,z';l_1,l_2)$. In order to obtain the formula

given in [4] from formula (A.20), we must first use expressions (A.33) and (A.31) to calculate $\hat{G}^{(1)}$ in (A.20) and then invoke the formula

$$\begin{aligned}&\mathrm{tr}\ln[A + A_1A_2] \qquad (A.34)\\ &= \mathrm{tr}\ln A + \mathrm{tr}\ln[1 + A^{-1}A_1A_2]\\ &= \mathrm{tr}\ln A + (-1)^P\mathrm{tr}\ln[1 + A_2A^{-1}A_1],\end{aligned}$$

which is valid for any of the operators A_1, A_2, and A, provided that $\det A \neq 0$. Here, $P = 1$ if both A_1 and A_2 obey Fermi statistics; otherwise, $P = 0$.

APPENDIX B

In order to obtain the first relation in (26), we calculate (A.19) for ω_{11} in the limit $k \to 0$ by substituting there formula (A.6) for the scalar function $J_1^{(1)}(t)$ at $\mu = \nu = 0$. The contour of integration with respect to z circumvents nondegenerate handles, but it can be transformed into a contour circumventing the points $z = u$ and $z = v$. Thus, the integral with respect to z is given by the sum of the residues at these points. The integral with respect to z' reduces to an integral along the cut of the logarithm in $J_1^{(1)}(t)$ and can easily be calculated because its integrand is the superderivative (7) of a local function. The integrals with respect to z_1 and z_2 in expression (A.18) for $\Phi_m^{(r)}(L;\{q\})$ can be calculated in a similar way. Considering that, in the limit $k \to 0$, only the function $J_1^{(1)}(t)$ in the integrands in (A.18) and (A.19) is singular at $z = u$ and $z = v$ and using expression (A.11), we can obtain the required relation. In order to derive the second relation in (26), we again substitute expression (A.6) for $J_1^{(1)}(t)$ into formula (A.19) for ω_{1l} and calculate the integral with respect to t in the same way as in deriving the first relation in (26). In the limit $k \to 0$, the integral in (A.19) with respect to t is equal to the sum of the residues of the integrand at the points $z = u$ and $z = v$. Finally, the relation for J_1 in (26) can be obtained by substituting expression (A.6) for $J_1^{(1)}(t)$ into the integral in (A.17) for $J_r^{(n)}(t;\{q\};L)$ and by subsequently calculating the integral in the limit $k \to 0$. The contour of integration with respect to t_1 in this integral circumvents nondegenerate handles. In just the same way as in the preceding cases, the integral is equal to the sum of the residues at the points $z = u$ and $z = v$. With allowance for formula (A.11), there arises the required relation. In order to obtain formula (30), we use expression (A.11). For $z \to u$, the regular part in (30) is given by the contribution of the pole that is situated at $z_1 = z = u$ and which is induced by the logarithmic term in (29). In a similar way, one can prove formula (31) and derive formulas for scalar functions. Taking into account (12), we thereby arrive at expressions (33) and (34). Following the same method and using formulas (19)–(21) and (A.20), we can calculate the function $\hat{Z}^{(n-1)}_{\tilde{L},\tilde{L}'}(\{q,\bar{q}\})$ in (24).

REFERENCES

1. M. Green, J. Schwartz, and E. Vitten, *The Theory of Superstrings* (Cambridge Univ. Press, Cambridge, 1987, 1988; Mir, Moscow, 1990), Vols. 1, 2.
2. D. Friedan, E. Martinec, and S. Shenker, Nucl. Phys. B **271**, 93 (1986).
3. B. E. W. Nilsson and A. K. Tollstén, Phys. Lett. B **240**, 96 (1990).
4. G. S. Danilov, Phys. Rev. D **51**, 4359 (1995); Erratum: **52**, 6201 (1995).
5. G. S. Danilov, Nucl. Phys. B **463**, 443 (1996).
6. G. S. Danilov, Yad. Fiz. **59**, 1837 (1996) [Phys. At. Nucl. **59**, 1774 (1996)].
7. P. Di Vecchia, K. Hornfeck, M. Frau, *et al.*, Phys. Lett. B **211**, 301 (1988).
8. J. L. Petersen, J. R. Sidenius, and A. K. Tollstén, Phys. Lett. B **213**, 30 (1988); Nucl. Phys. B **317**, 109 (1989); B. E. W. Nilsson, A. K. Tollstén, and A. Wätterstam, Phys. Lett. B **222**, 399 (1989).
9. G. S. Danilov, Yad. Fiz. **52**, 1143 (1990) [Sov. J. Nucl. Phys. **52**, 727 (1990)]; Phys. Lett. B **257**, 285 (1991).
10. E. Verlinde and H. Verlinde, Phys. Lett. B **192**, 95 (1987).
11. J. Atick and A. Sen, Nucl. Phys. B **296**, 157 (1988); **299**, 279 (1988).
12. G. Moore and A. Morozov, Nucl. Phys. B **306**, 387 (1988); A. Yu. Morozov, Teor. Mat. Fiz. **81**, 24, 293 (1989).
13. N. Berkovits, Nucl. Phys. B **395**, 77 (1993).
14. S. Mandelstam, Phys. Lett. B **277**, 82 (1992).
15. E. D'Hoker and D. H. Phong, hep-th/0110247; hep-th/0110283.
16. E. Martinec, Nucl. Phys. B **281**, 157 (1986).
17. G. S. Danilov, Pis'ma Zh. Éksp. Teor. Fiz. **58**, 790 (1993) [JETP Lett. **58**, 736 (1993)].
18. M. A. Baranov and A. S. Shvartz, Pis'ma Zh. Éksp. Teor. Fiz. **42**, 340 (1985) [JETP Lett. **42**, 419 (1985)]; D. Friedan, in *Proceedings of the Santa Barbara Workshop on Unified String Theories,* Ed. by D. Gross and M. Green (World Sci., Singapore, 1986).
19. D. V. Volkov, A. A. Zheltukhin, and A. I. Pashnev, Yad. Fiz. **27**, 243 (1978) [Sov. J. Nucl. Phys. **27**, 131 (1978)].
20. L. Crane and J. M. Rabin, Commun. Math. Phys. **113**, 601 (1988); J. D. Cohn, Nucl. Phys. B **306**, 239 (1988).
21. N. Seiberg and E. Witten, Nucl. Phys. B **276**, 272 (1986).
22. G. S. Danilov, Yad. Fiz. **60**, 1495 (1997) [Phys. At. Nucl. **60**, 1358 (1997)].

23. G. S. Danilov, Yad. Fiz. **57**, 2272 (1994) [Phys. At. Nucl. **57**, 2183 (1994)].
24. G. S. Danilov, Yad. Fiz. **58**, 2095 (1995) [Phys. At. Nucl. **58**, 1984 (1995)].
25. L. Hodkin, J. Phys. Gravity **6**, 333 (1989).
26. G. S. Danilov, Pis'ma Zh. Éksp. Teor. Fiz. **58**, 790 (1993) [JETP Lett. **58**, 736 (1993)].
27. P. Di Vecchia, M. Frau, A. Lerda, and S. Sciuto, Phys. Lett. B **199**, 49 (1987).
28. G. S. Danilov, Yad. Fiz. **49**, 1787 (1989) [Sov. J. Nucl. Phys. **49**, 1106 (1989)].
29. A. A. Belavin and V. G. Knizhnik, Zh. Éksp. Teor. Fiz. **91**, 364 (1986) [Sov. Phys. JETP **64**, 214 (1986)].

Translated by A. Isaakyan

Physics of Atomic Nuclei, Vol. 66, No. 7, 2003, pp. 1375–1383. Translated from Yadernaya Fizika, Vol. 66, No. 7, 2003, pp. 1416–1425.

ELEMENTARY PARTICLES AND FIELDS
Theory

Unitary Scalar–Vector Mixing in the ξ Gauge

A. E. Kaloshin* **and A. E. Radzhabov**

Institute of Applied Physics, Irkutsk State University, bul'v. Gagarina 20, Irkutsk, 664003 Russia

Received February 14, 2002; in final form, August 16, 2002

Abstract—The effect of the unitary mixing of scalar and vector fields is considered in the ξ gauge. For this effect to emerge, it is necessary that the vector current not be conserved; in the ξ gauge, there arise additional complications because of the presence of an unphysical scalar field. Solutions to the Dyson–Schwinger equations are obtained, and the renormalization of complete propagators is investigated. The use of the Ward identity, which relates a few different Green's functions, is a key point in performing this renormalization. It is shown that the dependence on the gauge parameter ξ disappears in the renormalized matrix element. © *2003 MAIK "Nauka/Interperiodica"*.

1. INTRODUCTION

The mixing of scalar and vector fields (S–V mixing) arises at a loop level if there exists an off-diagonal loop that relates a scalar and a vector propagator to each other. For this, it is necessary that the relevant vector current not be conserved.

A similar effect was noticed long ago [1, 2] in studying the Standard Model in the ξ gauge, where there arose the mixing of gauge-boson fields and an unphysical field—that is, the so-called Higgs ghost, whose propagator has a pole at the point $p^2 = \xi M^2$.[1)] However, a physical scalar field may also participate in mixing. By way of example, we indicate that, in [3], this effect was examined in the π–a_1 system and that, in [4], the S–V mixing between gauge bosons and Higgs particles was explored in various extended electroweak models. However, no attention was given in [4] either to the renormalization problem, which is nontrivial in the case being considered, or to the problem of gauge dependence. We note that, in the ξ gauge, S–V mixing leads to an interesting effect that was discovered in [5]: upon taking into account Ward identities, the dressing procedure leads to a transition to a different type of singularity for some propagators—namely, a simple pole of a bare propagator at the point $p^2 = \xi M^2$ transforms into a second-order pole of the corresponding total propagator. In view of this, there naturally arises the question of whether the Standard Model is renormalizable in principle in this gauge [5].

In the present study, we examine the unitary mixing of a physical scalar field and a vector field in the ξ gauge, pursuing our analysis to the stage of deriving a renormalized matrix element and investigating the dependence on ξ. We consider both the case of boson loops and the case of fermion loops because either case has its own special features. In particular, our consideration is applicable to electroweak models involving an extended Higgs sector.[2)]

In the ξ gauge, the Lagrangian is supplemented with the gauge-fixing term

$$L_{gf} = -\frac{1}{2\xi}(\partial^\mu A_\mu)^2. \qquad (1)$$

In taking into account loop contributions, there arises the mixing of three bare propagators (see Fig. 1): the scalar-particle propagator, the vector-field propagator in the ξ gauge, and the ghost propagator.

It is convenient to break down the vector propagator into the transverse and the longitudinal component; that is,

$$\pi_{22}^{\mu\nu} = T^{\mu\nu}\frac{1}{p^2 - M^2} + L^{\mu\nu}\frac{\xi}{\xi M^2 - p^2}, \qquad (2)$$
$$T^{\mu\nu} = -g^{\mu\nu} + \frac{p^\mu p^\nu}{p^2}, \quad L^{\mu\nu} = \frac{p^\mu p^\nu}{p^2}.$$

We recall that only the longitudinal vector-propagator component not associated with the spin of $J = 1$ can be mixed with a scalar field. For this effect to emerge, it is necessary that the vector current with

*e-mail: kaloshin@physdep.isu.runnet.ru

[1)]Different terms are used for this field. In what follows, we will refer to it merely as a ghost, nourishing the hope that this will not lead to a terminological confusion.

[2)]Loop transitions between massive gauge fields and Higgs scalars may arise only if the theory being considered features charged or pseudoscalar Higgs particles. It should also be recalled that, upon a spontaneous breakdown of symmetry, currents remain conserved, but that currents with which vector fields interact are not Noether currents; therefore, there is no contradiction between spontaneous symmetry breaking and the occurrence of scalar–vector transitions.

1063-7788/03/6607-1375$24.00

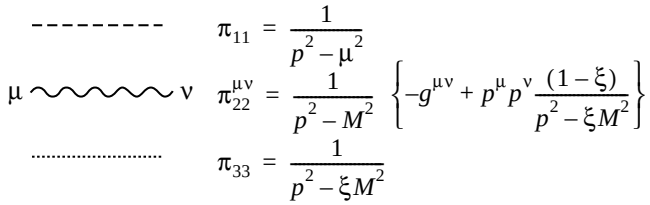

Fig. 1. Scalar-particle, vector-particle, and ghost propagators.

which this vector field interacts not be conserved. In the longitudinal component of the vector-particle propagator, there appeared an unphysical pole at the point $p^2 = \xi M^2$, but it was noticed long ago (see, for example, [6]) that the sign of this pole is opposite with respect to the scalar-meson contribution. In order to cancel this pole at the tree level, it is therefore sufficient to introduce an unphysical scalar field of mass ξM^2. As a result, there arises, at a loop level, the mixing of the aforementioned three propagators; in addition, there appear total off-diagonal propagators, which were absent at the tree level. Upon dressing, there therefore arise the problem of renormalizing coupled propagators and the problem of the gauge-parameter (in)dependence of the relevant S matrix.

2. SET OF DYSON–SCHWINGER EQUATION

In the case of mixing, propagators and loops become matrices; as a result, the set of Dyson–Schwinger equations takes the form[3)]

$$\Pi_{11} = \pi_{11} - \Pi_{11}J_{11}\pi_{11} - \Pi^\mu_{12}J^\mu_{21}\pi_{11} - \Pi_{13}J_{31}\pi_{11}, \tag{3}$$
$$\Pi^\mu_{12} = -\Pi_{11}J^\nu_{12}\pi^{\nu\mu}_{22} - \Pi^\gamma_{12}J^{\gamma\nu}_{22}\pi^{\nu\mu}_{22} - \Pi_{13}J^\nu_{32}\pi^{\nu\mu}_{22},$$
$$\Pi_{13} = -\Pi_{11}J_{13}\pi_{33} - \Pi^\mu_{12}J^\mu_{23}\pi_{33} - \Pi_{13}J_{33}\pi_{33},$$
$$\Pi^\mu_{21} = -\Pi^\mu_{21}J_{11}\pi_{11} - \Pi^{\mu\gamma}_{22}J^\gamma_{21}\pi_{11} - \Pi^\mu_{23}J_{31}\pi_{11},$$
$$\Pi^{\mu\nu}_{22} = \pi^{\mu\nu}_{22} - \Pi^\mu_{21}J^\gamma_{12}\pi^{\gamma\nu}_{22} - \Pi^{\mu\gamma}_{22}J^{\gamma\rho}_{22}\pi^{\rho\nu}_{22} - \Pi^\mu_{23}J^\gamma_{32}\pi^{\gamma\nu}_{22},$$
$$\Pi^\mu_{23} = -\Pi^\mu_{21}J_{13}\pi_{33} - \Pi^{\mu\gamma}_{22}J^\gamma_{23}\pi_{33} - \Pi^\mu_{23}J_{33}\pi_{33},$$
$$\Pi_{31} = -\Pi_{31}J_{11}\pi_{11} - \Pi^\mu_{32}J^\mu_{21}\pi_{11} - \Pi_{33}J_{31}\pi_{11},$$
$$\Pi^\mu_{32} = -\Pi_{31}J^\nu_{12}\pi^{\nu\mu}_{22} - \Pi^\gamma_{32}J^{\gamma\nu}_{22}\pi^{\nu\mu}_{22} - \Pi_{33}J^\nu_{32}\pi^{\nu\mu}_{22},$$
$$\Pi_{33} = \pi_{33} - \Pi_{31}J_{13}\pi_{33} - \Pi^\mu_{32}J^\mu_{23}\pi_{33} - \Pi_{33}J_{33}\pi_{33},$$

where π_{ij} are bare propagators, Π_{ij} are total propagators, and J_{ij} are single-particle-irreducible loop contributions. In these equations, we will break down each quantity carrying two indices into a transverse and a longitudinal component; that is,

$$\Pi^{\mu\nu}_{22} = T^{\mu\nu}\Pi^T_{22}(p^2) + L^{\mu\nu}\Pi^L_{22}(p^2), \tag{4}$$
$$\pi^{\mu\nu}_{22} = T^{\mu\nu}\pi^T_{22}(p^2) + L^{\mu\nu}\pi^L_{22}(p^2),$$
$$J^{\mu\nu}_{22} = T^{\mu\nu}J^T_{22}(p^2) + L^{\mu\nu}J^L_{22}(p^2),$$

where

$$T^{\mu\nu} = -g^{\mu\nu} + \frac{p^\mu p^\nu}{p^2}, \qquad L^{\mu\nu} = \frac{p^\mu p^\nu}{p^2}.$$

In the quantities carrying one index, we go over to scalar functions according to the relations

$$\Pi^\mu_{12}(p) = p^\mu\Pi_{12}(p^2), \quad \Pi^\mu_{21}(p) = p^\mu\Pi_{21}(p^2), \tag{5}$$
$$J^\mu_{12}(p) = p^\mu J_{12}(p^2), \quad J^\mu_{21}(p) = p^\mu J_{21}(p^2),$$
$$\Pi^\mu_{23}(p) = p^\mu\Pi_{23}(p^2), \quad \Pi^\mu_{32}(p) = p^\mu\Pi_{32}(p^2),$$
$$J^\mu_{23}(p) = p^\mu J_{23}(p^2), \quad J^\mu_{32}(p) = p^\mu J_{32}(p^2).$$

The equation for the transverse component is separated from the set of equations in question. As a result, it assumes the same form as in the absence of scalar–vector mixing; that is,

$$\Pi^T_{22} = \pi^T_{22} - \Pi^T_{22}J^T_{22}\pi^T_{22}. \tag{6}$$

A solution to this equation can be written in the form

$$\Pi^T_{22} = \frac{1}{p^2 - M^2 + J^T_{22}}. \tag{7}$$

As to the longitudinal components, the following set of equations arises for them in the ξ gauge:[4)]

$$\Pi_{11} = \pi_{11} - \Pi_{11}J_{11}\pi_{11} - p^2\Pi_{12}J_{21}\pi_{11} - \Pi_{13}J_{31}\pi_{11}, \tag{8}$$
$$\Pi_{12} = -\Pi_{11}J_{12}\pi_{22} - \Pi_{12}J_{22}\pi_{22} - \Pi_{13}J_{32}\pi_{22},$$
$$\Pi_{21} = -\Pi_{21}J_{11}\pi_{11} - \Pi_{22}J_{21}\pi_{11} - \Pi_{23}J_{31}\pi_{11},$$
$$\Pi_{22} = \pi_{22} - p^2\Pi_{21}J_{12}\pi_{22} - \Pi_{22}J_{22}\pi_{22} - p^2\Pi_{23}J_{32}\pi_{22},$$
$$\Pi_{13} = -\Pi_{11}J_{13}\pi_{33} - p^2\Pi_{12}J_{23}\pi_{33} - \Pi_{13}J_{33}\pi_{33},$$
$$\Pi_{31} = -\Pi_{31}J_{11}\pi_{11} - p^2\Pi_{32}J_{21}\pi_{11} - \Pi_{33}J_{31}\pi_{11},$$

[3)] In relation to the analysis of the unitary gauge in [3], we redefined here the off-diagonal scalar–vector propagators as $i\Pi_{12} \to \Pi_{12}$ and $i\Pi_{21} \to \Pi_{21}$ in order to obtain a more symmetric form of the equations in question. In addition, we do not assume that off-diadonal transitions possess some specific symmetry or asymmetry properties—the form of symmetry relations is dictated by the form of interaction, so that these relations may be different in different cases. We also note that a change in the form of the equations corresponds to redefining the loops involved.

[4)] Below, we use longitudinal components, suppressing the superscript L, unless otherwise stated.

$$\Pi_{23} = -\Pi_{21}J_{13}\pi_{33} - \Pi_{22}J_{23}\pi_{33} - \Pi_{23}J_{33}\pi_{33},$$
$$\Pi_{32} = -\Pi_{31}J_{12}\pi_{22} - \Pi_{32}J_{22}\pi_{22} - \Pi_{33}J_{32}\pi_{22},$$
$$\Pi_{33} = \pi_{33} - \Pi_{31}J_{13}\pi_{33} - p^2\Pi_{32}J_{23}\pi_{33} - \Pi_{33}J_{33}\pi_{33}.$$

A solution to this set of equations has the form

$$\Pi_{11} = \frac{1}{D}\left[(\pi_{22}^{-1} + J_{22})(\pi_{33}^{-1} + J_{33}) - sJ_{23}J_{32}\right],$$
$$\Pi_{12} = -\frac{1}{D}\left[J_{12}(\pi_{33}^{-1} + J_{33}) - J_{13}J_{32},\right], \quad (9)$$
$$\Pi_{21} = -\frac{1}{D}\left[J_{21}(\pi_{33}^{-1} + J_{33}) - J_{23}J_{31}\right],$$
$$\Pi_{22} = \frac{1}{D}\left[(\pi_{11}^{-1} + J_{11})(\pi_{33}^{-1} + J_{33}) - J_{31}J_{13}\right],$$
$$\Pi_{13} = -\frac{1}{D}\left[J_{13}(\pi_{22}^{-1} + J_{22}) - sJ_{12}J_{23}\right],$$
$$\Pi_{31} = -\frac{1}{D}\left[J_{31}(\pi_{22}^{-1} + J_{22}) - sJ_{32}J_{21}\right],$$
$$\Pi_{23} = -\frac{1}{D}\left[J_{23}(\pi_{11}^{-1} + J_{11}) - J_{21}J_{13}\right],$$
$$\Pi_{32} = -\frac{1}{D}\left[J_{32}(\pi_{11}^{-1} + J_{11}) - J_{31}J_{12}\right],$$
$$\Pi_{33} = \frac{1}{D}\left[(\pi_{11}^{-1} + J_{11})(\pi_{22}^{-1} + J_{22}) - sJ_{21}J_{12}\right],$$

where $s = p^2$ and

$$D(s) = (\pi_{11}^{-1} + J_{11})(\pi_{22}^{-1} + J_{22})(\pi_{33}^{-1} + J_{33}) \quad (10)$$
$$- (\pi_{11}^{-1} + J_{11})sJ_{32}J_{23} - (\pi_{22}^{-1} + J_{22})J_{31}J_{13}$$
$$- (\pi_{33}^{-1} + J_{33})sJ_{21}J_{12} + sJ_{12}J_{23}J_{31} + sJ_{32}J_{21}J_{13}.$$

We note that the transverse and the longitudinal component of the vector-particle propagator are not completely independent. For the relevant matrix element to be free from a $1/p^2$ pole, fulfillment of the condition $J_{22}^T(0) + J_{22}^L(0) = 0$ is necessary.

3. BOSON LOOPS: π–a_1 SYSTEM

We will examine the model identical to that which was studied in the unitary gauge in [3]—specifically, we consider the π–a_1 system dressed by a $\pi\sigma$ intermediate state.[5)]

The Feynman rules for this model are illustrated in Fig. 2.

For unphysical poles to be canceled in the matrix element at the tree level, it is necessary that

$$g_{G\pi\sigma} = \frac{g_{a\pi\sigma}}{M}. \quad (11)$$

We now present results obtained by calculating the relevant self-energy parts at the one-loop level. We note that, upon specifying the Feynman rules, loops must be determined consistently with Dyson–Schwinger equations. With respect to the unitary gauge, there appear new contributions that relate the ghost propagator to other particles. Loops are calculated by means of a procedure in which the application of a unitary cut is followed by the restoration of an integral over the discontinuity; that is,

$$J_{11}(p^2) = -i\,g_{\sigma\pi\pi}^2\int\frac{d^4l}{(2\pi)^4}\,\frac{1}{(l^2-\mu^2)((l-p)^2-m^2)}, \quad (12)$$
$$J_{12}^{\mu}(p) = -\,g_{a_1\pi\sigma}\,g_{\sigma\pi\pi}\int\frac{d^4l}{(2\pi)^4}\,\frac{(2l-p)^{\mu}}{(l^2-\mu^2)((l-p)^2-m^2)},$$
$$J_{13}(p^2) = -i\frac{g_{\pi\pi\sigma}g_{a_1\pi\sigma}}{M}\int\frac{d^4l}{(2\pi)^4}\,\frac{(p\cdot(2l-p))}{(l^2-\mu^2)((l-p)^2-m^2)},$$
$$J_{22}^{\mu\nu}(p) = -i\,g_{a_1\pi\sigma}^2\int\frac{d^4l}{(2\pi)^4}\,\frac{(2l-p)^{\mu}(2l-p)^{\nu}}{(l^2-\mu^2)((l-p)^2-m^2)},$$
$$J_{23}^{\mu}(p) = \frac{g_{a_1\pi\sigma}^2}{M}\int\frac{d^4l}{(2\pi)^4}\,\frac{(2l-p)^{\mu}(p\cdot(2l-p))}{(l^2-\mu^2)((l-p)^2-m^2)},$$
$$J_{33}(p^2) = -i\frac{g_{a_1\pi\sigma}^2}{M^2}\int\frac{d^4l}{(2\pi)^4}\,\frac{(p\cdot(2l-p))(p\cdot(2l-p))}{(l^2-\mu^2)((l-p)^2-m^2)},$$

where $m = m_\sigma$ and $\mu = m_\pi$.

The Feynman rules lead to the following symmetry relations for off-diagonal loops:

$$J_{21}^{\mu} = -J_{12}^{\mu}, \quad (13)$$
$$J_{32}^{\mu} = -J_{23}^{\mu},$$
$$J_{31} = J_{13}.$$

In just the same way as in the case of the unitary

[5)] We recall that π–a_1 transitions at the tree level arise in chiral models [7, 8]; therefore, their emergence at a loop level is quite natural.

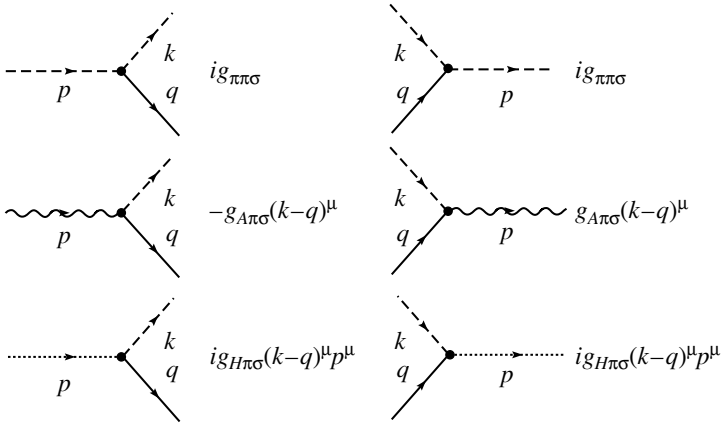

Fig. 2. Vertices for the $\pi-a_1$ model.

gauge in [3], all loops are expressed in terms of one function $H(p^2)$, apart from subtraction polynomials to be determined in the renormalization process. Specifically, we have

$$H(p^2) = \frac{1}{\pi}\int \frac{ds}{s(s-p^2)}\left(\frac{\lambda(s,m^2,\mu^2)}{s^2}\right)^{1/2}, \quad (14)$$

$$J_{11}(s) = g_1^2[P_{11} + sH(s)], \quad (15)$$
$$J_{12}(s) = -ig_1g_2[P_{12} + H(s)],$$
$$J_{13}(s) = \frac{g_1g_2}{M}[P_{13} + sH(s)],$$
$$J_{22}(s) = g_2^2[P_{22} + H(s)],\ J_{23}(s) = i\frac{g_2^2}{M}[P_{23} + H(s)],$$
$$J_{33}(s) = \frac{g_2^2}{M^2}[P_{33} + sH(s)],$$

where P_{ij} are polynomials in s with real-valued coefficients. We have also introduced the following notation: $g_1 = g_{\sigma\pi\pi}/\sqrt{16\pi}$, $g_2 = (\mu^2 - m^2)g_{a_1\pi\sigma}/\sqrt{16\pi}$, and $\lambda(a,b,c) = (a-b-c)^2 - 4bc$.

For total propagators, the $\pi\sigma \to \pi\sigma$ matrix element has the form

$$\frac{1}{16\pi}\mathcal{M}^{J=0} = -g_1^2\Pi_{11} - 2ig_1g_2\Pi_{12} - 2\frac{g_1g_2}{M}\Pi_{13} + 2i\frac{g_2^2}{M}\Pi_{23} - \frac{g_2^2}{s}\Pi_{22} - \frac{g_2^2}{M^2}\Pi_{33}. \quad (16)$$

Renormalization of the pion pole. We will perform renormalization by means of on-shell subtractions. Needless to say, the procedure is somewhat modified with allowance for the mixing of the propagators. The most economical formulation of the requirements on pion-pole renormalization is as follows:

(i) The function $D(s)$ must possess a simple zero at the point $s = \mu^2$ for any values of the coupling constants g_1 and g_2, which are assumed to be independent.

(ii) The total pion propagator Π_{11} must have a pole with a residue equal to unity, in just the way as the bare pion propagator π_{11} does have such a pole. This means the sum of all loop insertions into the external pion line is equal to zero.

These requirements lead to conditions on loops at the point $s = \mu^2$—that is, on subtraction polynomials:

$$J_{11}(\mu^2) = J'_{11}(\mu^2) = 0, \quad (17)$$
$$J_{12}(\mu^2) = 0, \quad J_{13}(\mu^2) = 0.$$

Renormalization of ξ. Since the mass of a vector particle is renormalized in the transverse part of the vector-particle propagator, the quantity M can be treated as a mass that has already been renormalized. Therefore, the renormalization of the unphysical pole at the point $s = \xi M^2$ is the renormalization of the gauge parameter ξ.

We will try to follow a line of reasoning similar to that in the case of the pion pole and formulate the following requirements on the renormalization in question:[6)]

(i) The function $D(s)$ must possess a second-order pole at the point $s = \xi M^2$ for any values of the coupling constants.

(ii) At this point, the total propagators Π_{22} and Π_{33} must have a simple pole.

By using the explicit form of the relevant solutions, we find that this leads to the conditions

$$J_{22}(\xi M^2) = J_{33}(\xi M^2) = J_{12}(\xi M^2) = J_{13}(\xi M^2) = J_{23}(\xi M^2) = 0. \quad (18)$$

[6)] These requirements are minimal, implying that the character of the singularity remains unchanged upon dressing the bare propagators. Since a ghost appears only in the form of propagators—and not in the form of external legs—we impose no conditions on the residues of the propagators.

It can easily be seen that, among total propagators, only Π_{23}, apart from Π_{22} and Π_{33}, can have a pole at the point $s = \xi M^2$. In order to trace the unphysical pole in the matrix element, it is therefore sufficient to consider only these contributions:

$$\frac{1}{16\pi}\hat{\mathcal{M}}^{J=0} = -\frac{g_2^2}{p^2}\Pi_{22}(p^2) - \frac{g_2^2}{M^2}\Pi_{33}(p^2) + 2i\frac{g_2^2}{M}\Pi_{23}(p^2). \quad (19)$$

Substituting solutions to the Dyson–Schwinger equations and using conditions (18), we find that, for an unphysical pole to be absent from the matrix element, it is necessary that the function $Y(s)$,

$$Y(s) = M^2 J_{33}(s) + sJ_{22}(s) + 2iMsJ_{23}(s), \quad (20)$$

have a second-order zero at the point ξM^2. This imposes constraints on the subtraction polynomials since, from (15), it can be seen that the loop function $H(s)$ cancels in (20).

We recall that the absence of a $1/p^2$ pole relates J_{22}^T to J_{22}^L:

$$J_{22}^T(0) + J_{22}^L(0) = 0. \quad (21)$$

With allowance for (18), the polynomial in the loop J_{22}^L must have the form

$$P_{22} = E\left(1 - \frac{s}{\xi M^2}\right) - \frac{s}{\xi M^2}H(\xi M^2), \quad (22)$$

where E is a constant that is determined in the transverse part of the loop J_{22}. We can now write renormalized loops that satisfy the condition in (20):

$$J_{22} = g_2^2\left[E\left(1 - \frac{s}{\xi M^2}\right) - \frac{s}{\xi M^2}H(\xi M^2) + H(s)\right], \quad (23)$$

$$J_{23} = i\frac{g_2^2}{M}\left[H(\xi M^2) - H(s)\right],$$

$$J_{33} = \frac{g_2^2}{M^2} \times \left[-\xi M^2 H(\xi M^2) - E\xi M^2\left(1 - \frac{s}{\xi M^2}\right) + sH(s)\right].$$

The remaining loops, which are not involved in the function $Y(s)$ (20), are given by

$$J_{11} = g_1^2\left[-sH(\mu^2) - \mu^2 H'(\mu^2)(s-\mu^2) + sH(s)\right], \quad (24)$$

$$J_{12} = -ig_1 g_2\left[\frac{\xi M^2 H(\mu^2) - \mu^2 H(\xi M^2)}{\mu^2 - \xi M^2} + s\frac{H(\xi M^2) - H(\mu^2)}{\mu^2 - \xi M^2} + H(s)\right],$$

$$J_{13} = \frac{g_1 g_2}{M}\left[\mu^2\xi M^2\frac{H(\xi M^2) - H(\mu^2)}{\mu^2 - \xi M^2} - \frac{\xi M^2 H(\xi M^2) - \mu^2 H(\mu^2)}{\mu^2 - \xi M^2} - sH(s)\right].$$

Having determined the subtraction polynomials in loops, we can now calculate the matrix element (16). Upon the substitution of total propagators, we arrive at a cumbersome expression in which there remains a dependence on the gauge parameter ξ. This means that an unphysical pole cannot be renormalized by a method similar to that applied to the physical pole, so that it is necessary to seek some other ways.

Ward identity. The use of a Ward identity that relates a few different total propagators is a key point in renormalizing ξ. This identity was derived in [5] by means of the Bechi–Rouet–Stora–Tyutin (BRST) transformation in a somewhat simpler situation where there is no a physical scalar. To test this derivation, we will obtain the Ward identity by a different method.

The Feynman rules presented above correspond to the Lagrangian[7)]

$$\mathcal{L} = -\frac{1}{4}(\partial_\mu A_\nu - \partial_\nu A_\mu)^2 + \frac{1}{2}M^2 A_\mu A^\mu - \frac{1}{2\xi}(\partial A)^2 + \frac{1}{2}(\partial_\mu\varphi)^2 - \frac{1}{2}\xi M^2\varphi^2 + A_\mu J^\mu + \frac{1}{M}\partial_\mu\varphi J^\mu, \quad (25)$$

where φ is the ghost field and J^μ is a vector current whose explicit form is immaterial here. We have presented here only terms involving the vector field and the ghost field. The equations of motion have the form

$$(\partial_\alpha\partial^\alpha + M^2)A_\mu - \left(1 - \frac{1}{\xi}\right)\partial_\mu(\partial A) = -J_\mu, \quad (26)$$

$$(\partial_\alpha\partial^\alpha + \xi M^2)\varphi = -\frac{1}{M}(\partial J). \quad (27)$$

From these two equations, it follows that

$$(\partial_\alpha\partial^\alpha + \xi M^2)((\partial A) - \xi M\varphi) = 0, \quad (28)$$

which means that the combination $(\partial A) - \xi M\varphi$, which appeared in (28), is a noninteracting field. If one examines the vacuum expectation value of the time-ordered product of these fields, such a Green's

[7)] We do not explicitly write isotopic indices here because they are trivial in the model being considered.

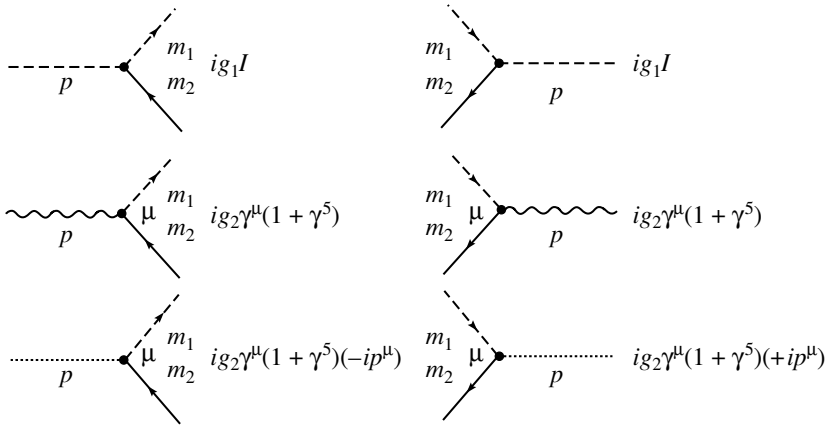

Fig. 3. Vertices for the $W^\pm - H^\pm$ model.

function must not change upon switching on the interaction. Calculating it for the respective bare quantities, we find that the result vanishes:

$$\langle 0|T\{((\partial A(x)) - \xi M\varphi(x))((\partial A(y)) - \xi M\varphi(y))\}|0\rangle = 0. \quad (29)$$

We note that, in order to go over in this expression to the propagators, it is necessary to differentiate the time-ordered product of vector fields accurately. The point is that this operation generates additional terms that are proportional to single-time commutators of interacting fields. It is well known, however, that single-time commutation relations for interacting fields commute with those for the corresponding free fields (see, for example, [9]). Upon performing the required calculations, we arrive at

$$\frac{\partial}{\partial x_\mu}\frac{\partial}{\partial y_\nu}\langle 0|T\{A_\mu(x)A_\nu(y)\}|0\rangle = \langle 0|T\{\partial A(x)\partial A(y)\}|0\rangle - i\xi\delta^4(x-y). \quad (30)$$

As a result, we find that, in the momentum representation, the required Ward identity in terms of the total propagators assumes the form[8)]

$$s\Pi_{22}^L(s) - 2is\xi M\Pi_{23}(s) + \xi^2 M^2\Pi_{33}(s) + \xi = 0. \quad (31)$$

Substituting the explicit form (9) of the total propagators into the Ward identity (31) and equating to zero the coefficients of the identical powers of the coupling constants g_1 and g_2, we obtain the following set of relations:

$$M^2J_{33} + sJ_{22} + 2isMJ_{23} = 0, \quad (32)$$
$$J_{22}J_{33} + s(J_{23})^2 = 0,$$
$$2isMJ_{12}J_{13} - M^2J_{13}^2 + s^2J_{12}^2 = 0,$$
$$-J_{22}J_{13}^2 + sJ_{33}J_{12}^2 + 2sJ_{12}J_{13}J_{23} = 0.$$

Solving these equations, we arrive at simple relations between the loops:

$$J_{33} = \frac{s}{M^2}J_{22}, \quad (33)$$
$$J_{23} = \frac{i}{M}J_{22}, \quad J_{13} = i\frac{s}{M}J_{12}.$$

We note that, in (32), there appeared the same function $Y(s)$ (20), which ensures the absence of unphysical poles in the matrix element.

Let us now calculate the total propagators by using relations (32), which follow from the Ward identity. It immediately turns out that, in the function $D(s)$, the dependence on the gauge parameter factors out:[9)]

$$D(s) = -\frac{(s-\xi M^2)^2}{\xi M^2}\hat{D}(s), \quad (34)$$

where there appeared the function

$$\hat{D}(s) = (\pi_{11}^{-1} + J_{11})(M^2 + J_{22}) + s(J_{12})^2, \quad (35)$$

which plays the role of the determinant in the unitary gauge [3].

The total propagators assume a rather simple form; that is,

$$\Pi_{11} = \frac{M^2 + J_{22}}{\hat{D}}, \quad (36)$$
$$\Pi_{12} = \frac{\xi M^2 J_{12}}{(s-\xi M^2)\hat{D}} \quad \Pi_{13} = -i\frac{MsJ_{12}}{(s-\xi M^2)\hat{D}},$$

[8)] We note that, in the literature, there is no consensus on the exact form of this relation. By way of example, we indicate that, in [10], it is written without the term ξ, although the corollaries from it coincide with our Eqs. (33).

[9)] Upon dressing the propagator, the pole lying above the threshold usually goes to the complex plane. In the presence of the Ward identity, however, the pole remains here on the real axis.

$$\Pi_{23} = i\frac{\xi M\left[(\pi_{11}^{-1}+J_{11})J_{22}+s(J_{12}^2)\right]}{(s-\xi M^2)^2\hat{D}},$$

$$\Pi_{22}$$
$$= -\xi\frac{(\pi_{11}^{-1}+J_{11})(M^2(s-\xi M^2)+sJ_{22})+s^2(J_{12})^2}{(s-\xi M^2)^2\hat{D}},$$

$$\Pi_{33}$$
$$= M^2\frac{(\pi_{11}^{-1}+J_{11})((s-\xi M^2)-\xi J_{22})-\xi s(J_{12})^2}{(s-\xi M^2)^2\hat{D}}.$$

Substituting the total propagators into the matrix element $\pi\sigma\to\pi\sigma$ (16), we obtain

$$\frac{1}{16\pi}\mathcal{M}^{J=0} = -g_1^2\frac{M^2+J_{22}}{\hat{D}} + 2ig_1g_2\frac{J_{12}}{\hat{D}} - g_2^2\frac{\pi_{11}^{-1}+J_{11}}{\hat{D}}. \quad (37)$$

The dependence on the gauge parameter ξ disappeared, and this expression coincides with the matrix element in the unitary gauge [3] if one imposes no conditions on the loop J_{11}, J_{12}, and J_{22} at the point $s=\xi M^2$.

Finally, we note that, if the terms in the matrix element (16) are arranged as

$$\frac{1}{16\pi}\mathcal{M}^{J=0} = -g_1^2\Pi_{11} - 2ig_1g_2\left(\Pi_{12}-\frac{i}{M}\Pi_{13}\right) - g_2^2\left(\frac{1}{s}\Pi_{22}+\frac{1}{M^2}\Pi_{33}-\frac{2i}{M}\Pi_{23}\right), \quad (38)$$

one can easily notice that, not only is the entire sum independent of the gauge parameter ξ, but also each of the above three terms individually possesses this property.

4. FERMION LOOPS: MIXING OF GAUGE BOSONS AND HIGGS PARTICLES IN EXTENDED MODELS

We recall that the unitary mixing of gauge bosons with Higgs particles is possible only in extended electroweak models since either pseudoscalar or charged Higgs particles are required for this. We will not specify the choice of model—it is sufficient to fix the form of vertices. For the sake of simplicity, we assume that only one physical scalar participates in mixing.

***$W^{\pm}$–$H^{\pm}$* mixing.** The interaction vertices are displayed in Fig. 3.[10)]

[10)]The longitudinal component of the $W^{\pm}$ field is mixed with the field of the charged Higgs particle. As will be seen from Eq. (41), which is given below, off-diagonal transitions vanish for the neutral Higgs field ($m_1=m_2$).

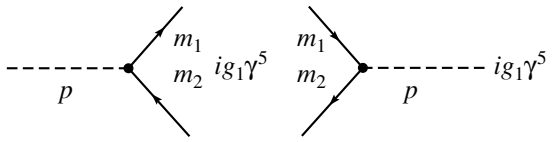

Fig. 4. Vertices for Z^0–pseudoscalar Higgs boson model.

The expressions for the loops are given by

$$J_{11}(p^2) = -ig_1^2\int\frac{d^4l}{(2\pi)^4} \times \mathrm{tr}\left\{\frac{1}{\hat{l}-\hat{p}-m_2}\frac{1}{\hat{l}-m_1}\right\}, \quad (39)$$

$$J_{12}^{\mu}(p) = -ig_1g_2\int\frac{d^4l}{(2\pi)^4} \times \mathrm{tr}\left\{\frac{1}{\hat{l}-\hat{p}-m_2}\gamma^{\mu}(1+\gamma^5)\frac{1}{\hat{l}-m_1}\right\},$$

$$J_{13}(p^2) = \frac{g_1g_2}{M}\int\frac{d^4l}{(2\pi)^4} \times \mathrm{tr}\left\{\frac{1}{\hat{l}-\hat{p}-m_2}\hat{p}(1+\gamma^5)\frac{1}{\hat{l}-m_1}\right\},$$

$$J_{22}^{\mu\nu}(p) = -ig_2^2\int\frac{d^4l}{(2\pi)^4} \times \mathrm{tr}\left\{\gamma^{\mu}(1+\gamma^5)\frac{1}{\hat{l}-\hat{p}-m_2}\gamma^{\nu}(1+\gamma^5)\frac{1}{\hat{l}-m_1}\right\},$$

$$J_{23}^{\mu}(p) = \frac{g_2^2}{M}\int\frac{d^4l}{(2\pi)^4} \times \mathrm{tr}\left\{\gamma^{\mu}(1+\gamma^5)\frac{1}{\hat{l}-\hat{p}-m_2}\hat{p}(1+\gamma^5)\frac{1}{\hat{l}-m_1}\right\},$$

$$J_{33}(p) = -\frac{g_2^2}{M^2}\int\frac{d^4l}{(2\pi)^4} \times \mathrm{tr}\left\{\hat{p}(1+\gamma^5)\frac{1}{\hat{l}-\hat{p}-m_2}\hat{p}(1+\gamma^5)\frac{1}{\hat{l}-m_1}\right\}.$$

The symmetry properties differ somewhat from those of boson loops; that is,

$$J_{21}^{\mu}(p) = J_{12}^{\mu}(p), \quad J_{31}(p) = -J_{13}(p), \quad J_{32}^{\mu}(p) = -J_{23}^{\mu}(p). \quad (40)$$

In the case of fermion loops, all longitudinal loops are expressed in terms of two functions $H_1(p^2)$ and $H_2(p^2)$, apart from subtraction polynomials. Specifically, we have

$$H_1(p^2) = \frac{1}{\pi}\int\frac{(m_1+m_2)^2-s}{s(s-p^2)}$$

$$\times \left(\frac{\lambda(s,m_1^2,m_2^2)}{s^2}\right)^{1/2} ds,$$

$$H_2(p^2) = \frac{p^2}{\pi}\int \frac{(m_1-m_2)^2 - s(m_1^2+m_2^2)}{s^2(s-p^2)} \times \left(\frac{\lambda(s,m_1^2,m_2^2)}{s^2}\right)^{1/2} ds,$$

$$J_{11} = f_1^2\left[P_{11}+sH_1(s)\right], J_{12} = f_1 f_2\left[P_{12}+H_1(s)\right], \quad (41)$$

$$J_{13} = i\frac{f_1 f_2}{M}\left[P_{13}+sH_1(s)\right], J_{22} = \hat{f}_2^2\left[P_{22}+H_2(s)\right],$$

$$J_{23} = i\frac{\hat{f}_2^2}{M}\left[P_{23}+H_2(s)\right], J_{33} = \frac{\hat{f}_2^2}{M^2}\left[P_{33}+sH_2(s)\right],$$

where P_{ij} are polynomials in s with real-valued coefficients. We have also used the following notation: $f_1 = g_1/\sqrt{8\pi}$, $f_2 = (m_1-m_2)g_2/\sqrt{8\pi}$, $\hat{f}_2 = g_2/\sqrt{4\pi}$.

Examining relations (33), which follow from the Ward identity, we can easily see that the Ward identity imposes constraints only on the subtraction polynomials, the loop integrals H_1 and H_2 identically satisfying Eqs. (33). Upon imposing the conditions in Eqs. (33), we arrive at a very simple dependence of the propagators on ξ in the form (36). It only remains to trace the ξ dependence in the matrix element.

The $f_1(q_1)\overline{f}_2(q_2) \to f_1(k_1)\overline{f}_2(k_2)$ matrix element has the form

$$\mathcal{M}^{J=0} = -g_1^2\Pi_{11}\,\overline{v}(q_2)u(q_1)\cdot\overline{u}(k_1)v(k_2) \quad (42)$$
$$- g_1 g_2\left(\Pi_{12} - \frac{i}{M}\Pi_{13}\right)\overline{v}(q_2)u(q_1)\cdot\overline{u}(k_1) \times \hat{p}(1+\gamma^5)v(k_2) - g_1 g_2\left(\Pi_{21} + \frac{i}{M}\Pi_{31}\right)\overline{v}(q_2) \times \hat{p}(1+\gamma^5)u(q_1)\cdot\overline{u}(k_1)v(k_2)$$
$$- g_2^2\left(\frac{1}{s}\Pi_{22} + \frac{1}{M^2}\Pi_{33} - \frac{i}{M}\Pi_{23} + \frac{i}{M}\Pi_{32}\right)\overline{v}(q_2) \times \hat{p}(1+\gamma^5)u(q_1)\cdot\overline{u}(k_1)\hat{p}(1+\gamma^5)v(k_2).$$

This expression can be simplified by using the equations of motion for spinors; however, it can be seen even at this stage that different spinor matrix elements appear with factors that are independent of ξ [see Eq. (38)]. Thus, the dependence on the gauge parameter disappeared.

Mixing in the system formed by the pseudoscalar Higgs boson and the Z^0 gauge boson. The vertex of Higgs boson interaction with fermions is shown in Fig. 4.

The form of the $f_1(q_1)\overline{f}_2(q_2) \to f_1(k_1)\overline{f}_2(k_2)$ matrix element changed slightly to become

$$\mathcal{M}^{J=0} = -g_1^2\Pi_{11}\overline{v}(q_2)\gamma^5 u(q_1)\cdot\overline{u}(k_1)\gamma^5 v(k_2) \quad (43)$$
$$- g_1 g_2\left(\Pi_{12} - \frac{i}{M}\Pi_{13}\right)\overline{v}(q_2)\gamma^5 u(q_1)\cdot\overline{u}(k_1) \times \hat{p}(1+\gamma^5)v(k_2) - g_1 g_2\left(\Pi_{21} + \frac{i}{M}\Pi_{31}\right)\overline{v}(q_2) \times \hat{p}(1+\gamma^5)u(q_1)\cdot\overline{u}(k_1)\gamma^5 v(k_2)$$
$$- g_2^2\left(\frac{1}{s}\Pi_{22} + \frac{1}{M^2}\Pi_{33} - \frac{i}{M}\Pi_{23} + \frac{i}{M}\Pi_{32}\right)\overline{v}(q_2) \times \hat{p}(1+\gamma^5)u(q_1)\cdot\overline{u}(k_1)\hat{p}(1+\gamma^5)v(k_2).$$

In relation to the case of the scalar Higgs bosons, some of the loops changed:

$$J_{11}(p^2) = -ig_1^2\int\frac{d^4l}{(2\pi)^4} \times \mathrm{tr}\left\{\gamma^5\frac{1}{\hat{l}-\hat{p}-m_2}\gamma^5\frac{1}{\hat{l}-m_1}\right\}, \quad (44)$$

$$J_{12}^{\mu}(p) = -ig_1 g_2\int\frac{d^4l}{(2\pi)^4} \times \mathrm{tr}\left\{\gamma^5\frac{1}{\hat{l}-\hat{p}-m_2}\gamma^{\mu}(1+\gamma^5)\frac{1}{\hat{l}-m_1}\right\},$$

$$J_{13}(p^2) = \frac{g_1 g_2}{M}\int\frac{d^4l}{(2\pi)^4} \times \mathrm{tr}\left\{\gamma^5\frac{1}{\hat{l}-\hat{p}-m_2}\hat{p}(1+\gamma^5)\frac{1}{\hat{l}-m_1}\right\},$$

$$J_{21}^{\mu}(p) = J_{12}^{\mu}(p), \quad J_{31}(p^2) = -J_{13}(p^2). \quad (45)$$

In relation to the mixing of charged fields, the only change is that the function $H_1(p^2)$ took a different form; that is,

$$H_1(p^2) = \frac{1}{\pi}\int\frac{(m_1-m_2)^2 - s}{s(s-p^2)} \times \left(\frac{\lambda(s,m_1^2,m_2^2)}{s^2}\right)^{1/2} ds,$$

$$J_{11} = f_1^2\left[P_{11}+sH_1(s)\right],\ J_{12} = f_1 f_2\left[P_{12}+H_1(s)\right],$$
$$J_{13} = i\frac{f_1 f_2}{M}\left[P_{13}+sH_1(s)\right],$$

where $f_2 = (m_1+m_2)g_2/\sqrt{8\pi}$.

The renormalized matrix element for the transition $f_1(q_1)\overline{f}_2(q_2) \to f_1(k_1)\overline{f}_2(k_2)$ assumes the form

$$\mathcal{M}^{J=0} = -g_1^2\frac{(M^2+J_{22})}{\hat{D}}\overline{v}(q_2) \quad (46)$$
$$\times \gamma^5 u(q_1)\cdot\overline{u}(k_1)\gamma^5 v(k_2) + 2g_1 g_2\frac{J_{12}}{\hat{D}} \times (\overline{v}(q_2)\gamma^5 u(q_1)\cdot\overline{u}(k_1)\hat{p}(1+\gamma^5)v(k_2)$$

$$+\overline{v}(q_2)\hat{p}(1+\gamma^5)u(q_1)\cdot\overline{u}(k_1)\gamma^5 v(k_2))$$
$$-g_2^2\frac{(\pi_{11}^{-1}+J_{11})}{\hat{D}}\overline{v}(q_2)\hat{p}(1+\gamma^5)$$
$$\times u(q_1)\cdot\overline{u}(k_1)\hat{p}(1+\gamma^5)v(k_2).$$

There are no other changes—in particular, the renormalized matrix element remains independent of ξ.

5. DISCUSSION

Thus, we have examined, at the loop level, the effect of scalar–vector mixing in the ξ gauge and found that, if one employs a Ward identity, the renormalized matrix element becomes independent of the gauge parameter. A complete disappearance of the dependence on ξ is quite surprising, since we have studied only that part of Dyson–Schwinger equations which have bearing on the dressing of propagators. There are therefore reasons to conjecture that relations (33) are of a more general character.

A change in the character of the singularity upon dressing is an ineresting phenomenon, which was previously found in [5] for a simpler situation. Specifically, a simple pole $1/(p^2-\xi M^2)$ in bare propagators transforms, upon dressing, into the second-order pole of total propagators. There is always such a possibility in the mixing of two bare propagators corresponding to equal masses, but it is realized only if loops satisfy some specific relations that are dictated by the Ward identity.

Hung Cheng and S.P. Li [5] calculated bosonic loop contributions and found that the position of the second-order unphysical pole is ultraviolet-divergent with allowance for the Ward identity. In this connection, it was argued that, in the ξ gauge, the Standard Model is unrenormalizable in principle.[11] As was shown above, however, the Ward identity leads to fulfillment of relations (33) for the loops. If these relations are satisfied, the position of second-order poles is ultraviolet stable [see Eqs. (36)]. It can therefore be conjectured that, in the course of the calculations performed in [5], loops did not satisfy the Ward identity for some reason or another, although this identity was used there in a general form.

After our study, there arises the impression that the use of the ξ gauge is not very convenient in extended Higgs models. Nonetheless, this gauge (or particular cases of ξ) is extensively used in studying electroweak models. In particular, one can test the correctness of calculations by varying ξ and tracing the respective variation of the matrix element.

As to physical implications of unitary scalar–vector mixing in electroweak models, this issue deserves a dedicated investigation.

REFERENCES

1. L. Baulieu and R. Coquereaux, Ann. Phys. (N.Y.) **140**, 163 (1982).
2. K. Aoki *et al.*, Prog. Theor. Phys. Suppl. **73**, 1 (1982).
3. A. E. Kaloshin, Yad. Fiz. **60**, 1306 (1997) [Phys. At. Nucl. **60**, 1179 (1997)].
4. M. C. Peyranere, Int. J. Mod. Phys. A **14**, 429 (1999).
5. Hung Cheng and S. P. Li, hep-ph/0107103.
6. J. C. Taylor, *Gauge Theories of Weak Interaction* (Cambridge Univ. Press, Cambridge, 1976; Mir, Moscow, 1978).
7. S. Gasiorowicz and D. A. Geffen, Rev. Mod. Phys. **41**, 531 (1969).
8. M. K. Volkov, Fiz. Élem. Chastits At. Yadra **17**, 433 (1986) [Sov. J. Part. Nucl. **17**, 186 (1986)].
9. N. N. Bogolyubov and D. V. Shirkov, *Introduction to the Theory of Quantized Fields* (Nauka, Moscow, 1976).
10. G. Passarino, Nucl. Phys. B **574**, 451 (2000).

Translated by A. Isaakyan

[11] The authors of [5] studied the mixing of the longitudinal part of W and a ghost in the Standard Model. This is a particular case of our consideration in the absence of a physical scalar.

Physics of Atomic Nuclei, Vol. 66, No. 7, 2003, pp. 1384–1394. Translated from Yadernaya Fizika, Vol. 66, No. 7, 2003, pp. 1426–1436.

ELEMENTARY PARTICLES AND FIELDS
Theory

Monopole Vacuum in Non-Abelian Theories

L. D. Lantsman[1)]* and V. N. Pervushin**

Joint Institute for Nuclear Research, Dubna, Moscow oblast, 141980 Russia

Received May 10, 2002; in final form, October 17, 2002

Abstract—It is shown that, in the theory of interacting Yang–Mills fields and a Higgs field, there is a topological degeneracy of Bogomol'nyi–Prasad–Sommerfield (BPS) monopoles and that there arises, in this case, a chromoelectric monopole characterized by a new topological variable that describes transitions between topological states of the monopole in Minkowski space (in just the same way as an instanton describes such transitions in Euclidean space). The limit of an infinitely large mass of the Higgs field at a finite density of the Bogomol'nyi–Prasad–Sommerfield monopole is considered as a model of the stable vacuum in pure Yang–Mills theory. It is shown that, in QCD, such a monopole vacuum may lead to a growing potential, a topological confinement, and an additional mass of the η_0 meson. The relationship between the result obtained here for the generating functional of perturbation theory and the Faddeev–Popov integral is discussed. © *2003 MAIK "Nauka/Interperiodica".*

1. INTRODUCTION AND FORMULATION OF THE PROBLEM

The problem of choosing, in a non-Abelian theory, a physical vacuum and variables that adequately reflect the topological properties of the manifold of initial data for non-Abelian fields [1–3] in Minkowski space is still considered to be one of the most important problems in these realms. There are reasons to believe that solving this problem will contribute to obtaining, within QCD, deeper insights into the nature of confinement, hadronization, and a spontaneous breakdown of scale invariance in the infrared region.

The present study is devoted to employing monopole solutions [4] to the equations of a non-Abelian theory to construct a model of a topologically invariant vacuum of Yang–Mills theory in Minkowski space. The respective Lagrangian of the theory has the form

$$\mathcal{L} = -\frac{1}{4}G^a_{\mu\nu}G^{\mu\nu}_a, \qquad (1)$$

where

$$G^a_{\mu\nu} = \partial_\mu A^a_\nu - \partial_\nu A^a_\mu + g\varepsilon_{abc}A^b_\mu A^c_\nu. \qquad (2)$$

From the mathematical point of view, the main problem in the theory of gauge fields is to find general solutions to the equations of the theory,

$$D^{ab}_\mu G^{\mu\nu}_b = 0 \quad (D^{ab}_\mu = \delta^{ab}\partial_\mu + g\varepsilon_{acb}A^c_\mu), \qquad (3)$$

and to construct, in order to describe processes in terms of probability amplitudes normalized per time and spatial-volume units, a generating functional for the S matrix in the class of functions such that the energy density is finite [5–7]. In QED, such functions have an $O(1/r^{1+m})$ behavior at spatial infinity. They are referred to as monopoles if $m = 0$ and as multipoles if $m > 0$.

Solving differential equations in theoretical physics presumes specifying initial data. Such initial data are measured by a set of physical instruments with which one associates a reference frame. In the present study, we will consider reference frames that are determined by the timelike unit vector $l^{(0)}_\mu = (1,0,0,0)$ and various Lorentz transformations of it, $l^{(1)}_\mu$.

There are two types of groups of transformations of the differential equations of a gauge theory. These are relativistic transformations, which change initial data (that is, reference frame), and gauge transformations,

$$\hat{A}^u_\mu(t,\mathbf{x}) := u(t,\mathbf{x})\left(\hat{A}_\mu + \partial_\mu\right)u^{-1}(t,\mathbf{x}), \qquad (4)$$
$$\hat{A}_\mu = g\frac{\tau^a}{2i}A^a_\mu,$$

which are associated with the gauge of physical fields and which do not affect the readings of an instrument.

The set of Eqs. (3) is referred to as a relativistically covariant set of equations if the total manifold of its solutions for each specific reference frame coincides with its counterpart for any other reference frame (see [7–12]).

In each reference frame, the set of all equations is broken down into the equations of motion $D^{ab}_\mu G^{\mu i}_b =$

[1)]Permanent address: Wissenschaftliche Gesellschaft, bei Judische Gemeinde zu Rostock, Wilhelm-Külz Platz, 18055 Rostock, Germany.

*e-mail: llantsman@freenet.de

**e-mail: pervush@thsun1.jinr.ru

0 $(i = 1, 2, 3)$—to solve these equations, it is necessary to measure initial data—and the constraint equations $D^{ab}_{\mu}G^{\mu 0}_{b} = 0$, which relate initial data for the spatial components of the fields involved to initial data for their time components. The time component of a field is singled out since it has no canonical momenta. In view of this, Dirac [13] and, after him, other authors of the first classic studies devoted to quantizing gauge theories (see [14, 15]) eliminated the time component by a gauge transformation. In our case, such a transformation,

$$\hat{A}^{\mathrm{D}}_{k} = v(\mathbf{x})T\exp\left\{\int\limits_{t_0}^{t} d\bar{t}\hat{A}_0(\bar{t},\mathbf{x})\right\}\left(\hat{A}_k + \partial_k\right) \quad (5)$$

$$\times\left[v(\mathbf{x})T\exp\left\{\int\limits_{t_0}^{t} d\bar{t}\hat{A}_0(\bar{t},\mathbf{x})\right\}\right]^{-1}$$

(here, the symbol T denotes time ordering of the matrices under the exponential sign), specifies a non-Abelian analog of Dirac's variables, apart from arbitrary time-independent matrices $v(\mathbf{x})$, which are considered as initial data at the instant t_0 for solving the equation $U(\hat{A}_0 + \partial_0)U^{-1} = 0$. At the level of Dirac's variables, Lorentz transformations of original fields become nonlinear, while the group of gauge transformations reduces to a group of time-independent transformations that specify the degeneracy of initial data for physical fields (including the classical vacuum $A_0 = A_i = 0$, which is defined as the zero-energy state). By gauge fixing, one means, in this case, presetting initial data in perturbation theory as the transversality condition [9–12].

In a non-Abelian theory, the set of time-independent gauge transformations is a set of three-dimensional paths in the space of the $SU_c(2)$ group that are broken down into topological manifolds characterized by integers (exponents of mapping):

$$\mathcal{N}[n] = -\frac{1}{24\pi^2}\int d^3x\,\epsilon^{ijk} \quad (6)$$

$$\times\,\mathrm{tr}\left[v^{(n)}\partial_i {v^{(n)}}^{-1} v^{(n)}\partial_j {v^{(n)}}^{-1} v^{(n)}\partial_k {v^{(n)}}^{-1}\right] = n.$$

The exponent of mapping indicates how many times the three-dimensional path $v(\mathbf{x})$ goes about $SU_{\mathrm{c}}(2)$ as the coordinate $\mathbf{x}_i$ runs over the entire three-dimensional space where this coordinate is specified. The condition in (6) means that the entire set of three-dimensional paths has the homotopic group $\pi_{(3)}(SU_c(2)) = Z$ and that all fields $v^{(n)}\partial_i {v^{(n)}}^{-1}$ are defined in the class of functions for which the integral in (6) is finite. This is the class of monopole functions [1, 2]. Naturally, the fields $A^{\mathrm{D}}_i(t,\mathbf{x})$ themselves must also belong to this class of monopole functions and have an $O(1/r^{1+m})$, $m > 0$ asymptotic behavior.

Thus, our objective is to quantize non-Abelian fields in the class of monopole functions that involves a topological degeneracy. Such a quantization presumes the choice of Dirac's variables in which this degeneracy occurs. The first Hamiltonian quantization of non-Abelian gauge theories in terms of Dirac's variables without allowing for their topological degeneracy was due to Schwinger [10], who proved the relativistic covariance of the transverse gauge at the level of commutation relations for the generators of the algebra of the Poincaré group that were constructed in the above class of functions. This Hamiltonian quantization of non-Abelian fields was reproduced by Faddeev [16], who employed the method of a path integral $Z_{l^{(0)}}$ explicitly dependent on a reference frame. In [17], it was shown that the relativistic transformation at the level of fundamental operator quantization according to Schwinger [10] corresponds to the relativistic transformation $l^{(0)} \to l^{(1)}$ of the time axis on which the path integral $Z_{l^{(0)}}$ depends. The dependence of this integral on a reference frame is called an implicit relativistic covariance.[2)]

That the path integral $Z_{l^{(0)}}$ is independent of a reference frame for on-shell amplitudes of elementary-particle scattering was first discovered by Feynman [21] and was proven by Faddeev [16] as a validation of the heuristic Faddeev–Popov path integral [22]. This integral was proposed as a generating functional of unitary perturbation theory for any gauges, including those that are independent of a reference frame. Schwinger noticed that gauges that are independent of a reference frame may be physically inadequate to fundamental operator quantization; that is, they may distort the spectrum of the original system.[3)]

In the present study, we verify Schwinger's statement in a non-Abelian theory, answering the question concerning the spectrum of a theory quantized in the class of monopole functions that involves a topological degeneracy of initial data and the question concerning the relationship between fundamental quantization and the heuristic Faddeev–Popov integral in a gauge that is independent of a reference frame.

The ensuing exposition is organized as follows. Section 2 is devoted to describing the topological degeneracy of known monopole solutions and to considering zero modes of the constraint equation. In Section 3, we examine the limiting transition to pure

[2)] The choice of the time axis for such an integral is discussed elsewhere [18–20].

[3)] "We reject all Lorentz gauge formulations as unsuited to the role of providing the fundamental operator quantization" [10].

Yang–Mills theory having a monopole vacuum. In Section 4, we analyze the $U(1)$ problem. In the Conclusion, we discuss the connection with the Faddeev–Popov integral.

2. TOPOLOGICAL DEGENERACY OF BOGOMOL'NYI–PRASAD–SOMMERFIELD MONOPOLE

Let us consider the well-known example of interacting Yang–Mills fields and a scalar Higgs field for the case where there is a spontaneous breakdown of symmetry. This situation is described by the Lagrangian density [4]

$$\mathcal{L} = -\frac{1}{4}G^a_{\mu\nu}G^{\mu\nu}_a \tag{7}$$
$$+\frac{1}{2}\left(D_\mu\varphi^a\right)\left(D^\mu\varphi_a\right) - \frac{\lambda}{4}\left(\frac{m^2}{\lambda} - \varphi^2\right)^2,$$

where

$$G^a_{\mu\nu} = \partial_\mu A^a_\nu - \partial_\nu A^a_\mu + g\varepsilon_{abc}A^b_\mu A^c_\nu$$

is the strength tensor of our non-Abelian field and φ^a, $a = 1, 2, 3$, is a scalar field forming a triplet of the adjoint representation of the $SU(2)$ group. The potential energy depends on the square of the vector φ^a, while the covariant derivative of the field has the form

$$D_\mu\varphi^a = \partial_\mu\varphi^a + g\varepsilon_{abc}A^b_\mu\varphi^c. \tag{8}$$

The Lagrangian density (7) possesses a manifest gauge invariance under transformations of the $SU(2)$ group.

The classical vacuum is defined as the asymptotic solution

$$r = |\mathbf{x}| \to \infty, \qquad E \to \min E,$$

providing the minimum of the field energy E.

For $m^2 \geq 0$ and $\lambda \geq 0$, the vacuum loses the $SU(2)$ symmetry of the Lagrangian; that is,

$$r = |\mathbf{x}| \to \infty, \qquad \varphi^a \to n^a\frac{m}{\sqrt{\lambda}},$$

with n^a being an arbitrary unit vector ($|\mathbf{n}| = 1$) in isotopic space. Choosing a specific vacuum reduces to choosing a specific direction of the vector $\mathbf{n}$, and this violates the symmetry of the $SU(2)$ group. This phenomenon is referred to as a spontaneous breakdown of symmetry.

In the Standard Model, a non-Abelian vector field develops a mass in precisely this way. Usually, quantum field theory is then constructed as a perturbation theory over this vacuum,

$$\varphi^a = n^a\frac{m}{\sqrt{\lambda}}, \tag{9}$$

in the class of functions such that the energy density is finite.

In addition to the trivial vacuum in (9), there are monopole solutions in the system described by the Lagrangian density in (7). These are solutions having an $O(1/r)$ type of behavior at spatial infinity:

$$r \to \infty; \quad \varphi^a - n^a\frac{m}{\sqrt{\lambda}} = O(1/r), \quad A^a_i = O(1/r). \tag{10}$$

The Bogomol'nyi–Prasad–Sommerfield (BPS) solution [4]

$$\varphi^a = \frac{x^a}{gr}f_0^{\mathrm{BPS}}(r), \quad f_0^{\mathrm{BPS}}(r) = \left[\frac{1}{\epsilon\tanh(r/\epsilon)} - \frac{1}{r}\right], \tag{11}$$

$$A^a_i(t,\mathbf{x}) \equiv \Phi_i^{a\mathrm{BPS}}(\mathbf{x}) = \varepsilon_{iak}\frac{x^k}{gr^2}f_1^{\mathrm{BPS}}(r), \tag{12}$$

$$f_1^{\mathrm{BPS}} = \left[1 - \frac{r}{\epsilon\sinh(r/\epsilon)}\right],$$

which was obtained in the limit

$$\lambda \to 0, \quad m \to 0; \qquad \frac{1}{\epsilon} \equiv \frac{gm}{\sqrt{\lambda}} \neq 0, \tag{13}$$

is a monopole solution satisfying the Yang–Mills equations, having a finite minimum energy, and violating $SU(2)$ symmetry. In the limit specified in (13), the Bogomol'nyi–Prasad–Sommerfield solution has a finite minimum energy that is proportional to

$$\int d^3x[B^a_iB^a_i] = 4\pi\frac{gm}{g^2\sqrt{\lambda}} = \frac{4\pi}{g^2\epsilon}, \tag{14}$$

where B^a_i is the magnetic induction,

$$B^a_i(\Phi_k^{c\mathrm{BPS}}) = \varepsilon_{ijk}\left(\partial_j\Phi_k^{a\mathrm{BPS}} + \frac{g}{2}\varepsilon^{abc}\Phi_j^{b\mathrm{BPS}}\Phi_k^{c\mathrm{BPS}}\right).$$

That this energy value corresponds to a minimum is ensured by the requirement that the magnetic field in question be of a potential character; that is,

$$B^a_i(\Phi_k^{c\mathrm{BPS}}) = D^{ab}_i(\Phi_k^{c\mathrm{BPS}})\varphi_b, \tag{15}$$

where the covariant derivative is specified by Eq. (8). It is precisely this condition (which ensures, as was indicated immediately above, the potential character of the magnetic field)—it is referred to as the Bogomol'nyi equation—that will play an important role in our construction of the stable vacuum of a non-Abelian theory (see below).

We will now show that the equation of potentiality means a topological degeneracy of fields under the time-independent gauge transformations

$$\hat{A}^{(n)}_i(t_0,\mathbf{x}) = v^{(n)}(\mathbf{x})\left[\hat{A}^{(0)}_i(t_0,\mathbf{x}) + \partial_i\right]v^{(n)}(\mathbf{x})^{-1}. \tag{16}$$

Dynamical fields can be represented in the form of the sum of the Bogomol'nyi–Prasad–Sommerfield monopole $\Phi_i^{\mathrm{BPS}}(\mathbf{x})$ and perturbations $\bar{A}_i^{(0)}$:

$$\hat{A}_i^{(0)}(t,\mathbf{x}) = \hat{\Phi}_i^{\mathrm{BPS}}(\mathbf{x}) + \hat{\bar{A}}_i^{(0)}(t,\mathbf{x}). \qquad (17)$$

Perturbations are considered as weak multipole fields [23]:

$$\bar{A}_i(t,\mathbf{x})|_{\mathrm{asymp}} = O\left(\frac{1}{r^{1+l}}\right) \quad (l>1). \qquad (18)$$

In the lowest order of perturbation theory, the equation for the time component,

$$\left[D^2(A)\right]^{ac} A_0^c = [D_i^{ac}(A)\partial_0 A_i^c], \qquad (19)$$

in Dirac's variables $A_0^{\mathrm{D}c} = 0$ assumes the form

$$\partial_t A^{a||}[A_i^{c(0)}(t,\mathbf{x})] = 0, \qquad (20)$$
$$A^{a||}[A_i^{c(0)}] \equiv [D_i^{ac}(\Phi^{\mathrm{BPS}})A_i^{c(0)}],$$

and implies that the time derivative of the longitudinal fields $A^{a||}$ vanishes. This equation can be solved if we have initial data at our disposal. We assume that there are no longitudinal fields at the initial instant of time; that is,

$$A^{a||}(t=t_0) \equiv [D_i^{ac}(\Phi^{\mathrm{BPS}})A_i^{c(0)}] = 0. \qquad (21)$$

We refer to this condition as the covariant Coulomb gauge. There arises the question of the degree of arbitrariness in Dirac's variables associated with this gauge, since it should be recalled that they are defined apart from time-independent gauge transformations.

In order to answer this question, we make the transformations

$$\hat{A}_i^{(n)} = v^{(n)}(\hat{A}_i^{(0)} + \partial_i)v^{(n)-1}, \quad v^{(n)} = \exp[n\Phi_0(\mathbf{x})], \qquad (22)$$

and require that, upon the transformations in (22), the fields in (17),

$$\hat{A}_i^{(n)}(t,\mathbf{x}) = \hat{\Phi}_i^{(n)\mathrm{BPS}}(\mathbf{x}) + \hat{\bar{A}}_i^{(n)}(t,\mathbf{x}),$$

satisfy the same covariant Coulomb gauge:

$$D_i^{ab}(\Phi_k^{(n)\mathrm{BPS}})\bar{A}_i^{b(n)} = 0. \qquad (23)$$

From the last condition of gauge conservation, we then obtain the so-called Gribov equation [24] for the phases of gauge transformations:

$$[D_i^2(\Phi_k^{\mathrm{BPS}})]^{ab}\Phi_0^b = 0. \qquad (24)$$

The Gribov Eq. (24) coincides with the Bogomol'nyi–Prasad–Sommerfield equation for the scalar field, the latter following from condition (15), which ensures the potential character of the magnetic field of the Bogomol'nyi–Prasad–Sommerfield monopole. Therefore, the Gribov Eq. (24) has a nontrivial solution in the form of the Bogomol'nyi–Prasad–Sommerfield monopole (11):

$$\hat{\Phi}_0 = -i\pi\frac{\tau^a x^a}{r}\left[\frac{1}{\tanh(r/\epsilon)} - \frac{\epsilon}{r}\right]. \qquad (25)$$

Thus, we have shown that the Bogomol'nyi–Prasad–Sommerfield monopole and transverse gauge physical fields have Gribov's replicas in the form of topological degeneracy (22).

It should be recalled that a topological degeneracy is associated primarily with a classical vacuum of zero energy, where this degeneracy is characterized by the Pontryagin index or by the Chern–Simons functional [1] (which we consider in a finite spacetime of volume V within the time interval $t_{\mathrm{in}} < t < t_{\mathrm{out}}$)

$$\nu[A] = \frac{g^2}{16\pi^2}\int\limits_{t_{\mathrm{in}}}^{t_{\mathrm{out}}} dt \int\limits_V d^3x G^a_{\mu\nu}\widetilde{G}^{a\mu\nu} \qquad (26)$$
$$= X[A^{\mathrm{D}}_{\mathrm{out}}] - X[A^{\mathrm{D}}_{\mathrm{in}}],$$

where

$$X[A] = -\frac{1}{8\pi^2}\int\limits_V d^3x\varepsilon^{ijk}\mathrm{tr}\left[\hat{A}_i\partial_j\hat{A}_k - \frac{2}{3}\hat{A}_i\hat{A}_j\hat{A}_k\right], \qquad (27)$$

which is a topological functional of gauge fields that reduces to an integer for a purely gauge field characterized by the degree of mapping in (6).

The functional in (27) generates the quantum wave function

$$\Psi_{\mathrm{ins}}[A] = \exp\left\{\pm\frac{8\pi^2}{g^2}X[A]\right\} \qquad (28)$$

as an exact solution to the Schrödinger equation [2, 25]

$$\hat{H}\Psi_{\mathrm{ins}}[A] = 0, \quad \hat{H} = \frac{1}{2}\int d^3x[\hat{E}^2 + \hat{B}^2], \qquad (29)$$
$$\hat{E} = \frac{\delta}{i\delta A},$$

at zero energy, $H = 0$. In just the same way as the oscillator wave function at zero energy, $[\hat{p}^2 + q^2]\Psi[q] = 0$, this wave function is nonnormalizable, which means that the corresponding eigenenergy $H = 0$ belongs to unphysical values in the spectrum. This fact may suggest that the instanton corresponding to transitions between vacua characterized by unphysical zero values of energy is itself an unphysical solution. Moreover, it is assumed in the wave function (28) that the topological motion $X[A]$ is a functional of local degrees of freedom that are denoted by A. In this case, the operators of local gauge transformation $\hat{T}X[A] = X[A] + 1$ do

not commute with the Hamiltonian $\hat{H}$. One of the simplest ways to remove all of these flaws, including the nonnormalizability of the wave function

$$\Psi_{\text{ins}}[A] = \exp\{iP_X X[A]\} \tag{30}$$

and the unphysical values of the energy and the momentum P_X of the topological motion,

$$H = 0, \quad P_X = \pm i\frac{8\pi^2}{g^2}, \tag{31}$$

consists in separating the topological motion from the local variables via the introduction of an independent topological degree of freedom $N(t)$ by means of a gauge transformation [25, 26]:

$$\hat{A}_i^{(N)} = \exp[N(t)\hat{\Phi}_0(\mathbf{x})][\hat{A}_i^{(0)} + \partial_i]\exp[-N(t)\hat{\Phi}_0(\mathbf{x})]. \tag{32}$$

By means of a direct calculation, it can be proven [27] that, for the vacuum of Bogomol'nyi–Prasad–Sommerfield monopoles $\Phi_i^{(n)}$, this degree of freedom is completely separated from the local degrees of freedom that are specified in the class of multipole functions:

$$X[A_i^{(N)}] = X[A_i^{(0)}] + N(t). \tag{33}$$

In this case, the instanton wave function (30) acquires a new independent degree of freedom,

$$\Psi_{\text{ins}}[A^N] = \exp\{iP_N X[A^N]\} = \exp\left\{iP_N(X[A_i^{(0)}] + N)\right\}, \tag{34}$$

and describes the topological motion of this degree of freedom at physical values of the momentum P_N. An independent topological motion arises as the inevitable consequence of a general solution to the equation $D_\mu G^{\mu 0} = 0$ for the time component of the field [25, 26]. This equation has the form

$$[D_k(A)]^{ab}\,[D_k(A)]^{bc}\,A_0^c = D_i^{ac}(A)\partial_0 A_i^c, \tag{35}$$

with the initial data being those that correspond to the Bogomol'nyi–Prasad–Sommerfield monopole:

$$\partial_0 A_i^c = 0, \quad A_i(t,\mathbf{x}) = \Phi_i^{\text{BPS}}(\mathbf{x}). \tag{36}$$

According to the theory of differential equations, a general solution to a nonhomogeneous equation can be represented as the sum

$$A_0^a = \mathcal{Z}^a + \tilde{A}_0^a, \tag{37}$$

where $\tilde{A}_0^a$ is a particular solution to the nonhomogeneous equation being considered and $\mathcal{Z}^a$ is a solution to the corresponding homogeneous equation

$$(D^2(A))^{ab}\mathcal{Z}^b = 0. \tag{38}$$

Apart from the factor $\dot{N}(t)$, which plays the role of a new variable (that is, a zero mode), the topological-degeneracy phase $\Phi_0(\mathbf{x})$ is the required solution $\mathcal{Z}^a$ to the homogeneous equation in the lowest order of perturbation theory:

$$\hat{\mathcal{Z}}(t,\mathbf{x}) = \dot{N}(t)\hat{\Phi}_0(\mathbf{x}). \tag{39}$$

The solution to the homogeneous equation describes an electric monopole,

$$G_{i0}^a(\mathcal{Z}) = D_i^{ab}(\Phi^{\text{BPS}})\mathcal{Z}^b = \dot{N}(t)D_i^{ab}(\Phi^{\text{BPS}})\Phi_0^b, \tag{40}$$

which cannot be completely eliminated from the action functional of the theory or from the Pontryagin index by going over to Dirac's variables with the aid of the gauge transformation (32). As was shown in [27], the Pontryagin index

$$\nu[A] = \frac{g^2}{16\pi^2}\int\limits_{t_{\text{in}}}^{t_{\text{out}}} dt \int\limits_V d^3x G_{\mu\nu}^a \tilde{G}^{a\mu\nu} = N(t_{\text{out}}) - N(t_{\text{in}}) \tag{41}$$

depends only on the difference of the final and initial values of the topological degree of freedom.

In the lowest order of perturtion theory in the coupling constant, the action functional of the theory being considered contains, in addition to the Bogomol'nyi–Prasad–Sommerfield monopole, an electric monopole and describes the dynamics of the new topological variable $N(t)$ in the form of a free rotor; that is,

$$W_{\mathcal{Z}}[N,\Phi^{\text{BPS}}] = \int\limits_{t_{\text{in}}}^{t_{\text{out}}} dt \int\limits_V d^3x \frac{1}{2} \times \left\{[G_{i0}^b(\mathcal{Z})]^2 - [B_i^b(\Phi_k^{b\text{BPS}})]^2\right\} = \int dt \frac{1}{2}\left\{I\dot{N}^2 - \frac{4\pi}{g^2\epsilon}\right\}, \tag{42}$$

where

$$I = \int\limits_V d^3x (D_i^{ac}(\Phi_k)\Phi_0^c)^2 = \frac{4\pi}{g^2}(2\pi)^2\epsilon \tag{43}$$

is the angular momentum of the rotor and $\epsilon = \sqrt{\lambda}/gm$ is the size of the Bogomol'nyi–Prasad–Sommerfield monopole in terms of the canonical momentum $P_N = \dot{N}I$:

$$H = \frac{2\pi}{g^2\epsilon}\left[P_N^2\left(\frac{g^2}{8\pi^2}\right)^2 + 1\right]. \tag{44}$$

Upon introducing new Dirac's variables with the aid of the transformation in (32), the topological degeneracy of all fields reduces, for such Dirac's variables, to the degeneracy of only one topological variable $N(t)$ with respect to a change in this variable by integers ($N \to N+n,\ n=\pm1,\pm2,...$). The wave function for the topological motion in Minkowski space has the form of the free-rotor wave function

$$\Psi_{\rm mon}[N] = \exp\{iP_N N\}, \qquad (45)$$

with the momentum spectrum being determined from the condition $\Psi_{\rm mon}[N+1] = e^{i\theta}\Psi_{\rm mon}[N]$. The result is

$$P_N = \dot{N}I = 2\pi k + \theta, \qquad (46)$$

where k is the number of a Brillouin zone and θ is the angle that specifies the spectrum of physical values of the Hamiltonian in (44). This Hamiltonian has zero eigenvalue ($H=0$) for the unphysical momentum values of $P_N = \pm i8\pi^2/g^2$, at which the instanton wave function (34) coincides with the wave function (45) for the monopole vacuum under the assumption that the topological degree of freedom is determined by a functional of local variables exclusively. Thus, the basic distinction between the monopole vacuum and the instanton vacuum is that, in the first case, there arises an independent Goldstone mode associated with the spontaneous breakdown of symmetry of physical states under the transformations of the $\pi_{(3)}(SU(2)) = Z$ homotopy group.

Equation (46) and condition (15), which ensures the potential character of the magnetic field, determine the spectrum of the electric-field strength:

$$G^b_{i0} = \dot{N}[D_i(\Phi^{(0)})A_0]^b = \alpha_s\left(\frac{\theta}{2\pi}+k\right)B^b_i(\Phi^{(0)}). \qquad (47)$$

Expression (47) is an analog of the spectrum of the electric-field strength, $G_{10} = e(\theta/(2\pi)+k)$, in two-dimensional electrodynamics [28–30] characterized by the same topology of degeneracy of initial data:

$$\pi_{(1)}(U(1)) = \pi_{(3)}(SU(2)) = Z.$$

The vanishing of the topological momentum does not imply that the degeneracy of physical states disappears. Physical implications of such a degeneracy will be considered in the next section.

3. YANG–MILLS THEORY FEATURING TOPOLOGICAL DEGENERACY OF PHYSICAL STATES

It is well known that perturbation theory constructed for non-Abelian fields by analogy with QCD [10, 16] is infrared-unstable [31, 32]. A conventional vacuum of perturbation theory, A = 0, is not a stable state. As a rule, uniform ([31]) or singular fields including instantons ([1]), the equation for which involves delta-function-like singularities in Euclidean space, are used for nonzero vacuum fields. If one explains physical effects by a uniform (or by an instanton) vacuum, it is also necessary to explain the emergence of capacitors at spatial infinity that generate uniform fields (or the origin of sources of delta-function-like singularities).

Bogomol'nyi–Prasad–Sommerfield monopoles provide a unique possibility for introducing, in the class of regular functions associated with topologically nontrivial gauge transformations, vacuum fields in such a way that the equations of Yang–Mills theory [Eqs. (1) in our case] do not develop any additional sources.

In order to introduce such a monopole vacuum, we include the interaction of gauge fields with a Higgs field in space of finite volume $V = \int d^3x$. The scalar-field condensate forms a Bogomol'nyi–Prasad–Sommerfield monopole characterized by a finite mass of the scalar field:

$$\frac{1}{\epsilon} = \frac{m}{\sqrt{\lambda}} \equiv V\langle\langle B^2\rangle\rangle\frac{g^2}{4\pi}. \qquad (48)$$

If we go over to the infinite-volume limit $V\to\infty$ under the condition that $\langle\langle B^2\rangle\rangle$ is finite, the scalar field acquires an infinitely large mass and disappears from the spectrum of physical excitations, while the regular solution representing a Bogomol'nyi–Prasad–Sommerfield monopole smoothly transforms into a Wu–Yang monopole [33]; this means that the equations of the theory do not develop, at the origin of coordinates, a singularity inherent in the Wu–Yang monopole and that the energy density does not go to infinity. In this limit, the finite energy density of the Bogomol'nyi–Prasad–Sommerfield monopole has the form

$$\int d^3x[B^a_i]^2 \equiv V\langle\langle B^2\rangle\rangle, \qquad (49)$$

where $\langle\langle B^2\rangle\rangle$ is the quantity that one has for the order parameter of the physical vacuum of the gauge field upon the the elimination of the scalar field.

We recall that the Wu–Yang monopole [33] is an exact solution to the classical equations of pure Yang–Mills theory, Eqs. (3), everywhere, with the exception of a small vicinity of the origin of coordinates. It is precisely in this small region around the origin of coordinates that the Wu–Yang monopole is regularized by the scalar-field mass, and this region disappears in the infinite-volume limit $V\to\infty$ [see Eq. (49)]. It should be noted here that, in quantum field theory, a transition to the limit $V\to\infty$ is performed upon calculating physical observables, such

as scattering cross sections and decay probabilities, that are normalized per unit time and per unit volume. Therefore, all special features of the above theory involving a Bogomol'nyi–Prasad–Sommerfield monopole, which include a topological degeneracy of initial data and an electric monopole, survive at any finite value of the volume.

On the other hand, there are, in the Yang–Mills theory specified by the Lagrangian density (1), direct indications that the scale symmetry of the vacuum is broken by solutions belonging to the type of a Wu–Yang monopole [33]. In particular, the topological classification of classical solutions to pure Yang–Mills theory specifies the class of solutions that possess zero topological index ($n = 0$),

$$X[A = \Phi^{(0)}] = 0, \qquad \left.\frac{\delta X[A]}{\delta A_i^c}\right|_{A=\Phi^{(0)}} \neq 0, \quad (50)$$

and which have the form

$$\hat{\Phi}_i^{(0)} = -i\frac{\tau^a}{2}\varepsilon_{iak}\frac{x^k}{r^2}f(r), \quad (51)$$

where there is only one unknown function, $f(r)$. An equation for this function can be obtained by substituting expression (51) into the classical Eq. (3):

$$D_k^{ab}(\Phi_i^{(0)})G_b^{kj}(\Phi_i^{(0)}) = 0 \Rightarrow \frac{d^2f}{dr^2} + \frac{f(f^2-1)}{r^2} = 0. \quad (52)$$

In the region $r \neq 0$, there exist the following three solutions to this equation:

$$f_1^{\mathrm{PT}} = 0, \qquad f_1^{\mathrm{WY}} = \pm 1\,. \quad (53)$$

The first, trivial, solution $f_1^{\mathrm{PT}} = 0$ corresponds to ordinary unstable perturbation theory involving "asymptotic freedom" [31, 32]. The two nontrivial solutions $f_1^{\mathrm{WY}} = \pm 1$ represent Wu–Yang monopoles, which, in the model being considered, emerge from Bogomol'nyi–Prasad–Sommerfield monopoles in the infinite-volume model without their singularities, along with the Goldstone model accompanying the breakdown of scale invariance.

Thus, the monopole vacuum characterized by a topological degeneracy of all physical states has the following features distinguishing it from the topologically degenerate instanton vacuum: Minkowski space; a topological Goldstone mode associated with scale-symmetry breaking that generates a nonzero order parameter $\langle\langle B^2\rangle\rangle \neq 0$; and a clear physical origin of scale-symmetry breaking, which is due to the condensate of a scalar Higgs field and which survives upon the elimination of the scalar field.

Physical implications of the theory being considered, which involves a monopole vacuum, are controlled by the generating functional for unitary perturbation theory in the covariant Coulomb gauge. Reproducing the calculations performed in [16] (see also [17]), one can obtain, as the generating functional for such a perturbation theory, a Feynman path integral in a reference frame with a specified time axis, $l_\mu = (1, 0, 0, 0)$; that is,

$$Z^*[l, J^*] = \int\int \prod_t dN(t) \int \prod_{c=1}^{3} [d^2A^{*c}d^2E^{*c}] \quad (54)$$

$$\times \exp\{iW^*[N, A^*, E^*] + i\int d^4x J^*A^*\},$$

where A^* are Dirac's variables (32); E^* are their canonically conjugate momenta; J^* are their sources; and $W^*[N, A^*, E^*]$ is the original action functional taken on the manifold spanned by solutions of the constraint equation

$$\frac{\delta W}{\delta A_0} = 0 \Rightarrow D_i^{cd}(A)G_{0i}^d = 0 \quad (55)$$

for the non-Abelian electric-field strength G_{0i}^d represented in the form of the sum of the transverse momentum E^* and the longitudinal component:

$$G_{0i}^d = E_i^{*d} + D_i^{db}(\Phi)\sigma^b \quad \left(D_i^{cd}(\Phi^{N(\mathrm{WY})})E_i^{*d} = 0\right). \quad (56)$$

If one assumes that, in perturbation theory, independent Dirac's variables $A_i^{*d} = \Phi_i^{dN(\mathrm{WY})} + \bar{A}_i^{*d}$ given by (32) satisfy the gauge conditions

$$D_i^{cd}(\Phi^{N(\mathrm{WY})})A_i^{*d} = 0, \quad (57)$$

which were considered above, then the constraint Eq. (55) reduces to an equation for the function σ^b; that is,

$$D_i^{cd}(A^*)D_i^{db}(\Phi^{N(WY)})\sigma^b = j_0^c, \quad (58)$$

where the quantity on the right-hand side is the current of independent non-Abelian variables,

$$j_0^a = g\varepsilon^{abc}[A_i^{*b} - \Phi_i^{bN(\mathrm{WY})}]E_i^{*c}. \quad (59)$$

One can solve Eq. (58), which involves a zero mode (described above), by means of perturbation theory, employing a Green's function of the Coulomb type. In the lowest order of perturbation theory, this Green's function $C^{bc}(\mathbf{x}, \mathbf{y})$ in the field of the usual Wu–Yang monopole Φ^{WY} is determined by the equation

$$[D^2(\Phi^{\mathrm{WY}})]^{ab}(\mathbf{x})C^{bc}(\mathbf{x}, \mathbf{y}) = \delta^{ac}\delta^3(\mathbf{x} - \mathbf{y}). \quad (60)$$

A solution to this equation specifies, in the Hamiltonian, an instantaneous interaction of non-Abelian currents,

$$-\frac{1}{2}\int_{V_0} d^3x d^3y j_0^b(\mathbf{x})C^{bc}(\mathbf{x}, \mathbf{y})j_0^c(\mathbf{y}), \quad (61)$$

as an analog of the Coulomb interaction of the currents in QED. A solution to Eq. (60) in the presence of a Wu–Yang monopole, where

$$[D^2(\Phi^{\mathrm{WY}})]^{ab}(\mathbf{x}) = \delta^{ab}\Delta - \frac{n^a n^b + \delta^{ab}}{r^2} + 2\left(\frac{n_a}{r}\partial_b - \frac{n_b}{r}\partial_a\right),$$

$n_a(x) = x_a/r$, $r = |\mathbf{x}|$, was obtained in [27] by means of an expansion of C^{ab} in terms of a complete set of orthogonal vectors; that is,

$$C^{ab}(\mathbf{x},\mathbf{y}) = [n^a(\mathbf{x})n^b(\mathbf{y})V_0(z) + \sum_{\alpha=1,2} e^a_\alpha(x)e^b_\alpha(y)V_1(z)], \quad z = |\mathbf{x}-\mathbf{y}|,$$

where $V_0(z)$ and $V_1(z)$ are potentials. Substituting this expansion into Eq. (60), one can derive an equation for the potentials. The result is

$$\frac{d^2}{dz^2}V_n + \frac{2}{z}\frac{d}{dz}V_n - \frac{n}{z^2}V_n = 0, \quad n = 0,\ 1.$$

Solving this equation, we obtain the potentials

$$V_n(|\mathbf{x}-\mathbf{y}|) = d_n|\mathbf{x}-\mathbf{y}|^{l_1^n} + c_n|\mathbf{x}-\mathbf{y}|^{l_2^n}, \quad n = 0,1, \tag{62}$$

where d_n and c_n are constants, while l_1^n and l_2^n are the roots of the equation $(l^n)^2 + l^n = n$; that is,

$$l_1^n = -\frac{1+\sqrt{1+4n}}{2}, \quad l_2^n = \frac{-1+\sqrt{1+4n}}{2}. \tag{63}$$

At $n = 0$, we have $l_1^0 = -(1+\sqrt{1})/2 = -1$ and $l_2^0 = (-1+\sqrt{1})/2 = 0$, so that there arises the Coulomb potential

$$V_0(|\mathbf{x}-\mathbf{y}|) = -(1/4\pi)|\mathbf{x}-\mathbf{y}|^{-1} + c_0; \tag{64}$$

at $n = 1$, $l_1^1 = -(1+\sqrt{5})/2 \approx -1.618$ and $l_2^1 = (-1+\sqrt{5})/2 \approx 0.618$, in which case one arrives at a growing potential for the golden-section equation $(l^1)^2 + l^1 = 1$:

$$V_1(|\mathbf{x}-\mathbf{y}|) = -d_1|\mathbf{x}-\mathbf{y}|^{-1.618} + c_1|\mathbf{x}-\mathbf{y}|^{0.618}. \tag{65}$$

As was shown in [34–36], the instantaneous interaction of color currents through a growing potential rearranges perturbation-theory series and leads to the constituent mass of the gluon field in Feynman diagrams; this changes the asymptotic-freedom formula at low momentum transfers, so that the coupling constant $\alpha_{\mathrm{QCD}}(q^2 \sim 0)$ becomes finite. The growing potentials of the instantaneous interactions of color currents [34–36] also lead to a spontaneous breakdown of chiral invariance for quarks.

Growing potentials do not remove poles of Green's functions in perturbation theory for amplitudes of processes not involving color degrees of freedom. Perturbation theory is formulated in terms of fields that are characterized by zero topological quantum numbers and which can be called partons:

$$\hat{A}^*(N|A^{(0)}) = U_N[\hat{A}^{(0)} + \partial]U_N^{-1}.$$

By virtue of gauge invariance, the phase factors of topological degeneracy, $U_N = \exp\{N(t)\hat{\Phi}_0(\mathbf{x})\}$, disappear. However, these factors survive at the sources of physical fields in the generating functional (54). A theory featuring a topological degeneracy of initial data, where the sources of physical fields involve the Gribov factors

$$\mathrm{tr}[\hat{J}_i v^{(n)} \hat{\bar{A}}_i^{(0)} {v^{(n)}}^{-1}],$$

differs from a theory that is free from degeneracy and which involves the sources $\mathrm{tr}[\hat{J}_i\hat{\bar{A}}_i^{(0)}]$. In a theory featuring degeneracy of initial data, it is necessary to average amplitudes over degeneracy parameters. Such averaging may lead to the disappearance of a number of physical states.

In [26, 37], it was shown that amplitudes for the production of physical color particles may vanish because of the destructive interference between the phase factors of topological degeneracy. In this case, the probability-conservation law for the S-matrix elements $\langle i|S = I + iT|j\rangle$ in the form

$$\sum_f \langle i|T|f\rangle\langle f|T^*|j\rangle = 2\mathrm{Im}\langle i|T|j\rangle$$

is saturated exclusively by the production of color-singlet states (hadrons) $f = h$. By virtue of the probability-conservation law, the sum over all hadronic channels becomes equal to the doubled imaginary part of the color-singlet amplitude ($2\mathrm{Im}\langle i|T|j\rangle$). In turn, the dependence on the factors of topological degeneracy disappears completely in the color-singlet amplitude. Owing to gauge invariance, the Hamiltonian of the theory, $H[A^{(n)}] = H[A^{(0)}]$, depends only on the fields of the zero topological sector, $A^{(0)}$, which play the role of Feynman's partons. In the high-energy parton region, where the imaginary part of the color-singlet amplitude, $\mathrm{Im}\langle i|T|j\rangle$, can be calculated on the basis of perturbation theory, quark–hadron duality, which is used to measure directly parton quantum numbers coinciding with the quantum numbers of physical color particles, arises from the probability-conservation law.

4. ESTIMATING THE QUANTITY $\langle\langle B^2\rangle\rangle$ WITHIN QCD

Let us estimate the quantity $\langle\langle B^2\rangle\rangle$ within QCD. In the monopole vacuum of QCD, the antisymmetric

Gell-Mann matrices λ_2, λ_5, and λ_7 play the role of the matrices τ_1, τ_2, and τ_3. The simultaneous interaction of color quark currents through a growing potential leads to the spectrum of mesons—in particular, to the pseudoscalar η_0 meson. Its anomalous interaction with gluons is described in terms of the Veneziano effective action [38]

$$W_{\text{eff}} = \int dt \left\{ \frac{1}{2} \left(\dot{\eta}_0^2 - M_0^2 {\eta_0}^2 \right) V + C_0 \eta_0 \dot{X}[A^{(N)}] \right\} \tag{66}$$

in the rest frame of this meson. Here, V is the volume of space, $C_0 = (N_f/F_\pi)\sqrt{2}/\pi$ is the coupling constant for the anomalous interaction of the meson with the topological functional $X[A^{(N)}] = X[A] + N$, F_π is the weak-pion-decay constant, and $N_f = 3$ is the number of flavors. A calculation of a similar action functional for QCD and for $\text{QED}_{(3+1)}$, where the topological functional describes the decay of parapositronium into two photons, is presented in [12]. In all probability, expression (66) for the effective anomalous interaction of a pseudoscalar state with gauge fields is common to all gauge theories. For electrodynamics in two-dimensional spacetime, one can obtain the same effective action [29, 30], where it leads to the mass of the Schwinger bound state.

In $\text{QCD}_{(3+1)}$, the extra mass of a bound pseudoscalar state,

$$\triangle m_\eta^2 = C_0^2 / I_{\text{QCD}} V,$$

can be determined, upon adding the action functional that is specified by Eqs. (42) and (43) and which controls the topological dynamics of zero modes,

$$W_{\text{QCD}} = \frac{1}{2} \int dt \int\limits_V d^3x G_{0i}^2 = \int dt \frac{\dot{N}^2 I_{\text{QCD}}}{2}$$

$$\left(I_{\text{QCD}} = \left(\frac{2\pi}{\alpha_{\text{QCD}}} \right)^2 \frac{1}{V \langle\langle B^2 \rangle\rangle} \right),$$

to the anomalous Veneziano action, by diagonalizing the total Lagrangian

$$L = \left[\frac{\dot{N}^2 I_{\text{QCD}}}{2} + C_0 \eta_0 \dot{N} \right]$$

$$= \left[\frac{(\dot{N} + C_0 \eta_0 / I_{\text{QCD}})^2 I_{\text{QCD}}}{2} - \frac{C_0^2}{2 I_{\text{QCD}}} \eta_0^2 \right].$$

In $\text{QED}_{(1+1)}$, the analogous formula describes the mass of the Schwinger state [29, 30], whereas, in $\text{QCD}_{(3+1)}$, we obtain the extra mass of the η_0 meson:

$$L_{\text{eff}} = \frac{1}{2} [\dot{\eta}_0^2 - \eta_0^2(t)(m_0^2 + \triangle m_\eta^2)] V, \tag{67}$$

$$\triangle {m_\eta}^2 = \frac{C_\eta^2}{I_{\text{QCD}} V} = \frac{N_f^2}{F_\pi^2} \frac{\alpha_{\text{QCD}}^2 \langle\langle B^2 \rangle\rangle}{2\pi^2}. \tag{68}$$

This result makes it possible to assess the strength of the vacuum chromomagnetic field in $\text{QCD}_{(3+1)}$, $\langle\langle B^2 \rangle\rangle \alpha_{\text{QCD}}^2 = 2\pi^2 F_\pi^2 \triangle {m_\eta}^2 / N_f^2 = 0.06$ GeV^4, by using the estimate $\alpha_{\text{QCD}}(q^2 \sim 0) \sim 0.24$ [34, 39]. Upon the calculation, we can remove infrared regularization by going over to the limit $V \to \infty$.

CONCLUSION

The monopole-vacuum model considered here demonstrates that the quantization of a non-Abelian theory featuring a topological degeneracy of the initial data for all physical states in a specific reference frame describes a destructive interference of degeneracy phase factors, which leads to quark–hadron duality; a Goldstone mode that is associated with a spontaneous breakdown of scale invariance and which leads to an extra mass of the η_0 meson; and a growing potential that controls the interaction of currents and which is thought to be responsible for a spontaneous breakdown of chiral invariance. These hidden features of non-Abelian fields manifest themselves upon switching on and off gauge-field interaction with a Higgs field, which acquires an infinitely large mass in the the infinite-volume limit. There arises the question of the extent to which such a fantastic possibility may be realized in nature.

The generating functional found in the form of a Feynman path integral with respect to Dirac's variables can be recast [16] into the form of a Faddeev–Popov integral [22] by means of the change of variables

$$\hat{A}_i^*(N|A) = U_N U^{\text{D}}[A] \left[\hat{A}_i + \partial_i \right] (U_N U^{\text{D}}[A])^{-1},$$

where

$$U^{\text{D}}[A] = \exp \left\{ \frac{1}{D^2(\Phi^{\text{WY}})} D_k(\Phi^{\text{WY}}) \hat{A}^k \right\} \tag{69}$$

is Dirac's "dressing" of non-Abelian fields. Upon this change of variables, the Feynman integral reduces to the Faddeev–Popov integral

$$Z^*[l, J^*] = \int \prod_t dN(t) \int \int \prod_{c=1}^{3} d^4 A^c \delta(f(A)) \tag{70}$$

$$\times \det M_{\text{FP}} \exp \{ i W[A] + i \int d^4x J^* A^*(N|A) \}$$

in an arbitrary gauge of the physical variables, $f(A) = 0$; here, the Faddeev–Popov determinant is determined in terms of the linear response of this gauge to a gauge transformation, $f(e^\Omega (A + \partial) e^{-\Omega}) = M_{\text{FP}} \Omega +$

$O(\Omega^2)$, while W is the original action functional in the theory being considered. At the same time, there remains the Dirac gauge of the sources in (69). As a relic of the fundamental quantization, the Dirac phase factors in the integral in (70) "remember" the entire body of information about the reference frame; monopoles; the growing potential of instantaneous interaction; and other initial data, including their topological degeneracy and confinement. As was predicted by Schwinger [10], all these effects disappear, leaving no trace, if these Dirac factors are removed by means of the substitution $A^*(N|A) \rightarrow A$ [16], which is made with the only purpose of removing the dependence of the path integral on a reference frame and initial data. On getting rid of this dependence, we obtain, instead of hadronization and confinement in Dirac's quantization, only the amplitudes for the scattering of free partons in the "relativistic" Faddeev–Popov integral, which do not exist as physical observables in Dirac's scheme of quantization that is dependent on initial data.

The same metamorphosis occurs in QED as well: going over from the Dirac gauge of sources to the Lorentz gauge in order to remove the dependence on a reference frame and initial data, we replace perturbation theory emerging upon fundamental quantization and featuring two singularities in the photon propagators (a single-time singularity and that at the light cone) by perturbation theory in the Lorentz gauge; the latter involves only one singularity in the propagators (that at the light cone), but by no means can it describe single-time Coulomb atoms, containing only Wick–Cutkosky bound states whose spectrum is not observed in nature [40].

ACKNOWLEDGMENTS

We grateful to B.M. Barbashov, D. Blaschke, E.A. Kuraev, and V.B. Priezzhev for discussion. V.N. Pervushin is indebted to W. Kummer for providing information about Wick–Cutkosky bound states and to A.S. Schwartz for a critical comment.

REFERENCES

1. A. A. Belavin *et al.*, Phys. Lett. B **59B**, 85 (1975); R. Jackiw and C. Rebbi, Phys. Lett. B **63B**, 172 (1976); C. G. Callan, Jr., R. Dashen, and D. Gross, Phys. Rev. D **17**, 2717 (1978).
2. L. D. Faddeev, *Proceedings of the IV International Symposium on Nonlocal Quantum Field Theory*, D1-9768, JINR (Dubna, 1976), p. 267; R. Jackiw, Rev. Mod. Phys. **49**, 681 (1977).
3. G. 't Hooft, Phys. Rep. **142**, 357 (1986); hep-th/0010225.
4. M. K. Prasad and C. M. Sommerfield, Phys. Rev. Lett. **35**, 760 (1975); E. B. Bogomol'nyĭ, Yad. Fiz. **24**, 861 (1976) [Sov. J. Nucl. Phys. **24**, 449 (1976)].
5. N. N. Bogolyubov and D. V. Shipkov, *Introduction to the Theory of Quantized Fields* (GITTL, Moscow, 1957).
6. A. I. Akhiezer and V. B. Berestetskiĭ, *Quantum Electrodynamics* (Fizmatgiz, Moscow, 1959).
7. S. Schweber, *An Introduction to Relativistic Quantum Field Theory* (New York, 1961; Inostr. Lit., Moscow, 1963).
8. J. Schwinger, Phys. Rev. **74**, 1439 (1948).
9. B. Zumino, J. Math. Phys. (N. Y.) **1**, 1 (1960).
10. J. Schwinger, Phys. Rev. **127**, 324 (1962).
11. I. V. Polubarinov, Preprint No. P2-2421 (Joint Inst. for Nucl. Res., Dubna, 1965); Fiz. Élem. Chastits At. Yadra **34** (2003) (in press).
12. V. N. Pervushin, *Dirac Variables in Gauge Theories, Lecture Notes in DAAD Summerschool on Dense Matter in Particle Physics and Astrophysics, JINR, Dubna, Russia, 2001*; hep-th/0109218; Fiz. Élem. Chastits At. Yadra **34** (2003) (in press).
13. P. A. M. Dirac, Proc. R. Soc. London, Ser. A **114**, 243 (1927); Can. J. Phys. **33**, 650 (1955).
14. W. Heisenberg and W. Pauli, Z. Phys. **56**, 1 (1929); **59**, 166 (1930).
15. E. Fermi, Rev. Mod. Phys. **4**, 87 (1932).
16. L. D. Faddeev, Teor. Mat. Fiz. **1**, 3 (1969).
17. Nguyen Suan Han and V. N. Pervushin, Mod. Phys. Lett. A **2**, 367 (1987).
18. N. P. Ilieva, Nguyen Suan Han, and V. N. Pervushin, Yad. Fiz. **45**, 1169 (1987) [Sov. J. Nucl. Phys. **45**, 725 (1987)].
19. Yu. L. Kalinovskiĭ *et al.*, Yad. Fiz. **49**, 1709 (1989) [Sov. J. Nucl. Phys. **49**, 1059 (1989)].
20. V. N. Pervushin, Nucl. Phys. B (Proc. Suppl.) **15**, 197 (1990).
21. R. Feynman, Phys. Rev. **76**, 769 (1949).
22. L. Faddeev and V. Popov, Phys. Lett. B **25B**, 29 (1967).
23. R. Akhoury, J.-H. Jun, and A. S. Goldhaber, Phys. Rev. D **21**, 454 (1980).
24. V. N. Gribov, Nucl. Phys. B **139**, 1 (1978).
25. V. N. Pervushin, Teor. Mat. Fiz. **45**, 394 (1980) [Theor. Math. Phys. **45**, 1100 (1981)].
26. V. N. Pervushin, Riv. Nuovo Cimento **8** (10), 1 (1985).
27. D. Blaschke, V. Pervushin, and G. Röpke, in *Proceedings of International Seminar "Physical Variables in Gauge Theories," Dubna, 1999*, Ed. by A. Khvedelidze, M. Lavelle, D. McMullan, and V. Pervushin, E2-2000-172, JINR (Dubna, 2000), p. 49; hep-th/0006249.
28. S. Coleman, Ann. Phys. (N. Y.) **93**, 267 (1975).
29. N. P. Ilieva and V. N. Pervushin, Yad. Fiz. **39**, 1011 (1984) [Sov. J. Nucl. Phys. **39**, 638 (1984)].
30. S. Gogilidze, N. Ilieva, and V. Pervushin, Int. J. Mod. Phys. A **14**, 3531 (1999).
31. S. G. Matinyan and G. K. Savvidy, Nucl. Phys. B **134**, 539 (1978).
32. A. A. Vladimirov and D. V. Shirkov, Usp. Fiz. Nauk **129**, 407 (1979) [Sov. Phys. Usp. **22**, 860 (1979)].
33. T. T. Wu and C. N. Yang, Phys. Rev. D **12**, 3845 (1975).

34. A. A. Bogolubskaya, Yu. L. Kalinovsky, W. Kallies, and V. N. Pervushin, Acta Phys. Pol. B **21**, 139 (1990).
35. Yu. L. Kalinovsky, W. Kallies, L. Münhow, *et al.*, Few-Body Systems **10**, 87 (1991).
36. V. N. Pervushin, Yu. L. Kalinovsky, W. Kallies, and N. A. Sarikov, Fortschr. Phys. **38**, 333 (1990).
37. V. N. Pervushin and Nguyen Suan Han, Can. J. Phys. **69**, 684 (1991).
38. G. Veneziano, Nucl. Phys. B **159**, 213 (1979).
39. D. Blaschke *et al.*, Phys. Lett. B **397**, 129 (1997).
40. W. Kummer, Nuovo Cimento **31**, 219 (1964); G. C. Wick, Phys. Rev. **96**, 1124 (1954); R. E. Cutkosky, Phys. Rev. **96**, 1135 (1954).

Translated by A. Isaakyan